

24th INTERNATIONAL MULTIDISCIPLINARY SCIENTIFIC GEOCONFERENCE - SGEM 2024

01 – 07 July 2024 - Albena, Bulgaria

CONFERENCE PROCEEDINGS OF SELECTED PAPERS in

NANO, BIO, GREEN & SPACE – TECHNOLOGIES FOR A SUSTAINABLE FUTURE

ISSUE 6.1

DISCLAIMER

The **International Multidisciplinary Scientific GeoConference SGEM (Survey, Geology, Ecology, and Management)** serves as a global platform for pioneering research and scientific dialogue across the diverse fields of geosciences. It is dedicated to advancing interdisciplinary solutions for the most pressing environmental challenges of our time — **Global Warming, Climate Change, CO_2 Reduction, Biodiversity Conservation, and the Development of Green Technologies**. By fostering a collaborative exchange of knowledge and **aligning its objectives** with the **United Nations Sustainable Development Goals (SDGs), SGEM aims to inspire scientific excellence and drive sustainable practices toward a greener, more resilient future for our planet.**

Authors are responsible for the content and accuracy of the written papers. Opinions expressed are not meant to represent or reflect the position of the SGEM International Scientific Committee members.

No part of this book may be reproduced or transmitted in any form or by any means, electronic or mechanical, for any purpose, without the express written permission of the SGEM International Scientific Committee on Earth and Planetary Sciences.

Copyright © SGEM WORLD SCIENCE (SWS) Scholarly Society 2024
Haidingergasse 1, C / 1113, Vienna 1030, Austria
Published by STEF92 Technology
Total print: 5000

E-mail: **sgem@sgem.org** | URL: **www.sgem.org**

ISBN 978-619-7603-74-3
ISSN 1314-2704
DOI: 10.5593/sgem2024/6.1

FOREWORD

Dear Readers,

We are honored to present the sixth issue of **the 24th volume of the SGEM GeoConference 2024 Conference Proceedings**, which brings together cutting-edge research **in Micro and Nano Technologies, Advances in Biotechnologies, Green Building Technologies and Materials, Green Design and Sustainable Architecture, and Space Technologies and Planetary Science**. These sections highlight the synergy between innovation and sustainability, providing comprehensive insights into some of the most dynamic fields of science and technology today.

A Vision for Sustainable Innovation

This collection of papers is a testament to the global commitment to sustainable development through technological advancement. From groundbreaking research in **nanomaterials** and **biotechnology** applications to **innovative approaches in green construction and space exploration, the studies featured here reflect a holistic approach to solving the world's pressing challenges.**

Issue Highlights

- Micro and Nano Technologies: This section delves into **advancements in nanostructured materials, nanofertilizers, and nanoscale sensors**, showcasing their potential to revolutionize industries such as agriculture, healthcare, and manufacturing.
- **Advances in Biotechnologies**: Highlighting the intersection of biology and technology, this section covers research on antimicrobial agents, fermentation techniques, and bio-based innovations aimed at **enhancing environmental and human health**.
- **Green Building Technologies and Materials**: Researchers present innovative solutions for sustainable construction, including **eco-friendly materials, energy-efficient systems**, and fire-resistant building technologies.
- **Green Design and Sustainable Architecture**: This section emphasizes the integration of green design principles and digital technologies in modern architecture, fostering **urban sustainability and resilience**.
- **Space Technologies and Planetary Sciences**: Bridging Earth and space, this section explores planetary exploration, space weather analysis, and **sustainable practices for lunar and satellite missions**.

Responding to Global Challenges

The research in this edition aligns with the United Nations Sustainable Development Goals (SDGs), including **SDG 9 (Industry, Innovation, and Infrastructure), SDG 11 (Sustainable Cities and Communities), and SDG 13 (Climate Action)**. These contributions pave the way for transformative solutions that address global challenges such as climate change, urbanization, and resource scarcity.

Peer Review and Scientific Excellence

Every paper in this volume has undergone a rigorous **peer-review process, ensuring the highest standards of scientific quality and relevance**. The **diversity of topics** and

international collaboration reflect the conference's commitment to fostering a multidisciplinary and inclusive research environment.

Towards a Sustainable Future
As technology continues to shape our world, this volume serves as a valuable resource for researchers, policymakers, and practitioners dedicated to building a more sustainable and innovative future. We hope these proceedings will inspire **continued exploration and innovation across these critical domains.**

On behalf of the SGEM GeoConference community, we extend our deepest gratitude to the authors, reviewers, and organizers for their invaluable contributions to this volume.

Sincerely yours,

Prof. Dr. hab. oec. Baiba Rivza
Editor-in-Chief of XXIV SGEM GeoConference Proceedings
Member of the Presidium of the Latvian Academy of Sciences, LATVIA
President of the Latvian Academy of Agricultural and Forestry Sciences
Vice-chair of the Latvian Council of Higher education
President of Latvian universities professors' association
Expert from the European Academy of Sciences Academic Advisory Board (EASAC)

Prof. DSc. Oleksandr Trofymchuk
Editor-in-Chief of XXIV SGEM GeoConference Proceedings
National Academy of Sciences of Ukraine, UKRAINE

CONFERENCE PROCEEDINGS CONTENTS

MICRO AND NANO TECHNOLOGIES

1. A BIOBASED NANO/MICRO-STRUCTURED MATERIAL FOR MICROORGANISMS' IMMOBILIZATION, Drd. Emanuel Gheorghita Armanu, Dr. Eng. Marius Sebastian Secula, Prof. Dr. Habil. Eng. Nicanor Cimpoesu, Dr. Hermann J. Heipieper, Prof. Dr. Habil. Eng. Irina Volf.....3

2. CLASSIFICATION OF NANOBEARINGS AND MATHEMATICAL FORMULATION OF THEIR OPERATION, Prof. Dr. Alexander Vorobyov, PhD Ress. Kirill Vorobyev, Prof. Dr. Zhamaletdin Mamasaidov, PhD Ress. Alawiyeh Mohamad Ali, Assoc. Prof. Dr. Tatiana Chekushina 11

3. COMPARISON OF SURFACE PLASMON RESONANCE RESPONSES FROM THREE DIFFERENT SENSOR STRUCTURES, Ing. Dominik Jursa, doc. Dr. Ing. Michal Lesňák, Ing. Marek Miskay, doc. RNDr. Barčová Karla, Ph.D. 17

4. DEVELOPMENT OF METAL-POLYMER LAMINATE WITH HIGH MECHANICAL PROPERTIES, Dr. Giorgi Baliashvili, Dr. Sophiko Kvinikadze, Dr. Tamar Iashvili, Davit Tsverava, Aleksandre Vanishvili 25

5. DEVELOPMENT OF RECOMMENDATIONS ON THE APPLICATION OF CORROSION-RESISTANT NANO-CEC FOR HEC WATER PUMPS PROTECTION, PhD Aiman Kemelzhanova, Gulsara Zhamanbayeva, PhD Rustem Atchibayev, PhD Sandugash Kemelzhanova 33

6. CORROSION DISSOLUTION OF AN IMPLANT MADE OF NZ30K ALLOY ALLOYED WITH Ag AND COATED WITH A LAYER OF SILVER IN A MODEL SOLUTION OF THE OSTEOSYNTHESIS PROCESS, Prof. Viktor Greshta, Prof. Oleksii Narivskyi, Assistant Anna Dzhus, Assoc. Prof. Vasyl Vynar, PhD Oleksandr Kuprin 41

7. EFFECT OF ZINC OXIDE NANOPARTICLES AGAINST PHYTOPHTHORA SPP. CAUSING DURIAN DISEASES IN VITRO, Dr. Kanchalar Keeratirawee, Assoc. Prof. Dr. Pornprapa Kongtragoul, Miss Sansanee Pantakan 51

8. EVALUATION AND PREDICTION OF RESISTANCE OF PLATE-LIKE HEAT EXCHANGERS MADE OF 06KhN28MDT ALLOY (ANALOGOUS TO AISI904L STEEL) TO CREVICE CORROSION IN RECYCLED WATER OF ENTERPRISES, Assistant Dzhus A.V., Prof. Dr. Greshta V.L., Prof. Dr. Pulina T.V., Prof. Dr. Snizhnoi G.V. 59

9. POLYLACTIC ACID/ZINC OXIDE NANOSTRUCTURED FIBROUS MATERIAL BY NEEDLELESS ONE SOLVENT ELECTROSPINNING FOR PROTECTION AGAINST TICK-BORNE DISEASES, Liga Rampane, Zane Zelca, Chaima Salmi 69

10. RESEARCH OF THE PROTECTION OF CHILDRENS RESPIRATOTY TRACTS WITH THE AIM OF ESTABLISHING STANDARDS FOR THE PRODUCTION OF CHILDRENS RESPIRATORS USING NANOMATERIALS, Ing. Ruzena Langova, Ing. Melanie Barabasova, doc. Ing. et Ing. Karel Klouda, CSc., Ph.D. 77

11. SIMULATION AND OPTIMIZATION OF EQUIPMENT FOR UNLOADING LONG METAL BARS, Assoc. Prof. Dr. Paul Ciprian Patic, Dr. Gabriela Măntescu.....85

12. IMPACT OF COLLOIDAL PROPERTIES OF PHOSPHORUS-BASED NANOFERTILIZERS IN FOLIAR APPLICATION ON PRODUCTION PARAMETERS, PHYSIOLOGY, AND MINERAL NUTRIENT CONTENT OF SUNFLOWER, Assoc. Prof. Dr. Marek Kolenčík, Asst. Prof. Dr. Dávid Ernst, Assoc. Prof. Dr. Martin Šebesta, PhD Viktor Straka, Assoc. Prof. Dr. Ľuba Ďurišová 95

13. ZINC OXIDE NANOPARTICLES INHIBIT SOME FUNGAL PATHOGENS INFECTION ON DURIAN SEEDLINGS, Assoc. Prof. Dr. Pornprapa Kongtragoul, Miss Sansanee Pantakan 107

ADVANCES IN BIOTECHNOLOGIES

14. AIR QUALITY TRENDS IN LIVESTOCK BARNS, Assist. Prof. Dr. Kristina Dineva, Prof. Dr. Tatiana Atanasova, Dr. Victor Danev.....117

15. ANTIMICROBIAL POTENTIAL OF METHANOLIC AND N-HEXANE EXTRACTS OF VISCUM ALBUM, Assoc. Prof. Dr. Marioara Nicoleta Caraba, Lecturer dr. Ion Valeriu Caraba, Prof. Dr. Gabi Dumitrescu, Prof. dr. Elena Pet, Prof. Dr. Roxana Popescu 125

16. CHEMOMETRIC PROFILE OF WHITE AND RED WINES FROM DIFFERENT AREAS OF ROMANIA, Drd. Petronela Anca Onache, Dr. Alina Florea, Prof. Dr. Dorin Ioan Sumedrea, Prof. Dr. Ovidiu Tița.....133

17. COMPARATIVE STUDY ON PHENOLICS, FLAVONOIDS, TANNINS AND ANTIOXIDANT PROPERTIES OF CALENDULA OFFICINALIS EXTRACTS OBTAINED BY DIFFERENT EXTRACTION TECHNIQUES, Lucia-Florina Popovici, Simona Oancea.....141

18. DEVELOPMENT OF A METHOD FOR PRODUCING A FEED ADDITIVE FROM THE GREEN MASS OF AMARANTH, SvetlanaValerevna Obraztsova, Olga Vladimirovna Bondareva, Dariya Sergeevna Khodasevich, Assistant professor Olga Leonidovna Meshcheryakova, Assistant professor TatiyanaVasilevna Sviridova**,** Professor Olga Sergeevna Korneeva 149

19. EVALUATION OF THE EFFICIENCY AND INTENSITY OF HOMOGENIZATION BY CHANGING THE GEOMETRY OF THE TURBINE IMPELLER BLADES, DSc., University Prof. Igor Korobiichuk, Ph.D., Assoc. Prof. Vladyslav Shybetskyi, Ph.D., Assoc. Prof. Sergii Kostyk, Ph.D., Myroslava Kalinina, Dariia Hunchenko, Zhanna Korobiichuk.....157

20. EVALUATION OF THE PROPERTIES OF YOGURT ENRICHED WITH CRUDE POLYSACCHARIDES OBTAINED FROM DIFFERENT MUSHROOMS, Dr. Oana Popa, Prof. Dr. Ovidiu Tița.....165

21. GLYCEROL-BASED FERMENTATION BY PLANT GROWTH PROMOTING ASPERGILLUS NIGER FOR ITS FURTHER FORMULATION AND APPLICATION IN TOMATO GROWTH, Nikolay Vassilev, Luis García del Moral Garrido, Vanessa Martos Nuñes, Giuseppe Falvo D'Urso Labate, Maria Vassileva.....173

22. RESEARCH ABOUT THE BEST SWEETENERS USED TO DESIGN A FOOD SUPPLEMENT WITH HIGH ANTIOXIDANT POTENTIAL, PhD Constantin Butoi, PhD AlexandraIoana Ionescu.....183

23. STUDY OF PROPERTIES OF GLUCOSE OXIDASE IMMOBILIZED ON MODIFIED WITH CHITOSAN AND SODIUM TRIPOLYPHOSPHATE MAGNETITE, Prof. Dr. Valentina G. Matveeva, Assoc. Prof. Ph.D. Boris B. Tikhonov, Mr. Daniil R. Lisichkin, Prof. Dr. Ajay Sh. Desai, Prof. Dr. J.C.S. dos Santos 191

24. STUDY REGARDING THE BEST SWEETENERS USED IN GREEN-TEA BASED SUPPLEMENTS, PhD. Ress. Alexandra-Ioana Ionescu, PhD. Ress. Constantin Butoi.....199

25. THE INFLUENCE OF APPLE VARIETIES AND THE ENZYMES ROHAPECT PTE-100 AND PECTINASE ON THE OBTAINING OF APPLE JUICES, Denisa Marica (Sopîrlă), Maria Lidia Iancu, Ovidiu Tița3.....207

26. THE POTENTIAL OF OLIVE POMACE BIOCHAR FOR METAL RETENTION, Prof. Dr. Paulo Mourao 215

GREEN BUILDINGS TECHNOLOGIES AND MATERIALS

27. CHARACTERISTIC STUDY OF ARTIFICIAL FLY ASH SAND AS A REPLACEMENT TO NATURAL RIVER SAND FOR MINIMIZING THE ENVIRONMENTAL IMPACT OF SAND MINING, Abhishek Khupsare, Ajay K. Agarwal, Swapnil P. Wanjari 225

28. EVALUATION OF THE INITIAL VOLUME STABILITY OF CURRENT CEMENTS, Dr. Božena Dohnálková, Dr. Jiří Grošek, Tomáš Zavřel, Dr. Theodor Staněk 239

29. FLUOROGRAPHENE-DOPED MAGNESIUM OXYCHLORIDE CEMENT COMPOSITES FOR CONSTRUCTION, Ing. Martina Záleská, Ph.D., prof. Ing. Milena Pavlíková, Ph.D., Ing. Adam Pivák, Ph.D., prof. Ing. Zbyšek Pavlík, Ph.D., prof. Ing. Ondřej Jankovský, Ph.D. 247

30. FUNCTIONALITY OF TWO-COAT SYSTEM FOR CONCRETE PROTECTION AND REPAIR, Prof. Ing. Zbysek Pavlik, Ph.D., Ing. Adam Pivak, Prof. Ing. Milena Pavlikova, Ph.D. 255

31. IMMOBILISATION OF HEAVY METALS IN FLY ASH-DIATOMITE MODIFIED MAGNESIA CEMENT COMPOSITE, Ing. Adam Pivak, prof. Ing. Milena Pavlikova, Ph.D., Ing. Martina Zaleska, Ph.D., assoc. prof. Mgr. Jana Nabelkova, Ph.D., prof. Ing. Zbysek Pavlik, Ph.D. 263

32. IMPROVEMENT OF PHYSIOLOGICAL DATA COLLECTION BY IMPROVING SENSOR ACCURACY BASED ON THE SENSOR LOCATION, PhD Angel Dogeanu 271

33. POLYMERIC COATING FOR THE INSULATION, PROTECTION AND SURFACES FINISHING OF THE REINFORCED BUILDINGS CONCRETE EXPOSED TO CORROSIVE ENVIRONMENTS, Prof. dr. ing. hab. Ion Rusu, Senior Lecturer dr. chem. Loredana Judele, Assoc. prof. dr. ing. hab. Daniel Lepadatu 279

34. RETROREFLECTIVE GUARDRAIL BEAMS TO IMPROVE TRAFFIC SAFETY, Dr. Jiří Grošek, Dr. Michal Janků, Jakub Motl, Leo Jeniš 287

35. SOLID RESIDUES FROM THE COBUSTION OF BIOMASS – HEAVY METALS CONTAMINATION AND POSSIBLE REUSE, Prof. Ing. Milena Pavlíková, Ph.D., Ing. Martina Záleská, Ph.D., Assoc. Prof. Mgr. Jana Nábělková, Ph.D., Ing. Adam Pivák, Prof. Ing. Zbyšek Pavlík, Ph.D. 295

36. STUDY OF REACTION TO FIRE IN HYBRID_BASED CORE INSULATORS INTENDED FOR THE OF VACUUM INSULATION PANELS, Prof. Ing. Jiří Zach, Ph.D., Ing. Petra Zachová, Ing. Jitka Peterková, Ph.D., Ing. Vítězslav Novák, Ph.D., Bc. Jindřich Havelka 303

37. SUSTAINABILITY ANALYSIS OF COPPER SLAG AND REPLACEMENT FOR CONCRETE, María José Pérez Verbal, Marcos Diaz González, Andrés Gabriel César Torres, Dr. Mauricio Pradena-Mique 311

38. THE ASSESSMENT OF STRENGTH PROPERTIES OF HISTORICAL MORTARS FOR SUSTAINABLE RENOVATIONS, Eng. Jaroslav Pokorný, Ph.D., Doc. Eng. Jan Fořt, Ph.D., Eng. Lenka Scheinherrová, Ph.D., Eng. Tomáš Navara, Eng. David Javorský 319

39. THE EFFECT OF DIFFERENT DEGRADATION ENVIRONMENTS ON CHLORIDE CONTENT AND CARBONATION IN CONCRETE, Dipl. Eng. et Dipl. Eng. Kristýna Hrabová, Ph.D., Dipl. Eng. Dita Vořechovská, Ph.D., Dipl. Eng. Tomáš Mazán, Dipl. Eng. Dominik Lisztwan, Dipl. Eng. Dalibor Kocáb, Ph.D., Prof., RNDr. Pavla Rovnaníková, CSc., Assoc. Prof., Dipl. Eng. Petr Konečný, Ph.D. 325

40. UNSTEADY STATE THERMAL ANALYSIS OF GLULAMINATED TIMBER ELEMENTS SUBJECTED TO FIRE, Lecturer Dr. Ing. Ruxandra Erbașu, Assist. Dr. Ing. Ioana Teodorescu, PhD Ress. Andrei Sabău, Lecturer Dr. Ing. Daniela Țăpuși 333

GREEN DESIGN AND SUSTAINABLE ARCHITECTURE

41. BIM APLICATIONS IN THE DESIGN OF DEEP FOUNDATIONS FOR WIND TURBINES, Bogdan Chelaru, Cătălin Onuțu, Adrian Alexandru Șerbănoiu 343

42. BIM STRATEGY, IMPLEMENTATION AND EXPECTATIONS IN EDUCATIONAL PROGRAM, Lect. Dr. Marina Lute, Lect.Dr. Luminita Fekete-Nagy 351

43. DIGITAL TWIN OF BRATISLAVA CITY FOR ESTIMATION OF SUSTAINABLE ENERGY PRODUCTION AND UTILIZATION, Ing. arch. March. Roman Hajtmanek, PhD. Univ. Assoc. Prof., Mgr. art. Martin Uhrík, PhD. Assoc. Prof., Ing. arch. Vladimír Hain, PhD. Univ. Assoc. Prof., Ing. arch. Alexander Kupko 357

44. THE EFFECTIVENESS OF THE RECONSTRUCTION OF HISTORIC COUNTRY HOUSES, Ing. Arch. Jaroslava Rolínková.....365

45. EVOLUTION AND DISTRIBUTION OF GREEN COVER AND ITS INFLUENCE ON URBAN PLANNING, THE CASE OF THE HISTORIC CENTRE OF LOJA, ECUADOR, Assoc. Prof. Valarezo-Jaramillo Sandra, Assoc. Prof. Aguirre-Maldonado Eduardo, Assoc. Prof. Dr. Balcázar-Arciniega Cristian, Assoc. Prof. Alvarado-Rodríguez Lorena 373

46. ILHA DE MOÇAMBIQUE AND ITS BUFFER ZONE – PROPOSAL FOR A LANDSCAPE STRUCTURE, Assist. Prof. Dr. Rute Sousa Matos, Assist. Prof. Dr. Paula Simões, Assist. Prof. Dr. Desidério Batista 381

47. INFLUENCE OF A FACADE BASED ON GABIONS AND PLANTS ON THE INDOOR AIR TEMPERATURE IN A TROPICAL CLIMATE OF THE AMAZON REGION, PhD. Balcázar- Arciniega, Cristian, Arq. Román- Vargas, Patricio, Assoc. Prof. Aguirre- Maldonado, Eduardo, Assoc. Prof. Valarezo- Jaramillo, Sandra, Assoc. Prof. Alvarado- Rodríguez, Lorena 389

48. MARGINAL CONDITIONS FOR MEASURING THE LIGHT TRANSMISSION OF WINDOWS, Ing. Dagmar Richtrová, Doc. Ing. Lenka Prokopová, Ph.D, Doc. Ing. Daniela Bošová, Ph.D. 397

49. NATURE A CONSTANT INSPIRATION FOR HUMAN BEINGS – AESTHETIC CHANGES IN ARCHITECTURE OVER THE CENTURIES, M. Eng. Arch. Ewa Kuhnert, ...403

50. THE METHODOLOGY OF TECHNICAL DUE DILIGENCE FOR THE REHABILITATION OF AN ABANDONED BUILDING, Bogdan Chelaru, Cătălin Onuțu, Adrian Alexandru Șerbănoiu 409

51. VALORIZATION OF THE LANDSCAPE THROUGH THE APPLICATION OF MODERN ENERGY SOLUTIONS FOR THE CONSTRUCTION OF GREEN BUILDINGS AND THE DEVELOPMENT OF GREEN ARCHITECTURE, Assoc. Prof. Dr. Metodi Ivanov.....417

SPACE TECHNOLOGIES AND PLANETARY SCIENCES

52. A SCIENTIFIC AND ENGINEERING APPROACH FOR PLANETARY LAVA TUBES EXPLORATION, Homero Aguilar Diaz, Gustavo Jamanca-Lino, Yury Vasquez Charcape, Daniel Suarez Zelada 429

53. ANALYSIS OF GEOMAGNETIC DATABASES IMPACTING SPACE WEATHER, Dr. Laurentiu Asimopolos, Dr. Natalia-Silvia Asimopolos, Dr. Vijdea Anca-Marina, Dinu Luminita, Assist. Prof. Adrian-Aristide Asimopolos.....441

54. EXPENDITURE OPTIMAL CONTROL FOR A SATELLITE MOVING CLOSE TO THE LIBRATION POINT, Prof. DSc. L. K. Babadzanjanz, Assoc. Prof. Dr. I. Yu. Pototskaya, Assoc. Prof. Dr. Yu. Yu. Pupysheva, Assoc. Prof. Dr. V. S. Korolev 451

55. LANDSLIDE SUSCEPTIBILITY MAPPING IN LUNAR SOUTH POLE RIGION, Andrea Ermini, Assoc. Prof. Riccardo Salvini, Full Prof. Pier Simone Marrocchesi 459

56. PROSPECT AND PROVOCATION OF SUSTAINABLE LUNAR ACTIVITIES, Dr. eng. cosm. Dumitru-Dorin Prunariu, Prof. dr. eng. habil. Ildiko Tulbure 467

57. SUSTAINABLE AEROSPACE PROPULSION: THE SPINLOOP ROTARY ACCELERATOR WITH MAGNETIC LEVITATION FOR LOW EARTH ORBIT VEHICLE DEPLOYMENT, Piotr Mamczura, Dawid Pekala 471

SECTION

MICRO AND NANO TECHNOLOGIES

A BIOBASED NANO/MICRO-STRUCTURED MATERIAL FOR MICROORGANISMS' IMMOBILIZATION

Drd. Emanuel Gheorghita Armanu[1]

Dr. Eng. Marius Sebastian Secula[1]

Prof. Dr. Habil. Eng. Nicanor Cimpoesu[2]

Dr. Hermann J. Heipieper[3]

Prof. Dr. Habil. Eng. Irina Volf[1]

[1]"Gheorghe Asachi" Technical University of Iasi, Faculty of Chemical Engineering and Environmental Protection "Cristofor Simionescu", **Romania**
[2]"Gheorghe Asachi" Technical University of Iasi, Faculty of Materials Science and Engineering, **Romania**
[3]Helmholtz Centre for Environmental Research (UFZ), Department of Molecular Environmental Biotechnology, **Germany**

ABSTRACT

Microbial immobilization is a promising strategy for various applications, including environmental remediation and bioprocess engineering. However, the efficacy of immobilization largely depends on the characteristics of the carriers. Biomass wastes are renewable and abundant resources that can be subjected to hydrothermal carbonization (HTC) for hydrochar production, a resulting carbonaceous material with a porous structure. This porous architecture offers extensive surface area and facilitates the colonization and growth of microorganisms, working as a protective buffer zone in highly polluted environments. This study points out the development of a novel biobased nano/micro-structured material for microorganism immobilization, integrating locally available feedstock for thermochemical conversion processes. To tailor a bio-based porous material suitable for bacterial immobilization, the biomass waste was processed through HTC. The influence of main HTC parameters on biomass conversion was established. Chemical, structural, and thermochemical analyses, encompassing proximate and ultimate analysis, Fourier Transform Infrared Spectroscopy (FTIR), Scanning Electron Microscopy (SEM), Chemical Composition Analyzer (EDS) and Thermogravimetric analysis (TGA), were conducted on both the feedstock and resulting hydrochar. SEM analyses revealed the nano/micro-structured morphology of the hydrochar, characterized by a wide distribution of pores ranging from nano to micrometer scale. A bacterial strain of *Pseudomonas* sp. was immobilized on hydrochar in order to evaluate the bacterial cell proliferation, their capacity and rate of forming stable colonies on the support material. The hydrochar obtained from locally biomass feedstocks represents an eco-friendly and sustainable biobased nano/micro-structured material, with promising applications in bioremediation and bioprocess engineering, thereby advancing green technologies and circular bioeconomy initiatives.

Keywords: wheat straws, porous structure, bacterial immobilization, biofilm, sustainable technologies

https://doi.org/10.5593/sgem2024/6.1/s24.01

INTRODUCTION

Hazardous compounds resulted from plastic industry (e.g. plasticizers, polychlorinated biphenyls), mining industry (e.g., hydrochloric acids, sulphuric acid, cyanide, mercury), agriculture (e.g., insecticides, herbicides, fungicides), construction sites and unproper waste management (e.g. agriculture, silviculture) generate a long-lasting impact on the environment [1]. Nevertheless, significant amounts of agricultural wastes (1 billion tons) are produced annually worldwide and disposed unproperly. This agricultural feedstock could be used to develop value added materials (such as hydrochars) with an immediate impact towards a circular bioeconomy [2]. Bioremediation of affected environmental factors could be achieved using this available feedstock, converted through a thermochemical process. A good candidate of such feedstock is represented by wheat straws (WS) [3].

The biomass conversion is strongly dependent on the thermal process applied (pyrolysis or hydrothermal carbonization) [4]. In order to choose the proper thermal conversion, the energy input and the value/quality of the obtained products have to be considered. Pyrolysis is an intensive energy consumer process commonly used to generate biooil as well as biochar. A cost-efficient path, the hydrothermal carbonization (HTC) is an emerging technique for converting raw (wet) biomass under autonomous pressure, resulting in a valuable rich material (hydrocar). The hydrochar structure can be tailored based on the main parameters of HTC conversion: (i) temperatures: (ii) solid-to-liquid ratio, and (iii) residence time [5], [6]. Thus, a porous structure suitable for bacterial immobilization can be achieved. A suitable candidate for immobilization, *Pseudomonas* sp. strain is a nonpathogenic bacterium with a metabolic plasticity and adaptation flexibility, ubiquitously met in water bodies and soil [7], [8].

The hydrochar structure improves the *Pseudomonas* sp. biofilm formation and consequently leads to higher tolerance and pollutant efficiency degradation.

This study addresses the thermochemical conversion of WS biomass to obtain a nano/micro porous structure suitable for bacterial immobilization. For this goal, the main parameters (temperature, w/v ratio, and residence time) of HTC process are investigated and optimized. The most favorable hydrochar structure is further used for *Pseudomonas* sp. immobilization. Also, the assessment of the immobilization process was carried out to reveal the interaction between the HTC carrier and biofilm colonies.

MATERIALS AND METHODS

Wheat straws (WS) biomass was obtained from the annual field harvesting of wheat, from hilly, unpolluted area in North-East of Romania. The straws were dried, grinded with a lab mill (Grindomix GM200), and placed in a sealed box for future analyses. WS thermochemical conversion was carried in a stainless-steel micro pressure reactor (model KQSA-250 ML, 10 MPa, 450°C). For each experiment the glass vessel (used to mix the raw material and deionized water) was placed in the micro reactor and set the operating parameters. For each HTC carbonization 10 g of WS and 100 mL deionized water were added. After the experimental run the reactor is stopped and let to cool down till 0 MPa. The obtained hydrochar is filtered (filter paper 150 mm) and dried in an oven at 105°C for 24 h.

Pseudomonas sp. used in the present study originates from a private collection from Leipzig, Germany. Many of these strains come from soil samples and belong to private collection and are publicly on the BacDive database (free access).

This bacterium is characterized by the rod shape, one or multiple flagella and non-pathogenic activity. Pseudomonas sp. was cultivated in mineral media with succinate as sole carbon source, according to Hartmans et al. [9] the bacterial cells were grown in 100 ml Erlenmeyer, under shaking, at 30°C. Then, 1mL of bacterial biomass was transferred in a 50 mL Erlenmeyer that contains 10 mL mineral media and 50 mg hydrochar, placed for 24 hours incubation at 30°C and shaking (150 rpm). Afterwards, the material is filtered and dried at 30°C for 24 hours, and followingly weighed.

To observe the biofilm adhesion on the hydrochar surface, Scanning Electron Microscopy (SEM) was carried with VegaTescan LMH II, SE detector, 30 and 8 kV, high vacuum, VegaTc software (aperture size 2 mm O.D. x 0.1 mm, magnification 23x, speed 3, stigmator 0.1%, WD 31.9 mm). Before SEM analysis, the immobilized *Pseudomonas* sp. on hydrochar was coated with 7 nm gold, using a Luxor coating device). Images were taken at 200, 100 and 20 μm with 30 kV acceleration voltage in vacuum environment. SEM equipped is also equipped with a Bruker detector (XFlash QUANTAX) sensor that can measure the energy dispersive X-ray spectroscopy (EDS) allowing the surface analysis of the non-immobilized hydrochar and map some trendlines of elemental composition [10].

For modeling and optimizing the hydrothermal conversion process, a face centered (α = 1) central composite design was generated using Design Expert software (State-Ease Inc., Minneapolis, MN, USA, Version 7.1.5). The suggested mathematical models contain only the statistically significant factors in agreement to ANOVA analysis.

RESULTS

The raw WS considered in the present study was physical-chemically characterized. The proximate analysis pointed out a moisture content of 7.4%, ash, 4%, while extractables are of 5.1%. As regard the main components, WS presents a hemicellulose and cellulose contents of 38.2 and 33.8%, respectively. A significantly lower content of 18.9% lignin is common to annual plants [11].

The independent variables and their range of variations were considered based on prior work of our team [12]: temperature (220-260°C) and time (30-60 min) as shown in Table 1. The coefficients of the models were kept based on a confidence level higher than 95%. The suitability of proposed models was evaluated by means of the coefficient of determination and the adjusted R^2 coefficient.

The effects of the two factors on the considered responses were assessed based on ANOVA for a confidence interval of 95%. The plot as residuals versus predicted data, Fig. 1a, outlines the consistent variation throughout the prediction range, revealing a random scatter of predicted residuals. The models' adequacy was determined by means of normal probability plot of residuals. Further diagnostic plots of internally studentized residuals point out the values align on a straight line, whereas residuals vs predicted form no trends as shown in Figure 1.

https://doi.org/10.5593/sgem2024/6.1/s24.01

Table 1. Experimental matrix design and values of the independent variables and responses

Run	A	B	Temperature (°C)	Time (min)	Response 1 (R1) Mass yield (%)	Response 2 (R2) Conversion degree (%)
1	1	1	260	60	33.56	66.44
2	0	1	240	60	38.78	61.22
3	-1	0	220	45	48.61	51.39
4	0	0	240	45	37.73	62.27
5	-1	-1	220	30	48.38	51.62
6	0	-1	240	30	36.62	63.38
7	1	0	260	45	31.94	68.06
8	0	0	240	45	37.74	63.26
9	-1	1	220	60	47.88	52.12
10	1	-1	260	30	31.66	68.34

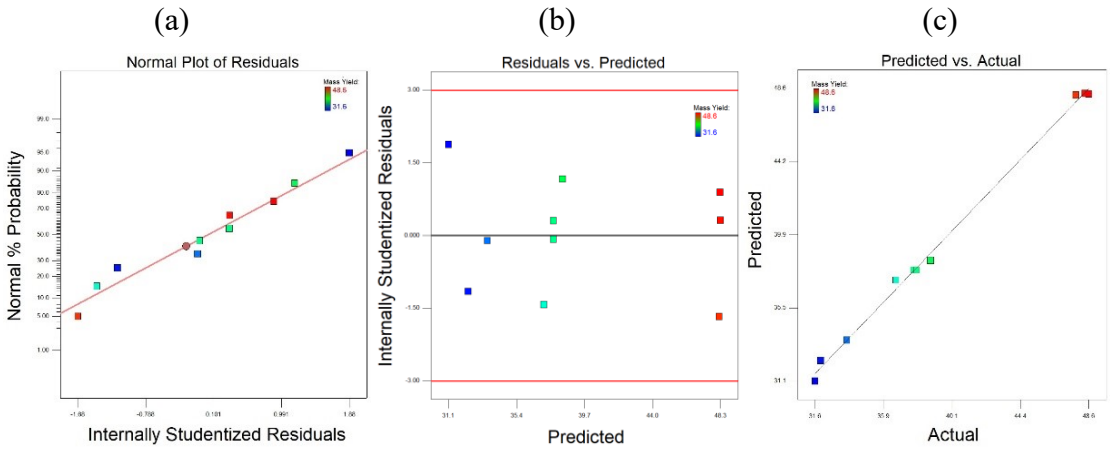


Figure 1. (a) Normal probability plot of residuals for Mass Yield. (b) Plot of residuals versus predicted values for Mass Yield. (c) Plot of residuals versus experimental values of Mass Yield.

In figure 2 shows the effects of the two factors and that of the interaction between temperature and time on the mass yield response.

The models obtained can be expressed in actual factors as:

$$MY = 523 - 3.56\ Temperature - 0.463\ Time + 0.00212\ Temperature\ Time + 6.4\ 10^{-3}\ A^2 - 6.67\ 10^{-5}\ B^2 \quad (1)$$

$$CD = -460 + 3.56\ Temperature + 0.562\ Time - 0.00212\ Temperature\ Time - 7.02\ 10^{-3}\ A^2 - 1.04\ 10^{-3}\ B^2 \quad (2)$$

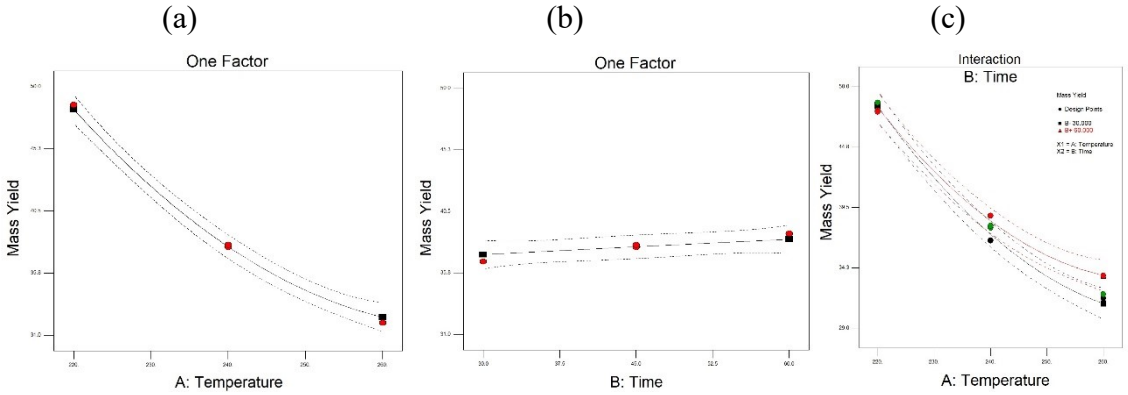


Figure 2. Plots of mass yield as a function of (a) temperature (45 min); (b) time (240 °C); (c) interaction temperature-time

Figure 3 presents the response surface of mass yield and desirability surface plot as a function of the two investigated factors.

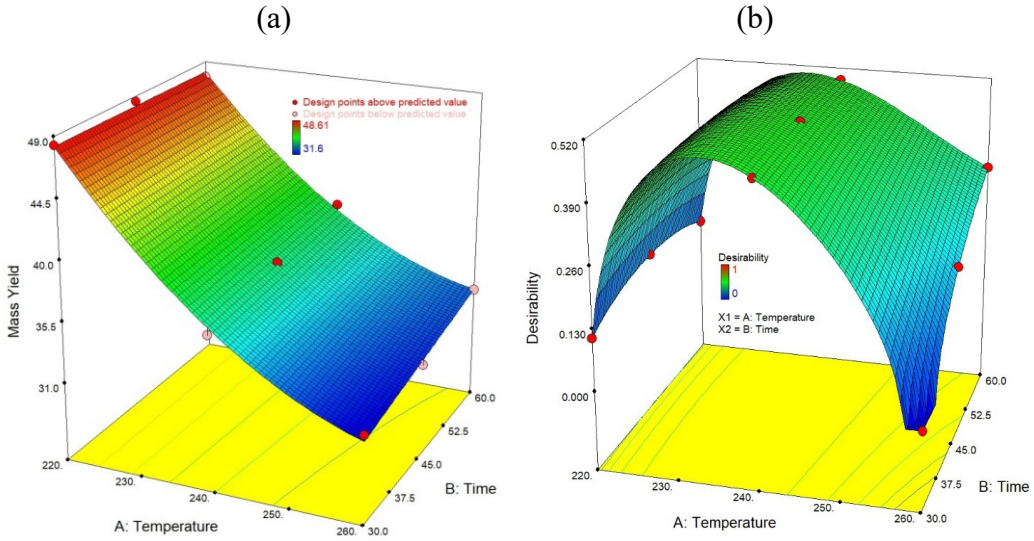


Figure 3. (a) Response surface plot and (b) desirability surface plot of mass yield as a function of temperature and time

Based on the suggested models, the optimal conditions of HTC process were established, a desirability function of 0.512, a mass yield of 40.2%, a conversion degree of 60.2% corresponding to a temperature of 234 °C and 45.2 min of HTC.
Hydrothermal carbonization (HTC) of WS was carried out in a stainless-steel autoclave at 260°C, 30 min, and 1:10 w/v ratio.

Figure 4 shows SEM images obtained for WS raw biomass (Fig. 4a), WS hydrochar (Fig. 4b), and immobilized hydrochar (Fig. 4c).

https://doi.org/10.5593/sgem2024/6.1/s24.01

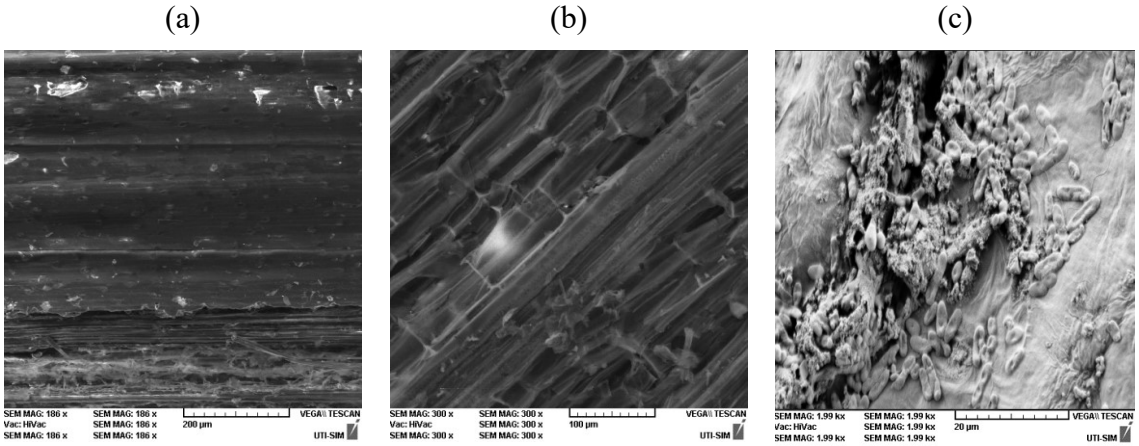


Figure 4. SEM images of the (a) raw biomass of wheat straws, (b) hydrochar obtained at 260°C, 30 min, 1:10 w/v ratio from WS and (c) immobilized *Pseudomonas* sp. on the hydrochar

SEM-EDS measurements identified Carbon as the major compound with 61,83 % and other elements such as Oxygen (37.96%), Hydrogen (5.2%), Potassium (0.17%), Silicon (0.03%) and traces of Copper (0.00096%).

DISCUSSION

The ANOVA analysis points out that the model obtained is significant, with the F value of 265. Also, the determination coefficient is very high, 0.997, indicating the suggested model fits the experimental data.

As shown in Fig. 2, the mass yield decreases (the conversion degree decreases) strongly with temperature, and slightly increases in time, the interaction pinpointing that the time factor influence is stronger at higher values of temperature.

Response surface shown in Fig. 3a pinpoints the effect of residence time increase significantly at 240 °C, being strongest at the highest investigated level of temperature. Meanwhile, the desirability surface shows a maximum at a 40.2% mass yield/60.2% conversion degree, obtained at 234 °C and 45.2 min of HTC. The obtained optimal parameters were validated experimentally.

As showed in Fig. 4a, the raw material has a compact lamellar structure, a typical morphology for a light material, characterized by a high content of cellulose and hemicellulose, and a relatively lower lignin concentration [13]. This structure presents no capacity for biofilm adhesions due to the lamellar morphology. SEM-EDS analysis show that carbon was found as a major compound but also S, K, Si, O and traces of Cu as shown in Results section.

HTC process has the potential to break down the cellulosic long polymeric chain resulting in micro structures of honeycomb shapes. This scaffold is a suitable support for bacterial immobilization. *Pseudomonas* sp.

After the thermochemical conversion, the hemicellulose and cellulose structures start to break down at 125 °C and 200°C, respectively resulting in micropores, thus enhancing the specific surface and consequently the biofilm adhesion (Fig. 4b). The obtained

hydrochar is a carbon-rich material and together with microelements (e.g., Ca, S, Zn, Fe) favors the biofilm formation and survivability in high polluted environments.

In order to perform the immobilization, a stock culture of *Pseudomonas* sp. strain was prepared in a Hartmans mineral media having an optical bacteria density of 0.74 cells/mL, under shaking (150 rpm), at 30°C. In mixture with hydrochar, the cell suspension was then attached on the surface forming stable biofilms as showed in Fig. 4c. At 20 μm field view, long (4 μm), rod shapes bacteria were noticed. The presence of flagella confirmed the strain genus. Its motility helps the bacteria to migrate (chemotaxis) and find a source of nutrients for the replication process. The biofilm is disposed on the hydrocarbon surface in so called "hotspots" with most abundance of carbon (C found along the linear sides of the pores). Bacterial cells size is around 0.5 μm up to 3-4 μm (with the flagellum).

CONCLUSION

This study demonstrates that hydrothermally converted WS biomass is a suitable nano/micro-structured carrier for *Pseudomonas* strains immobilization.

A face centered composite design was established for modeling and optimization of the hydrothermal process of WSs. An optimal mass yield of 40.2%, a conversion degree of 60.2% were obtained at a temperature of 234 °C and 45.2 min of HTC.

The process carried out under optimal conditions leads to a hydrochar where carbon was identified as major element, together with some other microelements such as C, S, K, Si, O, and traces of Cu. Aforementioned elements could provide a source of nutrients for bacterial biofilm formation in nutrient-depleted environments.

Pores suitable for bacterial biofilm colonization were observed by SEM analysis. Bacterial cells were visible at 20 μm field view, presenting rod shape morphology and a length of maximum 4 μm, including single/multiple polar oriented flagella. The bacterial cells display preferential biofilm formation in higher C and Si locations.

The SEM-EDS analyses confirm the structural porosity and compositional characteristics of the hydrochar, suggesting its suitability for immobilization and use in various biotechnological applications.

ACKNOWLEDGEMENTS

This work was supported by a grant from the Ministry of Research, Innovation and Digitization, CNCS-UEFISCDI, project number PN-III-P4-PCE-2021-1455, (118/2022) within PNCDI III.

REFERENCES

[1] Modupe S. A., Olubukola O. B., Bioremediation of environmental wastes: the role of microorganisms, Front. Agron., Sec. Plant-Soil Interactions, South Africa, Volume 5, 2023;

[2] Singh P., Singh V. K., Singh R., Borthakur A., Madhav S., Ahamad A., Kumar A., Pal D. B., Tiwary D., Mishra P. K., Chapter 1 - Bioremediation: a sustainable approach for management of environmental contaminants, Abatement of Environmental Pollutants, Elsevier, India, Pages 1-23, 2020;

https://doi.org/10.5593/sgem2024/6.1/s24.01

[3] Armanu G. E., Volf I., Natural carriers for bacterial immobilization used in bioremediation, Bulletin of Polytechnic Institute of Iasi, Chemistry and Chemical Engineering section, Romania, Issue 68 (72), vol. 3, pp 109-122, 2022;

[4] Jain A., Balasubramanian R., Srinivasan M. P., Hydrothermal Conversion of Biomass Waste to Activated Carbon with High Porosity: A Review, Chemical Engineering Journal, Singapore, 283, 2016;

[5] Barbato A. Robyn and Reynolds C. Mike, "22 - Bioremediation of contaminated soils", Principles and Applications of Soil Microbiology (Third Edition), Elsevier, United States, Pages 607-631, 2021;

[6] Bejenari I., Hristea G., Cărăușu C., Mija A., Volf I., A Sustainable Approach on Spruce Bark Waste Valorization through Hydrothermal Conversion, Processes, Romania, vol. 10, pp 111, 2022;

[7] Eberlein C., Baumgarten T., Starke S., Heipieper J. H., Immediate response mechanisms of Gram-negative solvent-tolerant bacteria to cope with environmental stress: cis-trans isomerization of unsaturated fatty acids and outer membrane vesicle secretion, Applied Microbiology and Biotechnology, Germany, vol. 102, pp 2583–2593, 2018;

[8] Heipieper H. J., Diefenbach R., Keweloh H Conversion of cis unsaturated fatty acids to trans, a possible mechanism for the protection of phenol-degrading Pseudomonas putida P8 from substrate toxicity, Appl Environ Microbiol, Germany, vol. 58(6), pp 1847-1852, 1992;

[9] Hartmans S., Smits J. P., van der Werf M. J., Volkering F., de Bont J. A., Metabolism of Styrene Oxide and 2-Phenylethanol in the Styrene-Degrading Xanthobacter Strain 124X, Appl Environ Microbiol., The Netherlands, 1989;

[10] Cimpoeşu N., Trincă L. C., Dascălu G., Stanciu S., Gurlui S. O., Mareci D., Electrochemical Characterization of a New Biodegradable FeMnSi Alloy Coated with Hydroxyapatite-Zirconia by PLD Technique, Journal of Chemistry, Romania, 2016;

[11] Zhang L., Larsson A., Moldin A., Edlund U., Comparison of lignin distribution, structure, and morphology in wheat straw and wood, Industrial Crops and Products, Volume 187, Part B, Swedem, 2022;

[12] Pătrăuțanu O. A., Ciupercă O. T., Popa V. I., Volf I., Contributions on Spruce Bark Polyphenols Identification Using Instrumental (UV-VIS Spectrometry), Qualitative (Thin Layer Chromatography) and Quantitative (HPTLC Densitometry) Methods, REV. CHIM. (Bucharest), Romania, 71, pp 1, 2020;

[13] Sharma I., Bioremediation Techniques for Polluted Environment: Concept, Advantages, Limitations, and Prospects, Trace Metals in the Environment - New Approaches and Recent Advances. IntechOpen, India, 2021.

CLASSIFICATION OF NANOBEARINGS AND MATHEMATICAL FORMULATION OF THEIR OPERATION

Prof. Dr. Alexander Vorobyov [1]

PhD Ress. Kirill Vorobyev [2]

Prof. Dr. Zhamaletdin Mamasaidov [3]

PhD Ress. Alawiyeh Mohamad Ali [2]

Assoc. Prof. Dr. Tatiana Chekushina[2]

[1] Grozny State Petroleum Technical University, **Russian Federation**
[2] RUDN University, **Russian Federation**
[3] Ferghana Institute of Public Health, **Uzbekistan**

ABSTRACT

Nanomechanical systems necessitate components with unparalleled precision and minimal frictional resistance to achieve optimal performance. Nanobearings represent a critical class of components that facilitate rotational or linear motion at the nanoscale. This paper presents a comprehensive classification of nanobearings, encompassing their structural attributes, materials employed, and operational mechanisms. Additionally, it provides a detailed mathematical formulation that describes the static and dynamic behavior of nanobearings, including equations for load capacity, friction torque/force, and stiffness. Numerical examples illustrate the application of these mathematical models in analyzing the performance of diverse nanobearing types. The findings provide invaluable insights for designing and optimizing nanobearing-based devices utilized in a wide range of applications spanning precision engineering, microfluidics, and biomedical engineering domains.

This expanded version delves deeper into the significance of nanobearings in nanomechanical systems and highlights the crucial role they play in enabling precise and low-friction motion at the nanoscale. It also emphasizes the importance of the mathematical formulation presented in understanding and predicting the behavior of nanobearings, which is essential for designing and optimizing nanobearing-based devices for various applications.

Keywords: nanoparticles, natural nanobearings, gravitational forces, electromagnetic forces, mass transport

INTRODUCTION

Nanotechnology is becoming an increasingly important and promising area in modern science and technology. They make it possible to create devices and materials at the micro- and nanoscale that have unique properties and abilities. One of the key aspects of nanotechnology is the development of nano-sized bearings, which play an important

https://doi.org/10.5593/sgem2024/6.1/s24.02

role in various technical devices and mechanisms. The classification of nanobearings and their mathematical description are of great importance for optimizing and improving technical systems at the nanoscale.

There are several types of nanobearings, which differ in operating principles, materials from which they are made, and sizes. One common type of nanobearing is ball bearing. They consist of nanoballs that rotate inside a nanoring, providing smooth movement and minimal friction.

Another type of nanobearings are roller bearings, which are nanorollers rotating around a nanoring. This type of bearing is widely used in precision applications where high precision and reliability are required.

In addition, there are planar nanobearings that provide linear motion at the nanoscale. They are widely used in nanorobots, nanodetectors and other devices that require precise positioning and motion control.

A mathematical description of the operation of nanobearings makes it possible to predict and optimize their characteristics, such as friction force, rotation speed and wear resistance. Simulations and analysis of mathematical equations help engineers and scientists design more efficient and durable nanobearings for a variety of engineering applications.

MATERIALS AND METHODS

The main research method was differential calculus, which is a branch of mathematical analysis that studies the concepts of derivative and differential and how to apply them to the study of various functions. The available mathematical apparatus allows us to extract a wide range of data during the study, including data on position, speed and force, angular velocity, momentum and kinetic energy arising from the rotation of nanobearings during the movement of landslide geomass.

In this case, the mathematical apparatus is understood not only as formal calculus, developed in accordance with the existing rules of mathematical operation, but also as individual fragments of the theory used.

The connection of these fragments is carried out by referring to theoretical schemes, which makes it possible to correct the transformations of mathematical equations of the accepted formalism.

RESULTS

Types of natural nanobearings. Several types of bearings are involved in the actual movement of landslide geomass - rotation and sliding nanotubes, nanospheres and “liquid” bearings (nanofluids).

Moreover, all known types of nanotubes have different unit cell parameters, as well as different wall-to-wall distances (10-12 nm) and chirality angles for their inner and outer walls.

Operation of nanotubes rotation. The rather weak interactions in multiwalled nanotubes, formed from at least two cylinders, allow the cylinders to slide or rotate within each other, acting as linear or rotational bearings.

Natural nanotubes (60-120 nm long, with an interwall distance of 0.34 nm), which in some way represent natural (natural) nanobearings, are very interesting objects that perform the work of moving the geomass of landslides, since their structure consists of shells nested inside each other, with a subnanometer distance between them and without any pronounced physicochemical bonds, which ensures relatively easy movement, with a fairly low friction value.

To study the characteristics of the relative rotation of the walls of nanotubes, it is necessary to calculate how the value of the interaction energy changes in the coordinate system describing their relative position.

Initially, mathematical modeling was carried out to study the rotational motion of concentric double-walled nanotubes.

By calculation, the value of the energy of wall-to-wall interaction of nanotubes was established, which ranges from 20 to 35 meV per atom for different types of nanotubes, as well as the values of the static and dynamic shear moduli, equal to 0.04 and 0.05 MPa, respectively.

In this case, the basic partial differential equation for a uniform rotating nanotube was obtained taking into account the existing non-local scale effects, and the variable coefficient for the centrifugal term was replaced by the maximum centrifugal force. As a result, the general problem of studying the parameters of a rotating nanotube was transformed into a more local case when it is subjected to only an axial force.

In the course of further research, the dependence of the resistance force (friction) on the size of nanotubes was revealed, which increases with increasing their length or radius, which is determined by a change in the contact area.

Thus, friction in a natural nanobearing depends linearly on the rotation speed, length and radius of the nanotubes and increases with decreasing distance between the nanotubes. Friction also depends linearly on temperature.

DISCUSSION

When moving the landslide geomass, the nanotubes act as translational bearings, implementing the translational sliding mode, in which the nanotube shells slide parallel to the axis, relative to each other.

The frictional force generated during such sliding is caused by the van der Waals interaction (which was calculated based on the measured geometry of the nanotubes and ranges from 0.5 to 20 nN, depending on the diameter of the moving wall) between adjacent sliding shells and is the derivative of the energy with respect to the sliding distance and is directly proportional to the existing contact area. Therefore, in such a bearing, in addition to the van der Waals force, both static and dynamic friction forces act, proportional to the contact area.

During the experimental work, it was found that the force required to continue the movement of such nanobearings decreases in proportion to the length of the overlapping

https://doi.org/10.5593/sgem2024/6.1/s24.02

contact area to a certain constant value at zero overlap area. This is clearly consistent with the assumption of area-dependent frictional forces plus the manifestation of a constant van der Waals force.

Their linear approximation makes it possible to qualitatively and quantitatively estimate the value of these constant forces, and the friction value obtained by theoretical calculations is so small that it cannot be detected by existing instruments. It was found that the rotational force was significantly lower than the linear sliding force.

Operation of nanoball bearings. Ball nanobearings are more efficient when moving landslide geomass, which is due to their unlimited degrees of freedom.

Operation of “liquid” nanobearings. In addition, when moving the geomass of a landslide, so-called “liquid” nanobearings, which are nanofluids with very low friction values, operate.

Moreover, for almost all types of nanobearings it is necessary to take into account the amplitude with which the resistance force changes, which correlates with the conversion of rotational motion into phonons, which leads to a possible loss of energy in the form of heat. Thus, friction is the rate of energy dissipation divided by the speed of movement of the nanoparticle.

Numerous experiments show that surfaces that come into contact with water or any other liquid with a high dielectric constant tend to develop a surface charge.

Using a zero mean square wave electromagnetic field, nanoparticles move through potential barriers along gentle slopes without net fluid flow. The speed of such movement is characterized by the dependence of the distance between charged particles and the underlying surface, and their maximum speed of movement is up to 50 μm/s.

Moreover, when nanoparticles move, they naturally choose predominantly areas with fewer restrictions.

CONCLUSION

The classification of nanobearings represents a significant advancement in the field of nanoengineering and tribology, offering a new frontier for applications across various industries. This article systematically categorizes nanobearings based on materials, structure, and operational principles, emphasizing the diverse mechanisms that underpin their performance. Various types, including carbon-based nanobearings, polymeric nanobearings, and metal-based nanobearings, each have unique properties that make them suitable for specific applications, from microelectronics to biomedical devices.

Mathematical formulations presented in this article provide a fundamental understanding of the operational mechanisms of nanobearings. These equations establish relationships between critical parameters such as load capacity, friction, wear, and lifespan, allowing for predictive modeling of nanobearing behavior under different operational conditions. The integration of classical mechanics with quantum effects highlights the necessity for a multidisciplinary approach in designing and optimizing nanobearing systems.

The insights gained from this classification and mathematical modeling pave the way for future research aimed at enhancing the performance and reliability of nanobearings.

Understanding the intricacies of nano-scaled interactions will enable engineers to develop more efficient designs, ultimately leading to innovations in technology that utilize these components. Future work should focus on experimental validation of the mathematical models, as well as exploring new materials and designs to push the boundaries of existing capabilities. The continuous evolution of nanobearings promises to play a crucial role in advancing technology, with implications that extend far beyond their immediate applications.

ACKNOWLEDGEMENTS

The study was supported by a grant from the Russian Science Foundation № 23-27-00444, https://rscf.ru/project/23-27-00444/, 2023.

REFERENCES

[1] Vorobyov A.E., Vorobyev K.A. Nanodiamonds. Monograph – Moscow: Mir nauki, 2018. – 161 p., ISBN 978-5-6041426-4-6.

[2] Martínez-Rodríguez R. A. Vidal-Iglesias F. J. Solla-Gullón J. Cabrera C. R. Juan M. F. Synthesis of Pt nanoparticles in water-in-oil microemulsion: effect of HCl on their surface structure J Am Chem Soc. 2014 136 4 1280 1283 . DOI: 10.1021/ja411939d

[3] Vorobyov A.E., Vorobyev K.A., Dzhumagaliev N.I. Nanodiamonds of petroleum origin // "Ecology and the oil and gas complex": Collection of materials of the International scientific and practical Conference. Atyrau: Atyrau University of Oil and Gas, 2018. pp. 272-274.

[4] Mai T. N. Lianlian D. Tetsu Y. Control of nanoparticles synthesized via vacuum sputter deposition onto liquids: a review Soft Matter 2022 18 19 47 . DOI: 10.1039/D1SM01002F

[5] Gahlawat G. Chaudhary A. R. A review on the biosynthesis of metal and metal salt nanoparticles by microbes RSC Adv. 2019 9 23 12944 12967 . DOI: 10.1039/C8RA10483B [6] Vorobyov A.E., Kozhogulov K.C., Karimov E.M. Zher koch kulordun talaa izildoolor (Field studies of landslides) // Izvestiya Osh Technological University (Kyrgyzstan). 2023. No. 2-1. pp. 214-221, ISSN: 1694-660X.

[7] Vorobyov A.E., Kozhogulova G.K. Possibilities and conditions of formation of nanoparticles in rock mass // Gorny vestnik of Uzbekistan, No. 1 (92). 2023. pp. 71-76, ISSN 2181-7383, DOI: 10.54073/gv.2022.1.92.015.

[8] Vorobyov A.E., Kozhogulova G.K. Identification of the basic mechanisms and main features of the movement of landslide geomass // Gorny vestnik of Uzbekistan, No. 3(90). 2022. pp. 20-26, ISSN 2181-7383, DOI: 10.54073/gv.2022.3.90.004.

[9] Charitidis C. A. Georgiou P. Koklioti M. A. Trompeta A-F. Markakis V. Manufacturing nanomaterials: from research to industry Manuf Rev. 2014 1 11 . DOI: 10.1051/mfreview/201400

[10] Vorobyov A.E., Kozhogulova G.K. Investigation of rapid and extended clay landslides // Proceedings of the National Academy of Sciences of the Kyrgyz Republic. No. 2. 2022. pp. 32-41, ISSN 0002-3221.

https://doi.org/10.5593/sgem2024/6.1/s24.02

[11] Jiang T. Wang X. Zhou J. Chen D. Zhao Z. Hydrothermal synthesis of Ag@MSiO2@Ag three core–shell nanoparticles and their sensitive and stable SERS properties Nanoscale. 2016 8 9 4908 4914 . DOI: 10.1039/C6NR00006A

[12] Pan A. Wu H. B. Yu L. Lou X. W. Template-free synthesis of VO2 hollow microspheres with various interiors and their conversion into V2O5 for Lithium-Ion batteries Angew Chem. 2013 125 8 2282 2286 . DOI: 10.1002/anie.201209535

[13] Bruno E. Strano V. Mirabella S. Donato N. Leonardo S. G. Neri G. Comparison of the Sensing Properties of ZnO nanowalls-based sensors toward low concentrations of CO and NO2 Chemosensors. 2017 5 3 20 . DOI: 10.3390/chemosensors5030020

[14] Kumar N. Reddy L. Parashar V. Ngilla J. C. Controlled synthesis of microsheets of ZnAl layered double hydroxides hexagonal nanoplates for efficient removal of Cr(VI) ions and anionic dye from water J Environ Chem Eng. 2017 5 2 1718 1731 . DOI: 10.1016/j.jece.2017.03.014

[15] Prost, J.; Cihak-Bayr, U.; Neacșu, I.A.; Grundtner, R.; Pirker, F.; Vorlaufer, G. Semi-Supervised Classification of the State of Operation in Self-Lubricating Journal Bearings Using a Random Forest Classifier. Lubricants 2021, 9, 50. https://doi.org/10.3390/lubricants9050050

COMPARISON OF SURFACE PLASMON RESONANCE RESPONSES FROM THREE DIFFERENT SENSOR STRUCTURES

Ing. Dominik Jursa[2]

doc. Dr. Ing. Michal Lesňák[1,2]

Ing. Marek Miskay[2]

doc. RNDr. Barčová Karla, Ph.D. [2]

[1] Nanotechnology Centre, VŠB - Technical University of Ostrava, **Czech Republic**
[2] Faculty of Safety Engineering, VŠB -Technical University of Ostrava, **Czech Republic**

ABSTRACT

This study presents a theoretical and experimental investigation of three distinct surface plasmon resonance (SPR) sensor configurations, evaluating their sensitivity and practical applications. The first configuration utilizes a commercially available SPR sensor, employing a coupling prism integrated with a thin gold layer in the well-established Kretschmann-Raether configuration for SPR excitation. The second configuration features an advanced design, incorporating a coupling prism combined with an optical multilayer structure and an additional magneto-optical layer, aimed at enhancing the sensor's response to magnetic fields and potentially broadening its application scope. The third configuration is a variation of the second, maintaining the optical multilayer but omitting the magneto-optical layer to assess its impact on sensor performance. Experimental results reveal that the third configuration exhibits the highest sensitivity among the three, making it a promising candidate for applications requiring precise detection capabilities.

Keywords: surface plasmon resonance (SPR), biochip, sensitivity

INTRODUCTION

Conventional surface plasmon resonance (SPR) optical sensors lack the high sensitivity required for applications like detecting chemical and biological compounds, studying biomolecular interactions, or medical diagnostics for pharmacological treatment. Researchers have proposed an SPR sensor with a gold grating on a silicon wafer [1] where the coupled SPR excites free electrons on the gold surface. This allows detection as a current signal by a Schottky barrier diode formed at the gold/silicon interface. Another novel design is an SPR temperature sensor using a depressed double cladding fiber (DDCF), theoretically proposed and experimentally demonstrated in [2]. Experimental results showed this 50-nm gold-coated DDCF-SPR sensor achieved an exceptionally high sensitivity of 7002 nm/RIU (refractive index unit). These designs aim to significantly enhance the performance of SPR sensors compared to conventional optical methods.

A novel fiber-optic temperature sensing system was proposed and demonstrated in [3]. It is based on surface plasmon resonance (SPR) and integrated with a smart-phone platform. Experimental results showed the sensor could achieve a measurement resolution of 0.83°C over the range of 30 to 70°C, corresponding to a high linear correlation coefficient of 0.9798. Researchers reported a phase SPR sensing technology

https://doi.org/10.5593/sgem2024/6.1/s24.03

using white light polarized interference in a common-path geometry configuration in [4]. Experimental demonstrations revealed this system had an exceptional sensitivity of 1.3 x 10^{-7} RIU (refractive index units) and a broad dynamic detection range of 0.029 RIU. These innovative SPR sensor designs leverage advanced fiber-optics, smart devices, phase detection methods, and common-path interferometry. This allows ultra-high resolution and sensitivity for temperature monitoring and refractive index sensing applications across multiple fields. The smart-phone integration also provides a portable, user-friendly platform ideal for field deployment of the sensors.

Researchers proposed and investigated a sensitivity-enhanced surface plasmon resonance (SPR) sensor with molybdenum diselenide ($MoSe_2$) as a modifying overlayer in [5]. The sensor is constructed by physically depositing $MoSe_2$ onto the surface of a conventional Kretschmann configuration SPR sensor. Experimentally, the highest achieved sensitivity was 2524.8 nm/RIU, which required two deposition cycles of the $MoSe_2$ overlayer. In [6], a D-shaped plastic optical fiber (D-POF) SPR biosensor was proposed and demonstrated for detecting DNA hybridization. It is based on a graphene/gold (G/Au) film structure. Compared to other plastic optical fiber experiments, this sensor exhibited improved sensitivity, reaching a calculated value of 1227 nm/RIU over a range of glucose solution concentrations. These designs utilize advanced 2D materials like $MoSe_2$ and graphene as surface overlayers to enhance SPR sensor performance. The $MoSe_2$ overlayer enabled exceptionally high 2524.8 nm/RIU sensitivity, while the G/Au film structure improved D-POF sensitivity to 1227 nm/RIU. Such hybrid material strategies coupled with optimized sensor configurations unlock new levels of sensitivity for biomolecular detection and other sensing applications.

Researchers have proposed using III-V semiconductor materials for far-infrared and terahertz plasmonic applications [7]. The surface plasmon properties of semiconductors in the THz range resemble those of noble metals in the visible and near-infrared, while being tunable by doping or applied magnetic fields. This opens new opportunities for engineered plasmonics and sensing in the THz regime. In [8], a plasmonic sensor design based on heavily doped silicon and a metallic grating structure was analyzed for operation in the mid-infrared region. Numerical results showed the reflection spectrum of a phosphorus-doped silicon grating with heavily doped silicon exhibits a sharp asymmetric Fano resonance dip. This dip is highly sensitive to changes in the surrounding refractive index. The proposed sensor displayed exceptional projected sensitivities - 8000 nm/RIU in air or 950 nm/RIU in water media. These values are remarkably high compared to existing mid-infrared plasmonic sensor devices. Leveraging highly doped semiconductor materials allows achieving ultra-high refractive index sensitivities not possible with traditional plasmonic materials like metals. Overall, these works highlight the emerging potential of engineered semiconductor plasmonics from terahertz to mid-infrared frequencies for developing extremely sensitive biochemical sensors and other applications benefiting from dynamic optical properties.

The magneto-optical permittivity tensor spectra of undoped, n-doped, and p-doped indium antimonide (InSb) crystals were determined using terahertz time-domain spectroscopy and Fourier transform far-infrared spectroscopy. A remarkably large polar magneto-optical (MO) Kerr effect, with rotation up to 20 degrees, accompanied by simultaneous plasmonic behavior, was experimentally observed at room temperature under a relatively low magnetic field of 0.4 T [9].

SPR SAMPLES

(a) A commercial SPR sensor using a coupling prism (SF-10) with one side coated with a 44-nm gold layer for the Kretschmann-Raether configuration. This is referred to as the "Au only" sample.

(b) A combined structure consisting of a coupling prism, a photonic crystal (PC), a magneto-optic layer, and a gold (Au) layer, as illustrated in Figure 1. The PC is implemented by alternating thin films of Ta_2O_5 and SiO_2 ($[Ta_2O_5/SiO_2]_4/Ta_2O_5$). The film parameters used in the modeling were determined by the sample preparation technology: [Ta_2O_5: 127 nm/SiO_2: 136 nm]4/[Ta_2O_5: 97 nm]. The induced anisotropy film (Fe layer) had a thickness of 8 nm, and the Au film that generates plasmonic phenomena had a thickness of 19 nm (Fig. 1). This structure is designated as "PC + Fe + Au."

(c) A structure similar to (b) but without the magneto-optic (Fe) layer. The film parameters used in the modeling were: [Ta_2O_5: 160 nm/SiO2: 70 nm]4/[Ta_2O_5: 75 nm]. The thickness of the gold film in this case was 44 nm. This structure is designated as "PC + Au."

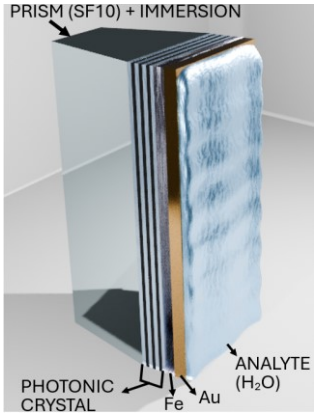


Fig. 1: Geometry of the sensor samples described in the text
(b) – [Ta_2O_5:127 nm/ SiO_2:136 nm]4 / Ta_2O_5: 97 nm/ Fe: 8 nm/ Au: 19 nm
(c) – as (b) without the Fe film, and, with a multilayer of [Ta_2O_5:160 nm/ SiO_2:70 nm]4 / Ta_2O_5: 75 nm/ Au: 44 nm

In our comparative tests, sample a) was a standard commercial sensor used in typical SPR experimental systems. Samples b) and c) were prepared using the vacuum electron beam evaporation technique. The coating system employed was the SYRUSpro 710 by Bühler (formerly Leybold Optics). This system is equipped with a plasma ion source (manufacturer's name APSpro) and is capable of plasma ion-assisted deposition (PIAD), where argon ions enhance the deposition process. The kinetic energy of the ions is transferred to the evaporated coating material atoms, resulting in more compact, less porous structures with higher refractive indices compared to those prepared by the standard electron beam evaporation technique.

The substrates were mechanically cleaned and placed into the coating system. Prior to the actual deposition process, the plasma cone from the APSpro was used to clean and prepare the surface of each sample. The deposition process was monitored using a quartz crystal monitor. The deposition rates were set to 0.2 nm/s for Ta_2O_5 and 0.4 nm/s for SiO_2.

https://doi.org/10.5593/sgem2024/6.1/s24.03

THEORY

Numerical results were obtained using a matrix formulation of the Rigorous Coupled-Wave Analysis (RCWA) implemented in a MATLAB code. The incidence angle step $\Delta\varphi = 0.001°$ refers to the prism/PC interface. The optical parameters of isotropic materials at the wavelength of 633 nm were as follows: refractive index of SF10 glass ng = 1.7231, gold nAu = 0.1838 - 3.4310i [11], tantalum pentoxide nTa = 2.1358 [14], silica oxide nSi = 1.457 [12], iron film nFe = 2.87 - 3.46i, and Voigt parameter of iron QFe = 0.0386 + 0.0034i [10]. In the theoretical treatment, several effects were considered that affect the reflection properties of the SPR sensor samples.

(A) Ta_2O_5/ SiO_2 multilayer

An angle reflectivity dependency of the structure [Ta_2O_5:160 nm/ SiO_2:70 nm]4 / Ta_2O_5: 75 nm/ Au: 44 nm on the angle of an incident wave was analyzed for the p-polarization. This was a sample of the sensor (c) (the magneto-optic film not present). Water was used as an analyte. Results are shown in Figure 2.

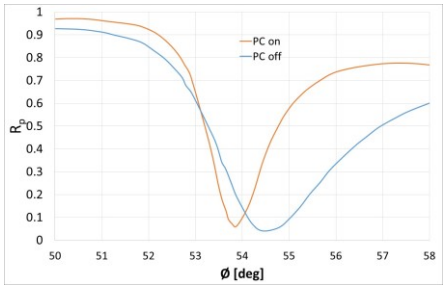


Fig. 2: Reflectance versus angle of incidence of structures (a), (c) for p-polarization
Solid line – complete structure with photonic crystal with four double layers [Ta_2O_5:160 nm/ SiO_2: 72 nm]$_4$ (PC on) Dashed line – structure without photonic crystal (PC off)

It is seen in Figure 2 that the resonance minimum is distinctly narrower in the presence of a quadruple double layer. Experimentally it points to a more accurate determination of the minimum itself that, in turn, leads to an increase in sensitivity of the structure.

(B) Standard SPR structure

In order to evaluate how the studied effects (surface plasmon resonance, multilayers, magneto-optic film) affect the overall sensor's response, the reflectivity dependence of a standard SPR structure, (a) above, on the refractive index changes of an analyte was simulated for p-polarization. The result is shown in Figure 3.ΔR_p angle of incidence [deg]

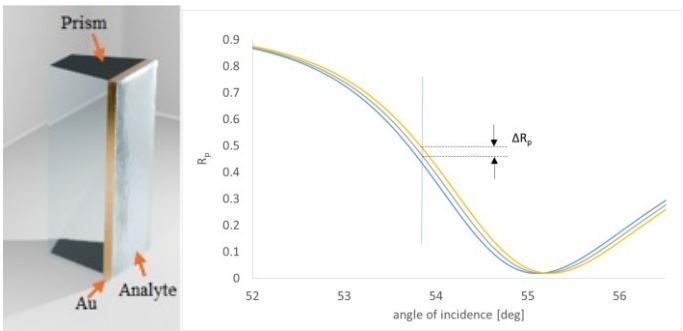


Fig. 3: SPR's reflectance versus analyte refractive index changes (1.331-1.335, step 0.001 RIU)

Figure 3 shows changes in the reflectivity due to changes in the analyte refractive index for p-polarization at different incident angles. One can see that for a fixed incident angle the structure sensitivity limit can be determined depending on, for example, substance concentration in the analyte.

(C) Magneto-optic effect

The linear magneto-optic effect for the [Ta_2O_5:127 nm/ SiO_2: 136 nm]$_4$ / Ta_2O_5: 97 nm /Fe: 8 nm / Au: 19 nm structure was modelled in the transversal configuration whereby TE and TM polarizations can be studied separately [13]. The external magnetic field strength was chosen such that sample saturation was reached in this configuration. Opposite polarity of the electric source for magnetic coils was used to produce antiparallel direction of the magnetization vector in the Fe layer. Signs + and – below indicate the reflectivity R_p for p-polarization of a planar structure with induced anisotropy at one or the other direction of the external magnetic field (antiparallel configuration, transversal geometry).

Breaking reciprocity of the reflectivity response due to a polarity change of an external magnetic field leads to a shift of the reflectance minima of the p-polarized optical beam at an incidence angle at which SPR is excited. This effect can be studied with the help of a response function

$$\rho(\phi) = \frac{R_p^+ - R_p^-}{R_p^+ + R_p^-}\ , \qquad (1)$$

where ϕ is the incidence angle. Superscript signs denote the orientation of the external magnetic field. The response quality is measured by a factor $F = |\rho_{max}| + |\rho_{min}|$ changing from 0 to 2 along with the shift $\Delta\phi_0$ which is the point where $\rho = 0$.

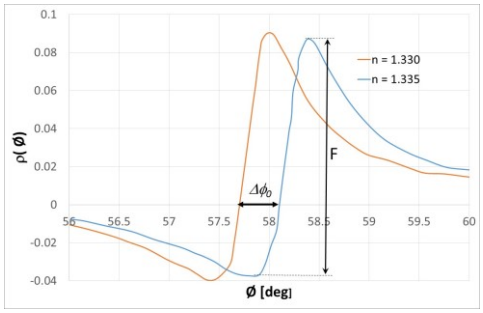


Fig. 4: Parameter ρ versus incident angle in vicinity of resonance for two values of analyte refractive index

Figure 4 shows a dependence of the parameter ρ, found from Eq. (1), on the incidence angle of a laser beam, impinging on the prism contact plane, around the resonance state. Both opposite orientations of an external magnetic field are plotted for the transversal configuration. The figure also illustrates modulation of the recorded shift $\Delta\phi_0$ due to a change in the analyte refractive index.

The analysis of this magneto-optic structure demonstrates an important fact that the Fe film thickness strongly controls sensing performance. Noticeable changes in reflectivity characteristics occur even with Fe film changes on the order of 1 nm. Drastic modulation of sensitivity extremes and shifts of resonance location were observed [14]. The main motivation for applying a modelling approach was an ability to determine

https://doi.org/10.5593/sgem2024/6.1/s24.03

responses of individual analyzed structures as they depend on the concentration of ethyl alcohol in water, and to compare their respective sensitivities. The modelling analysis of above mentioned structures yielded the following limit sensitivities (ethyl alcohol concentration in water): system „Au only“ - 0.110 %, structure „PC + Fe + Au“ – 0.136 %, sample „PC + Au“ – 0.067 %. In order to determine the ethyl alcohol concentration in water with an accuracy of a tenth of a percent, it was necessary to be able to measure changes in the reflectivity ΔR_p to a thousandth, which means obtaining $\Delta R_{p,min} = 0.001$ (see Fig. 3).

EXPERIMENT

The samples were prepared using SF-10 coupling prisms, onto which structures (b) and (c) were implemented. The coupling prisms and their geometries were selected to match the coupling prism in the J-Y Horiba SPRi-Lab+ measurement system. This approach enabled us to utilize the professional J-Y Horiba system for testing our individual prism sensors. In the measurement system, a polarized laser beam is incident on a computer-controlled mirror that varies the incidence angle on the sample base using software algorithms. The reflected light is detected by a CCD camera, and the resulting signal is processed by the SPRi-View software. Figure 5 summarizes the experimental results, showing the responses of all individual sensor samples as a function of changes in the analyte (ethyl alcohol concentration in water).

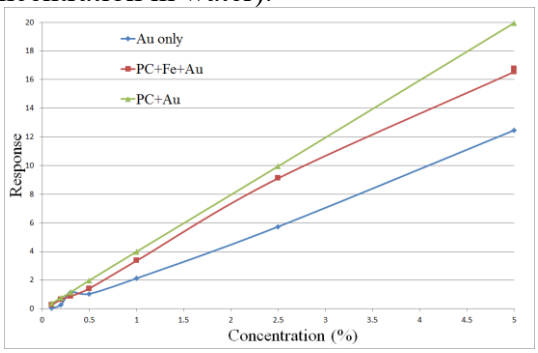


Fig. 5: Sensitivities of different sensor structures versus concentration of ethyl alcohol in water

The results show that the highest sensitivity was achieved with the "PC + Au" structure. Similar sensitivity parameters were obtained with the "PC + Fe + Au" system. The lowest sensitivity was displayed by the standard arrangement consisting of a coupling prism with a gold film for the Kretschmann-Raether configuration.

DISCUSSION

Based on the theoretical analysis and experimental results, the following conclusions can be drawn:

(i) The application of more layers (in this case, four double layers of $[Ta_2O_5/SiO_2]_4$) yields a clear enhancement of the resonance, resulting in a distinctly narrower resonance minimum. This leads to an increase in ΔRp (Fig. 3).

(ii) Experiments showed that the "PC + Fe + Au" structure exhibited slightly lower sensitivity compared to the "PC + Au" system. However, two aspects should be noted. The theoretical analysis revealed an extreme sensitivity to changes in the Fe layer, whereby variations in the Fe film thickness on the order of 1 nm strongly modulate the reflectivity dependence on the analyte. On the other hand, structures with a magneto-optic layer offer the possibility to incorporate a triggering signal into the detecting light.

This is achieved by changing the orientation of the external magnetic field in the transversal configuration (as in our study). This enables lock-in detection.
(iii) The response of all studied structures showed a linear behavior up to ethyl alcohol concentrations of 5%.
(iv) The structure with a magneto-optic layer exhibited an angle shift of 0.36° for its reflectance minimum, which corresponded to an analyte refractive index change of 0.005 (from na1 = 1.330 to na2 = 1.335). Considering the experimental precision limit in measuring this angle, one can determine the smallest detectable analyte refractive index changes as 0.0001, along with the corresponding concentrations of a material in solutions.
(v) If we consider variants (a) and (c) that work directly with the reflection response versus the concentration dependence, a relation between the modeled and measured data cannot be immediately established, because the experimental data in Figure 5 are not scaled as reflectance. However, the linearity of both dependencies (see Fig. 6) enables a comparison of the enhancement in resolution ability. Denoting w0 and wPC as the responses in the "PC off" and "PC on" cases, respectively, the resolution increase (in percent) can be expressed as:

$$\eta = \frac{w_{PC} - w_0}{w_0}.100 \quad [\%] \qquad (2).$$

The obtained results, namely η = 62.5 % for the model and η = 60.1 % in the laboratory test, show a very good agreement.

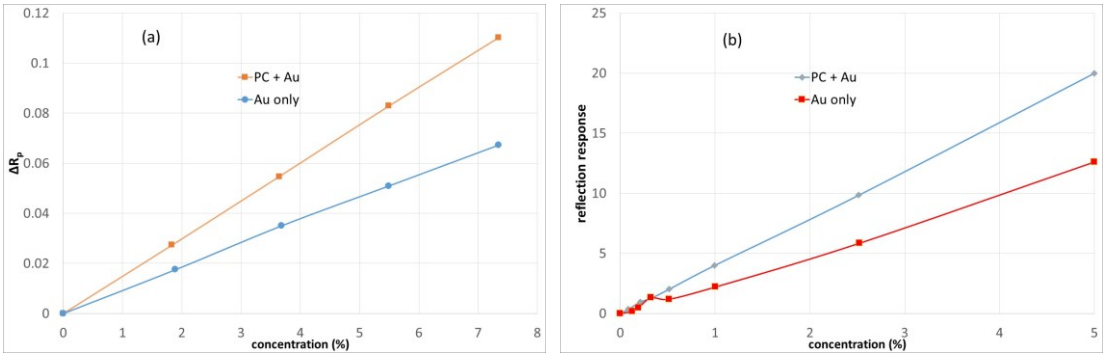


Fig. 6: Comparison of reflection response: (a) numerical model, (b) experimental data.

CONCLUSIONS

The study showed that the use of a larger number of layers in the form of a photonic crystal ($[Ta_2O_5/SiO_2]_4$) leads to a significant enhancement of the resonance effect and a narrower resonance minimum, increasing the detection sensitivity. The "PC + Au" structure exhibited the highest sensitivity, while the addition of an iron magneto-optic layer ("PC + Fe + Au") led to a slight decrease in sensitivity. However, theoretical analysis revealed an extreme sensitivity to changes in the iron layer thickness on the order of 1 nm. Furthermore, the magneto-optic layer allows the incorporation of a triggering signal for lock-in detection. The responses of all structures were linear up to 5% ethyl alcohol concentration. Using the magneto-optic structure, it was possible to detect changes in the analyte refractive index of 0.0001. A comparison of the modeled and experimental data showed very good agreement in the enhancement of detection resolution ability by 60-62.5% with the use of the photonic crystal.

https://doi.org/10.5593/sgem2024/6.1/s24.03

ACKNOWLEDGEMENTS

The authors would like to acknowledge support from the Faculty of Safety Engineering, VSB – Technical University of Ostrava for project SP2023/063.

REFERENCES

[1] Y. Saito, Y. Yamamoto, T. Kan, T. Tsukagoshi, K. Noda, and I. Shimoyama, "Electrical detection SPR sensor with grating coupled backside illumination," Opt. Express 27(13), 17763-17770, 2019.
[2] Z. Yang, J. Xia, S. Li, R. Qi, G. Zuo, and W. Li, "Ultrawide temperature range operation of SPR sensor utilizing a depressed double cladding fiber coated with Au-Polydimethylsiloxane," Opt. Express 28(1), 258-269, 2020.
[3] L. Lu, Z. Jiang, Y. Hu, H. Zhou, G. Liu, Y. Chen, Y. Luo, and Z. Chen, "A portable optical fiber SPR temperature sensor based on a smart-phone," Opt. Express 27(18), 25420-25427, 2019.
[4] Y. Zeng, X. Wang, J. Zhou, R. Miyan, J. Qu, H. Ho, K. Zhou, B. Z. Gao, and Y. Shao,"Phase interrogation SPR sensing based on white light polarized interference for wide dynamic detection range,". Opt. Express 28(3), 3442-3450, 2020.
[5] Y. Luo, S. Hu, H. Wang, Y. Chen, J. Dong, Z. Jiang, X. Xiong, W. Zhu, W. Qiu, H. Lu, H. Guan, Y. Zhong, J. Yu, J. Zhang, and Z. Chen,"Sensitivity-enhanced surface plasmon sensor modified with MoSe2 overlayer,". Opt. Express 26(26), 34250-34258 , 2018.
[6] W. Gong, S. Jiang, Z. Li, C. Li, J. Xu, J. Pan, Y. Huo, B. Man, A. Liu, and C. Zhang,"Experimental and theoretical investigation for surface plasmon resonance biosensor based on graphene/Au film/D-POF," Opt. Express 27(3), 3483-3495, 2019.
[7] J. Chochol, K. Postava, M. Cada, M. Vanwolleghem, M. Micica, L. Halagacka, JF. Lampin, J. Pistora,"Plasmonic behavior of III-V semiconductors in far-infrared and tera-hertz range. JOURNAL OF THE EUROPEAN .
[8] N. Nguyen-Huu, M. Cada, Y. Ma, F. Che, J. Pistora, K. Yasumoto, Y. Ma, J. Lin, H. Maeda,"Mid-infrared Fano resonance in heavily doped silicon and metallic nanostructures due to coupling of Wood-Rayleigh anomaly and surface plasmons," Journal of Physics D-Applied Physics 50, 20, 2017.
[9] J. Chochol, K. Postava, M. Cada, M. Vanwolleghem, L. Halagačka, J. F. Lampin, J. Pištora: Magneto-optical properties of InSb for terahertz applications. AIP ADVANCES 6, 11, 2016.
[10] K. Postava, J. Pištora, T. Yamaguchi: Magneto-optic vector magnetometry for sensor applications. SENSORS AND ACTUATORS A-PHYSICAL 110, 1 – 3, 2004.
[11] P.B. Johnson, R.W. Christy, Optical constants of the noble metals, Phys. Rev. B 6 (12), 5056–5070, 1972.
[12] https://www.filmetrics.com/refractive-index-database/SiO2/Fused-Silica-Silica-Silicon-Dioxide-Thermal-Oxide-ThermalOxide.
[13] K. Postava, J. Pištora, Š. Višňovský: Magneto-optical effects in ultrathin structures at transversal magnetization. Czechoslovak Journal of Physics 49(8), 1185 – 1204, 1999.
[14] P. Otipka, J. Vlček, M. Lesňák, J. Sobota: Design of MO-SPR sensor element with photonic crystal. Photonics and Nanostructures - Fundamentals and Applications 31, 77 – 80, 2018.

DEVELOPMENT OF METAL-POLYMER LAMINATE WITH HIGH MECHANICAL PROPERTIES

Dr. Giorgi Baliashvili[1]

Dr. Sophiko Kvinikadze[1]

Dr. Tamar Iashvili[1]

Davit Tsverava[1-2]

Aleksandre Vanishvili[1]

[1] G. Tsulukidze Mining Institute, Tbilisi, **Georgia**

[2] Georgian Technical University, Tbilisi, **Georgia**

ABSTRACT

Basalt fiber-reinforced metal-polymer composites represent a cutting-edge class of materials that merge the robustness of metal with the pliability of polymer. Originating from natural volcanic rocks, basalt fibers possess remarkable mechanical properties, such as high tensile strength, resistance to extreme temperatures, and chemical inertness. Integrating basalt fibers into a polymer matrix like epoxy or thermoplastic resins significantly boosts the composite's resistance to dynamic impacts and its energy absorption capacity. The metal component ensures structural integrity and strength, while the polymer matrix distributes energy through elastic deformation. Basalt fibers find application across various industries, including aviation, automotive, and military technology.

There are research centers and scientific groups whose work is focused on developing polymer composite materials reinforced with basalt fibers. These metal-polymer composites are especially valuable for their application in an automotive industry, aerospace and construction, due to their high strength to weight ratio, as well as for the ability to absorb impact energy, flexibility in design and chemical resistance.

The objective of this study is to develop a technology for producing basalt fiber-based metal-polymer composites and to investigate the physical and mechanical properties of these materials. Using Vacuum Infusion Process (VIP) technology, metal-polymer composites incorporating basalt fiber were produced. The resulting samples exhibit high bonding strength, uniform polymer distribution within the matrix, and a straightforward manufacturing process. Experimental samples of the metal-polymer composites, produced using VIP technology, were tested under mechanical and dynamic loads.

Keywords: Composites, Metal-polymer laminate, Dynamic loading, Material Characteristics

INTRODUCTION

Composite is a material that is made up of two or more discrete materials combined to achieve desirable properties. Commonly, composite consists of a matrix material and

https://doi.org/10.5593/sgem2024/6.1/s24.04

some kind of reinforcements [1]. Such composite materials include metal-polymer laminates which consist of layers of metal and reinforced fibers, usually bonded together with polymeric matrix (figure 1). They offer a combination of structural strength of metal and flexibility and impact resistance of polymers. Metal-polymer laminates offer several notable advantages over traditional metal structures. By utilizing thin metal layers supported by polymer materials, these laminates achieve lighter structures without compromising strength. Metal-polymer laminates deliver significant weight savings compared to solid metal counterparts. Weight reduction is especially valuable in industries where minimizing weight is crucial [2],[3].

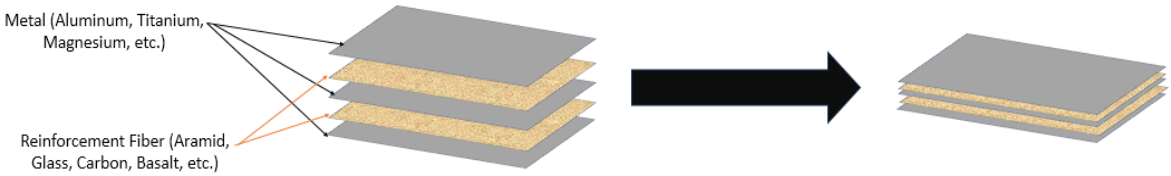


Fig. 1. Schematic presentation of Metal-Polymer laminate composite

Basalt fiber originates from igneous rock that is abundantly found in the Earth's crust. The primary benefit of basalt is its abundance and the simplicity of its mining process, making it comparatively inexpensive. Moreover, basalt can be easily extruded into fibers. Since these fibers are derived from igneous rock, they are also remarkably eco-friendly [4],[5]. Research has been carried out on the effectiveness of basalt-based fiber as a material for enhancing blast resistance [6].

MATERIALS AND METHODS

Laminate Manufacturing

Laminate samples were produced using following technique: stacking of consisting layers of bidirectional basalt fiber weaves (surface density – 380 tex, tensile strength ≈ 2 GPa) and aluminum metal plates of different thickness (figure 2), secondly injecting matrix resin using Vacuum Infusion Process (**VIP**) Method (figure 3), which involved injection in a low-pressure environment (10^{-3} torr) VIP method particularly distinguished with high resin impregnation rate. The prepared sample was placed in vacuum for 20 hours and underwent an additional 48-hour drying at room temperature. Basalt fiber textile weaves were provided by "LLC Basalt Fibers, Georgia" (https://basalt-fibers.com/). Epoxy resin (XRL ER80AB) was used as a binding matrix of layers.

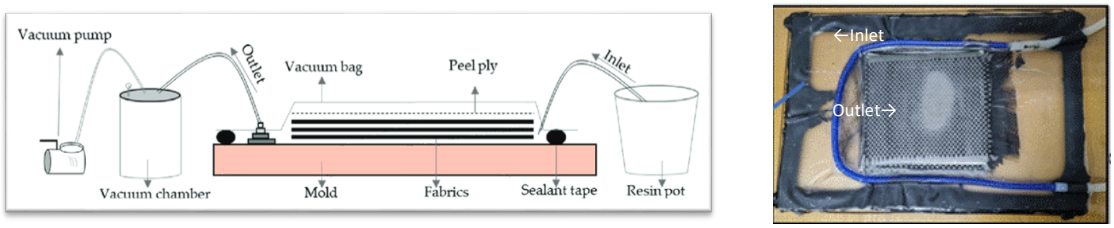


Fig 2. General scheme of manufacturing laminate using Vacuum Infusion Process (**VIP**)

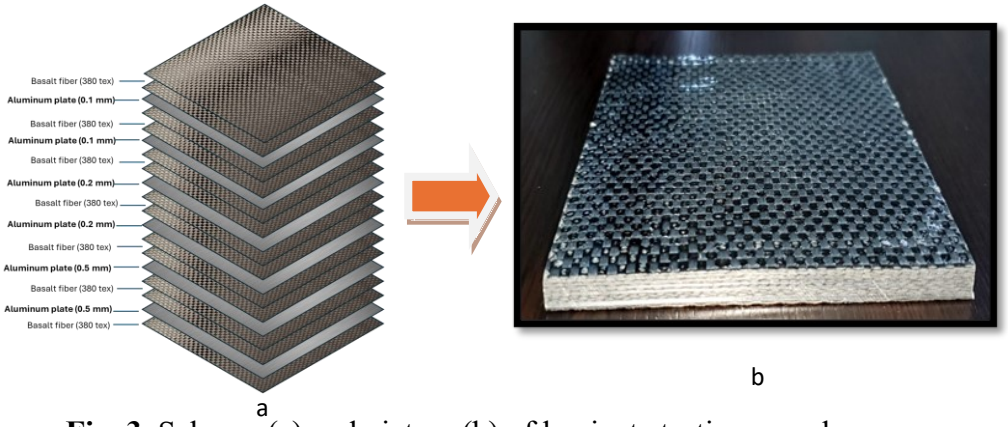


Fig. 3. Scheme (a) and picture (b) of laminate testing sample

Methodology

Tensile Test: The obtained product was evaluated for its mechanical properties. Tensile strength was measured using tensile test machine Mark-10™ ESM303 Tension Test Stand. Experiments were carried out according to international standard ISO 527 to obtain the experimental data. Ultimate tensile strength (MPa) and relative deformation (%) data were measured.

Impact testing: The impact strength experiment was conducted on Charpy impact test machine (figure 4) to measure the amount of energy absorbed (J) by the material during fracture. According to ISO 179-2000 standard method 6 samples were made. The following parameters were used for measuring impact energy: Start angle - 160°, Impact speed - 3.5 m/s and impact energy - 7.5 J. Average values were used to analyze test results.



Fig. 4. Charpy impact test machine

https://doi.org/10.5593/sgem2024/6.1/s24.04

Explosion-resistance experiment: During the dynamic loading experiment, the effects of shock waves generated by explosions (15 g hexogen) on plates were measured. Experiments were conducted on a test bench (figure 5). Reference material to compare test samples was aluminum plate (figure 6). The charge is placed vertically at 400 mm from the sample. Data, such as deformation, acceleration and pressure were recorded by a digital oscilloscope.

The following parameters were registered during the explosions:

- Shock wave overpressure on the plate (using PCB pressure sensors),
- Plate center displacement (using a hall sensor fixed in the center of the inner surface),
- Plate center acceleration (using PCB acceleration sensor).

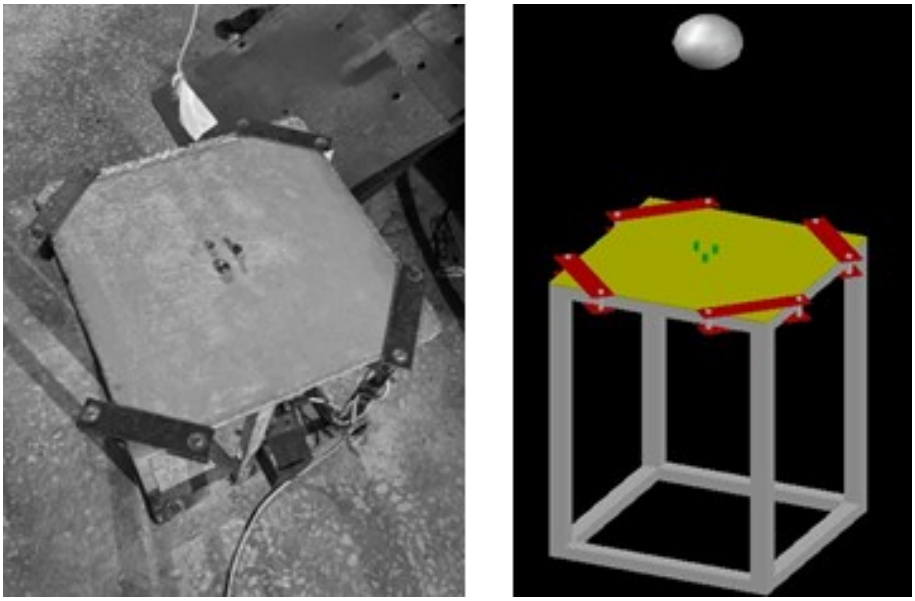


Fig. 5. Test bench for dynamic loading



Fig 6. Aluminum plates used for reference

TEST RESULTS

Tensile testing

Tensile strength test was conducted on the samples, which displayed as stress-strain curve (Figure 7). The ultimate tensile strength of test samples was 62 MPa and a relative deformation of 14.4 %

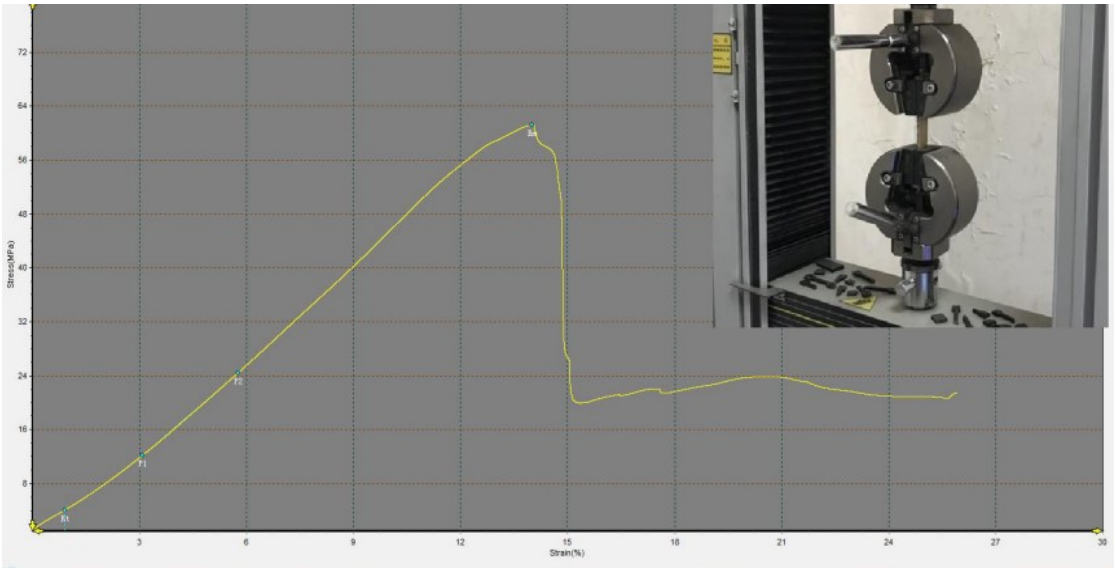


Fig. 7. Stress-strain curve

Impact testing

The laminate impact test was conducted using a Charpy impact tester. The sample for the experiment was prepared according to the ISO 179-2000 standard, considering the sample geometry (4x10x80 mm). A total of 6 samples were tested (Figure 8). During the experiment, the impact energy was 7.5 J, the speed was 3.5 m/s, and the impact angle was 159°.



Fig. 8. Tested experimental samples

https://doi.org/10.5593/sgem2024/6.1/s24.04

Explosion-resistance experiment

A total of seven experiments were conducted, of which four were for reference (aluminium plate) and three –composite laminate samples.

The testing results are presented on Table 1.

Table 1. Average values of overpressure, displacement and acceleration

#	Sample	Overpressure, kPa	Displacement, mm	Acceleration, g
1	Aluminium plate	700	20	92
2	Polymer composite	700	17	74

Based on the analysis of the results obtained during dynamic loading from an explosion-generated shock wave, differences between the reference material and the polymer composite were identified. According to experimental data, under the same conditions of dynamic impact, the displacemrnt of the polymer composite decreases from 20 mm to 17 mm, and the acceleration – from 92g to 74g compared to the aluminium plate.

CONCLUSIONS

- Vacuum Infusion Process (VIP) technology was used to fabricate the metal-polymer composite, through which test samples were produced. This technology ensures uniform impregnation of the reinforcing component with epoxy resin and fills free space.
- A tensile test machine was used for determining ultimate tensile strength (MPa) and relative deformation (%) of laminate sample. Analysis of a stress-strain curve obtained during testing tensile strength of material was 62 MPa and relative deformation was 14.4 %.
- Impact Strength test experiment was conducted on a Charpy impact test machine. The analysis of obtained data showed energy that was absorbed during material fracture which was 3.9 J.
- To evaluate resistance to explosion, an aluminum sheet of the same geometry as the laminate (400mmx400mmx4mm) was used as a benchmark. The experiment revealed that the displacement of the laminate decreased by 15% compared to the aluminum sheet, while acceleration decreased by 20%.
- Based on these results, the metal-polymer composite can be considered a promising material for structures designed to mitigate dynamic loads.

ACKNOWLEDGEMENTS

This work is in progress with the support of the Shota Rustaveli National Science Foundation of Georgia (SRNSFG) – Grant # AR–22–1445. Title - "Production of

multifunctional metal-polymer laminate with high mechanical characteristics and determination of technological parameters.

Special thanks to Dr. Edgar Mataradze and Chief engineer Karlo Tavlalashvili for support in testing of metal-polymeric composites and determination of explosion-resistant properties.

REFERENCES

[1] Hazell PJ. Armour: Materials, Theory, and Design. 2nd ed. CRC Press; 2022. Available from: https://doi.org/10.1201/9781003322719

[2] Langdon G, Nurick G, Karagizova D, Cantwell W. Fiber–metal panels subjected to blast loading. In: Dynamic Failure of Materials and Structure. Springer; 2010. pp. 269-296. https://doi.org/10.1007/978-1-4419-0446-1_9

[3] Fatt MS, et al. Ballistic impact of GLARE™ fiber-metal laminates. Composite Structure.2003;61(1-2):73-88. http://dx.doi.org/10.1016/j.compstruct.2009.08.023

[4] Spagnuolo DM, Napadensky E, Sano T, Wolbert JP. Investigation of Basalt Woven Fabrics for Military Applications. Aberdeen Proving Ground, MD: Army Research Laboratory; 2011.

[5] Prasad S, Chouhan H, Kartikeya K, Singh KK, Bhatnagar N. An experimental investigation into mechanical behaviour of Basalt PEI laminates at various strain rates. Composite Structures. 2021; 267:113800. Available from: https://doi.org/10.1016/j.compstruct.2021.113800

[6] A. Vanishvili, S Kvinikadze, D Tsverava, T Iashvili, G Baliashvili, G Abashidze; Development and characteristics of Metal-Polymer Laminates, Nanotechnology Perceptions, v 19, n 3, pp 47-52, 2023, ISSN 1660-6795

https://doi.org/10.5593/sgem2024/6.1/s24.04

DEVELOPMENT OF RECOMMENDATIONS ON THE APPLICATION OF CORROSION-RESISTANT NANO-CEC FOR HEC WATER PUMPS PROTECTION

PhD Aiman Kemelzhanova[1]

Gulsara Zhamanbayeva[1]

PhD Rustem Atchibayev[1]

PhD Sandugash Kemelzhanova[1]

[1]Al-Farabi Kazakh National University, Almaty, **Kazakhstan**

ABSTRACT

Modern electrochemical technologies for surface treatment of chromium based electrolytic coatings to create protective, antifriction materials are considered.The physicochemical fundamentals of the processes of electrolytic formation of conversion and composite electrolytic coatings are highlighted. The purpose of our researches is working out technology of nano-structured composite electrolytic coatings obtaining and revealing optimum mode for effective corrosion proof coatings electroplating. The coatings were developed for Heat Electro Central (HEC) equipment, in particular for water pumps details. Coatings were obtained from electrolytes with different concentrations of silicon dioxide at temperatures and current densities for corrosion resistance using the gravimetric and potentiodynamic method in a 3% NaCl solution. The results showed that the highest corrosion resistance have coatings, received at current density 4 A/dm^2 and temperature 333 K with concentration 20-30 g/ dm^3 SiO_2.

Keywords*:* nano-structured composition electrolytic coatings (nano-CEC), corrosion resistance, electro deposition, temperature dependency

INTRODUCTION

Particular interest in composite materials and coatings has appeared in recent decades due to a sharp increase in requirements for the level of performance properties of materials operating in aggressive environments, friction and wear [1-7]. In this regard, the development of effective and economical methods for producing nanostructured composite electrolytic coatings of nano-CECs, the study of electrodeposition processes [8-11], as well as the study of the influence of microstructure [12-14] on the properties of electrolytic coatings is one of the pressing problems of modern materials science [15-20].

The purpose of our research is to develop a technology for producing nano-CECs and to identify the optimal mode for deposition of effective corrosion-resistant coatings for pump rods and cylinders, which are used at JSC AlES CHPP-1 for pumping cold water (Figure 1).

https://doi.org/10.5593/sgem2024/6.1/s24.05



a b

a – hydraulic cylinder rods made of SCh 25 cast iron;
b – pump hydraulic cylinder made of steel ST 45
Figure 1 - External view of the rods and cylinder of cold water pumps

MATERIALS AND METHODS

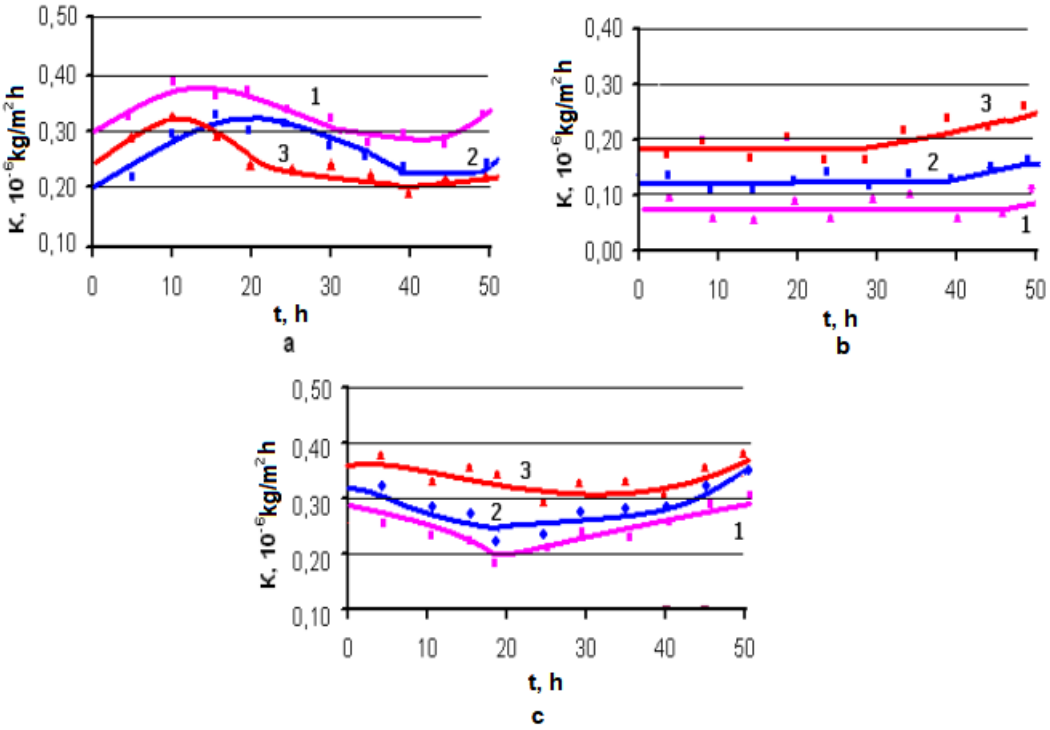
To establish the corrosion resistance of nanostructured chrome-white soot coatings, gravimetric and potentiodynamic research methods were used. Nano-CECs were obtained on samples made of St 45 steel and SCh 25 cast iron with dimensions of 50x25x2 mm. The choice of sample material is dictated by the fact that the rods and sediment cylinders traditionally used for pumping cold unfiltered water to JSC Almaty Electric Network CHPP-1 are made from the appropriate materials. The production modes and composition of the electrolyte suspension are presented in Table 1.

Table 1- Modes and composition of the electrolyte suspension

Name	Units of measurement	Indicators
Chromic anhydride CrO_3	g/l	250,0-300,0
Sulfuric acid H_2SO_4	g/l	2,5-3,0
White soot SiO_2	g/l	5,0 – 45,0
Deposition temperature, T	K	303-343
Current Density, j	A/m^3	3,0-7,0

At the first stage, the task was set to establish the optimal composition of the electrolyte and the deposition mode of nano-CECs. Gravimetric and potentiodynamic research methods were used. For testing, nano-CECs were obtained on samples made of St 45 steel and SCh 25 cast iron with dimensions of 50x25x2 mm. The choice of sample material is dictated by the fact that the sediment rods and cylinders, traditionally used for pumping cold unfiltered water to JSC AlES CHPP-1, are made from the appropriate materials. The production modes and composition of the electrolyte suspension are presented in Table 1.

We examined coatings obtained from electrolytes with different concentrations of silicon dioxide at temperatures and current densities for corrosion resistance using the gravimetric and potentiodynamic method in a 3% NaCl solution.
Before testing, the samples were first degreased and washed with distilled water until completely wet. After 5 hours of corrosion tests, the samples were dried, packed in filter paper, kept in a desiccator with a desiccant for 1 hour and weighed on an analytical balance with an accuracy of 0.0001 g. The results were processed according to GOST 9.506-87, clause 2.6 accuracy indicator - E determined according to GOST 9.502-82.
Figure 1 shows kinetic corrosion curves, which clearly shows that for nano-CECs obtained from electrolytes containing 5-15 g/l SiO_2, dissolution and passivation are observed (Figure 1, a). Nano-CECs obtained from electrolytes containing 20-30 g/l SiO_2 corrode from a state of complete passivation (Figure 1, b). For coatings formed from electrolytes containing 35-45 g/l SiO_2 (Fig. 1, c), the corrosion process begins from a passivation state.



a - 1-5; 2- 10; 3- 15, b- 1-20; 2- 25; 3- 30, c - 1-35; 2- 40; 3- 45
Fig. 2. Kinetic curves of corrosion nano-CEC Cr-SiO_2, obtaining from electrolytes with SiO_2 (g/dm^3):

Figure 2 shows potentiodynamic corrosion curves that are in satisfactory agreement with the kinetic curves given above. For nano-CEC 5-15 g/l SiO_2, the region of complete passivation is short 0.05 V. (Figure 2, a). Nano-CECs formed from electrolytes containing 20-30 g/l SiO_2 (Figure 2, b) the length of the complete passivation region is 0.60-0.85 V. For coatings 35-45 g/l SiO_2 (Figure 2, c) the region of complete passivation decreases with increasing concentration of the dispersed phase in the electrolyte.

https://doi.org/10.5593/sgem2024/6.1/s24.05

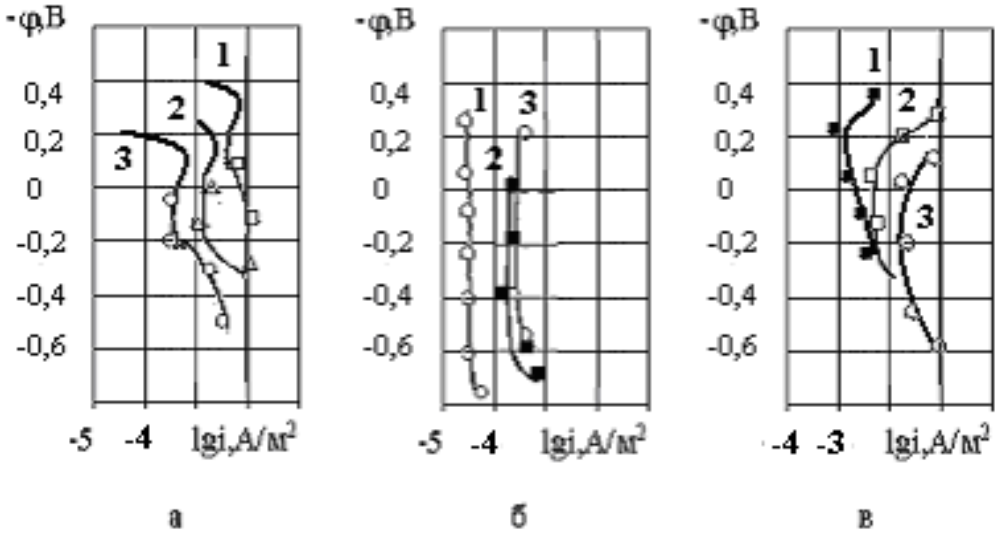
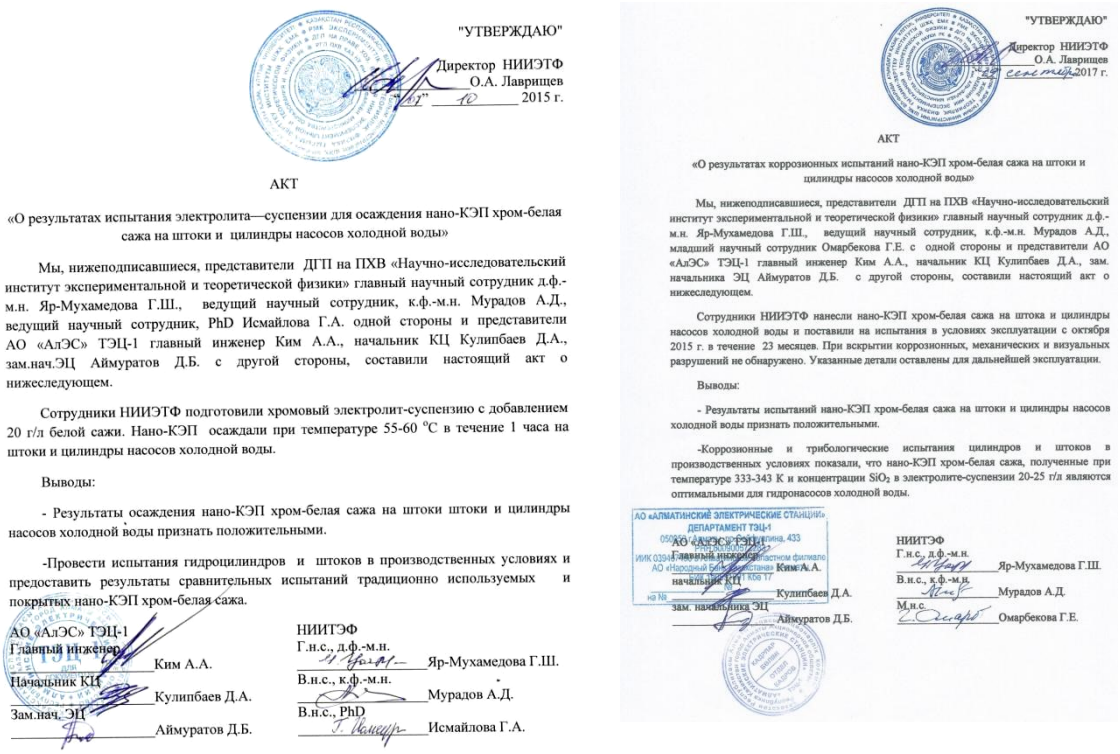


Fig. 3. Potentiodynamical curves of nano-CEC Cr-SiO_2, obtaining from electrolytes with SiO_2 (g/dm^3):
a - 1-5; 2- 10; 3- 15, b- 1-20; 2- 25; 3- 30, c - 1-35; 2- 40; 3- 45

At the second stage, coatings of the optimal composition (20 g/l) were applied at 333 K to parts of a cold, unfiltered water pump. The appearance of parts with nano-CEC chrome-white soot and test reports for the electrolyte suspension are presented in Figures 3 and 5, a.



Figure 4 - Appearance of cold water pumps' rod and hydro-cylinder after chrome-white soot nano-CEC deposition



"УТВЕРЖДАЮ"
Директор НИИЭТФ
О.А. Лаврищев
"__" 10 2015 г.

АКТ

«О результатах испытания электролита—суспензии для осаждения нано-КЭП хром-белая сажа на штоки и цилиндры насосов холодной воды»

Мы, нижеподписавшиеся, представители ДГП на ПХВ «Научно-исследовательский институт экспериментальной и теоретической физики» главный научный сотрудник д.ф.-м.н. Яр-Мухамедова Г.Ш., ведущий научный сотрудник, к.ф.-м.н. Мурадов А.Д., ведущий научный сотрудник, PhD Исмайлова Г.А. одной стороны и представители АО «АлЭС» ТЭЦ-1 главный инженер Ким А.А., начальник КЦ Кулипбаев Д.А., зам.нач.ЭЦ Аймуратов Д.Б. с другой стороны, составили настоящий акт о нижеследующем.

Сотрудники НИИЭТФ подготовили хромовый электролит-суспензию с добавлением 20 г/л белой сажи. Нано-КЭП осаждали при температуре 55-60 °С в течение 1 часа на штоки и цилиндры насосов холодной воды.

Выводы:

- Результаты осаждения нано-КЭП хром-белая сажа на штоки штоки и цилиндры насосов холодной воды признать положительными.

-Провести испытания гидроцилиндров и штоков в производственных условиях и предоставить результаты сравнительных испытаний традиционно используемых и покрытых нано-КЭП хром-белая сажа.

АО «АлЭС» ТЭЦ-1
Главный инженер Ким А.А.
Начальник КЦ Кулипбаев Д.А.
Зам.нач. ЭЦ Аймуратов Д.Б.

НИИТЭФ
Г.н.с., д.ф.-м.н. Яр-Мухамедова Г.Ш.
В.н.с., к.ф.-м.н. Мурадов А.Д.
В.н.с., PhD Исмайлова Г.А.

"УТВЕРЖДАЮ"
Директор НИИЭТФ
О.А. Лаврищев
"__" сентября 2017 г.

АКТ

«О результатах коррозионных испытаний нано-КЭП хром-белая сажа на штоки и цилиндры насосов холодной воды»

Мы, нижеподписавшиеся, представители ДГП на ПХВ «Научно-исследовательский институт экспериментальной и теоретической физики» главный научный сотрудник д.ф.-м.н. Яр-Мухамедова Г.Ш., ведущий научный сотрудник, к.ф.-м.н. Мурадов А.Д., младший научный сотрудник Омарбекова Г.Е. с одной стороны и представители АО «АлЭС» ТЭЦ-1 главный инженер Ким А.А., начальник КЦ Кулипбаев Д.А., зам. начальника ЭЦ Аймуратов Д.Б. с другой стороны, составили настоящий акт о нижеследующем.

Сотрудники НИИЭТФ нанесли нано-КЭП хром-белая сажа на штока и цилиндры насосов холодной воды и поставили на испытания в условиях эксплуатации с октября 2015 г. в течение 23 месяцев. При вскрытии коррозионных, механических и визуальных разрушений не обнаружено. Указанные детали оставлены для дальнейшей эксплуатации.

Выводы:

- Результаты испытаний нано-КЭП хром-белая сажа на штоки и цилиндры насосов холодной воды признать положительными.

-Коррозионные и трибологические испытания цилиндров и штоков в производственных условиях показали, что нано-КЭП хром-белая сажа, полученные при температуре 333-343 К и концентрации SiO_2 в электролите-суспензии 20-25 г/л являются оптимальными для гидронасосов холодной воды.

АО «АЛМАТИНСКИЕ ЭЛЕКТРИЧЕСКИЕ СТАНЦИИ»
ДЕПАРТАМЕНТ ТЭЦ-1
Главный инженер Ким А.А.
начальник КЦ Кулипбаев Д.А.
зам. начальника ЭЦ Аймуратов Д.Б.

НИИТЭФ
Г.н.с., д.ф.-м.н. Яр-Мухамедова Г.Ш.
В.н.с., к.ф.-м.н. Мурадов А.Д.
М.н.с. Омарбекова Г.Е.

a b

a - electrolyte-suspension, b - nano-CEC under operating conditions

Figure 5 - Test certificates in HEC-1"AlES" JSC

At the last stage, we conducted industrial tests of chromium-silicon dioxide nano-CECs for corrosion resistance under operating conditions at AlES JSC from October 2015 for 23 months. When opening the equipment after the test period, no damage, pitting corrosion, cavities, or scratches were found. After a detailed inspection, the hydraulic cylinders and rods were installed for further operation. Test reports are presented in Figure 5, b.

CONCLUSIONS

From the results obtained it follows:

- It has been established that nano-CECs obtained from an electrolyte containing 20 g/l SiO_2 at a current density of 4 A/dm2 and a temperature of 333 K have the best corrosion resistance. The depth corrosion rate is 0.2-0.4.10-3 mm/year . High anti-corrosion properties were demonstrated by nanostructured composite electrolytic coatings formed from electrolytes with 20-30 g/l Aerosila-300.

-The corrosion resistance of nano-CECs, which are obtained from electrolytes with a low content of dispersed phase (5-15 g/l SiO_2), is almost the same as that of pure chromium electrolytic coatings. Obviously, the above amount of the second phase is not enough to change the structure and properties of chromium coatings.

- An increase in the concentration of the second phase in the electrolyte from 35 to 45 g/l leads to a decrease in current efficiency and a sharp deterioration in the quality of chromium deposits.

- Industrial testing has shown that the durability of nano-CEC chrome-white carbon black is 9.5-10.2 times higher than that of traditional uncoated pump parts used in the industry.

https://doi.org/10.5593/sgem2024/6.1/s24.05

ACKNOWLEDGEMENTS
This research has bee n funded by the Science Committee of Kazakhstan's Ministry of Science and Higher Education (BR21882188).

REFERENCES

[1] Narivskyi O.E., Belikov S.B., Subbotin S.A., Pulina T.V. Influence of Chloride-Containing Media on the Pitting Resistance of AISI321 Steel. Materials Science, 2021, 57(2), pp. 291-297. DOI: https://doi.org/10.1007/s11003-021-00544-z.

[2] Narivs'kyi, O.E., Subbotin S. A., Pulina T. V.et.al. Assessment and Prediction of the Pitting Resistance of Plate-Like Heat Exchangers Made of AISI304 Steel and Operating in Circulating Waters//Materials science., 2022, vol.58. pp.41–46 DOI: 10.1007/s11003-022-00628-4

[3] Yar-Mukhamedova, G.Sh. Internal adsorption of admixtures in precipitates of metals / Materials Science, 1999, 35(4), pp. 598–600. 14 DOI: 10.1007/BF02365760

[4] Aldabergenova, T.M., Kislitsin, S.B. et.al. Effect of low-energy alpha-particles irradiation on surface structure and physical-mechanical properties of high-purity tungsten / AIP Conf. Proceed., 2016, 1783, 020003. DOI: 10.1007/s11182-018-1562-8

[5] Narivs'kyi O.E. The influence of heterogeneity steel AISI321 on its pitting resistance in chloride - containing media. Materials Science, 2007, 2 (43). pp. 256-264. DOI: https://doi.org/10.1007/s11003-007-0029-9.

[6] Yar-Mukhamedova, G., Ved', M. et.al. Effect of electrodeposition parameters on the composition and surface topography of nanostructured coatings by tungsten with iron and cobalt / Euras. Chem-Techn. J., 2020, 22(1), pp. 19–25. DOI: 10.18321/ectj697

[7] Yar-Mukhamedova, G.S. A mathematical model of formation of the structure of composite films by the cut-off method / Materials Science, 2000, 36(4), pp. 598–601. DOI: 10.1023/a:1011382609756

[8] Narivskiy A., Yar-Mukhamedova G. et. al. Corrosion losses of alloy 06XN28MDT in chloride-containing commercial waters / Int. Multidisc. Sc. GeoConf. SGEM, 2016, pp. 63–70 1. DOI: 10.5593/sgem2018/6.1/S24.036

[9] Sachanova, Y.I., Ermolenko, I.Y. Influence of the Contents of Refractory Components on the Corrosion Resistance of Ternary Alloys Based on Iron and Cobalt / Materials Science, 2019, 54(4), pp. 556–566. DOI:10.1007/s11003-019-00218-x

[10] Imanbayeva A.K., Syzdykova R.N., Temirbayev A.A. Concept formulation and university teaching methodology for dynamic chaos. Journal of Physics: Conference Series, 2018, 1136(1), 012029.

[11] Mishchenko V. G., Snizhnoi G. V., Narivs'kyy O. Eh. Magnetometric investigations of corrosion behaviour of AISI 304 steel in chloride-containing environment. Metallofizika i noveishie tekhnologii, 2011, 33(6), pp. 769–774.

[12] Yar-Mukhamedova, G.S. A mathematical model of formation of the structure of composite films by the cut-off method / Materials Science, 2000, 36(4), pp. 598–601. DOI: 10.1023/a:1011382609756

[13] Narivs'kyi O.E., Subbotin S.O., Pulina T.V., Khoma M.S., Ratska N.B. Mechanisms of Pitting Corrosion of Austenitic Steels of Heat Exchangers in Circulating Waters and its Prediction. Materials Science, 2023, 59(3), pp. 275–282.

[14] Karakurkchi, H.V., Sakhnenko, N.D. Features of Plasma-Electrolyte Synthesis of Heterooxide Nanocomposites on Multicomponent Alloys of Valve Metals / Springer Proceedings in Physics, 2023, 280, pp. 123–147. 10.1007/978-3-031-18104-7_10

[15] Ashurov, N., Oksengendler, B., Maksimov, S. et. Al. Perovskite-Based Solar Cells: Some Problems and Ways of their Solution / Eurasian Chemico-Technological Journal, 2022, 24(3), pp. 229–239. DOI: 10.18321/ectj1436

[16] Imanbayeva A., Tursynbek Y., Syzdykova R., Mukhamedova A., Evaluating the effectiveness of information security based on the calculation of information entropy. Journal of Physics: Conference Series, 2021, 1783(1), 012042.

[17] Narivs'kyi O., Atchibayev R. Mathematical modeling of the corrosion behavior of austenitic steels in chloride-containing media during the operation of plate-like heat exchangers / Eurasian Chemico-Technological Journal, 2022, 24(4), pp. 19–25 DOI: 10.18321/ectj1473

[18] Yar-Mukhamedova, G., Ved', M. Corrosion and Mechanical Properties of the Fe-W-WO_2 and Fe-Mo-MoO_2 Nanocomposites / Advances in Materials Science and Engineering, 2021, 2021, 5511127. DOI: 10.1155/2021/5511127

[19] Yar-Mukhamedova, G., Ved, M. Research on the improvement of mixed titania and Co(Mn) oxide nano-composite coatings / IOP Conference Series: Materials Science and Engineering, 2018, 369(1), 012019. DOI: 10.1088/1757-899X/369/1/012019

[20] Komarov, F.F., Ismailova, G.A. et. al. Effect of thermal processing on the structure and optical properties of crystalline silicon with GaSb nanocrystals formed with the aid of high-doze ion implantation / Technical Physics, 2015, 60(9), pp. 1348–1352 DOI: 10.1134/S1063784215090078

https://doi.org/10.5593/sgem2024/6.1/s24.05

CORROSION DISSOLUTION OF AN IMPLANT MADE OF NZ30K ALLOY ALLOYED WITH Ag AND COATED WITH A LAYER OF SILVER IN A MODEL SOLUTION OF THE OSTEOSYNTHESIS PROCESS

Prof. Viktor Greshta[1]
Prof. Oleksii Narivskyi[1]
Assistant Anna Dzhus[1]
Assoc. Prof. Vasyl Vynar[2]
PhD Oleksandr Kuprin[3]
[1]Zaporizhzhia Polytechnic National University, Zaporizhzhia, **Ukraine**
[2]Physics and Mechanics Karpenko Institute, National Academy of Sciences of Ukraine, Lviv, **Ukraine**
[3]National Research Center «Physics and Technology Kharkiv Institute», Kharkiv, **Ukraine**

ABSTRACT

In this paper, the magnesium alloy NZ30K alloyed with 0.1 wt. % Ag and clad with a 900 nm thick silver layer. It has been found that in the Ringer-Locke solution, the cylindrical sample underwent contact corrosion over the entire surface and crevice corrosion at the transition from the cylindrical to the flat part, which caused the coating delamination from the alloy under the mechanical action of hydrogen "bubbles" formed at the cathodic areas and corrosion products in the crevice, which have a higher specific volume than the Ringer-Locke solution. It has been found that the sample has subjected to the greatest localized corrosion damage during the first 1020 seconds of testing in this solution, since its corrosion potential E_{cor} during this period was rapidly shifting to the negative side at a rate of 0.04 mV/s. This is due to an intensive increase in the contact area of the alloy with the Ringer-Locke solution, since the standard potential of the alloy is about 3V more negative than that of the silver coating. It was recorded that the rate of shift of the corrosion potential E_{cor} of the sample to the negative side slowed down to 0.0063 mV/s until its stationary value E_{cor} = -1.471 V has been established after 2300 seconds of testing. This is due to the "inhibition" of anodic corrosion processes from crevice corrosion in the above-mentioned areas of the sample and the development of contact corrosion at a constant rate. The NZ30K + 0.1 wt.% Ag alloy clad with a 900 nm thick silver layer is recommended for the manufacture of biodegradable implants for the treatment of bone fractures and its research in clinical conditions, given the negative impact of stress concentrators in its manufacture.

Keywords: biodegradable magnesium alloy implants, silver coating on the surface of implants, contact and crevice corrosion of magnesium alloys in Ringer-Locke solution, selective dissolution of magnesium alloy.

INTRODUCTION

In traumatology, implants made of stainless steels, cobalt-containing and titanium alloys are used to fix broken bones, which are surgically removed after treatment. However, this is a problem for pediatric patients [1], increases the cost of treatment, and

https://doi.org/10.5593/sgem2024/6.1/s24.06

the materials can contribute to allergic reactions, infections, and muscles necrosis in the vicinity [2]. Magnesium does not have such disadvantages, but it is not able to form self-protective oxide films and dissolves rapidly in human body fluids, so it is not suitable for the production of biodegradable implants [3]. Alloying magnesium [4] and plastic deformation of its alloys to an ultrafine microstructure [5] allows controlling the rate of its corrosion dissolution and increases the mechanical characteristics to the values required for implant materials [6]. In particular, biodegradable implants are made from aluminum-containing [7] and Mg-Mn, Mg-Mn-Zn, Mn-Y-Zn, and Mg-Ca [8] magnesium alloys. However, the first one can contribute to some biological complications during treatment, including muscle destruction, reduced osteoclastogenesis, Alzheimer's disease, etc. [9]. The others do not have these disadvantages, as Zn has a positive effect on human metabolism, is non-toxic, and increases the strength and relative elongation of magnesium alloys [10]. The alloying of magnesium alloys with Zr contributes to a significant grinding of their grains, which increases its specific shock absorption capacity and resistance to vibration loads during human movement, and the modification of aluminum-free magnesium alloys with Nd provides its high strength and relative elongation. Therefore, in [11], the authors considered the magnesium alloy NZ30K as the basis for the development of a new alloy with antibacterial properties and improved mechanical characteristics that are required for materials used to produce biodegradable implants. At the same time, in addition to alloying, the rate of biodegradation of implants in the human body is regulated by coating [12, 13]. For this reason, the dissolution processes of the silver-alloyed NZ30K alloy coated with a 900 nm thick silver layer were studied in this paper.

MATERIALS AND METHODS

We studied samples of silver-alloyed magnesium alloy NZ30K, which were smelted in an induction crucible furnace and subjected to aging [11]. The diameter of the samples was 12 and the length was 30 mm. Its chemical composition by the X-ray spectral method using the INKA ENERGY 350 has been determined (Table 1).

Table 1 - Chemical composition of silver alloy NZ30K

Alloy	Content of chemical elements, wt. %				
NZ30K+Ag	Mg	Zn	Zr	Nd	Ag
	95,57	0,69	0,86	2,76	0,09

The samples of the alloy under study were clad with a 900 nm thick layer of silver using a DC magnetron sputtering system equipped with a circular source and an Ag target (50 mm in diameter) in a gas discharge. The vacuum chamber of the system was a cylinder with an internal diameter and height of 500 mm. Cylindrical samples made of silver-alloyed NZ30K alloy (Table 1) were chemically degreased and cleaned by ultrasonication in a hot ethanol bath for 10 minutes and dried in warm air. Then they were mounted on a rotating (9 Hz) fixture located 90 mm from the sputtering source. Before deposition of the silver coating, air was pumped out of the chamber by a diffusion oil pump to a residual pressure of $1\text{-}10^{-3}$ Pa. The samples were ion-etched at a bias potential of 1000 V for 15 minutes at a pressure of 1.5 Pa. An unbalanced magnetron was used in a 600 mA DC

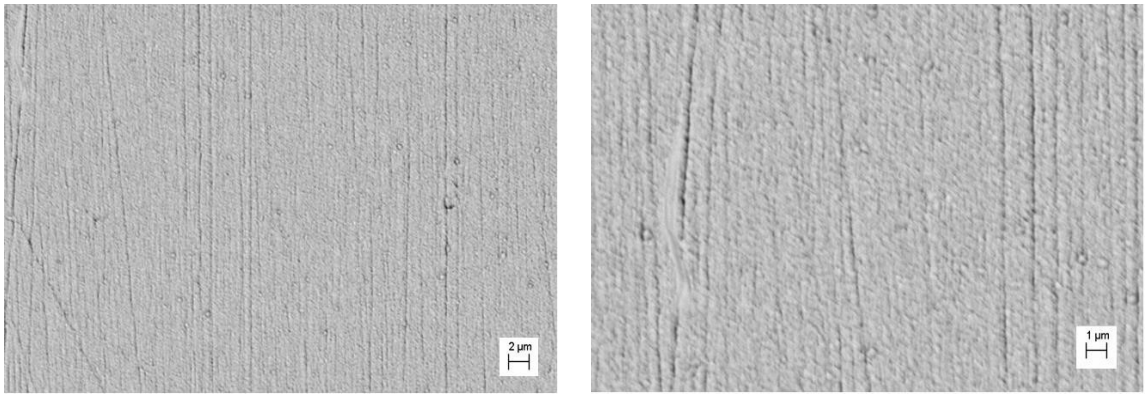
mode at 400 V. The silver coating was applied at a constant magnetron power of 240 W and a substrate bias voltage of 100 V. The argon pressure in the deposition chamber was 1.0 Pa. The time of silver deposition on the surface of the studied magnesium alloy was 20 minutes for a coating thickness of 900 nm.

Corrosion tests of silver clad samples in a Ringer-Locke solution have been carried out (an aqueous solution of distilled water with the following chemical reagents, in mg/l NaCl - 9; $NaHCO_3$; $CaCl_3$; $KCl_{0.2}$; $C_6H_{12}O_6$ - 1) at a temperature of 20±1°C.

The establishment of the stationary value of the corrosion potential E_{cor} on the tested samples on the PN-2MK-10A potentiostat in automatic mode has been recorded. The surface of corrosion damage on the samples after its testing in the Ringer-Locke solution using an optical microscope MMR-2P has been examined.

RESULTS AND DISCUSSION

According to the results of metallographic analysis of the surface of a sample made of NZ30K alloy additionally alloyed with Ag and clad with a 900-nm thick silver layer, point and linear defects due to the application technology have been discovered (Fig. 1).



a b

Figure 1 - Point and linear defects of a 900 nm thick silver clad layer on the surface of NZ30K alloy + 0.1 wt.% Ag (a) × 500; (b) × 1000

The analysis of local corrosion damage of the test sample with a coating thickness of 900 nm showed that it was located along linear defects on the silver coating (Figs. 1, 2), and its size varied from 50 to 150 µm (Fig. 2).



Figure 2 - Surface of NZ30K alloy + 0.1 wt.% Ag clad with a 900 nm thick silver layer after corrosion tests in Ringer-Locke solution

https://doi.org/10.5593/sgem2024/6.1/s24.06

At the same time, in (Fig. 2), in the area of the intersection of the cylindrical and flat parts of the sample, we observed the delamination of the silver coating. Most likely, it is caused by contact corrosion between the studied magnesium alloy and the silver coating, which originated and developed due to the adsorption of chloride ions from the Ringer-Locke solution on point and linear imperfections of the coating (Figs. 1, 2) and was accelerated by the high potential difference between silver and NZ30K alloy (≈3 V). This is consistent with the literature data on the adsorption of chloride ions on imperfections in the structure of steels and alloys, which contribute to the development of local corrosion processes [14-17], actively accelerated by the galvanic effect in contact pairs with a high potential difference [18]. The contact corrosion ulcers near the end of the sample, together with the increased stresses that are usually present when a cylindrical surface transitions to a flat one, were the primary cause of the delamination of the silver coating from the NZ30K alloy in these places (see the upper part of Fig. 2). This process was actively accelerated by crevice corrosion, which formed in the gap between the NZ30K alloy and the silver coating (see Fig. 2, right corner). It is known [19] that in the crevices on the surface of steels and alloys in neutral chloride-containing media, an acidic corrosive media is formed as a result of the hydrolysis of ions of dissolved chemical elements, which can accelerate the corrosion dissolution of steels and alloys. During the corrosion tests of the investigated samples in the Ringer-Locke solution, very active hydrogen emission was visually observed in these places, which may indicate local corrosion of the sample in an acidic chloride-containing media formed in the aforementioned crevice (Fig. 2) from corrosion products. It should be noted that they usually have a much higher specific volume than the media in which steels and alloys are tested [18]. This and the mechanical effect of hydrogen bubbles on the silver coating on the surface of the NZ30K alloy accelerated its delamination. On the cylindrical part of the test specimen, as well as on the flat part, we observed an accumulation of localized corrosion damage (Fig. 3) caused by contact corrosion in characteristic places, which are obviously related to microdefects in the silver coating on the surface of the specimen (Fig. 1).

At the same time, it should be noted that the number of localized corrosion damage here is much smaller than on the flat part of the sample (Fig. 2), which may be due to different technologies for forming surfaces, in particular, flat surfaces are formed by cutting, and cylindrical surfaces are formed without machining after casting.

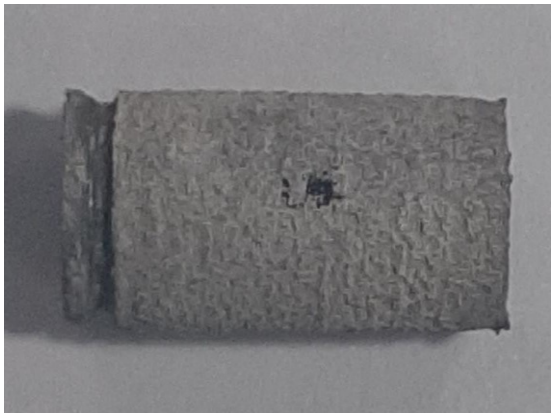


Figure 3 - Localized corrosion damage on the cylindrical surface of a sample of NZ30K alloy + 0.1 wt.% Ag clad with a 900-nm thick silver layer caused by contact corrosion in Ringer-Locke solution

Summarizing the above, it can be noted that a sample of NZ30K alloy + 0.1 wt.% Ag clad with a 900 nm thick silver layer was subjected to contact and crevice corrosion in a Ringer-Locke solution. Corrosion damage from contact corrosion is located on the point and linear imperfections of the coating, which are caused by the technology of its deposition. The number, size, and nature of localized corrosion damage on the flat and cylindrical surfaces of the sample differ significantly, which is due to the characteristic features of coating application on its surface and the technologies of its processing. Ulcers of contact corrosion and increased stresses at the intersection of the cylindrical surface of the sample with the flat surface contributed to crevice corrosion with intense hydrogen release at the cathodic areas, and the mechanical effect of hydrogen bubbles and an increase in the volume of corrosion products in the gap between the coating and the alloy contributed to its delamination from the surface. Intense hydrogen release and delamination of the coating from the alloy surface in the human body can cause muscles necrosis during the treatment of bone fractures [20]. Therefore, the peculiarities of corrosion dissolution of NZ30K + 0.1 wt.% Ag alloy samples coated with a 900-nm thick silver layer require investigation by electrochemical methods.

Based on the results of analyzing the dependence E_{cor} - τ (Fig. 4), it has been found that the steady-state value of the corrosion potential E_{cor} of the sample made of NZ30K alloy additionally alloyed with 0.1 wt % Ag and clad with a 900-nm thick silver layer in two stages has been formed. In particular, at the first stage, E_{cor} intensively shifted to the negative side from -1.4224 V (point 1 of Table 2) to -1.46272 V (point 22 of Table 2) within 1016 seconds.

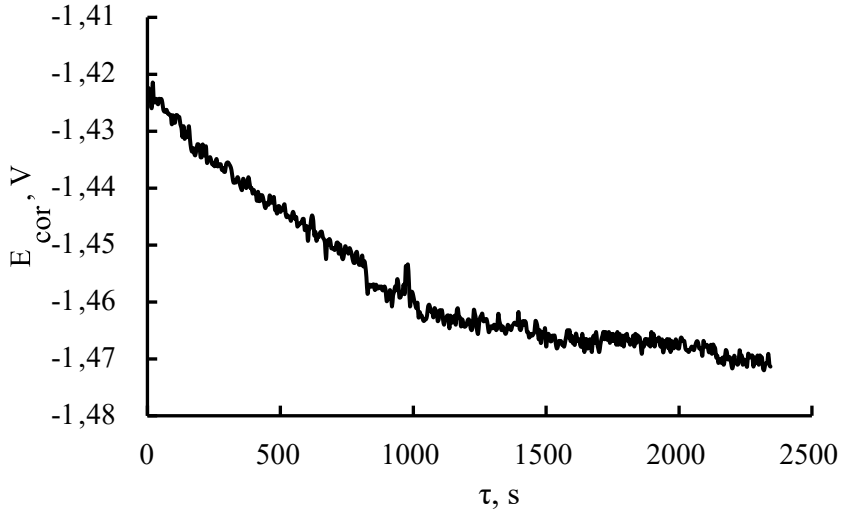


Figure 4 - Dependence between the corrosion potential E_{cor} of NZ30K alloy + 0.1 wt.% Ag clad with a 900 nm thick silver layer and the exposure time (τ) of the sample in Ringer-Locke solution

It turns out that at this stage of the test, the test sample's potential E_{cor} shifted to the negative side at a rate of 0.04 mV/s, which is 0.006 mV faster than that of the 500 nm thick silver clad sample. This is due to similar mechanisms of corrosion destruction of the samples at this stage of the formation of the stationary value of the potential E_{cor} . In particular, they are characterized by an intense increase in the contact area of the alloy with the Ringer-Locke solution due to contact and crevice corrosion and delamination of the silver coating from the alloy at the points of transition of the cylindrical part of the samples to the flat part by the above mechanism (Fig. 2).

https://doi.org/10.5593/sgem2024/6.1/s24.06

Table 2 - Corrosion potentials E_{cor} of NZ30K alloy + 0.1 wt.% Ag clad with a 900 nm thick silver layer depending on the time (τ) of exposure of samples in Ringer-Locke solution

No. of points	τ, s	E_{cor} , V	No. of points	τ, s	E_{cor} , V	No. of points	τ, s	E_{cor} , V
1	4	-1,4224	21	1000	-1,45888	41	1500	-1,46784
2	44	-1,42432	22	1020	-1,46272	42	1540	-1,46816
3	84	-1,4272	23	1040	-1,46336	43	1580	-1,46496
4	124	-1,4288	24	1080	-1,46112	44	1620	-1,46688
5	204	-1,43456	25	1100	-1,46144	45	1660	-1,46752
6	244	-1,43584	26	1120	-1,46304	46	1700	-1,4688
7	284	-1,43648	27	1160	-1,464	47	1740	-1,4672
8	364	-1,43872	28	1180	-1,46432	48	1780	-1,46688
9	404	-1,44096	29	1200	-1,464	49	1820	-1,46688
10	484	-1,44384	30	1220	-1,46496	50	1860	-1,46912
11	524	-1,44512	31	1240	-1,46496	51	1900	-1,46752
12	564	-1,44672	32	1280	-1,464	52	1940	-1,4688
13	604	-1,44928	33	1300	-1,46464	53	1980	-1,46816
14	684	-1,44896	34	1340	-1,46464	54	2020	-1,46688
15	724	-1,44992	35	1360	-1,46464	55	2060	-1,46784
16	764	-1,45088	36	1380	-1,46368	56	2100	-1,46784
17	804	-1,45344	37	1400	-1,46464	57	2180	-1,4688
18	884	-1,45792	38	1420	-1,46336	58	2220	-1,47104
19	924	-1,45888	39	1460	-1,46336	59	2260	-1,46912
20	964	-1,45696	40	1480	-1,4672	60	2300	-1,47104

It should be noted that the area of corrosion damage on the end surface of the tested sample, calculated by the Image J computer program, was 7.45 mm^2 . This is 14.8% of its total area and 1.67 times larger than the area of localized corrosion damage on the end surface of the 500-nm-thick silver clad sample studied earlier. This is due to the fact that only point defects were found on the surface of the 500-nm-thick silver clad sample, and linear defects with a thickness of 900 nm (Fig. 1), where local corrosion damage was formed due to contact corrosion between the coating and the alloy, which was the anode section. It is known [19] that in localized corrosion pits, which are anodic areas on the surface of steels and alloys, its chemical elements dissolve selectively. A characteristic feature of the selective dissolution of metals from localized corrosion damage is that the chemical element with the most negative value of the standard electrode potential dissolves most intensively. This process is supported by the solid-phase diffusion of chemical element atoms in the nanoscale metal volumes in the vicinity of localized corrosion damage. At the same time, the metal with the most negative value of the standard electrode potential moves to its surface, creating microcavities, corrosion

channels, etc., which contribute to the local corrosion processes characteristic of crevice corrosion, in particular with the formation of acidic, highly corrosive media formed from corrosion products. This accelerates the destruction of micro volumes of metal in localized corrosion damage by the mechanisms mentioned above. Metallographic analysis revealed that the local corrosion damage of the test sample has a developed surface characteristic of selective metal dissolution in the anode areas. At the same time, in the NZ30K alloy + 0.1 wt.% Ag, magnesium has the most negative standard electrode potential and dissolves most intensively, which promotes its solid-phase diffusion to localized corrosion damage and accelerates metal destruction in them according to the above mechanism, which has been established in studies [14, 19].

According to the results of the analysis (Fig. 4), it has been found that the potential E_{cor} of the sample made of NZ30K alloy + 0.1 wt.% Ag clad with a 900 nm thick silver layer slowly shifted to the negative side from -1.46272 (point 22, Table 2) to -1.47104V (points 58, 60, Table 2). This tendency characterizes the second stage of corrosion destruction of the test sample in the Ringer-Locke solution. It should be noted that at this stage of the test, the rate of displacement of the sample E_{cor} in the negative direction was only 0.0063 mV/s. This is 6.35 times slower than at the first stage of corrosion tests (Fig. 4). At the same time, the analysis of the data (Fig. 4 and Table 2) showed that after 2300 s of testing the sample of NZ30K alloy + 0.1 wt.% Ag clad with a 900 nm thick silver layer in Ringer-Locke solution, a stationary value of the potential E_{cor} was established on it. This shows that the corrosion dissolution of the sample under such conditions proceeds at a constant rate without active hydrogen release at the cathode sites.

Summarizing the above, it can be noted that in the Ringer-Locke solution, the NZ30K alloy + 0.1 wt.% Ag clad with a 900 nm thick silver layer underwent intense contact and crevice corrosion on point and linear imperfections of the coating with its delaminate from the alloy at the points of transition of the cylindrical surface of the sample to a flat one. These processes were most intense in the first 1020 seconds of testing with active hydrogen release at the cathodic areas of the sample, but then this process slowed down significantly, and after 2300 seconds, a stationary value of the potential E_{cor} was established with a constant rate of anodic corrosion processes. These research results showed that samples of NZ30K+0.1 wt.% Ag alloy clad with a 900nm thick silver layer can be recommended for clinical research, taking into account the influence of the edge effect on the delamination of the coating from the alloy during implant manufacturing.

CONCLUSIONS

According to the results of corrosion tests of a sample of NZ30K alloy + 0.1 wt.% Ag clad with a 900 nm thick layer of silver in Ringer-Locke solution, it has been found that it was subjected to contact and crevice corrosion. It has been found that localized corrosion damage from contact corrosion originated and developed on point and linear imperfections of the coating, and delamination of the coating at the points of transition of the cylindrical part of the sample to the flat part due to the influence of corrosion products and mechanical action of hydrogen bubbles on it due to crevice corrosion, which is caused by the influence of contact corrosion and increased stresses in these places. It was recorded that at the first stage of the corrosion tests of the sample, the corrosion potential E_{cor} shifted to the negative side at a rate of 0.04 mV/s for 1020 seconds. This is due to the intensive growth of the area of localized corrosion damage from contact corrosion and delamination of the coating from crevice corrosion. It was shown that the rate of shift of the potential E_{cor} in the negative direction slowed down to 0.0063 mV/s until the steady-

https://doi.org/10.5593/sgem2024/6.1/s24.06

state value of the potential E_{cor} =-1.471 V after 2300 seconds of testing has been established. This is due to the slowdown of anodic corrosion processes, which is also confirmed by a significant decrease in the intensity of hydrogen release at the cathodic areas of the sample, which was recorded visually. Samples of NZ30K+0.1 wt.% Ag alloy clad with a 900 nm thick silver layer are recommended for clinical researches, and when manufacturing implants using this technology, it is warned that angles are unacceptable to prevent the coating delamination from alloy.

LITERATURE

[1] Busam M.L., Ester R.J. and Obremskey W.T. Hardware removal: indications and expectations. Journal of the American Academy of Orthopaedic Surgeons, 2006, 14(2): p 113-120. https://doi.org/10.5435/00124635-200602000-00006

[2] Ratner B.D., Haffman A.S., Schoen F.J. and Lemons J.E. Biomaterials Science - An Introduction to Materials in Medicine. Third edition: Academic Press, 2013. https://doi.org/10.1016/C2009-0-02433-7

[3] Pilling, N. and Bedworth, R.J. The Oxidation of Metals at High Temperatures. Inst. Metals, 1993, 29, pp. 529-593.

[4] Cui L.V., Li X.T., Zeng R.C., Li S.Q., Han E.N., Song L. In vitro corrosion of Mg-Ca alloy - The influence of glucose content. Frontiers of Materials Science, 2017, 11, pp. 284-295. http://dx.doi.org/10.1007/s11706-017-0391-y

[5] Xu W., Birbilis N., Sha G. and Wang Y. A high-specific-strength and corrosionresistant magnesium alloy. Nature Materials. 2015, 14 (12), pp. 1229-1235. http://dx.doi.org/10.1038/nmat4435.

[6] Cowin S.C., Goodship A.E. and Cunningham J.L. "Bone adaptation" in Bone mechanics Handbook; Second Edition. CRC Press, Boca Raton, FL, 2001, ch. 5.

[7] Xu L., Yu G., Zhang E., Pan F. and Yang, K. In vivo corrosion behavior of MgMn-Zn alloy for bone implant application // Journal of Biomedical Materials Research Part A: An Official Journal of The Society for Biomaterials, The Japanese Society for Biomaterials, and The Australian Society for Biomaterials and the Korean Society for Biomaterials, 2007, Vol. 83(3), pp. 703-711. https://doi.org/10.1002/jbm.a.31273

[8] Friedrich H. E. et al. Magnesium technology. - Springer-Verlag Berlin Heidelberg, 2006, Vol. 212.

[9] Ferreira P.C., Piai K.D.A., Takayanagui A.M.M. and Segura-Muñoz S.I. Aluminum as a risk factor for Alzheimer's disease // Revista latino-americana de enfermagem, 2008, Vol. 16, pp.151-157. https://doi.org/10.1590/S0104-11692008000100023

[10] Lastra M.D., Pastelin R., Camacho A., Monroy B. and Aguilar A.E. Zinc intervention on macrophages and lymphocytes response. Journal of trace elements in medicine and biology, 2001, Vol. 15(1), pp. 5-10. https://doi.org/10.1016/S0946-672X(01)80019-5

[11] Greshta V.L., Shalomeev V.A., Dzhus A.V., Mityaev O.A. Study of the effect of silver alloying on the microstructure and properties of magnesium alloy NZ30K for implants in osteosynthesis // New Materials and Technologies in Metallurgy and Engineering, 2023, (2), pp. 14-19. https://doi.org/10.15588/1607-6885-2023-2-2

[12] Yar-Mukhamedova G.S. A mathematical model of formation of the structure of composite films by the cut-off method Materials Science, 2000, 36(4), pp. 598–601. DOI: 10.1023/a:1011382609756

[13] Muradov, A.D., Mukashev, K.M., Yar-Mukhamedova, G.S., Korobova, N.E. Impact of silver metallization and electron irradiation on the mechanical deformation of polyimide films. Technical Physics, 2017, 62(11), pp. 1692–1697. DOI: 10.1134/s1063784217110226.

[14] Narivs'kyi O. E. Corrosion Fracture of Platelike Heat Exchangers. Fiz.- Khim. Mekh. Mater., 2005, 41 (1), pp. 104-108. DOI: https://doi.org/10.1007/s11003 005-0140-8

[15] Narivskyi O.E., Subbotin S.O., Pulina T.V., Khoma M.S. Assessment and Prediction of the Pitting Resistance of Plate-Like Heat Exchangers Made of AISI304 Steel and Operating in Circulating Waters. Materials Science, 2022, 58, pp. 41-46. https://doi.org/10.1007/s11003-022-00628-4.

[16] Mishchenko V.G., Snizhnoi G.V., Narivs' kyy O. E. Magnetometric investigations of corrosion behavior of AISI 304 steel in chloride-containing environment. Metallofizika i noveishie tekhnologii, 2011, 33(6), pp. 769-774.

[17] Narivskyi O.E., Belikov S.B., Subbotin S.A., Pulina T.V. Influence of ChlorideContaining Media on the Pitting Resistance of AISI321 Steel. Materials Science, 2021, 57(2), pp. 291-297. DOI: https://doi.org/10.1007/s11003-021-00544-z.

[18] Narivskiy A., Yar-Mukhamedova G., Temirgaliyeva E., Mukhtarova M., YarMukhamedov Y. Corrosion losses of alloy 06KhN28MDT in choride-containing commercial waters. International Multidisciplinary Scientific GeoConference Surveying Geology and Mining Ecology Management, SGEM, 2016, 1, pp.63-70. DOI: 10.5593/sgem2018/6.1/S24.036

[19] Narivs'kyi O.E. Micromechanism of corrosion fracture of the plates of heat exchangers // Materials Science, 2007, 43(1), pp. 124-132. DOI: https://doi.org/10.1007/s11003-007-0014-3.

[20] Golovakha M.L., Neryanov Y.M., Ivchenko D.V., Kudievsky A.V. and others. General issues of traumatology and orthopedics, 2nd edition. Study guide for practical classes. Zaporizhzhia State Medical University, Department of Traumatology and Orthopedics. Zaporizhzhia, 2016, 200 p.

https://doi.org/10.5593/sgem2024/6.1/s24.06

EFFECT OF ZINC OXIDE NANOPARTICLES AGAINST *PHYTOPHTHORA* SPP. CAUSING DURIAN DISEASES *IN VITRO*

Dr. Kanchalar Keeratirawee[1]*

Assoc. Prof. Dr. Pornprapa Kongtragoul[2]

Miss Sansanee Pantakan[2]

[1]Department of General Sciences, King Mongkut's Institute of Technology Ladkrabang Prince of Chumphon Campus, Chumphon 86160, **Thailand**

[2]Department of Agricultural Technology, King Mongkut's Institute of Technology Ladkrabang Prince of Chumphon Campus, Chumphon 86160, **Thailand**

ABSTRACT

The efficiency of zinc oxide nanoparticles (ZnO-NPs) in inhibiting *Phytophthora* spp. growth in both durian fruits and stems is demonstrated. The size of ZnO-NPs used was in range of 25-50 nm in diameter. Diseased durian sample were collected from a durian orchard located in southern of Thailand. The pathogen of diseased durian was isolated for subsequent morphological identification. Three distinct strains of *Phytophthora* spp. (designated as PHY41, PHY45, PHY49) were successfully isolated and were found in colonies with rings and stellate pattern, ovoid, limoniform sporangium with semi-papillate or papillate, and formation chlamydospores. All isolates were exhibiting 100% pathogenicity on durian, as indicated by the disease incidence (DI). The concentration of ZnO-NPs played a crucial role in suppressing the growth of *Phytophthora* spp. in all isolates. Higher concentration of ZnO-NPs resulted in increased inhibition of growth. ZnO-NPs at the concentration of 2000 µg/mL effectively suppressed the mycelial growth of all fungi isolates at 57.76-69.84%. Additionally, ZnO-NPs at the concentration of 500 µg/mL completely inhibited the sporulation only in the PHY49 strains. Furthermore, ZnO-NPs concentration ranging from 1000-2000 µg/mL resulted in completed inhibition in sporulation in all *Phytophthora* spp. isolates. The result demonstrated that ZnO-NPs at all concentrations effectively delayed the germination of *Phytophthora* spp.

Keywords: Durian diseases, Pathogenicity test, *Phytophthora* spp., ZnO-NPs, Inhibit

INTRODUCTION

Zinc oxide nanoparticles (ZnO-NPs) are of particular interest for antimicrobial applications. They are approved by the Food and Drug Administration (FDA) as a food additive and are generally recognized as safe and non-toxic at low concentrations [1]. ZnO-NPs demonstrate several mechanisms of antimicrobial activity. First, the release of antimicrobial Zn^{2+} ions. Second, the use of light radiation to generate reactive oxygen species (ROS) such as hydrogen peroxide (H_2O_2), hydroxyl radicals (-O.H.), and superoxide (O^{2-}). Finally, electrostatic interactions contribute to their antimicrobial properties. They can enter microbial cell walls via carrier proteins or ion channels, where they form bonds with various organelles and cause cell damage [2]. Although

https://doi.org/10.5593/sgem2024/6.1/s24.08

nanoparticles have already been used as an alternative to control the growth of *Phytophthora* spp. [3], the most effective ones, based on their nature, chemical composition, and optimal concentration, are still unknown.

Durian is widely known as the 'King of Fruit' in Southeast Asia. Particularly, Thailand is the largest producer among Southeast Asian countries. However, durian is seriously threatened by numbers of fungal diseases, such as *Phytophthora* sp., which can cause stem rot, root rot, and fruit rot. These disease causes major crop damage and significant economy loses for farmer. Traditionally, Thai durian growers have relied on chemical fungicides to oppose these pathogens. Nonetheless, prolongs use these chemicals can lead to the development of fungicide resistance and produce mutant genes as they evolve and become immune to fungicides [4-8]. Therefore, it is critical to utilize economical, environmentally friendly solutions for the control this fungus. The aim of the present study was to isolate and identify the fungal pathogens causing durian diseases, perform pathogenicity tests, and evaluate the *in-vitro* antifungal capacity of ZnO-NPs on the fungus *Phytophthora* spp., the causal agent of durian disease.

MATERIALS AND METHODS

1. Collection, Isolation, and Identification by morphology

Diseased durian samples were collected in southern Thailand. The infected parts of the durian plant were cut into small pieces, and the surfaces were sterilized with 10% Clorox® before being washed in sterilized distilled water. The plant tissue was placed on the PAR(PH)-V8 selective medium and incubated at room temperature. After the hyphal tips appeared, the culture was removed and transferred to clarified V8 juice agar. The identification of *Phytophthora* spp. was followed the procedure established by Gallegly and Hong [9].

2. Pathogenicity test

Phytophthora spp. was grown on carrot agar (CA) at RT °C for 7-10 days. Six-month-old Monthlong durian seedlings were sprayed with a spore suspension of *Phytophthora* spp. at a concentration of $1x10^5$ spores/mL. Then, the seedlings were covered with a plastic bag for 24 hours. Afterward, the durian seedlings were taken out of the bag, with four replicates in total. The experiment assessed the percentage of disease occurrence.

3. Effect of ZnO-NPs on mycelial growth, and sporulation of *Phytophthora* spp.

ZnO-NPs were tested using the poisoned food method by mixing ZnO-NPs in PDA medium at concentrations of 0 (control), 500, 1000, and 2000 µg/mL. Next, the edge of the fungal colony was cut using a sterile cork borer with a diameter of 0.5 cm. The culture dish was placed at the center of agar plates containing various concentrations of ZnO-NPs and incubated at room temperature. This experiment used a completely randomized design (CRD) with 4 replicates. The colony diameters were measured, and the percentage of inhibition of mycelial growth was calculated.

The number of *Phytophthora* spp. sporangium was counted on slides under a microscope. Fungal colonies were cut out at each concentration using a cork borer with a diameter of 0.5 cm. Then, 10 pieces were transferred to 10 mL of sterilized distilled

water. The density of the sporangium numbers was counted to calculate the percentage of inhibition of sporulation.

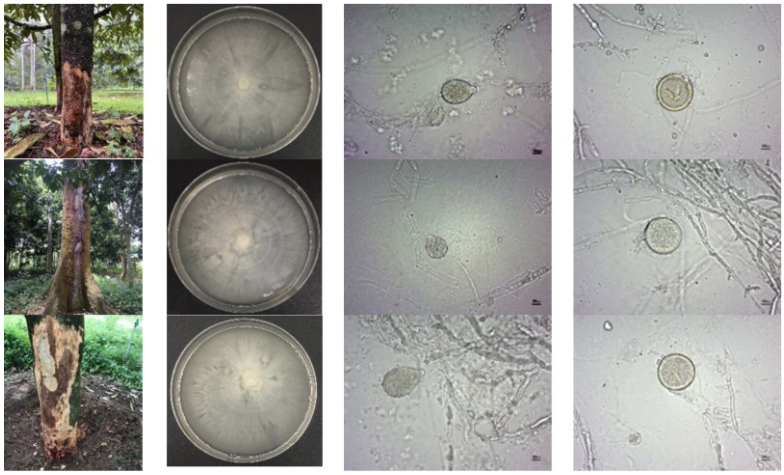
4. Effect of ZnO-NPs on germ tube length of *Phytophthora* spp.

CA medium was mixed with ZnO NPs at concentration levels of 0 (control), 500, 1000, and 2000 µg/mL. Agar pieces were cut to a size of 1.5x1.5 cm and placed on a slide. The spore concentration was adjusted to $1x10^5$ spores/mL, with 40 µL of spore suspension placed on the agar peiecs, covered with a cover slip, and incubated in a humid box at room temperature. The length of the germ tube of sporangium was measured at 0, 3, and 6 hours under a microscope at 400 times magnification, with 5 replicates counted.

RESULTS

1. Collection, Isolation, and Identification by morphology

Symptoms of durian stem rot caused by *Phytophthora* disease is depicted in Fig. 1. The colony, spores, and chlamydospores of each sample are shown in Fig. 1(a), 1(b), and 1(c) respectively. A piece of sample affected by *Phytophthora* disease leading to stem rot was collected to further investigation, including pathogenicity testing, and assessing the potential impact of ZnO-NPs on the growth of mycelial, and sporulation of *Phytophthora* spp.



(a) (b) (c) (d)

Figure 1 Symptoms of durian stem rot (a), colony (b), sporangium (c), and chlamydospores of *Phytophthora* spp. isolates.

Morphology characterization of *Phytophthora* spp. isolates causing stem rot and fruit rot disease of durian is shown in Table 1. Based on the data, isolate PHY41 exhibits a stellate colony pattern with a growth rate of 16.00 mm per day. Its sporangia are globose and semi-papillate with a length of approximately 23 µm and a width of 18.2 µm. In contrast, isolate PHY45 presents a rings colony pattern with a slower growth rate

https://doi.org/10.5593/sgem2024/6.1/s24.08

of 7.18 mm per day. Its sporangia are also globose but papillate with a length of around 23 µm and a width of 17 µm. On the other hand, the sporangia of PHY49 are also globose but semi-papillate with a longer length of around 27 µm and a width of 21.2 µm.

Table 1 Morphology characterization of *Phytophthora* spp. isolates causing stem rot and fruit rot disease of durian.

Isolates	Colony pattern	Growth rate (mm/day)	Sporangia characteristics			
			Shape	Papillate	Length (µm)	Width (µm)
PHY41	stellate	16.00±0.23	Ovoid	semi-papillate	23±1.9	18.2±1.48
PHY45	rings	7.18±0.54	Globose	semi-papillate	23±1.22	17.2±1.79
PHY49	stellate	13.81±0.24	Ovoid	semi-papillate	27.2±2.7	21.2±2.77

2. Pathogenicity test

According to the disease susceptibility test, injecting *Phytothora palmivora* isolate PHY41, PHY45, and PHY49 onto durian seedlings yielded different result. After 2 days of injection, isolates PHY41 and PHY49 caused watery lesions of indistinct shapes, yellowing leaves, and subsequent leaf drop. Meanwhile, isolate PHY45 exhibited leaf drop only after 7 days of injection (Fig. 2). After 7 days of injection, isolates PHY41 and PHY49 induced disease 100% of seedling (Table 2), whereas isolate PHY45 caused disease in 75% of the seedling.

Table 2 Disease incidence (DI) of PHY41, PHY45, and PHY49 of *Phytophthora* spp. isolates after inoculation on durian seedlings for 7 days.

Isolate code	Disease incidence (%)[1/]			
	0 days	3 days	5 days	7 days
PHY41	0	75	100	100
PHY45	0	50	50	75
PHY49	0	100	100	100

[1/]Values are evaluated with 4 durian seedlings.



Figure 2 Symptoms on durian seedlings after inoculation with PHY41 (A-D), PHY45 (E-H), and PHY49 (C-L) of *Phytophthora* spp. isolates for 7 days.

3. Effect of ZnO-NPs on mycelial growth, and sporulation of *Phytophthora* spp.

The inhibitory effects of zinc oxide nanoparticles on the growth of on mycelial of *Phytophthora palmivora* were test at concentrations of 500, 1000, and 2000 µg/mL. As result depict in Table 3, all three isolates mycelial growth was inhibited. The statistical difference was significant as the concentration of ZnO-NPs increased. The percentage of inhibition of mycelial growth increased with the rise in concentration. The most effective inhibition percentage was observed at a concentration of 2000 µg/mL, which was 57.76%, 58.50%, and 69.84% respectively. Subsequently, at a concentration of 1000 µg/mL, inhibition percentages were 50.11%, 37.23%, and 63.56% respectively. Additionally, observations around the colonies revealed deformities. Examination of mycelial images under a microscope at 100x magnification revealed that concentrations ranging from 500 to 2000 µg/mL resulted in decreased branching and increased curving at the mycelial tips of all three isolates as the concentration increased (Fig. 3).

Table 3 Inhibitory effects of zinc oxide nanoparticles at 500, 1000, and 2000 µg/ml on mycelial growth of *Phytophthora* spp. PHY41, PHY45, and PHY49 after incubation for 4 days.

ZnO NPs (µg/mL)	**Inhibition of mycelial growth (%)[1/]**		
	PHY41	**PHY45**	**PHY49**
Control	0d	0d	0d
500	41.47c	17.00c	49.94c
1000	50.11b	37.23b	63.56b
2000	57.76a	58.50a	69.84a
F-Test	**	**	**

[1/]Values expressed are means with 4 replications. The different letters in the same column are significantly different as determined by the least significant difference test at $p<0.01$.

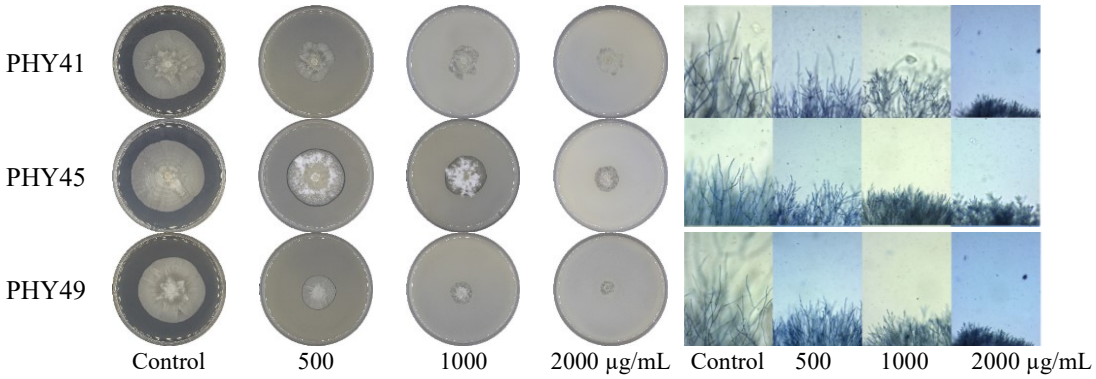


Figure 3 The effect of the zinc oxide nanoparticles test at various concentrations for controlling PHY41, PHY45, and PHY49 isolates of *Phytophthora* spp. on V8 agar for 4 days.

Inhibitory effects of zinc oxide nanoparticles at 500, 1000, and 2000 µg/ mL on sporulation of *Phytophthora* spp. PHY41, PHY45, and PHY49 after inoculation for 4

https://doi.org/10.5593/sgem2024/6.1/s24.08

days was investigated. The result shows in Table 4 revealed that all three isolates sporulation was inhibited. The statistical difference was significant as the concentration of ZnO-NPs increased. Specifically, all concentrations were able to inhibit sporulation ranging from 88-100%

Table 4 Inhibitory effects of zinc oxide nanoparticles at 500, 1000, and 2000 µg/ml on sporulation of *Phytophthora* spp. PHY41, PHY45, and PHY49 after inoculation for 4 days.

ZnO NPs (µg/ml)	**Inhibition of sporulation (%)[1/]**		
	PHY41	**PHY45**	**PHY49**
Control	0b	0b	0b
500	99.34a	88.24a	100.00a
1000	100.00a	100.00a	100.00a
2000	100.00a	100.00a	100.00a
F-Test	**	**	**

[1/]Values expressed are means with 4 replications. The different letters in the same column are significantly different as determined by the least significant difference test at $p<0.01$.

4. Effect of ZnO-NPs on germ tube length of *Phytophthora* spp.

The efficiency of zinc oxide nanoparticles on germ tube length of *Phytophthora palmivora* isolates PHY41, PHY45, and PHY49 on V8 agar according to incubation periods is shown in Table 5. The result revealed that ZnO-NPs significantly reduce germ tube length of *Phytophthora palmivora* isolates PHY41, PHY45, and PHY49 on V8 agar. The most inhibition occureed at a concentration of 2000 µg/mL at both 3 hours and 6 hours. Lower concentration of 500 µg/mL and 1000 µg/mL also reduced germ tube growth but less effectively.

Table 5 Efficiency of zinc oxide nanoparticles on germ tube length of *Phytophthora palmivora* isolates PHY41, PHY45, and PHY49 on V8 agar according to incubation periods.

Concentration ZnO NPs (µg/ml)	**Length of germ tube (µm)[1/]**					
	3 hr.			**6 hr.**		
	PHY41	**PHY45**	**PHY49**	**PHY41**	**PHY45**	**PHY49**
Control	49.30d	47.60c	48.65d	117.50d	110.50d	115.00d
500	8.60c	7.50bc	9.10c	80.50c	78.75c	89.25c
1000	5.15b	4.20b	6.00b	63.00b	57.75b	66.75b
2000	0.50a	0.20a	0.35a	41.75a	43.25a	43.75a
F-Test	**	**	**	**	**	**

DISCUSSION

The results from this research show that ZnO-NPs with a diameter ranging from 25-50 nm can effectively inhibit the germination of durian pathogens. The inhibitory effect on fungal growth increases with increasing ZnO-NPs concentrations. Previous studies have reported that ZnO-NPs can attach to fungal surfaces through pinocytosis and accumulate in the outer membrane or cytoplasm. This causes the release of Zn ion

which can damage the cell membrane, proteins, and genome, thus fungal germination is inhibited. Higher concentrations of ZnO-NPs enhance this effect due to the increased amount of Zn ions. Our observations are consistent with those of Wanger et al. [10] who found that ZnO-NPs could inhibit *P. tabacica* infection in tobacco leaves. Similarly, Arciniegas-Grijalba et al. [11] observed cytoplasmic liquefaction and cell wall detachment in the coffee fungus *Erythricium salmonicolor.* These studies confirm the effectiveness of ZnO-NPs in preventing fungal infection in durians.

The efficiency of zinc oxide nanoparticles on germ tube length of *Phytophthora palmivora* isolates PHY41, PHY45, and PHY49 on V8 agar revealed a significant decline in germ tube length with increasing the concentration of ZnO-NPs. Particularly, at the concentration of 2000 μg/mL, the most inhibition of germ tube growth was observed at both 3 hours and 6 hours of the experiment time. This resulted in more effective inhibition of germ tube development. The 500 μg/mL and 1000 μg/mL concentrations also reduced germ tube growth but to a lesser extent.

CONCLUSION

According to the results of this study, durian pathogen germination can be successfully inhibited by zinc oxide nanoparticles (ZnO-NPs). With diameters ranging from 25 to 50 nm, these nanoparticles exhibited strong antifungal activity that rose with applied concentration. In particular, the germ tube length of the Phytopthora palmivora isolates was significantly shortened at a concentration of 2000 μg/mL. This effectiveness was attributed to the interaction between the fungal cells and ZnO-NPs, which led to the release of zinc ions that damage the cell and stop the fungus from growing. After ZnO-NPs were applied, all *Phytophthora* spp. examined in this investigation demonstrated complete pathogenicity. ZnO-NPs effectively delayed the germination of *Phytophthora* spp. and inhibited the mycelial growth of all fungal isolates. These findings demonstrated the potential of zinc oxide nanoparticles (ZnO-NPs) as an effective crop protection material that could strengthen the fungal resistances of durian crops.

ACKNOWLEDGEMENTS

The authors sincerely thank King Mongkut's Institute of Technology Ladkrabang, Prince of Chumphon Campus, Chumphon, Thailand, for support.

REFERENCES

[1] C. R. Mendes *et al.*, "Antibacterial action and target mechanisms of zinc oxide nanoparticles against bacterial pathogens," *Scientific Reports,* vol. 12, no. 1, p. 2658, 2022/02/16 2022, doi: 10.1038/s41598-022-06657-y.

[2] A. Miri, N. Mahdinejad, O. Ebrahimy, M. Khatami, and M. Sarani, "Zinc oxide nanoparticles: Biosynthesis, characterization, antifungal and cytotoxic activity," *Materials Science and Engineering: C,* vol. 104, p. 109981, 2019/11/01/ 2019, doi: https://doi.org/10.1016/j.msec.2019.109981.

[3] S. Ritmontree and P. Kongtragoul, "Antifungal effect of zinc oxide nanoparticles against disease in durian caused by Phytophthora palmivora," 2021.

https://doi.org/10.5593/sgem2024/6.1/s24.08

[4] P. Kongtragoul, K. Ishikawa, and H. Ishii, "Metalaxyl Resistance of Phytophthora palmivora Causing Durian Diseases in Thailand," *Horticulturae,* vol. 7, no. 10, p. 375, 2021. [Online]. Available: https://www.mdpi.com/2311-7524/7/10/375.

[5] L. T. KWEE, N. C. CHONG, and C. C. LAN, "Etiology and control of durian foliar blight and dieback caused by Rhizoctonia solani," *Annals of Applied Biology,* vol. 111, no. 2, pp. 301-307, 1987, doi: https://doi.org/10.1111/j.1744-7348.1987.tb01456.x.

[6] T. Lim and S. Sangchote, "Diseases of durian," *Diseases of tropical fruit crops,* pp. 241-251, 2003.

[7] R. Piasai, P. Chalmers, O. Piasai, and N. Khewkhom, "Postharvest fungicide dips to control fruit rot of 'Monthong' durian (Durio zibethinus)," *European Journal of Plant Pathology,* vol. 160, no. 2, pp. 325-336, 2021/06/01 2021, doi: 10.1007/s10658-021-02246-3.

[8] R. Pongpisutta *et al.*, "Comprehensive Investigation of Die-Back Disease Caused by Fusarium in Durian," *Plants,* vol. 12, no. 17, p. 3045, 2023. [Online]. Available: https://www.mdpi.com/2223-7747/12/17/3045.

[9] M. E. Gallegly and C. Hong, *Phytophthora: identifying species by morphology and DNA fingerprints*. APS Press, 2008.

[10] G. Wagner, V. D. Korenkov, J. D. Judy, and P. M. Bertsch, "Nanoparticles Composed of Zn and ZnO Inhibit Peronospora tabacina Spore Germination in vitro and P. tabacina Infectivity on Tobacco Leaves," *Nanomaterials,* vol. 6, 2016.

[11] P. A. Arciniegas-Grijalba, M. C. Patiño-Portela, L. P. Mosquera-Sánchez, J. A. Guerrero-Vargas, and J. E. Rodríguez-Páez, "ZnO nanoparticles (ZnO-NPs) and their antifungal activity against coffee fungus Erythricium salmonicolor," *Applied Nanoscience,* vol. 7, no. 5, pp. 225-241, 2017/06/01 2017, doi: 10.1007/s13204-017-0561-3.

EVALUATION AND PREDICTION OF RESISTANCE OF PLATE-LIKE HEAT EXCHANGERS MADE OF 06KhN28MDT ALLOY (ANALOGOUS TO AISI904L STEEL) TO CREVICE CORROSION IN RECYCLED WATER OF ENTERPRISES

Assistant Dzhus A.V.

Prof. Dr. Greshta V.L.

Prof. Dr. Pulina T.V.

Prof. Dr. Snizhnoi G.V.

Zaporizhzhia Polytechnic National University, Zaporizhzhia, **Ukraine**

ABSTRACT

The article develops one-dimensional linear regression mathematical models that establish the relationship between the activation potentials E_{crev}, repassivation E_{rep}, and corrosion E_{cor} of the 06KhN28MDT alloy used in the production of plate-like heat exchangers and its chemical composition and structure components in model recycled water. It has been found that the limiting potential Elim of the alloy shifted in the positive direction with an increase in the content of Cr, Mo, Si, S, the volume of titanium sulphides Vs, and a decrease in Mn. It has been found that its positive effect on Elim increased in the following order: S, Mo, Ti, Cr, Vs, Si. It is assumed that silicon, chromium, titanium, and molybdenum create mixed oxide films on the alloy surface that contribute to the repasivation of local corrosion damage in the gap between adjacent heat exchanger plates. It has been found that the corrosion potential of E_{cor} alloy shifted to the negative side with an increase in its Ni content and a decrease in Ti. It has been found that Ni increases and Ti decreases the alloy's resistance to crevice corrosion in chloride-containing media, since the higher the value of $\Delta E = E_{lim} - E_{cor}$, the higher it is. In general, it has been found that the higher the Ti content in the alloy, the higher its resistance to crevice corrosion in a chloride-containing media, since Ti has a 6-times stronger effect on the potential E_{lim} than E_{cor}. It has been found that the crevice corrosion potential of E_{crev} alloy shifted in the positive direction with an increase in the content of Cr and Ti and a decrease in C. It is assumed that Cr and Ti create mixed oxide films that effectively counteract the activating effect of chloride ions, and C creates carbides that activate local corrosion processes. The developed mathematical one-dimensional linear regression models are recommended for use in assessing and predicting the resistance of plate-like heat exchangers made of 06KhN28MDT alloy (analogue of AISI 904 L steel) to crevice corrosion in recycled water of enterprises.

Keywords: Plate-like heat exchanger made of 06KhN28MDT alloy, crevice corrosion of 06KhN28MDT alloy, recycled chloride-containing water of enterprises, selective dissolution of metals in localized corrosion damage.

https://doi.org/10.5593/sgem2024/6.1/s24.09

INTRODUCTION

Heat exchangers made of 06KhN28MDT alloy (analogous to AISI904L steel) are used in the production of sulfuric, orthophosphoric, hydrofluoric acid, etc., as this alloy is resistant to these media. Plate-like heat exchangers are most commonly used in the technological processes of enterprises, as they are more efficient than shell-andtube heat exchangers and have smaller overall dimensions. To cool the process product in the production of these acids, enterprises use water from recycling systems containing chloride ions and other local corrosion activators that can cause pitting or crevice corrosion of heat exchange equipment [1,2]. To predict the pitting resistance of heat exchangers made of 06KhN28MDT alloy in recycled water, phenomenological models were built in [3], which establish the relationship between the critical pitting temperatures (CPT) of the alloy and its chemical composition, components of the structure and parameters of model recycled water, and in [4,5], the correlation between the potentials of this alloy (E_{rep}, E_{pit}, E_{cor}) and its chemical composition and structural heterogeneity has been established. To predict and prevent pitting corrosion of heat exchangers made of AISI 304, 08Kh18N10 [6,7], AISI 321, 12Kh18N10T steels [8-10] and 06KhN28MDT alloy [11] in the recycled water of enterprises, we used the developed mathematical models based on multivariate regressions of various orders and neural models of direct signal propagation, that establish the relationship with the CPT of these steels and alloys and its chemical composition, structure components, and parameters of recycled water. This showed a positive result in the operation of heat exchangers at enterprises. However, plate-like heat exchangers under the same operating conditions can be subject to crevice corrosion in the gap (≈0.3 mm) between adjacent heat transfer plates. Coating the heat transfer plates of plate-like heat exchangers with composite [12] or nanostructured coatings [13] is a promising direction for solving this problem, but to date, they have positive results only at the stage of laboratory research. Therefore, the issue of predicting and preventing crevice corrosion of plate-like heat exchangers in the recycled water of enterprises remains relevant. The article develops mathematical models that establish the relationship between the potentials (E_{rep} , E_{crev} , E_{cor}) of the 06KhN28MDT alloy and its chemical composition and structure components in model recycled water. The established dependencies between them are recommended for assessing, predicting, and preventing crevice corrosion of plate-like heat exchangers made of 06KhN28MDT alloy in recycled water of enterprises.

MATERIALS AND METHODS

Five industrial melts of the cold-rolled alloy 06KhN28MDT has been studied. The chemical composition of its melts (Table 1) and structural heterogeneity previously have been determined [3]. Polished samples 30 × 20 × 10 mm with a hole ⌀6 mm in stacks have been collected. A gap of 0.3 mm (the size of the gap between adjacent plates of plate-like heat exchangers) was established between the sample and the counterbody, which was fixed with fluoroplastic washers. Electrochemical studies were performed on a potentiostat P5848, the setup included test samples made of 06KhN28MDT alloy, a counterbody made of the same alloy, a saturated chloride-silver comparison electrode, a Lugin capillary, an auxiliary platinum electrode, a potentiostat, a cathode voltmeter, microammeters, and a thermostat to maintain a temperature of ±1°C (Degree Celsius). Electrochemical studies were performed at room temperature ($20^{\pm1}$ °C (Degree Celsius)) in a 3% NaCl solution. Prior to polarization, the samples were kept in the solution for 10

minutes until the steady-state value of the corrosion potential E_{cor} was established and anodically polarized at a rate of 1.8 V/h. Potentiodynamic anode curves were taken up to a current density of 30 mA/cm^2, and the reverse curves were taken until the minimum cathodic currents have been recorded (0.005 mA/cm^2). The deviation of the activation potentials in the gap E_{crev} and the repassivation potential E_{rep} did not exceed ±0.01 V. The values of these potentials are given in Table 2.

Table 1 - Chemical composition of alloy 06KhN28MDT

Melt number	Content of alloying elements, wt. %									
	C	Si	Mn	Cr	Ni	Mo	Cu	Ti	S	P
1	0,050	0,60	0,32	24,31	27,39	2,90	2,75	0,79	0,006	0,029
2	0,067	0,57	0,46	22,68	27,65	2,78	2,68	0,59	0,005	0,027
3	0,068	0,55	0,54	21,84	27,45	2,55	2,60	0,55	0,004	0,038
4	0,048	0,62	0,57	22,67	27,73	2,56	2,53	0,67	0,006	0,028
5	0,050	0,57	0,31	23,46	27,51	2,51	2,78	0,89	0,004	0,032

Table 2 - Electrochemical parameters of 06KhN28MDT alloy

Potentials, V	Melts number of alloy				
	1	2	3	4	5
E_{cor}	-0,40	-0,43	-0,42	-0,40	-0,38
E_{crev}	+1,10	+0,58	+0,58	+1,10	+1,13
E_{rep}	+0,80	+0,50	+0,22	+0,55	+0,60

Multivariate linear regression as the basis for building mathematical models has been used [14]. The first-order multivariate linear regression equation is as follows:

$$y = \sum_{j=1}^{N} w_j x_j^s,\ s = 1, 2, \ldots, S, \quad (1)$$

y^S - the value of the initial characteristic for the *s-th* observation of the sample (E_{cor}, E_{crev}, E_{rep}) dependent variables, °C (Degree Celsius),

w_j is the weight of the *j-th* feature,

x_j^s - the value of the *j-th* characteristic of the *s-th* sample instance (independent variables), in particular x_1 - carbon (C) content, wt. %; x_2 - silicon (Si) content, wt. %; x_3 - manganese (Mn) content, wt. %; x_4 - chromium (Cr) content, wt. %; x_5 - nickel (Ni) content, wt. %; x_6 - molybdenum (Mo) content, wt. %; x_7 - copper (Cu) content, wt. %; x_8 - titanium (Ti) content, wt. %; x_9 - sulfur (S) content, wt. %; x_{10} - phosphorus (P) content, wt. % (Table 1); x_n - volume of titanium nitrides ($V_н$) (0.0931...0.1918, vol. %); x_{12} - volume of titanium sulfides (V_c), (0.0031...0.0091, vol. %); x_{13} - mean austenite grain diameter ($d_з$), (11...31 μm), S - number of sample specimens.

The quality of the model was assessed by the sum of squared instantaneous mistakes (2):

https://doi.org/10.5593/sgem2024/6.1/s24.09

$$E = \sum_{s=1}^{S} (y^s - y^{s*})^2 , \quad (2)$$

where: y^s – is the actual value of the output feature for the *s-th* observation of the training sample (Table 2);

y^{s*} – the estimated value of the output feature for the *s-th* observation of the training set.

The least squares method to determine the coefficients of linear regression models has been used [14].

RESULTS AND DISCUSSION

Based on the results of the analysis of the developed multifactorial linear mathematical model (3), it was found that the activation potential E_{crev} of the 06KhN28MDT alloy in the gap shifts to the positive side with an increase in the content of Cr (x_4), Ti (x_8), and a decrease in C (x_1)

$$E_{crev} = 0.61+0.08x_4 +0.58x_8 -9.27x_1 \quad (3)$$

According to model (3) and the data (Table 1), it was found that the potential E_{crev} of the 06KhN28MDT alloy in the model chloride-containing media shifts by 0.198 V to the positive side with an increase in its chromium content from 21.84 melt 3 to 24.31 wt. % melt 1. At the same time, it was found that it shifts to the positive side by 0.197 V with an increase in the titanium content from 0.55 melt 3 to 0.89 wt. % melt 5 (Table 1). It should be noted that under such conditions, the positive effect of Cr and Ti on the resistance of the 06KhN28MDT alloy to activation in the crevice is almost the same. This is most likely due to the fact that Cr and Ti create mixed oxide films on the alloy surface that better resist activation by chloride ions in the crevice. It should be noted that in chloride-containing media, Cr plays a major role in enhancing the protective properties of austenitic steels [7, 9], since studies [6-8] found that among all the chemical elements in the composition of AISI304, 08Kh18N10, 12Kh18N10T, and AISI321 steels, only Cr significantly increases the CPT of these steels in model recycled waters. At the same time, the role of Cr content in the steels was half that of the structure components, in particular, the mean austenite grain diameter and the mean distance between oxides in the vicinity of which pitting occurred and developed on the surface of AISI304 and 08Kh18N10 [6,15] and AISI321 and 12Kh18N10T steels [8,10]. At the same time, in [11], under the same test conditions, the opposite dependencies between the CPT of the 06KhN28MDT alloy and the Cr content and mean austenite grain diameter have been found. This is due to the fact that at such a concentration of chromium in the alloy, oxide films of Cr and Mo reduce the number of metastable pitting on its surface and thus contribute to the growth of the current density in the rest, facilitating its transition from a metastable to a stable state. A decrease in the mean diameter of the austenite grain increases the likelihood of inclusions intersecting with the boundaries of the alloy's austenite grains, which increases the number of metastable pitting on its surface and decreases the current density in more pits. This "inhibits" the transition of metastable pitting to stable pitting and increases the pitting resistance of the 06KhN28MDT alloy in model recycled water with a pH of 4...8 and a chloride concentration of 350 to 600 mg/L [11]. In the crevice between the tested samples, the corrosive chloride-containing media is more aggressive than the above with a higher chloride concentration and a much lower pH, so Cr and Ti create mixed oxide films that counteract the activation of the 06KhN28MDT alloy in an acidic chloride-containing media. Under such conditions, the negative effect of carbon in alloys

and steels is associated with a decrease in the overvoltage of hydrogen ionization on carbides that it forms with Cr, Ti, and Mo, which can contribute to its activation in chloride-containing media [3]. Most likely, this is why the potential E_{crev} of the 06KhN28MDT alloy in the crevice according to model (3) shifts to the negative side by 0.185 V with an increase in its carbon content from 0.048 wt.% of melt 4 to 0.068 wt.% of melt 3 (Table 1).

Summarizing the above, it can be noted that in an acidic chloride-containing media in the crevice, the negative effect of carbon on the activation of the 06KhN28MDT alloy is compensated by the positive effect of Cr and Ti, increasing the protective properties of the oxide films on it.

Based on the results of the analysis of the developed multifactorial mathematical model (4), which establishes the relationship between the repassivation potential E_{rep} of the 06KhN28MDT alloy in the crevice and its chemical composition and structure components, it was found that it shifts towards the positive side with an increase in the content of Cr (x_4), Ti (x_8), Mo (x_6), Si (x_2), S (x_9), the volume of titanium nitrides (x_{12}), and a decrease in Mn (x_3).

$$E_{rep} = -0.501+0.0185X_4+0.09X_8+0.065X_6+11.21X_2+1.31X_9+29.65X_{12}-0.095X_3; \quad (4)$$

From the analysis of the mathematical model (4) and the data (Table 1), it follows that the potential E_{rep} of the 06KhN28MDT alloy shifts in the positive direction by 0.046; 0.031; 0.023; 0.785; 0.003; 0.163V; with an increase in its Cr content from 21.84 melt 3 to 24.31 wt.% melt 1; Ti from 0.55 melt 3 to 0.89 wt.% melt 5; Mo from 2.51 melt 5 to 2.90 wt.% melt 1; Si from 0.55 melt 3 to 0.62 wt.% melt 4; S from 0.004 melt 3; 5 to 0.006 wt.% melt 1, 4 and the volume of titanium sulfides from 0.0036 melt 5 to 0.0091 vol.% melt 1[3] and in the negative direction by 0.025V with an increase in the Mn content from 0.31 melt 5 to 0.57 wt.% melt 4. Thus, the positive effect of alloy components on its ability to repassivation in the crevice increases in the following order: S, Mo, Ti, Cr, Si, and the volume of titanium sulfides. It should be noted that Si and Cr increase the ability of the 06KhN28MDT alloy to repassivation in the crevice the most among all chemical elements. In addition, Si has a 17.1 times higher value than Cr, but according to the mathematical model (3), Si in the alloy does not affect its activation resistance in the crevice at all, which is characterized by the potential E_{crev}. Most likely, this is due to the fact that Si does not create mixed oxide films of Cr, Ti, and Mo on the surface of the 06KhN28MDT alloy and local corrosion damage during its repassivation, but promotes its solid-phase diffusion to the surface. This hypothesis is also based on the significant positive effect of titanium sulfides on the ability of the alloy under study to repassivate in the crevice, since it is known [16, 17] that the nature of inclusions in steels and its volume affect its critical potential, which determines the direction of solid-phase diffusion of chemical elements in the vicinity of local corrosion damage and the processes of its repassivation or growth. These anodic processes are characterized by the peculiarities of selective dissolution of metals in localized corrosion damage, in particular, the solid-phase diffusion of metal atoms in the vicinity of inclusions where these damages occur is simplified [18], and Mn, which is less thermodynamically stable than Fe, dissolves selectively and accelerates its dissolution [19]. That is why, according to model (4), Mn contributes to a shift in the repassivation potential E_{rep} of the 06KhN28MDT alloy to the negative side and "inhibits" the repassivation of localized corrosion damage on its surface. It should be noted that the positive effect of sulfur on the repassivation ability of the

https://doi.org/10.5593/sgem2024/6.1/s24.09

06KhN28MDT alloy (4) is most likely due to the fact that it creates its sulfides with titanium, The much smaller total effect of the Ti and S content in the alloy on its repassivation potential E_{rep} than the volume of titanium sulfides shows that the selective dissolution of metals in the vicinity of these inclusions is supported by the simplified solid-phase diffusion of its atoms. Consequently, the defectiveness of the austenite structure has a greater effect on the E_{rep} potential of the alloy than Cr, Mo, and Ti. At the same time, it should be noted that the positive effect of Cr on the CPT of AISI304, 08Kh18N10[6], 12Kh18N10T, AISI321[8] steels and the negative effect of 06KhN28MDT alloy [11] in chloride-containing model recycled water is associated with the number of metastable pitting on its surface in the vicinity of inclusions of different nature, which can contribute to the repassivation of the majority, the growth of current density in the rest and its transformation into stable ones. It also depends on the protective properties of chromium-containing oxide films on its surface, in particular, in the 06KhN28MDT alloy they are higher than in steels [7,9], which contributes to a smaller number of metastable pitting on its surface, but a higher probability of its transition to a stable state due to higher density currents in them, and a decrease in its CPT, unlike these steels. Therefore, in our opinion, the positive effect of Cr on the repassivation potential E_{rep} of the 06KhN28MDT alloy in the crevice is associated with the formation of mixed oxides of Mo and Ti on the surface of local corrosion damage, which contribute to its repassivation. This is consistent with the data of [20] on the mechanisms of pitting of austenitic stainless steels in chloride-containing media.

Summarizing the above, it can be noted that Cr, Mo, and Ti contribute to the shift of the repassivation potential E_{rep} of the 06KhN28MDT alloy in the crevice to the positive side due to the creation of mixed oxide films on the surface of corrosion damage. Silicon contributes to the enrichment and Mn - to the depletion of its surface Cr, Mo and Ti, which affects the solid-phase diffusion of its atoms in the vicinity of localized corrosion damage, which usually forms near titanium sulfides. This determines the directions of solid-phase diffusion of Cr, Mo, and Ti atoms to the surface of localized corrosion damage in its vicinity, and Fe - in the opposite direction. This tendency contributes to the repassivation of localized corrosion damage on the alloy surface in the crevice.

According to the results of the analysis of the developed multifactorial linear mathematical model (5), which establishes the relationship between the corrosion potential E_{cor} of the 06KhN28MDT alloy and its components in the crevice, it was found that it shifts to the positive side with an increase in the Ti content and a decrease in Ni

$$E_{cor} = 0.95 + 0.03X_8 - 0.05X_5 \quad (5)$$

It should be noted that the minimum absolute value of the instantaneous mistake modulus for model (5) E_{min} is 0.0012 V, and E_{max} = 0.0098 V, E_{ev} = 0.0056 V, E_{sum} = 0.61 V. This model is quite suitable for assessing and predicting the potential E_{cor} of the 06KhN28MDT alloy in the crevice depending on the change in its components. It should be noted that, according to the data of the mathematical model (5), the structural heterogeneity of the 06KhN28MDT alloy does not affect its potential E_{cor} in the crevice. However, it shifts to the positive side by 0.01 V with an increase in the Ti content from 0.55 of melt 3 to 0.89 wt% of melt 5 and 0.017 V with a decrease in the Ni content from 27.39 of melt 1 to 27.73 wt% of melt 4. It turns out that even a small change in the Ni content in the studied alloy has a 1.7 times more intense effect on its E_{cor} in the crevice than a more significant change in the Ti content. At the same time, it should be noted that

it has a 3 times greater effect on the repassivation potential E_{rep} of the 06KhN28MDT alloy and a 19.7 times greater effect on its activation potential in the crevice E_{crev}. Thus, it can be noted that Ti mainly contributes to the resistance of the 06KhN28MDT alloy to local activation in the acidic chloride-containing media formed in the crevice [1] due to the formation of mixed Cr, Mo, and Ti oxide films on its surface, and its effect on the reparation of corrosion damage is almost an order of magnitude less. This is most likely due to a more aggressive corrosive media in localized corrosion damage than in the crevice between the sample and the counterbody.

The parameters $\Delta E = E_{rep} - E_{cor}$, or $\Delta E = E_{crev} - E_{cor}$ are used as additional criteria for assessing the resistance of steels and alloys to crevice corrosion in chloridecontaining media present in the crevice. The higher the values, the higher its resistance to crevice corrosion. Therefore, it turns out that Ti somewhat reduces this criterion by contributing to the shift of the corrosion potential E_{cor} of the 06KhN28MDT alloy in the positive direction (5), but, as mentioned above, it contributes to a much more intense shift of the potentials E_{rep} and E_{crev} in the positive direction, contributing to the growth of the ΔE criterion and the resistance of the alloy to crevice corrosion. Most likely, the negative effect of Ti on the resistance of 06KhN28MDT alloy to crevice corrosion due to the shift of the potential E_{cor} in the positive direction is associated with a decrease in the number of local corrosion damage on its surface in the metastable state, its repassivation and an increase in the current density in the remaining ones, which may contribute to its transition to a stable state, as mentioned in studies [20] for pitting corrosion, the mechanisms of which are similar to crevice corrosion.

Summarizing the above, it can be noted that Cr and Ti in the 06KhN28MDT alloy contribute to a positive shift in its activation potential in the crevice by creating mixed oxide films on its surface, while carbon, creating carbides in the acidic media in the crevice, causes the opposite effect.

Chromium, Mo, Ti, Si, and titanium sulfides contribute to the shift of the repassivation potential of the 06KhN28MDT alloy in the crevice to the positive side, and Mn to the negative side. This is due to the fact that Cr, Mo, and Ti create mixed oxides on the surface of localized corrosion damage in the crevice, contributing to their repassivation, while Si contributes to the enrichment and Mn to the depletion of its surface with these chemical elements.

Titanium helps to shift the corrosion potential E_{cor} of the 06KhN28MDT alloy to the positive side and Ni to the negative side, which affects the number of localized corrosion damage on its surface and its ability to repassivate.

CONCLUSION

We have developed multifactorial linear mathematical models of the first order that establish the relationship between the activation potentials E_{crev}, repassivation E_{rep}, and corrosion E_{cor} of the 06KhN28MDT alloy in a chloridecontaining media in the crevice and its components. The analysis of the developed mathematical models showed that the potential E_{crev} of the alloy in the crevice shifts to the positive side with an increase in the content of Cr, Ti and a decrease in C, which is due to the formation of mixed Cl, Ti oxide films on its surface and a decrease in the overvoltage of hydrogen ionization on carbides in the acidic chloridecontaining media formed in the crevice. It was found that the potential E_{rep} of the 06KhN28MDT alloy shifts to the positive side with an increase in the

https://doi.org/10.5593/sgem2024/6.1/s24.09

content of Cr, Mo, Ti, Si, S, the volume of titanium sulfides, and a decrease in Mn. This is due to the formation of mixed Cr, Mo, and Ti oxide films on the surface of localized corrosion damage and its repassivation. Silicon and titanium sulfides, in the vicinity of which they originate and develop, contribute to the enrichment of oxide films with these chemical elements, and Mn - to the depletion, given the known characteristics of selective dissolution of metals in local corrosion damage on the surface of stainless steels and alloys. It has been found that the potential E_{cor} of the 06KhN28MDT alloy shifts to the positive side with an increase in its Ti content and a decrease in Ni. Such an effect of Ti on E_{cor} somewhat reduces ΔE, the alloy criterion, affecting the repassivation and redistribution of currents in localized corrosion damage on its surface, but it shifts the potential E_{rep} to the positive side by 19.7 times more intensively than E_{cor}. This contributes to an increase in this criterion and an increase in the alloy's resistance to crevice corrosion. The developed mathematical models are used to evaluate and predict the resistance of plate-like heat exchangers made of 06KhN28MDT alloy to crevice corrosion in the recycled water of enterprises.

REFERENCES

[1] Narivs'kyi O.E. Micromechanism of corrosion fracture of the plates of heat exchangers, Materials Science, 2007, 43(1), p. 124-132. DOI: https://doi.org/10.1007/s11003-007-0014-3.

[2] Narivs'kyi O.E. Corrosion fracture of plate-like heat exchanger, Fiz.-Khim. Mekh. Mater., 2005, 1 (41), p. 104-108.

[3] Narivs'kyi O.E., Belikov S.B. Pitting resistance of 06KhN28MDT alloy in chloride-containing media. Materials Science, 2008, 44 (4), pp. 573-580. DOI: https://doi.org/10.1007/s11003-009-9107-5.

[4] Narivskiy A., Temirgaliyeva. E., Mukhtarova M. and Yar-Mukhamedov Y. Corrosion losses of alloy 06KhN28MDT in chloride-containing commercial waters, International Multidisciplinary Scientific GeoConference Surveying Geology and Mining Ecology Management: SGEM. 2016, 1, pp. 63–70.

[5] Narivskiy A., Atchibaev R., Muradov A., Mukashev K., Yar-Muchamedov Y. Investigation of electrochemical properties in chloride-containing commercial waters, International Multidisciplinary Scientific GeoConference Surveying Geology and Mining Ecology Management, SGEM, 2018, 18 (6.1), pp. 267-274. DOI: 10.5593/sgem2018/6.1/S24.036.

[6] Narivskyi O.E., Subbotin S.A., Pulina T.V. and Khoma M.S. Assessment and Prediction of the Pitting Resistance of Plate-Like Heat Exchangers Made of AISI304 Steel and Operating in Circulating Waters. Materials Science, 2022, 58, pp. 41–46. DOI: https://doi.org/10.1007/s11003-022-00628-4.

[7] Narivs'kyi O., Atchibayev R., Kemelzhanova A., Yar-Mukhamedova G., Snizhnoy G., Subbotin S., Beisebayeva A. Mathematical modeling of the corrosion behavior of austenitic steels in chloride-containing media during the operation of plate-like heat exchangers, Eurasian Chemico-Technological Journal, 2022, Vol. 24. No. 4, pp. 295-301. DOI: https://doi.org/10.18321/ectj1473

[8] Narivskyi O.E., Belikov S.B., Subbotin S.A. Influence of Chloride-Containing Media on the Pitting Resistance of AISI321 Steel, Materials Science, 2021, 57(2), pp. 291-297. DOI: https://doi.org/10.1007/s11003-021-00544-z.

[9] Narivs'kyi O.E., Subbotin S.O., Leoshchenko S.O., Khoma M.S., Ratska N.B. Modeling of pitting of heat exchangers made of 18/10 type steel in circulating waters, Materials Science, 2023, 58(5), pp.1-7. DOI: https://doi.org/10.1007/s11003-023-00725-y.

[10] Narivs'kyi O.E. The influence of heterogeneity steel AISI321 on its pitting resistance in chloride - containing media, Materials Science, 2007, 2 (43). pp. 256-264. DOI: https://doi.org/10.1007/s11003-007-0029-9.

[11] Dzhus A., Subbotin S., Pulina T., Leoshchenko S., Sniznoi G. Evaluation and prediction of pitting resistance of heat exchangers made of alloy 06KhN28MDT (similar to AISI904L steel) to crevice corrosion. Book Proceedings of 23rd International Multidisciplinary Scientific GeoConference SGEM 2023, 2023, Vol. 23. issue. 6.1, pp. 25-34. https://doi.org/10.5593/sgem2023/6.1/s24.03

[12] G. Yar-Mukhamedova, A. Muradov, K. Mukashev, G. Ismailova, Y. Yar-Mukhamedov. Mathematical model of composite materials formation, Int. Multidisc. Sc. GeoConf. SGEM, 2017, 17(61), pp. 201–208. DOI: 10.5593/sgem2017/61/S24.027

[13] Yar-Mukhamedova, G., Ved', M., Yermolenko, I., Karakurkchi, A., Kemelzhanova, A. Effect of electrodeposition parameters on the composition and surface topography of nanostructured coatings by tungsten with iron and cobalt, Eurasian Chemico-Technological Journal, 2020, 22(1), pp. 19–25. DOI: 10.18321/ectj697

[14] Freedman D.A. Statistical models: theory and practice, Cambridge University Press, 2009, 442 p. https://doi.org/10.1017/CBO9780511815867

[15] Narivs'kyi O.E. Corrosion fracture of platelike heat exchangers, Materials Science, 2005, 41(1), pp. 122–128. https://doi.org/10.1007/s11003-005-0140-8

[16] Mishchenko V. G., Snizhnoi G. V., Narivs'kyy O. Eh. Magnetometric investigations of corrosion behaviour of AISI 304 steel in chloride-containing environment, Metallofizika i noveishie tekhnologii, 2011, 33(6), pp. 769–774.

[17] Pickering H.W. Characteristic features of alloy polarization curves. Corrosion Science, 1983, Vol. 23, Issue 10, pp. 1107-1109, 1111-1120. https://doi.org/10.1016/0010-938X(83)90092-6

[18] Fritz J.D., Pickering H.W. Selective anodic dissolution of Cu-Al alloys: TEM and current transient study, Electrochem. Soc., 1991, Vol. 11, pp. 3209-3219.

[19] Pourbaix M., De Zoubov N. Atlas of electrochemical equilibrium in aqueous solutions, Oxford: Pergamon press, 1966. 493 p.

[20] Narivs'kyi O.E., Subbotin S.O., Pulina T.V., Khoma M.S., Ratska N.B. Mechanisms of Pitting Corrosion of Austenitic Steels of Heat Exchangers in Circulating Waters and its Prediction, Materials Science, 2023, 59(3), pp. 275–282.

https://doi.org/10.5593/sgem2024/6.1/s24.09

POLYLACTIC ACID/ZINC OXIDE NANOSTRUCTURED FIBROUS MATERIAL BY NEEDLELESS ONE SOLVENT ELECTROSPINNING FOR PROTECTION AGAINST TICK-BORNE DISEASES

Liga Rampane[1]
Zane Zelca[1]
Chaima Salmi[2]
[1] Riga Technical University, Institute of Architecture and Design, **Latvia**
[2] El-Oued University, Faculty of Technology**, Algeria**

ABSTRACT

Ticks (*Ixodidae* and *Argasidae*) pose significant health risks as vectors for infectious diseases, with their prevalence expanding across Europe and North America. Ticks employ sophisticated sensory mechanisms, notably utilizing Haller's organs, to locate and sense their hosts. These sensory structures detect various cues, including chemosensation, changes in atmospheric CO_2 concentration, and radiant heat emitted by potential hosts. Once a host is detected, landing is facilitated by electrostatic attraction, accelerating the precise positioning of the tick for feeding.

Reports indicate that ZnO nanoparticles exhibit acaricidal activity. The strong thermal and electrical conductivity of ZnO may effectively impede tick host-seeking mechanisms. This study focuses on fabricating ZnO-containing nanostructured polylactic acid (PLA) fiber material for tick repellency.

In this research, acetone, chosen for its low toxicity and compatibility with natural acaricides, is utilized in a single-solvent system to produce nanofibers with long-lasting acaricidal properties. Successful electrospinning of acetone-based systems has been limited to needle electrospinning. Here, we present a method employing needleless electrospinning to fabricate ZnO nanoparticle-loaded PLA nanofibers by using pike-type electrode.

The PLA-ZnO solutions were characterized by density, conductivity, viscosity, and other parameters, while the resulting fiber mats underwent analysis via FTIR, SEM, and evaluation of thermal conductivity. Optimization of spinning parameters including critical voltage, collector distance, and environmental factors such as temperature and humidity was conducted.

Our study demonstrates the creation of PLA-ZnO fibers in a single solvent system through needleless electrospinning. Obtained membranes contain 1-3 wt% ZnO within an 8-10 wt% PLA matrix solution and exhibit heightened electrical conductivity. This advancement underscores the potential of ZnO in tick-repellent materials and strategies against tick-borne diseases.

Keywords: electrospinning, single-solvent, ZnO nanoparticles, ticks, repellent

https://doi.org/10.5593/sgem2024/6.1/s24.12

INTRODUCTION

The primary risks associated with ticks are insect-borne infectious diseases such as tick-borne encephalitis and Lyme disease, as well as the risk of anaphylactic shock caused by allergies.
While ticks cannot directly see their host; they possess light receptors capable of perceiving contrasting silhouettes and movement resulting from changes in light [1].
Ticks can determine the location of their host from a distance using a complex anatomical structure - Haller's organ, located at the base of the tick's front legs and unique to animals of the *Acari* class [2]. The function of Haller's organ is associated with chemical sensitivity, specifically olfactory sensitivity. Haller's organs also contain heat-sensing receptors, which can detect the potential presence of a host from a distance of up to 50 cm [1]. Contrary to common belief, ticks do not jump onto their hosts; rather, they are dislodged from grass or foliage when a host passes by, either due to the movement of the host's fur or aided by static electricity, which can passively draw ticks onto the host's fur from a distance greater than several times the tick's body length. The magnitude of this charge is 752 ± 679 pC (mean ± SD, N = 20) [3].
In recent years zinc oxide (ZnO) has garnered significant attention in a field of passive radiative cooling due to its high emissivity in the atmospheric window wavelength range [4], high refractive index $n \approx 2$ [4], [5], little absorption from visible to NIR wavelengths [5]. ZnO also exhibits semiconducting properties, large surface to volume ratio and high thermal and chemical stability [6] and acaricidal activity [7], [8]. Collectively, these properties underscore its potential to impact tick host-seeking mechanisms.

Herbal extracts were prepared from Indian Neem tree (*Azadirachta indica*) leaves which contain Azadirachtin. It is a complex tetranortriterpenoid, which is one of the most prominent biopesticides, with low mammalian toxicity [9] and carries the potentials to replace synthetic insecticides, of which acaricide resistance in some tick populations is reported [10].

Polylactic acid (PLA) was selected for the fiber matrix and the active ingredient carrier due to its high mechanical strength, hydrophobicity, biocompatibility, and future prospects of becoming a low-carbon material, while being biodegradable bio-based polymer [11]. For polymer solution preparation, acetone is chosen as it is an accessible and comparatively green solvent [12], compared to solvents that are typically used in binary and tertiary systems for PLA dissolution.

The electrospinning method enabled the incorporation of a variety of active ingredients into different polymer fiber structures. The aim of this research was to evaluate PLA-ZnO biocomposites for further investigation of their acaricidal efficiency.

MATERIALS AND METHODS

Materials

Polylactic acid in a form of 3D printing filament (color: natural, D = 1.75 mm) was obtained from Spectrum Group Sp. z.o.o. Acetone manufactured by OKKO, (EC number: 200-662-2) was used for the basic PLA solution preparation.
Additive materials - ZnO nanopowder was purchased from Nanjing High Technology Nano material Co., Ltd.; 99.5% purity; D = 20 nm. Neem leaf powder was obtained from Herbals Diet™ (labelled SI-EKO-003 Non-EU Agriculture).

Neem leaf extract preparation

The Neem leaf – acetone extract (NEA) was obtained in laboratory by mixing neem leaf powder and acetone and magnetic stirring (Lab Logistics Group LLG-uniSTIRRER) with 300 RPM at 57 °C for 1h. The mixture was cooled to a room temperature and set in a sealed jar at the dark in a 21±2 °C for 10 days. The majority of powder particles were separated by centrifugation (Ohaus Frontier 5816) with 2000 RPM for 20 min. Finally, the extract was filtered through 10±2 nm filter.

PLA, PLA/ZnO and PLA/ZnO/NEA solutions preparation

PLA basic solutions were prepared from a PLA 3D printing filament by mechanically graining the filament and completely dissolving in acetone at 57 °C with magnetic stirring of 300 RPM. The polymer concentration in basic solution was 8 wt%.
To prepare the PLA/ZnO solutions, ZnO nanoparticles were added at 1, 3 and 5 wt% based on the solution weight.
To prepare the PLA/ZnO/NEA solution, the weight of the PLA solution containing 3 wt% ZnO was reduced by 10% and then substituted with NEA.
Both PLA/ZnO and PLA/ZnO/NEA solutions were magnetically stirred with 300 RPM at 57 °C. As a final step the mixed solutions were processed using an ultrasound mixer (Hielscher UP200H) for 30 minutes with a cycle of 0.5 and an amplitude of 80%.

Solution parameters

A successful single solvent PLA-Acetone electrospinning using needle at 10 wt% has been reported [13]. Here, experimentally it was observed that the least interrupted process using needle-less electrospinning was with using 8 wt% polymer solution, therefore this concentration was chosen for the further experiments. ZnO was incorporated at concentrations of 1 wt%, 3 wt% and 5 wt% of the 8PLA solution and respective solution designations assigned are presented in Table 1.

Table 1. Electrospinning solution parameters

Sample	8PLA	1ZnO8PLA	3ZnO8PLA	5ZnO8PLA	3ZnO8PLA-NEA
PLA wt%	8	8	8	8	8
ZnO wt%	0	1	3	5	3
NEA wt%	0	0	0	0	10
Conductivity, µS/cm	0	9	13	16	16
Density, kg/m^3	815	814	830	836	822
Viscosity, cSt	52	55	50	48	31

Electrospinning parameters

Electrospinning was carried out with an Elmarco NS LAB 200 machine, using pike-type electrode. The distance between electrodes was 11 cm. Electrospinning was carried out in a controlled climate of temperature of 21 ± 1 °C and relative humidity of 26 ± 1 °C. Fibers were spun at the voltage of 16-20 kV onto a fixed nonwoven polypropylene support material (30 g/m^2).

Material characterization

FTIR analysis of four specimens was conducted using a Bruker Tensor II with 10 measurements, each consisting of 31 scans. Surface morphologies of all membranes were observed using a Verios 5 UC scanning electron microscope, and diameters of 100 fibers per sample were measured with ImageJ software. X-ray diffraction (XRD) analysis of the

https://doi.org/10.5593/sgem2024/6.1/s24.12

ZnO-containing membranes and pure ZnO was performed using a Rigaku Ultima X-ray diffractometer.

RESULTS

FTIR analysis

The FTIR results (Fig. 1) indicate the presence of characteristic peaks for both PLA and ZnO in the fabricated nanofiber materials. The observed peaks for PLA correspond to its known vibrational modes: 873 cm^{-1} (C–O–C stretching) [14], 1082 and 1180 cm^{-1} (C-O stretching) [15], 1453 cm^{-1} (CH bending) [16], 1648 cm^{-1} (C=O stretching) [17], 3002 cm^{-1} (C-H stretching) [18], and 3380 cm^{-1} (O-H stretching) [19]. These peaks confirm the presence of PLA within the nanofibers.
Additionally, peaks corresponding to ZnO are observed at 523 cm^{-1} (Zn-O stretching), indicative of the presence of ZnO nanoparticles in the nanofiber material. The presence of these peaks confirms the successful incorporation of ZnO into the PLA matrix.
Interestingly, the spectra of 3ZnO8PLA exhibit shorter peak heights compared to the 1ZnO8PLA. This observation could suggest changes in the molecular environment or interactions within the nanofiber structure at higher ZnO concentrations. The decrease in peak intensity at higher ZnO concentrations may indicate potential alterations in the crystallinity or dispersion of ZnO nanoparticles within the PLA matrix. At higher concentrations, ZnO nanoparticles might start to aggregate or affect the polymer chain mobility, leading to changes in molecular interactions and consequently affecting the observed FTIR peaks.

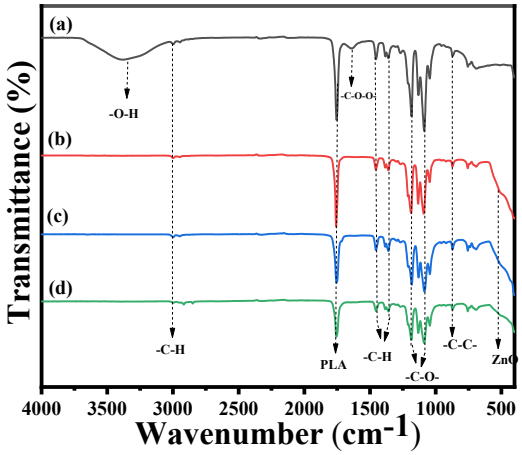


Figure 1. FTIR spectra of a) 8PLA; b) 1ZnO8PLA; c) 3ZnO8PLA; d) 3ZnO8PLA-NEA

SEM analysis

SEM images reveal uneven fiber morphology with most of diameters below 382 nm and elongated beads in 8PLA sample (Fig. 2a). Upon the addition of 1 wt% ZnO nanoparticles to spinning solution, a reduction in bead size and fiber diameter is evident, with a maximum diameter of 356 nm observed (Fig. 2b). Conversely, the incorporation of 3% ZnO (Fig. 2c) leads to an increase in diameter, reaching 430 nm, and the presence of uneven fiber shapes suggests particles embedded within fibers, some forming agglomerates. In contrast, 5 wt% ZnO additive (Fig. 2d) notably decreases the fiber

diameter with most fibers below 143 nm, but an excessive amount of agglomerates is present. Sample with the NEA additive (Fig. 2e) shows relatively moderate fiber sample diameter mostly being below 286 nm, ZnO is visibly incorporated, but agglomerates are present. It was observed that the additive of NEA appears to influence fiber shape, tending to flatten it.

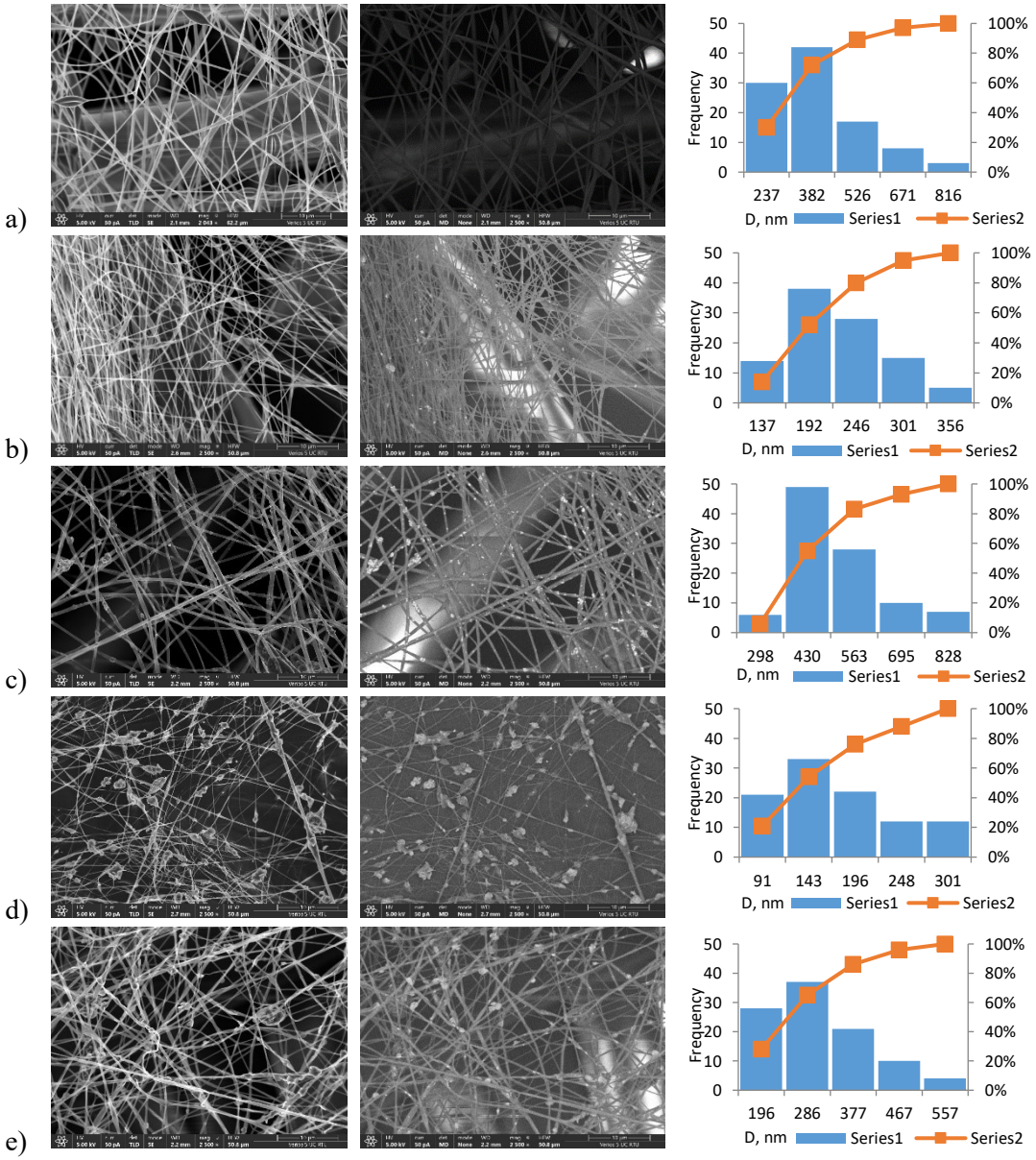


Figure 2. Morphology of fiber surface and ZnO NP's in fiber volume, and diameter distribution of nanofibers: a) 8PLA; b) 1ZnO8PLA; c) 3ZnO8PLA; d) 5ZnOPLA; e) 3ZnO8PLA-NEA

XRD analysis

The XRD analysis revealed distinctive patterns (Fig. 3) for both pure ZnO nanoparticles and 3ZnO8PLA. The peaks observed at 2θ values of 31.7°, 34.4°, 36.2°, 47.5°, 56.5°, 63.01°, 66.5°, 68.1°, 69.3°, 72.7°, and 77.2° corresponded to crystallographic planes (1 0 0), (0 0 2), (1 0 1), (1 0 2), (1 1 0), (1 0 3), (2 0 0), (1 1 2), (2 0 1), (0 0 4), and (2 0 2), respectively, affirming the hexagonal crystal structure of ZnO nanoparticles, as supported

https://doi.org/10.5593/sgem2024/6.1/s24.12

by JCDPS Card N°. (01-075-0576). Furthermore, in the XRD spectrum of the 3ZnO8PLA, the peaks corresponding to ZnO NPs are still discernible but with decreased intensity compared to the pure ZnO NPs spectrum. This reduction in peak intensity suggests a potential interaction or incorporation of ZnO nanoparticles within the PLA matrix, altering the crystallinity or orientation of the ZnO crystallites. Notably, two additional peaks emerge at 2θ values of 14.2° and 17.01° in the 3ZnO8PLA spectrum. These new peaks indicate potential changes in the crystalline structure or arrangement of the PLA matrix induced by the presence of ZnO nanoparticles. These findings suggest promising structural characteristics for the synthesized materials, which may have implications for their performance in tick repellency applications and warrant further investigation into their crystalline behavior and interactions within the composite matrix.

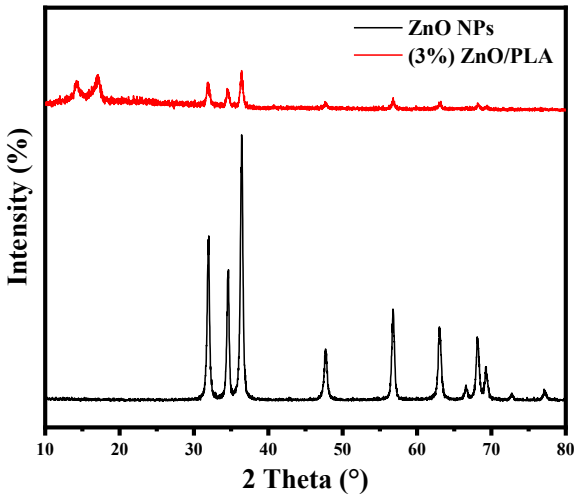


Figure 3. XRD of ZnO NPs and the composite 3ZnO8PLA

CONCLUSIONS

This study presents the synthesis and characterization of PLA-based nanofibers loaded with ZnO nanoparticles and NEA additive, offering potential applications in tick repellency. The observed alterations in FTIR spectra, corresponding to varying ZnO concentrations, indicate intricate molecular interactions between ZnO nanoparticles and the PLA matrix. This suggests potential modifications in the material's chemical environment and structure, supported by the emergence of new peaks in the XRD spectrum and SEM images depicting fibers with incorporated NPs. Incorporating 1% ZnO NPs into the electrospinning solution enhances solution conductivity and improves fiber quality, reducing the average diameter to 199 nm. However, higher concentrations of the ZnO additive lead to NP agglomerations within the fiber mat. Further investigations of the synthesized biomaterial are necessary to assess its acaricidal activity.

ACKNOWLEDGEMENTS

This research is co-financed by Riga Technical university within the project “Insect repellent containing textile material” No. 04000-1.3-e/23 | ZM-2023/13 | 4816.

REFERENCES

[1] Carr, A. L., & Salgado, V. L. (2019). Ticks home in on body heat: A new understanding of Haller's organ and repellent action. *PloS One*, *14*(8), e0221659. https://doi.org/10.1371/journal.pone.0221659.

[2] Gebremedhin, M. B., Xu, Z., Kuang, C., Shumuye, N. A., Cao, J., Zhou, Y., Zhang, H., & Zhou, J. (2023). Current knowledge on Chemosensory-Related candidate molecules potentially involved in tick olfaction via Haller's organ. Insects, 14(3), 294. https://doi.org/10.3390/insects14030294.

[3] England, S. J., Lihou, K., & Robert, D. (2023). Static electricity passively attracts ticks onto hosts. CB/Current Biology, 33(14), 3041-3047.e4. https://doi.org/10.1016/j.cub.2023.06.021.

[4] Liang, L., Bai, S., Lin, K., Kwok, C. T., Chen, S., Zhu, Y., & Tso, C. Y. (2024b). Advancing Sustainable Development: Broad applications of passive radiative cooling. *Sustainability*, *16*(6), 2346. https://doi.org/10.3390/su16062346.

[5] Cai, L., Song, A. Y., Li, W., Hsu, P. C., Lin, D., Catrysse, P. B., Liu, Y., Peng, Y., Chen, J., Wang, H., Xu, J., Yang, A., Fan, S., & Cui, Y. (2018a). Spectrally selective nanocomposite textile for outdoor personal cooling. Advanced Materials, 30(35). https://doi.org/10.1002/adma.201802152.

[6] Shirley, J. A., Florence, S. E., Sreeja, B. S., Padmalaya, G., & Radha, S. (2020). Zinc oxide nanostructure-based textile pressure sensor for wearable applications. Journal of Materials Science. Materials in Electronics, 31(19), 16519–16530. https://doi.org/10.1007/s10854-020-04206-9.

[7] Norouzi, R., Ataei, A., Hejazy, M., & Shahbazi, P. (2019b). Acaricidal activity of zinc oxide nanoparticles against Hyalomma spp. in vitro. DOAJ (DOAJ: Directory of Open Access Journals). https://doi.org/10.22034/nmrj.2019.04.005.

[8] Gandhi, P. R., Jayaseelan, C., Mary, R. R., Mathivanan, D., & Suseem, S. (2017b). Acaricidal, pediculicidal and larvicidal activity of synthesized ZnO nanoparticles using Momordica charantia leaf extract against blood feeding parasites. Experimental Parasitology, 181, 47–56. https://doi.org/10.1016/j.exppara.2017.07.007.

[9] Kilani-Morakchi, S., Morakchi-Goudjil, H., & Sifi, K. (2021b). Azadirachtin-Based Insecticide: Overview, risk assessments, and future directions. Frontiers in Agronomy, 3. https://doi.org/10.3389/fagro.2021.676208.

[10] Quadros, D. G., Johnson, T. L., Whitney, T. R., Oliver, J. D., & Chávez, A. S. O. (2020). Plant-Derived Natural Compounds for tick pest control in livestock and wildlife: pragmatism or utopia? Insects, 11(8), 490. https://doi.org/10.3390/insects11080490.

[11] Wu, Y., Gao, X., Wu, J., Zhou, T., Nguyen, T. T., & Wang, Y. (2023b). Biodegradable polylactic Acid and its composites: characteristics, processing, and sustainable applications in sports. Polymers, 15(14), 3096. https://doi.org/10.3390/polym15143096.

[12] Tobiszewski, M. (2016b). Metrics for green analytical chemistry. Analytical Methods, 8(15), 2993–2999. https://doi.org/10.1039/c6ay00478d.

https://doi.org/10.5593/sgem2024/6.1/s24.12

[13] Casasola, R., Thomas, N., Trybala, A., & Georgiadou, S. (2014). Electrospun poly lactic acid (PLA) fibres: Effect of different solvent systems on fibre morphology and diameter. Polymer, 55(18), 4728–4737. https://doi.org/10.1016/j.polymer.2014.06.032.

[14] Salmi, C., Laouini, S. E., Meneceur, S., & Mohammed, H. A. (2024b). Biosynthesized MgO@SnO2 nanocomposite and their modification with polyvinylpyrrolidone. Efficiency for removal of heavy metals and contaminants from industrial petroleum wastewater. Clean Technologies and Environmental Policy. https://doi.org/10.1007/s10098-024-02766-6.

[15] Heydari-Majd, M., Ghanbarzadeh, B., Shahidi-Noghabi, M., Abdolshahi, A., Dahmardeh, S., & Mohammadi, M. M. (2020). Poly(lactic acid)-based bionanocomposites: effects of ZnO nanoparticles and essential oils on physicochemical properties. Polymer Bulletin, 79(1), 97–119. https://doi.org/10.1007/s00289-020-03490-z.

[16] Boutalbi, A., Mohammed, H. A., Meneceur, S., Eddine, L. S., Abdullah, J. a. A., Alharthi, F., & Hasan, G. G. (2023b). Photocatalytic dye degradation efficiency and reusability of potassium polyacrylate hydrogel loaded Ag@ZnO nanocomposite. Transition Metal Chemistry, 48(5), 353–363. https://doi.org/10.1007/s11243-023-00548-5.

[17] Mohammed, H. A., Eddine, L. S., Souhaila, M., Hasan, G. G., Kir, I., & Abdullah, J. a. A. (2023). Green Synthesis of SnO2 Nanoparticles from Laurus nobilis L. Extract for Enhanced Gelatin-Based Films and CEF@SnO2 for Efficient Antibacterial Activity. Food and Bioprocess Technology, 17(5), 1364–1382. https://doi.org/10.1007/s11947-023-03209-8.

[18] Chai, M. N., & Isa, M. I. N. (2013b). The oleic acid composition effect on the carboxymethyl cellulose based biopolymer electrolyte. Journal of Crystallization Process and Technology, 03(01), 1–4. https://doi.org/10.4236/jcpt.2013.31001.

[19] Mohammed, H. a. M., Souhaila, M., Eddine, L. S., Hasan, G. G., Kir, I., & Mahboub, M. S. (2023). A novel biosynthesis of MgO/PEG nanocomposite for organic pollutant removal from aqueous solutions under sunlight irradiation. Environmental Science and Pollution Research International, 30(19), 57076–57085. https://doi.org/10.1007/s11356-023-26422-6.

RESEARCH OF THE PROTECTION OF CHILDRENS RESPIRATOTY TRACTS WITH THE AIM OF ESTABLISHING STANDARDS FOR THE PRODUCTION OF CHILDRENS RESPIRATORS USING NANOMATERIALS

Ing. Ruzena Langova[1]

Ing. Melanie Barabasova[1]

doc. Ing. et Ing. Karel Klouda, CSc., Ph.D.[1,2]

[1] Faculty of Safety Engineering, VSB Technical University of Ostrava, **Czech Republic**
[2] Occupational Safety Research Institute (OSRI), **Czech Republic**

ABSTRACT

There are situations in which human health is at risk from inhalation of hazardous substances and particles (viral epidemics, biological weapons, chlorine leaks, nuclear accidents, asbestos removal, quarrying). In response to these scenarios, emphasis is placed on respiratory protection and minimising exposure to these substances and particles. One of the most commonly used respiratory protective devices is respirators. However, respiratory protection for children is not addressed by any manufacturing or testing technical standard. There are children's respirators on the market that are rather scaled-down versions of adult respirators. Yet there is a very significant difference between these target groups in terms of body morphology and respiratory physiology. Therefore, there is an urgent need to develop a standard that precisely defines the requirements for respirators intended for children to ensure effective protection of their airways. Based on the research carried out, four groups of sizes of children's respirators were proposed using existing standards, taking into account the requirements of the child user.

Keywords: children's respirators, lung capacity, material, respirator sizes, prototype design

INTRODUCTION

The respiratory tract provides viruses with the basic conditions necessary for reproduction, as they are unable to continue to exist on their own. Viruses can be transmitted by touching where droplets of virus have landed, which may contain a very small space, invisible to the eye, with virus dimensions in nanometres (nm). Droplets that fly out when coughing or sneezing, multiplying viruses in the body, can also create micrometer-sized viruses. [1]

Thus, a suitable protection option should be a barrier that prevents the virus from entering the respiratory tract, whether it is from the person spreading the virus or also for people inhaling ambient air. This kind of protection is provided by protective devices called respirators. The devices are able to clean the air we breathe in or out by trapping aerosol droplets containing viruses. [1]

https://doi.org/10.5593/sgem2024/6.1/s24.13

The basic requirements for respiratory protective masks according to the test standard CSN 17553:2022 are that the protective masks must not show any visible defects such as cracks or deformations and must be fitted with a means of attachment around the head or ears. Protective masks shall be adapted to the minimum dimensions of the wearer so that they always cover the critical zone of the nose, mouth and chin. The dimensions given in CEN/TS 17553:2022 will serve as a model for anthropometric data in future design. The quality of the porous material used for the manufacture of protective masks is indicated by the filtration efficiency category, but may not be indicative of the useful protective efficiency. A material with a high filtration efficiency alone does not guarantee overall protective effectiveness unless it meets the appropriate face seal. [1]

The amount of air in each breath is affected by the size of the lung volume. The average volume of air inhaled by the average adult is 6 litres. In children, this value is considerably lower. Thus, this parameter must be taken into account in the manufacture of protective masks. [2]

MATERIALS AND METHODS

The topic of lung vital capacity in children has not yet been evaluated in detail. In the literature it is reported that the average values of lung vital capacity are around 4 litres (l). A trained person reaches 5 to 7 litres. [4] The value of pulmonary vital capacity in children is not reported, what some foreign sources, in which lung capacity in children has been addressed, report a value from 0.1 l to 2 l (in children from one year to 14 years of age). The range of the size of the vital capacity of the lungs in children depends not only on their age but mainly on their body proportions such as weight and height. Physical activity also has an effect on lung capacity, and a gradual increase in lung capacity is possible, especially in water sports (but also in other aerobic exercises).

The "Balloon method", which relies on the principle of inhaling and exhaling fully into a balloon, is used to measure vital lung capacity and has been used for various measurements. According to the volume of exhaled air (one inhalation and exhalation) in the balloon, the vital capacity of the lungs of a person is determined. It is basically the amount of air your lungs can expel in one breath. [5]

To measure the vital capacity of the lungs without hands-on measurement, this data can be determined based on the person's height in centimetres and the person's age in years. Due to the impracticality of finding these data in practice, for the purposes of this article, values were calculated based on the variability of height in children of the same age. Using the average values, the children's vital lung capacity values in litres of air were determined for the given age groups. [5]

The calculation of the vital capacity of the lungs is performed using the following equation:

$$V = 0.041*h - 0.018*a - 2.69$$

V - vital lung capacity in litres of air

h - height in centimetres

a - age in years [5]

The used values were entered into a formula, based on which we found the data of vital lung capacity in children according to their average height and age.

Using data determined by calculating the vital capacity of the lungs in children aged 1 to 15 years, it is possible to assess that the vital capacity of the lungs in children ranges from 0.36 l to 4 l of air. Children older than 15 years are no longer young children. At this teenage age, adult-sized respirators can be used for them. Information on the vital capacity of children's lungs is a useful means of selecting suitable materials for the manufacture of respirators for children, taking into account inspiratory and expiratory resistance, and the correct material with satisfactory breathability can be designed.

RESULTS

The design of multiple sizes of protective masks - respirators for children is based mainly on practical considerations. Considering the diversity of faces, age interface, it is of course very important to have an exact fitting size in order to achieve higher protection (especially the fit of the prototypes). As an example, we could give a three year old preschooler and a thirteen year old school child, where the difference between these two children would be huge.

Four sizes of masks were designed for the purpose of practical implementation in production. These were divided into groups according to age. Approximate sizes for children between the ages of 1 and 15 years were suggested based on the observed values. For newborn children up to children over two years of age, the use of protective bags was assumed, and this subject has been dealt with in the past by Jiří Slabotinský, who provided his materials to broaden the horizon. [1]

The first group we can call group A. It consists of children from 3 to 5 years of age, and in this group the range of vital lung capacity according to the above calculation is estimated at 1.233 – 1.833 litres. The vital capacity of the lungs for the second group, group B, is determined to be in the range of 1.833 – 2.724 litres and includes the group of children from 6 to 9 years of age. Group C, which includes the group of children aged 10 to 12 years, has a lung vital capacity value of 2.724 to 3.388 litres. The last group is group D, comprising children aged 13 to 15 years with a range of vital lung capacity from 3.388 to 4.010 litres. This is summarised in Table 1 below.

Table 1 Overview of the proposed size distribution of children's respirators (author)

Group	Age range [years]	Vital lung capacity range [l]
A	3-5	1.23 – 1.83
B	6-9	1.83–2.72
C	10-12	2.72 – 3.38
D	13-15	3.38 – 4.01

In order to establish a design standard for the manufacture of children's respirators, it is necessary to prepare prototypes of the so-called "hooves", which will be designed in four sizes, which are described in detail in Table 1.

https://doi.org/10.5593/sgem2024/6.1/s24.13

The public face shield shall be designed and manufactured to meet the requirements for use by children. The face and head size ranges are shown in Figure 1 and are used as a guide." [7]

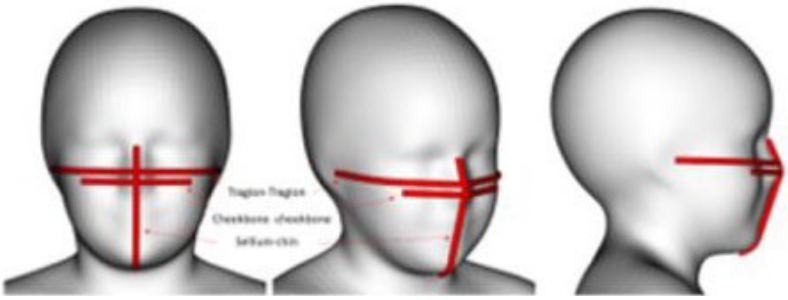


Figure 1 Types of children's respirators [7]

According to the specified dimensions of children's faces within the standard CEN/TS 17553:2023 in the manufacture of facepieces will also be the design of "hooves", indicating the dimensions for four groups of sizes of children's respirators (group A to D). The design has been prepared according to the standard requirements. The dimensions are given in Table 2.

Table 2 Dimensions of children's face and head (author)

Age	Cheekbone – cheekbone	Root of nose – chin	Tragion – Tragion	Head circumference
3-5 years	88–109 mm	93–127 mm	202–253 mm	477–549 mm
6-9 years	94–116 mm	105–130 mm	220–279 mm)	500–560 mm
10-12 years	98–121 mm	114–133 mm	233–290 mm	515–570 mm
13-15 years	104–132.5 mm	123–135 mm	251–300 mm	525–580 mm

Czech technical standard EN 14683 + AC, 855812:2020 Medical face masks - Requirements and test methods is the original document for the purpose of testing medical masks, which is available in the English original. The standard will be used together with the Public Facepiece standard as a basis for designing a solution for children's respirators. According to EN 14683+AC:2020, the same requirements for testing masks can be considered in addition to the requirement - resistance to arterial bleeding. The newly designed children's respirators will be tested for resistance to viral penetration and also for breathability. The design of the respirators was inspired by the material used based on this standard.

The different sizes of respirators A to D are summarised in Table 3 and their sketch is described in Figure 2, on the basis of which laboratory samples of selected materials capable of further testing for breathability and virus capture will be prepared.

Table 3 shows the dimensions of the width and length of the proposed respirators, called hoofs, based on the average values of the determined dimensions of the child's face and head.

Table 3 Respirator sizes A-D (author)

Size	Respirator sizes	
	WIDTH[1]	**LENGHT[2]**
A	50 mm	110 mm
B	53 mm	117 mm
C	55 mm	123 mm
D	58 mm	129 mm

[1] distance from the cheekbone to the root of the nose

[2] distance from the root of the nose to the chin

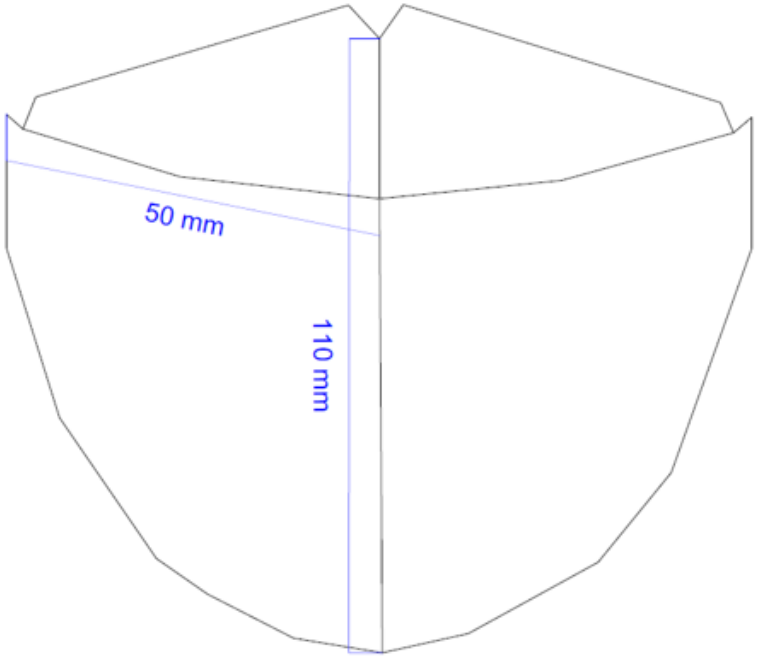


Figure 2 Sketch with dimensions of a child respirator size A (author)

Respirators were designed according to standards that address respirator design according to the vital capacity of the lungs. After consulting the prototypes for the development of a standard for the production of children's respirators with the Medical Chamber. According to the recommendations of the experts, it will be necessary to redesign the prototypes and focus on the characteristics of the breathing resistance (the force of the child's exhalation), i.e. the breathability of the material, when designing them.

Detailed methods, reference values, indications and other properties influencing the design of a respirator for children are addressed in the book Respiratory Function in Children and Adolescents 1984 by authors Zapletal Alois, Šamánek Milan and Paul Tomáš, which will be used to analyse in more detail the airway resistance currents in the position of functional residual capacity (i.e. in the position of resting expiratory flow), depending on body height, age and body surface in boys and girls.

https://doi.org/10.5593/sgem2024/6.1/s24.13

The research conducted and the design that was initially developed according to the vital capacity of the lungs was determined with respect to the height and age of the children, with sizes and values determined for children aged 3 to 15 years. The values used from the book (Respiratory Function in Children and Adolescents 1984) were from 6 years and 115 cm, therefore further values were calculated according to the various equations in force [8].

The Czech market has a large number of well-known and lesser-known manufacturers, who started to develop their production of children's respirators especially at the time of the Covid-19 pandemic. Most of them meet the requirements as a medical device according to Directive 93/42/EEC and at the same time as a personal protective equipment according to Regulation 2016/425.

The type of material and quality of production is very variable, because the Czech Republic does not yet have a standard that would determine according to which parameters and from which materials to produce child protective respirators, this topic is still open on the Czech market and is still waiting, for its solution by the resolution of standards, for their legal production.

The prevailing standard materials for adult respirators were polyvinyl fluoride nanotextiles laminated with polypropylene - a non-woven fabric.

CONCLUSION

The aim of this article was to determine the parameters for the design of the basis for the production of children's respirators. The design of the respirators was divided into four groups A-D according to age, this division taking into account the dimensions of the face, head and vital lung capacity of the children. Designing a suitable material for the manufacture of the children's respirators, with polyvinyl fluoride nanotextiles most likely to be used and laminated with polypropylene.

Further development of the design of children's respirators will focus on taking into account the resistance that children are required to overcome to breathe through the material. In particular, the choice of material will take into account the parameters of the inspiratory and expiratory force of the children. New prototypes of children's respirators will be designed based on the new knowledge gained.

ACKNOWLEDGEMENTS

Special thanks go to the Research Institute of Occupational Safety, v. v. i. in Prague, which provided facilities for the scientific activities. For expert consultations we would like to thank Mrs. Ing. Munzarová from Nonamedical s.r.o. in Liberec and the management of the Children's Respiratory Department of the University Hospital Ostrava. Furthermore, MUDr. Petr Konečný Ph. D. for expert consultation.

REFERENCES

[1] Slabotinsky, J., Castulik, P., & Dekonta CBRN, s.r.o. (2022). *Neni respirator jako respirator*. Brno: Dekonta CBRN, s.r.o.

[2] Javorka, K. (2001). *Lekarska fyziologia: ucebnica pre lekarske fakulty*. (Vysokoskolske ucebnice). Martin: Osveta. ISBN 80-806-3023-2.

[3] Ganong, W. F. (2005). *Prehled lekarske fyziologie: dvacate vydani*. Praha: Galén. ISBN 80-726-2311-7.

[4] Mereni plicni vitalni kapacity. (2016). Retrieved May 10, 2023, from https://pardubice.nempk.cz/uploads/facilitywing/189/doc/mereni-plicni-vitalni-kapacity.pdf

[5] The Grainger College of Engineering. (2007, October 22). *Physics Van*. Published by Tamara. Retrieved April 5, 2024, from https://van.physics.illinois.edu/ask/listing/786

[6] Crayola. (2024). How do I select the proper Crayola Face Mask size? Retrieved April 5, 2024, from https://www.crayola.com/faq/online-shopping/how-do-i-select-the-proper-crayola-face-mask-size/

[7] Urad pro technickou normalizaci, metrologii a statni zkousenictvi (UNMZ). (2020). *Technicka normalizacni informace: Oblicejove rousky pro verejnost – Minimalni pozadavky, zkusebni metody a pouzivani*. CWA 17553. TNI, CEN CWA 17553:2020. Retrieved from chrome-extension://efaidnbmnnnibpcajpcglclefindmkaj/https://www.mpo.gov.cz/assets/cz/podnikani/standardizace/2020/11/TNI.pdf

[8] Lung Volumes and Forced Ventilatory Flows: Report working party standardization of lung function tests european community for steel and coal. (1993). *European Respiratory Journal*, 6(Suppl. 16), 5-40. Printed in UK - all rights reserved. Eur Respir J. ISBN: 87-16-15024-4. Retrieved May 10, 2023, from https://erj.ersjournals.com/content/erj/6/Suppl_16/5.full.pdf

https://doi.org/10.5593/sgem2024/6.1/s24.13

SIMULATION AND OPTIMIZATION OF EQUIPMENT FOR UNLOADING LONG METAL BARS

Assoc. Prof. Dr. Paul Ciprian Patic[1]

Dr. Gabriela Mănțescu[2]

[1] Valahia University of Targoviste, 13, Sinaia Alley, **Romania**
[2] Valahia University of Targoviste, 13, Sinaia Alley, **Romania**

ABSTRACT

The dynamics of human society is directly related to the dependence on automation, and we can no longer produce almost anything without industrial automation. Automation is often associated with the industrial field, but automation has penetrated many areas of everyday life. Domains such as environmental protection, global trade, car, naval or rail traffic (increasingly intense), agriculture, construction and last but not least the medical field are some examples in which automation is present and in which they have a decisive role. This studied equipment is part of a technological flow to produce rectified and chromed bars intended to produce rods for hydraulic cylinders. Also, it can be used in two points of the manufacturing flow (translation for the rectification operation, or translation for the packaging operation) and has the role of moving the bars from one production line to another or from the chrome-plating operation to the packaging. The equipment was modelled virtually and checked for correct operation. During operation, there is sometimes a need for a mobile system of the equipment to be able to be positioned in various operating points, an operation that must be performed in the shortest possible time. This repositioning is ensured by a property called controllability. These positionings were performed through virtual simulations of the behaviour of the functional components of the equipment.

Keywords: Bars, Conveyor belt, Guidance system, Rollers, Pneumatic cylinders, Sensors, SolidWorks.

INTRODUCTION

The great advantage of using industrial automation is the increase in productivity, in any manufacturing system, and the quality of any product. The increase in productivity and product quality using automation led to significant reductions in production costs. Hydraulic cylinders are linear motors that work with oil pressure and are very demanding from the point of view of the quality of the execution of the component parts. Their rods must be executed correctly to the prescribed tolerances with a perfect cylindrical surface, without bumps or deformations. Human handling of these parts can lead to such defects. That is why the automation of the equipment that produces the bars from which these rods are built is very important [10]. The equipment for translating the bars is called an intermediate bench and has the role of taking over the long bars, from the first rectification line, and transferring them to the next line, for the second rectification operation. In short, the equipment has the role of passing (translation) the bars from one line to another for a process of two passes of the bar through the rectification operation.

https://doi.org/10.5593/sgem2024/6.1/s24.15

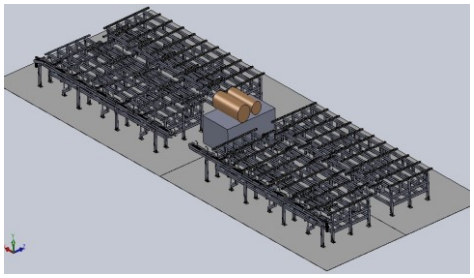


Figure 1. Automatic grinding flow for long bars

The equipment for translating the bars is composed of:

- automatic bar loading bench;
- feeding system with groups of rollers;
- grinding machine without centres;
- exhaust system with groups of rollers;
- intermediate automatic bank for bar translation and roller transport system 1;
- intermediate automatic bar transfer bench and roller transport system 2;
- ATM for final unloading of bars [8].

Also, the explanation from below will contain a part of positioning and dimensioning calculations necessary to determine the functional parameters, the parameters that are directly related to the choice of automatic operation control devices [17].

OPTIMIZING AND SIMULATING EQUIPMENT'S OPERATION

The intermediate unloading equipment operates within a flexible long bar manufacturing flow for the production of hydraulic cylinder rods. It is a component of a technological process, a process that takes place according to certain well-established parameters (Figure 1).

A. Virtual simulation of equipment operation

This equipment has the role of taking the bars from a mechanical system, translating them, following certain stages, and evacuating them to the next equipment in the flow. The operation of the equipment depends on the intermediate stages and times of the technological process and must be adapted to these stages. At the same time, the equipment must be able to adapt to possible problems of dysfunctionality in the flow, accidental blockages, voluntary stops for control. All these problems can occur before or after the equipment in the technological flow. The equipment must have the capacity to store, for a period, a number of bars coming from the technological flow, if there is a blockage after the equipment and to be able to pick them up and handle them, one by one, after fixing the malfunction or stopping the stoppage [3]. The main functions of the equipment are: 1 - taking over the bar by lifting it from the groups of rollers and lowering the bar on the inclined plane; 2 - free rolling up to the adjustable stops; 3 - selection and lifting of the bar, its free translation and its lowering on the rollers; 4 - discharge of the bar to the intermediate loading equipment;

Each main function must take place in well-defined steps and times:

1. Taking over the bar by lifting it from the groups of rollers and lowering the bar on the inclined plane; Steps: a. Lifting the bar from the rollers:

- pneumatic cylinder at minimum stroke L_0 = 30 mm;
- raising the lever system, s = 70 mm; lifting bar;
- stationary, free rolling time, along the length l = 580 mm;
- the lowering of the lever system, s = 70 mm; lowering the bar on the inclined plane.

The times for raising and lowering the bar on the inclined plane are small and will not be considered. Free rolling time is longer approx. 5 s (determined in simulation) [16]. The time a bar travels through the grinding machine depends on the speed of the driving stone and from the technological process this average speed is:

$$v_{bar} = 20 \text{ mm/s}$$

For a bar length l_{bar} = 6000 mm, the bar grinding time is:

$$t_{rectificare} = \frac{l_{bară}}{v_{bară}} = \frac{6000}{30} = 200\text{s} = 3{,}33 \text{ min}$$

This time must also be the time in which a bar arrives, brought by the transport system, next to the intermediate unloading equipment. An intermediate time of 2 s will also be taken into account from the stop of the bar to the actuation of the levers that lift it from the rollers, according to Figure 2.

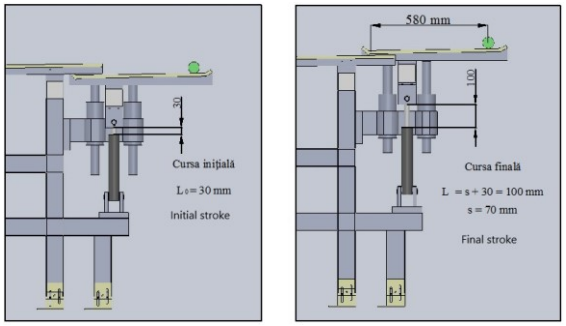


Figure 2. Lifting from the groups of rollers and lowering the bar on the inclined plane – Function 1

2. Free rolling up to the adjustable stops

This function takes place in a single step, i.e., the free rolling of the bar on the inclined plane until they reach the adjustable stops or stop one in the other (storage). The time required for the free rolling of the bar along the length of the slope (2150...2250 mm) is 5 s, as one can see in Figure 3.

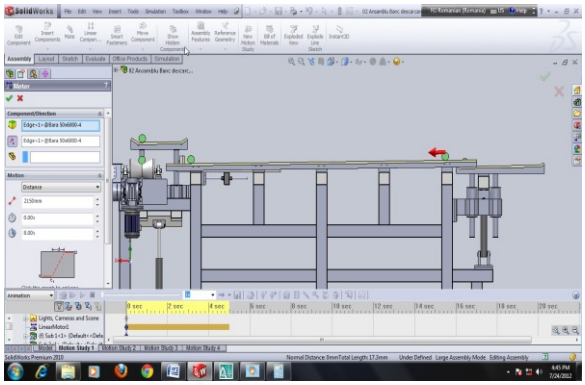


Figure 3. Free rolling up to the adjustable stops - Establishing times - Function 2

https://doi.org/10.5593/sgem2024/6.1/s24.15

3. Selection and lifting of the bar, free translation and its lowering on rollers
Working steps: b. Lifting the bar from the inclined plane:
- the pneumatic cylinder is at the minimum stroke

$$L_0 = 25 \text{ mm};$$

- raising the lever system, s = 100 mm; lifting bar;
- stationary, free rolling time along the length l = 300 mm;
- the lowering of the lever system, s = 100 mm; lowering bar on the roller bed [7].

The times for raising and lowering the bar on the rollers are small and will not be taken into account. The free rolling time is slightly longer approx. 3 s. The roller transport speed of the bar will be variable (Figure 4).

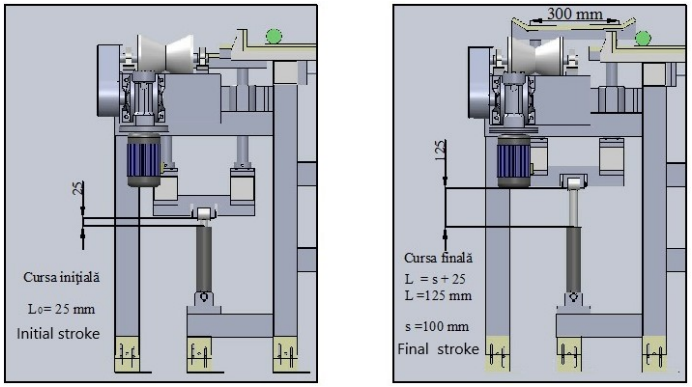


Figure 4. Free rolling up to the adjustable stops - Establishing times - Function 3

$$v_{bar} = v_{roll} = 0{,}05...0{,}15 \text{ m/s} = 50...150 \text{ mm/s}$$

The time required to evacuate the bar to the intermediate loading equipment, for a bar length: l_{bar} = 6000 mm is:

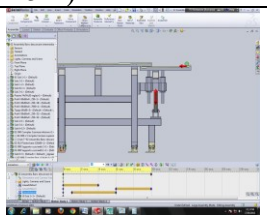
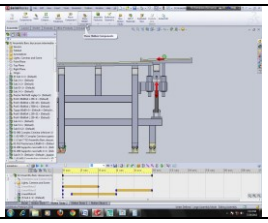
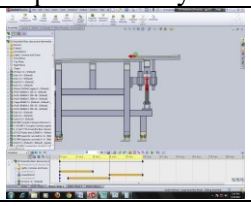
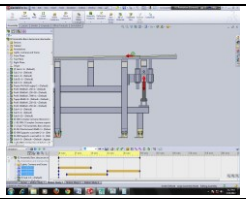
$$t_{evacuare} = \frac{l_{bară}}{v_{bară}} = \frac{6000}{150} = 40\text{s}$$

All the parameters established so far are necessary for the simulation of the movements of the intermediate equipment components, a simulation necessary to visualize the correct operation and if it fits into the manufacturing flow of which it is a part. The virtual simulations are performed in SolidWorks Motion and verified with the MOTION Analysis module. The intermediate bar unloading equipment was designed and modeled in SolidWorks, assembled in subassemblies, taking into account that the motor elements are positioned in the final assembly. The elements motors were positioned as a whole for the virtual simulation of the analysed movements [16].

B. Virtual simulation of the operation of the first lever system

One finds 3 stages. In the first stage it can be observed that the lifting of the lever system is carried out by the rod of a pneumatic cylinder. In the virtual simulation, a virtual linear motor will be attached to the cylinder rod, initially positioned at the bottom stroke L_0 = 30 mm, which has the role of lifting the pneumatic cylinder rod together with the entire lever system, for a stroke s = 70 mm, during of 4 s. The actual operating time is 2 s, but for a better visualization of the movements, a time of 4 s was chosen. The second stage is the assignment of weight force for the bar on the lever and the establishment of a coefficient of friction with the rubber protection. The bar is in the

raised position. Rolling of the bar starts as soon as it is no longer in contact with the rollers. So, the start of the movement of the virtual motor must be 2 s before the stop time of the virtual motor to raise the lever system to its maximum stroke [6]. The third stage is the assignment of a virtual linear motor, to the cylinder rod, for lowering the lever system to the initial stroke and depositing the bar on the surface of the inclined plane [11]. The established stages (steps) can be visualized in the following figures (Figure 5.1 - 5.4).

<table>
<tr><td>  </td><td>  </td></tr>
<tr><td>Figure 5.1. Stage 1 - virtual motor at the rod of the pneumatic cylinder</td><td>Figure 5.2. Stage 2.1 - Free rolling of the bar</td></tr>
<tr><td>  </td><td>  </td></tr>
<tr><td>Figure 5.3. Stage 2.2 - Reaching the bar at the end of the lever</td><td>Figure 5.4. Stage 3 - Lowering the lever system</td></tr>
</table>

C. Virtual simulation of rolling of the bar on the inclined plane

For this stage, the same settings are made as for rolling on the levers. The time determined for the free rolling of the bar along the entire length of the slope is 5s, as one can see in Figure 6 [12].

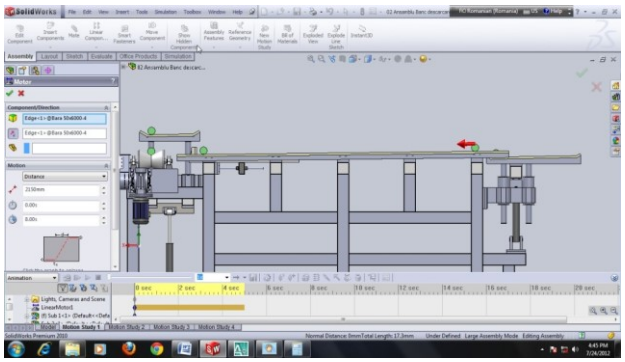


Figure 6. Stage 3 - Lowering the lever system

D. Virtual simulation of the operation of the lever system 2

As in the case of the first pneumatic cylinder, in reality the lifting of the levers is carried out by a pneumatic cylinder. In the simulation performed in SolidWorks, a virtual linear motor is assigned to the rod of the pneumatic cylinder, initially positioned at the initial stroke L_0 = 25 mm. This motor raises the rod of the pneumatic cylinder together with the entire system of levers, for a stroke s = 100 mm, between a time of 4 s. The actual operating time is 2 s, but for a better simulation of the behavior it was set a time of 4 s. The second step is to assign a virtual linear motor to the bar, which is raised, or one can assign weight to the bar and it will roll under the action of gravity. The free rolling of the bar starts as soon as it is no longer in contact with the rollers and will travel a

https://doi.org/10.5593/sgem2024/6.1/s24.15

distance of 300 mm. The start of the virtual engine must be set 2 s before the stop time of the virtual engine to raise the maximum stroke [2]. The third step is the assignment of a virtual linear motor, to the rod of the pneumatic cylinder, to lower the lever system to the initial stroke and deposit the bar on the exhaust rollers from the equipment. The following figures (Figure 7.1-7.4) show the stages carried out in SolidWorks.

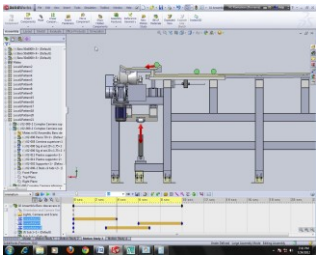


Figure 7.1. Step 1 - Virtual linear motor

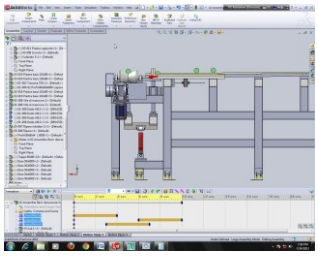


Figure 7.2. Step 2 - Selecting the bar

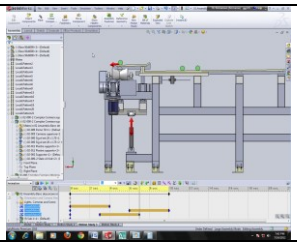


Figure 7.3. Step 3 - Free rolling of the bar

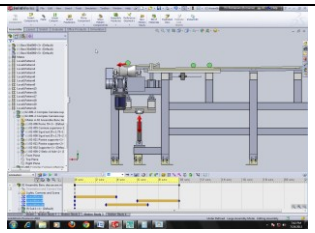


Figure 7.4. Step 4 - Laying the bar on the discharge rollers

E. Simulation of the evacuation of the bar on the automatic roller system 1

For this simulation, a virtual linear motor was assigned to the bar on the rollers in the transport direction to the next equipment and it was determined that the bar could be evacuated in 10 s (Figure 8) [18].

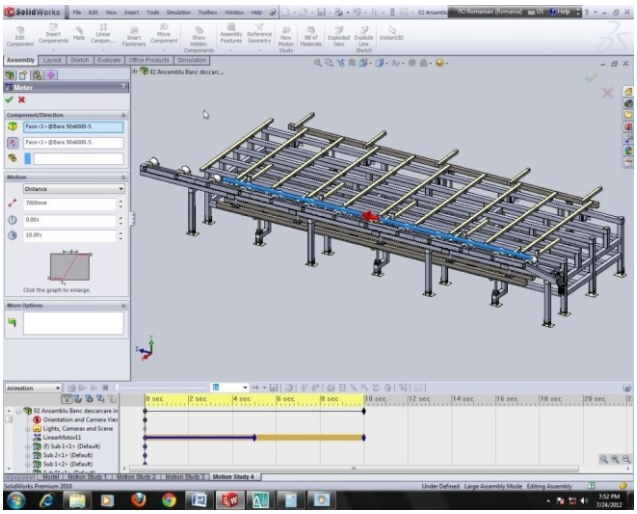


Figure 8. Evacuation of the bar from the equipment

AUTOMATION OF THE INTERMEDIATE DISCHARGE BANK

For the designed equipment to become functional, it is required that it be well determined, which was done by designing the equipment and verifying its functionality

in a virtual environment. The equipment must be able to function in a correct equilibrium regime. During operation, there is sometimes a need for a mobile system of the equipment to be able to be positioned in various operating points, an operation that must be performed in the shortest possible time. This repositioning is ensured by a property called controllability. Also, in order to manage various automatic driving strategies, it is important to know the positioning of equipment systems at a given moment, and even the individual positioning of each mobile system. The control must be performed automatically, based on the measurement of the output quantities of the technological process being conducted [1]. Figure 9 shows the general logic diagram for the automatic control of the bar translation equipment [4] and [5].

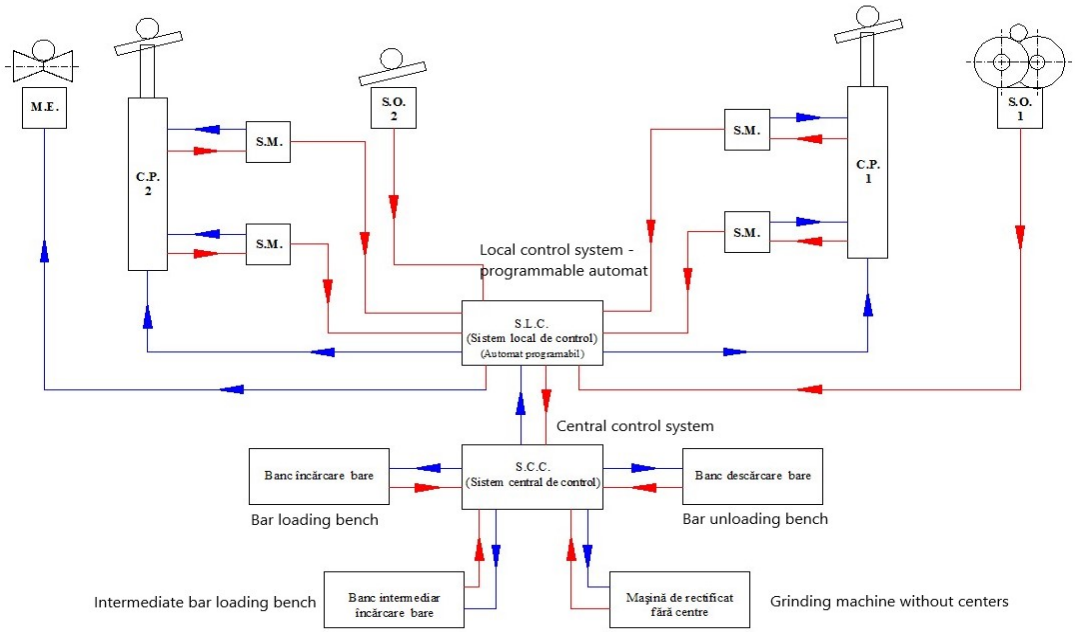


Figure 9. Logic diagram for equipment automation
Where, C.P.1 – equipment pneumatic cylinder; C.P.2 – pneumatic cylinder exhaust from the equipment

M. E. – electric motor driving the exhaust rollers;
S.M. – pneumatic cylinder stroke magnetic sensor;
S.O.1. – optical sensor for the presence of a bar on the group of inclined rollers;
N.O.2. – optical sensor for the presence of a bar next to the stop;

After the bar is discharged from the grinding machine, it is transported to the intermediate unloading equipment by the group of inclined rollers. The appearance of the bar in this position and the stopping of the bar movement is controlled by the optical sensor O.P.1 [15]. This sensor, through the local control system (automatically programmable) sees the lifting command of the pneumatic cylinder C.P.1. C.P.1 performs the lifting stroke, stroke which is limited by magnetic sensors S.M. assembly at the beginning and end of the stroke. The bar raised by the lever system rolls along the length of the lever towards the inclined plane. After the set time has passed, for the free roll of the bar, the pneumatic cylinder descends to the minimum stroke, stroke limited by the second magnetic sensor S.M. From this moment the bar rolls freely until it reaches the adjustable stops. At this point, the optical sensor S.O.2 detects the presence of the bar and commands the operation by raising the pneumatic cylinder C.P.2, which

https://doi.org/10.5593/sgem2024/6.1/s24.15

cylinder is controlled, to limit the upper and lower stroke, by two magnetic sensors S.M. At the moment of passing the free rolling time of the bar on the lever system, the pneumatic cylinder C.P. 2 is actuated and the bar descends with the lever system on the rollers of the exhaust system. The signal given by the end of stroke of the pneumatic cylinder C.P.2, given by the magnetic sensor S.M., is received by the local control system that starts the electric motor that sets the roller system in motion and the bar is evacuated from the equipment. Stopping the electric motor is controlled by a presence sensor of the bar in the working position at the intermediate loading equipment [13]. All information received and commands given are managed by a local control system, which is a programmable automaton [9]. The programmable automaton must be in an informational and control connection with the other equipment in the flexible bar rectification system through a central control system [14].

CONCLUSION

The automation of this equipment was designed based on the knowledge of the functional characteristics and the stages of the technological process it serves. Determining the strokes of the pneumatic cylinder rods are the parameters related to the choice and positioning of the stroke limiters which can be electrical contactors properly mounted on the lifting and lowering systems or the stroke can be controlled from the air flow required for the stroke determined by a pressure transducer and all the components auxiliary (automatic pressure distributors, automatic direction and overpressure valves etc.). The movement of the bar on the inclined plane was controlled by presence sensors. The actuation of the bar lifting systems were controlled by devices that are connected to the presence sensors. Monitoring the number of bars stored on the inclined plane is also important. This monitoring was done with an optical sensor mounted at a certain distance from the end of the inclined plane. The virtual simulation of the operation of the equipment systems helped me in choosing automation solutions. This equipment can be improved from the point of view of automation by positioning a presence sensor on the inclined plane to signal that there are a certain number of bars on this plane. The positioning can be done at a distance equal to the number of diameters of the bars and then the presence of the last bar of a number "n" can be signalled or the number of bar crossings can be recorded and through the software the number of bars present on the inclined plane can be known.

REFERENCES

[1] Anand K. Bewoor, Vinay A Kulkarni, Metrology & Measurement, Tata McGraw-Hill Publishing House, New Delhi, 2009.

[2] Bessai H. J., MIMO Signals and Systems, Springer Publishing House, 2005.

[3] Bradley D., Seward D., Dawson D., Burge S., Mechatronics and the design of intelligent machines and systems, Informa, 2000.

[4] Demian T., Pascu A., Stoica G., Measuring devices in coordinates, Tehnica Publishing House, Bucharest, 1991.

[5] Dodoc P., Modern measuring methods and means in fine mechanics and machine construction, Tehnica Publishing House, Bucharest, 1978.

[6] Dodoc, P., General metrology, Didactical and Pedagogical Publishing House, Bucharest, 1990.

[7] Filipoiu I. D., Tudor A., Design of mechanical transmissions, Bren Publishing House, Bucharest, 2006.

[8] Gheorghe Gheorghe I., Palade D. D., Pau V., Spineanu, N. U., Engineer's manual of fine mechanics, mechatronics and integronics, CEFIN Publishing House, Bucharest, 2006.

[9] Gheorghe, Gheorghe I, Palade D. D., Pau V, Sensors and transducers for industrial applications, CEFIN Publishing House, Bucharest, 2003.

[10] Gheorghe, Gheorghe I., Integrative Engineering, CEFIN Publishing House, Bucharest, 2007.

[11] Gheorghe, Gheorghe I., Spineanu, N. U., Palade D. D., Pau V., Systems and information engineering, CEFIN Publishing House, Bucharest, 2005.

[12] Gheorghe, Gheorghe I., Intelligent Measurement Technique, CEFIN Publishing House, Bucharest, 2004.

[13] Grama L., Basics of manufacturing technologies in machine construction, Petru Maior University Publishing House, Targu Mures, 2000.

[14] Ispas V., Pop I. I., Bocu M., Industrial robots, Dacia Publishing House, Cluj Napoca, 1985.

[15] Oprescu T., Ionescu D., Andrei G., Measurement in Coordinates, Documentary Information Office for the Machine Construction Industry.

[16] Patic P. C., Simulation of a Flexible Manufacturing System for Machining Some Industrial Parts, Design, Construction, Maintenance, An Open Access International Journal of Engineering, pp. 173 – 178, Volume 3, 2023.

[17] Potorac, Alexandru, Podan, Tolerances and dimensional control, University "Ştefan Cel Mare" Suceava Faculty of Mechanical Engineering, Mechatronics and Management.

[18] Vasilescu A., Ciocirlea A., Industrial Metrology, Volume II – Applications in the Length Domain, Printech Publishing House, Bucharest, 2006.

https://doi.org/10.5593/sgem2024/6.1/s24.15

IMPACT OF COLLOIDAL PROPERTIES OF PHOSPHORUS-BASED NANOFERTILIZERS IN FOLIAR APPLICATION ON PRODUCTION PARAMETERS, PHYSIOLOGY, AND MINERAL NUTRIENT CONTENT OF SUNFLOWER

Assoc. Prof. Dr. Marek Kolenčík [1]

Asst. Prof. Dr. Dávid Ernst [1]

Assoc. Prof. Dr. Martin Šebesta [2]

PhD Viktor Straka [1]

Assoc. Prof. Dr. Ľuba Ďurišová [3]

[1] Institute of Agronomic Sciences, Faculty of Agrobiology and Food Resources, Slovak University of Agriculture in Nitra, **Slovakia**
[2] Institute of Laboratory Research on Geomaterials, Faculty of Natural Sciences, Comenius University in Bratislava, **Slovakia**
[3] Institute of Plant and Environmental Sciences, Faculty of Agrobiology and Food Resources, Slovak University of Agriculture in Nitra, **Slovakia**

ABSTRACT

In contemporary agricultural practice, ensuring sufficient bioavailable macronutrients, particularly phosphorus, for plants in phosphorus-deficient soils remains a significant challenge. As a promising alternative, the application of phosphate-calcium-based nanofertilizers (NFs), with or without zinc, emerges as a suitable solution, offering targeted effects through foliar dispersion. However, current knowledge gaps persist regarding the development and colloidal properties of applied NFs and their impact on sunflower (*Helianthus annuus* L.), a globally significant oilseed crop known for its broad leaves and an intensive photosynthetic apparatus.

This study aimed to evaluate the physicochemical properties and colloidal characteristics of two phosphate fertilizers: nano-hydroxylapatite (n-HA) and a mixture of nano-calcium zinc phosphate and macro-sized parascholzite (nano/macro-CaZnP), compared to a NF-free control. The work focused on their effects on selected yield parameters and physiological responses, specifically examining changes of major mineral nutrients in sunflower leaves during the 2022 growing season in Nitra, Slovakia, Central Europe.

Result indicates that the treatment with nano/macro-CaZnP, produced via chemical route along with n-HA performed though biotechnological protocol, resulted in higher yield parameters in sunflowers compared to the NF-free control. Notably, the treatment with nano/macro-CaZnP exhibited higher yields, likely attributable to its favorable colloidal properties, including smaller hydrodynamic size, higher (positive) zeta potential (ζ-potential), or quantitatively higher content of ionically-soluble species during foliar deposition. This was statistically reflected via photochemical reflectance index (PRI), an important physiological indicator, for the particular treatment. Still, the unequal relative distribution of major macronutrients (N, P, K) of sunflower in leaves among the treatments poses a challenge to be overcome.

Keywords: phosphate nanofertilizers, sunflower, spray application, field conditions, colloidal properties

https://doi.org/10.5593/sgem2024/6.1/s24.16

INTRODUCTION

Currently, the nanotechnology is in many ways utilized in various industries, including agriculture [1]. Here, one of the promising field is nanofertilizers (NFs), which are typically less than 100 nm in size and possess distinct properties such as gradual nutrient release, lower effective concentration ranges, and more targeted effects compared to ion-soluble or macro-sized counterparts [2]. However, we have insufficient knowledge of their colloidal properties when considering the relation of their hydrodynamic size and ζ-potential to their leaf entry and subsequent effects [3]; alteration of surface structures such as stomata or trichomes [4], or impact on the leaf's chemical properties with regards to mineral nutrients ratio and pigment diversity [5]. Also, varying nanoparticles (NPs) concentrations of can significantly influence symbiotic organisms or the development and functions of plant root systems [6], where their fate is governed by soil environmental properties [7].

One of the most suitable candidates in the plant kingdom providing proof-of-concept studies with the NFs application, with typically broad leaves, diverse morphological structures, and global distribution, is sunflower (*Helianthus annuus* L.) [8]. It demonstrated the capacity to absorb, distribute, and metabolize NFs trough leaves structures [9] and NFs applied at different concentrations could evoke physiological stress or modulate hormone levels with varying intensity [10]. Moreover, the NF influence also had impact on crop yield and yield-related parameters, as shown in studies on sunflower [4], lentil [11], and foxtail millet [12].

NFs can be classified into macronutrient-based, micronutrient-based, for instance zinc phosphate and nanostimulants, depending on the nutrient essentiality incorporated to nano-domain [13]. In this context, information is absent about the combined effects of phosphate-based NFs, synthesized through biological or chemical protocols, also containing calcium, and zinc. The principles of biomimetics and biotemplating in their formation seems to increase their efficiency in natural cycles [14], and in our case, we employed these principles in synthesis of n-HA or through chemical precipitation of nano/macro-CaZnP. In addition, to fish bones [15], microscopic fungi are also used in the NF synthesis, with their challenges in agricultural applications due to their specific properties outlined in study by Šebesta et al. [16].

Currently, in this academic field, there is a greater focus on fundamental research on the NF effects than field studies. Hence, the aim of this study was to assess the physicochemical and colloidal properties of our prepared two types of phosphate-based NFs, with or without zinc, and their impact on sunflower crop yield parameters and physiological responses, as well as the potential effects on leaf's mineral nutrients during the 2022 growing season in field conditions in the Central European region compared to an NF-free control.

MATERIALS AND METHODS

Production and Characterization of Phosphorus-based Nanofertilizers Foliar Applicated on Sunflower

Sheelavati fish bones (*Roho labio*) from the Krishna River act as the biological source for n-HA formation, where were integrated multi-step procedure that included the removal of organic residues, drying, mechanical disintegration, and thermal treatment at 600 °C

[15]. In the case of nano/macro-CaZnP production, the co-precipitation method was used followed by [17].

For the visualization of the size and morphology of n-HA, scanning electron microscopy (SEM) was utilized using a JEOL 7610 F+ instrument (JEOL, Akishima, Tokyo, Japan), and the chemical verification through energy-dispersive X-ray spectroscopy (EDS) using a Phillips XL30 device. The morphology of nano/macro-CaZnP was investigated using the scanning transmission electron microscope (STEM) JEOL JSM-7610F Plus, Tokyo, Japan with a Schottky cathode at 30 keV in high vacuum chamber with elemental analysis using the energy-dispersive X-ray spectroscope (EDS) AZtec Ultima Max 65 (Oxford Instruments, Abingdon, UK).

Before foliar deposition, the colloidal properties of the NFs were analyzed for hydrodynamic diameter, ζ-potential, and conductivity, correspond to solution ionic strength using the nanoPartica SZ-100 analyzer (Horiba, Kyoto, Japan) according to Kolenčík et al., [11].

Climatic and Seasonal Fluctuations at the Experimental Site

During the growing season, data on average daily temperature (in °C) and precipitation (in mm) (Fig. 1b) were obtained from Meteoblue data [18].

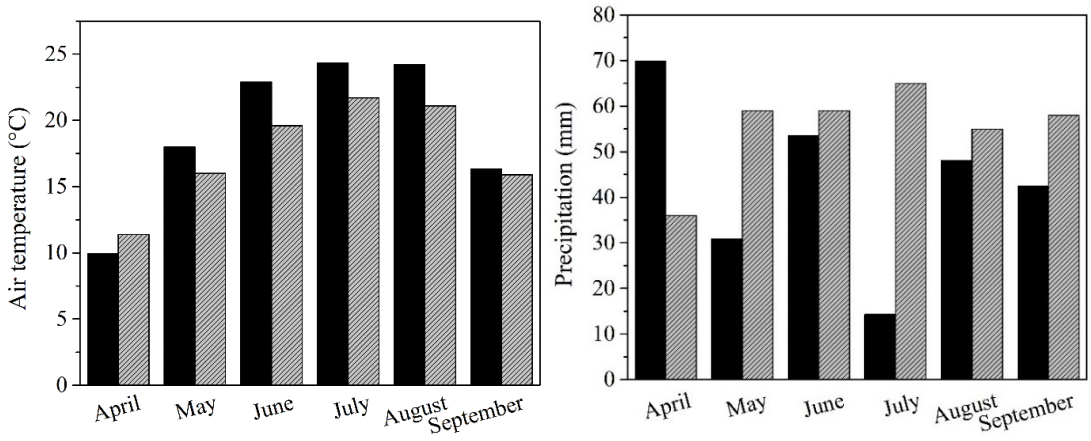


Fig. 1. Analyzation of the monthly variations in (a) air temperature and (b) precipitation at the experimental field site in Dolná Malanta near Nitra, Slovakia, within the Central European region. Dark black columns represent measured data for the vegetation season compared to the ideal climatic norm (sparse texture) for both cases.

Description of Natural Condition Conditions at the Site and Establishment of Sunflower Experiment

Field experiments were conducted at the Slovak University of Agriculture in Nitra (SUA Nitra) in Dolná Malanta, near Nitra, Slovak Republic. This site belongs to the agronomic Central European region. At the site, the soil was identified as silt loam haplic Luvisol [19] and sunflowers were integrated into a 7-plot crop rotation system. The experiment was conducted using a split-plot design, including randomly assigned controls, as described by [4], with three replications. Standard procedures were followed during sowing, including the cultivation of winter wheat (*Triticum aestivum* L.) as forecrop, and soil integrated macronutrients N, P, K using 15-15-15 DUSLOFERT fertilizer (Duslo, a. s., Šaľa, Slovak Republic).

https://doi.org/10.5593/sgem2024/6.1/s24.16

For our field experiment, we used the SY Neostar hybrid (*Helianthus annuus* L.) developed by Syngenta in Basel, Switzerland. This hybrid, tailored for the ClearField Plus® system is resistant to two-line imidazoline, and highly resistant to *Sclerotinia sclerotiorum* and *Diaporte helianthi*, with tolerance to *Plasmopara halstedii* [20].

To combat plant pests, Wing® herbicide (BASF, Ludwigshafen am Rhein, Germany) and Pictor® fungicide (BASF, Ludwigshafen am Rhein, Germany) were applied. Spray dispersed NFs were both deposited with at a concentration of 33 $mg \cdot L^{-1}$ and for NF-free control water was used. The initial spray was done on day 40 during leaf development, followed by a second spray on day 80 during stem elongation and flower bud formation. Before each application, NFs samples underwent a 15-minute ultrasonic treatment to improve colloidal dispersion.

The Photochemical Reflectance Index Analysis, Nanofertilizers Impact on Sunflower Yield Parameters and Mineral Nutrient Profile of Sunflower Biomass

After sunflowers reached full seed maturity at an optimal moisture level, samples were collected. Quantitative parameters such as head diameter (mm) using Texi 4007 laboratory equipment (Texi GmbH, Berlin, Germany), and head weight (g) using Kern PCB3500-2 lab scale (KERN & Sohn GmbH, Balingen, Germany) were determined [8].

The photochemical reflectance index (PRI) was used for physiological assessment, quantified using the PlantPen 200-U device (Photon Systems Instruments, Brno, Czech Republic), gathering reflected wavelengths (R_{531}, R_{570}) ranging from 531 to 570 nm from the leaf surface [21], determined by the equation:

$$PRI = (R_{531} - R_{570})/(R_{531} + R_{570}).$$

To enhance the interpretation of physiological indicators, changes in the mineral nutrients profile in sunflower leaves were investigated week after the second application. Additionally, a more detailed evaluation of potential phosphorus translocation was also quantified. Phosphorus, along with potassium content in leaf biomass, was determined following the method described by Knoppová, et al., [22], while nitrogen was assessed using the Kjeldahl method with HNO_3 as the digesting agent.

Data evaluation

The statistical analysis for quantitative parameters and physiological response was applied with TIBCO Statistica®, version 14.0 (TIBCO Software Inc., Palo Alto, CA, USA). Prior to the evaluation of the multifactorial analysis of variance (ANOVA) with Fisher's least significant difference (LSD) was used.

RESULTS

In Fig. 2., there is shown a homogeneous compound, n-HA, in solid-state prepared through biotechnological route. The crystalline phase contains mainly P and Ca. Compared to the second applied NFs, nano/macro-CaZnP, it has a smaller particle size distribution and a little bit different morphology. It's the difference of the nano/macro-CaZnP in chemical nature, size and shape is visualized in Fig. 3a, 3b. This form of NF has chemically heterogeneous nature, containing a mixture of nano-sized and macro-sized particles. It was produced through chemical synthesis. Both NFs were dispersed in distilled water and formed colloidal dispersions before being deposited on sunflower leaves.

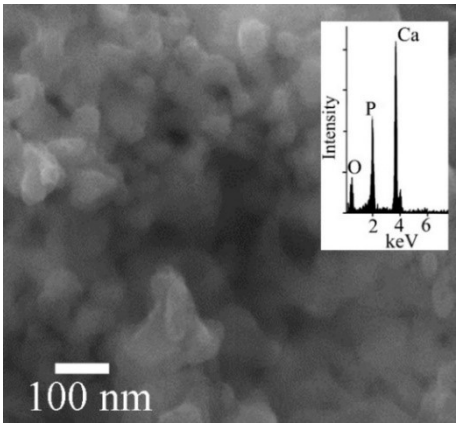


Fig. 2. Scanning electron microscopy visualization of morphology n-HA which was applied to sunflower leaves. Inset: chemical confirmation of elements such as P and Ca trough EDS regime.

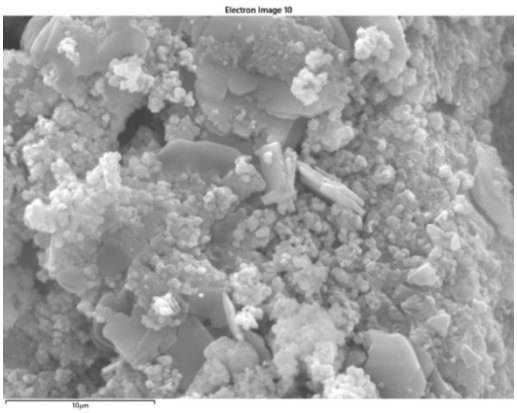


Fig. 3a The SEM image of nano/macro-CaZnP with mixture of nano- and micro-sized fertilizers.

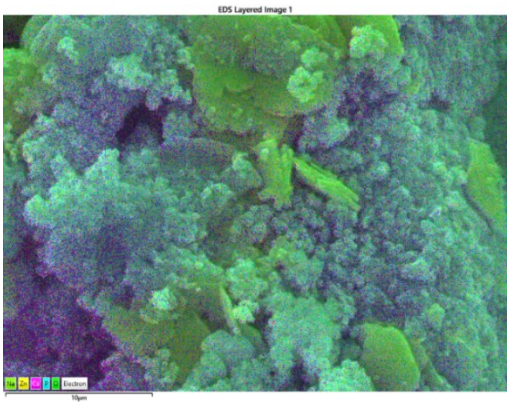


Fig. 3b. EDS chemical verification of nano/macro-CaZnP containing macronutrients such as O, P, Ca, and Zn.

In the dispersions, the n-HA and nano/macro-CaZnP NFs exhibit slightly different colloidal properties (Tab. 1.). Regarding hydrodynamic diameter (nm), the nano/macro-CaZnP showed lower values and a higher ζ-potential, which indicates relatively higher stability in colloidal dispersion compared to the n-HA. Additionally, based on electrical conductivity (representing the quantitative content of dissolved ions), the nano/macro-CaZnP reached equilibrium with a higher quantity of dissolved species than the n-HA.

Tab. 1. Colloidal properties of applied nanofertilizers

The designation of applied nanofertilizer	Hydrodynamic diamater (nm)	ζ-potencial (mV)	Electrical conductivity (mS/cm)
nano/macro-CaZnP	1390.9 ± 173	4 ± 6	1.31 ± 0.03
n-HA	1795 ± 96.5	-0.15 ± 0.2	0.09 ± 0.001

After the preparation of colloidal dispersions, the NFs were deposited on sunflower leaves and the physiological response was analyzed through physiological reflectance index

https://doi.org/10.5593/sgem2024/6.1/s24.16

(Tab. 2.). According to the seasonal physiology, the statistically most effective treatment was nano/macro-CaZnP compared to the NFs-free control. Surprisingly, the least suitable treatment appeared to be n-HA, which achieved the lowest values.

Tab. 2. Summary physiological response to the application of P and Ca-based NFs compared to the NF-free control evaluated on the photochemical reflectance index during vegetation season 2022.

Parameter	Control without NF application	n-HA	nano/macro-CaZnP
PRI	-0.006 ± 0.039	-0.009 ± 0.058 ^{ns}	0.004 ± 0.046 *

* p value < 0.05, ** p value < 0.01.

In the case of vegetation week after the 1st application of both NF types, no significant trend on PRI was noted. During the week after the 2th application, a unexpected, relatively positive indication of PRI was observed for the NF-free control, which persisted until harvest. However, the nano/macro-CaZnP variant proved the most physiologically effective, which was statistically evident in the final phase of vegetation (Fig. 4).

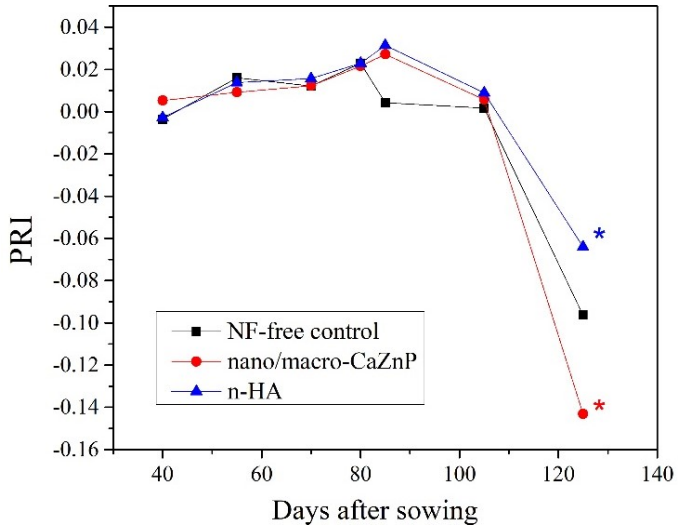


Fig. 4. Evaluation of the physiological response to spray dispersed n-HA and nano/macro-CaZnP compared to NF-free control during the vegetation season of 2022 based on the photochemical reflectance index (PRI).* p value < 0.05.

The response to NFs was also reflected in the varying profile of mineral nutrients founded in sunflower leaves after the second application (Tab. 3.). The highest contents of P and K were related to NFs-free control, while the highest N-content was observed with application of nano/macro-CaZnP.

Tab. 3. The content of selected macronutrients in sunflower leaves after the second application (mg.kg^{-1})

Examined elements	NFs-free Control	n-HA	nano/macro-CaZnP
Phosphorus	2541.66 ± 72.17	1958.67 ± 35.8	2104.3 ± 35.8
Nitrogen	29735.75 ± 1585	28875.1 ± 598.08	30891.5 ± 729.21
Potassium	46500.05 ± 500	41666.67 ± 288.67	38833.33 ± 288.6

DISCUSION

Physicochemical and Colloidal Properties of Nanofertilizers and the Impact on Sunflower Yield Parameters and Physiology in Field Conditions

The n-HA applied on leaves was produced from natural materials inspired by a biotechnological protocol published in [15]. In a stable state, these NPs belong to one crystalline phase, exhibit a mostly spherical NP morphology or they are elongated in one direction and correspond to a pseudo-hexagonal shape. These NFs are found in larger aggregates, with individual particles with size distribution around 50 nm. According to [23], they are classified as macro-essential nanofertilizers because they contain calcium and phosphorus elements, commonly known macronutrients.

Similarly, the second applied NF, the nano/macro-CaZnP, comprises of a mixture of nano-sized and macro-sized particles with two crystalline phases formed through chemical synthesis, i.e., precipitation (Fig. 3a). This NF shows morphologically distinctive "flake-like aggregates," predominantly contains the micronutrient Zn (Fig. 3b), with a slightly lower phosphorus content than n-HA variant [17].

In dispersion, n-HA and nano/macro-CaZnP exhibit little different colloidal properties (Tab. 1.), which the most probably are reflected in their slightly higher yield potential compared to the control (Tab. 4.).

Tab. 4. Comparison of quantitative parameters of nano/macro-CaZnP and n-HA treatments with NF-free control recorded in the 2022 vegetation season [17].

Parameter	nano/macro-CaZnP Treatment	n-HA Treatment	Control Variant No NF Application
Head diameter (mm)	203 ± 27 *	192 ± 36 ns	178 ± 22
Weight of dry head (g)	136 ± 47 *	125 ± 52 ns	88 ± 34

The significance: * P value < 0.05, ** *P* value < 0.01, ns Non-significant.

The increased yield parameters (Tab. 4) could be directly attributed, for instance, to smaller hydrodynamic radii or hydration of the NFs, which often determines the absorption rate or penetration into plant leaf structures at smaller dimensions [3], although our findings indicated that both NFs had a sufficiently large hydrodynamic diameter (Tab. 1.). Yield-forming intensification could have been synergistically done by the positive ζ-potential of nano/macro-CaZnP, which influences leaf absorption due to its positive values (Tab. 1.). Generally, the positively charged cationic geochemical metal-species may predominantly bind to the partly negatively charged membrane surfaces of sunflower leaves [24]. Furthermore, n-HA value of a ζ-potential in dispersion approaching to zero, where according to the DLVO theory aggregation and potentially reduced NFs effect may appeared [25], although in both cases, the ζ-potential was not significantly different. Logically, however, in the case of nano/macro-CaZnP, the higher content of soluble forms represented by solution electrical conductivity may have also contributed to absorption and leaves nutrient uptake (Tab. 1).

During vegetation, NFs were applied on leaves of sunflower twice, in key growth stages with various physiological responses. In this regard, PRI particularly reflected a higher pigment content, i.e., chlorophyll and carotenoids, as also investigated by [5]. A positive response in the case of NF application was already recorded with sunflower [4], which

https://doi.org/10.5593/sgem2024/6.1/s24.16

indeed may also be attributed to other environmental plant-stress factors [26]. Our results seem to be logical because of the highest PRI value was observed in the nano/macro-CaZnP variant compared to n-HA (Tab. 2.), suggesting a potentially more yield-stimulating effect related to structurally integrated zinc (Tab. 4.). Zinc in nanoparticulate distribution is active component of many stress regulating enzymes and due to its micronutrient nature [27] even when applied at a relatively low concentration, it may have relatively large effect.

Although both NFs had approximately similar chemical formulation of the macronutrients, it is likely that the content of Zn caused the most effective physiological stimulation in the final phase of vegetation (Fig. 4). This has already been confirmed by the vegetation extension trend previously observed in sunflower [4]. Furthermore, it should be emphasized that the n-HA treatment positively impacted yield-forming parameters, confirming that the macronutrients Ca and P significantly enhance sunflower production compared to the NF-free control.

The response of foliar spray application of nanofertilizers on the mineral nutrient profile of sunflower leaves

The response of physiological and metabolic processes to NFs was also reflected in the varying profile of mineral nutrients found in sunflower leaves after the second application (Tab. 3.). Surprisingly, P-content increase in leaves after the second application was observed in the control variant, where it was not actively applied in comparison with n-HA or nano/macro-CaZnP variants, where the lowest concentrations was recorded (Tab. 4.). Phosphorus is a key element in many plant metabolic and energy processes, including supporting photosynthesis, ATP formation, and nucleic acid synthesis [28]. Its higher-level content may indicate active metabolic processes and development, or reflection of harmful environmental stress [29]. Paradoxically, it may also indicate soil-deficiency content, or a more efficient uptake in P-deficient soils, as kind of a compensatory mechanism for the plant's metabolic needs. This could be facilitated by soil organism activity [30], and most likely this trend was also reflected in our P-content leaf findings (Tab. 3.). From phosphate content, it is obvious that there was no significant transport and accumulation in the leaves after their foliar deposition. One of the scenarios shows the P potential absorption, transport, and accumulation in other parts of the plant tissues [31] or a higher quantitative production of sunflower biomass or corresponding leaf index area [32], considering the reduced P-content were redistributed into the leaves in various organic and inorganic forms [33].

In relation to N-content, the most effective was nano/macro-CaZnP treatment. The higher levels could suggest sunflowers' active growth and development under optimal physiology [34], appropriate agro-climate and environmental conditions [35] or sufficient bioavailable N forms in the soil. Oppositely, in the case of soil N-deficiency, it may indicate imbalanced stress conditions [34] but these conditions were not present in the soil where sunflowers were grown.

Relatively contradictory results were observed in the K-content of the leaves, which was highest in the NF-control than P-nanofertilizers application (Tab. 3). Generally, potassium regulates physiological processes such as the stomata movements [36], the regulation of osmotic pressure [37], the protein synthesis, metabolism or carbon assimilation [38], and stress responses against drought [39]. Authors [40] also present that insufficient K-absorption and abnormal plant development attributable to excessive P-

fertilization, or nitrogen, or their combination. However, this does not align with our NFs-applied experiments, which applied relatively low P-content corresponding to a few milligrams per liter. In this context, we utilize P- and Ca-based NFs supporting concepts of precision agriculture which currently absent in the academic research and potentially introduce new insights into this area of research.

CONCLUSION

In this agronomic study, two next-generation nanofertilizers based on P and Ca (macronutrients) compared to an NP-free control were applied to leaves of sunflowers in field conditions. The experiment was conducted during the 2022 growing season in Nitra, Slovakia, within the Central European agronomic region. In terms of yield-forming parameters, the NFs were more effective than the NP-free control, with the nano/macro-CaZnP treatment being the most effective. This could be attributed to the examined colloidal properties, where the yield benefits could be supported by smaller hydrodynamic size, higher (positive) ζ-potential, and the presence of ionically-soluble species. These factors were particularly associated with the most effective Zn-containing NFs. This was formed through a chemical synthesis route, compared to the second most effective NFs, the biotechnologically prepared n-HA. In the context of sunflower physiological effects that were based on photochemical reflectance index, the nano/macro-CaZnP treatment was also the most effective compared to both NP-free control and n-HA-treatments. Additionally, the induced plant physiology likely contributed positively to the beneficial yield-forming parameters in sunflowers. However, the profile of mineral nutrients in the sunflower leaves, selected one week after the 2^{th} application, presents a slight discrepancy. Contents of P and K were surprisingly most accumulated in the NP-free variant samples than the other variants, while nitrogen, an indicator of active plant-growth and development, was quantitatively higher in the nano/macro-CaZnP treatment. Our results confirmed that, at low concentrations, the spray-dispersion of macro-based NFs supports the implementation of new precision and sustainable agriculture concepts in field conditions.

ACKNOWLEDGEMENTS

This research was funded by the Grant Agency of the Slovak Republic Ministry of Education and the Slovak Academy of Sciences under contract VEGA 1/0655/23, VEGA 1/0359/22, VEGA 1/0331/23 and the operational program "*Research on the Impact of Biotic and Abiotic Factors on System Counterparts such as Soil-Water-Atmosphere-Plant Cover*" (313011T620), co-financed by the European Regional Development Fund.

REFERENCES

[1] Kolenčík, M., Nemček, L., Šebesta, M., Urík, M., Ernst, D., Kratošová, G., Konvičková, Z., Effect of TiO_2 as plant-growth stimulating nanomaterial on crop production, In: Singh, V.P., et al., editors. Plant responses to nanomaterials, Recent interventions, and physiological and biochemical responses. 1 ed. Springer Nature Switzerland AG: Springer International Publishing; 2021. pp. 129-144;

[2] Mousavi Kouhi, S.M., Lahouti, M., Ganjeali, A., Entezari, M.H., Comparative phytotoxicity of ZnO nanoparticles, ZnO microparticles, and Zn^{2+} on rapeseed (*Brassica napus* L.): investigating a wide range of concentrations. Toxicological & Environmental Chemistry, vol. 96, 2014, pp. 861-868;

https://doi.org/10.5593/sgem2024/6.1/s24.16

[3] Avellan, A., Yun, J., Zhang, Y., Spielman-Sun, E., Unrine, J.M., Thieme, J., Nanoparticle size and coating chemistry control foliar uptake pathways, translocation, and leaf-to-rhizosphere transport in wheat, ACS Nano, vol. 13:, 2019, pp. 5291-5305;

[4] Kolenčík, M., Ernst, D., Urík, M., Ďurišová, Ľ., Bujdoš, M., Šebesta, M., Dobročka, E., Kšiňan, S., Illa, R. and Qian, Y., Foliar application of low concentrations of titanium dioxide and zinc oxide nanoparticles to the common sunflower under field conditions, Nanomaterials, vol. 10, 2020, pp. 1-8, 1619;

[5] Genaidy, E.A.E., Abd-Alhamid, N., Hassan, H.S.A., Hassan, A.M., Hagagg, L.F., Effect of foliar application of boron trioxide and zinc oxide nanoparticles on leaves chemical composition, yield and fruit quality of *Olea europaea* L. cv. Picual, Bulletin of the National Research Centre, vol. 44, 2020, p. 106;

[6] Yusefi-Tanha, E., Fallah, S., Rostamnejadi, A., Pokhrel, L.R., Responses of soybean (*Glycine max* [L.] Merr.) to zinc oxide nanoparticles: Understanding changes in root system architecture, zinc tissue partitioning and soil characteristics, Science of the Total Environment, vol. 835, 2022, 155348;

[7] Transport a distribúcia syntetických nanočastíc v pôdach a sedimentoch, Chem listy, vol. 111, 2017, pp. 322-328;

[8] Ernst D, Kolenčík M, Šebesta M, Ďurišová Ľ, Ďúranová H, Kšiňan S, Illa, R., Safarik, I., Černý, I., Kratošová, G., Žitniak Čurná, V., Ivanič Porhajašová, J., Babošová, M., Feng, H., Dobročka, E., Bujdoš, M., Pospiskova, K. Afzal, S., Singh, N. K., Swamiappan, S., Aydın, E., Agronomic investigation of spray dispersion of metal-based nanoparticles on sunflowers in real-world environments, vol. 12, 2023, 1789;

[9] Li, C., Wang, P., van der Ent, A., Cheng, M., Jiang, H., Lund Read, T., Absorption of foliar-applied Zn in sunflower (*Helianthus annuus*): importance of the cuticle, stomata and trichomes, Annals of Botany, vol. 123, 2019, pp. 57-68;

[10] Al-Dhalimi, A.M., Al-Ajeel, S.A.H., Effect of plant regulators, zinc nanoparticles and irrigation intervals on leaf content of endogenous hormones and nutrients in sunflower (*Helianthus annuus* L.), Plant Archives, vol. 20, 2020, pp. 2720-2725;

[11] Kolenčík, M., Ernst, D., Komár, M., Urík, M., Šebesta, M., Ďurišová, Ľ., Bujdoš, M., Černý, I., Chlpík, J., Juriga, M., Illa, R., Qian, Y., Feng, H., Kratošová, G., Čech Barabaszová, K., Ducsay, L., Aydın, E., Effect of foliar application of ZnO nanoparticles to lentil production, physiology, and nutrients seed quality at field conditions, Nanomaterials, vol. 12, 2022, 310;

[12] Kolenčík, M., Ernst, D., Komár, M., Urík, M., Šebesta, M., Dobročka, E., Dobročka, E., Černý, I., Illa, R., Kanike, R., Qian, Y., Feng, H., Orlová, D. Kratošová, G., Effect of foliar spray application of zinc oxide nanoparticles on quantitative, nutritional, and physiological parameters of foxtail millet (*Setaria italica* L.) under field conditions, Nanomaterials, vol. 9, 2019, 1559;

[13] Yadav, A., Yadav, K., Abd-Elsalam, K.A., Nanofertilizers: types, delivery and advantages in agricultural sustainability, Agrochemicals, vol. 2, 2023, pp. 296-336;

[14] Paris, O., Burgert, I., Fratzl, P., Biomimetics and biotemplating of natural materials, MRS Bulletin, vol. 35, 2010, pp. 219-25;

[15] Sunil, B.R. and Jagannatham, M., Producing hydroxyapatite from fish bones by heat treatment. Materials Letters, vol. 185, 2016, pp. 411-414;

[16] Šebesta, M., Vojtková, H., Cyprichová, V., Ingle, A.P., Urík, M., Kolenčík, M., Mycosynthesis of metal-containing manoparticles - Fungal metal resistance and mechanisms of synthesis, International Journal of Molecular Sciences, vol. 23, 2022, 14084;

[17] Ernst, D., Kolenčík, M., Šebesta, M., Ďurišová, Ľ., Kšiňan, S., Tomovičová, L., Kotlárová, N., Kalúzová, M., Černý, I., Kratošová, G., Žitniak Čurná, V., Ivanič Porhajašová, J., Babošová, M., Dobročka, E., Qian, Y. Swamiappan, S., Illa, R., Gayathri Radhakrishnan, S., Ratna Sunil, B., Ducsay, L. Significance of phosphate nano-fertilizers foliar application: A brief real-field study of quantitative, physiological parameters, and agro-ecological diversity in sunflower, Agronomy, vol. 13, 2023, 2606;

[18] Meteoblue Available online: https://www.meteoblue.com/sk/ (accessed on March 2022);

[19] Šimanský, V., Kovačik, P., Long-term effects of tillage and fertilization on pH and sorption parameters of haplic Luvisol, Journal of Elementology, vol. 20/ no. 4, 2015, pp.1033-1040;

[20] Skala, O., Complex technology for oil crops cultivation, Česká zemědělská univerzita, Praha, 2016;

[21] Gamon, J.A., Peñuelas, J., Field CB. A narrow-waveband spectral index that tracks diurnal changes in photosynthetic efficiency, Remote Sensing of Environment, vol. 44, 1992, pp. 35-44;

[22] Knoppová, A., Pirkl, J., Kalina, J., Stanovení popelovin v rostlinném materiálu přesními expeditívními metodami, Vědecké práce. Praha: VÚRV, 1955;

[23] Liu, R., Lal, R., Potentials of engineered nanoparticles as fertilizers for increasing agronomic productions, Science of the Total Environment, vol. 514, 2015, 131-139;

[24] Benaïssa, H., Elouchdi, M.A., Removal of copper ions from aqueous solutions by dried sunflower leaves, Chemical Engineering and Processing: Process Intensification, vol. 46, 2007, pp. 614-622;

[25] Bal, V., Stability characteristics of nanoparticles in a laminar linear shear flow in the presence of DLVO and non-DLVO forces, Langmuir, vol. 35, 2019, pp. 11175-11187;

[26] Kohzuma, K., Tamaki, M., Hikosaka, K., Corrected photochemical reflectance index (PRI) is an effective tool for detecting environmental stresses in agricultural crops under light conditions, Journal of Plant Research, vol. 134, 2021, pp. 683-694;

[27]] Sturikova, H., Kryštofová, O., Huska, D., Adam, V., Zinc, zinc nanoparticles and plants, The Journal of Hazardous Materials. vol. 349, 2018, pp. 101-110;

[28] Plesnicar, M., Kastori, R., Petrovic, N., Pankovic, D., Photosynthesis and chlorophyll floorescence in sunflower (*Hellianthus annuss* L.) leaves as affected by phosphorus-nutrition, Journal of Experimental Botany, vol. 45, 1994, pp. 919-924.

[29] Sharma, B., Afonso, L.O.B., Singh, M.P., Soni, U., Cahill, D.M., Zinc- and magnesium-doped hydroxyapatite-urea nanohybrids enhance wheat growth and nitrogen uptake, Scientific Reports, vol. 12, 2022, 19506;

https://doi.org/10.5593/sgem2024/6.1/s24.16

[30] López-Arredondo, D.L., Leyva-González, M.A., González-Morales, S.I., López-Bucio, J., Herrera-Estrella, L., Phosphate nutrition: improving low-phosphate tolerance in crops, Annual Review of Plant Biology, vol. 65, 2014, 95-123;

[31] Lambers, H., Phosphorus acquisition and utilization in plants, Annual Review of Plant Biology, vol. 73, 2022, pp. 17-42;

[32] de Oliveira, A.K.S., Soares, E.B., dos Santos, M.G., Lins, H.A., de Freitas Souza, M., dos Santos Coêlho, E., Lindomar Maria Silveira, L.M., Mendonça, V., Paes Barros, A., Lopes, W.A.L., Efficiency of phosphorus use in sunflower. Agronomy, vol. 12, 2022, 1558;

[33] Suriyagoda, L.D.B., Ryan, M.H., Gille, C.E., Dayrell, R.L.C., Finnegan, P.M., Ranathunge, K., Nicol, D., Lambers, L., Phosphorus fractions in leaves, New Phytologist, vol. 237, 2023, pp. 1122-1135;

[34] Eaton, S.V., Effects of phosphorus deficiency on growth and metabolism of sunflower, Botanical Gazette, vol. 110, 1949, pp. 449-464;

[35] Nasim, W., Belhouchette, H., Tariq, M., Fahad, S., Hammad, H.M., Mubeen, M., Correlation studies on nitrogen for sunflower crop across the agroclimatic variability, Environmental Science and Pollution Research, vol. 23, 2016, 3658-3670;

[36] Outlaw, W.H., Current concepts on the role of potassium in stomatal movements, Physiologia Plantarium, vol. 59, 1983, pp. 302-311;

[37] Lindhauer, M.G., Potassium and phosphorus, Journal of Plant Nutrition, vol. 10, 1987, pp. 1965-1973;

[38] Shah, I.H., Jinhui, W., Li, X., Hameed, M.K., Manzoor, M.A., Li, P, Exploring the role of nitrogen and potassium in photosynthesis implications for sugar: Accumulation and translocation in horticultural crops, Scientia Horticulturae, vol. 327, 2024, 112832;

[39] Saeed Akram, M., Ashraf, M., Shahbaz, M., Aisha Akram, N., Growth and photosynthesis of salt-stressed sunflower (*Helianthus annuus*) plants as affected by foliar-applied different potassium salts, Journal of Plant Nutrition and Soil Science, vol. 172, 2009, pp. 884-893;

[40] Yahaya, S.M., Mahmud, A.A., Abdullahi, M., Haruna, A., Recent advances in the chemistry of nitrogen, phosphorus and potassium as fertilizers in soil: A review, Pedosphere, vol. 33, 2023, pp. 385-406.

ZINC OXIDE NANOPARTICLES INHIBIT SOME FUNGAL PATHOGENS INFECTION ON DURIAN SEEDLINGS

Assoc. Prof. Dr. Pornprapa Kongtragoul [1]

Miss Sansanee Pantakan [1]

[1] Department of Agricultural Technology, King Mongkut's Institute of Technology Ladkrabang Prince of Chumphon Campus, **Thailand**

ABSTRACT

Durian disease-causing organisms such as fungi can infect durian trees at any stage of development. Chemical fungicides are widely used because they are convenient and simple to use. However, it impacts the health of producers, consumers, and the environment. As a result, recommendations have been developed and established for researching zinc oxide nanoparticles (Zn-ONPs) that can inhibit fungal growth as an alternative for preventing and eliminating such fungi. The purpose of this study is to collect and isolate some fungi that cause durian diseases and their pathogenicity test, as well as to investigate the efficacy of Zn-ONPs ranging in size from 25 to 50 nm in inhibiting germination and fungal infection on durian seedlings. Three isolates of *Phytophthora* sp. (CL4_F1, CL4_S5, CL4_F10), two isolates of *Fusarium* sp. (CL6_FL1, CL6_FL2), two isolates of *Phomopsis* sp. (CH1_PF1, CH1_PF2), and two isolates of *Rhizoctonia* sp. (CL1_RL1, CL1_RL2) were successfully isolated as durian pathogenic fungi. All isolates were pathogenic on durian seedlings, with a 100% disease incidence. As a result, it was found that increasing the concentration of ZnO-NPs could further inhibit growth in the germination and infection of durian seedlings. All tested isolates had delayed germination by ZnO-NPs at all concentrations. Furthermore, as the severity of the disease decreased, ZnO-NPs could inhibit infection in durian seedlings at higher concentrations.

Keywords: durian diseases, zinc oxide nanoparticles, *Phytophthora* sp., *Fusarium* sp., *Phomopsis* sp., and *Rhizoctonia* sp.

INTRODUCTION

Thai Durian is one of the important economic fruits, with high international demand. However, these commercially important crops are affected by some fungal pathogens, for example, *Phytophthora* sp. causing fruit, stem, and root rot disease [1, 2], *Fusarium* sp. causing dieback disease [3], *Phomopsis* sp. causing leaf spot disease [4], and *Rhizoctonia* sp. causing leaf blight disease [5] and significant economic losses. Therefore, most Thai durian farmers selected chemical fungicides to control. Farmers believe that chemical fungicides can be managed promptly, used efficiently, and that was bought easily. However, using fungicides for an extended period will negatively affect farmers, consumers, and the environment directly and indirectly. Furthermore, the fungicide resistance of plant pathogens may occur in orchards [1].

https://doi.org/10.5593/sgem2024/6.1/s24.17

One potential alternative is using zinc oxide nanoparticles (ZnO-NPs) since these offer an environmentally friendly means of preventing plant disease for a sustainable future [6]. It is an inorganic compound that typically forms an insoluble white powder. There are some mechanisms by which zinc oxide nanoparticles can perform their antimicrobial activity. The first of these occurs through the release of antimicrobial Zn^{2+} ions. The second involves the use of light radiation to generate reactive oxygen species (ROS), such as hydrogen peroxide (H_2O_2), hydroxyl radicals (-O.H.), and superoxides (O^{2-}). Third, electrostatic interactions produce antimicrobial effects. ZnO-NPs can enter microbial cell walls via carrier proteins or ion channels, forming bonds with various organelles, allowing them to cause damage to the cells [7]. Previous research has determined the antifungal activity of zinc oxide nanoparticles against various fungal pathogens that attack plants, including *P. palmivora*, which causes durian disease [8], *Botrytis cinerea*, and *Penicillium expansum*, which affects fruit after harvesting [9], Fusarium wilt disease in eggplant [10], and *Rhizoctonia solani*, which causes black scurf disease in potatoes [11]. Other worthy of investigation are *Ralstonia solanacearum*, *Phomopsis vexans*, and *Meloidogyne incognita* [12]. However, ZnO-NPs carry out their antifungal activity is not entirely understood. However, the authors are unaware of any studies examining the effects of some diseases affecting durian crops. The objectives of this study were as follows: 1) to isolate the fungal pathogens causing durian diseases and their pathogenicity tests and 2) to assess ZnO-NPs sized 25-50 nm to determine their infections on durian seedlings.

MATERIALS AND METHODS

1. Collection, isolation, and pathogenicity test of fungal pathogens.

The disease samples were collected from commercial durian orchards. They were isolated the fungal pathogen using the tissue transplantation technique. The samples were cut into 0.5×0.5 cm pieces, disinfected with 10% Clorox for 3-5 minutes, dried on sterile tissue paper, then placed on water agar (WA) and incubated at room temperature (RT) for 2–3 days. As fungal hyphae grow, use a cork borer to cut off the tip and place it on potato dextrose agar (PDA). The fungus is separated and purified with a single spore isolate (SSI). They grow on a PDA medium and are stored in PDA slants.

Pathogenicity tests of all fungi were carried out with durian seedling assay. The tested fungi, including *Fusarium* sp., *Phomopsis* sp., and *Rhizoctonia* sp., were grown onto PDA and *P. palmivora* on carrot agar (CA) at RT for 7-10 days. They were prepared as inoculum at a concentration of 1×10^5 spores/ml, sprayed onto 6-month-old "Monthong" durian seedlings, and covered with plastic bags for 24 hours with four replicates. The disease incidence (DI) percentage was assessed from the occurrence of symptoms on durian seedlings. The disease severity index (DSI) was rated up to 4 levels of symptoms: level 0 indicates no disease symptoms, level 1 indicates 1-25% of disease symptoms, level 2 indicates >25-50% of disease symptoms, level 3 indicates >50-75% of disease symptoms, and level 4 indicates more than 75-100%.

2. Effect of ZnO-NPs on germination and infection of fungal pathogens on durian seedling

The spore suspensions of *P. palmivora*, *Fusarium* sp., and *Phomopsis* sp. were adjusted about $1x10^5$ spores/ml, and *Rhizoctonia* sp. were prepared mycelial suspension mixed with ZnO-NPs concentrations at 0 (control), 500, 1000, and 2000 µg/ml respectively.

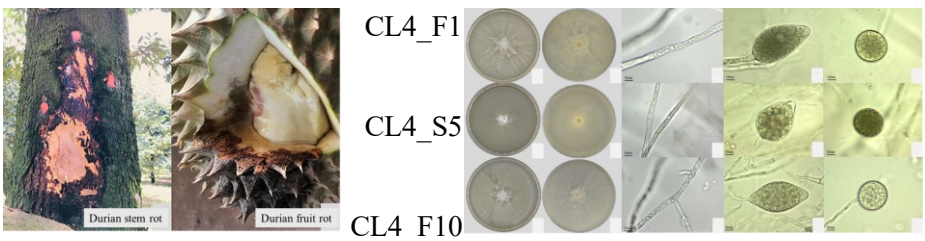
The 40 µl of mixer were dropped onto 1.5x1.5 cm of WA pieces and incubated in a moist box at room temperature. The spore germination of *P. palmivora*, *Fusarium* sp., *Phomopsis* sp., and mycelial germination of *Rhizoctonia* sp. was observed at 0, 3, and 6 hr under a microscope 400 times. Experiments were planned to use a completely randomized design (CRD) with 5 replicates. Count the number of spores and hyphae germinating to calculate the percentage of germination inhibition. Calculate the percentage inhibition of germination (PISG) in an area of 1 square millimeter. (TS = total number of spores, SG = number of spores that germinate)

The effect evaluation of ZnO-NPs of fungal pathogens was tested on the infection on durian seedlings. The inoculum of all fungal isolates was prepared using the experimental method in Section 1. They were sprayed onto 6-month-old "Monthong" durian seedlings and covered with plastic bags for 24 hours. Then, ZnO-NPs at 500, 1000, and 2000 µg/ml were sprayed on durian seedlings every 7 days 3 times. The inoculation with only pathogens and without pathogens were used as control treatments. A completely randomized design (CRD) with 4 replications was used in the experiment. The percentage of DI and DSI were recorded.

RESULTS

1. Collection, Isolation, and Pathogenicity test

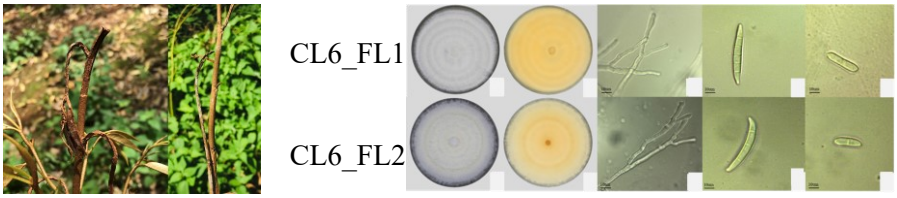
The results showed that 4 genera of durian pathogenic fungi with different diseases were successfully isolated and identified by morphological characteristics. The stem and fruit rot disease (Figure 1A) were three isolates of *Phytophthora* sp., namely CL4_F1, CL4_S5, and CL4_F10. They were rings and stellate pattern colonies and produced ovoid, limoniform sporangium with semi-papillate or papillate and formation chlamydospores (Figure 1B). The dieback diseases (Figure 2A) were isolated as two isolates of *Fusarium* sp., CL6_FL1 and CL6_FL2. They were the creamy white colonies, septate-hyphae, producing 2 forms of conidia: crescent-shaped macroconidia and elliptical microconidia (Figure 2B). The leaf spot diseases (3A) were isolated as two isolates of *Phomopsis* sp., namely CH1_PF1 and CH1_PF2. They appeared as colonies with flat growth on the surface media and slightly yellow of the central colony, greyish white mycelium, forming 2 conidia, alpha conidia ellipsoid, and beta conidia elongated with slightly bent (3B). Leaf blight diseases (4A) were isolated as two isolates of *Rhizoctonia* sp., CL1_RL1 and CL1_RL2. They were initially white colonies on the surface media when mature mycelium turned brown to dark brown. The hypha is perpendicular to the septum (4B).



(1A) (1B)

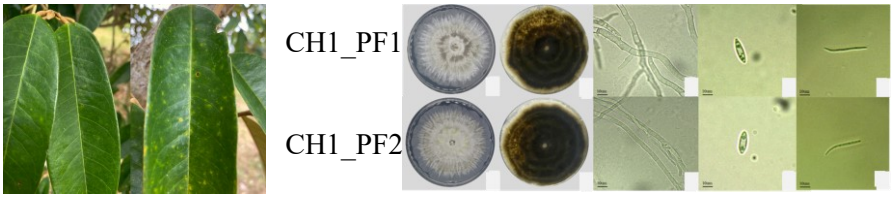
Figure 1 Symptoms of durian stem and fruit rot disease (1A), morphological characteristics of *Phytophthora* spp. with colony, mycelium, sporangium, chlamydospore on V8 agar for 10 days (1B).

https://doi.org/10.5593/sgem2024/6.1/s24.17



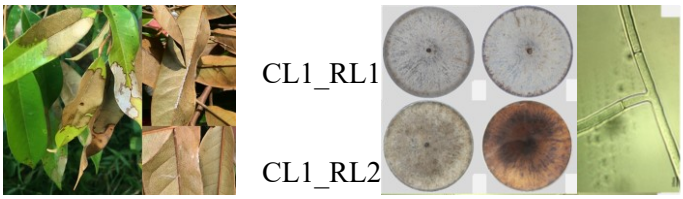
(2A) (2B)

Figure 2 Symptoms of durian dieback disease (2A), morphological characteristics of *Fusarium* sp., colony, mycelium, macroconidia, microconidia on PDA for 14 days (2B).



(3A) (3B)

Figure 3 Symptoms of durian leaf spot disease (3A), morphological characteristics of *Phomopsis* sp., colony on PDA for 14 days, mycelium, alpha conidia, beta conidia (3B).



(4A) (4B)

Figure 4 Symptoms of leaf blight disease on naturally infected durian leaves (4B), morphological characteristics of *Rhizoctonia* sp., colony for 7 days and 21 days grown on PDA, mycelium, sclerotium (4B).

All isolates were pathogenic on durian seedlings at 100% disease incidence (DI) with different disease severity indexes (DSI) shown in Table 1.

Table 1 Disease incidence (DI) of *Phytophthora palmivora* isolates after inoculation on durian seedlings for 7 days.

Fungal pathogen	**Isolate code**	**Disease Severity Index (DSI)**
Phytophthora sp.	CL4_F1	4.00
	CL4_S5	2.25
	CL4_F10	4.00
Fusarium sp.	CL6_FL1	4.00
	CL6_FL2	3.00
Phomopsis sp.	CH1_PF1	2.75
	CH1_PF2	2.50
Rhizoctonia sp.	CL1_RL1	2.50
	CL1_RL2	2.00

2. Effect of ZnO-NPs on germination and infection of fungal pathogens

Table 2 shows the efficacy of ZnO-NPs at 500, 1,000, and 2,000 µg/ml on germination of 4 genera of fungal pathogen causing durian diseases for 3 hr. after incubation. ZnO-NPs were found to inhibit growth further with increasing concentration. The 1,000 and 2,000 µg/ml concentration could completely inhibit spore germination of all P. palmivora and Fusarium sp isolates. Moreover, it was found that 1,000 and 2,000 µg/ml of ZnO-NPs inhibited the germination of all *Phomopsis* sp. and *Rhizoctonia* sp. isolates at 68.99-86.08% and 80.54-98.64% respectively.

Table 2 Efficiency of zinc oxide nanoparticles at 500, 1,000, and 2,000 µg/ml on germination of 4 genera of fungal pathogen causing durian diseases for 3 hr. after incubation.

Fungal pathogen	Isolate code	Inhibition of spore germination (%)[1/]				
	ZnO-NPs	Control	500	1000	2000 µg/ml	F-Test
Phytophthora sp.	CL4_F1	0.00c	77.42b	100.00a	100.00a	**
	CL4_S5	0.00c	83.17b	100.00a	100.00a	**
	CL4_F10	0.00c	80.00b	100.00a	100.00a	**
Fusarium sp.	macroconidia					
	CL6_FL1	0.00b	86.21a	100.00a	100.00a	**
	CL6_FL2	0.00c	68.62b	100.00a	100.00a	**
	microconidia					
	CL6_FL1	0.00c	47.62b	100.00a	100.00a	**
	CL6_FL2	0.00c	50.00b	100.00a	100.00a	**
Phomopsis sp.	CH1_PF1	0.00c	42.41b	68.99ab	86.08a	**
	CH1_PF2	0.00c	33.53b	72.46a	79.64a	**
Rhizoctonia sp.	CL1_RL1	0.00c	23.98b	80.54a	98.64a	**
	CL1_RL2	0.00c	28.11b	80.65a	94.47a	**

[1/]Values expressed are means with 4 replications. The letters in the same row are significantly different, as determined by the least significant difference test at $p<0.01$.

Table 3 shows the efficacy of zinc oxide nanoparticles at 500, 1000, and 2000 µg/ml, which were sprayed every 7 days for a total of 3 times after inoculation with (*Phytophthora* sp., *Fusarium* sp., *Phomopsis* sp., and *Rhizoctonia* sp.) and without pathogens on durian seedlings. It was found that spraying ZnO-NPs at all tested concentrations could not inhibit the disease occurrence in all tested pathogens. However, it was found that spraying ZnO-NPs with increasing concentration tended to reduce DSI compared to spraying only pathogens. ZnO-NPs at a 2000 µg/ml concentration show the best reduced DSI of all tested isolates. Moreover, it could reduce the DSI at 1.25-1.75 after inoculation with *Phytophthora* sp., 0.75-2.25 of *Fusarium* sp., 0.50-0.75 *Phomopsis* sp., and 0.25-0.75 *Rhizoctonia* sp.

https://doi.org/10.5593/sgem2024/6.1/s24.17

Table 3 Inhibitory effect of zinc oxide nanoparticles at 2000, 4000, and 8000 µg/ml on durian seedlings of 4 genera of fungal pathogen causing durian diseases on disease severity index (DSI).

Fungal pathogen Isolate code	Disease Severity Index (DSI)					
	Non-pathogen	pathogen	ZnO-NPs (µg/ml)			
			500	1,000	2,000	F-test
Phytophthora sp.						
CL4_F1	0.00a	3.75d	3.00cd	2.25bc	1.75b	**
CL4_S5	0.00a	2.50b	2.50b	1.75b	1.25ab	**
CL4_F10	0.00a	3.25c	3.50c	2.00b	1.75b	**
Fusarium sp.						
CL6_FL1	0.00a	1.50b	1.50b	1.00ab	0.75ab	*
CL6_FL2	0.00a	1.00ab	3.00b	2.50b	0.25ab	**
Phomopsis sp.						
CH1_PF1	0.00a	2.00b	2.00b	1.50ab	0.75ab	*
CH1_PF2	0.00a	2.25cd	2.75d	1.25bc	0.50ab	**
Rhizoctonia sp.						
CL1_RL1	0.00a	2.25c	1.50bc	1.00abc	0.25ab	**
CL1_RL2	0.00a	2.75b	3.00b	2.50b	0.75a	**

1/Values expressed are means with 4 replications. The different letters in the same row are significantly different as determined by the least significant difference test at $p<0.01$

DISCUSSION

The world's highest durian-growing region is Thailand. Thus, it is significant to research safe methods for preventing and controlling diseases. Consequently, samples of durian disease were taken from commercial durian orchards exhibiting symptoms such as root rot, stem rot, dry branches, leaf spots, and leaf blight. After being successfully isolated, it was discovered that *Phytophthora* sp., *Fusarium* sp., *Phomopsis* sp., and *Rhizoctonia* sp. are pathogenic for durian diseases. Other significant durian producers, such as Australia, Malaysia, Vietnam, and Indonesia, have explicitly tested for all pathogens [2, 13, 14].

These results indicate that ZnO-NPs (25-50 nm) may be effective in limiting the germination of durian pathogens; however, the overall efficacy of ZnO-NPs in terms of antifungal properties is concentration-dependent. Previous research has demonstrated that ZnO-NPs can more readily bind to the surface of fungi with pinocytosis due to their ability to absorb ZnO-NPs within the cells [6, 7]. ZnO-NPs can accumulate in either the outer membrane or the cytoplasm of a fungal cell, stimulating the release of Zn ion, destroying the fungal cell membrane, damaging the membrane protein, and causing genomic instability, all of which serve to inhibit fungal germination [6, 7]. This process is more efficient at higher concentrations because more zinc particles can exert influence. This could be due to fungi absorbing ZnO-NPs. Higher ZnO-NP concentrations were required to achieve a comparable infection reduction to the effects on germination. Our findings were consistent with those of Wagner et al. (15), who reported that ZnO-NPs could reduce *P. tabacica* infection in tobacco leaves.

Furthermore, Arciniegas-Grijalba et al. [16] investigated the effects of ZnO nanoparticles on the coffee fungus *Erythricium salmonicolor*. Their TEM images revealed cytoplasmic liquefaction, resulting in less electron density, several vacuoles, and significant cell wall detachment. These findings suggested that ZnO-NPs can function as an antifungal agent, preventing infection in durians.

CONCLUSION

As durian diseases, three isolates of *Phytophthora* sp., which causes stem and fruit rot disease, and two isolates of each genus, *Fusarium* sp., which causes dieback; *Phomopsis* sp., which causes leaf spot; and *Rhizoctonia* sp., which causes leaf blight, were collected and isolated. Every isolate was pathogenic on durian seedlings at 100% disease incidence, with varying disease severity indexes. ZnO-NPs 25–50 nm in size are the most effective at preventing fungal pathogen germination and reducing fungal infection in durian seedlings when applied at 2,000 µg/ml. Furthermore, it was found that increasing the concentration of ZnO-NPs (500–2,000 µg/ml) could further stop infection and germination in durian seedlings. In every tested isolate, ZnO-NPs at any concentration resulted in delayed germination. ZnO-NPs could therefore, at higher concentrations (2,000 µg/ml), prevent infection in durian seedlings as the disease severity decreased. These results suggest that ZnO-NPs could be a useful and secure alternative to fungicides in the treatment of durian disease.

ACKNOWLEDGEMENTS

The authors express their sincere gratitude for the support provided by King Mongkut's Institute of Technology Ladkrabang, Prince of Chumphon Campus, Chumphon, Thailand.

REFERENCES

[1] Kongtragoul P., Ishikawa K., Ishii H., Metalaxyl resistance of *Phytophthora palmivora* causing durian diseases in Thailand, Horticulturae, Netherlands, vol. 7/ issue 10, pp 375, 2021, https://doi.org/10.3390/horticulturae7100375;

[2] Lim T.K., Sangchote S., 2003. Diseases of durian. Diseases of tropical fruit crops, England, pp 241-251, ISBN 978-0-85199-390-4.

[3] Pongpisutta R., Keawmanee P., Sanguansub S., Dokchan P., Bincader S., Phuntumart V., Rattanakreetakul C., Comprehensive investigation of dieback disease caused by *Fusarium* in durian, Plants, Switzerland, vol. 12/ issue 17, p.3045. 2023, https://doi.org/10.3390/plants12173045;

[4] Piasai R., Chalmers P., Piasai O., Khewkhom N., Postharvest fungicide dips to control fruit rot of 'Monthong'durian (*Durio zibethinus*), European Journal of Plant Pathology, Netherlands, vol. 160, pp 325-336. 2021, https://doi.org/10.1007/s10658-021-02246-3;

[5] Kwee L.T., Chong N.C., Lan C.C., Etiology and control of durian foliar blight and dieback caused by *Rhizoctonia solani*, Annals of applied biology, United Kingdom, vol. 111/issue 2, pp 301-307. 1987, https://doi.org/10.1111/j.1744-7348.1987.tb01456.x;

https://doi.org/10.5593/sgem2024/6.1/s24.17

[6] Thounaojam T.C., Meetei T.T., Devi Y.B., Panda S.K., Upadhyaya H., Zinc oxide nanoparticles (ZnO-NPs): a promising nanoparticle in renovating plant science, Acta Physiologiae Plantarum, Poland, vol. 43, pp.1-21. 2021, https://doi.org/10.1007/s11738-021-03307-0;

[7] Miri A., Mahdinejad N., Ebrahimy O., Khatami M., Sarani M., Zinc oxide nanoparticles: Biosynthesis, characterization, antifungal and cytotoxic activity, Materials Science and Engineering C, Netherlands, 104, p.109981. 2019, https://doi.org/10.1016/j.msec.2019.109981;

[8] Ritmontree S., Kongtragoul P., December. Antifungal effect of zinc oxide nanoparticles against disease in durian caused by *Phytophthora palmivora*, In III Asian Horticultural Congress-AHC2020, Thailand, 1312, 2020. pp 423-430, https://doi.org/10.17660/ActaHortic.2021.1312.61;

[9] He L., Liu Y., Mustapha A., Lin M., Antifungal activity of zinc oxide nanoparticles against *Botrytis cinerea* and *Penicillium expansum*, Microbiological research, Germany, vol. 166/ issue 3, pp 207-215, 2011, https://doi.org/10.1016/j.micres.2010.03.003;

[10] Abdelaziz A.M., Salem S.S., Khalil A.M., El-Wakil D.A., Fouda H.M., Hashem A.H., Potential of biosynthesized zinc oxide nanoparticles to control Fusarium wilt disease in eggplant (*Solanum melongena*) and promote plant growth, BioMetals, Netherlands, vol. 35/issue 3, pp 601-616. 2022, https://doi/10.1007/s10534-022-00391;

[11] Al-Zaidi W.J., Ali A.M., Muhsen T.A., Efficacy of nanoparticle zinc oxide in the resistance of fungus *Rhizoctonia solani* causing black scurf disease in local potatoes, Caspian Journal of Environmental Sciences, Iran, vol. 21/issue 1, pp 95-103. 2023, https://doi.org/10.22124/CJES.2023.6199 ;

[12] Khan M., Siddiqui Z.A., Zinc oxide nanoparticles for the management of *Ralstonia solanacearum*, *Phomopsis vexans,* and *Meloidogyne incognita* incited disease complex of eggplant, Indian Phytopathology, United States, vol. 71, pp 355-364. 2018, https://doi.org/10.1007/s42360-018-0064-5;

[13] Mohamed Azni I.N.A., Sundram S., Ramachandran V., Pathogenicity of Malaysian *Phytophthora palmivora* on cocoa, durian, rubber, and oil palm determines the threat of bud rot disease, Forest Pathology, United Kingdom, vol. 49/issue 6, pp e12557, 2019, https://doi.org/10.1111/efp.12557;

[14] O'Gara E., Guest D.I., Vawdrey L., Langdon P., Diczbalis Y., 6.6 Phytophthora Diseases of Durian, and Durian-Decline Syndrome in Northern Queensland, Australia. Diversity and Management of *Phytophthora* in Southeast Asia, Australia, pp 143-151. 2004, ISBN 1863204059.

[15] Wagner G., Korenkov V., Judy J.D. and Bertsch P.M., Nanoparticles composed of Zn and ZnO inhibit *Peronospora tabacina* spore germination in vitro and *P. tabacina* infectivity on tobacco leaves, Nanomaterials, Switzerland, vol. 6/issue 3, p 50, 2016, https://doi.org/10.3390/nano6030050;

[16] Arciniegas-Grijalba P.A., Patiño-Portela M.C., Mosquera-Sánchez L.P., Guerrero-Vargas J.A., Rodríguez-Páez J.E., ZnO nanoparticles (ZnO-NPs) and their antifungal activity against coffee fungus *Erythricium salmonicolor*, Applied Nanoscience, Switzerland, vol. 7, pp 225-241, 2017, https://doi.org/10.1007/s13204-017-0561-3;

SECTION

ADVANCES IN BIOTECHNOLOGY

AIR QUALITY TRENDS IN LIVESTOCK BARNS

Assist. Prof. Dr. Kristina Dineva

Prof. Dr. Tatiana Atanasova

Dr. Victor Danev

Institute of Information and Communication Technologies – Bulgarian Academy of Sciences, **Bulgaria**

ABSTRACT

Livestock barns are integral to modern agriculture, providing essential environments for raising animals. The air quality in these barns directly impacts livestock health, quality of production and environmental sustainability. Trends in key metrics such as gas concentrations, particulate matter levels, humidity content, and temperature can influence the overall health of livestock, barn operations, and broader ecological factors. Understanding these trends and their interrelationships is crucial for managing barn conditions effectively.

To investigate air quality trends in livestock barns, data was collected using IoT multiple sensors device. These sensors recorded various metrics, including gas concentrations (hydrogen sulfide, ammonia, volatile organic compounds), particulate matter levels (PM2.5 and PM10), and humidity-related metrics such as relative humidity and dewpoint temperature. The collected data was analyzed using correlation and trend analyses to explore relationships between these variables and their influence on barn conditions. The analysis reveals key trends and positive correlations between the collected data.

Keywords: Internet of things, Air quality, Data analysis, Correlation, Livestock barns

INTRODUCTION

The air in livestock premises differs significantly from that of ambient air. The air in buildings where animals are kept is polluted with decomposition products of organic substances [1]. Numerous studies prove that the content of microbiological and chemical components in the air increases with the dustiness of the air. In turn, the concentration of dust depends on the activity of the animals, the efficiency of the ventilation and the physicochemical properties of the litter. The seasons and how animals are raised also affect the qualitative and quantitative composition of the air. The high humidity in the buildings and the higher, in contrast to the outside, air temperature, contribute to the transfer of aerosols containing microbiological and chemical components, and these are prerequisites for the occurrence of different disease states in animals.

Recently, there has been a trend towards intensification of livestock systems to increase productivity. However, it may have adverse effects on animal health. At the same time, technologically oriented approaches for animal welfare monitoring are being developed [2]. Neglecting the welfare of animals can hinder growth, reduce productivity and

https://doi.org/10.5593/sgem2024/6.1/s25.18

increase the incidence of disease. Important factors for animal welfare are the temperature-humidity relations, air flow and the content of ammonia, carbon dioxide, dust and microorganisms in the air [3]. The study [4] examines the complex transmission process of fine dust and offers the potential for adjusting the barn environment. Considering the influence of the microclimate and the dustiness led to an understanding of the need for regular measurements of the dust level in the barns.

A wide range of pollutants are released into the atmosphere with intensive livestock farming like emissions of ammonia (NH_3), nitrous oxide (N_2O), methane (CH_4), nitric oxides, a variety of organic species and reduced sulfur compounds, and primary PM2.5. There is growing interest in applying machine learning [5] methods to build models for predicting air concentrations of livestock-specific air constituents as it is proposed, for example in [6], where it is noted that the concentrations of bioaerosols are influenced by the type of farms, farm-level individual practices, manure handling procedures, feeding practices, housing conditions and ventilation systems. Many environmental impact studies have focused on ammonia, dust and methane emissions from livestock farms [6]. Ammonia emissions from cattle farms threaten ecosystems through acidification and eutrophication and are a key precursor to PM2.5 formation a in the atmosphere [7, 8]. The study [7] found that temperature, air velocity and relative humidity are important indoor factors that mark NH_3 emissions from livestock buildings.

The welfare of dairy cows is multifaceted. Achieving the goals of precision animal husbandry and improving animal health requires a system that integrates measurements of barn climate and air quality with measurements from individual caws, bearing in mind that the barn environment is an important factor of animal welfare [9].

The proposed article explores trends in air quality metrics over time, highlighting factors influencing livestock barn conditions and their implications for animal wellbeing.

MATERIALS & METHODS

The data for this study was collected over nearly a year, encompassing all four seasons, to capture a comprehensive range of climatic conditions. The data was gathered using an IoT multi-sensor device designed and built by our team, which was installed in a barn with natural ventilation in Troyan, Central Bulgaria. The IoT multi-sensor device used in this study was custom-built to measure various environmental parameters critical to barn air quality. The device comprised the following sensors:

1. MQ-137 Ammonia NH3 Gas Sensor Module
2. MQ-136 Hydrogen Sulphide Gas Sensor Modul
3. Nova PM Sensor SDS011 Laser PM2.5 PM10
4. CCS811 Total Volatile Organic Compound & equivalent Carbon Dioxide
5. SI7021 Temperature & Humidity Sensor
6. BMP280 Temperature & Barometric pressure combined Three-in-one Sensor

Table 1 provides an overview of the variables measured in the study.

Table 1: Description of collected parameters and associated hypotheses

Variable Name	Description	Hypothesis
Time	A DateTime variable indicates when the readings were taken.	Time of day may correlate with changes in environmental metrics, reflecting potential daily cycles and seasons.
Humidity %	Numerical variable showing the humidity percentage at the time of recording.	High humidity may affect air quality, influencing gas levels and particulate concentrations.
H2S ppm	Numerical variable indicating the concentration of hydrogen sulphide (H2S) in parts per million.	High H2S levels may correlate with poor air quality, impacting livestock health.
Pressure hPa	Numerical variable indicating atmospheric pressure in hectopascals.	Pressure changes may correlate with variations in environmental conditions, including gas levels and humidity.
PM2.5 µg/m3	Numerical variable representing the concentration of particulate matter < 2.5 microns, in µg/m3.	PM2.5 levels may correlate with other pollutants, affecting air quality and livestock health outcomes.
PM10 µg/m3	Numerical variable representing the concentration of particulate matter < 10 microns, in µg/m3.	PM10 levels may reflect environmental conditions, impacting livestock health and air quality.
Dewpoint C^{o}	Numerical variable showing the dewpoint temperature in degrees Celsius in the barn.	Dewpoint may influence or correlate with humidity, affecting overall barn conditions.
NH3 ppm	Numerical variable representing the concentration of ammonia (NH3) in parts per million.	High ammonia levels may indicate poor air quality, impacting livestock health.
TVOC ppb	Numerical variable showing the concentration of Total Volatile Organic Compounds (VOCs) in parts per billion.	TVOC levels may correlate with other air pollutants, reflecting overall environmental quality.
eCO2 ppm	Numerical variable indicating the equivalent concentration of carbon dioxide in parts per million.	eCO2 levels may correlate with other pollutants, reflecting barn conditions and air quality.

https://doi.org/10.5593/sgem2024/6.1/s25.18

RESULTS

The IoT multi-sensor device was configured to collect data continuously throughout the year. The data was stored and processed using the pandas-profiling Python library, which provided comprehensive profiling reports and facilitated the analysis of environmental metrics. The collected data included time-stamped records of all measured parameters, allowing for the analysis of daily cycles and seasonal variations in barn conditions.

A specific set of data points or metrics changes over some time making a trend in the overall direction. In the case of livestock barns, trends indicate the changing environmental conditions and various factors that affect the well-being and health of the livestock as well as the overall processes of the barn.

The hypotheses were formulated to explore how different environmental factors might interact and influence air quality, thereby affecting livestock health and overall barn conditions. The significance of the measured variables, and the expected relationships between these variables and the environmental conditions in the barn are shown in the Table 1. The hypothesizes are combined and summarized into three main suggestions that form the basis for presenting the research results.

Hypothesis 1: Increased humidity in livestock barns correlates positively with higher gas levels such as hydrogen sulfidic, ammonia, and total volatile organic compounds, suggesting that humidity facilitates the release or retention of these gases.

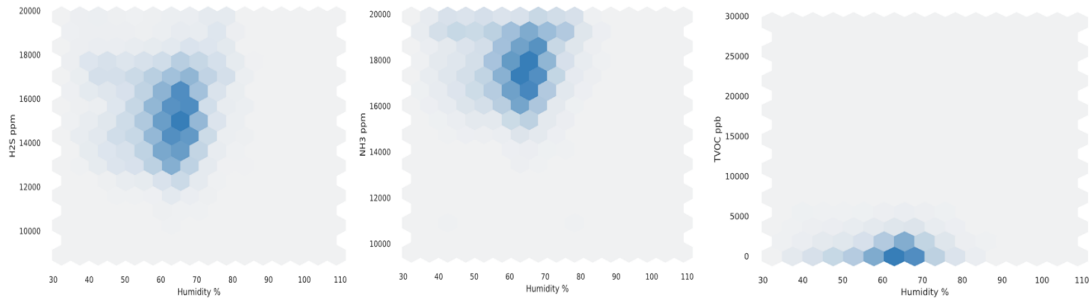


Figure 1. Scatter plots comparing humidity with various gas levels metrics: a) humidity % vs H2S, b) humidity % vs NH3, c) humidity % vs TVOC.

The relationship between humidity and pollutant concentrations shows trends, particularly when observing hydrogen sulfide (H2S), ammonia (NH3), and total volatile organic compounds (TVOCs). Figures 1a, 1b and 1c collectively demonstrate a concentration of data points within a central humidity range, typically between 50% and 70%. This suggests a positive correlation between humidity and pollutant levels, where increased humidity facilitates releasing or retaining these gases.

For H2S, as visualized in Figure 1a, humidity levels between 50% and 70% show higher concentrations of data points, indicating that this humidity range promotes H2S release in the barn environment. This could be due to the humid conditions enhancing microbial activity or the decomposition of organic matter, leading to more significant H2S emissions. As a result, this impacts barn air quality and potentially affects livestock health due to elevated gas concentrations.

Similarly, Figure 1b reveals a similar pattern for NH3, where ammonia levels are higher within the 50% to 70% humidity range. Increasing humidity may heighten microbial

activity or accelerate manure decomposition, contributing to more significant NH3 emissions. This underscores the importance of managing barn humidity to control ammonia levels, ensuring better air quality and safeguarding livestock health.

Figure 1c highlights the relationship between humidity and TVOC concentrations. The data points are mainly concentrated between 60% and 75% humidity, and the TVOC levels are primarily below 5,000 ppb, indicating that higher humidity levels may facilitate the emission of volatile organic compounds. This trend suggests that elevated humidity can contribute to increased TVOC levels, affecting overall environmental quality.

The lower pollutant concentrations observed under 50% and above 70% humidity can be attributed to different mechanisms. Below 50% humidity, the environment might be too dry for optimal microbial activity, reducing the breakdown of organic materials and subsequent gas emissions. Above 70% humidity, the air might become saturated, potentially slowing down further gas emissions or promoting the dissolution of these gases into moisture, thereby reducing their concentration in the air. These insights emphasize the critical role of maintaining optimal humidity levels in barns to manage pollutant concentrations effectively.

Hypothesis 2: Increased humidity in livestock barns correlates positively with PM2.5 and PM10 µg/m3 concentrations.

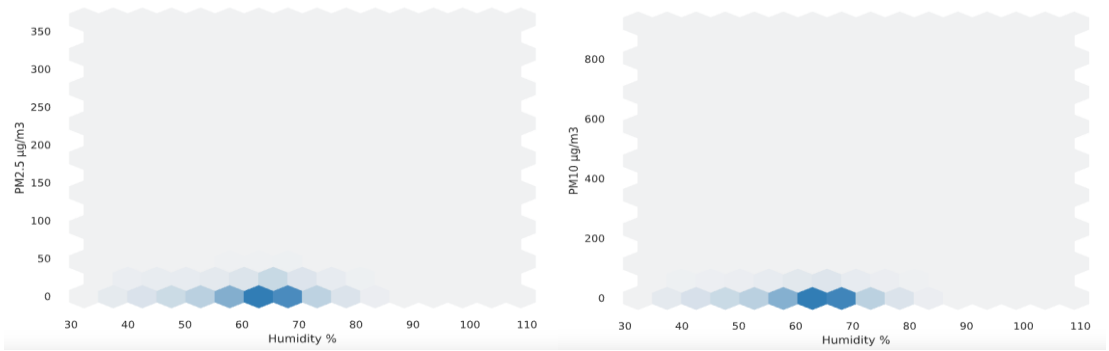


Figure 2. Scatter plots comparing humidity with different concentrations of particulate matter a) humidity % vs PM2.5, b) humidity % vs PM10

The relationship between Humidity % and particulate matter concentrations is visualized in Figure 2, showing a concentration of data points in the range between 60% and 70% humidity.

This suggests a positive correlation between humidity and both PM2.5 and PM10 levels, indicating that higher humidity corresponds to increased particulate concentrations. This relationship may arise from several factors: humid conditions might facilitate the generation or retention of particulate matter, potentially through chemical or microbial processes. Additionally, humidity could affect barn activities or conditions, contributing to dust or particulate accumulation.

This trend may arise from several factors: humid conditions might facilitate the generation or retention of particulate matter, potentially through chemical or microbial processes. Additionally, humidity could affect barn activities or conditions, contributing to dust or particulate accumulation. Furthermore, elevated humidity levels can enhance the binding of particles, keeping them suspended in the air longer. It can also boost

https://doi.org/10.5593/sgem2024/6.1/s25.18

chemical reactions and microbial activities that generate or transform particulate matter, contributing to their increased concentrations.

Hypothesis 3: Increased humidity in livestock barns correlates positively with higher dewpoint temperatures, reflecting the interdependence between moisture content and temperature.

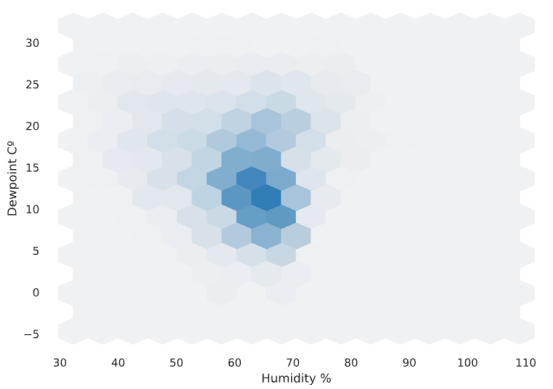


Figure 3. Scatter plots presenting the relationship between humidity and dewpoint Cº in the livestock barn.

The scatter plot shows a concentration of data points in the range between 55% and 75% humidity, with dewpoint Cº ranging from 5 to 20 degrees Cº, indicating a positive correlation between Humidity % and Dewpoint. This reflects the physical relationship between these variables, where dewpoint temperature represents the point at which air reaches saturation or 100% relative humidity. As the air's humidity content increases, so does its dewpoint temperature, leading to this observed relationship.

Elevated dewpoint temperatures can lead to higher perceived temperatures, potentially causing heat stress in animals.

DISCUSSION

The results of this study underscore the significant impact of humidity on air quality within livestock barns. The positive correlation between humidity levels and the concentrations of hydrogen sulfide concentration, atmospheric pressure, fine and coarser dust particles, dew point temperature, ammonia concentration, volatile organic compounds and carbon dioxide equivalent, highlights the crucial role of moisture in facilitating the release or retention of these politeness. These findings emphasize the need for precise humidity management to mitigate the release of harmful gases and ensure better air quality for both livestock and workers.

These findings are consistent with previous research that highlights the critical role of the barn microclimate in influencing air quality and animal health [10]. However, the study's limitations, including its specific geographic and climatic focus, should be considered when generalizing the results. Future research should explore the impact of humidity in different types of livestock barns and under varying environmental conditions to validate and extend these findings. Practical applications of this research include the development of targeted ventilation and humidity control strategies to optimize barn conditions, thereby enhancing both animal welfare and productivity. The insights gained underscore the importance of regular monitoring and environmental

control in livestock barns to ensure a healthier and more sustainable agricultural practice.

CONCLUSION

The dataset reveals several key trends in air quality metrics within livestock barns. Firstly, there is a positive correlation between humidity and gas levels, including hydrogen sulfide, ammonia, and volatile organic compounds, suggesting that higher humidity facilitates the release or retention of these gases. Additionally, the data shows a positive correlation between humidity and particulate matter concentrations (PM2.5 and PM10), indicating that increased humidity may contribute to particulate accumulation through microbial or chemical processes. Lastly, a positive correlation is observed between humidity and dewpoint temperatures, highlighting the interdependence between humidity content and temperature. These trends emphasize the dynamic interplay between environmental factors in barns, affecting air quality and highlighting the need for effective management practices to regulate moisture content, control gas emissions, and ensure optimal conditions for livestock health and environmental sustainability to gain better insights into the mechanisms underlying the effects. Overall, the research provides valuable insights into the environmental dynamics of livestock barns, highlighting the need for targeted ventilation and humidity control strategies. By optimizing barn conditions, it is possible to enhance animal welfare and productivity while minimizing the environmental impact of intensive livestock farming.

ACKNOWLEDGEMENTS

The research leading to these results received funding from the Ministry of Education and Science of the Republic Bulgaria under the National Science Program INTELLIGENT ANIMAL HUS-BANDRY, grant agreement No. Д01-62/18.03.2021/.

REFERENCES

[1] Chmielowiec-Korzeniowska A., Trawińska B., Tymczyna L., Bis-Wencel H., Matuszewski Ł. Microbial contamination of the air in livestock buildings as a threat to human and animal health—a review. Annals of Animal Science21(2):417–431, 2021. https://doi.org/10.2478/aoas-2020-0080

[2] Dineva K., Atanasova T. Health Status Classification for Cows Using Machine Learning and Data Management on AWS Cloud. Animals, MDPI, vol. 13(20), 3254, 2023. https://doi.org/10.3390/ani13203254

[3] Benić M. Behaviour and well-being of dairy cows in modern livestock production. Veterinarska stanica, 55(2), 2024. https://doi.org/10.46419/vs.55.2.3

[4] Mostafa E., Paßmann J., Abdellatif H. R. S., Buescher W. Improving the forecast of fine dust emission and transmission from cattle barns: a comprehensive data package and analysis. Environmental Sciences Europe, 36(42), 2024. https://doi.org/10.1186/s12302-024-00845-5

[5] Dineva K., Atanasova T. Machine Learning Solution for IoT Big Data. 20th International Multidisciplinary Scientific GeoConference SGEM, 20(2.1), 2020. https://doi.org/10.5593/sgem2020/2.1/s07.027

https://doi.org/10.5593/sgem2024/6.1/s25.18

[6] Hewitt B. C., Smit L.A.M., van Kersen W., Wouters I.M., Heederik D.J.J., Kerckhoffs J., Hoek G., de Rooij M.M.T. Residential exposure to microbial emissions from livestock farms: Implementation and evaluation of land use regression and random forest spatial models. Environmental Pollution. April, 1;346:123590. 2024. https://doi.org/10.1016/j.envpol.2024.123590

[7] Tabase R. K., Næss G., Larring Yn. Ammonia and methane emissions from small herd cattle buildings in a cold climate. Science of The Total Environment, p. 166046, 2023. https://doi.org/10.1016/j.scitotenv.2023.166046

[8] Burns A. M., Chandler G., Dunham K. J., Carlton A. G. Data Gap: Air Quality Networks Miss Air Pollution from Concentrated Animal Feeding Operation. Environ. Sci. Technol. 57(49), 20718–20725, 2023. https://doi.org/10.1021/acs.est.3c06947

[9] Leliveld L. M. C. Brandolese C., Grotto M., Marinucci A., Fossati N., Lovarelli D., Riva E., Provolo G. Real-time automatic integrated monitoring of barn environment and dairy cattle behaviour: Technical implementation and evaluation on three commercial far Computers and Electronics in Agriculture, 216, article id: 108499, 2024. https://doi.org/10.1016/j.compag.2023.108499

[10] Mylostyvyi R., Izhboldina O., Chernenko O., Khramkova O., Kapshuk N., Hoffmann G. Microclimate modeling in naturally ventilated dairy barns during the hot season: Checking the accuracy of forecasts. Journal of Thermal Biology, 93, 102720, 2020. https://doi.org/10.1016/j.jtherbio.2020.102720

ANTIMICROBIAL POTENTIAL OF METHANOLIC AND N-HEXANE EXTRACTS OF VISCUM ALBUM

Assoc. Prof. Dr. Marioara Nicoleta Caraba[1,2,3]

Lecturer dr. Ion Valeriu Caraba[3,4]

Prof. Dr. Gabi Dumitrescu[3,4]

Prof. dr. Elena Pet[5]

Prof. Dr. Roxana Popescu[2,3]

[1]Faculty of Chemistry, Biology, Geography, West University of Timisoara, **Romania**

[2]Faculty of Medicine, "Victor Babes" University of Medicine and Pharmacy of Timisoara, **Romania**

[3]ANAPATMOL Research Center, "Victor Babes" University of Medicine and Pharmacy of Timisoara, **Romania**

[4]Faculty of Bioengineering of Animal Resources, University of Life Sciences "King Mihai I" from Timisoara, **Romania**

[5]Faculty of Management and Rural tourism, University of Life Sciences "King Mihai I" from Timisoara, **Romania**

ABSTRACT

Plants are sources of compounds with medicinal potential, an impressive number of medicines have in their composition compounds isolated from natural sources, many of them being used since ancient times, in traditional medicine. Aromatic and medicinal plants are sources of various nutrients and non-nutritive molecules, many of which exhibit antimicrobial and antioxidant properties. *V. album* extracts have a complex chemical composition, some of the identified compounds being responsable for their antibacterial and antifungal potential. The chemical composition of *V. album* extracts differs depending on the provenance and especially with respect to the host plant. The antimicrobial effect of extracts in methanol and n-hexane from leaves and young branches of *V. album* was tested by the diffusimetric method on agar. In the study, five concentrations were tested for each extract, on four Gram positive bacterial strains: *Streptoccoccus pyogenes*, *Enterococcus faecalis*, *Clostridium perfringens*, *Staphylococcos aureus* and three Gram negative: *Escherichia coli*, *Pseudomonas aeruginosa*, *Legionella pneumophila*, respectively two antibiotics: ampicillin and chloramphenicol were used as a reference control. Gram+ and Gram- bacterial strains showed an intermediate sensitivity at the first two concentrations tested for both extracts (methanolic and n-hexane), after which the antibacterial potential decreases with the decrease in concentration until it disappears completely. The effects of the methanolic extract of *V. album* is more obvious in Gram+ bacteria compared to Gram-. The n-hexane extract of *V. album* determines an antimicrobial effect only at the first concentrations tested, there are variations depending on the bacterial strain.

Keywords: extracts, natural compounds, antimicrobial

https://doi.org/10.5593/sgem2024/6.1/s25.19

INTRODUCTION

Nature has been a source of medicines for thousands of years and an impressive number of modern medicines have been isolated from natural sources, many based on their use in traditional medicine. Various medicinal plants have been used for years in everyday life to treat diseases all over the world. They have been used as a source for obtaining new natural drugs without adverse, side effects. In fact, plants contain a diverse range of bioactive molecules, making them a rich resource for obtaining different types of products with therapeutic effect [1].

In many studies, a variety of pharmaceutical effects of different types of V. album extracts have been highlighted and different types of activities have been reported: antidiabetic [2], antioxidant [3], vasodilator [4], sedative, antiepileptic, antipsychotic [5], antihypertensive [1,6], anti-inflammatory, immunostress-stimulating, antimutagenic [7], anticarcinogenic [8,9], antimicrobial [1,8].

V. album contains glycoproteins (lectins), polypeptides (viscotoxins), flavonoids, alkaloids, amines, caffeic and other acids, terpenoids, lignans and acetylcholine [10]. Other studies revealed a complex structure determined by triterpene saponosides (β-amyrin and oleanolic acid derivatives), β and α viscol, amines (choline and acetylcholine), β-phenylethylamine, inositol, free amino acids, fatty substances formed from oleic acid, linoleic, palmitic, etc., vitamins C and E, mucilages, glycosidic substances (syringin), quercetin, sugars, viscotoxin (polypeptide that is inactivated by heating and hydrolysis), viscid acid, a polysaccharide with antitumor action, mineral salts, etc. [1]. The mentioned compounds are responsible for the properties of the previously mentioned extracts.

Viscum album is part of the Loranthaceae family, it includes semi-parasitic shrubs that attach to the host tree by means of haustoria. The mistletoe has a wide area, central European, southern European and Asian. In Romania, numerous woody species are parasitized, which leads to the drying of already weakened trees; it occurs frequently in hilly and mountain areas [9].

There are no studies in the specialized literature, so there are no published data that highlight possible antibacterial effects of *Viscum album* extracts on bacterial strains - *Enterococcus faecalis*, *Clostridium perfringes* and *Legionella pneumophila*. So, the novelty element of our study is the testing of the possible antibacterial effects of the *V. album* extract on the bacterial strains listed above and at the same time the use of different concentrations than those presented in the literature.

MATERIALS AND METHODS

The compound tested

The V album extracts were made from plants harvested from Săcuieni (Bihor County, Romania), the buds, stems and young leaves represented the biological material used to obtain the methanolic extract and in n-hexane. The methanolic extract of V. album was tested in 5 concentrations: c1-29.10 mg/mL, c2-19.4 mg/mL, c3-11.64 mg/mL, c4-5.82 mg/mL, c5-2.91 mg/mL. The n-hexane extract of V, album showed the following concentrations: c1-23.44 mg/mL, c2-15.62 mg/mL, c3-9.37 mg/mL, c4-4.68 mg/mL, c5-2.34 mg/mL.

Bacterial strains

In vitro, the amtimicrobial effect was tested on 4 Gram positive bacterial strains: *Streptoccoccus pyogenes* (ATCC 196415), *Enterococcus faecalis* (ATCC 29212), *Clostridium perfringens* (ATCC 13124), *Staphylococcos aureus* (ATCC 25923), respectively 3 Gram negative strains: *Escherichia coli* (ATCC 8739), *Pseudomonas aeruginosa* (ATCC 10145), *Legionella pneumophila* (ATCC 33152).

Assessment of minimum inhibitory concentration

The assessment of antibacterial activity of chitosan was undertaken by employing the agar diffusion method (Kirby-Bauer method) that allows one to estimate the MIC based on inhibition distances (mm) around the culture media. The solid culture medium employed was Tripton soy agar (TSA). 50µL of the liquid culture medium with the bacteria tested was transferred onto a Petri dish. The discs were applied and on each disc a volume of 10 µL of different concentrations of chitosan were applied. The bacterial plates were incubated at 37°C for 48 h. The test was carried out in triplicates. The zones of inhibition were measured afterwards by using a scale and the antimicrobial activity was calculated [11,12,13]. Two antibiotics were used as control: ampicillin (100 mg/mL) and chloramphenicol (25 mg/mL). All experiments were conducted in triplicate.

Statistical analysis

The data were analyzed using variance analysis. The significance between samples was determined using Mann-Whitney test. The difference was considered significant when $p < 0.05$, highly significant when $p < 0.01$ and non-significant when $p > 0.05$.

RESULTS

The methanolic and n-hexane extracts obtained from *V. album* were tested on the microtablets applied in Petri dishes with solidified culture medium and inoculated with the bacterial strains of interest. The values of the zones of inhibition were determined after the completion of the incubation period of the plates, as all concentrations of extracts were tested on each bacterial strain in triplicate, the values presented graphically are the averages of the determinations.

Analyzing the antibacterial potential of the methanolic extract on Gram+ bacterial strains, we identify a moderate antibacterial potential for *Enteroccus faecalis* at c1 (11.33±0.03 mm) and c2 (10.66±0.03 mm) of the tested extract, in the case of the *Streptoccoccus pyogenes* strain, the moderate antibacterial potential being identified only at c1 (9.66±0.13 mm). For the other 2 bacterial strains, regardless of the concentration, the antibacterial effect could not be highlighted.

In the case of the n-hexane extract of mistletoe, a moderate antibacterial effect against Enteroccus faecalis is evident at c1 (13.33±0.06 mm), c2 (12.33±0.17 mm), respectively at c3 (9.33±0.23 mm) of the extract. For the strain of *Clostridium perfringens*, the moderate antibacterial effect is highlighted only when testing c1 (9.33±0.16 mm). The extract in n-hexane from leaves and young branches of mistletoe did not show antibacterial potential to *Streptoccoccus pyogenes*, respectively *Staphylococcos aureus*.

https://doi.org/10.5593/sgem2024/6.1/s25.19

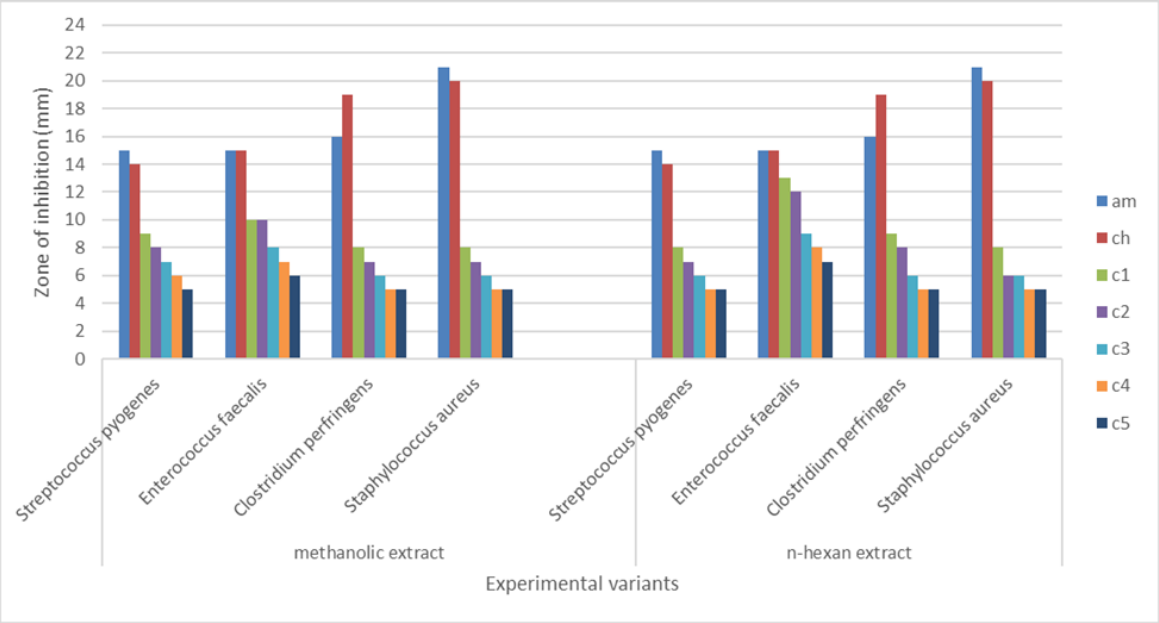


Figure 1. Antibacterial potential of methanolic and n-hexane extracts of *V. album* on Gram+ bacterial strains

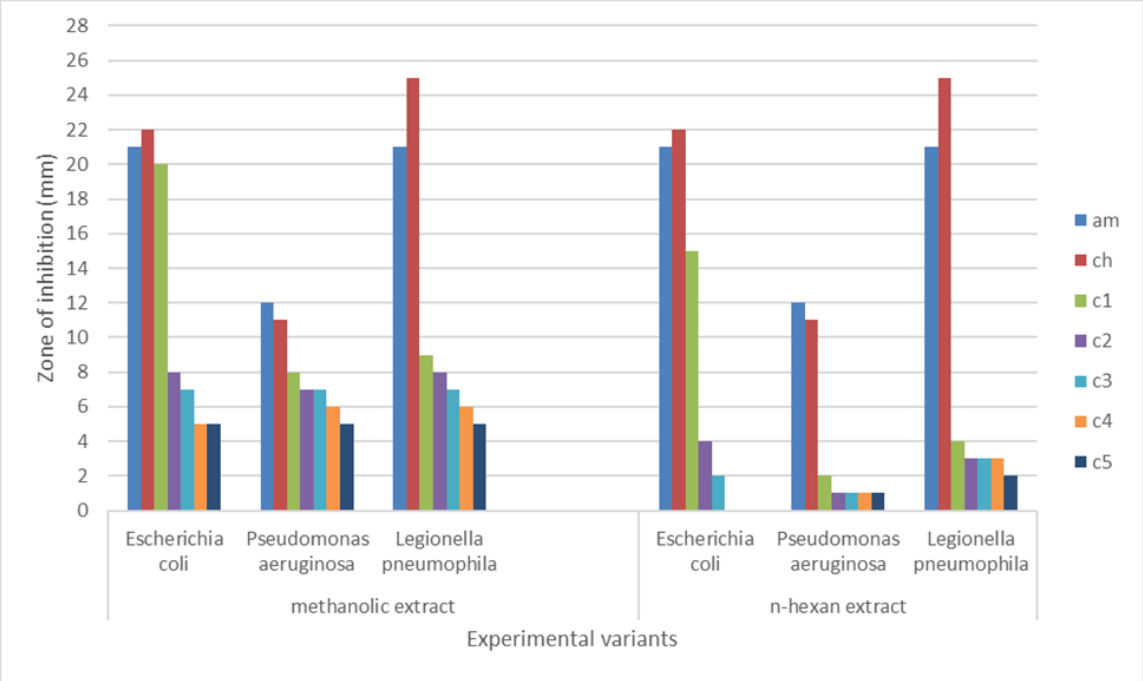


Figure 2. The antibacterial potential of the methanolic and n-hexane extracts of *V. album* on Gram-

From the analysis of the inhibition zone values determined by the methanolic extract on the Gram- bacterial strains, we identified an antibacterial potential in the *Escherichia coli* strain at c1 (20.66±0.08 mm). The moderate antibacterial effect is identified for *Legionella pneumophila* at c1 (9.33±0.03 mm). In the case of *Pseudomonas aeruginosa*, the antibacterial effect was not highlighted regardless of the tested concentration. The extract in n-hexane of mistletoe has an obvious antibacterial effect on Escherichia coli

at c1 (15.83±0.16 mm), on the other 2 bacterial strains the effect is absent regardless of the tested concentration.

DISCUSSION

Aromatic and medicinal plants are known for their ability to produce bioactive molecules that interact with microorganisms, having the property of inhibiting the growth of different groups of bacteria or fungi. Substances that can inhibit pathogens and have low toxicity to host cells are being considered for the development of new drugs with antimicrobial properties. The chemical composition of mistletoe extracts differs depending on the origin and especially with respect to the host plant, the effects being closely related to the chemical composition of the extract and the type of solvent used for extraction.

Studies are presented in the literature that test the effects of mistletoe extracts made in solvents such as ethyl acetate, chloroform, the results obtained differ compared to those obtained in our study, a fact due to the different solvent used to make the extract, the extract concentrations used (higher compared to those applied in our study), respectively the bacterial strain under study.

Thus, the extract made from the leaves of *V. album* in ethyl acetate showed prominent antibacterial activity against the bacterial strains of *Staphylococcus aureus, Bacillus subtilis, Escherichia coli, Bordetella bronchiciptica, Pseudomonas aeruginosa* and *Pseudomonas syringae,* the values of the inhibition zones determined for these strains being 24.33±0.17 mm *(Staphylococcus aureus)*, 19.66±0.33 mm (*Bacillus subtilis*), 24.96±0.23 mm *(Escherichia coli),* 24.83±0.17 mm *(Bordetella bronchiciptica),* 19.66±0.33 mm *(Pseudomonas syringae),* 19.66±0.33 mm *(Pseudomonas aeruginosa*). Also, the same extract, in the same concentrations, did not show an antibacterial effect on the microbial strains of *Enterococcus faecium, Salmonella typhae, Saccharomyces cerevisiae* and *Aspergillus flavus* [14,15].

In another study, the effect of the extract from the branches of V. album plants also in ethyl acetate was tested, the extracts showed appreciable antibacterial activity against *Staphylococcus aureus, Bacillus subtilis, Enterococcus faecium, Escherichia coli, Bordetella bronchiciptica, Pseudomonas aeruginosa, Pseudomonas syringae and Salmonella typhae.* The values of the determined inhibition zones were: 15.83±0.17 mm *(Staphylococcus aureus),* 15.06±0.06 mm *(Bacillus subtilis),* 20.06±0.6 mm *(Enterococcus faecium)*, 24.83±0.17 mm *(Escherichia coli),* 15.06±0.03 mm (*Bordetella bronchiciptica*), 19.66±0.33 mm *(Pseudomonas aeruginosa),* 22.66±0.33 mm *(Pseudomonas syringae)*, 15.06±0.06 mm *(Salmonella typhae*). Fungal strains of *Saccharomyces cerevisiae* and *Aspergillus flavus* did not show antifungal sensitivity to the same type of extract tested [15].

Extracts made from leaves of *V. album* in methanol showed antibacterial activity on *Enterococcus faecium* (19.83±0.17 mm), *Pseudomonas aeruginosa* (19.83±0.17 mm) and *Pseudomonas syringae* (20.93±0.06 mm). The antibacterial potential was not highlighted in the case of *Escherichia coli, Staphylococcus aureus, Bacillus subtilis, Bordetella bronchiciptica, Salmonella typhae, Saccharomyces cerevisiae* and *Aspergillus flavus*. The extract from the twigs of V. album also in methanol determined antibacterial action only on the bacterial strains *Staphylococcus aureus* (19.83±0.16

https://doi.org/10.5593/sgem2024/6.1/s25.19

mm) and *Escherichia coli* (24.83±0.17 mm), in the case of the other bacterial and fungal strains the antimicrobial effect could not be highlighted [15].

The mistletoe leaf extract in chloroform showed antibacterial activity against *Escherichia coli* (19.76±0.23 mm), *Pseudomonas aeruginosa* (10.00± .00 mm), *Pseudomonas syringae* (15.16±0.16 mm). In the species of *Staphylococcus aureus, Bacillus subtilis, Bordetella bronchiciptica, Salmonella typhae, Saccharomyces cerevisiae* and *Aspergillus flavus,* no antimicrobial potential was demonstrated. The extract of V. album branches in chloroform showed moderate antibacterial activity on most of the microorganisms studied, except for *Saccharomyces cerevisiae* and *Aspergillus flavus* [15].

In another study carried out with mistletoe extract in n-hexane, the antibacterial effect of the tested product on the development of Gram+ and Gram- bacteria taken in the study was highlighted: *B. subtilis, E. coli, P. aeruginosa, S. aureus, E. cloacae, P. vulgaris*. Also, the n-hexane extract of mistletoe showed antibacterial activity and antifungal activity against *Candida albicans* [1].

The results of these studies confirmed existing data in the literature regarding the effects of V. album extracts in different solvents, only that in the case of our study, the values of the determined inhibition zones do not indicate an obvious antibacterial potential for most of the bacterial strains studied.

CONCLUSION

The extract in methanol from leaves and young branches of V. album showed an intermediate antibacterial effect at high concentrations on Gram+ bacteria: Enterococcus *faecalis, Streptococcus pyogenes*, the antibacterial potential being absent for *Clostridium perfringens* and *Staphylococcos aureus.* The n-hexane extract of V. album showed an intermediate antibacterial effect at high concentrations on Gram- bacteria: *Enterococcus faecalis* and *Clostridium perfringens*, the antibacterial effect being absent at all concentrations tested on *Streptoccoccus pyogenes* and *Staphylococcos aureus*. The methanol extract of mistletoe in the tested concentrations has an obvious antibacterial effect on *Escherichia coli,* a moderate antibacterial effect on *Legionella pneumophila*, the antibacterial effect being absent on *Pseudomonas aeruginosa.* The n-hexane extract of mistletoe showed an obvious antibacterial effect only on the bacterial strain *Escherichia coli* at c1, the antibacterial potential is absent on *Pseudomonas aeruginosa* and *Legionella pneumophila*. The decrease in the concentration of the extract causes a decrease in the antibacterial effect of the bacterial strains studied. In the perspective of resuming the studies on a larger number of bacterial strains, the inclusion of fungal strains in the study, the testing of more varied concentrations is necessary to confirm the antimicrobial potential of mistletoe extracts harvested from trees in Romania.

REFERENCES

[1] Erturk O., Hatice K., Yayli N., Demirbag Z., Antimicrobial Activity of Viscum album L. subsp. abietis (Wiesb), Turk. J. Biol., vol. 27, pp 255-258, 2003.

[2] Shahaboddin M.E., Pouramir M., Moghadamnia A-A., Lakzaei M., Mirhashemi S.M., Motallebi M., Antihyperglycemic and antioxidant activity of *Viscum album* extract, Afr J Pharm Pharmaco, vol. 5/issue 3, pp 432-436, 2011.

[3] Orhan D.D., Aslan M., Sendogdu N., Ergun F., Yesilada E., Evaluation of the hypoglycemic effect and antioxidant activity of three *Viscum album* subspecies (European mistletoe) in streptozotocin-diabetic rats, J Ethnopharmacol, vol 98/issue 1-2, pp 95-102, 2005.

[4] Tenorio F.A., del Valle L., González A., Pastelín G., Vasodilator activity of the aqueous extract of *Viscum album*, Fitoterapia, vol. 76/issue 2, pp 204-209, 2005.

[5] Gupta G., Kazmi I., Afzal M., Rahman M., Saleem S., Ashraf M.S., Khusroo M.J., Nazeer K., Ahmed S., Mujeeb M., Zubair A., Anwar F., Sedative, antiepileptic and antipsychotic effects of *Viscum album* L. (Loranthaceae) in mice and rats, J Ethnopharmacol, vol 141/issue 3, pp 810-816, 2012.

[6] Ofem O.E., Eno A.E., Imoru J., Nkanu E., Unoh F., Ibu JO., Effect of crude aqueous leaf extract of Viscum album (mistletoe) in hypertensive rats, Indian J Pharmacol, vol 39, pp 15-19, 2007.

[7] Onay-Uçar E., Erol O., Kandemir B., Mertoğlu E., Karagöz A., Arda N., *Viscum album* L. Extracts Protects HeLa Cells against Nuclear and Mitochondrial DNA Damage, Evid-Based Compl Alt Med, vol. 2, pp 10-11, 2012.

[8] Turker A.U., Yıldırım A.B., Karakas F.P, Antitumor and antibacterial activities of *Viscum album* L. grown on different host trees, Spatula DD., vol 2/ issue 4, pp 229-236, 2012.

[9] Vlad D.C., Popescu R., Dumitrascu V., Cimporescu A., Cristian S.V., Vágvölgyi C., Krisch J., Dehelean C., Horhat F.G, Phytocomponents identification in mistletoe (Viscum album) young leaves and branches, by GC-MS and antiproliferative effect on HEPG2 and MCF7 cell lines, Farmacia, vol. 64/issue 1, pp 82-87, 2016.

[10] Ochocka J., Piotrowski A., Biologically active compounds from European mistletoe (*Viscum album* L.), Can J Plant Pathol, vol 24, pp 21-28, 2002.

[11] Filimon M.N., Popescu R., Sinitean A., Maniu P., Dumitrescu G., Verdes D., Vlad C.S., The assessment of chitosan solutions effects on bacterial strains, Revista de Chimie (Bucharest), vol. 69/issue 6, pp 1485-1488, 2018.

[12] Popescu R., Filimon MN., Vlad DC., Verdes D., Moatar A, Moisei G., Gurani K., Caraba IV., Petculescu Ciochina L., Pinzaru I., Dehelean CA., Dumitrescu G., Antiproliferative and antibacterial potential of tetrahexylammonium bromide-based ionic liquids, Experimental and Therapeutic Medicine, vol. 22, pp. 672, 2021. DOI: 10.3892/etm.2021.10104.

[13] Vlad C.S., Vlaia L., Vlaia V., Dumitraşcu D., Filimon M.N., Popescu R., Cimporescu A., Dehelean C., Onwubiko C.E., Vlad D.C., Chromatographic analysis and antibacterial potential of extracts of *Gnetum africanum*, Farmacia, vol. 67/issue 6, pp 1083-1090, 2019.

https://doi.org/10.5593/sgem2024/6.1/s25.19

[14] Eloff J.N.E., Famakin J.O., Kathrene D.R.P., Cembretum woodii leaf extracts have high activity against Gram-negative and Gram-possitive bacteria, Africen Journal of Biokethnology, vol. 4/ issue 10, pp1161-1166, 2005.

[15] Hussain M.A., Khan M.Q., Hussain N., Antimicrobial Screening of *Viscum Album* L. Extracts, IACSIT Press., vol. 6, pp 203-207, 2011.

CHEMOMETRIC PROFILE OF WHITE AND RED WINES FROM DIFFERENT AREAS OF ROMANIA

Drd. Petronela Anca Onache[1,2]

Dr. Alina Florea[2]

Prof. Dr. Dorin Ioan Sumedrea[2]

Prof. Dr. Ovidiu Tița[3]

[1] Doctoral School "Lucian Blaga", University of Sibiu, **Romania**
[2] National Research & Development Institute for Biotechnology in Horticulture Stefanesti-Arges, **Romania**
[3]„Lucian Blaga" University of Sibiu, **Romania**

ABSTRACT

In this research, we studied wines from eleven wine regions of Romania (Stefanesti, Dragasani, Dealul Mare, Minis, Blaj, Babadag, Focsani, Tarnave, Silagiu, Iasi, Cotnari), but also for two years of different production (2019 and 2021), to observe their chemometric profile according to the geographical origin. The chemical composition was determined for 40 white wines and 34 red wines. The studied chemical parameters were alcohol concentration, wine density, total acidity, free and total sulfur dioxide, non-reducing dry extract, glucose and fructose, pH, organic acids (tartaric acid, malic and lactic) and macro-elements - calcium, potassium, copper, iron, nitrogen primary aminic and nitrogen ammonia. There are differences between the wine varieties on geographical areas, the alcoholic concentration has values ranging from 10.22-15.7% the lowest values are observed in white wines from the Iasi wine center, the total acidity has values ranging from 4.37-7.6 g/l tartaric acid, and the high values are found in the Blaj wine center for red varieties (Burgund - 7.11 g/l tartaric acid), but also to a specific variety Riesling de Rihn (9.25 g/l tartaric acid) from Dragasani vineyard. A good correlation is also observed between the geographical area and the pH. Principal component analysis (PCA) and related methods were used in order to achieve discrimination, classification and correlation of wines by geographical areas and varieties.

Keywords: wine, chemical composition, chemometric profile

INTRODUCTION

The authenticity and typicality of wines is an important issue for both producers and consumers, and it could be solved by a correct quantification of a wide range of issues starting from the conditions of vine culture [1], production technology, variety or geographical origin and climatic area, variety [2] and year of production. The share of adulterated wines on the global market is rising and this trend and experts estimate the global proportion of falsified wines to be approximately 5% [3,4]. The authenticity of wine is guaranteed by strict guide-lines laid down by the responsible authorities [1] the International Organisation of Vine and Wine (OIV) and the European Union. The UE regulations protects the authenticity of regional food by regulations 2081/82 and

https://doi.org/10.5593/sgem2024/6.1/s25.20

2082/92 (amended in 2006 – 510/2006 and 509/2006) [3]. These regulations concern the protection of indications of geographical origin and the control of names of agricultural and food products [3,5].

Adulteration of varietal wines is relatively common. Varietal authenticity and typicality of wines can be evaluated by determination of the chemical composition of wines with univariate and multivariate data processing [6,7]. Wine analysis is only part of the research, and selecting an appropriate method of data analysis is very important for the purpose of authenticating wine varieties [3]. Data exploration, discriminatory and classification techniques such as main component analysis (PCA), linear discrimination (ALD) analysis, hierarchical cluster analysis (HCA), etc, and others are commonly used as basic chemometric instruments [1,3]. These methods provide a graphical and numerical representation of discrimination, especially in the form of discriminatory functions, which can be further used to classify known wine [3,8].

MATERIALS AND METHODS

Sample collection

A total number of seventy-four samples of wines, from eleven regions of Romania (Stefanesti, Dragasani, Dealul Mare, Minis, Blaj, Babadag, Focsani, Iasi, Silagiu, Tarnave, Cotnari). The wines used for this study were from the 2019 and 2021 production years, and the varieties are in Table 1. All samples were analyzed in triplicate.

Table 1. The wine samples

Wine varieties	Symbol	Geographic region	Wine center/ Vineyard	Year of production
Riesling Italian	RI_19/21 M	Muntenia	Ștefănești	2019, 2021
	RI_19/21 Bl	Transilvania	Blaj	2019
Fetească Regală	FR_19/21 M	Muntenia	Ștefănești	2019, 2021
	FR_19 DM	Muntenia	Dealul Mare	2019
	FR_19/21 O	Oltenia	Drăgășani	2019, 2021
Sauvignon Blanc	SB_19/21 M	Muntenia	Ștefănești	2019, 2021
	SB_19/21 O	Oltenia	Drăgășani	2019, 2021
	SB_19 Is	North Moldova	Iași	2019
	SB_19 F	South Moldova	Focșani	2019
Pinot Gris	PG_19/21 D	Dobrogea	Babadag	2019, 2021
Muscat Ottonel	MO_19/21 M	Muntenia	Ștefănești	2019, 2021
	MO_19 Bl	Transilvania	Blaj	2019
	MO_19 B	Banat	Silagiu	2019
Riesling de Rihn	RR_19/21	Muntenia	Drăgășani	2019, 2021
Crâmpoșie Selecționată	CrS_19/21	Muntenia	Drăgășani	2019, 2021
Fetească Albă	FA_19/21	Muntenia	Ștefănești	2019, 2021
	FA_19 Is	North Moldova	Iași	2019
	FA_19 B	Banat	Silagiu	2019
Tămâioasă Românească	TR_19/21 M	Muntenia	Ștefănești	2019, 2021
	TR_19 O	Oltenia	Drăgășani	2019
Aligote	A_19/21 D	Dobrogea	Babadag	2019, 2021
Chardonnay	CH_19/21 D	Dobrogea	Babadag	2019, 2021

	CH_19 M	Muntenia	Ștefănești	2019
Traminer Roz	TR 19 Bl	Transilvania	Blaj	2019
Busuioacă de Bohotin	BB 19 DM	Muntenia	Dealul Mare	2019
Muscat de Maderat	MM 19 B	Transilvania	Târnave	2019
Grasă de Cotnari	GC 19C	North Moldova	Cotnari	2019
Burgund Mare	BM_19/21M	Muntenia	Ștefănești	2019, 2021
	BM_19/21 Bl	Transilvania	Blaj	2019
	BM_19 B	Banat	Silagiu	2019
Cabernet Sauvignon	CS_19/21M	Muntenia	Ștefănești	2019, 2021
	CS_19/21O	Oltenia	Drăgășani	2019, 2021
	CS_19 Iș	North Moldova	Iași	2019
Fetească Neagră	FN_19/21 M	Muntenia	Ștefănești	2019, 2021
	FN_19 C	North Moldova	Cotnari	2019
	FN_19 O	Oltenia	Drăgășani	2019
	FN_19 D	Dobrogea	Babadag	2019
Merlot	M_19/21 M	Muntenia	Ștefănești	2019, 2021
	M_19 Iș	North Moldova	Iași	2019
	M_19 F	South Moldova	Focșani	2019
	M_19/21 D	Dobrogea	Babadag	2019, 2021
Pinot Noir	PN_19/21 M	Muntenia	Ștefănești	2019, 2021
	PN_19/21 D	Dobrogea	Babadag	2019, 2021
Baluerzweigelt	Bl_19 M	Muntenia	Ștefănești	2019
Negru de Drăgășani	ND_19 O	Oltenia	Drăgășani	2019, 2021
Syrah	Sy_19 O	Oltenia	Drăgășani	2019, 2021
Cabernet Franc	CF_19/21 O	Oltenia	Drăgășani	2019, 2021
	CF_19 Bl	Transilvania	Blaj	2019
	CF_19 B	Banat	Silagiu	2019
Petit Verdot	PV_19/21 O	Oltenia	Drăgășani	2019, 2021
Cadarcă	CD_19 B	Transilvania	Târnave	2019

Methods of analysis

The alcoholic strength is achieved by distillation, with an oenological distiller SUPER DEE, procured from the company Gibertini Elettronika, Novate Milanese, Italy. The hydrostatic balance method, method C type I (OIV-MA-AS312-02; Resolution Oeno 24/2003 - 377/2009) is based on the training of alcohol with the vapors produced by a distillation apparatus. Total acidity was performed by the titrimetric method (OIV-MA-AS313-02, revised 551/2015). Determination of non-reducing dry wine extract was used a densimetric method (OIV-MA-AS2-03B, revised 465/2012). Determination of volatile acidity was achieved by distillation and capture of volatile acids using the super DEE oenological distiller, procured from the the company Gibertini Elettronika, Novate Milanese, Italian company (OIV-MA-AS313-02, revised 549/2015). Free sulphur dioxide (OIV-MA-AS323-04B, A17 revisited 377/2009) and total (OIV-MA-AS323-04B, A17 resold 377/2009) was determined by the Iodometric method. The determination of the total sugar content, expressed as the sum of fructose and glucose (g/l), is made by defecation using the Schoorl method (OIV-MA-AS311, Oeno 11/2006 revised 377/2009; Schoorl, Schoorl, 1929). Organic acids, nitrous substances in wine (ammoniacal nitrogen and aminic nitrogen) and macroelements - Cu, Fe, Ca, K (mg/l)

https://doi.org/10.5593/sgem2024/6.1/s25.20

they were determined using the enzyme method using the Shenzhen Midray BS 200 automatic analyser. The pH analysis was performed using a pH meter Mettler Toledo Seven Easy (OIV-MA-AS313-15, A31 revised Oeno 438-2011) calibrated.

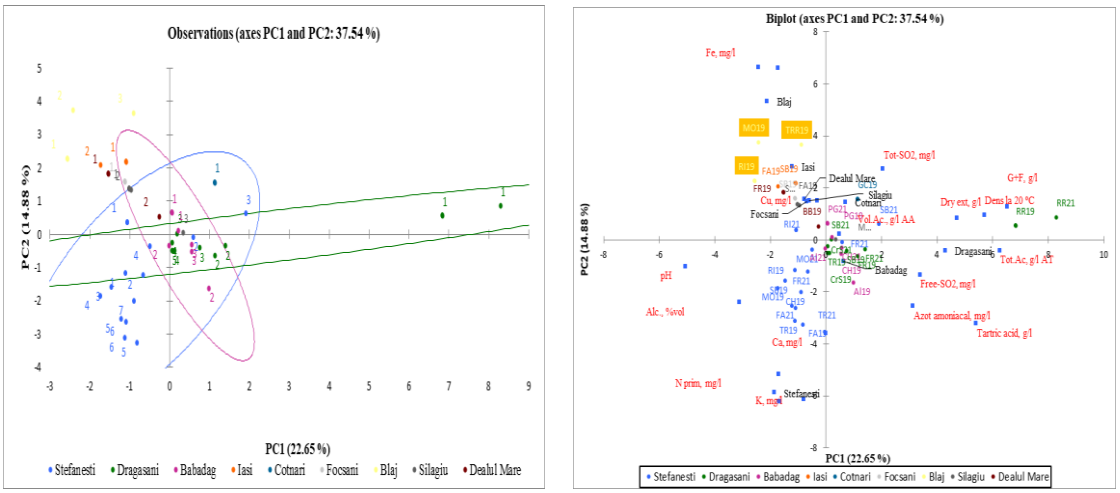
Statistical analysis

Analysis of variance (ANOVA) was used to find significant differences between concentrations of selected elements in wine samples from different regions of origin. In this analysis, the difference was taken as significant at $p < 0.05$ for 95% confidence level. The elements concentration was evaluated by descriptive statistical analysis. Multivariate analysis, heat map, agglomerative hierarchical clustering (AHC) and principal component analysis (PCA), was employed in wine differentiation and classification according to the geographical origin. Statistical analysis and PCA were performed using commercial software packages such as Microsoft Excel and XLSTAT 2016.

DISCUSSION

Elementary analyses of white and red wines show that they depend on the variety they are obtained from, the area of production and the climatic conditions of the year of production.

In our study, possible influences of geographic regions on wine varieties (A) and chemical parameters (B) were evaluated in Figure 1.



(A) **(B)**

Fig. 1 The PCA bi-plot analysis of white wine samples by region and by grape variety (A) and the PCA bi-plot analysis of white wine samples and compounds data (B)

In our study, white wines are noted that the highest alcoholic concentrations are in the geographical areas Stefanesti and Babadag, these being between the values of 13.9-16.3% vol. There are a few exceptions, such as the Sauvignon Blanc variety in Stefanesti with 12.9% vol and 9.9%vol for Riesling de Rihn in Dragasani, in the other geographical areas, alcoholic concentrations remain between the values of 12.1-14.7% vol. To dry extract there are no large differences between white wine varieties and geographical areas, it is comprised between the values of 16.5-21 g/l, there are differences between sweet varieties, and, such as Riesling de Rihn and Tamaioasa Romaneasca at values of 25-26 g/l.

The total acidity of wines there are no large differences (4.5-6.0 g/l AT), except Riesling de Rihn with 9.25 g/l AT (Dragasani) and Grasa from Cotnari with 7.35 g/at g/l AT (figure 2). In the analysis of K there are essential differences between the geographical areas, large quantities are in the Stefanesti (161-499 mg/l) and Dealul Mare (183-210 mg/l) areas, the smallest amounts of K are found in the Iasi area (10 mg/l). Regarding the iron content, all wines fall within the legal limits, except for wines from Blaj area (13 mg/l).

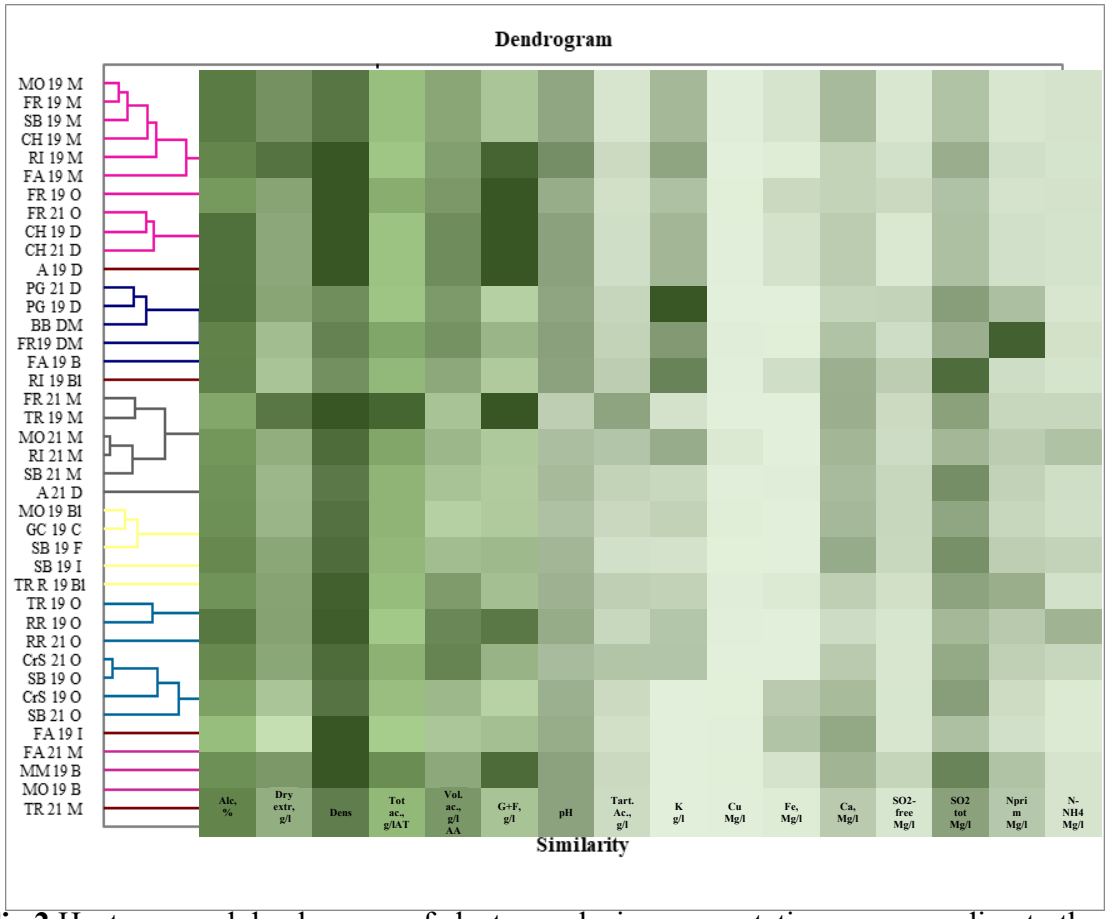
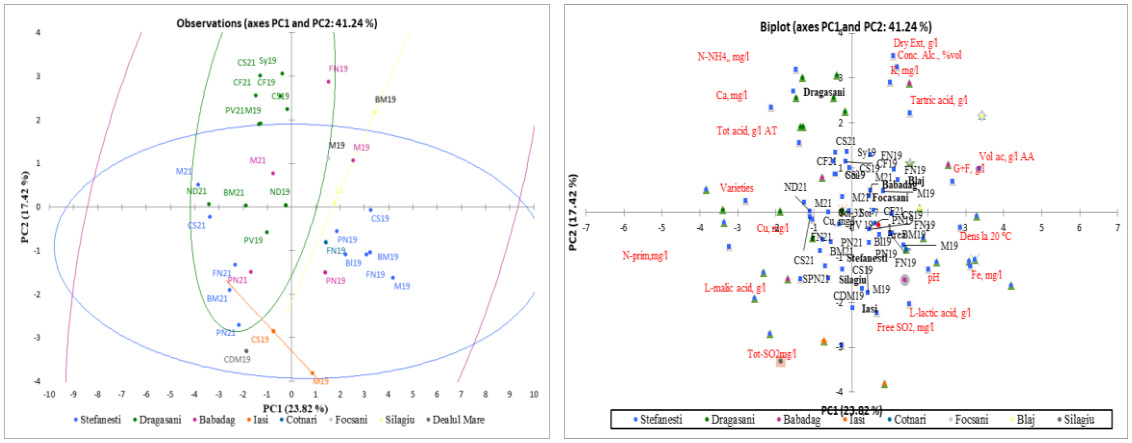


Fig.2 Heat map and dendrogram of cluster analysis representation corresponding to the 40 monovarietal white wines. The relative content of each compound is illustrated through a chromatic scale (from light green, minimum, to dark green, maximum). Dendrogram for the HCA (hierarchical cluster analysis) results, was also included.

Figure 2 shows the hierarchical dendrogram for grouping the 40 wine samples. It can be concluded that two specific models of descriptors of interest determine the quality of wine samples. Two similarity models could be easily distinguished— lower cluster 1 includes samples 24-40 and upper cluster 2-samples 1–23. Both groups are well separated and represent two different types of wine quality. This separation is reasonable if the input data is carefully checked. Wine samples from 1 to 40 are white wines, dominant from the Riesling grape types, Feteasca Regala, Sauvignon Blanc and Muscat Ottonel are in large numbers in terms of variety, as the other 23 (1-23) have a fairly high alcoholic concentration above 13.5% vol.

https://doi.org/10.5593/sgem2024/6.1/s25.20



(A) **(B)**

Fig. 3 The PCA bi-plot analysis of redwine samples by region and by grape variety (A) and the PCA bi-plot analysis of red wine samples and compounds data (B)

In figure 3 shows the PCA analysis of red wine varieties by geographical area (A). In the dark blue circle are the varieties from the Stefanesti geographical area, with blue Cotnari area, Dragasani is outlined with green, Babadag with magenta, Silag with yellow, Silagiu with yellow, Focsani with light grey and the Dealul Mare with dark grey. The alcoholic strength of red wines does not vary greatly and is in the range of 11.9 – 15.25 % vol, the lowest alcoholic strength is found at Merlot 2019 in the Iasi geographical area and the highest value at Burgund Mare in the Dealul Mare with the value of 15.53%vol. The highest total acidity is observed at Burgund Mare (7.11 g/l AT) Dealul Mare area and on Syrah (6.59 g/l AT) in Dragasani area.



Fig. 4 Heat map and dendrogram of cluster analysis representation corresponding to the 34 monovarietal red wines. The relative content of each compound is illustrated through a chromatic scale (from light pink, minimum, to dark orange-red, maximum). Dendrogram for the HCA (hierarchical cluster analysis) results, was also included.

Figure 4 shows the hierarchical dendrogram for grouping the 34 red wine samples. It can be concluded that three specific models of descriptors of interest determine the quality of wine samples. There are three different clusters, two similar to 2 wine varieties and one with most homogeneous wine varieties in the studied parameters. Three models could be easily distinguished— lower cluster includes two samples of wine, upper cluster 2-samples, 2-samples , cluster 2 contains most wine varieties 32–3 and final cluster 3 – two wine sample. Both groups are well separated and represent two different types of wine quality. Wine samples from 1 to 34 are red wines, dominant from the types of grapes Burgund Mare, Cabernet Sauvignon, Feteasca Neagra, Merlot, Pinot Noir. In the 2nd cluster wine varieties are in large number in terms of the quantity depending on the alcoholic strength.

CONCLUSION

In this paper were studied the elementary composition of 74 varieties of wines (40 white wines and 34 red wines) from the most important geographical areas of Romania in 2019 years of production and 2021. After selecting the elemental markers (Alcoholic concentration, dry extract, Fe, Ca, K, N-prim, N-NH4) and introducing organic parameters (total acidity, pH, tartaric acid) able to differentiate wines by geographic regions, we get a PCA score of 37.54% on white wines and 41.24% on red wines. A satisfactory separation of wine samples was made for the eleven geographical regions, even for the very close areas of the same region (Iasi, Cotnari-North of Moldova), North and South of Romania. Also, good discrimination on wine varieties from different geographical areas. Our results show the geographical origin of the wine and the variety can be distinguished based on elementary analysis. We intend to improve our classification criteria by analyzing polyphenolic compounds of the same wine varieties from the studied geographical areas.

REFERENCES

[1] Arvanitoyannis, I.S., Katsota, M.N., Psarra, E.P., Soueros, E.H., Kallithrakay, S. - Application of quality control methods for assessing wine authenticity: Use of multivariate analysis (chemometrics), Review, Trends in Food Science & Technology, issue 10, Elsevier, pp. 321-336, 2000;

[2] Feher, Ioana; Magdas, Dana Alina; Dehelean, Adriana; Sarbu, C. - Characterization and classification of wines according to geographical origin, vintage and specific variety based on elemental content: a new chemometric approach, J Food Sci Technol, vol. 56, issue 12, pp. 5225–5233, 2019. https://doi.org/10.1007/s13197-019-03991-4

[3] Porizka, J., Divis, P., Dvorak, M. - Elemental analysis as a tool for classification of Czech white wines with respect to grapevine varieties, Journal of Elementology, 23(2), pp. 709-727, 2018. http://doi.10.5601/jelem.2017.22.4.1379

[4] Luykx D.M.A.M., van Ruth S.M. - An overview of analytical methods for determining the geographical origin of food products. Food Chem., 107(2), pp. 897-911, 2008. http://doi.org/10.1016/j.foodchem.2007.09.038

[5] Bora1, F.D., Ripanu, Oana; Donici, Alina; Bunea, C.I., Pop, Nastasia; Lung, M.L., Popescu, Daniela - Influence Of Micro-, Macroelements And Heavy Metals On Wine Quality, Annals. Food Science and Technology, Valahia University Press, Romania, 2016. www.afst.valahia.ro

https://doi.org/10.5593/sgem2024/6.1/s25.20

[6] Kaur, Arshpreet; Chadha, Raman; Shashvat, Kumar - Classification Of Wines Based On Quality Assessment Using Its Chemical Properties With Application Of Discriminant Analysis, International Journal Of Engineering Sciences & Research Technology, 5(6), pp. 119-129, 2016.

[7] Zamfir C.I., – „Studiul autenticităţii şi tipicităţii vinurilor roşii obţinute din soiuri autohtone", Thesis, USAMV Iasi, Romania, 2009.

[8] Gonzalves, M., Guardia, M. - Basic chemometric tools. Comprehensive Anal. Chem., 60, pp. 299-315, 2013. http://dx.doi.org/10.1016/B978-0-444-59562-1.00012-8

COMPARATIVE STUDY ON PHENOLICS, FLAVONOIDS, TANNINS AND ANTIOXIDANT PROPERTIES OF *CALENDULA OFFICINALIS* EXTRACTS OBTAINED BY DIFFERENT EXTRACTION TECHNIQUES

Lucia-Florina Popovici[1]
Simona Oancea[1]
[1]"Lucian Blaga" University of Sibiu, Department of Agricultural Sciences and Food Engineering, **Romania**

ABSTRACT

The aim of this study was to evaluate the influence of several extraction methods on the content of bioactive compounds of polyphenolic structure and antioxidant properties of petals from marigold flowers (*Calendula officinalis*).

Ethanolic extracts prepared using maceration, turbo-extraction and bead-beating techniques were investigated for total phenolics, flavonoids and tannins, and antioxidant activities as measured by FRAP and DPPH assays, as well.

The results showed that the highest phenolic content (1316.367 ± 4.316 mg GAE/100 g DW) and antioxidant activity by FRAP (505.755 ± 4.623 mg ascorbic acid/100 g DW) were obtained by maceration for 24 h at room temperature, while the highest flavonoid content (2729.521 ± 7.261 mg quercetin /100 g DW) and tannin content (476.748 ± 4.126 mg catechin /100 g DW) were recorded in the sample subjected to turbo-extraction for 5 min. Turbo-extraction proved to be an efficient technique for extraction of total phenolics at an extraction time of 10 min, and for total flavonoids and tannins at an extraction time of 5 min. Extracts obtained by short maceration (5 min, 10 min) showed lower values of phenolic content, flavonoid content and antioxidant activity by FRAP, compared to those of sample subjected to maceration for 24 h. Extracts obtained by bead-beating technique at extraction times of 5 and 10 min indicated the lowest phenolic, tannin and flavonoid contents compared to all the other extraction methods. Ceramic (zirconium oxide) bead-beating technique generated lower contents compared to those of sample obtained using metal (stainless steel) bead-beating technique, except for the antioxidant activity by DPPH, which was found the highest among all investigated samples at an extraction time of 10 min (17.726 ± 0.015 %).

Our results suggest that extraction time is a key factor for the investigated techniques. The ethanolic extracts of *Calendula officinalis,* in particular using turbo-extraction, showed high phenolic content and ferric reducing antioxidant power, using a short extraction time, properties that increase their potential to be applied as bioactive ingredients.

Keywords: *Calendula officinalis*, extraction, phenolics, flavonoids, tannins, FRAP, DPPH.

INTRODUCTION

Calendula officinalis Linn. (*C. officinalis*), also named marigold, is a plant from the *Calendula* genus (approx. 25 species), family Asteraceae, with multiple uses in the

https://doi.org/10.5593/sgem2024/6.1/s25.21

medical and cosmetic fields. It has been known for centuries for its therapeutic and healing properties. This plant is rich in bioactive compounds such as flavonoids, polyphenols, carotenoids, tannins, and volatile oils, providing its antioxidant, anti-inflammatory, antimicrobial, and cicatrizing properties [1].

Extraction is a crucial process used in various fields such as chemistry, pharmaceuticals, food processing, and environmental science, enabling the separation, purification, and concentration of compounds for further analysis, process, and utilization. Bioactive compounds of polyphenolic structure have been extracted from *C. officinalis* flowers applying Soxhlet extraction, ultrasound assisted extraction, supercritical CO_2 assisted extraction, microwave-assisted extraction, maceration, mainly using ethanol, methanol, or H_2O as a solvent, in various proportion, with or without agitation [2]. Choosing the best extraction method involves carefully evaluating issues such as temperature, extraction time, plant-solvent ratio, in order to achieve the desired results in an efficient, economical, and sustainable manner.

The aim of the present paper was to investigated the efficiency of three extraction techniques, maceration, turbo-extraction, and bead-beating, respectively, investigated for 2 extraction times (5 and 10 min), at room temperature, on the phytochemical contents and on the antioxidant activity of flowers of *C. officinalis*.

MATERIALS AND METHODS

I. Raw plant material and chemical reagents

The marigold flower petals (*C. officinalis*) were collected from the Sibiu region, Romania. The moisture content of the samples was determined using a moisture analyzer (MAC 210/NP Radwag, Poland). Samples were stored at −70 °C until analysis.

All chemical reagents were of analytical grade.

II. Extraction techniques

Extraction was performed in 70% ethanol at a solvent/sample ratio of 20/1, at room temperature using maceration, turbo-extraction, and bead-beating techniques.

Maceration: Approximately 1 g of plant material was subjected to extraction by soaking in 20 ml of 70% ethanol, at room temperature. A set of three intervals of extraction times were investigated: 5 min, 10 min, and 24 h, respectively.

Turbo-extraction: Approximately 1,5 g of plant material were extracted in 30 ml of 70% ethanol, using a digital high-shear stirrer device (T 18 digital Ultra-Turrax®, IKA, Germany), at 6000 rpm. The investigated extraction times were 5 min and 10 min.

Bead-beating: Approximately 1 g of plant material in 20 ml of ethanol 70% was subjected to a vertical mixing motion using the bead beater device (Bead Genie SI-B100, Scientific Industries, USA), at room temperature. Two types of beads were used: 1.4 mm of ceramic (zirconium oxide) and metal beads (stainless steel), respectively.

After the extraction, the mixtures were centrifuged at 8000 rpm, at 4°C for 10 min using the refrigerated centrifuge (Universal 320-R, Hettich, Germany).

III. Determination of polyphenols

The total phenolics content of the marigold extracts was determined spectrophotometrically by the Follin-Ciocalteu assay [3], using a Specord 200 Plus UV-

Vis spectrophotometer (Analytik Jena,Germany). The results were expressed in mg of gallic acid equivalents per 100 g dry weight (mg GAE/100 g DW).

The total flavonoids content was determined spectrophotometrically by the aluminium chloride assay [4]. The results were expressed in mg quercetin equivalents per 100 g dry weight (mg QE/100 g DW).

The total condensed tannins content was determined spectrophotometrically using the vanillin assay, as described in the literature [5]. The results were expressed in mg catechin equivalents per 100 g dry weight (mg CE/100 g DW).

IV. Determination of antioxidant activity

The antioxidant activity of the extracts was determined using two assays, the ferric reducing antioxidant power (FRAP) assay [6] and the 1,1-diphenyl-2-picrylhydrazyl (DPPH) assay [7]. The results of the FRAP assay were expressed in mg ascorbic acid equivalent per 100 g dry weight (mg AAE /100 g DW). The results of the DPPH assay were expressed as inhibition percentage calculated according to the following formula:

$$\text{Radical Scavenging Activity (\%)} = 100 \times (A_0 - A) / A$$

where A_0 is the absorbance at 515 nm of the control and A is the absorbance at 515 nm of the sample.

V. Statistical analysis

All measurements were performed in duplicate. Results were calculated and expressed as mean ± standard deviation.

RESULTS

1. Evaluation of total phenolic content of the C. officinalis flower extracts

The total phenolics content of the *C. officinalis* flower extracts obtained by maceration, turbo-extraction, and bead-beating techniques are presented in Figure 1. The highest content (1088.314 ± 3.343 mg GAE/100 g DW) was recovered after turbo-extraction, for 10 min.

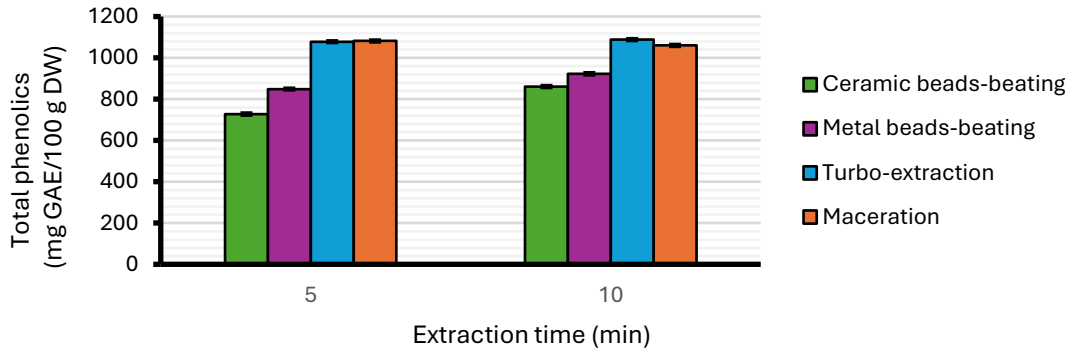


Figure 1. Total phenolic content of the *C. officinalis* flower extracts developed using different techniques.

However, high phenolic content (1081.620 ± 3.310 mg GAE/100 g DW) was also obtained after maceration, and after extraction using the turbo-extraction technique for 5

https://doi.org/10.5593/sgem2024/6.1/s25.21

min (1078.166 ± 3.083 mg GAE/100 g DW), as well. Maceration at 24 h recorded the highest content values among all extraction methods (1316.367 ± 4.316 mg GAE/100 g DW).

2. Evaluation of total flavonoid content of the C. officinalis flower extracts

A significant total flavonoid content was obtained by turbo-extraction method for 5 min (2729.521 ± 7.261 mg QE /100 g DW) and 10 min (2253.728 ± 7.261 mg QE /100 g DW) (Figure 2), and also by the 24 hours maceration (2543.678 ± 6.839 mg QE /100 g DW).

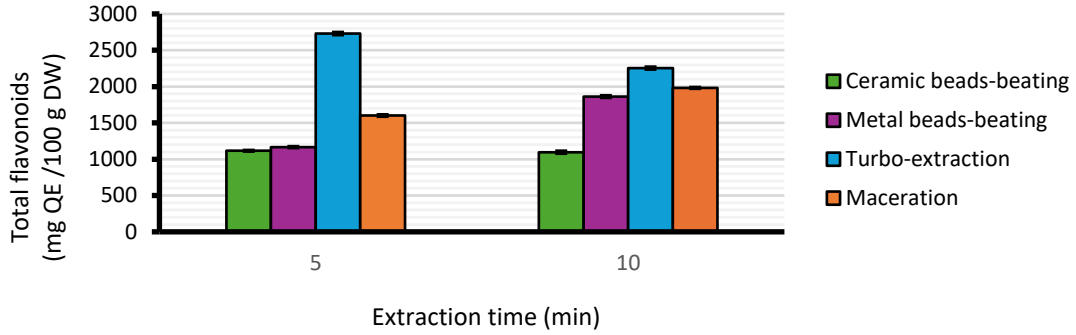


Figure 2. Total flavonoid content of the *C. officinalis* flower extracts developed using different techniques.

The total flavonoid content of extracts obtained by maceration for 10 min was 1981.378 ± 4.189 mg QE /100 g DW, while lower contents of flavonoids were recovered using the beads-beating techniques with both type of beads, ceramic and metallic.

3. *Evaluation of total tannin content of the C. officinalis flower extracts*

The highest content of the total condensed tannins and was obtained by turbo-extraction for 5 min (476.748 ± 4.126 mg CE /100 g DW) and 10 min (426.618 ± 4.191 mg CE /100 g DW), as shown in Figure 3. Similar content was registered by the extracts obtained by the maceration technique, for 5 min (433.939 ± 3.030 mg CE /100 g DW), with higher content than the 24 h maceration (428.239 ± 2.381 mg CE /100 g DW). The extracts prepared by the metal bead-beating technique for 10 min showed a content of 378.226 ± 2.387 mg CE /100 g DW.

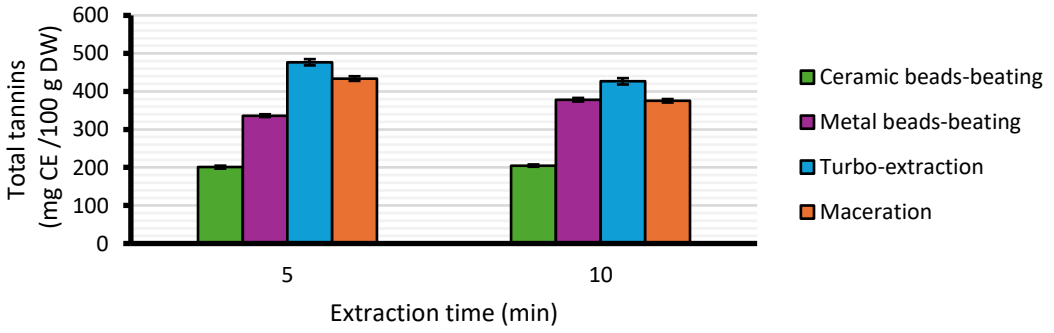


Figure 3. Total tannins content of the *C. officinalis* flower extracts developed using different techniques.

4. Evaluation of the antioxidant activity of the C. officinalis flower extracts

The most significant antioxidant activity of the *C. officinalis* extracts, determined by FRAP assay (Figure 4), was recorded in extracts prepared by the turbo-extraction method, for both extraction times, 10 min (479.463 ± 2.768 mg AAE/100 g DW), and 5 min (470.915 ± 3.543 mg AAE/100 g DW), respectively. Similar antioxidant activity was registered in extracts prepared by maceration for 5 min (464.963 ± 2.519 AAE/100 g DW), but the highest activity by maceration was at 24 h (505.755 ± 4.623). The lowest antioxidant activity was obtained in extracts prepared by ceramic beads-beating for 5 min.

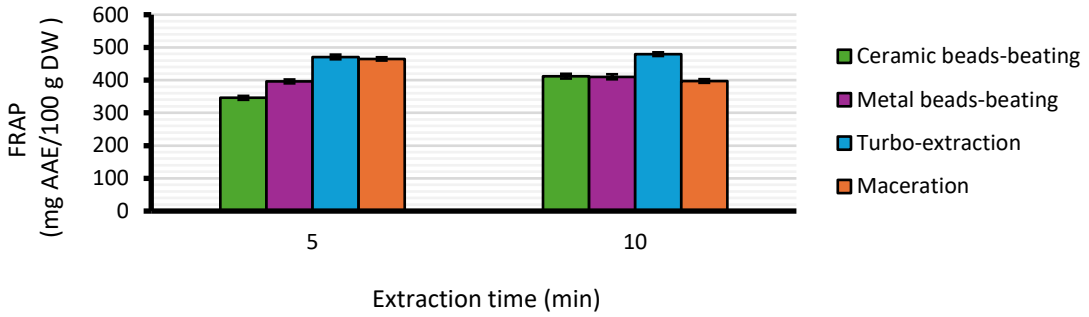


Figure 4. The antioxidant activity measured by FRAP of the *C. officinalis* flower extracts developed using different techniques.

As shown in Figure 5, the highest antioxidant activity determined using the DPPH assay was found in extracts prepared by the ceramic beads-beating technique, at an extraction time of 10 min (17.726 ± 0.015 %). Among the results in extracts prepared for 5 min using different extraction techniques, the antioxidant activity was higher when using the metal-beads beating method (8.497 ± 0.051 %), followed by the maceration for 24 h (7.478 ± 0.028 %).

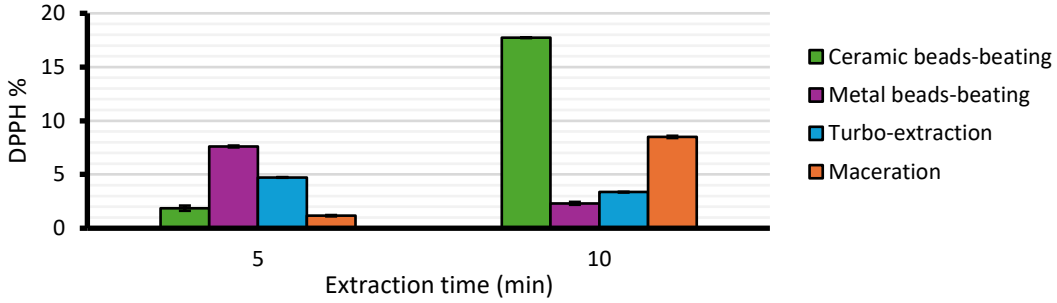


Figure 5. The antioxidant activity measured by DPPH of the *C. officinalis* flower extracts developed using different techniques.

5. Correlation of the antioxidant activities and polyphenols content of C. officinalis extracts

The correlations between bioactive content and activity are indicated in Table 1. Very significant Pearson's correlations ($p < 0.01$) were observed between total phenolic and total flavonoid contents, and between total phenolic content and antioxidant activity determined by FRAP. Significant Pearson's correlations ($p < 0.05$) were found for total tannin content and antioxidant activity determined by FRAP. No significant correlations were found between the antioxidant activity as measured by DPPH assay and the content of the investigated polyphenols.

https://doi.org/10.5593/sgem2024/6.1/s25.21

Table 1. The significance of Pearson's correlation coefficient (*r*) and *p* -value (*, **, ***) of the antioxidant activities and polyphenols content of *C. officinalis* extracts

	TP	TF	TT
TP	1	+0.83 **	+0.79 *
TF	+0.83 **	1	+0.84 **
TT	+0.79 *	+0.84 **	1
FRAP	+0.90 **	+0.76 *	+0.78 *
DPPH	-0.08 Ns	-0.26 Ns	-0.44 Ns

Note: Ns - not significant ($p > 0.05$), * - significant ($p < 0.05$), ** - very significant ($p < 0.01$)

For the total flavonoid content, a strong Pearson's correlation was found with the total condensed tannins, one of the very significant one ($p < 0.01$), but also a significant one ($p < 0.05$) for the total condensed tannins with the total phenolics content, which was also highly correlated.

DISCUSSIONS

Maceration is a passive method that requires time for extraction to occur, while turbo-extraction and bead-beating extraction are fast and active techniques that can accelerate the extraction process. The complexity differs between the three methods, with maceration being the simplest, and turbo-extraction and bead-beating extraction requiring more specialized equipment. Mostly, in speciality literature the solute/solvent extraction was used, especially maceration, at different extraction time, with or without agitation. The turbo-extraction method demonstrated high efficiency in extracting bioactive compounds of polyphenolic structure from *C. officinalis* flowers, and in the antioxidant activity as measured by FRAP assay for both investigated times, 5 min and 10 min, respectively, at room temperature. The highest total phenolic content was recorded after turbo-extraction for 10 min, surpassing all other tested extraction methods. The turbo-extraction method utilizes mechanical agitation and high-speed rotation to enhance the extraction process, facilitating the release of bioactive compounds from plant material. This mechanical action helps to break down the cell walls of the plant material more effectively, allowing faster and more efficient extraction of phenolic compounds.

Short maceration (5 min, 10 min) generated lower phenolic content, flavonoid content, and antioxidant activity by FRAP, compared to maceration for 24 h, suggesting that the conventional maceration with a long extraction time is better. Similar results were reported by Ak [2] showing a total phenolic content by maceration for 24 h of 34.27 ± 0.40 mg GAE/g extract prepared from *C. officinalis* flowers in methanol at a solvent/sample ratio of 20/1. This is different from using the turbo-extraction method which proved efficiency event at shorter extraction time (5 min). This might be attributed to the efficient penetration of the solvent into the plant material at a high-speed rotation, resulting in a quick extraction of phenolic compounds. Moreover, the inherent characteristics of *C. officinalis*, such as the structure of its tissues and the solubility of phenolic compounds, could contribute to the extraction efficiency even within shorter extraction time. The results of Ak [2] showed a total phenolic content of 32.18 ± 0.40 mg GAE/g in *C. officinalis* flower extracts prepared under similar conditions as ours, by homogenizer-assisted (HAE) using ultra-turrax (5 min).

The study of de Souza [8] reported that the best conditions for achieving the highest flavonoid content differed between the maceration and turbo-extraction processes. At a

12.5% (w/v) plant material, maceration yielded optimal results over a 15-day period, whereas the turbo-extraction process achieved similar performance within a shorter duration of 5 min. Regarding the antioxidant activity as measured by DPPH assay, the highest values were recorded in extracts prepared by bead-beating, in particular for 10 min using ceramic beads followed by those obtained for 5 min extraction using metal beads. The different efficiency might be linked to the fact that the presence of non-phenolic antioxidants such as vitamin C, vitamin E, and carotenoids, contributes significantly to the overall antioxidant activity [9]. In a study of Verma [10], phytochemical constituents and antioxidant potential in floral extracts of *C. officinalis* were analyzed. A significant presence of phenolics and tannins and antioxidant activity measured by the free radical scavenging (DPPH%) and ferric reducing antioxidant power (FRAP) in ethanol-based extracts, as opposed to aqueous extracts, renders this organic solvent as ideal and selective for extracting numerous bioactive polyphenolic compounds. Because of the differences in how extraction is carried out, it's probable that the composition of the extract varies between studies. This factor could account for the differences noticed in other reported results [11].

CONCLUSIONS

Calendula officinalis, also known as marigold, represents a medicinal plant with rich history in traditional medicine and phytotherapy practice. It is recognized for its therapeutic properties, particularly due to its rich content of bioactive compounds. Extracts from *C. officinalis* exhibit various biological activities, including antioxidant, anti-inflammatory, antimicrobial, and wound-healing properties.

Our study demonstrated that the turbo-extraction method yielded the highest content of antioxidant compounds (phenolics, flavonoids, tannins) and antioxidant activity as measured by FRAP, compared to the other investigated extraction techniques, suggesting it as a more effective approach for extracting most polyphenolic compounds from marigold. However, bead-beating proved efficiency for a high antioxidant activity as measured by DPPH assay. Additionally, the results indicate a significant impact of extraction time on total phenolic content and antioxidant activity by FRAP assay. Generally, an extraction time of 10 min resulted in the highest recovery across all methods (except maceration), compared to the extraction time of 5 min, indicating that longer extraction time enhance the extraction efficiency of these bioactive compounds.

This research describes the optimal conditions for high recovery of antioxidant content and activity of marigold, representing a promising direction in researching and implementing more eco-friendly extraction methods.

ACKNOWLEDGEMENTS

This research was funded by the Lucian Blaga University of Sibiu (Knowledge Transfer Center) & Hasso Plattner Foundation research grants - grant number LBUS-HPI-ERG-2023-04.

REFERENCES

[1] Shahane K., Kshirsagar M., Tambe S., Jain D., Rout S., Ferreira M. K. M., Mali S., Amin P., Srivastav P. P., Cruz J., Lima R. R., An Updated Review on the Multifaceted

https://doi.org/10.5593/sgem2024/6.1/s25.21

Therapeutic Potential of *Calendula officinalis* L., *Pharmaceuticals,* Switzerland, vol. 16/ issue 4, pp. 1-21, 2023, DOI: https://doi.org/10.3390/PH16040611

[2] Ak G., Zengin G., Sinan K. I., Mahomoodally M. F., Picot-Allain M. C. N., Cakir O., Bensari S., Yilmaz M. A., Gallo M., Montesano D., A Comparative Bio-Evaluation and Chemical Profiles of *Calendula officinalis* L. Extracts Prepared via Different Extraction Techniques, *Applied Sciences,* Switzerland, vol. 10/ issue 17, pp. 1-16, 2020, DOI: https://doi.org/10.3390/APP10175920

[3] Singleton V. L., Rossi, J. A., Colorimetry of Total Phenolics with Phosphomolybdic-Phosphotungstic Acid Reagents, *American Journal of Enology and Viticulture*, U.S.A, vol. 16/ issue 3, pp. 144–158, 1965, DOI: https://doi.org/10.5344/AJEV.1965.16.3.144

[4] Kumar S., Kumar D., Jusha M., Saroha K., Singh N., Vashishta B., Antioxidant and free radical scavenging potential of *Citrullus colocynthis* (L.) Schrad. methanolic fruit extract, *Acta Pharmaceutica*, Croatia, vol. 58/ issue 2, pp. 215–221, 2008, DOI: https://doi.org/10.2478/V10007-008-0008-1

[5] Price M. L., Scoyoc S. Van, Butler L. G., A Critical Evaluation of the Vanillin Reaction as an Assay for Tannin in Sorghum Grain, *Journal of Agricultural and Food Chemistry*, U.S.A, vol. 26/ issue 5, pp. 1214–1218, 1978, DOI: https://doi.org/10.1021/JF60219A031/ASSET/JF60219A031.FP.PNG_V03

[6] Benzie I. F. F., Strain J. J., The Ferric Reducing Ability of Plasma (FRAP) as a Measure of 'Antioxidant Power': The FRAP Assay, *Analytical Biochemistry*, U.S.A, vol. 239/ issue 1, pp. 70–76, 1996, DOI: https://doi.org/10.1006/ABIO.1996.0292

[7] Brand-Williams W., Cuvelier M. E., Berset C., Use of a free radical method to evaluate antioxidant activity, *LWT - Food Science and Technology*, vol. 28/ issue 1, pp. 25–30, 1995, doi: https://doi.org/10.1016/S0023-6438(95)80008-5

[8] de Souza A. P. T. B., Barni S. T., Ferreira R. A., Couto A. G., Technological Development of Hydroalcoholic Extractive Solutions from *Calendula officinalis* L. Flowers by using Factorial Design, *Latin American Journal of Pharmacy*, Argentina, vol. 29/ issue 1, pp. 13–21, 2010, ISSN: 0326-2383 (printed ed.), 2362-3853 (on-line ed.)

[9] Untea A., Lupu A., Saracila M., Panaite T., Comparison of ABTS, DPPH, Phosphomolybdenum assays for estimating antioxidant activity and phenolic compounds in five different plant extracts., *Bulletin of the University of Agricultural Sciences & Veterinary Medicine Cluj-Napoca. Animal Science & Biotechnologies*, Romania, vol. 75/ issue 2, pp. 110–114, 2018, DOI: https://doi.org/10.15835/buasvmcn-asb

[10] Verma P. K., Raina R., Sultana M., Phytochemical constituents and antioxidant potential in floral extracts of *Calendula officinalis* Linn. *World Journal of Pharmaceutical Research*, vol. 3, pp. 2067-2083, 2014, ISSN: 2277-7105.

[11] Givol O., Kornhaber R., Visentin D., Cleary M., Haik J., Harats M., A systematic review of *Calendula officinalis* extract for wound healing, *Wound Repair and Regeneration*, vol. 27/ issue 5, pp. 548–561, 2019, DOI: https://doi.org/10.1111/WRR.12737

DEVELOPMENT OF A METHOD FOR PRODUCING A FEED ADDITIVE FROM THE GREEN MASS OF AMARANTH

SvetlanaValerevnaObraztsova[1]
Olga Vladimirovna Bondareva[1]
Dariya Sergeevna Khodasevich[1]
Assistant professor Olga Leonidovna Meshcheryakova[1]
Assistant professor TatiyanaVasilevna Sviridova[1]
Professor Olga Sergeevna Korneeva[1]
[1]Voronezh State University of Engineering Technologies, **Russia**

ABSTRACT

A comparative assessment of the chemical composition of amaranth green mass cultivated in 2022 and 2023 was carried out. It was revealed that the content of nitrates, tannins and phytates in the 2023 harvest exceeded these indicators compared to the 2022 harvest by 3.3, 1.4 and 4 times, respectively. The amount of oxalic acid was 16 times lower, and that of tannins did not exceed the maximum permissible concentration of 0.5%. At the same time, the content of proteins and fats decreased by 12.6 and 31.6%, respectively, and the amount of fiber increased by 8.5%. The process of enzymatic treatment of amaranth green mass with a multienzyme complex possessing xylanase, β-glucanase, cellulase, protease, amylase and phytase activities has been studied. It has been established that phytase, which is part of the enzyme complex, exhibits maximum ability to hydrolyze phytates in plant materials at pH 6.5 and temperature 37 °C. A rational treatment regime for the green mass of amaranth has been selected, ensuring not only the complete destruction of phytates, but also the release of nitrates from the plant raw materials under study and a reduction in fiber content by 29%. Thus, preliminary enzymatic treatment of amaranth green mass made it possible to obtain a feed additive with improved nutritional properties for further use in the diet of quails.

Keywords: amaranth, anti-nutritional substances, enzymatic hydrolysis, phytates

INTRODUCTION

Poultry farming in the Russian Federation occupies a leading position among other sub-sectors of livestock farming. The share of poultry meat in the total volume of meat production in 2023 was about 50.2%, and the cost of the carcass increased by 20% compared to 2022. The observed annual increase in the price of poultry products is mainly due to rising prices for compound feed and feed ingredients. In this regard, the further development of the poultry industry is closely related to the improvement and creation of the domestic feed supply [1].

The current global level of technology for feeding farm animals is based on the widespread use of biological components. However, the production of domestic compound feeds and premixes is largely carried out without the use of alternative sources of biologically active substances, which reduces the competitiveness of Russian livestock farming.

In this regard, the development of effective domestic feed additives that help improve feed digestibility is an urgent task. Currently, there is an emerging trend to replace feed

https://doi.org/10.5593/sgem2024/6.1/s25.22

additives obtained by chemical synthesis in the diet. There is an active search for new highly productive raw materials for producing feed additives using biological methods [2-3].

One of the most promising types of raw materials for the production of feed additives is amaranth, which attracts attention with its relatively low cost, high yield and ease of cultivation. It contains 14-20% of easily digestible protein, vitamins B, C, E, P, carotenoids, macro- and microelements. Amaranth proteins are not inferior in amino acid composition to soy protein and milk casein, have high digestibility (90%) [4], and are balanced in the amount of essential amino acids. The use of amaranth in feed makes the diet of animals more complete and balanced, helps to increase the productivity and safety of livestock, and makes it possible to replace products of animal origin in compound feed [5].

However, along with beneficial nutrients, amaranth, like other plant raw materials, can also accumulate anti-nutritional components, which contribute to the deterioration of feed absorption, slower growth and reduced animal productivity.

We previously established [6] that during the growth and development of the crop, oxalic acid, tannins, nitrates and phytates accumulate in the green mass of amaranth; trypsin inhibitors and saponins are absent. At the same time, the content of phytates in the green mass of amaranth is 1.5-2 times higher than in lentils, broad beans and wheat, but lower compared to soybeans, beans and lupine. The concentration of nitrates exceeded the maximum permissible by 20 times. The content of oxalic acid is lower than in the green mass of vetch (0.50–0.8%) and oats (1%). Thus, the removal of phytates and nitrates from amaranth is an important technological task in the production of feed additives that increase the nutritional value and improve the digestibility of feed. The most effective way to destroy phytic acid is enzymatic hydrolysis.

In connection with the above, the purpose of this study was to develop a method for the enzymatic destruction of phytates, ensuring their maximum extraction from the green mass of amaranth for further use in the diet of quails.

MATERIALS&METHODS

The object of the study was freshly cut and dried green mass of amaranth variety “Giant” (Amaranthus hypochondriacus), and a commercial enzyme preparation “Kemzyme Plus P dry” (KEMIN).

The green mass of amaranth was grown in the Khokhol district of the Voronezh region (harvest 2023) for 90 days. For sowing amaranth, a field of 16 hectares was used, mostly flat, but there were areas with a certain slope, the soil structure was fine-grained. The predecessor was barley. Sowing was carried out on May 23, 2023 in the usual row way (15 cm row spacing) using a grain-grass seeder. Seeding rate - 1.5 kg/ha. After sowing, the soil was compacted.

“Kemzyme Plus P dry” is a multi-enzyme complex containing 6% enzymes exhibiting the following activities, at least units/g: xylanase – 20,000 (producer Trichoderma viride NIBH FERM BP 4842), β-glucanase – 2350 (producer Aspergillus aculeatus CBS 589.94) , cellulase – 4000 (producer Trichiderma longibrachiatum CBS 592.94), protease – 450 (producer Bacillus amyloliquelaciens DSM 9554), amylase – 400 (producer Bacillus amyloliquefaciens DSM 9553), phytase – 630 (producer Trichoderma reesei CBS 126897); 81.8-91.8% calcium carbonate, 4-6% bentonite, 0.9-1.5% silicon dioxide and 0.7-1.3% vegetable oil.

The dry matter content and moisture content of the green mass were determined according to GOST 31640-2012 (ISO 5983-1:2005), the mass fraction of “crude protein” - by the Kjeldahl method (GOST 32044.1-2012), the mass fraction of “crude fat” - by the Soxhlet method (GOST 13496.15 -2016), mass fraction of “crude fiber” - by the Henneberg and Stohmann method (GOST 31675-2012), mass fraction of “raw ash” - according to GOST 32933-2014 (ISO 5984:2002).
The content of nitrogen-free extractives (NFE) was determined by subtracting from 100% the proportion of water, “crude ash”, “crude protein”, “crude fiber”, and “crude fat” content (in percent). The NFE group includes sugars, dextrins, gums, starch, hemicellulose, inulin, some organic acids and others.
Sample preparation for the determination of anti-nutritional substances was carried out by preparing extracts from the green mass of amaranth with a moisture content of 6.8%. The aerial part was crushed to a size of 2-3 mm, 50 g of green mass was thoroughly ground in a mortar with quartz sand, quantitatively transferred into a 500 cm3 volumetric flask, and adjusted to the mark with distilled water. The resulting mixture was infused for 24 hours at a temperature of 25 °C, the green mass was separated by filtration, and the content of antinutrients in the filtrate was controlled. The amount of nitrates was determined in accordance with GOST 13496.19–2015, oxalic acid - MU 1808-77, tannins - GOST 19885-74. The content of phytic acid and the accumulation of inorganic phosphate were determined according to the method described in RF Patent 2018102663.
Hydrolysis of the green mass of amaranth, previously dried to a moisture content of 8-9%, was carried out with the enzyme preparation “Kemzyme Plus P dry”, at 37 ° C, pH 6.5, hydromodule of 1:10, for 2-3 hours. During the hydrolysis process every 30 -60 min the content of inorganic phosphorus was monitored.
Experiments to study the influence of the dosage of the enzyme preparation, hydromodule, pH and temperature of hydrolysis on the efficiency of phytate destruction were carried out according to the classical research method, in which only one factor was varied while the others remained constant. The measurement error of the experiments did not exceed that established by the standard or the methodology used. Each experiment was performed in triplicate.

RESULTS & DISCUSSION

The component composition of the green mass of plants is not constant and varies depending on cultivation conditions. Analysis of experimental data (Table 1) showed that the content of anti-nutritional substances in the green mass of amaranth variety Giant of the 2023 harvest exceeds these indicators compared to the 2022 harvest: nitrates - 3.3, tannins - 1.4, phytates - 4 times, and the amount of oxalic acid is 16 times lower. At the same time, the content of proteins and fats decreased by 12.6 and 31.6% respectively, and the amount of fiber increased by 8.5%, which is associated with changes in the soil and climatic conditions of amaranth cultivation. The average monthly temperature during the amaranth cultivation period in 2022 and 2023 was 20.6 and 19.2 °C respectively, this could contribute to greater protein synthesis in the 2022 harvest. The main feature of this period of 2023 in the Voronezh region was a record amount of precipitation in June (71.4 mm) and especially in July (147.6 mm), which explains the increase in the amount of nitrates in the green mass of amaranth. The high content of oxalic acid in the 2022 harvest indicates that amaranth was cultivated on more alkaline soil compared to 2023. In addition, our research showed that the 2023 harvest contains more phytates, which accumulate in plants when grown on acidic soil [7]. The tannins content did not exceed

https://doi.org/10.5593/sgem2024/6.1/s25.22

the maximum permissible concentration of 0.5%, which can help improve feed intake, health, nutrition and performance of monogastric animals [8]. It should also be noted that the species used, Amaranthus hypochondriacus, contains more than 90 times less oxalic acid compared to other amaranth species cultivated in Russia (A. retroflexus, A. gangeticus, A. caudatus) [9].

Table 1 - The chemical composition of the green mass of amaranth

Name of indicators	Dry matter content, %	
	Harvest 2022	Harvest 2023
Nitrates	0,30 ± 0,005	0,99 ± 0,005
Tannins	0,30 ± 0,005	0,42 ± 0,005
Oxalic acid	0,31 ± 0,005	0,02 ± 0,005
Phytates	0,62 ± 0,005	2,50 ± 0,005
Crude protein	14,89 ± 0,01	13,01 ± 0,01
Crude fat	4,33 ± 0,01	2,96 ± 0,01
Crude fiber	17,05 ± 0,01	18,50± 0,01
Nitrogen-free extractive substances	39,61 ± 0,01	41,23± 0,01
Crude ash	15,32 ± 0,01	15,50 ± 0,01

Phytates contained in plant components of feed are not broken down in the gastrointestinal tract of farm animals and birds, reduce the activity of digestive enzymes and the digestibility of minerals, proteins, amino acids, fats, and also cause low availability of phosphorus. High levels of phytic acid in feed can lead to rickets [10]. Therefore, our further research was aimed at developing regimes for the enzymatic destruction of phytates in the green mass of amaranth.

Phytates are present in feed in the form of complex compounds with polysaccharides and proteins, which limit the action of phytases. The cleavage of globules by proteases and carbohydrases can facilitate the availability of phytases to the substrate, increasing the efficiency of hydrolysis of phytic acid and its salts [11]. In this regard, for the destruction of phytates in the green mass of amaranth, the multienzyme complex “Kemzyme Plus P dry” was used, which has xylanase, β-glucanase, cellulase, protease, amylase and phytase activities, which will not only facilitate the availability of phytases to the substrate, but also increase feed digestibility due to the destruction of non-starch polysaccharides.

The efficiency of biocatalysis is significantly influenced by the dosage of the enzyme preparation, the hydromodule, the pH of the reaction medium, the temperature and duration of hydrolysis.

Study of the effect of the hydromodule on the effectiveness of phytase action (Fig. 1) showed that the maximum accumulation of inorganic phosphorus was observed at a hydromodule of 1:10 after one and a half hours of hydrolysis. A further increase in the hydromodule to 1:25 reduced the effectiveness of phytase by 3 times. With a ratio of amaranth green mass to water of 1:8, the process of enzymatic destruction of phytates proceeds intensively for the first 30 minutes, but the maximum amount of released inorganic phosphorus is 1.5 times less than with a hydromodule of 1:10. In addition, a growth of the hydromodule increases the duration of drying of the hydrolyzate, thereby the energy costs of the process become greater, which is not expedient from an economic point of view.

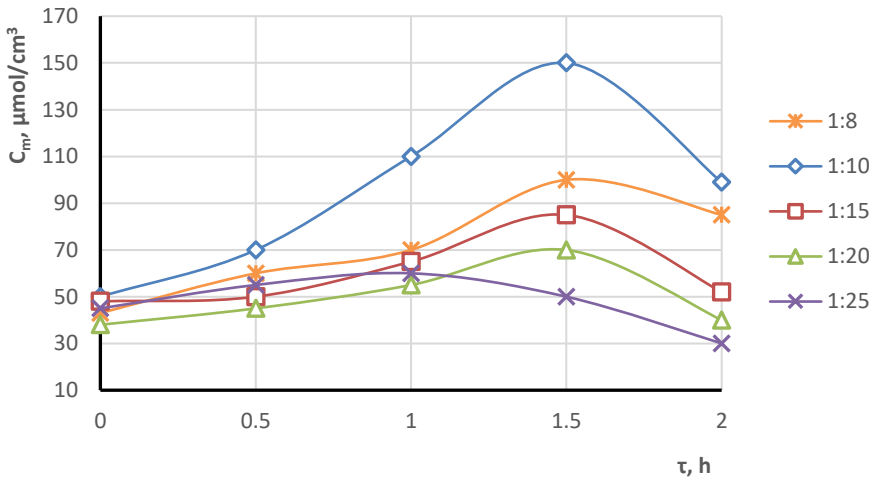


Fig. 1. Dynamics of accumulation of inorganic phosphates at an EP dosage of 2.5%, hydromodule: 1 – 1:10; 2 – 1:8; 3 – 1:15; 4 – 1:20; 5 – 1:25. C_m – molar concentration of inorganic phosphates, µmol/cm^3; τ – duration of hydrolysis, h

Another important parameter that has a significant impact on the process of hydrolysis of amaranth green mass is the dosage of the enzyme preparation, which was added in an amount of 1-3%.

In a series of experiments presented in Fig. 2, it was established that the maximum accumulation of inorganic phosphorus was observed when the enzyme preparation was added in an amount of 2.5-3%. With such dosages of the enzyme preparation, approximately the same amount of inorganic phosphorus was formed; from an economic point of view, it is more expedient to add 2.5% of the enzyme preparation to the reaction medium. Adding a smaller amount reduced the efficiency of phytate hydrolysis by 1.5-3 times.

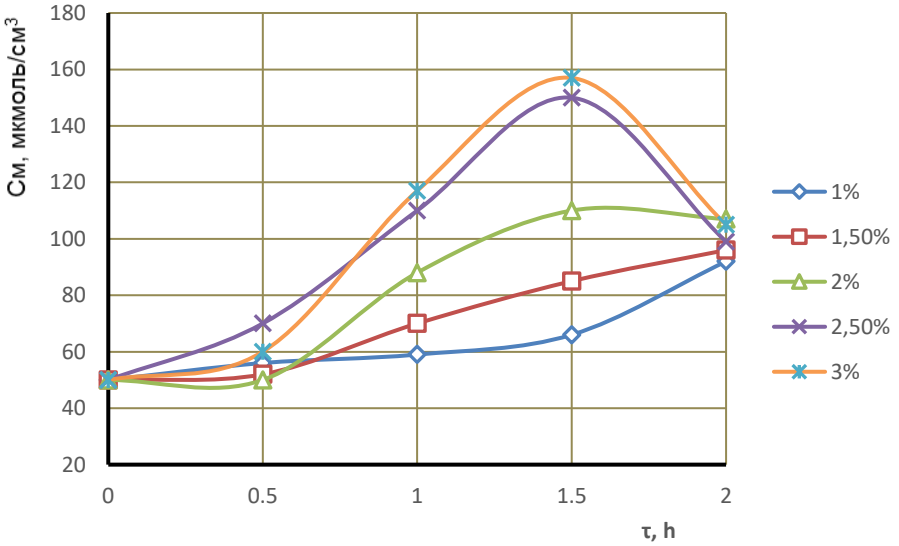


Fig. 2. Dynamics of accumulation of inorganic phosphates with a hydromodule of 1:10 and different dosage of the enzyme preparation. C_m – molar concentration of inorganic phosphates, µmol/cm^3; τ – duration of hydrolysis, h

https://doi.org/10.5593/sgem2024/6.1/s25.22

Experimental data on the influence of pH on the hydrolysis process showed (Fig. 3) that the phytase of the multienzyme complex is active in a wide pH range; it showed the greatest hydrolytic ability against phytates in a neutral medium, the maximum at 6.5. A change in pH to the acidic and alkaline side helped to slow down the hydrolysis process, the accumulation of inorganic phosphates decreased by 1.2-1.3 times.

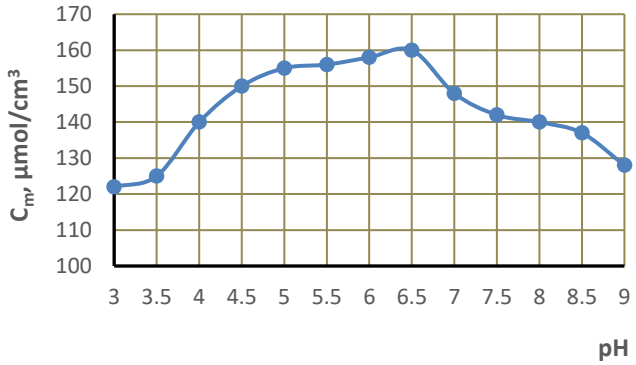


Fig. 3. The effect of pH on the accumulation of inorganic phosphates in the process of enzymatic destruction of phytates. C_m – molar concentration of inorganic phosphates, µmol/cm^3

The study of the influence of temperature on the efficiency of hydrolysis was carried out in the temperature range of 30-50 °C. Analysis of experimental data (Fig. 4) showed that the maximum accumulation of inorganic phosphorus is observed at 37-40 °C for 1.5 hours. At a temperature of 40 °C, the destruction of phytates was intense for the first 30 minutes, then a decrease in enzyme activity was observed. At temperatures of 30 and 50 °C, the effectiveness of phytase activity decreases by 1.7-2 and 3-4 times respectively. At a temperature of 45-50 °C, the content of inorganic phosphates increased slightly, which indicates inactivation of the enzyme.

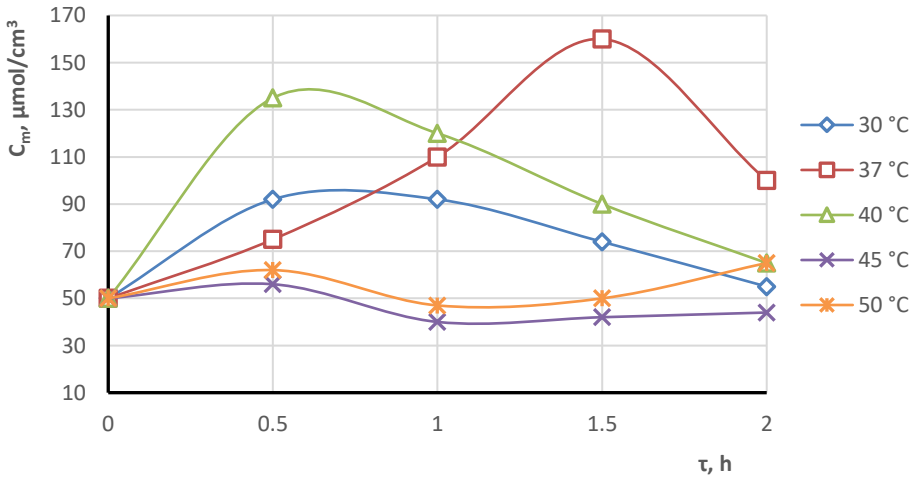


Fig. 4. Dynamics of accumulation of inorganic phosphates in the hydrolysate of amaranth green mass at a hydromodule of 1:10, dosage of an enzyme preparation of 2.5%, pH 6.5.C_m – molar concentration of inorganic phosphates, µmol/cm^3; τ – duration of hydrolysis, h

Thus, we have selected a rational regime for the enzymatic destruction of phytates in the green mass of amaranth using the enzyme preparation "Kemzyme Plus P dry": temperature 37 ° C; pH 6.5; hydromodule 1:10; the dosage of the enzyme preparation is 2.5% and the duration of hydrolysis is 90 minutes.

A comparative analysis of the chemical composition of amaranth green mass and the resulting hydrolyzate (Table 2) showed that the developed method of enzymatic processing of raw materials ensured a reduction in fiber and fat content by 1.4 and 3.2 times respectively, complete destruction of phytates and release of the final product from nitrates. The content of tannins and oxalic acid remained at the same level, the amount of protein decreased by 1%.

Table 2 – Comparative characteristics of the green mass of amaranth and hydrolysate

Name of indicators	Dry matter content, %	
	Green mass amaranth	Hydrolysate
Nitrates	0,99 ± 0,005	0
Tannins	0,42 ± 0,005	0,42± 0,005
Oxalic acid	0,02 ± 0,005	0,02± 0,005
Phytates	2,50 ± 0,005	0
Crude protein	13,01 ± 0,01	12,88± 0,01
Crude fat	2,96 ± 0,01	0,90± 0,01
Crude fiber	40,30 ± 0,01	28,50± 0,01
Nitrogen-free extractive substances	41,29 ± 0,01	45,82 ± 0,01
Crude ash	15,50 ± 0,01	15,30 ± 0,01

Thus, the proposed enzymatic treatment of the green mass of amaranth made it possible to obtain a high-quality feed additive free of phytates and nitrates for further use in the diet of quails.

CONCLUSION

1. It was revealed that the content of nitrates, tannins and phytates in the green mass of amaranth variety Giant of the 2023 harvest exceeds these indicators compared to the 2022 harvest by 3.3, 1.4, and 4 times respectively. The amount of oxalic acid is 16 times lower. At the same time, the content of proteins and fats decreased by 12.6 and 31.6%, respectively, and the amount of fiber increased by 8.5%.
2. It is recommended to use the multi-enzyme complex "Kemzyme Plus P dry" (KEMIN) for the decomposition of phytates in the green mass of amaranth, which has xylanase, β-glucanase, cellulase, protease, amylase and phytase activities, which will not only facilitate the availability of phytases to the substrate, increasing the effectiveness of their action, but also to increase the digestibility of feed due to the destruction of non-starchy polysaccharides.
3. It was established that phytase, which is part of the multi-enzyme complex, exhibits a high ability to hydrolyze amaranth phytates in the pH range of 4.5-7.0, the maximum at 6.5. The optimal operating temperature is 37 °C.
4. A rational treatment regime for amaranth green mass has been selected: temperature 37 °C; pH 6.5; hydromodule 1:10; dosage of the enzyme preparation is 2.5%, duration 90

https://doi.org/10.5593/sgem2024/6.1/s25.22

minutes, ensuring not only the complete destruction of phytates, but also the release of the studied plant raw materials from nitrates during the fermentation process.
5. It was noted that enzymatic hydrolysis of the green mass of amaranth by a multi-enzyme complex helps reduce fiber in the feed additive by 29%.

ACKNOWLEDGEMENTS

The work was carried out within the framework of the Russian Science Foundation grant no. 22-76-00062.

REFERENCES

[1] Shaaban Maysun Analysis of the Russian market of feed additives/ Animal husbandry and feed production, 2023. Vol. 106, No. 3. pp. 76-91.
[2] Walk C.L., Rama Rao S.V. Increasing dietary phytate has a significant anti-nutrient effect on apparent ileal amino acid digestibility and digestible amino acid intake requiring increasing doses of phytase as evidenced by prediction equations in broilers. Poultry Science, 2020, 99(1): 290-300. DOI: 10.3382/ps/pez489
[3] Babatunde O.O., Cowieson A.J., Wilson J.W., Adeola O. The impact of age and feeding length on phytase efficacy during the starter phase of broiler chickens. PoultryScience, 2019, 98(12): 6742-6750. DOI: 10.3382/ps/pez390
[4] Yusifov N.M. Protein nutrition and amino acid composition of amaranth protein of grain direction / N.M. Yusifov, K.S. Dashdemirov, S.A. Amirov// Eurasian Union of Scientists. - 2016. - No. 1. – pp. 117-118.
[5] Písaříková B. et [al.] The use of amaranth (genus Amaranthus L.) in the diets for broiler chickens // Veterinarny Medicina. 2006. № 51. Vol. 7. – P. 399-407
[6] Pavlenkova S.V., Bondareva O.V., Sviridova T.V., Anokhina E.P., Shuvaeva G.P., Korneeva O.S. The study of the dynamics of the accumulation of nutrients and anti-nutrients in the green mass of amaranth / 23rd International Multidisciplinary Scientific GeoConference SGEM 2023, 2023. – ISSUE 6. - P. 241-248 doi.org/10.5593/sgem2023/6.1/s25.30
[7] Kulikov, Yu. A., Ecological aspects of the introduction and use of plants of the genus Amaranthus L.: monograph / Yu. A. Kulikov, R. N. Sagitov, K. D. Matrosova. — Moscow: Rusains, 2019. — 161 p. — ISBN 978-5-4365-3475-6. — URL: https://book.ru/book/932732 — Text : electronic.
[8] TZahra Mohammed Hassan, Tlou Grace Manyelo, Letlhogonolo Selaledi and Monnye Mabelebelehe Effects of Tannins in Monogastric Animals with Special Reference to Alternative Feed Ingredients / Molecules, 2020 Oct; 25(20). 4680. doi: 10.3390/molecules25204680
[9] Officers E.N., Korosteleva Yu.A. The use of amaranth in solving the problem of hypocalcemia / Butlerov communications, 2005. - Vol. 6. - No.2. – C. 56-66
[10] Zinoviev, S. V. The anti—nutritional effect of phytates - the extraphosphoric effect of phytase (review)/ S. V. Zinoviev, V. S. Kryukov, H. M. Mutieva, I. V. Glebova, N. I. Yarovan// Genetics and animal breeding, 2021. - No. 4. – pp.74-84
[11] Kryukov V.S., Zinoviev S.V. New aspects in the interpretation of the role of phytase in the digestive processes in productive animals / Problems of biology of productive animals, 2021.- vol. 3. Pp. 5-19. doi: 10.25687/1996-6733

EVALUATION OF THE EFFICIENCY AND INTENSITY OF HOMOGENIZATION BY CHANGING THE GEOMETRY OF THE TURBINE IMPELLER BLADES

DSc., University Prof. Igor Korobiichuk[1]

Ph.D., Assoc. Prof. Vladyslav Shybetskyi [2]

Ph.D., Assoc. Prof. Sergii Kostyk[2]

Ph.D., Myroslava Kalinina [2]

Dariia Hunchenko[2]

Zhanna Korobiichuk[3]

[1] Łukasiewicz Research Network – Industrial Research Institute for Automation and Measurements PIAP, **Poland**
[2] National Technical University of Ukraine "Igor Sikorsky Kyiv Polytechnic Institute", **Ukraine**
[3] Warsaw University of Technology, Warsaw, **Poland**

ABSTRACT

This article presents a numerical study of the effects of changing the geometry of the turbine impeller blades on the efficiency and intensity of homogenization in a bioreactor. The mixing of liquid media is an important stage of technological processes in various industries. Modern Impellers are equipped with homogenizing devices for introducing energy into the liquid, they include hydraulic, pneumatic and mechanical devices or their combinations. Rational selection of the mixing device at the design stage is important for the efficiency of the homogenizer and the entire production line. Four types of impellers are considered: a classic turbine impeller with straight blades, and three modified impellers with different blade inclinations. The mixing process is simulated using the ANSYS Fluid Flow CFX module, based on the finite element method. The results show that the impeller with an upper inclined blade at an angle of 45° has the best performance in terms of mixing speed and vortex formation. The article demonstrates the potential of using computer modeling to optimize the design of mixing devices and to improve the quality and productivity of biotechnological processes. The results obtained in this work can be used by engineers and technologists to design bioreactors with reduced values of shear stresses.

Keywords: turbine impeller, ANSYS, hydrodynamics, homogenization.

INTRODUCTION

The mixing of liquid media is an important stage of technological processes in various industries, where it is used for various purposes, such as the preparation of emulsions, suspensions and homogeneous systems, as well as to increase the efficiency of chemical, thermal and diffusion processes.

The preparation of emulsions requires the creation of significant shear forces to grind the dispersed phase. This is achieved due to the velocity gradient in the fluid, where the greatest shear forces occur in regions with the greatest velocity gradient.

https://doi.org/10.5593/sgem2024/6.1/s25.23

Homogenization, preparation of suspensions, heating or cooling of a homogeneous medium requires reduction of concentration or temperature gradients in the apparatus. In the case of intensification of chemical, thermal, and diffusion processes in heterogeneous systems, mixing creates better conditions for bringing matter to the reaction zone or heat exchange. An increase in the turbulence of the system during mixing leads to a decrease in the thickness of the boundary layer and an increase in the rate of mass transfer and heat transfer, which accelerates the processes. Mixing is used in the processes of absorption, evaporation, extraction and other processes of chemical technology to improve the quality and speed of various operations [1].

Modern Impellers are equipped with homogenizing devices for introducing energy into the liquid, they include hydraulic, pneumatic and mechanical devices or their combinations. Rational selection of the mixing device at the design stage is important for the efficiency of the homogenizer and the entire production line.

The most important parameters by which mixing devices can be evaluated are efficiency and intensity. The efficiency of the mixing device is determined by the quality of the mixing process and depends on the purpose of this process. For example, in the case of the formation of suspensions, the efficiency is characterized by the uniformity of the distribution of the solid phase in the entire volume of the apparatus. When intensifying heat or mass processes, efficiency is determined by the ratio of heat or mass transfer coefficients with and without mixing. It is important to note that the efficiency of mixing depends not only on the design of the device and apparatus itself, but also on the energy introduced into the liquid [1]. The intensity of mixing is determined by the time required to achieve a certain technological result, or by the number of revolutions of the stirrer during a fixed period (in the case of mechanical stirrers). The higher the intensity of mixing, the faster the expected result is achieved. Intensification of mixing processes allows reducing the size of designed devices and increasing the productivity of existing ones [1]. The basis of this study is the possibility of estimating these parameters by changing the geometry of the blades of a classic turbine impeller using CAD. This principle is often used by other authors.

Prayush Jung Karki and co-authors investigates the potential of replacing conventional agitator impellers with golden angle impellers in mixing tanks to enhance performance and energy efficiency. A golden angle impeller is designed and analyzed using CAD modeling and Computational Fluid Dynamics (CFD). Numerical simulations reveal a 12.4% increase in power output and a 66.36% increase in average flow velocity compared to conventional marine impellers. Experimental validation shows a 5.39% increase in conductivity and 17.6% increase in power consumption for the golden angle impeller due to higher turbulence. The study concludes that the golden angle impeller offers significant optimization potential for mixing processes in industries such as pharmaceuticals, cosmetics, and waste water management [2].

Cuicui Yin and co-authors study compares the performance of two rotor-stator agitators (CSRS and HCSRS) with conventional axial-flow (A200) and radial-flow (Rushton) agitators in solid-liquid mixing operations. Computational Fluid Dynamics (CFD) modeling is employed to assess homogeneity, power consumption, and liquid level stability. Results show that while conventional agitators experience decreased homogeneity at higher stirring speeds, rotor-stator agitators maintain good mixing homogeneity even at 600 rpm. The CSRS agitator achieves superior performance with a

42% reduction in particle concentration deviation compared to the A200 agitators, along with significantly lower average liquid level velocity [3].

At YuanYuan Shen and co-authors study investigates the impact of a newly designed "V-shaped" horizontal baffle on the performance of agitators in liquid-liquid mixing processes. Traditional baffles are known to enhance mixing but can lead to high energy consumption. By introducing the "V-shaped" baffle attached to the inner wall of the agitator at the impeller height, the study compares various baffle configurations using computational fluid dynamics (CFD). Results show that the "V-shaped" baffle reduces energy consumption and enhances mixing, offering promising avenues for baffle optimization and innovation [4].

In work Sahrun Dongoran and co-autors research was carried out for four designs of stirrers for research was carried out for four designs of impellers for the production of biodiesel. The flow behavior in a biodiesel reactor with different types of agitators using computational fluid dynamics (CFD) simulations to determine the optimal agitator. Various parameters such as temperature and fraction distribution, turbulence intensity, and fluid vorticity were analyzed under transient and steady-state conditions using agitation types including helical screw, turbine, propeller, and anchor. The materials modeled included cooking oil and methanol with a mole ratio of 1:6, with mixing conducted at 500 rpm agitation speed and 60-65°C mixing temperature. The analytical hierarchy process method was employed to determine the optimal agitator, with scores obtained for each agitator: 0.314 (anchor), 0.350 (helical screw), 0.249 (propeller), and 0.087 (turbine). The helical screw type was identified as the optimal agitator based on the analysis [5].

Previously, a team of our researchers published research computer simulations to analyze the hydrodynamics of a bioreactor equipped with different types of turbine impellers: a standard open-type turbine impeller, a two-disc open-type turbine impeller with straight blades, and a novel design with blades oriented at 45º and 135º angles. Using ANSYS software, comparative analyses of liquid flow hydrodynamics resulting from mixing by these devices are conducted. Results show that the proposed turbine significantly reduces vortex formation, with depths of 0.06 m at 400 rpm and 0.012 m at 600 rpm [6].

MATERIALS AND METHODS

The most common is mechanical mixing with the help of agitators, which receive rotational movement from an electric motor through a gearbox. The process of mechanical mixing is an external problem of hydrodynamics, where a body is surrounded by a fluid stream. When the speed of movement increases, the separation of the liquid boundary layer from the surface of the body occurs, which leads to the formation of a turbulent wake following the movement of the body. The speed of rotation has the greatest effect on the periphery of the stirrer, where a zone of reduced pressure is formed, stimulating intensive mixing of the contents of the apparatus.

The problem of external flow around bodies under mixing conditions can be solved using the Navier-Stokes equations and flow continuity. The exact analytical solution of this problem is quite difficult and is possible only for individual cases. Therefore, the theory of similarity is used to solve this problem. As follows from the generalized equation of hydrodynamics, the forced radial movement of a liquid in conditions where the action of gravity cannot be neglected is described by the criterion equation [7, 8]:

https://doi.org/10.5593/sgem2024/6.1/s25.23

$$Eu = f(Re, Fr, G_1, G_2, ...) \quad (1)$$

Eu – Euler number;
Re – Reynolds number;
Fr – Froude number;
G_1, G_2, … – simplexes of geometric similarity.

To describe the mixing process, modified Euler, Reynolds, and Froude criteria are used, which can be obtained by transforming the usual expressions of these criteria by replacing the linear velocity of the liquid with a rotational velocity that is proportional to the frequency [7, 8]:

$$Re_m = \frac{\rho \cdot n \cdot d^2}{\mu} \quad (2)$$

$$Fr_m = \frac{n^2 \cdot d}{g} \quad (3)$$

$$Eu_m = \frac{\Delta P}{\rho (n \cdot d)^2} \quad (4)$$

n – rotation frequency, [s^{-1}];
d – diameter of impeller, [m];
ρ – density of the fluid, [kg/m^3];
μ – dynamic viscosity of the fluid, [Pa·s];
ΔP – pressure gradient, [Pa].

Euler's criterion includes the pressure difference between the front (on the side of the flow) and the back planes of the agitator blade. This pressure drop, which is overcome by the force F, which is applied to the agitator shaft, is expressed in terms of the useful power N, which is transmitted to the liquid. The value N is proportional to the product of the force on the shaft and the speed of rotation [7, 8]:

$$N \approx F(n \cdot d) \quad (5)$$

The pressure drop can be replaced by a proportional value, given that $S \sim d^2$:

$$\Delta P = \frac{F}{S} \approx \frac{N}{(n \cdot d)S} \approx \frac{N}{n \cdot d^3} \quad (6)$$

We can obtain the resulting expression for the modified Euler criterion, which is called the K_N power criterion:

$$Eu_m = \frac{N}{\rho \cdot n^3 \cdot d^5} = K_N \Leftrightarrow N = K_N \cdot \rho \cdot n^3 \cdot d^5 \quad (7)$$

It should also be noted that for the preparation of heterogeneous dispersion systems, it is necessary to consider a number of features that affect the efficiency and intensity of mixing. In general, establishing these parameters by analytical solution is quite a difficult task, especially in the case of a new agitator geometry, since there will be no data on the power criteria for them. In this case, it is possible to conduct empirical research using a natural experiment or computer modeling using CAD.

COMPUTER SIMULATION

In order to study mixing with new impeller designs, it is necessary to go from the development of technical documentation to conducting physical experiments and

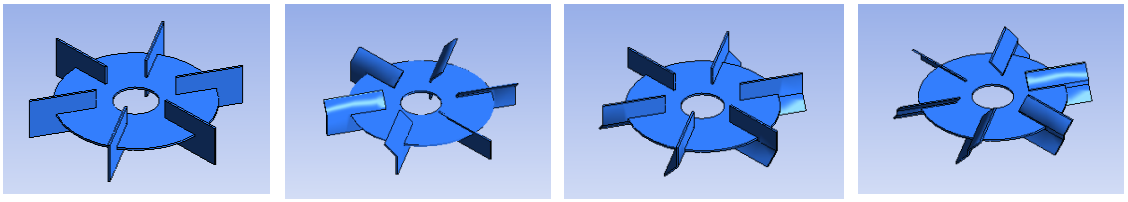
confirming the correctness of the assumptions underlying the design. Reducing the costs associated with conducting full-scale experiments and the time spent on preparing stands and manufacturing test samples can be implemented through the use of computer modeling [9].

The most progressive method of computer modeling of hydrodynamic, heat and mass transfer processes is the finite element method. This method is implemented in the following ANSYS, COMSOL, and SolidWorks programs [10-13].

The purpose of this study is to analyze the possibility of using stirrer designs in which only the upper or lower part of the blade is inclined; as well as a design in which both the upper and lower parts of the blade are inclined, but the middle part remains straight as an element of increasing the efficiency of the mixing process.

The relevance of the study is due to the use of bioreactors in most lines of biotechnological production, the implementation of energy saving during technological operations and strict control of process parameters to obtain products of appropriate quality [14-15].

The Fluid Flow CFX module of the ANSYS program was chosen for the simulation. Modeling was carried out for 3D models (Fig. 1).



a) b) c) d)

Fig. 1. Impeller s: A – classic turbine impeller with straight blades; B – turbine impeller with an upper inclined blade; C – a turbine impeller with a lower inclined blade; D – a turbine impeller with a slope on both sides

To implement the finite element method, geometric models were divided into a finite set of elements in the ANSYS «Mesh» system. During construction, the «Use adaptive Sizing» function is enabled with the Resolution=7 value, and the grid is also improved with the «Refinement» function, with the Refinement equal to 3. The mesh consists of 70886 elements and 14493 nodes.

The simulation type is «Transient», the timestep is 0.01 s, which ensures the convergence conditions and the Courant number at the level of 10. When modeling the mixing process, the material «Water» of the built-in library was selected as a liquid, for which physicochemical parameters are automatically determined.

Boundary and initial conditions of the process:

- the boundary condition «Fluid» is set by default.
- the agitator is set to the «Rotor» boundary conditions with a speed of rotation of the agitator of 3.3 s^{-1}.

RESULTS

In fig. 2 shows the speed of mixing throughout the volume depending on the selected type of mixing device. From the given results, it can be concluded that the speed of mixing with the modernized stirrer B at certain points of the volume is a slightly higher than when mixing with the standard stirrer A. The modernized turbine impeller with an upper

https://doi.org/10.5593/sgem2024/6.1/s25.23

inclined blade also has better indicators in terms of continuous volume.

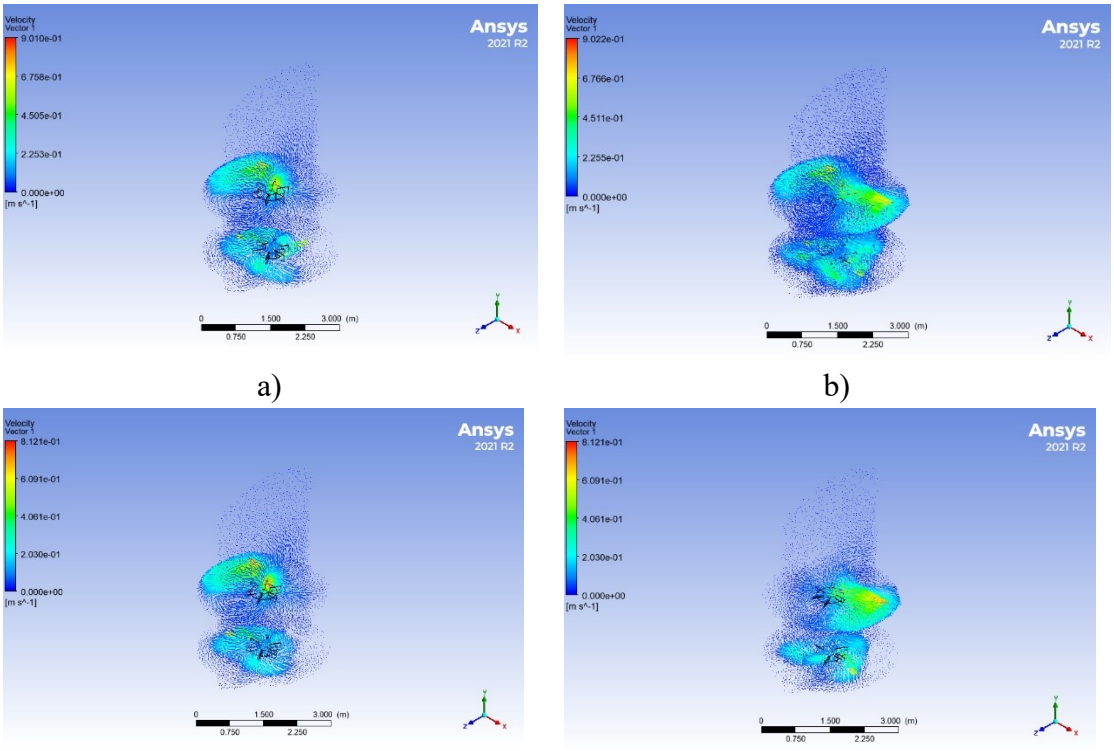


Fig. 2. Vectors of velocity and direction of liquid flow depending on the type of stirrer

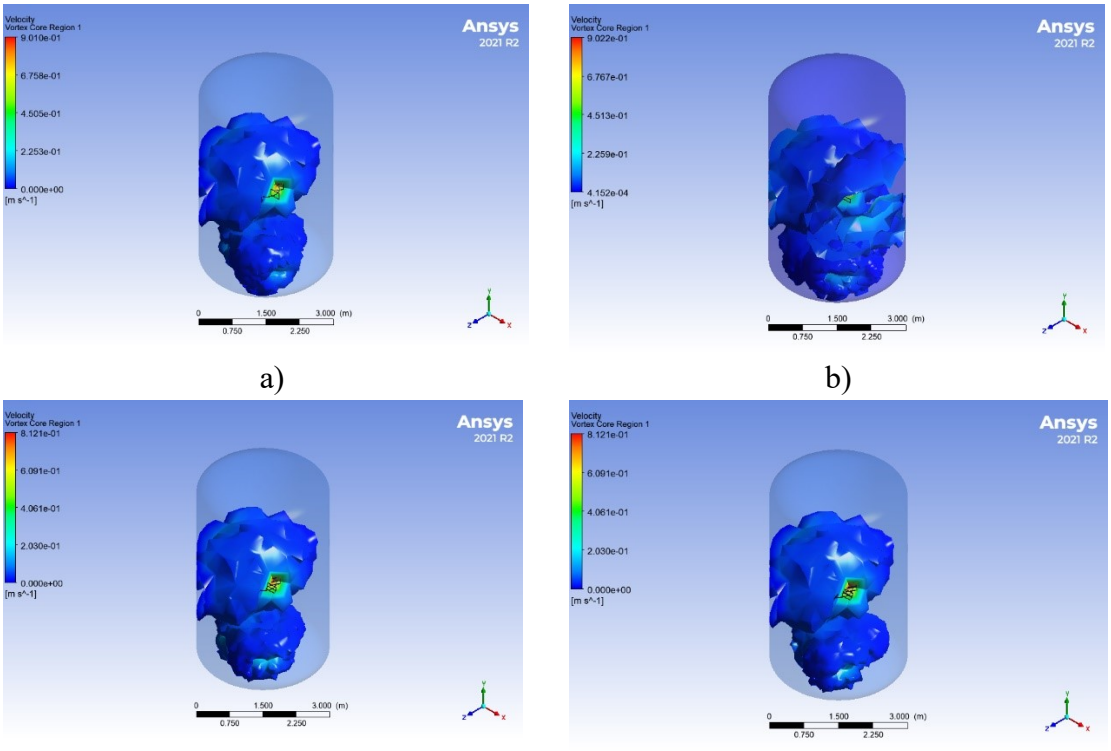


Fig. 3. Vortices created by mixing devices

The maximum speed of mixing for the classic stirrer was 9.01 $m \cdot s^{-1}$, and for the modernized one - 9.022 $m \cdot s^{-1}$. Also, the highest speed can be observed near the blades. However, the turbine impeller with an upper inclined blade also has the advantage that the speed of movement is natively preserved throughout the entire volume of liquid starting from the center, while for others there is an option of speed development only in certain parts of the volume.
In fig. 3. vortices formed during mixing and their velocities are demonstrated. As already mentioned, out of the above options of modernized stirrers, stirrer B performed best, surpassing the speed of classic stirrer A. According to the data obtained during this analysis, the vortex during mixing with a modernized stirrer occupies almost the entire volume of the apparatus, in contrast to mixing with a standard stirrer.

CONCLUSION

The computer model adequately describes the mixing process in the bioreactor, so it can serve to analyze the feasibility of using a modified design of the mixing device and to further optimize its geometry.
The simulation results demonstrate the feasibility of using the modified impeller. Comparing the presented models, in particular the indicators of the mixing speed, it should be noted that the impeller with the inclined upper part at an angle of 45° has better indicators than the classic impeller with straight blades.
Computer simulation convinced that a impeller with a blade tilted from above at an angle of 45° has more advantages than a classic impeller. The maximum mixing speed for the classic impeller was 9.01 $m \cdot s^{-1}$, and for the modernized turbine impeller with an upper inclined blade - 9.022 $m \cdot s^{-1}$. Also, maintaining the mixing speed throughout the volume of liquid is most present in the bioreactor with turbine impeller with an upper inclined blade. The results obtained in this work can be used by engineers and technologists to design bioreactors with reduced values of shear stresses.

REFERENCES

[1] Jaromir J. Ulbrecht, Gary K. Patterson, Mixing Liquids By Mechnanical, Taylor & Francis, p. 345, 1991.

[2] Prayush Jung Karki, Abishek Subedi, Anupama Gaihre, Bikalpa Chaulagain, Strena Shrestha, and Sailesh Chitrakar, Comparative numerical and experimental study of golden angle and conventional agitator impellers, Kathmandu University Journal of Science, Engineering and Technology, Vol. 15, No. 2, August 2021.

[3] Yin, C., Zheng, K., He, J., Xiong, Y., Tian, Z., Lin, Y., Long, D.,nTurbulent CFD Simulation of Two Rotor-Stator Agitators for High Homogeneity and Liquid Level Stability in Stirred Tank, Materials, 2022, Vol. 15, 8563. https://doi.org/10.3390/ma15238563.

[4] Shen, Y., Qin, B., Li, X. et al., Investigation of the flow characteristics of liquid–liquid two-phase mixing in an agitator equipped with a “V-shaped” horizontal baffle, Environ Dev Sustain, 23, 2298–2313 (2021). https://doi.org/10.1007/s10668-020-00675-4.

[5] Sahrun D., Dyah W., Desrial D., Investigation of Fluid Flow in Biodiesel Reactor with 4 Different Types of Agitator using Computational Fluid Dynamics Simulation, Urnal Keteknikan Pertanian, Vol. 10(2), 133-143, 2022. https://doi.org/10.19028/jtep.010.2.133-144

https://doi.org/10.5593/sgem2024/6.1/s25.23

[6] Korobiichuk, I., Shybetskyi, V., Kostyk, S., Kalinina, M., Tsytsiura, A., Ways to Reduce the Creation of Vortex During Homogenization of Liquid Products, In: Szewczyk, R., Zieliński, C., Kaliczyńska, M. (eds) Automation 2022: New Solutions and Technologies for Automation, Robotics and Measurement Techniques. AUTOMATION 2022. Advances in Intelligent Systems and Computing, vol 1427. Springer, Cham, 2022. https://doi.org/10.1007/978-3-031-03502-9_33.

[7] Strenk, F., Mixing and equipment with stirrers, Lviv: GHI, 1975, 384 p.

[8] Shterbachek Z., Tausk P., Mixing in the chemical industry, GSHCh, 1963, 416 p.

[9] Aboul Khail, A., Erişen, A., Improvement of Plate Heat Exchanger Performance Using a New Plate Geometry, Arab J Sci Eng, vol 46, 2877–2889, 2021.

[10] Cappello, V., Plais, C., Vial, C., Augier, F., Bubble size and liquid-side mass transfer coefficient measurements in aerated stirred tank reactors with non newtonian liquids, Chemical Engineering Science, 211, 115280, 2020.

[11] Gemello, L., Cappello, V., Augier, F., Marchisio, D., Plais, C., CFD-based scale-up of hydrodynamics and mixing in bubble columns, Chemical Engineering Research and Design, 136, 846–858, 2018.

[12] Akita, K., & Yoshida, F., Bubble size, interfacial area, and liquid-phase mass transfer coefficient in bubble columns, Industrial & Engineering Chemistry Process Design and Development, 13 (1), 84–91, 1974.

[13] Ameur, H., Mixing of shear thinning fluids in cylindrical tanks: effect of the impeller blade design and operating conditions, International Journal of Chemical Reactor Engineering, 14 (5), pp. 1025–1033, 2016.

[14] Ameur, H., Kamla, Y., & Sahel, D., CFD simulations of mixing characteristics of radial impellers in cylindrical reactors, ChemistrySelect, 1 (10), 2548–2551, 2016.

[15] Gimbun, J., Rielly, C. D., & Nagy, Z. K., Modelling of mass transfer in gas–liquid stirred tanks agitated by rushton turbine and CD-6 impeller: a scale-up study, Chemical Engineering Research and Design, 87 (4), 437–451, 2009.

EVALUATION OF THE PROPERTIES OF YOGURT ENRICHED WITH CRUDE POLYSACCHARIDES OBTAINED FROM DIFFERENT MUSHROOMS

Dr. Oana Popa[1]

Prof. Dr. Ovidiu Tița[2]

[1]Doctoral School of Lucian Blaga University of Sibiu, **Romania**
[2]Department of Agricultural Sciences and Food Engineering, Lucian Blaga University of Sibiu, **Romania**

ABSTRACT

With the development of food production technologies, the consumers attention has turned to products with specific nutritional and health-promoting properties. For this necessity, today's manufacturers have turned their attention to fortified foods, and a raw material that is found in great diversity and that can be used to enrich food is represented by mushrooms.

The purpose of this study consists in determining how the addition of different concentrations of crued polysaccharides extracted from mushrooms and added to milk to obtain new varieties of yogurts can influence its quality. The two mushroom species from which polysaccharides have been extracted are Champignon and Reishi.

The obtained analysis showed that the crued polysaccharides extracted from mushrooms consist in carbohydrates (~6% - *Champignon* mushrooms; ~30% - *Reishi* mushrooms), proteins (~6.2% - *Champignon* mushrooms; ~12.6% - *Reishi* mushrooms) and in a smaller amount in phenolic compounds (~ 0.5% - *Champignon* mushrooms; ~8% - *Reishi* mushrooms). To obtain the fortified yogurts, the polysaccharides were added to cow's milk at different concentrations of 0.3% and 0.5% from each species of mushroom. A control sample represented by plain milk that does not contain polysaccharides was also developed. All samples were fermented using commercially available starter cultures.

Following the determinations, it was found that the addition of polysaccharides led to a decrease in pH in the case of both types of samples with the addition of polysaccharides from mushrooms, compared to the control sample. The largest decreases in pH were recorded for concentrations of 0.5% added polysaccharides. In the case of syneresis, significant increases were recorded for the samples enriched with polysaccharides, especially for the samples to which concentrations of 0.5% polysaccharides were added (38.02g for the sample with *Reishi* polysaccharides and 42.22g for the sample with *Champignon* polysaccharides).

The results on the antioxidant activity following the determinations performed recorded the lowest values for the control sample (355µM).

The results showed that crude polysaccharides extracted from the two species of mushrooms added to milk before fermentation can improve its properties, but can also affect them, if the concentrations are not exceeded and are not kept under observation.

Keywords: polysaccharides, mushrooms, yogurt, antioxidant activity

https://doi.org/10.5593/sgem2024/6.1/s25.10

INTRODUCTION

Along with the development of food products, the attention of consumers has turned more and more to healthy foods that offer them benefits. Products or raw materials that provide a beneficial influence have been recognized as functional foods. These assortments can be produced using a wide range of raw materials such as cereals, dairy, fruits and vegetables [1].

Yogurts enriched with different plant-based ingredients have been increasing in the market, and the proposed research focuses on evaluating how the quality of plain yogurt enriched with mushroom polysaccharides is improved. One of the raw materials with different properties is represented by mushrooms, which are found in a great diversity. Both wild and cultivated mushrooms are a rich source of vitamins, phenolic compounds, selenium or vitamin D [2, 3]. A special attention is paid in this study to bioactive polysaccharides. These molecules exert antioxidant and antitumor activity, strengthen the immune system, act as prebiotics and are able to lower cholesterol levels [4].

In this work, the attention was focused on the mushrooms from the species *Ganoderma lucidum* (Reishi) and *Agaricus* (Champignon) and on the polysaccharides that can be extracted from them for the enrichment of yogurt.

Polysaccharides from *Ganoderma* mushrooms were first investigated in 1981 when they were shown to have antitumor activity. Most of the previous studies focused on the antitumor and immunoregulatory activities of these polysaccharides. According to previous investigations, polysaccharides isolated from Ganoderma mushrooms are composed of glucose, mannose, galactose, fuctose, xylose and arabinose. However, these polysaccharides are still quite rarely highlighted in research [5].

The *Agaricus bisporus* mushroom is one of the most important edible mushrooms from an economic point of view. This mushroom species have antioxidant and hypoglycemic activities due to their abundant nutritional components including proteins, polysaccharides, vitamins, nucleotides and unsaturated fatty acids [6, 7].

MATERIALS AND METHODS

- Hot water extraction of crude polysaccharides

20g of dried mushroom powder was extracted twice with hot water at different temperatures (60°C, 80°C and 100°C) at 200 rpm for 2 hours. Then, the extracted solutions were centrifuged (8,000 rpm for 10 min) to collect the supernatant. The concentrate was precipitated using 95% ethanol. After the centrifugation process, the precipitate was collected and dried at 50°C to obtain the crude polysaccharide extract [8].

- Chemical characterization of crude polysaccharides

This characterization involved the determination of the content of carbohydrates, proteins and phenolic compounds. To determine the carbohydrate content, the sample was dissolved in water and mixed with phenol (0.6mL) and concentrated sulfuric acid (3mL). This was incubated for 40 minutes and the absorbance was measured at 490nm using a spectrophotometer. For protein content the dissolved sample (50µL) was mixed with 2.5mL of Bradford reagent and incubated for 6 min at room temperature. Absorbance was read at 595nm. When determining the total content of phenols, the dissolved sample (0.1ml) was mixed with 0.1ml of Folin Ciocalteu reagent, 0.1ml of Na2CO3 and 0.7ml of water. The mixtures were incubated for 90min at room temperature and measured spectrophotometrically at 725nm [9].

- Bacterial culture

The starter cultures used in the preparation of fermented dairy products were: *Lactobacillus*, *Lactococcus*, *Streptococcus*, *Leuconostoc*, *Bifidobacterium* and *Pediococcus*. Lactic fermentation of milk was carried out with bacteria of the genus *Lactococcus* which includes three subspecies: subsp. lactis, subsp. cremoris and subsp. diacetylactis. Bacterial cultures were purchased from DR.Chr. Hansen.

- Preparation of flavored yogurts

The milk samples were supplemented by adding extracts from the two species of mushrooms. Two concentrations of extract from each species were used in the experiment: 0.3% and 0.5% resulting 4 samples of milk enriched with mushroom extract and also a sample of milk without any addition, used as control sample. All samples were pasteurized at a temperature of 85-90˚C for 20 minutes, cooled to 20˚C and then subjected to the operation of seeding with the help of bacterial cultures, 120g per 2l of milk. After that, the samples were subjected to the thermostat operation which was carried out at 30-32˚C for 12h and finally the fermented dairy products obtained were cooled to a temperature of 6-8˚C. After incubation, the yogurts obtained were kept for 24 hours at 5°C before performing the physico-chemical determinations [9].

- Determination of pH

The pH measurement for the samples enriched with different concentrations of mushroom extract as well as for the control sample was carried out using the portable pH meter for food and dairy products.

- Determination of the degree of syneresis

Syneresis of yogurt samples was determined according to Barkallah's method [10].
The principle of the method is based on filtering 100g of sample in a funnel lined with filter paper. After 24 hours of standing, the samples were drained for 6 hours and the whey volume was weighed. The following formula was used to express the results:

$$Syneresis = \frac{V1}{V2} x100$$

where:
V_1 = volume of whey collected after draining, ml
V_2 = the volume of the yogurt sample, ml

- Antioxidant capacity

The FRAP (ferric-reducing antioxidant power) test was performed to determine the antioxidant activity of the yogurts obtained. The methodology described by Benzie and Strain (Benzie, 1996) was used. 0.1 ml of each sample was mixed with 1.9 ml of FRAP reagent. The samples were subsequently incubated at 37°C for 15 minutes, and the absorbance was read at 593 nm using a spectrometer. Quantification of FRAP antioxidant capacity was performed using the calibration curve that was prepared with different concentrations of Trolox (synthetic vitamin E), and the results were expressed as Trolox µM [9].

- Statistical analyses

All assays were performed in triplicate. Results were expressed as mean values ± standard deviation (SD). Statistical analysis was performed using Minitab Statistical Software as well as Excel Calculation Software.

https://doi.org/10.5593/sgem2024/6.1/s25.10

The direction of the conducted research started as an idea from the work of researchers Wojciech Radzki et al. and it was followed how the use of other types of mushrooms can bring positive effects on dairy products [9].

RESULTS

- The results of the pH analysis

The results obtained from the pH analysis are presented in Figure 1. In the case of the PM sample which represents the control sample, a pH of 4.56 was reached. For the samples enriched with polysaccharides from the Reishi mushroom species, a decrease in the pH value was found, and this was proportional to the added polysaccharide concentration. Thus, at the highest concentration (0.5%), the recorded pH value was PR2=4.25. Regarding the Agaricus mushroom culture, the lowest pH value (PC2=4.23) was observed in the case of the sample with 0.5% polysaccharide concentration, similar to Reishi species.

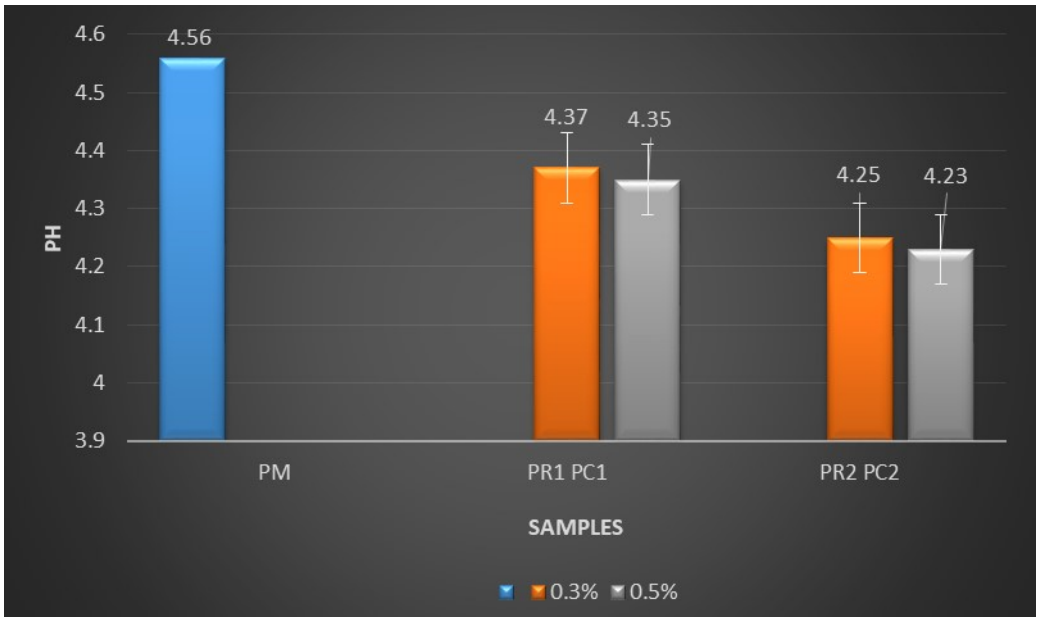


Figure 1. Comparison between the pH level of yogurts enriched with different concentrations of polysaccharides from Reishi and Agaricus mushrooms compared to a control sample (plain yogurt)

- Syneresis results

Syneresis of yogurts is a process by which the whey is released from the gel formed. As shown in Figure 2, the lowest level of syneresis in the analysis was recorded for the control sample (PM=3.10g). The highest values of the degree of syneresis were observed in yogurts containing 0.5% polysaccharides (PR2=38.02g for the sample with Reishi polysaccharides and PC2=42.22g for the sample with Agaricus polysaccharides).

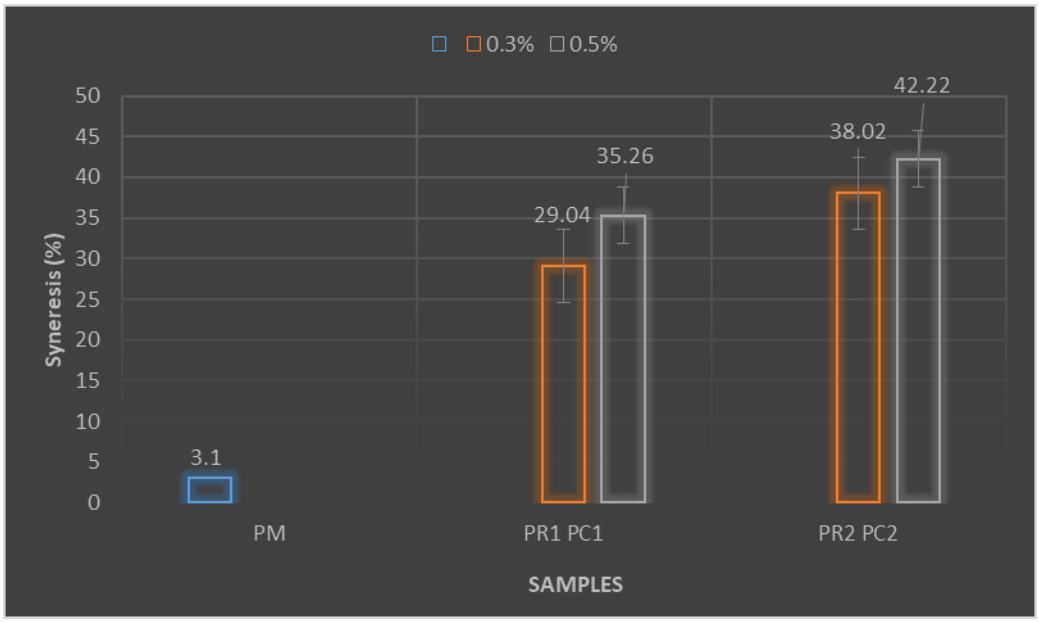


Figure 2. Syneresis of yogurts enriched with different concentrations of polysaccharides obtained from Reishi and Agaricus mushrooms compared to a control sample (plain yogurt)

- Antioxidant activity

The results on the antioxidant activity, measured by the FRAP method, are presented in Figure 3. Following the determinations, the lowest values were recorded for the control sample (PM=355µM).

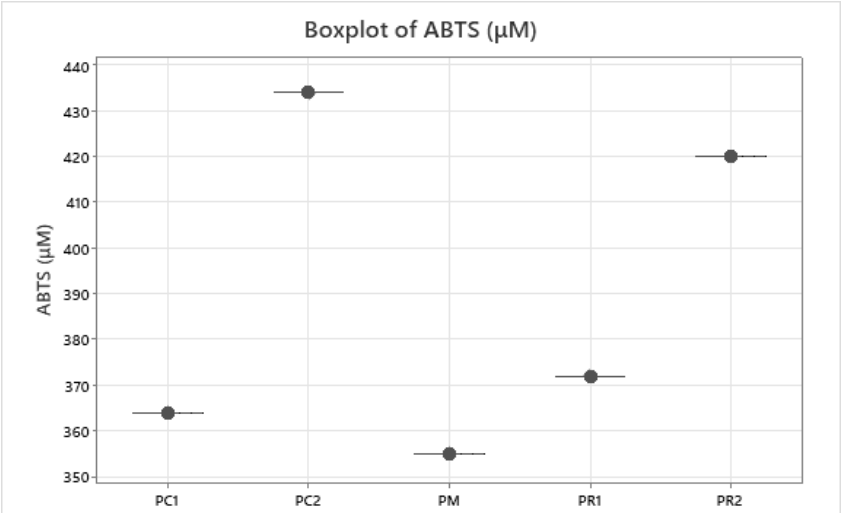


Figure 3. Antioxidant power of yogurts enriched with different concentrations of polysaccharides obtained from Reishi and Agaricus mushrooms compared to a control sample (plain yogurt)

https://doi.org/10.5593/sgem2024/6.1/s25.10

DISCUSSION

For the pH analysis, compared to the results obtained by other researchers, such as in the work of Hozová et al [11], the data obtained are contrary, because in the results obtained by the researcher, a lack of any effect of polysaccharides on pH was noted. This difference in results could be attributed to the much lower concentrations of polysaccharides involved in the researcher's work.
Regarding syneresis, the determinations carried out showed that syneresis increased proportionally with the added polysaccharide content, regardless of the type of polysaccharides. However, the obtained results do not support another study in which the addition of polysaccharides from the species *P. ostreatus* and *L. edodes* worsened the consistency of yogurts [11]. Singh et al. [12] concluded that the addition of barley β-glucans to yogurts at a level higher than 0.3% leads to excessive syneresis and significant deterioration of product quality. Therefore, the use of these molecules seems to be limited in the production of yogurts.
The antioxidant activity of plain yogurt results from the presence of various compounds that naturally exist in milk such as peptides, proteins, amino acids or vitamins. The lactic acid fermentation process can improve antioxidant capacity due to protein digestion and peptide leading to a stronger antioxidant effect.
For the samples developed with the addition of polysaccharides, slightly higher values were recorded for the antioxidant activity. The highest values were recorded for samples containing 0.5% polysaccharides. These increases could result from the presence of polysaccharides that exert antioxidant potential. Such a potential of mushroom polysaccharides was also highlighted in the works of Radzki, 2016 [13].

CONCLUSION

The purpose of the study was to determine how the quality of yogurt can be enriched with polysaccharides extracted from Reishi and Agaricus mushrooms. The addition of polysaccharides can affect the fermentation process of yogurts by stimulating the growth of lactic acid bacteria, which also results from pH and acidity analyses. However, a significant level of decreased syneresis was reported at higher polysaccharide concentrations. The current study is limited due to the lack of in-depth analysis of the polysaccharides used in the study. Detailed information about these molecules could provide additional insight into textural properties. Further research could also be conducted to examine other potential bioactivities of yogurts related to the presence of mushroom-derived polysaccharides.
Therefore, this study reinforces the idea that changing these parameters can limit the use of such macromolecules in yogurt production.

REFERENCES

[1] Kaur S., Das M., Functional Foods: An Overview, Food Sci. Biotechnol, 2011, pp 861–875;

[2] Witkowska A.M., Zujko M.E., Mirończuk-Chodakowska I., Comparative Study of Wild Edible Mushrooms as Sources of Antioxidants, Int. J. Med. Mushrooms**,** 2011, pp 335–341;

[3] Łysakowska P., Sobota A., Wirkijowska A., Medicinal Mushrooms: Their Bioactive Components, Nutritional Value and Application in Functional Food Production-A Review, Molecules, 2023, pp 5393;

[4] Radzki W., Sławińska A., Skrzypczak K., Michalak-Majewska M., The Impact of Drying of Wild-Growing Mushrooms on the Content and Antioxidant Capacity of Water-Soluble Polysaccharides, Int. J. Med. Mushrooms, 2019, pp 393–400;

[5] Shaoping N., Zhang H., Li W., Xie M., Current development of polysaccharides from *Ganoderma*: Isolation, structure and bioactivities, Bioactive Carbohydrates and Dietary Fibre, 2013, pp 10-20;

[6] Delgado-Povedano M.d.M., Sánchez de Medina V., Bautista J., Priego-Capote F., Luque de Castro M.D., Tentative identification of the composition of *Agaricus bisporus* aqueous enzymatic extracts with antiviral activity against HCV: A study by liquid chromatography–tandem mass spectrometry in high resolution mode, J. Funct Foods, 2016, pp 403-419;

[7] Li S., Liu H., Wang W., Wang X., Zhang C., Zhang J., Jing H., Ren Z., Gao Z., Song X., Jia L., Antioxidant and anti-aging effects of acidic-extractable polysaccharides by Agaricus bisporus, International Journal of Biological Macromolecules, 2018, pp 1297-1306;

[8] Benjarat T., Chuttida T., Supattra S., Kamolwan J., Impact of high pressure pre-treatment and hot water extraction on chemical properties of crude polysaccharide extract obtained from mushroom (Volvariella volvacea), Food Chemistry: X, 2023;

[9] Wojciech R., Katarzyna S., Bartosz S., Ewa J.R., Waldemar G., Properties of Yogurts Enriched with Crude Polysaccharides Extracted from *Pleurotus ostreatus* Cultivated Mushroom, Foods, 2023;

[10] Barkallah M., Dammak M., Louati I., Hadrich B., Mechichi T., Ayadi M.A., Fendri I., Attia H., Abdelkafi S., Effect of Spirulina platensis fortification on physicochemical, textural, antioxidant and sensory properties of yogurt during fermentation and storage, LWT - Food Science and Technology, 2017, pp 323-330;

[11] Hozová B., Kuniak Ľ., Kelemenová B., Application of β-d-glucans isolated from mushrooms *Pleurotus ostreatus* (pleuran) and *Lentinus edodes* (lentinan) for increasing the bioactivity of yoghurts, Czech Journal of Food Sciences, 2004, pp 204-214;

[12] Sang C.J., Sundar R.K., Yong T.J., Chi H.S., Gerald P., Macrophage Immunomodulating and Antitumor Activities of Polysaccharides Isolated from Agaricus bisporus White Button Mushrooms, Journal of Medicinal Food, 2012;

[13] Radzki W., Ziaja-Sołtys M., Nowak J., Rzymowska J., Topolska J., Sławińska A., Michalak-Majewska M., Zalewska-Korona M., Kuczumow A., Effect of Processing on the Content and Biological Activity of Polysaccharides from Pleurotus Ostreatus Mushroom, LWT Food Science Technology, 2016, pp 27–33.

https://doi.org/10.5593/sgem2024/6.1/s25.10

GLYCEROL-BASED FERMENTATION BY PLANT GROWTH PROMOTING *ASPERGILLUS NIGER* FOR ITS FURTHER FORMULATION AND APPLICATION IN TOMATO GROWTH

Nikolay Vassilev[1]

Luis García del Moral Garrido[1]

Vanessa Martos Nuñes[1]

Giuseppe Falvo D'Urso Labate[2]

Maria Vassileva[1]

[1]University of Granada, **Spain**
[2]EKROME srl, **Italy**

ABSTRACT

Sustainable crop production includes methods of growing food in a responsible manner avoiding application and dependence on chemically produced fertilizers and pesticides. The latter means development of approaches that lead to environmentally mild inputs based on the production-consumption-recycling principle. Biofertilizers are an important tool to achieve sustainable crop production. In this work, we report the results of experiments on growth and spore/mycelium production of plant growth promoting *A. niger* applying standard nutritional medium (potato-dextrose broth, PDB) enriched with 3% insoluble phosphate (20 to 200 mesh hydroxyapatite of animal-bone origin, HABO) and 0 to 80 g/L glycerol (a by-product of biodiesel production. Results showed the ability of *A. niger* to acidify the medium with the highest titratable acidity of 28.9 mmol/1 (at 5% of glycerol) and solubilize animal bone char under these conditions. As a second stage of the experimental work, the resulting final products were used to formulate gel-based inoculant. Both, the spores and mycelium produced during the fermentation process were further used as a base for formulation to make the biofertilizer production the key in the Sustainable Agriculture. Storage of the resulting products reported here was facilitated by the presence of glycerol in the formulation system.

Keywords: plant growth promoting microorganisms, fermentation, formulation, seedlings

INTRODUCTION

Microorganisms beneficial to plant growth and health are now widely recommended as potential alternatives to chemical fertilizers and pesticides in sustainable agriculture. During the last years, a large number of microorganisms have been isolated and characterized morphologically, physiologically and biochemically. Their potential as biofertilizers and biocontrol agents has been proved in controlled and natural conditions. Since the early studies in the field of microbial inoculants, the emphasis of the scientific

https://doi.org/10.5593/sgem2024/6.1/s25.24

activity during the last 15-20 years is on developing environmentally friendly and efficient microbial fermentations on cheap and assessable substrates [1] and formulation techniques adapted to these processes. **Production, formulation and application of biofertilizers** are the final steps in exploitation of specific beneficial microbial strains alone or in combination with phytostimulants in enhancing nutrient availability, improving soil properties, and increasing crop yield. In general, the results confirmed the beneficial effect of the selected microorganisms on plant growth and health, which is highly dependent on the formulation procedure and the number of microorganisms in one biopreparation [2]. The main roles of the formulation of inoculants are to ensure friendly micro-environment for the microorganisms, simultaneously protecting the cell viability from different physical and chemical agents during storage over a prolonged period and to help them in the competition with native soil microflora or reduce the negative effect of the micro-fauna after introduction into soil-plant systems while interacting with plants and soil microbiome [3]. Before formulation, spores and biomass of the plant-beneficial microorganisms must be produced, which, after formulation, should be delivered depending on the carrier, as liquids (sprays, drenches, and root dips) or as dry formulations applied at the appropriate time [4]. Independently of its form (liquid or solid) the formulated product should fulfil a number of requirements, the most important of which are to ensure high plant root (or rhizosphere) colonizing efficiency, sufficiently high competitiveness in conditions of biotic and abiotic harsh environment, simultaneously increasing plant health and nutrition [3]. One of the most promising formulation techniques is the encapsulation in macro- and micro-beads of (mainly natural) polysaccharides, which guarantees a continuous release of gel-embedded cells/spores into soil-plant systems [5]. It was proved that a simple entrapment of plant beneficial microorganisms in polysaccharide gel particles is not sufficient to ensure and desired advantages and agronomic efficiency of the formulated products [6]. Double/multiple inoculants combined with bio-stimulants and other additives (smart bio-formulates) should be developed to compete with the traditional chemical fertilizers [3].

The aim of this work was to study the behavior of a citric acid producing strain *Aspergillus niger* in the presence of glycerol as a medium component and animal bonechar as an insoluble phosphate source. Further formulation of the filamentous fungus was carried out and its storage for different time periods was tested.

MATERIALS AND METHODS

Microorganism and culture medium:

- The filamentous fungus *Aspergillus niger* NB2 (Collection of the Department of Chemical Engineering, University of Granada) was used throughout this study. It was maintained on potato-dextrose agar slants at a temperature of 4ºC and transferred every 3 months.
- The culture medium for growth and immobilization was Potato-Dextrose Broth supplemented with microbial protein (MP; from mechanically destroyed yeast culture), 5%.
- The medium for acid production and P-solubilization was PDB-MP supplemented with different amounts of glycerol (0-80.0 $g.L^{-1}$) and animal bonechar, of 3.0 $g.L^{-1}$. The initial pH of the medium was 6.5 and was left unadjusted. The medium was autoclaved at 120°C for 20 min. Animal bonechar (80, 50, and 20 mesh, 31% phosphate), kindly provided by BES Ltd, Scotland, was sterilized separately.

Entrapment of A. niger in gel-based carrier: Fungal mycelium and spores were obtained after the end of the fermentation in PDB/MP and glycerol (from 0 $g.L^{-1}$, control, to 80 $g.L^{-1}$).
Sodium alginate solution (4%, w/v) was prepared by continuously stirring at 70° C, autoclaved at 120 °C for 20 minutes, cooled down to environmental (lab) temperature and further mixed (1:1) with a fungal suspension ($1.4x10^8$ colony-forming units, CFU mL^{-1}) previously blended together with the spent liquid medium containing the rest of the un-consumed glycerol. The alginate-fungal suspension mixture $\pm$ 3% animal bonechar was dropped slowly by droplet generator-syringe device with a speed of 15-20 ml per hour into a gently stirred 0.5M $CaCl_2.2H_2O$ solution under a magnetic stirrer. The Ca-alginate beads were recovered after 30 min and washed in a sterile dH_2O water to remove excess calcium ion and un-entrapped cells before introduction into the fermentation flasks. Drying of beads was carried out in an oven for 30h at 30°C to reach a water activity close to 0.2-0.3.

Experimental procedure: The experiments were performed with free and gel-entrapped *A. niger* mycelium/spores.

- **Experiments with free *A. niger*** were performed in Erlenmeyer flasks (250 mL) containing 100 mL of sterilized medium supplemented or not with animal bonechar and inoculated with $1x10^7$ CFU mL^{-1} (collected from 6-day-old *A. niger* grown on potato-dextrose agar; 1 ml/flask). An orbital shaker at 250 rev min^{-1} 30° C was used to carry out the fermentations at 30°C. Each single batch with free *A. niger* for organic acid production and animal bonechar solubilization was carried out for 120 h.
- **Experiments with gel-entrapped cells** were performed under conditions of repeated-batch fermentation as follows: each single-batch cycle was carried out for 48 h and then immobilized cells in alginate were transferred (after careful washing with sterile dH_2O) to fresh medium. 20 Ca-alginate beads were used per flask with a total number of $1x10^8$ CFU.

***Analytical methods**:* **Biomass** was determined both in immobilized particles and as mycelium, freely suspended in the fermentation broth. Determination of fungal survival after immobilization or drying was determined as described by Mater et al. [7] after dissolution of the Ca-alginate beads using 25 fresh or dried beads in 0.2 M citrate buffer (chelating the Ca^{2+} of the Ca-alginate) agitated at 80-100 rpm by a magnetic stirrer. Dissolved fungal mass was diluted and incubated on PDA to determine the CFU. The free biomass was determined by vacuum filtration of the samples, washed with dH_2O, and dried at 70°C to a constant weight.
Titratable acidity was determined by titrating each sample to pH 7.0 with 0.1 M NaOH.
The concentration of **soluble phosphate** was determined by the molybdo-vanado method using vanadate-molybdate reagent (Sigma-Aldrich Cat. No 94686). All experiments were performed in triplicate (three flasks per treatment) and values were analysed and presented as means $\pm$ standard deviation.

https://doi.org/10.5593/sgem2024/6.1/s25.24

Soil-plant experiment

Plants were grown in 128-cell polystyrene (PS) trays (27.7 cm^3 $cell^{-1}$). The soil used was the top 0-20 cm of a Granada (Spain) field soil with pH of 7.5 and containing 15 mg phosphorus/g (Olsen test), total N 0.26% and organic matter 0.8%. Immobilized-cell beads were inoculated manually in soil-sand (5:2) steam-sterilized mixture (free mycelium/spores and different beads per PS cell, adjusted to 10^7 CFU per PS cell) in the surface layer. Tomato seeds, sterilized with 10% hypochlorite for 20 min, and then washed three times with sterile water, were placed in each PS cell (three/cell). After emergence, seedlings were thinned to one per PS cell. Seedlings were irrigated daily. All cells were cultivated in a greenhouse for four weeks under a day/night cycle of 16/8h, 21/15”C, 50% relative humidity. Throughout the experiment, water loss from field capacity was replaced by top watering. The variables measured were shoot height and root length, shoot dry mass, and root dry mass.

RESULTS AND DISCUSSION

Aspergillus niger grew well in the presence of glycerol in the medium (Table 1). However, the biomass concentration decreased, which was more pronounced at 8% glycerol while at 3% and 5% glycerol the biomass growth had similar profile with final values of 4.39 g/L and 4.34 g/L, respectively. Glycerol did not inhibit the citric acid formation expressed as titratable acidity. Higher concentrations of citric acid were registered at 3% and 5% of glycerol compared to the control. Under these conditions, the amount of citric acid produced per gram biomass (Y_{xp}: yield of product in terms of biomass or g product g^{-1} biomass) at the end of the process increased with increasing the glycerol concentration from 0% glycerol to 8% (0% - 4.2; 3% - 5.68; 5% - 6.66; 8% - 8.6) but in the last case this increase was due to the lower biomass growth compared to other treatment. The morphology of the fungal mycelium was found to be affected by the added glycerol and its concentration. In general, filamentous fungi have the tendency to develop different mycelium morphologies, such as suspended mycelium or pellets which depend on shear forces and determine fungal metabolic response and productivity [8]. When PDB was used without glycerol, filamentous mycelium was formed which, along the fermentation process, increased to the highest biomass concentration compared to all other treatment. When glycerol concentration was in the range of 30–50 $g.L^{-1}$, uniform but small (<1 mm on average) pellets were observed. As the glycerol concentration increased to 80 $g.L^{-1}$, the pellets formed clumps and the respective biomass decreased. It is widely accepted that *A. niger* produces a high citric acid yield when the culture grows in the form of small pellets [9]. On the other hand, when the glucose concentration was high in the medium (20% in PDB), particularly in the initial part of the process, glycerol was not consumed.

Table 1 Biomass accumulation and citric acid production by *A. niger* on potato-dextrose broth enriched with glycerol.

Medium Composition (PDB/MP) + Gly (%)	Time-course fermentation (h)	Biomass ($g.L^{-1}$)	Titratable acidity ($mmol.L^{-1}$)
0 (PDB)	40	1,80+0.06	11.0+0.5
	80	2,55±0.04	14.9±0.4
	120	5.32+0.03	21.0+0.6
3	40	1.87+0.05	18.0+0.1
	80	3.91±0.05	22.0±0.3
	120	4.39+0.02	26.0+0.7
5	40	1.71+0.06	13.1+0.2
	80	3.60±0.01	20.8±0.1
	120	4.34+0.04	28.9+0.4
8	40	1.22+0.02	9.2+0.3
	80	1.70±0.07	10.5±0.4
	120	2.20+0.07	12.0+0.2

After depletion of the glucose the glycerol consumption continued the acid production. As the biomass in the presence of glycerol, independently of its concentration, was lower, the metabolism of the fungus was oriented towards acid accumulation, which resulted in higher acidity registered in the fermentation medium. The consumed glycerol increased with increasing its initial concentration starting from 4.31 $g.L^{-1}$ and 5.88 $g.L^{-1}$, (3% and 5% glycerol, respectively) but decreased at 8% glycerol to 3.01 $g.L^{-1}$. Although the results of 3% and 5% glycerol were very similar, 5% initial glycerol was selected for further experiments as in this case the acid production was a bit higher while the residual glycerol was higher (data not shown) compared to all other treatments.

The addition of different size HABO particles to the medium resulted in different response of the *A. niger* (Table 2). In general, the presence of insoluble phosphate and its further solubilization due to the medium acidification and pH lowering, affected the biomass growth pattern. Normally, the acid-producing microorganisms increase their biomass growth in the presence of phosphate [10].

https://doi.org/10.5593/sgem2024/6.1/s25.24

Table 2 Solubilization of different particle size of HABO (3g.L^{-1}) by freely suspended *A. niger* in a single 120-h batch fermentation process and 5% glycerol in the medium

HABO (mesh)	Biomass (g.L^{-1})	Titratable Acidity (mmol.L^{-1})	$P_{soluble}$ (mg.L^{-1})
20	5.68±0.20	30.9±0.1	411±21
60	5.39±0.11	32.1±0.3	489±12
100	4.15±0.13	22.4±0.2	280±9
200	3.46±0.14	18.7±0.2	199±4

The higher fungal growth was also noted in this experiment but in treatments with higher HABO particles size (20 and 60 mesh). Powdered phosphate source did not positively affect biomass growth and acid-production. The results could be explained by an increase of the medium viscosity particularly in the last two particle sizes (100 and 200 mesh) when, in addition, theses small particles adhered to the fungal biomass thus limiting its activity [11]. Therefore, in our experiments, the close relation between the type, size, and concentration of the added substances and the microbial biomass growth and activity was observed.

Table 3 Gel-entrapped *Aspergillus niger* based solubilization of HABO (3 g.L^{-1}, 60 mesh) supplemented to the PDB/MP medium (A) or introduced in the alginate beads (B), in conditions of repeated batch cultivation

Batch No.	Titratable acidity (mmol.L^{-1})		P soluble (mg.L^{-1})	
	A	B	A	B
1	28.1±1.4	31.1±1.4	314±21	348±11
2	33.5±1.1	35.8±1.1	466±13	488±10
3	43.2±1.0	47.1±1.0	512±17	582±17
4	40.1±2.0	44.1±2.0	514±19	564±12
5	39.8±1.4	45.9±1.4	510±12	570±14

The next step was to use the fermentation specificity of our study and prepare a possible formulated product. The P-solubilizing capacity of two types of alginate beads was studied in repeated-batch fermentation of five batch cycles containing HABO in the gel

structure or the same amount of HABO particles were added to the PDB. In both cases, alginate beads contained the fungal biomass and spent fermentation liquid with residual glycerol.

The results (Table 3) showed a higher acid production particularly after the third batch cycle, which was well pronounced in the treatment with alginate-bead-entrapped HABO compared to the treatment with freely suspended HABO. Similarly, the P-solubilizing activity was higher when the P source was entrapped in the polysaccharide carrier thus producing 10 % more soluble total P solubilized by the gel-entrapped fungus. Therefore, the gel entrapped system containing both the fungus and the insoluble phosphate could be used as a formulated product and further tested in soil-plant system. The reason for the higher efficacy of this gel-entrapped system is the presence of glycerol (presented in the spent fermentation liquid) and HABO particles in the carrier. In the case of freely suspended HABO particles, abrasion effect of the solid P-source was observed on the outer surface of the gel-beads, which probably could affect the morphological structure of the fungal filaments developed out of the beads with a concomitant change in the metabolic (acid-producing) activity. Based on the above results, further studies were carried out to determine the viability of the entrapped fungus in dried alginate beads enriched with HABO. The CFU counts as determined at different stages of the experiment resulted as follows:

a) Initial CFU in the ALG/MP/±HABO mixture (ml) ……..1.4 x 10^8
b) CFU in 20 wet gel beads after entrapment and bead solidification 1.0 x 10^8
c) CFU in dried beads (from 20 wet beads)..…… ……. 1.3 x 10^7
d) CFU after a 90-d storage:
    a. at 4^o C……..1.5 x 10^6
    b. at 24^o C……..1.6 x 10^8

The resulting free and gel-formulated products were tested in substrate-tomato system for 25 days (Table 4). Although the highest results of plant growth (shoot and root length) were obtained in treatments with *A. niger* applied in the formulated form of wet cell-beads just after the immobilization, the highest plant dry weight was observed in the case of alginate beads dried for three months at 24^o C.

https://doi.org/10.5593/sgem2024/6.1/s25.24

Table 4. Tomato growth parameters after 25-day-treatments with different formulations of *A. niger*.

	Plant growth (cm)		Plant dry weight (g plant^{-1})	
Treatment	Shoot length	Root length	Shoot	Root
Control	41.33±1.43^{d}	14.1±1.26^{d}	6.1±0.21^{c}	4.00 ± 0.2^{c}
Free Mycelium/ Spores	48.3±0.55^{c}	21.1±0.21^{c}	6.85±0.1^{bc}	4.87±0.22^{bc}
Wet cell-beads-AI	60.73±0.15^{a}	32.16 ± 0.13^{a}	7.99±0.21^{b}	6.11±0.10^{a}
Dried cell-beads/BS	55.4±0.24^{b}	27.98 ± 0.25^{b}	6.96±0.25^{bc}	5.03±0.2^{b}
Dried beads/AS				
at 4^{o}C	54.0±0.25^{bc}	26.88 ± 0.13^{b}	7.76±0.2^{b}	5.26±0.13^{b}
at 24^{o}C	56.7±0.09^{b}	27.02 ± 0.12^{b}	8.89 ±0.37^{a}	6.33±0.07^{a}

Control: Plants without microbial treatment; *Free Mycelium/Spores*: Plants inoculated with free *A. niger* - without its inclusion into gel beads; *Wet Cell-beads*-AI: *A. niger* mycelium and spores applied just after immobilization; *Dried cell-beads-BS*: Dried cell-beads before storage; *Dried beads – AS*: Dried beads after storage at different temperatures.
(Each value represents mean ± S.E, standard error of three replications; Results not sharing a letter in common are show differences between treatments according to LSD test, P ≤ 0.05)

CONCLUSIONS

Microorganisms beneficial to plant growth and health are now widely recommended as potential alternatives to chemical fertilizers and pesticides in sustainable agriculture. The production and formulation stage of the biofertilizer production and its further storage characteristics have a great impact on the success of the final product in soil-plant systems. The results of this study demonstrated the possibility of applying glycerol as a substrate in the medium as shown before [12]. The inclusion of an insoluble phosphate source in the fermentation system showed the capability of free and gel-entrapped acid-producing fungal culture to solubilized it and even at higher production scheme level when the P-bearing material was included into the immobilized cell-gel system. The formulation of a mixture containing the acid-producing microorganism, spent fermentation broth with residual glycerol, and P-bearing particles was active after a three-month period with higher number of viable cells after storage at ambient temperature.

Dried gel-microorganism formulation after three-month-storage at room temperature demonstrated high plant growth promotion activity and could be used as an efficient inoculant at least in tomato growth. Further studies are needed to show the efficacy of the formulated product and its effect on field soil-plant system and the effect of the fungal phosphate solubilizer on soil-plant microbiome [13].

ACKNOWLEDGEMENTS

This work was funded by the European Union's Horizon 2020 Research and Innovation Program, project EXCALIBUR under grant agreement No. 817946 and by the EU project SUSTAINABLE, EU grant agreement no. 101007702. NV is thankful to EKROME SL-Italy for their help during the preparation of the manuscript.

REFERENCES

[1] Vassilev N, Vassileva M, Azcon R, Fenice M, Federici F, Barea JM (1998), Fertilizing effect of microbially treated olive mill wastewater on Trifolium plants, Biores, Technol., 66, 133-137, doi: 10.1016/S0960-8524(97)00141-7.

[2] Vassilev, N., Nikolaeva, I., Vassileva, M. Polymer-based Preparation of Soil Inoculants: Applications to Arbuscular Mycorrhizal Fungi. *Rev Environ Sci Biotechnol* 4, 235–243. doi.org/10.1007/s11157-005-2098-2, 2005.

[3] Bashan Y., de-Bashan L. E., Prabhu S. R., Hernandez J.-P. Advances in plant growth-promoting bacterial inoculant technology: formulations and practical perspectives (1998–2013). *Plant and Soil* 2014378:1–33. doi: 10.1007/s11104- 013- 1956- x, 2014.

[4] O'Callaghan, M. Microbial inoculation of seed for improved crop performance: issues and opportunities. Appl Microbiol Biotechnol 100, 5729– 5746. doi: 10.1007/s00253-016-7590-9, 2016.

[5] Bashan Y., de-Bashan L. E., Prabhu S. R. "Superior polymeric formulations and emerging innovative products of bacterial inoculants for sustainable agriculture and the environment," in *Agriculturally Important Microorganisms*. Eds. Singh H.B., Sarma B. K., Keswani C. (Singapur: Springer), 15–46, 2016.

[6] Malusà E., Berg G., Biere A., Bohr A., Canfora L., Jungblut A.D., Kepka W., Kienzle J., Kusstatscher P., Masquelier S., Pugliese M., Razinger J., Tommasini M.G., Meyling N.V., Xu X., Mocali S. A Holistic Approach for Enhancing the Efficacy of Soil Microbial Inoculants in Agriculture: From Lab to Field Scale. *Global J. Agricul. Innov. Res. Devel.* 8, 176-190, 2021.

[7] Mater, D.D.G., Barbotin, J.N., Saucedo, J.E.N., Truffaut, N., Thomas, D., 1995. Effect of gelation temperature and gel-dissolving solution on cell viability and recovery of two *Pseudomonas putida* strains co-immobilized within calcium alginate or κ-carrageenan gel beads. *Biotechnol. Tech*. 9, 747–752.

[8] Veiter L., Rajamanickam V., Herwig C. The filamentous fungal pellet—relationship between morphology and productivity. *Appl. Microbiol. Biotechnol*. 102 (2018) 2997–3006, https://doi.org/10.1007/s00253-018-8818-7.

[9] Kheirkhah, T., Neubauer, P., & Junne, S. (2023). Controlling Aspergillus niger morphology in a low shear-force environment in a rocking-motion bioreactor. *Biochemical Engineering Journal*, *195*, [108905]. https://doi.org/10.1016/j.bej.2023.108905

https://doi.org/10.5593/sgem2024/6.1/s25.24

[10] Kucey RMN (1987) Increased phosphorus uptake by wheat and field beans inoculated with a phosphorus-solubilizing *Penicillium bilaii* and with mycorrhizal fungi. Appl Environ Microbiol 55: 2699—2703.

[11] Malvern Panalytical. Changing the properties of particles to control their rheology. 2015. Saved from URL: https://www.azom.com/article.aspx?ArticleID=12304

[12] Jaiswal, A., Kumari, G., Upadhyay, V. K., Pradhan, J., Pramanik, H. S. K. (2023). A methodology to develop liquid formulation of biofertilizer technology. The Pharma Innovation Journal, 12, 875-881.

[13] Nasuelli, M., Novello, G., Gamalero, E., Massa, N., Gorrasi, S., Sudiro, C., Hochart, M., Altissimo, A., Vuolo, F., Bona, E. PGPB and/or AM Fungi Consortia Affect Tomato Native Rhizosphere Microbiota. *Microorganisms* 2023, 11, 1891. https://doi.org/10.3390/microorganisms11081891.

RESEARCH ABOUT THE BEST SWEETENERS USED TO DESIGN A FOOD SUPPLEMENT WITH HIGH ANTIOXIDANT POTENTIAL

PhD. Constantin Butoi[1]

PhD. Alexandra Ioana Ionescu[1]

[1]University of Life Sciences "Regele Mihai I", IRVA Doctoral School, Timișoara, **România**

ABSTRACT

Food supplements with strong antioxidant potential are increasingly being used by consumers to maintain good health [1], [5], [6], [8], [9], [10], [11], [15]. The best food supplements use natural and organic raw materials and "Mild Food Processing" operations. This work paper presents a management technique for food additives (used, in this case, in the testing and selection of used sweeteners) in the design of a black tea-based food supplement. The raw material used was tested by A.A.S. (Atomic Absorption Spectroscopy) to check for the absence of contamination with residues or heavy metals [2], [3], [12], [13], [14]. For the determination of the influence of sweeteners on the basic chemical composition, it was used UV-VIS optical spectrometry and some elements of mathematical statistics. The obtained results from this step of the research led to the establishment of the best sweetening option for food supplement based on black tea. The obtained and selected product can be used (as raw material) in the following technological steps, showed a chemical composition close to the unsweetened version but it also had much improved sensory properties. The best sweetening variant in this case was determined depending on the minimal change on the basic chemical composition of black tea and the preservation of the basic sensory characteristics. The development of innovative methods and technologies for the management of food additives facilitates the production of high-quality end products with high levels of food safety.

Keywords: black tea, sweeteners, innovative, food supplements

INTRODUCTION

Food supplements with high antioxidant potential are increasingly in demand in the consumer market. The use of raw materials that are free of natural or acquired toxicity leads to an increase in the healthiness of the supplement and an increase in demand from educated consumers.

All over the world, tea, both hot and cold, is a very popular beverage among consumers, always at the top of their preferences. Black tea is known for its sensory qualities, but also for being rich in antioxidants, stimulating because it contains active substances that act on the central nervous system, the circulatory system and has a diuretic effect [7].

Black tea is a "living food", with an extremely valuable chemical composition, in a continuous biodynamics, with the ability to change concentrations in nanoseconds. To enhance the sensory qualities of black tea, the main food additives used are natural and synthetic sweeteners [4], [7], [11].

https://doi.org/10.5593/sgem2024/6.1/s25.27

MATERIALS AND METHODS

The raw material used was tested by A.A.S. (Atomic Absorption Spectroscopy) to check for contamination by residues or heavy metals. UV-VIS optical spectrometry and mathematical statistics were used to determine the influence of sweeteners on the base chemical composition [2], [3].

Atomic Absorption Spectroscopy (AAS)

The first stage of sample preparation for atomic absorption spectrometry is mineralisation (microwave digestion). Microwave digestion is used to prepare samples of all types (plants, soil, food, pharmaceuticals) for elemental analysis by ICP, ICP-MS or AA, which requires the sample to be in solution before it is introduced into the analyser. Acid digestion is used to break down the sample matrix, leaving the elements of interest in solution and ready for analysis. CEM microwave digestion systems rapidly break down a wide variety of sample matrices, leaving behind a clear solution containing the analytes of interest [4], [7].

It was used a 1200W MARS mineralised microwave CEM system. CEM's MARS system is a multimodal platform equipped with a magnetic stirring plate and a rotor that allows multiple vessels per batch to be processed in parallel. We used HP-500 (Teflon insert (TFA)) (vessel volume 80 ml, maximum pressure 350 psi, maximum temperature 210ºC) and chem (glass insert (borosilicate)) (vessel volume 80 ml, maximum pressure 200 psi, maximum temperature 200ºC) vessel types, both based on a fourteen-position rotor. The system delivers continuous power between 0 and 1200 W. The temperature is controlled internally by a fibre optic probe in a control reference vessel.

Method: Briefly, 10 g of dry substance tea was weighed with analytical precision. For the mineralisation step, 10.00 g of product (black tea), 6 mL of concentrated nitric acid and 3 mL of 30% hydrogen peroxide were added to each digestion cartridge. A digestion cartridge containing no product, only reagents, was used as a control. The method is summarised in Table 1.

A Varian SpectrAA 220Z atomic absorption spectrometer furnace system with Varian SpectrAA 220Z autosampler, Varian GTA 110Z furnace, Varian UltrAA and related Windows interface software was used for the AAS method.

UV-VIS optical spectrometry

A range of natural and synthetic sweeteners were used in the laboratory analyses to study the effects of these sweeteners on the chemical composition of black tea.

In order to obtain the control version of the unsweetened black tea, approximately 10 grams of the black tea plant per 1000 ml of water were placed in a bowl. The tea was then heated, cooled and filtered to produce the experimental variant V0. From this experimental variant, the ten sweetened tea variants were made. This resulted in the following variants:

V0- unsweetened black tea variety

V1- black tea version sweetened with white sugar

V2- black tea version sweetened with brown sugar

V3- black tea variant sweetened with honey

V4- black tea version sweetened with saccharin

V5- black tea version sweetened with sucrose

V6- black tea version sweetened with Diamond (sodium cyclamate and sodium saccharin)

V7- black tea variant sweetened with fructose

V8- black tea variant sweetened with xylitol

V9- black tea version sweetened with sorbitol

V10- black tea version sweetened with stevia

To facilitate the passage of the incident light beam through the tea solution, a dilution of 1:50 (2%) was used. This dilution was obtained by sieving after filtering the black tea and passing it through the cuvettes of the spectrophotometer.

Molecular absorption spectra of the proposed experimental variants were obtained using a T92 Plus UV-VIS spectrophotometer manufactured by PG Instruments U.K.

The spectrophotometer was set up to work at a wavelength bandwidth of 1cm and record molecular absorption values from nanometre to nanometre in both the UV range (190-400 nm) and the visible range (400-700 nm).

Special parallelepipedal UV quartz cuvettes with a square side of 1 cm section were used to measure absorption.

TABLES, GRAPHS & FIGURES

Table 1. Stages of microwave digestion

Power, W	Time, min	Stirring	Comments
300	4	yes	For cartridge protection
0	1.5	no	To help the sedimentation process in the down side of vessels
400	2.5	yes	
600	2.5	yes	
200	1	no	
800	2.5	yes	
1000	4	yes	
0	10	no	Cooling for opening cartridges

https://doi.org/10.5593/sgem2024/6.1/s25.27

Table 2. Atomic Absorption Spectroscopy baseline for black tea

Indicator/ Constituent	BLACK TEA	
	Dry matter ppm (mg/kg)*	Watery extract 1:10 ppm (mg/L) Average value
Na^{+}	1012±3.56	153.04
K^{+}	16720.2±3.26	285.21
Ca^{2+}	742±2.46	7.98
Mg^{2+}	462±1.64	7.93
Zn^{2+}	48±2.48	1.79
Mn^{2+}	84.5±1.89	0.23
Fe^{2+}	74.24±1.84	0.68
Al^{3+}	10.42±0.67	0.49
Cu^{2+}	10.46±0.66	0.35
Pb^{2+}	0.036±0.001	missing

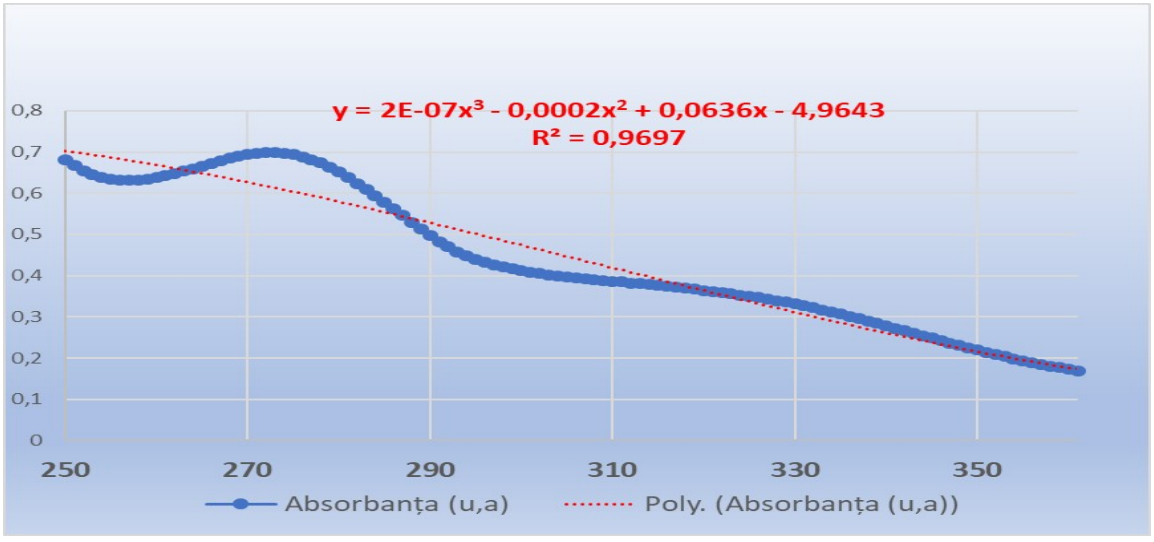


Fig. 1. Absorbance variation (a.u.) as a function of wavelength for V2 in the UV range

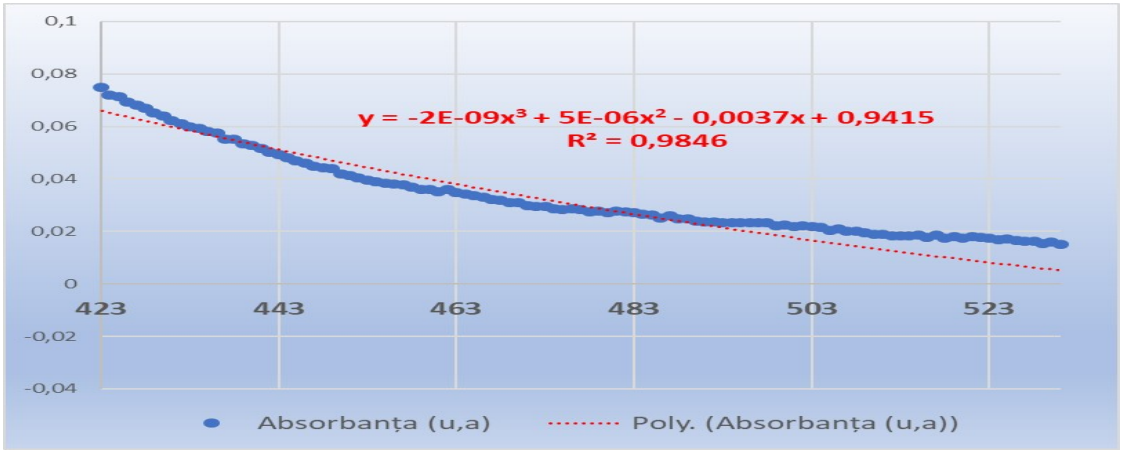


Fig. 2. Absorbance variation (a. u.) as a function of wavelength for V2 in the visible range

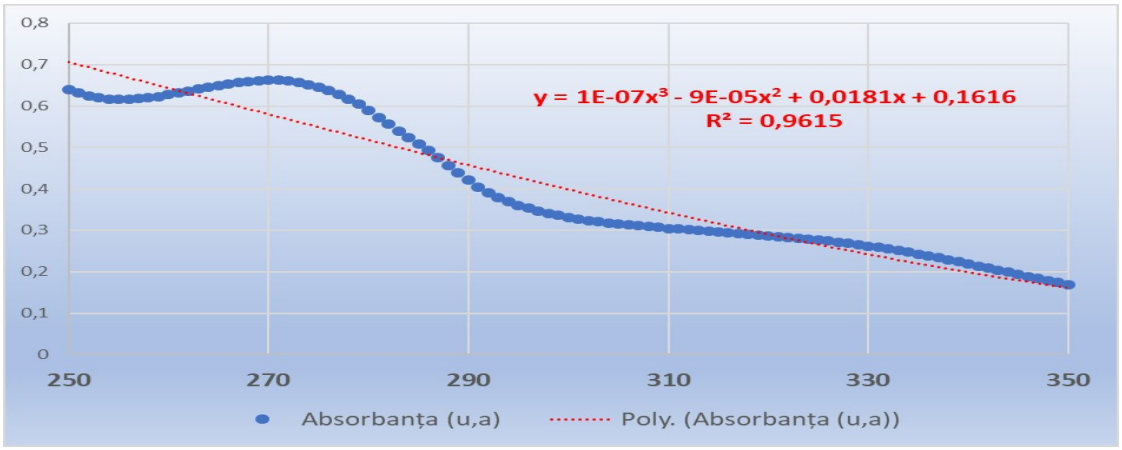


Fig. 3. Absorbance variation (a. u.) as a function of wavelength for V7 in the UV range

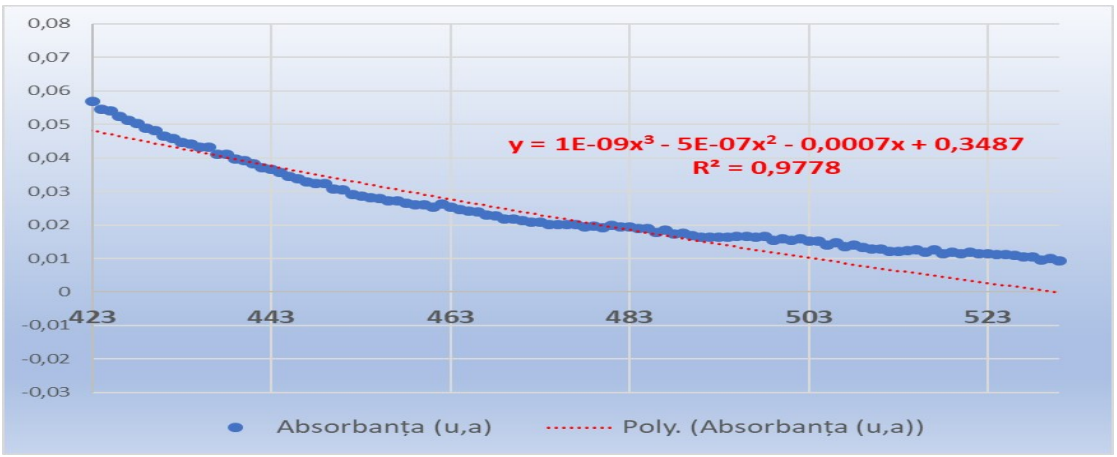


Fig. 4. Absorbance variation (a. u.) as a function of wavelength for V7 in the visible range

https://doi.org/10.5593/sgem2024/6.1/s25.27

RESULTS

The results obtained in this phase of the research led to the identification of the best sweetening option for the black tea-based dietary supplement. The product thus obtained and selected for use (as raw material) in the subsequent technological steps had a chemical composition similar to the unsweetened version, but also much improved sensory properties.

The use of the AAS technique revealed high concentrations of potassium, magnesium and calcium in the parts of the tea plant used (Table 2).

DISCUSSION

For the V0 variant we have a peak of NAD (Nicotinamide adenine dinucleotide) a decrease in tocopherol content and a high theobromine content. The white sugar introduced in V1 induces small changes in the content of pigments and a slight decrease in the content of certain alkaloids, in particular theobromine. The tendency to modify the flavoproteins is also observed when using brown sugar in V2, but more on the oxidised forms and in this case the influence on the pigments is much lighter. So brown sugar even though it alters the colour intensity and colour tone protects the reduced forms of flavoprotein, it is a better variant than white sugar sweetening. Saccharin has quite a strong effect on the concentration of the main active compounds in black tea. When sucrose is used, the isoalloxazines active nucleus in saccharin is slightly acidified (citric and fumaric acid) and buffered with bicarbonate. This treatment of the active core causes sucrose to induce fewer changes in the concentrations of the main active compounds in black tea. Acidification and then buffering of the active core from saccharin creates a levelling of the oxidative attack and at the same time a higher activity. By buffering the active core of saccharin, sucrose is more readily used by consumers inducing the sweet taste under low oxidation conditions. The use of a mixture of sodium cyclamate and saccharin ensures a certain conservatism in the concentrations of the hydrogenated forms of specific oxidoreductase coenzymes, while maintaining a strong antioxidant character. The use of V7 fructose (variant 7 in which fructose is used) has a lesser effect on colour intensity in the UV and visible range. This also preserves the colour tone. Very similar effects on the concentration of the main compounds in black tea are seen in the xylitol- and sorbitol-sweetened versions (V8 and V9).

CONCLUSION

The best sweetening option in this case was determined by minimising the change in the basic chemical composition of black tea and preserving the basic sensory characteristics. The development of innovative methods and technologies for the management of food additives facilitates the production of high quality and food safe end products.

For healthy consumers the best sweetening variant is the one using white sugar V1 and for consumers with health problems the best variant is V8 sweetened with xylitol.

By analysing the results and interpreting the values obtained, it is easy to draw a number of important conclusions:

Brown sugar, although it alters the colour intensity and shade, protects the reduced forms of phloavoprotein, making it a better variant than white sugar;

Honey, used as a sweetener in black tea, induces a higher oxidation state and causes a change in the clarity of the tea;

Saccharin has a strong effect on the concentration of the main active compounds found in black tea;

Sucrose becomes more readily usable by consumers by buffering the active core of saccharin, inducing the sweet taste under conditions of lowest oxidability;

The use of a mixture of sodium cyclamate and saccharin ensures a certain preservation of the concentration of hydrogenated forms of specific oxidoreductase coenzymes, while maintaining a strong antioxidant character;

The V8 xylitol and V9 sorbitol sweeteners have very similar effects on the concentration of the main constituents of black tea.

REFERENCES

[1] Belitz, H.-D.; Grosch, W.; Schieberle P. Food Chemistry, Springer-Verlag Berlin Heidelberg, Germania, Ed.4, 2009. 95-102.

[2] BV L'vov, BV Cincizeci de ani de spectrometrie de absorbție atomică ; J. Anal. Chem., 60:2005. 382–392.

[3] L'vov, B. Recent advances in absolute analysis by graphite furnace atomic absorbtion spectrometrie". Spectrochimica Acta Part B: Atomic Spectroscopy . 45 (7): 1990. 633–655. [4] Savescu P. (2017). A New Approach to Study the Sweetener's Effect on Green Tea Oxidative Status, Revista de Chimie, 68 (2), 294-299.

[5] Savescu P., Poenaru, M.M, Iacobescu F. (2016). Study regarding the Development of Organic Farming Systems in Romania as the Basis for obtaining of innocuity Agricultural Raw Materials – used in Functional Food, Annals Of The University Of Craiova, Series Agriculture, Montanology, Cadastre, No.1, 46, 281-285.

[6] Savescu, P. (2016). Improving the concentrations of bioactive compounds (with antioxidant properties) in alfaalfa and corn for their use in food supplements and functional food. Nano, Bio and Green-Technologies for a Sustainable Future, SGEM International Conference, Albena, BG, No.6, (1), 583-590.

[7] Savescu, P. (2017), Comparative Study on the Effect of Sweeteners on the Oxidative Status of Green Tea and Black Tea, Revista de Chimie, 68 (6), 1406-1412.

[8] Savescu, P. (2021). Chapter Natural Compounds with Antioxidant Activity-Used in the Design of Functional Foods. In Book Title -Functional Foods - Phytochemicals and Health Promoting Potential, IntechOpen Eds., London,U.K., DOI: http://dx.doi.org/10.5772/intechopen.97364, 1-25.

[9] Savescu, P. et all. (2006). Environmental risk's decreasing according to the European Standard (QMS ISO 9000:2000) applied to food factories, JEPE , 2006, Vol 6 (2), 447-453.

https://doi.org/10.5593/sgem2024/6.1/s25.27

[10] Savescu, P., Iacobescu, F., Poenaru, M.M. (2020). Study on the Use of Biomaterials as Protective Membranes for Certain Functional Foods. In Book Advances in Bionanomaterials II, Book Series: Lecture Notes in Bioengineering. Publisher: Springer International Publishing, Print ISBN: 978-3-030-47704-2, Springer Nature Switzerland AG 2020, S. Piotto et al. (Eds.),BIONAM 2019,LNBE, https://doi.org/10.1007/978-3-030-47705-9_16, 1-13.

[11] Savescu, P., (2017). A New Approach To Study The Sweetener`S Effect On Hibiscus Tea Oxidative Status, International Conference SGEM 2017, Section 25 - Advances in Biotechnology, Albena, Bulgaria, DOI: 10.5593/sgem2017/61/S25.059, ISSN 1314-2704, Vol 17, Nr. 1, Rev. 61, 455-460.

[12] Savescu, P., Badescu, G., Milut, M., Ciobanu, A., Apostol, L., Vladut, V. (2019).Healthy Food – Through Innovative Technologies. Vol. ISB-INMA-TEH Bucharest. 516-521.

[13] Savescu, P., Iacobescu, F., Poenaru, M.M. (2020). Patent Application -OSIM A00745, ” Innovative food supplement based on plant products obtained from organic farming”, OSIM, Romania.

[14] Skoog, DA; Holler FJ; Crouch SR Principles of Instrumental Analysis, Thomson Brooks/Cole, SUA, Ed. a 6-a, 2007, 349-351, 2007

[15] Tita, O., E Lengyel., E., Stegarus, D., Savescu, P., Ciubara, A.B., (2021). Identification and Quantification of Valuable Compounds in Red Grape Seeds, Appl. Sci. 11(11), 5124; https://doi.org/10.3390/app11115124, 5124-5139.

STUDY OF PROPERTIES OF GLUCOSE OXIDASE IMMOBILIZED ON MODIFIED WITH CHITOSAN AND SODIUM TRIPOLYPHOSPHATE MAGNETITE

Prof. Dr. Valentina G. Matveeva[1]

Assoc. Prof. Ph.D. Boris B. Tikhonov[1]

Mr. Daniil R. Lisichkin[1]

Prof. Dr. Ajay Sh. Desai[2]

Prof. Dr. J.C.S. dos Santos[3]

[1] Tver State Technical University, **Russia**
[2] Dr. Balasaheb Sawant Konkan Krishi Vidyapeeth, **India**
[3] University of International Integration of Afro-Brazilian Lusophony (UNILAB), **Brazil**

ABSTRACT

A new biocatalyst based on glucose oxidase immobilized on Fe_3O_4 magnetite nanoparticles modified with chitosan and sodium tripolyphosphate was synthesized. Magnetite nanoparticles were obtained by mixing solutions of $FeCl_2$ and $FeCl_3$ with ammonia while heating to a temperature of 65 ºC. To stabilize the nanoparticles and ensure the presence of amino groups on their surface, chitosan and sodium tripolyphosphate were sequentially deposited on magnetite. Immobilization of glucose oxidase on the support was carried out after preliminary activation of the carboxyl groups of the enzyme by 1-ethyl-3-(3-dimethylaminopropyl) carbodiimide hydrochloride and N-hydroxysuccinimide. The activity and stability of the biocatalyst were investigated in the oxidation reaction of D-glucose to D-glucono-δ-lactone. The immobilized biocatalyst was shown to retain more than 60% of the activity compared to the native form of the enzyme. The synthesized biocatalyst can be easily separated from the reaction mixture by a permanent magnet and reused without significant loss of activity. The optimal composition of the biocatalyst providing the maximum activity and operational stability was determined. It has been shown that the immobilization of glucose oxidase on modified magnetite leads to an expansion of the operating range of pH and temperatures by 15-20%, compared with the native enzyme. The successful modification of the magnetite with a fine layer of chitosan as well as the presence of target functional groups on the support surface were confirmed by the Fourier-transform infrared spectroscopy and low-temperature nitrogen adsorption.

Keywords: magnetite, chitosan, glucose oxidase, immobilization

INTRODUCTION

Glucose oxidase (GOx, EC 1.1.3.4) is an enzyme of the oxidoreductase class that catalyzes the oxidation of β-D-glucose to D-glucono-δ-lactone (δ-glucono-1,5-lactone) and H_2O_2 using molecular oxygen as an electron acceptor [1]. It is a dimeric flavoprotein consisting of two identical polypeptide chains connected by disulfide bridges. Glucose oxidase contains two Flavin adenine dinucleotide (FAD) molecules as

https://doi.org/10.5593/sgem2024/6.1/s25.29

a coenzyme [2]. This enzyme can be obtained from various fungi, most often *Aspergillus* and *Penicillium*. The molecular weight of GOx varies between 130-175 kDa depending on sources. The optimal pH range for the enzyme is from 4 to 7, and the optimal temperature range is 35-40 °C. GOx has been used in recent decades in a wide range of applications, primarily in chemical processes and analytical chemistry [3]. In this case, it is most advisable to use enzyme preparations immobilized on solid supports. This makes it possible to consolidate the conformation of the enzyme, significantly increase its resistance to inhibitory effects, including expanding the operating of pH and temperature ranges, and also makes it possible to use the enzyme repeatedly with no loss of activity [4].

In the scientific literature, there is evidence of successful immobilization of glucose oxidase on such supports as biopolymers modified by various functional groups, glass, inorganic oxides, and nanoparticles [2, 3, 5-8]. Currently, among the most promising supports for the immobilization of enzymes, the materials with magnetic properties are distinguished. Such supports can be easily separated from the reaction medium using a permanent magnet [9]. To stabilize magnetic particles and ensure the presence of target functional groups on their surface, they are chemically modified with multifunctional reagents [10].

In this study, a biocatalyst based on GOx and magnetic F_3O_4 nanoparticles modified with chitosan and sodium tripolyphosphate was synthesized.

MATERIALS AND METHODS

Solutions of $FeCl_3$ and $FeCl_2$ were mixed in a thermostatically controlled glass reactor to synthesize nanoparticles. The mixture was stirred at a rate of 300 min^{-1} for 15 minutes, after which it was heated to 65 °C. After reaching the synthesis temperature, the mixture was stirred for another 15 minutes, and a concentrated ammonia solution was added dropwise at a rate of 2 mL per minute. The reaction was allowed to continue for 15 minutes. Next, a chitosan solution in acetic acid was added and the mixture was stirred again for 15 minutes. To attach chitosan to the surface of the magnetic particles, the suspension was kept in a sodium tripolyphosphate solution for 1 hour. Then the particles were washed several times with distilled water and extracted using a permanent magnet. To immobilize GOx on the synthesized magnetic particles, the support was soaked in a mixture containing carbodiimide, N-hydroxysuccinimide, and glucose oxidase for 12 hours. The synthesized biocatalyst was thoroughly rinsed with distilled water several times, extracted using a strong magnet, and dried in the air.

Magnetization measurements of the samples were carried out in a developed vibrating sample magnetometer (VSM) with an accuracy better than ±0.01 emu/g. The apparatus allows measuring bulk and powder samples of 0.01-150 mg in temperature range -193÷726 °C and magnetic field 0-2.5 T. An optical microscope Biomed-2 (Russia) was used to obtain microphotographs of the samples.

The activity and stability of the synthesized biocatalyst were studied in the oxidation reaction of D-glucose to D-gluconolactone in a thermostatically controlled glass reactor with constant stirring (300 min^{-1}). A periodic sampling from the reaction mixture was carried out to analyze the H_2O_2. An indicator of GOx activity is the amount of hydrogen peroxide (equimolarly reacted D-glucose) formed in the reaction mixture. The content

of hydrogen peroxide was determined iodometrically by photometry of the resulting blue iodine-starch complex [11].

RESULTS AND DISCUSSION

The magnetite nanoparticles synthesized according to the method described above were found to have good magnetic properties and can be easily and completely separated from the reaction medium using a magnet. At the same time, the magnetization of particles decreased slightly after the application of chitosan, sodium tripolyphosphate, and glucose oxidase to magnetite (Figure 1).

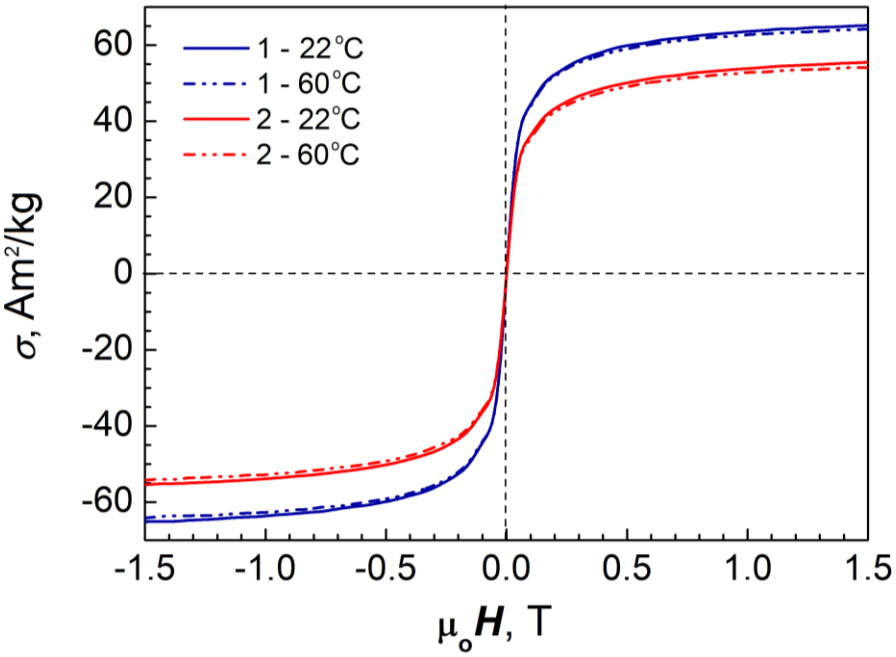


Figure 1 – Magnetization of samples: 1 – magnetite; 2 – biocatalyst

Optical microscopy of the samples showed that most of the particles have a spherical shape with the formation of small agglomerates, easily separated by mechanical action (Figure 2). The mean particle diameter was measured to be 220 ± 10 nm.

Figure 3 shows the dependence of the activity of the synthesized biocatalyst on the chitosan content in the enzymatic system. The activity was estimated as a dependence of the hydrogen peroxide content in the reaction mixture on time.

The results show that an increase in the chitosan content of more than 0.1 g per 1 g of the biocatalyst is impractical since the amount of hydrogen peroxide formed in the oxidation reaction of D-glucose significantly reduces.

https://doi.org/10.5593/sgem2024/6.1/s25.29

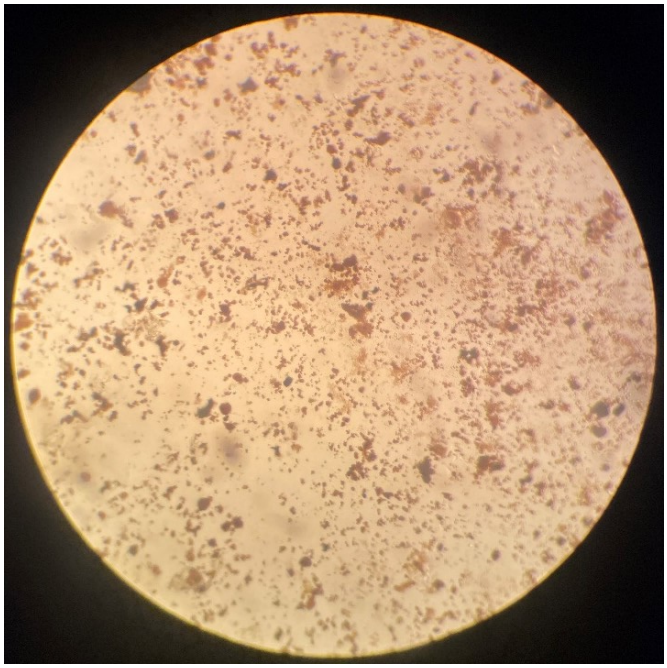


Figure 2 – Micrograph of synthesized magnetite nanoparticles obtained using an optical microscope (magnification 1000x)

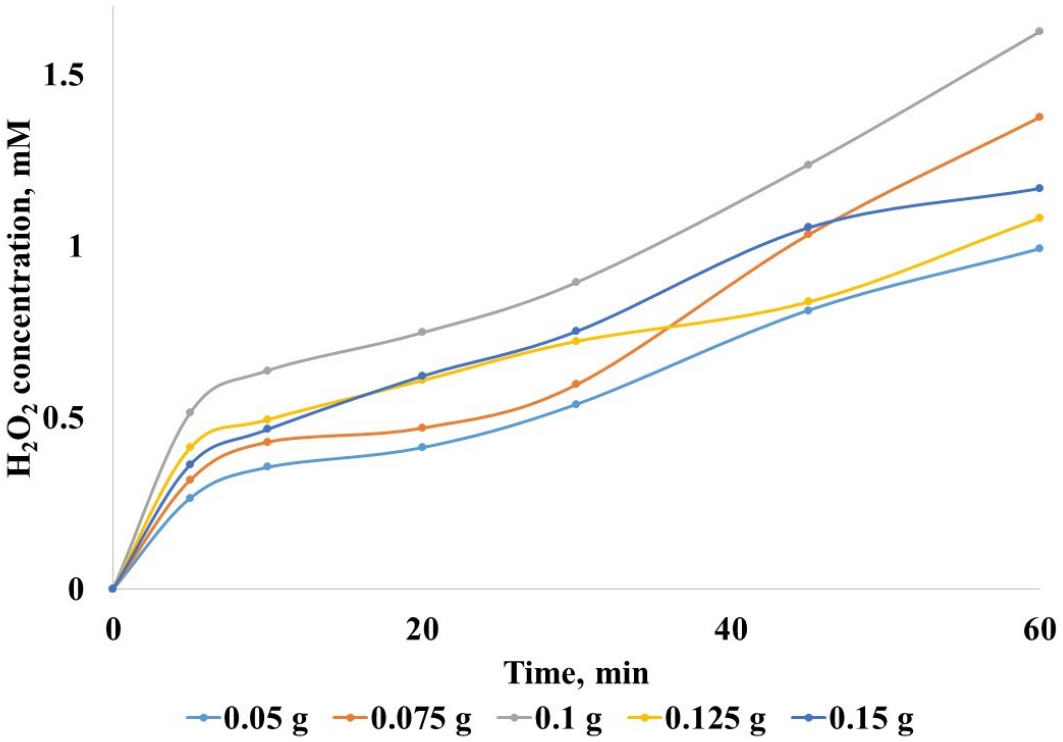


Figure 3 – Dependence of the activity of immobilized GOx on the chitosan content in the enzymatic system

The effect of the content of carbodiimide, N-hydroxysuccinimide, sodium tripolyphosphate, and glucose oxidase on the effectiveness of immobilization was also studied (Figures 4-6).

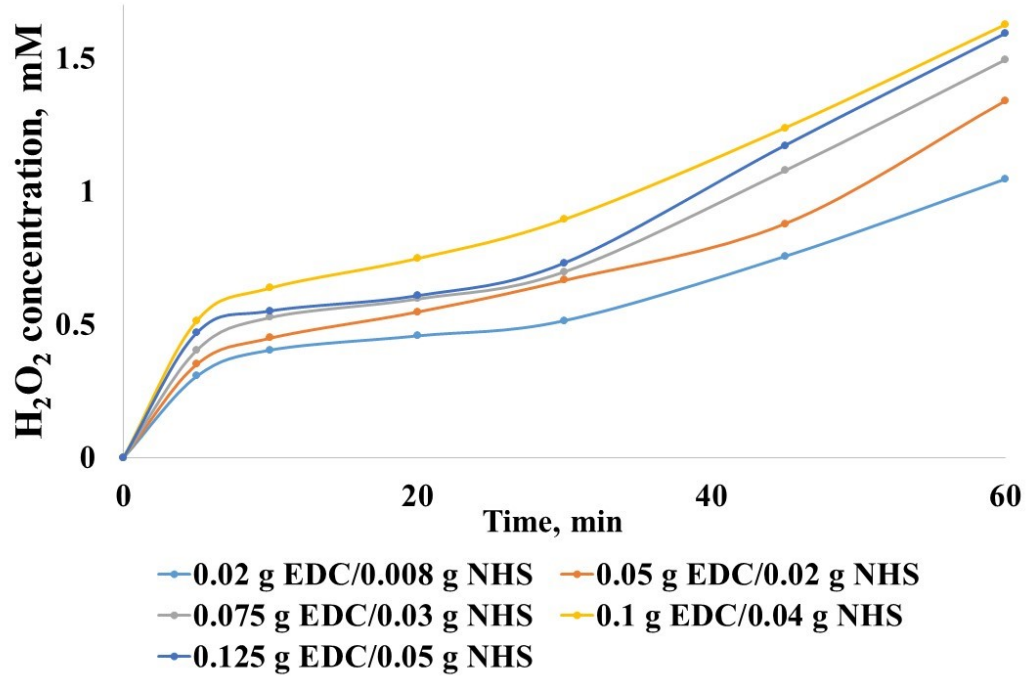


Figure 4 – Dependence of the activity of immobilized GOx on the content of carbodiimide and N-hydroxysuccinimide in the enzymatic system

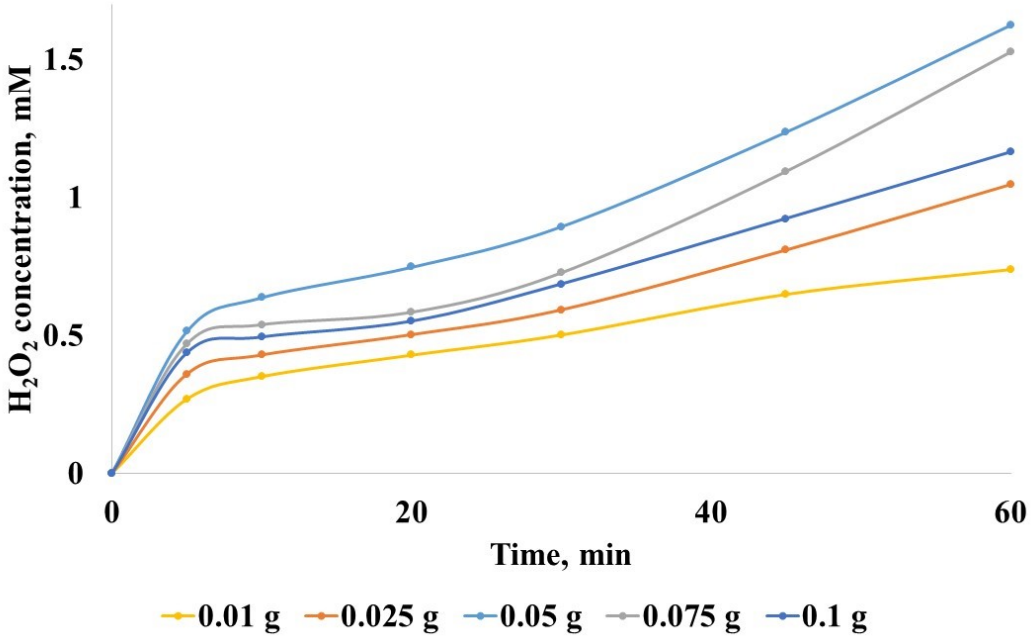


Figure 5 – Dependence of the activity of immobilized GOx on the content of sodium tripolyphosphate in the enzymatic system

https://doi.org/10.5593/sgem2024/6.1/s25.29

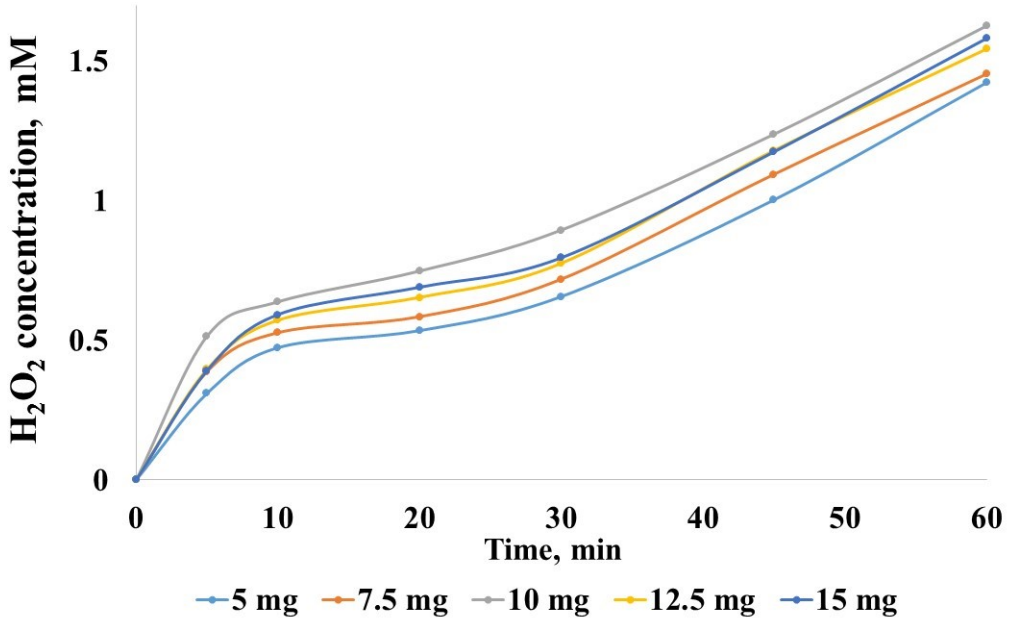


Figure 6 – Dependence of the activity of immobilized GOx on the GOx content in the enzymatic system

Based on the results obtained, it was revealed that the higher immobilization efficiency was achieved using 0.1 g of chitosan, 0.05 g of sodium tripolyphosphate, 0.125 g of carbodiimide, 0.05 g of N-hydroxysuccinimide and 0.05 g of glucose oxidase per 1 g of magnetic nanoparticles.

Experiments were carried out to vary the initial concentration of D-glucose. Experiments have shown that GOx immobilized on magnetic particles has a slightly lower activity compared to its native form. This is primarily due to diffusion limitations and difficulty in accessing the substrate to the active sites of the enzyme during the heterogenization of the process. However, immobilization makes it easy to separate the enzyme from the reaction medium and use it repeatedly. Based on the results of kinetic experiments, the kinetic parameters of the biocatalyst were calculated: activity A, the limiting reaction rate, and the Michaelis constant K_M are shown in Table 1.

Table 1 – Kinetic parameters of native and immobilized glucose oxidase

Parameter	Native GOx	Immobilized GOx
V_m, μmol/L·s	6,32	2,92 (46,2 %)
Activity, AU/mg	0,038	0,017 (44,7 %)
K_M, mmol/L	7,688	3,083 (40,1 %)

Table 2 shows the activity values of the synthesized biocatalyst during repeated use. As can be seen, the biocatalyst loses about 20% of its activity over 10 consecutive cycles.

Table 2 – Relative activity of the synthesized biocatalyst during repeated use

	Number of cycles									
	1	2	3	4	5	6	7	8	9	10
Relative activity, %	100	98,0	94,8	93,5	91,1	88,0	87,4	84,6	81,7	79,6

Thus, the possibility of successful immobilization of glucose oxidase on biopolymer-modified magnetite was confirmed. The decrease in the activity of the immobilized enzyme in comparison with its native form is compensated by the possibility of its repeated use. In this case, the enzyme is stabilized on the surface of the solid support in an effective conformation, which practically does not change in repeated cycles of use.

CONCLUSION

The effectiveness of GOx immobilization on magnetic nanoparticles modified with chitosan and sodium tripolyphosphate has been proven. Mesoporous magnetite particles with an average diameter of 220±10 nm with good magnetic properties were obtained. The magnetization of the particles decreased slightly after applying chitosan, sodium tripolyphosphate, and GOx to the magnetite. The activity and stability of the synthesized biocatalyst were studied in the oxidation reaction of D-glucose to D-gluconolactone in a thermostatically controlled glass reactor. The composition of the biocatalyst leading to the highest intensity of formation of the reaction product, hydrogen peroxide, in the reaction mixture has been optimized. Kinetic experiments have shown that the immobilization of GOx led to the stabilization of the enzyme, preservation of most of its activity, and increased resistance to inhibitory effects. The synthesized biocatalyst can be used for industrial production of D-gluconic acid and analytical determination of the concentration of D-glucose in various liquids.

ACKNOWLEDGEMENTS

This work was supported by the Ministry of Science and Higher Education, project 075-15-2022-1232.

REFERENCES

[1] Wilson R., Turner A.P.F., Glucose oxidase: an ideal enzyme, Biosensors and Bioelectronics, vol. 7, pp. 165-185, 1992

[2] Bankar S.B., Bule M.V., Singhal R.S., Ananthanarayan L., Glucose oxidase - An overview, Biotechnology Advances, vol. 27, pp. 489–501, 2009.

[3] Tikhonov B.B., Sulman E.M., Stadol'nikova P.Y., Sulman A.M., Golikova E.P., Sidorov A.I., Matveeva V.G., Immobilized enzymes from the class of oxidoreductases in technological processes: A review, Catalisys in Industry, vol.11 (3), pp. 251–263, 2019.

[4] Datta S., Christena L.R., Rajaram Y.R., Enzyme immobilization: an overview on techniques and support materials, 3 Biotechnology, vol. 3(1), pp. 1-9, 2013.

[5] Dong L. C., Wang G., Xiao Y., Xu Y., Zhou X., Jiang H., Luo Q., Immobilization of Glucose Oxidase on a Novel Crosslinked Chitosan Support Grafted with L-Lysine

https://doi.org/10.5593/sgem2024/6.1/s25.29

Spacers, Chemical and Biochemical Engineering Quarterly, vol. 25 (3), pp. 395–402, 2011.

[6] Wang X., Zhu K.-X., Zhou H.-M., Immobilization of Glucose Oxidase in Alginate-Chitosan Microcapsules, International Journal of Molecular Sciences, vol. 12, pp. 3042-3054, 2011.

[7] Hashemifard N., Mohsenifar A., Ranjbar B., Allameh A., Lotfi A.S., Etemadikia B., Fabrication and kinetic studies of a novel silver nanoparticles–glucose oxidase bioconjugate, Analytica Chimica Acta, vol. 675, pp. 181–184, 2010.

[8] Wang H., Huang J., Wang C., Li D., Ding L., Han Y. Immobilization of glucose oxidase using $CoFe_2O_4/SiO_2$ nanoparticles as carrier // Applied Surface Science, vol. 257, pp. 5739–5745, 2011.

[9] Ghadi A., Tabandeh F., Mahjoub S., Mohsenifar A., Roshan F. T., Alavije R., Fabrication and characterization of core-shell magnetic chitosan nanoparticles as a novel carrier for immoblization of *Burkholderia cepacia* lipase, Journal of Oleo Science, vol. 64(4), pp. 423-430, 2015.

[10] Ein Aliafjeh M., Pourahmad R., Akbari-Adergani B., Azin M., Characteristics of glucose oxidase immobilized on Magnetic Chitosan Nanoparticles, Food Science and Technology, Campinas, vol. 40(1), pp. 68-75, 2019.

[11] Graf E., Penniston J. T., Determination of Hydrogen Peroxide, with its Application Illustrated by Glucose Assay, Clinical Chemistry, vol. 26 (5), pp. 658-660, 1980.

STUDY REGARDING THE BEST SWEETENERS USED IN GREEN-TEA BASED SUPPLEMENTS

PhD. Ress. Alexandra-Ioana Ionescu[1]

PhD. Ress. Constantin Butoi[2]

[1]University of Life Sciences "Regele Mihai I", Calea Aradului 119, Timișoara, IRVA Doctoral School, 119 Calea Aradului, Timișoara, **România**

ABSTRACT

Green tea-based food supplements are very attractive to a large group of consumers and make an important contribution to maintaining good health.

In order to preserve the nutritional value of supplements of this type, pesticide and plant growth hormones-free green tea is used as raw material.

Choosing the best sweeteners in this case is an important part of scientific research, especially for consumers with certain digestive conditions.

The aim of this paper is to successfully identify the best way to sweeten green tea by testing and selecting the best sweetener. In this mode results an intermediate product with superior physical-chemical and sensory properties. This product will be used as a raw material in the next technological steps, providing a good basis for an innovative food supplement.

The used raw material (green tea) was tested by A.A.S. (Atomic Absorption Spectroscopy) to check for contamination by residues or heavy metals [2], [3], [5]. In order to determine the influence of sweeteners on the basic chemical composition, UV-VIS optical spectrometry and mathematical statistics were used.

The results of this phase of research led to the identification of the best sweetening option for green tea-based food supplements. The product obtained and selected for use (as raw material) in the following technological steps had a chemical composition similar to that of the unsweetened version, but also much improved sensory properties.

The best sweetening option in this case was determined by minimizing the change in the basic chemical composition of the green tea and preserving the basic sensory characteristics.

Keywords: green tea, sweeteners, innovative, food supplements

INTRODUCTION

Tea is made by processing the leaves of the *Camellia sinensis* tea plant. Tea contains active substances that act on the central nervous system, the circulatory system and is a good diuretic. It is rich in mineral salts and vitamins, especially vitamin C, and helps to strengthen the immune system [4], [7].

https://doi.org/10.5593/sgem2024/6.1/s25.30

Tea leaves contain tannins, amino acids, carbohydrates and essential oils that give the tea its colour and flavour. Green tea is recognized for its high antioxidant potential, being very rich in polyphenolic compounds, vitamins, and pro-vitamins [1], [5].

Tea is usually consumed with sweeteners, both natural and synthetic. These are added to improve sensory qualities. Sweeteners are food additives that make the food they are added to taste sweet. Like sugar, they stimulate sweet taste receptors, but some contain far fewer calories than sugar.

Producing an energy drink (food supplement) based on green tea is not easy, but introducing innovative extraction methods, additive management, product design, and packaging design can help a lot.

The use of such methods and technologies results in an extremely valuable end product, which is important for the healthiness and hedonic quality transmitted to the final consumer [6], [8], [9], [10], [11], [12], [13].

MATERIALS AND METHODS

The used raw material (green tea) was tested by A.A.S. (Atomic Absorption Spectroscopy) to check for contamination by residues or heavy metals. In order to determine the influence of sweeteners on the basic chemical composition, UV-VIS optical spectrometry and mathematical statistics were used [14], [15].

Subsection 2.1: Atomic Absorption Spectroscopy (AAS)

The first stage of sample preparation for atomic absorption spectrometry is mineralization (microwave digestion). Microwave digestion is used to prepare samples of all types (plants, soil, food, pharmaceuticals) for elemental analysis by ICP, ICP-MS or AA, which requires the sample to be in solution before it is introduced into the analyzer. Acid digestion is used to break down the sample matrix, leaving the elements of interest in solution and ready for analysis. CEM microwave digestion systems rapidly break down a wide variety of sample matrices, leaving behind a clear solution containing the analytes of interest. It was used a 1200W MARS mineralized microwave CEM system. CEM's MARS system is a multimodal platform equipped with a magnetic stirring plate and a rotor that allows multiple vessels per batch to be processed in parallel. We used HP-500 (Teflon insert (TFA)) (vessel volume 80 ml, maximum pressure 350 psi, maximum temperature 210^{o}C) and Greenchem (glass insert (borosilicate)) (vessel volume 80 ml, maximum pressure 200 psi, maximum temperature 200^{o}C) vessel types, both based on a fourteen-position rotor. The system delivers continuous power between 0 and 1200 W. The temperature is controlled internally by a fiber optic probe in a control reference vessel.

Method: Briefly, 10 g of dry substance tea was weighed with analytical precision. For the mineralization step, 10.00 g of product (green tea), 6 mL of concentrated nitric acid and 3 mL of 30% hydrogen peroxide were added to each digestion cartridge. A digestion cartridge containing no product, only reagents, was used as a control. The method is summarized in Table 1.

Subsection 2.2 UV-VIS optical spectrometry

A range of natural and synthetic sweeteners were used in the laboratory analyses to study the effects of these sweeteners on the chemical composition of green tea.

To obtain the control version of unsweetened green tea, approximately 10 grams of green tea plant per 1000 ml of water was placed in a bowl. The tea was heated, cooled and filtered to produce the experimental V0. This experimental variant was used to create the ten sweetened tea variants. This resulted in the following variants: V0- unsweetened green tea variety, V1- green tea version sweetened with white sugar, V2- green tea variant sweetened with brown sugar, V3- green tea variant sweetened with honey ,V4- green tea version sweetened with saccharin, V5- green tea version sweetened with sucrose, V6- green tea variant sweetened with Diamond, V7- green tea variant sweetened with fructose, V8- green tea variant sweetened with xylitol, V9- green tea variant sweetened with sorbitol, V10- green tea variant sweetened with stevia

Molecular absorption spectra of the proposed experimental variants were obtained using a T92 Plus UV-VIS spectrophotometer manufactured by PG Instruments U.K.

The spectrophotometer was set up to operate at a wavelength bandwidth of 1cm and to record molecular absorption values from nanometer to nanometer in both the UV (190-400nm) and visible (400-700nm) ranges. The equipment automatically records spectral curves, changing the deuterium and tungsten lamps at 361 nm by automatic programming. To double-check the values obtained, at each measurement the T92 Plus spectrophotometer was set to develop an automatic retracking. Special parallelepipedal UV quartz cuvettes with a square side in section of 1cm were used to measure absorption.

TABLES, GRAPHS & FIGURES

Table 1. Stages of microwave digestion

Power, W	Time, min	Stirring	Comments
300	4	yes	For cartridge protection
0	1.5	no	To help the sedimentation process in the base of vessels
400	2.5	yes	
600	2.5	yes	
200	1	no	
800	2.5	yes	
1000	4	yes	
0	10	no	Cooling for opening cartridges

https://doi.org/10.5593/sgem2024/6.1/s25.30

Table 2. Atomic Absorption Spectroscopy baseline for green tea

Indicator/ Constituent	GREEN TEA	
	Dry matter ppm (mg/kg)*	Watery extract 1:10 ppm (mg/L) Average value
Na +	872±1.74	77.86
K +	1484±1.86	72.43
Ca 2+	376±0.96	2.04
Mg 2+	212±0.88	2.10
Zn 2+	24.6±0.02	0.62
Mn 2+	288±0.94	0.95
Fe 2+	8.74±0.03	0.08
Al 3+	6.86±0.03	0.31
Cu 2+	4.267±0.03	0.18
Pb 2+	0.018±0.002	lipsa

*Values are expressed as mean ± SD of triplicate measurements

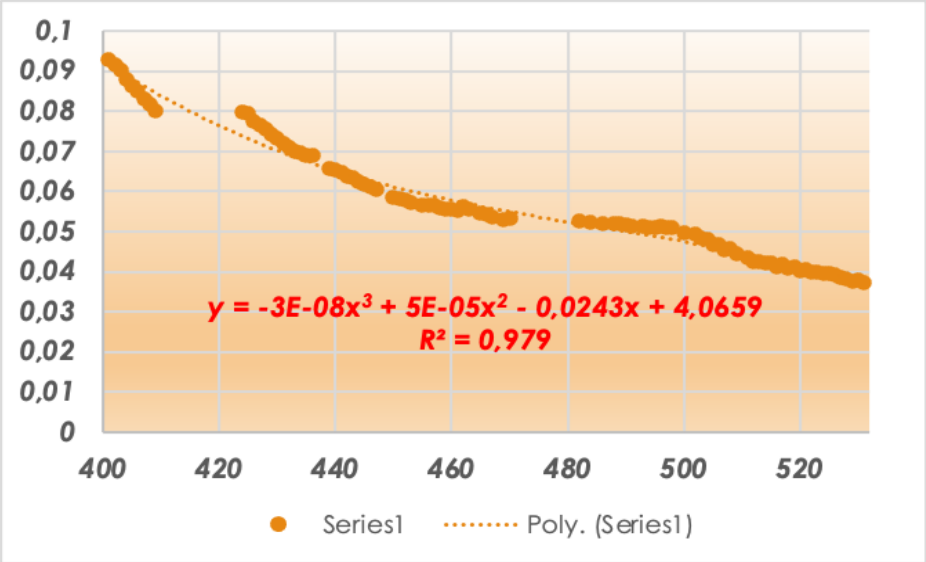


Fig. 1. Absorbance variation (a.u.) as a function of wavelength for V4 in the visible range

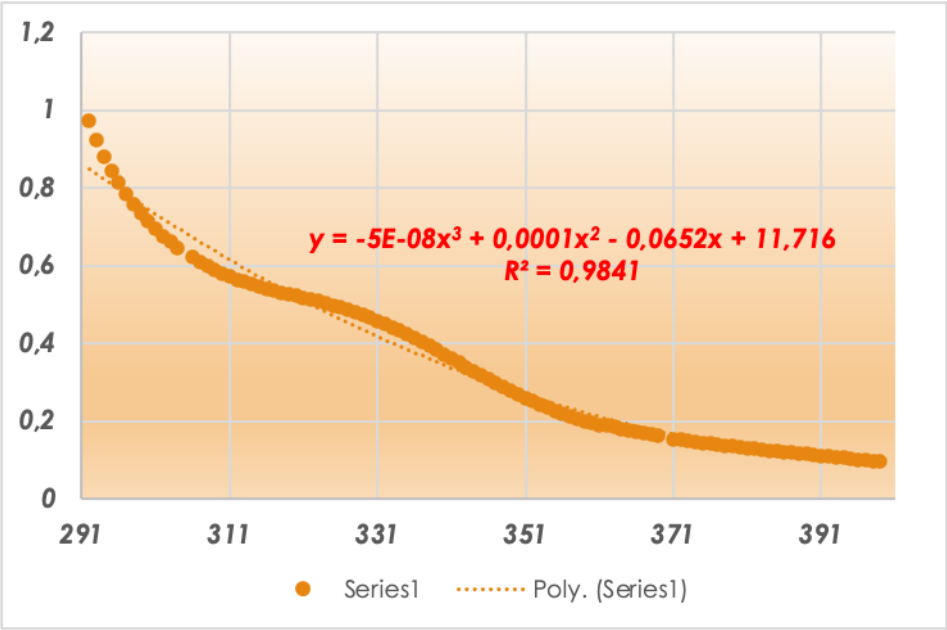


Fig. 2. Absorbance variation (a.u.) as a function of wavelength for V4 in the UV range

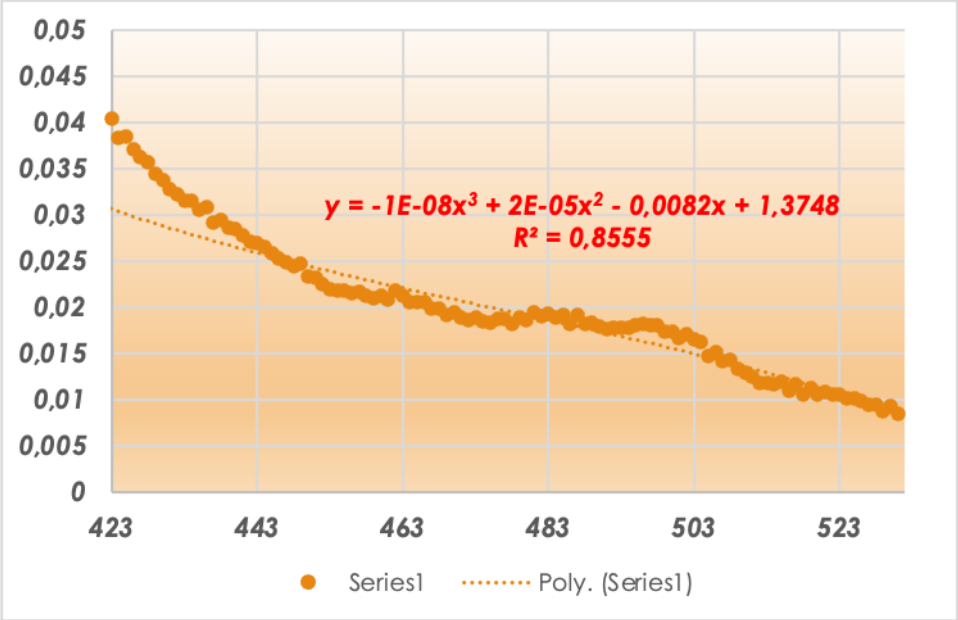


Fig. 3. Absorbance variation (a.u.) as a function of wavelength for V7 in the visible range

https://doi.org/10.5593/sgem2024/6.1/s25.30

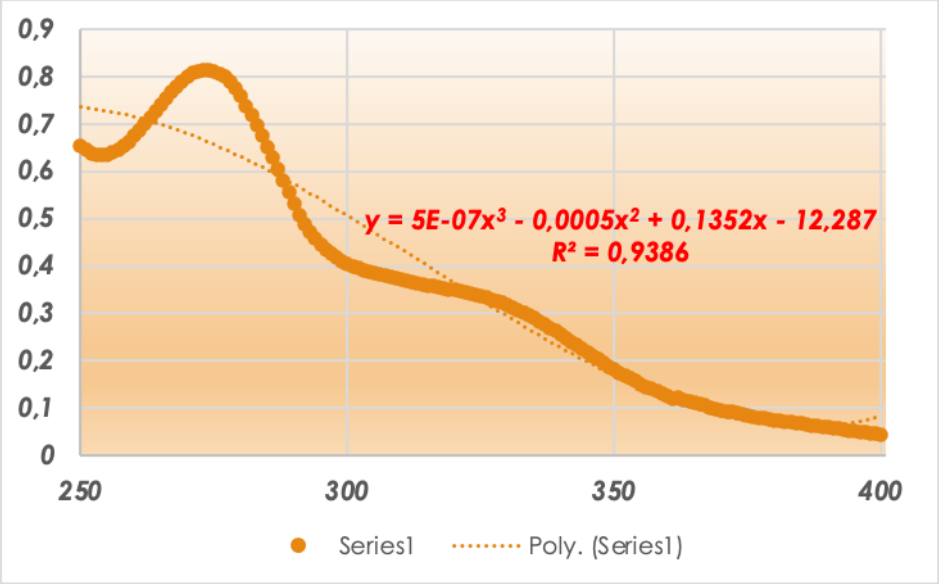


Fig. 4. Absorbance variation (a.u.) as a function of wavelength for V7 in the UV range

RESULTS

Subsection 3.1: Atomic Absorption Spectroscopy (AAS)

The use of the AAS technique revealed high concentrations of potassium, magnesium and calcium in the parts of the tea plant used. (Table 2).

Subsection 3.2: UV-VIS optical spectrometry

The results of this phase of research led to the identification of the best sweetening option for green tea-based food supplements which is white sugar for healthy people and sucrose for people with some sort of diseases.

DISCUSSION

The product obtained and selected for use (as raw material) in the following technological steps had a chemical composition similar to that of the unsweetened version, but also much improved sensory properties. Green tea has a high concentration of chlorophyll pigments, which is maintained at a high level even after boiling. However, this concentration is significantly affected by oxidation when brown sugar (experimental variant V2) and saccharin (experimental variant V4) are used as sweeteners. The use of white sugar in the experimental V1 variant produces much smaller changes on the concentration of the reduced forms, induces a state of lowed level of oxidability, and is more suitable for consumption by healthy people. When honey is used as a sweetener, the green tea environment loses transparency and clarity, both colour intensity and colour tone are affected and a slight oxidising effect occurs. The influence of honey on the characteristic pigments and thiophilic-type alkaloids in green tea varies according to the origin of the green tea and the temperature at which the sweetener is added. Saccharin induces strong oxidative effects in the chemical composition of green tea and alters both the hue and intensity of the colour, causing visible disturbances. When sucrose is added to the medium, the oxidation effects are much less as the coloured pigments are better protected. This is due to the additional

activation of the isoalloxazine nucleus of saccharin by acidification with an organic acid and buffering of this nucleus with bicarbonate. Fructose (V7) acts quite extensively within the fluid, altering the concentrations of some NAD-dependent oxidoreductase coenzymes. The experimental variants V8 and V9 with sorbitol and xylitol showed similar variations of the molecular absorption spectra curves, inducing almost the same effects.

CONCLUSION

From the analysis of the results of the laboratory experiments and the interpretation of the values, a number of clear conclusions can be drawn: Green tea has a high concentration of chlorophyll pigments, which is maintained at a high level even after boiling. However, this concentration is significantly affected by oxidation when brown sugar (experimental variant V2) and saccharin (experimental variant V4) are used as sweeteners.

The use of white sugar in the experimental V1 variant produces much smaller changes on the concentration of the reduced forms, induces a state of minimalised oxidability, and is more suitable for consumption by healthy people.

The optimum temperature at which honey should be used as a sweetener is between 45-55^{o}C, at which point it retains its strong antioxidant properties and optimum colour.

The use of saccharin affects certain reduced levels of bioactive compounds such as vitamins (vitamins B and C) and enzymes.

The use of sucrose in the experimental version of V5 gives a significantly improved result, which is beneficial for people with digestive, diabetic or cardiovascular problems and is recommended for these categories of consumers.

When monosodium saccharin is used together with cyclamate (the V6 experimental variant sweetened with 'Diamond' sweetener), the final effect is improved and is considered to be better than the saccharin sweetened variant.

Fructose (V7) acts quite extensively within the fluid, altering the concentrations of some NAD-dependent oxidoreductase coenzymes.

Experimental variants V8 and V9 using sorbitol and xylitol showed similar variations of the molecular absorption spectra curves, inducing almost the same effects. The use of one or the other of the two sweeteners to sweeten green tea is left to the consumer's choice.

The best sweetening option in this case was determined by minimizing the change in the basic chemical composition of the green tea and preserving the basic sensory characteristics. The development of innovative methods and technologies for the management of food additives facilitates the production of high-quality and safe food end products.

REFERENCES

[1] Belitz, H.-D.; Grosch, W.; Schieberle P. Food Chemistry, Springer-Verlag Berlin Heidelberg, Germania, Ed.4, 2009. 95-102.

[2] BV L'vov, BV Cincizeci de ani de spectrometrie de absorbție atomică ; J. Anal. Chem., 60:2005. 382–392.

[3] L'vov, B. Recent advances in absolute analysis by graphite furnace atomic absorbtion spectrometrie". Spectrochimica Acta Part B: Atomic Spectroscopy . 45 (7): 1990. 633–655.

https://doi.org/10.5593/sgem2024/6.1/s25.30

[4] Savescu P. (2017). A New Approach to Study the Sweetener's Effect on Green Tea Oxidative Status, Revista de Chimie, 68 (2), 294-299.

[5] Savescu P., Poenaru, M.M, Iacobescu F. (2016). Study regarding the Development of Organic Farming Systems in Romania as the Basis for obtaining of innocuity Agricultural Raw Materials – used in Functional Food, Annals Of The University Of Craiova, Series Agriculture, Montanology, Cadastre, No.1, 46, 281-285.

[6] Savescu, P. (2016). Improving the concentrations of bioactive compounds (with antioxidant properties) in alfaalfa and corn for their use in food supplements and functional food. Nano, Bio and Green-Technologies for a Sustainable Future, SGEM International Conference, Albena, BG, No.6, (1), 583-590.

[7] Savescu, P. (2017), Comparative Study on the Effect of Sweeteners on the Oxidative Status of Green Tea and Black Tea, Revista de Chimie, 68 (6), 1406-1412.

[8] Savescu, P. (2021). Chapter Natural Compounds with Antioxidant Activity-Used in the Design of Functional Foods. In Book Title -Functional Foods - Phytochemicals and Health Promoting Potential, IntechOpen Eds., London,U.K., DOI: http://dx.doi.org/10.5772/intechopen.97364, 1-25.

[9] Savescu, P. et all. (2006). Environmental risk's decreasing according to the European Standard (QMS ISO 9000:2000) applied to food factories, JEPE , 2006, Vol 6 (2), 447-453.

[10] Savescu, P., Iacobescu, F., Poenaru, M.M. (2020). Study on the Use of Biomaterials as Protective Membranes for Certain Functional Foods. In Book Advances in Bionanomaterials II, Book Series: Lecture Notes in Bioengineering. Publisher: Springer International Publishing, Print ISBN: 978-3-030-47704-2, Springer Nature Switzerland AG 2020, S. Piotto et al. (Eds.),BIONAM 2019,LNBE, https://doi.org/10.1007/978-3-030-47705-9_16, 1-13.

[11] Savescu, P., (2017). A New Approach To Study The Sweetener`S Effect On Hibiscus Tea Oxidative Status, International Conference SGEM 2017, Section 25 - Advances in Biotechnology, Albena, Bulgaria, DOI: 10.5593/sgem2017/61/S25.059, ISSN 1314-2704, Vol 17, Nr. 1, Rev. 61, 455-460.

[12] Savescu, P., Badescu, G., Milut, M., Ciobanu, A., Apostol, L., Vladut, V. (2019).Healthy Food – Through Innovative Technologies. Vol. ISB-INMA-TEH Bucharest. 516-521.

[13] Savescu, P., Iacobescu, F., Poenaru, M.M. (2020). Patent Application -OSIM A00745, " Innovative food supplement based on plant products obtained from organic farming", OSIM, Romania.

[14] Skoog, DA; Holler FJ; Crouch SR Principles of Instrumental Analysis, Thomson Brooks/Cole, SUA, Ed. a 6-a, 2007, 349-351, 2007

[15] Tita, O., E Lengyel., E., Stegarus, D., Savescu, P., Ciubara, A.B., (2021). Identification and Quantification of Valuable Compounds in Red Grape Seeds, Appl. Sci. 11(11), 5124; https://doi.org/10.3390/app11115124, 5124-5139.

THE INFLUENCE OF APPLE VARIETIES AND THE ENZYMES ROHAPECT PTE-100 AND PECTINASE ON THE OBTAINING OF APPLE JUICES

Denisa Marica (Sopîrlă)[1]

Maria Lidia Iancu[2]

Ovidiu Tița[3],

[1]Doctoral School of " Lucian Blaga" University of Sibiu, **România**
[2]Departament of Agricultural Sciences and Food Engineering, "Lucian Blaga" University of Sibiu, **România**
[3]Faculty of Agriculture Science, Food Industry and Environmental Protection, "Lucian Blaga" University of Sibiu, **România**

ABSTRACT

This thesis studies the impact of the addition of two types of enzymes: Rohapect PTE-100 and Pectinase to 6 varieties of apple, grown in the Valea Dâmboviței area in order to improve the quality of apple juice. The 6 apple varieties used are: Sirus, Florina, Red Topaz, Golden, Starkrimson and Rozela. Thanks to the new varieties planted, and the use of modern technology, the production of apples has increased, and the apples are used fresh or processed in the form of natural juice as such or mixed with other fruits.

The orchard area under analysis has 12,500 m2, of which 8,500 m2 are planted with 900 apple trees in an intensive system and 4,000 m2 with 1,200 apple trees in a super-intensive system.

Physic-chemical and sensory analyzes were applied to each apple variety to identify their quality.

The quality parameters such as vitamin C, acidity, anthocyanin content, enzyme activity, pH, and turbidity, were compared for the apple juices obtained with the addition of Rohapect PTE-100 enzyme, Rohapect PTE-100, and Pectinase enzymes and without enzymes.

This research provides the possibility of choosing suitable apple varieties and a database on the addition of Rohapect PTE-100 and Rohapect PTE-100 with Pectinase to the production of apple juices. Enzymes increase the juice yield when pressed, improve the clarification of clear juices and the stability of juices with pulp, and favor the extraction of color pigments and aromas. They help to reduce the amount of insoluble pectin, but enzyme concoctions are sensitive to variations in pH and temperature. Under these conditions, the yield of polyphenols increases in the obtained juices. Polyphenols have an antioxidant, anti-inflammatory, antibacterial, anti-tumor, and anti-atherogenic role.

Following the research, a higher yield resulted for the juice obtained with the addition of enzymes. The highest amount of vitamin C was identified in the juice obtained from the Starkrimson apples variety with the addition of Rohapect PTE-100 and Pectinase. A high turbidity was observed in the Rozela variety, but with the addition of Rohapect PTE-100 and Pectinase it decreased.

Keywords: apple varieties, apple juice, Rohapect PTE-100, Pectinase

https://doi.org/10.5593/sgem2024/6.1/s25.31

INTRODUCTION

It is studied the impact of adding two types of enzymes: Rohapect PTE-100 and Pectinase. From the 6 varieties analyzed (Florina, Red Topaz, Starkrimson, Sirius, Golden and Rozela) we obtained apple juice without additions, apple juice with the addition of Rohapect PTE-100 and apple juice with Rohatepect PTE-100 and Pectinase according to the technological scheme (variant 1, 2 and 3). The samples were grouped according to table no. 1.

Table no. 1 – The choice of work options

Variant 1	Sample 1 (E1)	Florina
(control)	Sample 2 (E2)	Red Topaz
	Sample 3 (E3)	Starkimson
	Sample 4 (E4)	Sirius
	Sample 5 (E5)	Golden
	Sample 6 (E6)	Rozela
Variant 2	Sample 1 (EL1)	Florina, Rohapect PTE-100
	Sample 2 (EL2)	Red Topaz, Rohapect PTE-100
	Sample 3 (EL3)	Starkimson, Rohapect PTE-100
	Sample 4 (EL4)	Sirius, Rohapect PTE-100
	Sample 5 (EL5)	Golden, Rohapect PTE-100
	Sample 6 (EL6)	Rozela, Rohapect PTE-100
Variant 3	Sample 1 (ELP1)	Florina, Rohapect PTE-100, Pectinaza
	Sample 2 (ELP2)	Red Topaz, Rohapect PTE-100, Pectinaza
	Sample 3 (ELP3)	Starkimson, Rohapect PTE-100, Pectinaza
	Sample 4 (ELP4)	Sirius, Rohapect PTE-100, Pectinaza
	Sample 5 (ELP5)	Golden, Rohapect PTE-100, Pectinaza
	Sample 6 (ELP6)	Rozela, Rohapect PTE-100, Pectinaza

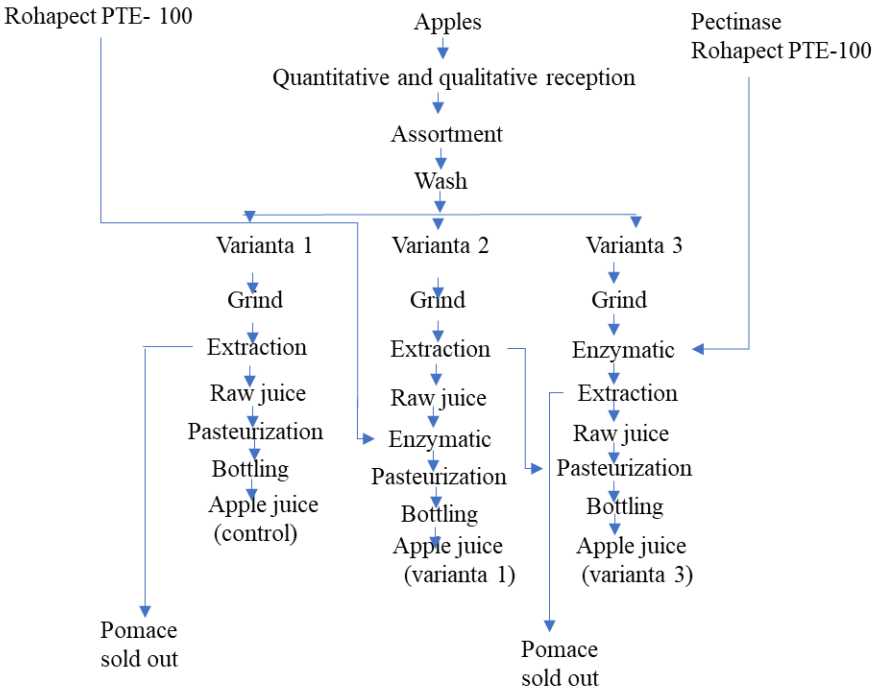


Figure no. 1- The technological scheme for obtaining apple juice in the chosen variants

In figure no. 2 below we can see the three types of juice obtained from the 6 varieties.

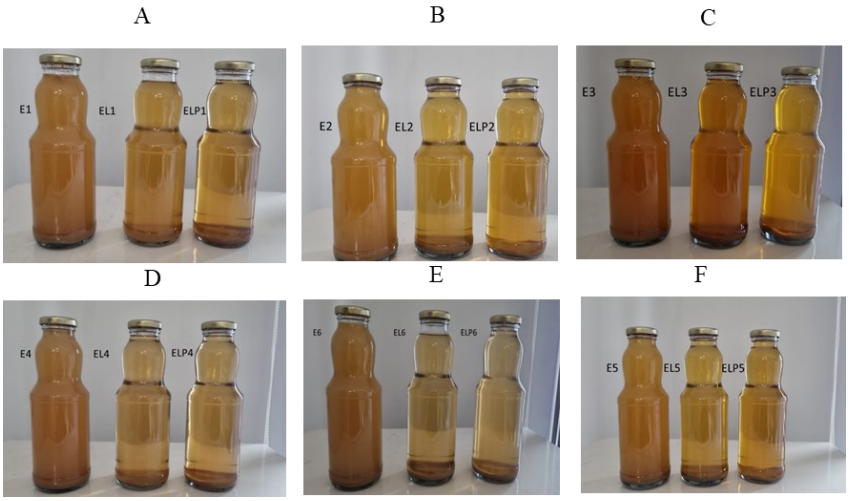


Figure no. 2 A,B,C,D,E,F – apple juice variant 1,2,3;

The apple juice was first treated with enzymes and then pasteurized.

METHODS AND MATERIALS

The 6 varieties of apples (Florina, Starkrimson, Rozela, Sirius, Golden and Red Topaz), ripe, small and medium-sized apples intended for obtaining apple juice, picked between October 15-25, 2023, were analyzed. The apples were stored in warehouses with a controlled atmosphere until February 15, 2024, when the research took place. The sensory analysis of each variety of apple was done by 52 students aged between 17-19 years old from the "Goga Ionescu" Technological High School in Titu, using the scoring method, each student assigning a grade from 1...5 to each sensory characteristic. The acidity was determined in the laboratory of the Faculty of Agricultural Sciences, Food Industry, Environmental Protection. The enzymes used are Rohapect PTE-100 and Pectinase.

Rohapect PTE-100. It is an enzyme concoction that mainly has pectintranseliminase or endo pectinolysis activity. The degradation of pectin takes place according to the transeliminative model without being preceded by deesterification. It improves the extraction time during the manufacture of juices and ensures the stability of the cloud, which is more stable during storage. The extraction time is also influenced by the variety and quality of the fruit used. According to research done by Jan Oszmianscki, from Poland, "turbid apple juice contains up to 4 times more polyphenols compared to clear apple juice". Polyphenols have an antioxidant, anti-inflammatory, antibacterial, antitumor and antiatherogenic role [1]. 60ml/100kg (for 4 hours) of this enzyme was added after extracting the raw juice to variant 2 and the same quantity together with the Pectinase after shredding to variant 3.

Pectinase. "Pectinase" produced by Oestreich GmbH [2] is used. We use pectinase to establish the turbidity of apple juice and to benefit from polyphenols. Pectinase prevents the juice from gelling and increases the production of free-flowing juice by breaking down pectin. In addition, pectinase improves the pre-stability of the puree, the extraction of colors and flavors and accelerates and improves the clarification of the

https://doi.org/10.5593/sgem2024/6.1/s25.31

juice. The yield is increased, and the viscosity of the must is reduced, thus avoiding clarification and filtration problems, reducing filtration costs. It increases the release of valuable aromatic substances, which determine the quality, and improves color stability. The enzyme used does not contain harmful depsidases and oxidases, therefore it does not cause premature aging [2]. Pectinase is added at 10 g/hl and left to act for 4 hours in variant 3.

By calculating the yield, the amount of juice resulted from each sample obtained from 100 kg of apples without and with the addition of enzyme was determined. For the determination of vitamin C content was used the HANNA kit (is based on titration with drops until the appearance of intensely colored samples, reducing substances interfere in the determination of ascorbic acid. Ascorbic acid undergoes an oxidation reaction with potassium iodate in an acidic state. The amount of potassium iodate consumed is then determined iodometrically). For the determination of anthocyanin content was used the pH-differentiated method (it applies to the determination of monomeric anthocyanins from fruits, juices, natural dyes and wines in the range of 20-3000 mg/L as cyanidin equivalent -3 - glucosidic)[3]. The determination of enzyme activity is used to establish the determination of the enzyme activity of pectinase (polygalacturonase) from microbial enzyme preparations that are intended for the juice industry. For the determination of density was used the pycnometer, aerometer and portable electronic densimeter (DMA35). Nephelometric turbidity (NTU) was determined with the B100 portable turbidimeter. All determinations were made 3 times and the arithmetic mean of the three determinations was expressed in the tables.

RESULTS AND DISCUSSION

Production in 2023 was 58t/12500m^2. In table no.2 we can see the distribution of fruits by category.

Table no. 2. The use of fruit from the orchard area under analysis

Distribution of fruits	Production 2023/ton
Fruit sold fresh	46,5
Fruit processed for juice	8
Fruit sold for brandy or other alcoholic products	2
Spoiled fruit	1,5
Total fruit	58

In table no. 3. the acidity of the apples is observed and in table no. 4 the result of the sensory analysis. In figure no. 3 it is observed that the most appreciated variety of apple is Rozela with a total of 19.5 points. It is appreciated for its sweet-sour taste and pleasant appearance. It is followed by Red Topaz with a total of 19 points, which is appreciated for its appearance and color, but the taste is too sour. Starkrimson apples are appreciated for their sweet and aromatic taste, but they are not crisp as most consumers appreciate. Sirius is crunchy, but the appearance, color and taste were not appreciated by all consumers because when obtaining the juice, we use second quality apples (and only the first quality ones, we noticed in a previous study, have extremely high sensory properties appreciated by consumers).

Golden has a pronounced sweet taste, so it was not appreciated by all consumers. And Florina is a crunchy apple, but it does not have the taste appreciated by consumers, it lacks sourness.

Table no.3. The acidity apples taken into analysis.

Apple variety	Acidity
Florina	0,4857%
Red Topaz	0,75 %
Starkrimson	0,2242%
Sirius	0,5980%
Golden	0,3364 %
Rozela	0,5978%

Table no.4 Sensory analysis based on the scoring scale

Apple variety	Appearance	Color	Consistency	Taste	Total
Florina	4	4	4,5	3,2	15,7
Red Topaz	4,5	5	5	3,5	19
Starkrimson	4,4	4,6	3,5	4	16,5
Sirius	4	4	4,5	4	16,5
Golden	4	4	4	4	16
Rozela	5	5	4,5	5	19,5

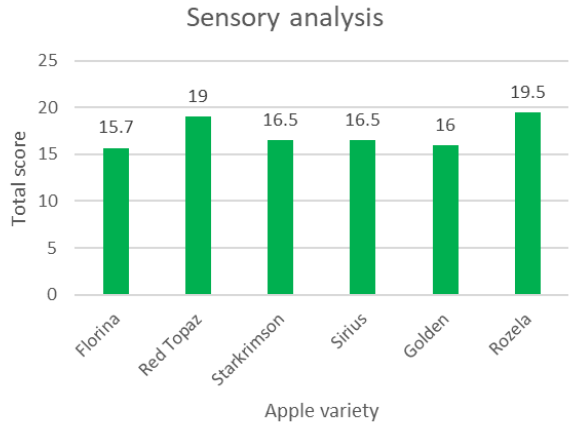


Figure no. 3 Sensory analysis results

In table no. 5 we observe the calculation of yield, specific consumption, and total losses. By adding Rohapect PTE-100 and Pectinase the yield is much higher compared to the other two variants.

Table no. 5 Juice yield, specific consumption, and total losses for each sample

Proba	Yield in juice [%]	Specific consume Cs, [kg/kg]	Total losses Pt ,[%]
E1	61,2 ±0,2	1,634±0,005	38,8±0,2
EL1	61,8±0,32	1,618±0,008	38,2 ±0,32
ELP1	64,2 ±0,17	1,558±0,004	35,8 ±0,17
E2	61,3±0,27	1,631±0,006	38,7±0,27
EL2	62,1 ±0,17	1,61±0,004	37,9 ±0,17
ELP2	64,8±0,33	1,543±0,007	35,2±0,31
E3	61,7±0,31	1,621±0,008	38,3±0,31
EL3	62±0,27	1,613±0,007	38±0,27
ELP3	64,9±0,2	1,541±0,004	35,1±0,2
E4	64,3±0,2	1,556±0,005	35,7±0,2
EL4	65,3±0,14	1,531±0,002	34,7±0,14
ELP4	67,6±0,28	1,480±0,006	32,4±0,28
E5	62,3±0,27	1,605±0,006	37,7±0,27
EL5	63,1±0,19	1,585±0,004	36,9±0,19
ELP5	65±0,25	1,538±0,006	35±0,25
E6	61,3±0,27	1,631±0,006	38,7±0,27
EL6	62±0,22	1,613±0,005	38±0,22
ELP6	64,2±0,11	1,558±0,003	35,8±0,11

https://doi.org/10.5593/sgem2024/6.1/s25.31

Table no. 6. pH, turbidity, flow time and total viscosity, determination of density by 3 methods

Sample	pH	Turbidity [NTU]	Flow time and total viscosity		Determination of density		
			Time (minutes, seconds, milliseconds) v= k*t m2/s	Kinematic viscosity[cSt]	The areometric method g/cm3	Pycnometer method g/cm3	The portable densimeter g/cm3
E1	3,741	890±0,2	*	-	1,065	1,0691	1,0661
EL1	3,735	196 ±0.32	02:20.60	1,4245±0,001	1,064	1,0669	1,0651
ELP1	3,645	556 ±0,33	02:28.83	1,51607±0,0045	1,0645	1,0677	1,0655
E2	3,372	336 ± 0,21	02:49.39	1,71957±0,0033	1,059	1,0626	1,0601
EL2	3,370	375 ± 0,13	02.17.92	1,40415±0,0012	1,060	1,0621	1,0596
ELP2	3,343	673 ± 0,21	02.21.05	1,43467±0,0021	1,058	1,0574	1,0604
E3	4,028	947±0,3	05:08.32	3,1339±0,0022	1,067	1,0718	1,0697
EL3	4,015	417± 0,34	02:30.69	1,53642±0,0022	1,072	1,07439	1,0693
ELP3	3,934	654±0,21	02:25.82	1,48555±0,0031	1,071	1,0727	1,0707
E4	3,522	875±0,23	02:37.73	1,60765±0,0012	1,052	1,0553	1,0532
EL4	3,551	256± 0,12	02:12.61	1,35327±0,0003	1,050	1,0551	1,0521
ELP4	3,493	989± 0,11	02:09.22	1,31257±0,00112	1,051	1,0552	1,0531
E5	4,084	671,3±0,2	02:42.12	1,64835±0,0078	1,060	1,0628	1,0589
EL5	4,023	163±0,12	02:11.59	1,3431±0,0026	1,057	1,0618	1,0585
ELP5	4,024	603±0,23	02:13.17	1,35327±0,0056	1,059	1,0621	1,0586
E6	3,871	1081 ± 0,26	03.24.14	2,0757±0,0024	1,057	1,0575	1,0535
EL6	3,755	672± 0,11	02:16.75	1,39397±0,0027	1,055	1,0558	1,0548
ELP6	3,849	743± 0,26	02:13.50	1,36345±0,0031	1,052	1,0564	1,0532

* Could not be determined, a larger viscometer is needed

In table no. 6 we notice that by adding enzymes, Rohapect PTE-100 and Pectinase, the pectin is broken down and the pectinase prevents the gelling of the juice which helps to increase the yield from 61.1% E2 to 64.8% ELP2. The lowest amount of losses is observed at ELP4 of 32,4; this is due to the apple variety and the action of the viscosity-reducing enzyme. If a temperature of 50^0C is also applied during the enzyme action, then according to research the yield would be even higher [4]. Knowledge of pH is necessary because it influences taste properties, clarity, and color in juices with anthocyanin pigments and determines the conditions for the development of beneficial and pathogenic microorganisms. The pH also influences the physical, chemical, and

biochemical processes that take place throughout the evolution of the juice. We note that, in general, the pH value is between 3-4, so an indicated pH could change during storage. We see that the turbidity is influenced by the type of apple used, but by adding pectinase it decreases and the mixture of the two enzymes stabilizes the turbidity. The results show that the addition of the two enzymes significantly reduces viscosity. We observe the highest clarity in E4 juice, which increases with the addition of enzymes up to 1.31257 in ELP4. Enzymes help extract color (improves color stability) and flavor and improves juice clarity. The density value is influenced by the apple variety, a slight difference is observed by the addition of enzymes. The evolution of vitamin C content and total anthocyanins from apple to apple juice obtained by different techniques is presented in table no. 7.

Table no. 7. Evolution of vitamin C content and total anthocyanins from apple to apple juice

Apple varieties	**Determination of anthocyanin [mg/l]**	**Amount of ascorbic acid [mg/100g]**	**Sample**	**Determination of the anthocyanin content of the juice variants obtained - the pH-differentiated method [mg/l]**	**Amount of ascorbic acid [mg/100g juice]**
Florina	12,52	22,04 ±0,2	E1	3,67	3,2 ±0,2
			EL1	2,00	5,1±0,2
			ELP1	22,54	5,2±0,1
Red Topaz	6,26	29,49±0,2	E2	3,92	4,1±0,2
			EL2	5,42	3±0,15
			ELP2	9,60	4,1±0,2
Starkrimson	5,76	22±0,1	E3	6,34	4,1±0,2
			EL3	6,84	4±0,2
			ELP3	5,51	3,2±0,2
Sirius	12.02	29,49±0,12	E4	23,62	4,3±0,2
			EL4	7,01	4,2±0,3
			ELP4	11,60	3,1±0,13
Golden	6,01	29,43±0,2	E5	12,35	5,3±0,2
			EL5	7,01	4,2±0,2
			ELP5	5,92	3,1±0,4
Rozela	5,76	18,64±0,12	E6	1,20	2,2±0,2
			EL6	7,26	2,1±0,2
			ELP6	6,09	3,4±0,2

Anthocyanins were present in apple juice at different levels depending on the varieties, cyanidin-3-galactoside present in apples, decreases in juice compared to fruit. The highest concentration was observed in ELP1 followed by E6. Cyandidin – 3-galactoside accumulates especially in the peel of ripe fruits [5]. It is observed that the fruits have a higher amount of vitamin C, in juice the amount of vitamin C decreases due to the treatment to which the juice is subjected (contact with light during storage for 4 hours for the action of the enzyme, the temperature to which the juice is subjected for preservation pasteurization at 80^0C and its contact with machinery).

CONCLUSIONS

The extraction yield is different for each apple variety and increases under the action of enzymes Rohapect PTE-100 and Pectinase. The best yield was obtained with the Sirius variety. Following the analysis, the varieties recommended for obtaining apple juice,

https://doi.org/10.5593/sgem2024/6.1/s25.31

from the most appreciated to the least appreciated, are Sirius, Rozela, Red Topaz, Golden, Starkrimson, Florina.

The juice obtained from the Florina variety has a high viscosity, but with the addition of enzymes it becomes clear. The filtration time decreases, with Starkrimson apples it decreases significantly (about 50%). The apple variety preferred by consumers is Rozela followed by Starkrimson which is characterized by a special aroma. The vitamin C content is much lower in the apple juice obtained, therefore future studies will try to find a way to improve it or avoid losses, and discover an ideal combination of apple varieties to obtain the juices. The polyphenol content will be analyzed with the possibility of obtaining apple juice mixed with cranberry juice to increase the content in polyphenols [6,7].

ACKNOWLEDGMENTS

This work was supported by the Center for Research in Biotechnologies and Food Engineering of "Lucian Blaga" University of Sibiu.

REFERENCES

[1] Artiomov, L. The influence of some polyphenols of vegetable origin on the microflora of foods and their safety. In: Competitiveness and innovation in the knowledge economy, Ed. 21, September 27-28, 2019, Chisinau. Chisinau Republic of Moldova: ASEM Editorial-Polygraphic Center, 2019, 21st Edition, pp. 279-282. ISBN 978-9975-75-968-7.

[2] Oestreich GmbH, Enzyme: https://www.gärfix.de/epages/62132971.sf/de_DE/?ObjectPath=/Shops/62132971/Categories/Kellereibedarf/Enzyme. (2023.11.2024).

[3] Lengyel E., Oprean L., Iancu R., Ketney O., Tita O., 2012 - Anthocyanins and polyphenols content in red Merlot, Cabernet Sauvignon and Pinot Noir wines from Recas vineyard, Acta Universitatis Cibiniensis Series E: FOOD TECHNOLOGY Vol. XVI (2012), no.1, https://saiapm.ulbsibiu.ro/cercetare/ACTA_E/AUCFT2012_I_51_56.pdf

[4] Will F., Schulz K., Ludwig M., Otto K., Dietrich H. The influence of enzymatic treatment of mash on the analytical composition of apple juice. Internațional Journal of Food Science and Technology 2002, 37, 653-660.

[5] Liu, Y., Che, F., Wang, L., Meng,R., Zhang, X., Zhao, Z. Fruit coloration and anthocyanin biosynthesis after bag removal in non-red and red apples (Malus× domestica Borkn). Molecules 18: 1549-1563. 2012.

[6] Sandru D., Niculescu V., Lengyel E., Tita O., 2016- Identification and quantification of total polyphenols in plants with bioactive potentially International Journal of Pharmacology, Phytochemistry and Ethnomedicine, 2016. ISSN: 2297-6922, Vol. 4, pp 47-51, doi:10.18052/www.scipress.com/IJPPE.4.47

[7] Frum A., Lengyel E., Georgescu C., Gligor F., Tița O. Analysis of phenolic compounds extracted from three types of berries, Journal of EcoAgriTourism, 2016. Vol. 12, No. 2, 5-9 ref. 7https://www.cabidigitallibrary.org/doi/full/10.5555/20173127760, https://rosita.ro/jeat/archive/2_2016.pdf

THE POTENTIAL OF OLIVE POMACE BIOCHAR FOR METAL RETENTION

Prof. Dr. Paulo Mourão
University of Évora, Department of Chemistry and Biochemistry, MED & CHANGE, IIFA, ECT, **Portugal**

ABSTRACT

This paper is a review of the potential of olive pomace, a by-product of the olive sector, as a precursor for the production of biochar. In general, it presents a panorama of this sector, which is so important worldwide and particularly in the Mediterranean region, the largest olive and olive oil producing area in the world, representing 90% of global production. We also address the problem of the large amount of waste (around 15 million tons/year), in the form of pomace, generated by this olive oil production industry, which has an impact on the environment and directly on the people living near the plants that process this by-product. Next, we explore the possibility of valorising this by-product, which in the quantities it is produced is even an environmental problem, by transforming it into biochar and revisit the main processes for producing this carbon material. We then focus on the potential for its application in metal retention (e.g. silver, arsenic), through the adsorption process, with a wide range of applications in areas ranging from mining to water treatment and environmental remediation, among others. This section presents the results that show the potential of valorising olive pomace by transforming it into a carbon material, biochar, with a developed porous structure and surface chemistry, which can be adjusted for its specific application in the retention or removal of metals present in liquid phase systems.

Keywords: biochar, olive pomace, metal, adsorption

INTRODUCTION

Biochar is defined by consensus as a solid material obtained from the carbonization thermochemical conversion process of biomass in an oxygen-limited environment [1]. However, in more *lato sensu*, biochar is produced by the thermal decomposition of organic material (e.g. multiple sources of biomass such as wood, slurry, leaves, husks) under a restricted amount of oxygen, and usually at temperatures below 700 ºC [1].

The cultivation of the olive tree, the harvesting of its fruit, the olive, and the production of olive oil, the natural vegetable oil that is the basis of the Mediterranean diet, are activities that date from the origins of mankind and have been intensified in countries such as Portugal, Spain, Greece, Italy, Morocco, Turkey and Egypt, among others. Statistics from the last 10 years show that Mediterranean countries together account for 90% of the world's production of this natural product [2]. However, along with this intensification of cultivation and olives production, which is the result of a certain amount of intensification (new varieties and modern irrigation systems), one of the negative aspects of this activity is becoming more and more evident, which is the production of huge quantities of olive pomace, one of the by-products of this activity (it takes 5 kg of olives to produce 1 litre of olive oil and it ends up producing between 3

https://doi.org/10.5593/sgem2024/6.1/s25.32

and 4 kg of pomace) [2, 3]. The current situation suggests that this growth will be boosted by the perception that olive oil, in its virgin or refined form, is a nutritious food rich in bioactive compounds and is therefore becoming an increasingly important part of traditional and modern diets.

This reality presents an opportunity for a circular economy approach that could transform the problem of huge quantities of olive pomace (e.g. 916 x 10^3 tonnes in 2021, the result of a record olive oil production of 229 x 10^6 million litres, only in Portugal) [4], into a source of raw material (of natural, vegetable and renewable origin) that can be converted into an adsorbent, a porous material with a surface chemistry enriched with functional groups, which has numerous applications due to its ability to retain both elemental and compound substances, the adsorptive [5, 6]. Among these substances, there are metals whose presence, especially in liquid systems, makes it necessary to retain them, to adsorb them, sometimes in order to recover a valuable metal (e.g. silver, gold) in mining processes, or in other cases to prevent environmental contamination by metals that are highly toxic due to their nature or quantity (e.g. mercury, arsenic) [7, 8]. The additional challenge is to finetune the adsorbent, either during the production process or at a later stage, to increase its specificity in order to enhance its adsorptive capacity, and finally, when possible, to regenerate it in order to extend its lifetime, closing the circularity loop.

MATERIALS AND METHODS

Biochar production

In this section, we revisit the main procedures for producing biochar from vegetable biomass, which are either already in use or show potential for use in obtaining biochar from olive pomace. It is important to note that the quality of the plant biomass used as a precursor in these processes is one of the determinants of the structural and surface chemical characteristics of the final carbonaceous material. Thus, the composition of the raw material in terms of hemicellulose, cellulose, and lignin will influence these characteristics, as the response of these components, whether isolated or combined in different proportions, to the thermochemical processes occurring during the preparation of biochar is distinct. Consequently, these lignocellulosic characteristics will also affect the applicability of biochar as an adsorbent, not only in liquid systems (e.g., aqueous) but also in solid systems (e.g., soils).

The methods for preparing biochar are essentially divided into pyrolysis, gasification, and hydrothermal carbonization. These processes always occur in an oxygen-limited environment and within a temperature range that never exceeds 700 ºC. In the case of pyrolysis, a thermochemical conversion of the plant biomass into bio-oil, syngas, and biochar occurs solely due to the contact of the biomass with the gas produced by the temperature increase, without any additional supply of an oxidizing agent. In gasification, a defined amount of an oxidizing agent, usually air or steam, is supplied to the system. On the other hand, in the process of hydrothermal carbonization, the conversion of biomass occurs in a liquid environment and under pressure, variables which, when combined, allow for the production of biochar with properties quite distinct from those obtained in a gaseous environment.

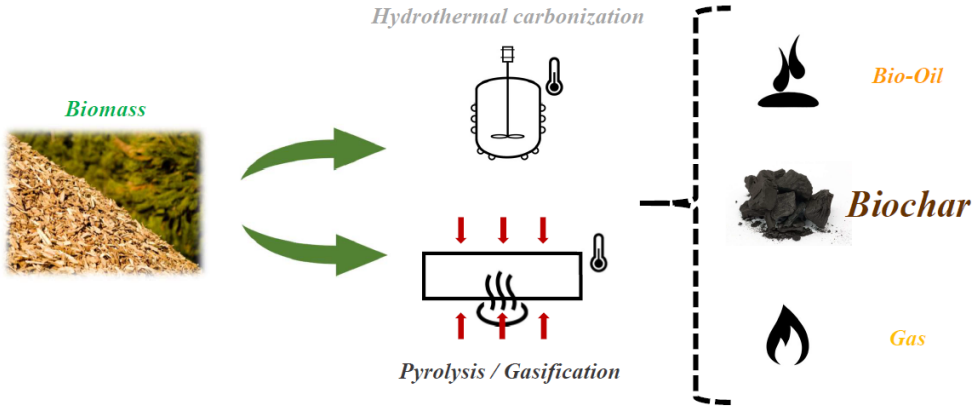


Figure 1: General process for biomass conversation by thermochemical process.

Literature and experience show that there is sometimes an ill-defined boundary between these three broad classes of processes. Furthermore, within each of these classes there are subtypes that can be used to produce materials with very different structural and chemical properties, thereby broadening their range of applications.

In brief, pyrolysis comprises the processes of slow pyrolysis (SP), intermediate pyrolysis (IP) and fast pyrolysis (FP). The conditions for these processes vary, with the most significant differences being the temperature, residence time and heating rate used. The temperature range is 300-550 ºC, 450-550 ºC and 450-600 ºC, the residence time ranges from hours to days, 10-20 seconds and less than 2 seconds and the heating rate ranges from 1-10 ºC/s and 10-100 ºC/s for SP, IP and FP processes respectively. The yield of these processes decreases significantly from slow to fast, with average values of around 35%, 25% and 12% for biochar, respectively. The analysis of the process in terms of liquid (bio-oil) and gaseous (syngas) products shows inverse behaviour. While the amount of bio-oil increases from 30% to 50% and 75% when moving from a slow to a fast process, the amount of syngas decreases from 35% to 25% and 13%. The values and trend of syngas amounts are similar to those of biochar in these pyrolysis processes.

The structural and chemical characteristics are also distinct and vary according to the process speed. Structurally, porosity increases significantly with rising temperature, always with a strong predominance of heterogeneous distribution, where microporosity predominates, followed by some mesoporosity and reduced macroporosity. In terms of surface chemistry, the characteristics are highly dependent on the type of biomass used. However, there is a tendency to obtain materials with a greater richness of surface chemical groups for intermediate processes, while an increase in pyrolysis temperature significantly increases the prevalence of condensed aromatic structures.

Gasification is not typically the most suitable process for the production of biochar, as it is usually a by-product of this type of operation. The primary objective of gasification is to produce a syngas containing H_2 (hydrogen), CO (carbon monoxide), CO_2 (carbon dioxide), CH_4 (methane), N_2 (nitrogen), and C_2H_2 (acetylene), which is generally quite clean and has a high calorific value due to its richness in hydrogen. The quantity and quality of biochar decrease significantly, with yields of approximately 15%, when the maximum temperature exceeds 750 ºC. Therefore, if biochar production is intended using an external oxidant (air, oxygen, or steam, or a mixture thereof), the maximum

https://doi.org/10.5593/sgem2024/6.1/s25.32

temperature should not exceed 700 ºC. Conversely, temperatures below 600 ºC do not allow the process to remain stable. Structurally and chemically, the biochar obtained from gasification typically has a high pore volume, and its surface chemistry is primarily determined by the precursor and the oxidant agent used.

On the other hand, if the aim is to obtain large quantities of biochar to maximise its application in terms of volume, the hydrothermal carbonisation process is the most suitable. The key to this process is the use of water, heat, and the effect of pressure (in the order of a few MPa), with the advantage that it operates at a low temperature range, usually between 200 and 350 ºC, and within a closed system for a few hours (1 to 16 hours). This process yields a mixture of products (biochar, bio-oil, and syngas) in equivalent proportions. However, it is common to find biochar amounts exceeding 35%. This process converts biomass into a gaseous product (comprising mainly H_2, CO, CH_4, and CO_2) and a hydrochar with an excellent H/C ratio. Structurally, hydrochar has low porosity and surface area, while its surface chemistry is characterised by the presence of large quantities of functional groups, particularly oxygenated ones. The carbon stability of hydrochar is lower than that of other biochars. From an environmental perspective, this is the most favourable process for the production of biochar.

Biochar aplication

Nowadays, the focus on biochar is mainly associated with carbon sequestration. However, there is a world of opportunities for this carbon material, which includes applications ranging from biogas production, construction (e.g., housing and roads), human and animal feed (e.g., preservative, aquaculture), technology (e.g., batteries), water treatment (e.g., pollutant retention), gas removal (e.g., carbon, odours), industry (e.g., steel, silicone), materials (e.g., bioplastics, carbon composites), and soil (e.g., soil conditioner, fertiliser, or remediator). In this work, the focus is on its use for the removal of metals from liquid and solid phases. These applications present enormous potential in areas such as the removal of metals in the treatment of natural or wastewater, environmental remediation in metal-contaminated areas like mining sites or the naval industry, landfills, and in the stabilisation and rebalancing of agricultural soils, among others.

RESULTS AND DISCUSSION

In this section, we review the state of the art concerning the types of biochar obtained from olive pomace and their uses in the field of metal retention from liquid or solid systems, with a particular focus on water treatment and the remediation of contaminated soils. To better characterise the current state of this field of research, the results from the last five years, between 2019 and 2024, are presented.

Olive pomace biochar production

The production of biochar from olive pomace is quite versatile, encompassing the three main processes identified above. However, there is a clear bias towards the pyrolysis and hydrothermal carbonisation processes, due to their higher yield in terms of biochar quantity. An analysis of the publications available on the ScienceDirect platform, considering only 'Research articles', using the term biochar in the title and throughout the text the terms: biochar, and 'olive pomace', reveals 56 publications in the last 5 years. More specifically, of these, 46 are associated with the pyrolysis process [e.g. 9-

11], and only 18 are related to the preparation of biochar by hydrothermal carbonisation [e.g. 12-14].

Part of the explanation for the disparity in these numbers is the relative ease with which the pyrolysis process is carried out. However, the analysis of publications and information provided by stakeholders in this area shows a trend towards a gradual shift to hydrothermal carbonisation. This is explained by the much lower environmental footprint of this process in terms of energy consumption, activating agents, waste generation, and other factors. The primary drawback of hydrothermal carbonisation is the initial investment required for equipment, such as autoclaves/reactors, considering their sizing to obtain significant quantities of biochar.

Olive pomace biochar aplication

A search of scientific publications on the ScienceDirect platform reveals 80 publications, including articles and book chapters, that contain the term ‘biochar’ in the title and/or abstract, and throughout the text the terms: biochar, ‘olive pomace’, metal, and water. A similar search identified 66 publications, including articles and book chapters, which contain the term ‘biochar’ in the title and/or abstract, and throughout the text the terms: biochar, ‘olive pomace’, metal, and soil.

However, a more comprehensive analysis, including other platforms, reveals additional publications demonstrating results in the field of water treatment with biochar prepared from olive pomace. These studies include the use of these materials to remove As (arsenic) [15, 16], Cr (chromium) [17], Cu (copper) [18] and Ni (nickel) [19]. Similarly, there are studies in which biochar prepared from olive pomace is used to retain metals in soil for various purposes, including agriculture and, more frequently, environmental remediation. Examples include the retention of N (nitrogen), P (phosphorus), and K (potassium) [20]; P, K, and Ca (calcium) [21]; Ca, Mg (magnesium), Na (sodium), and K [22] in the agricultural field, correlated with the cultivation of different species. In terms of heavy metals, there are instances of this type of biochar being used to remove Cd (cadmium), Pb (lead), Zn (zinc), As (arsenic) and Hg (mercury) [23], and Pb [24].

CONCLUSION

This brief review confirms the significant potential of olive pomace as a biomass source for the production of a new generation of adsorbent, biochar. The results indicate that studies utilising olive pomace as a precursor for biochar are beginning to garner interest within the scientific community, contrasting with the extensively studied production of high-porosity adsorbents, such as activated carbon. This shift could be particularly beneficial in the Mediterranean region, especially in countries with substantial olive oil production, which generates a large volume of precursor material. Hydrothermal carbonisation, an environmentally friendly method due to its low energy requirements (up to a maximum temperature of 350°C), the use of water as an activating agent, and the generation of waste that can be repurposed (e.g., as fertilisers or for energy production), is especially promising. The market for this product is substantial, including applications in soil improvement, agriculture, environmental remediation, and the treatment of liquid systems, such as potable water and waste water treatment. This option is reinforced by the size of the market available for the use of this product, with estimates suggesting it will reach a value of 126 ktons in 2024 and more than double to approximately 366 ktons by 2029, only on Europe [25]. Particular focus is being placed

https://doi.org/10.5593/sgem2024/6.1/s25.32

on its application to soil in agriculture or environmental remediation, or in the treatment of liquid systems, such as those associated with the treatment of water for human consumption or waste. In these areas, the retention of metals for permanent removal or controlled release presents a significant challenge with enormous potential for agricultural production or water supply in accordance with European legislation. The ability to manage this resource will make a decisive contribution to its valorisation, adhering to a truly circular approach.

ACKNOWLEDGEMENTS

The author thanks to the National Funds through FCT/MCTES from MED & CHANGE Research Centres within the scope of the project UIDB/05183/2020 for the financial support received.

REFERENCES

[1] https://iupac.org/project/2015-056-3-600

[2] Mehdi R., Naqvi S.R., Khan A.A., Mirani A.A., Optimization of olive oil extraction from olive pomace using solvent extraction and response surface methodology analysis of oil yield, Fuel, 348, 128633, 2023.

[3] Di Giovacchino L., Preziuso S.M., Di Serio M.G., Mucciarella M.R., Di Loreto G., Lanza B., Double extraction of olive oil in large oil mills of Southern Italy: Effects on extraction efficiency, oil quality, and economy of the process, European Journal of Lipid Science and Technology, 119, 1600161, 2017.

[4] Instituto Nacional de Estatística - Estatísticas Agrícolas : 2021. Lisboa : INE, 2022. Disponível na www: <url:https://www.ine.pt/xurl/pub/31589846>. ISSN 0079-4139. ISBN 978-989-25-0605-0

[5] IUPAC Compendium of Chemical Terminology, 3rd ed. International Union of Pure and Applied Chemistry; 2006. Online version 3.0.1, 2019. https://doi.org/10.1351/goldbook.A00153

[6] IUPAC Compendium of Chemical Terminology, 3rd ed. International Union of Pure and Applied Chemistry; 2006. Online version 3.0.1, 2019. https://doi.org/10.1351/goldbook.A00166

[7] Muqing Q., Lijie L., Qian L., Yawen C., Shujun Y., Shuqin W., Dong F., Baowei H., Xiangke W., Biochar for the removal of contaminants from soil and water: a review. Biochar, 4 (1), 2022.

[8] Mansoor S., Kour N., Manhas S., Zahid S., Wani A.O., Sharma V., Wijaya L., Alyemeni M.N., Alsahli A.A., El-Serehy H.A., Paray B.A., Ahmad P., Biochar as a tool for effective management of drought and heavy metal toxicity, Chemosphere, 271, 129458, 2021.

[9] Aissaoui M.H., Trabelsi A.B.H., Bensidhom G., Ceylan S., Leahy J.J., Kwapinski W., Insights into olive pomace pyrolysis conversion to biofuels and biochars: Characterization and techno-economic evaluation, Sustainable Chemistry and Pharmacy, 32, 101022, 2023.

[10] Ouazzani W.T., Farissi L.E., Monteiro E., Rouboa A., Automotive plastic waste and olive pomace valorization using the pyrolysis process, Energy Reports, 8 (9), 1577-1586, 2022.

[11] Abid N., Masmoudi M.A., Megdiche M., Barakat A., Ellouze M., Chamkha M., Ksibi M., Sayadi S., Biochar from olive mill solid waste as an eco-friendly adsorbent for the removal of polyphenols from olive mill wastewater, Chemical Engineering Research and Design, 181, 384-398, 2022.

[12] Di Caprio F., Altimari P., Astolfi M.L., Pagnanelli F., Optimization of two-phase synthesis of Fe-hydrochar for arsenic removal from drinking water: Effect of temperature and Fe concentration, Journal of Environmental Management, 351, 119834, 2024.

[13] Ramos J.S., Ferreira A.F., Techno-economic analysis and life cycle assessment of olive and wine industry co-products valorisation, Renewable and Sustainable Energy Reviews, 155, 111929, 2022.

[14] Gul E., Alrawashdeh K.A.B., Masek O., Skreiberg Ø., Corona A., Zampilli M., Wang L., Samaras P., Yang Q., Zhou H., Bartocci P., Fantozzi F., Production and use of biochar from lignin and lignin-rich residues (such as digestate and olive stones) for wastewater treatment, Journal of Analytical and Applied Pyrolysis, 158, 105263, 2021.

[15] Capobianco L., Di Caprio F., Altimari P., Astolfi M.L., Pagnanelli F., Production of an iron-coated adsorbent for arsenic removal by hydrothermal carbonization of olive pomace: Effect of the feedwater pH, Journal of Environmental Management, 273, 111164, 2020.

[16] Mourão P., Di Caprio F., Cansado I.P.P., Castanheiro J.E., Falcone I., Astolfi M.L., Altimari P., Pagnanelli F., Granulation and Activation of an Arsenic Adsorbent Made of Iron Oxide Doped Hydrochar, Chemical Engineering Transactions, 93, 91-96, 2022.

[17] Almezgagi, M., Guzel Kaya, G., Kar, Y., Deveci, H., Biochar Produced from Co-Pyrolysis of Olive Pomace & Crude Oil as an Adsorbent for Cr (VI) Removal from Aqueous Solutions, Iranian Journal of Chemistry and Chemical Engineering, 41(4), 2022.

[18] Mannaï I., Sayen S., Arfaoui A., Touil A., Guillon E., Copper removal from aqueous solution using raw pine sawdust, olive pomace and their derived traditional biochars, International Journal of Environmental Science and Technology, 19, 6981-6992, (2022).

[19] Mourgela R.N., Regkouzas P., Pellera F.M., Diamadopoulos E., Ni(II) Adsorption on Biochars Produced from Different Types of Biomass, Water, Air, & Soil Pollution, 231, 206, 2020.

[20] Das S.K., Adsorption and desorption capacity of different metals influenced by biomass derived biochar, Environmental Systems Research, 13, 5, 2024.

[21] El-Bassi L., Azzaz A.A., Jellali S., Akrout H., Marks E.A.N., Ghimbeu C.M., Jeguirim M., Application of olive mill waste-based biochars in agriculture: Impact on soil properties, enzymatic activities and tomato growth, The Science of the total environment, 755, 142531, 2021.

https://doi.org/10.5593/sgem2024/6.1/s25.32

[22] Kypritidou Z., Doulgeris C. Tziritis E., Kinigopoulou V., Jellali S., Jeguirim M., Geochemical Modelling of Inorganic Nutrients Leaching from an Agricultural Soil Amended with Olive-Mill Waste Biochar, Agronomy, 12, 480, 2022.

[23] Ceroni-Galloso A., Carbonel D., Huarcaya-Nina J., Esquivel-Lorenzo S., Colorado H., Gomez-Marroquin M., Mercury immobilization in mining waste soils using thiol-modified olive stones biochar, Environmental Engineering and Management Journal, 22(6), 1101-1115, 2023.

[24] Usama M., Rafique M.I., Ahmad J., Ahmad M., Al-Wabel M.I., Al-Farraj A.S.F., A Sustainable Approach towards the Restoration of Lead-Contaminated Soils through Nutrient-Doped Olive Waste-Derived Biochar Application, Sustainability, 15, 2606. 2023.

[25] Europe Biochar Market Size & Share Analysis - Growth Trends & Forecasts (2024 - 2029), Mordor Intelligence, 2024 (accessed on https://www.mordorintelligence.com/industry-reports/europe-biochar-market)

SECTION GREEN BUILDINGS

TECHNOLOGIES AND MATERIALS

CHARACTERISTIC STUDY OF ARTIFICIAL FLY ASH SAND AS A REPLACEMENT TO NATURAL RIVER SAND FOR MINIMIZING THE ENVIRONMENTAL IMPACT OF SAND MINING

Abhishek Khupsare[1,a]

Ajay K. Agarwal[2,b]

Swapnil P. Wanjari[3,c]

[1]Research Scholar, Department of Mining Engineering, Visvesvaraya National Institute of Technology, Nagpur, **India**

[2]Associate Professor, Department of Mining Engineering, Visvesvaraya National Institute of Technology, Nagpur, **India**

[3]Assistant Professor, Department of Civil Engineering, Visvesvaraya National Institute of Technology, Nagpur, **India**

ABSTRACT

The excess demand for natural River sand (NRS) as a construction material is increasing day by day. As a result of demand, there are server environmental impacts such as lowing the water table, damaging the flora and fauna etc. This study is to focus to prevent the environmental impact by developing artificial sand as a replacement for natural river sand (NRS). Development of artificial sand by mixing high volume fly ash, cement, natural river sand, and locally purchased high solid content polycarboxylate ether-based superplasticizer (HS-PCE). All the physical and chemical properties of polycarboxylate fly ash sand (PFS) were observed and satisfied the requirement of the Indian Standard code. As per IS: 383 – 2016 PFS is classified as Zone-I sand and has a specific gravity of 2.59. However, the angle of friction (41°), pH (11.6), and water absorption (3.58%) values were higher as compared to NRS. Soundness and Alkali aggregate test were within the permissible limit as per Indian Standard. The compressive strength of M25 grade concrete incorporating PFS was evaluated against the same for the control mix incorporating NRS. The trial mix with PFS achieved a 28-day compressive strength of 32.7 MPa which was roughly 4% lower than that of the control mix. This research indicates that PFS would be the best replacement for NRS as reduced the environmental impact of sand mining, also the utilization of waste.

Keywords: PFS; Fly ash; HS-PCE; polycarboxylate super-plasticize; PFS mortar

1. INTRODUCTION

The excess demand for natural river sand (NRS) as a construction material has led to a nationwide scarcity of good-quality natural river sand (NRS). Furthermore, many states in India have imposed a blanket ban on mining river sand to mitigate the negative impacts of sand-bed mining which include destruction of natural habitats, land scouring, lowering of the water table, and destroying the flora fauna etc. In 2008 Supreme Court of India stay

https://doi.org/10.5593/sgem2024/6.1/s26.33

orders in Tamin Nadu for banning sand mining [1]. Excess river sand mining causes environmental threats like the lower water table, sliding off the stream shores, disturbing the flora and fauna etc. [2]-[3]. Mining itself as of now prompts radical changes in the climate, however, without appropriate regulation and guidelines, the impacts can be devastating. The extraction of sand might prompt a decrease in the accessibility of sand and be hazardous to the environment [4]. However, in reverse, the power sector generates a numerous amount of fly ash which is huge for government and confidential substances in the field, a tremendous amount of this fly ash debris stays unused and is at last unloaded in landfills and debris dykes. This again leads to environmental problems due to the leaching process. Many publications have reported the use of quarry dust as a replacement of river sand for self-compacting concrete [5].

Different authors have published the article regarding the utilization of fly ash for construction work. It has been seen that fly ash can be replaced with natural river sand (NRS) in concrete [6]-[7]. Siddique et.al reported that the use of fly ash in concrete as a replacement for river sand was from 10% to 40%, however increasing the dosage of fly ash will reduce the strength [7]. Serval studies were also conducted on geopolymer sand and observed as per the Indian Standard. They reported that geopolymer sand can be replaceable with river sand as analysed the physical and chemical properties of sand within the permissible limit [8]. All physical and chemical properties like specific gravity, pH, direct shear, XRD, and SEM as per IS: 383- 2016 [9] were observed with developed polycarboxylate fly ash sand (PFS).

Other studies have been done on high solid polycarboxylate ether-based superplasticizer (PCE) in concrete containing high content of fly ash to increase the workability by reducing the water content. However, it results in increasing the strength of the concrete. Titiksh and Wanjari reported that using PCE in the concrete increase the physical, chemical, and durability properties of mix with high content of fly ash as a replacement for river sand. Tkaczewska et.al observed that the use of PCE superplasticizer in concrete mix helped to reduce the water content with the consistency of 47%-50% as compared to normal mix [10]. From previous research, it has been seen that PCE superplasticizer increases the pozzolanic action with fly ash and the same role will be considered to develop the PFS.

The main object of this study is to develop the polycarboxylate base fly ash (PFS) sand as a replacement for natural river sand (NRS) in the concrete mix for the mining industry and utilization of a huge amount of waste like fly ash and reduce the environmental impact of sand mining. Different dosages of superplasticizer were used to develop the PFS into a huge amount of fly ash and a little amount of cement and natural river sand. Optimum dosages were evaluated by comparing the compressive strength of mortar.

Hence, the current study is to develop the PFS and evaluate it as per Indian Standard to replace the natural river sand (NRS) to reduce the environmental effect of sand mining.

2. EXPERIMENTAL PROGRAM

2.1 Material

The development of PFS has been done by mixing the PCE superplasticizer, fly ash, cement, and river sand with different dosages (Table 3). The Polycarboxylate ether-based superplasticizer with 54% solid content was used from M/s Aradhya chemical,

Nagpur. As per IS: 8112-2013 confirmed the OPC 43 grade of cement. Natural river sand was available locally in Nagpur [11]. The physical properties of fly ash such as specific surface area by Blain's air permeability apparatus as per IS: 1727 (1967) [12], particle size distribution by Microtac Particle Size analyser shown in Fig 1, and chemical properties were determined as per XRF (X-ray fluorescence) and mentioned in Table 1. The specific gravity and specific surface area of the fly ash particles were 2.15 and 391.2 m^2/kg, respectively. It was classified as class-F fly ash as per ASTM [13] as SiO_2 = 58.52%, Al_2O_3 = 25.36%, Fe_2O_3 = 4.36%, CaO = 5.12% and SO_3 = 0.368% content in fly ash. However, the chemical properties of the PCE superplasticizer are given in Table 2.

Table 1 Physico-chemical properties of fly ash

Properties	Fly Ash %
Specific Gravity	2.15
Specific Surface Area	391.2 m^2/kg
Particle Size Distribution	41-391 μm
Median Particle Size	158.3 μm
SiO_2	58.52
Al_2O_3	25.36
CaO	5.12
Fe_2O_3	4.36
TiO_2	1.23
K_2O	0.42
SO_3	0.368
Na_2O	0.38
MnO	0.036
ZrO_2	0.029

Table 2 Chemical analyses of PCE superplasticizers

Properties	Values
Solid Content %	54
pH	13.1
Density (g/cm^3)	1.23
Colour	Yellowish Brown
Ash Content %	11

https://doi.org/10.5593/sgem2024/6.1/s26.33

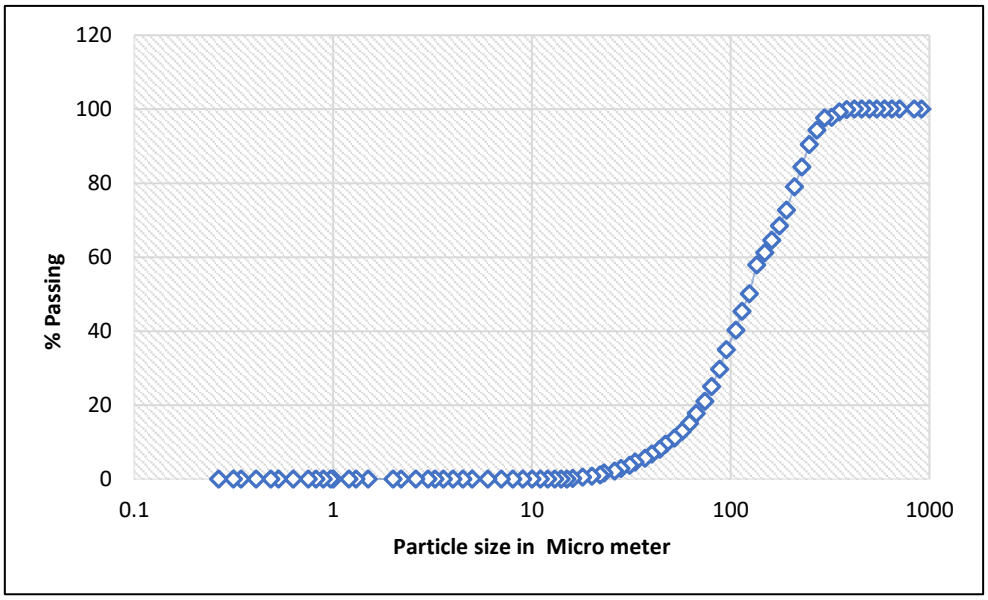


Fig. 1. Fly Ash Particle Size Analysis

2.2 Optimization of PFS

In the beginning, some trials were observed by adding a different dosage of PCE superplasticizer i.e. 0.5% to 1% of solid to develop the PFS as mentioned in table 3. The process of developing the PFS is a mixing of high-volume fly ash, cement, and some amount of river sand with water to solid ratio of 0.2. Then the addition of PCE superplasticizer with varying dosages into the mix. As the increasing dosage of superplasticizer decreases the water demand in the mix. However, the water content required for different dosages was neglected because our main objective was to maintain the binder properties of each particle. After preparing the sample, sieve the wet material from different sizes i.e. 4.75mm, 2.36 and 1.18mm IS sieves. 14 days of curing were conducted by the sprinkling of water to these PFS. Then, prepared the mortar specimen for evaluating the compressive strength as per IS: 2386 (Part-VI)-1986 [14]. As shown in Fig 2, it can be observed that increasing the PCE superplasticizer dosages led to improving the compressive strength properties of specimens up to 1%.

Table 3 Mix proportioning for PFS (sample size of 1kg)

Mix	Fly Ash (gm)	Cement (gm)	NRS (gm)	HS-PCE (g)
Mix-1	800	100	100	5.0g
Mix-2	800	100	100	7.5g
Mix-3	800	100	100	10g
Mix-4	800	100	100	12.5g

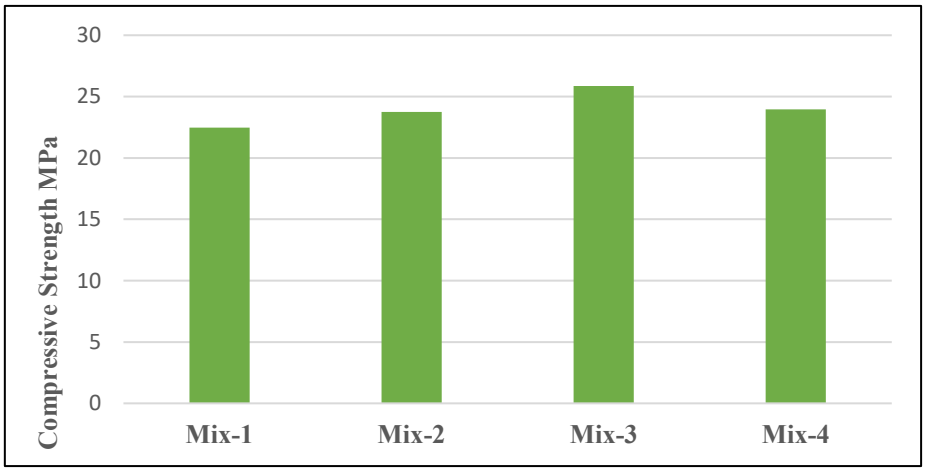


Fig. 2. PFS in terms of mortar compressive strength

2.3 Manufacturing of PFS

Initially, dry material has been mixed with the vortex mixture and adding the water: solid = 0.2. Ensuring the proper mixing by adding a PCE superplasticizer at a defined dosage. When the particle starts bonding to each other and forms a thin layer on each particle's surface, then sieve the material from 4.75mm, 2.36mm, and 1.18mm sieve. Sieved the material in a circular motion and obtained the shape and size of PFS similar to NRS Fig 3. Later on, provide the 14 days of curing by the sprinkling of water on PFS. Physical and chemical test as per Indian Standard has been conducted on PFS, like direct shear, frictional angle, water absorption, X-ray fluorescence, etc as discussed in chapter 3.

Table 4 Optimum mix proportion of PFS

Fly Ash	Cement	NRS
80%	10%	10%



Fig. 3. Different gradations of Polycarboxylate fly ash sand (PFS)

https://doi.org/10.5593/sgem2024/6.1/s26.33

3. RESULT AND DISCUSSION

3.1 Specific Gravity and Water Absorption

Specific gravity and water absorption were calculated according to the IS: 2386 (Part-III)- 1963 [15] of PFS and NRS and the outcomes are referenced in Table 5. The observed values for PFS and NRS are 2.59 and 2.96 respectively, which indicate that polycarboxylate-based fly ash sand (PFS) is light in weight as compared to natural river sand (NRS). The specific gravity of fly ash was observed as 2.15 (Table 1). However, PFS has higher specific gravity than fly ash because of the addition of cement in the manufacturing process. The evaluation of water absorption has been done as per the above Indian standard and observed as 3.58% which is higher as compared to natural river sand mentioned in table 5. Agarwal et.al. [8] have developed the geopolymer sand and observed 5.16% water absorption which is higher than PFS. PFS satisfied the requirement as per IS: 383-2016 [9].

3.2 Particle Size Distribution

The particle distribution curve as per IS: 2386 (Part-I)- 1963 [16] was observed for polycarboxylate-based fly ash sand (PFS) and natural river sand (NRS). The PFS and NRS sand was categorized as zone-I sand as per IS: 383-2016 (Bureau of Indian Standards, 2016) as shown in Fig. 4. Evaluation of coefficient of uniformity (Cu) and coefficient of curvature (Cc) was done as per IS: 1498-1970 [17]. It was observed that PFS has Cu = 4.35 and Cc = 1.8 which indicates that as poorly graded sand. Rao et.al [18] and Agrawal et.al. [8] also developed the geopolymer sand from fly ash which was also poorly graded sand as per IS:1498-1970 [17].

Table 5 Physical properties of PFS and NRS

Properties	PFS	NRS	Requirements as per IS: 383- 2016 [9]
Specific Gravity	2.59	2.96	>2.1
Water Absorption	3.58%	2.1%	<5%
Frictional Angle in degree	41	37	-
pH	11.6	8.38	-
Soundness	8%	-	<10% using Na_2SO_4 after 5 cycle
Alkali Aggregate Reaction	0.07%	-	<0.1% after 16 days

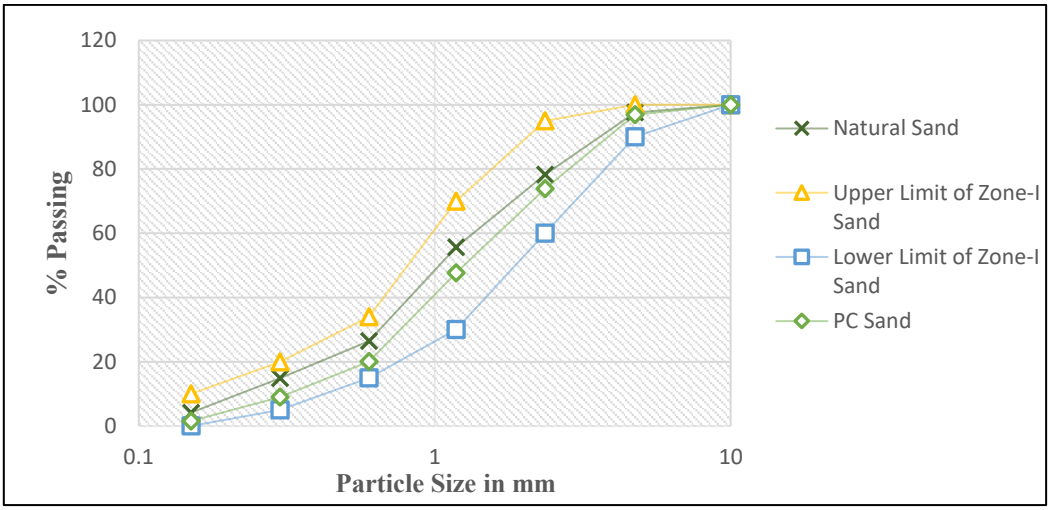


Fig. 4. Particle Size Distribution of PFS and NRS

3.3 Direct Shear Test & pH

To determine the friction angle of the PFS, a test has been carried out as per IS 2720 (Part-13)-1986 [19] the normal stress of 25kPa and 50 kPa as shown in Fig 5. The observed friction angle for PFS 41° (Table 5). However, the same procedure has been followed for NRS and the observed 37° (Table 5). As referred to IS: 2720 (Part-13)-1986 [19], if the angle of friction is 45°, it indicates the particles are angular and densely packed. On the other hand, if the angle of friction is 27°, it indicates the particles are rounded and loosely packed. However, PFS has a higher angle of friction due to the proper bonding of fly ash particles with the PCE superplasticizer. The similar results obtained by Agarwal et.al. [8] for geopolymer sand as 42°, indicate a rounded particle.

The pH test was conducted on PFS and NRS as per IS: 2720 (Part-26)- 1987 [20] by using Hanna HI 2211 pH meter, and the observed values as 11.6 and 8.38 (Table 5). The addition of a PCE superplasticizer to develop the PFS exhibits higher pH. Greater pH indicates the potential to induce an alkaline environment while mixing with the cement. Agarwal et.al [8] also observed similar results for geopolymer sand as 12.12.

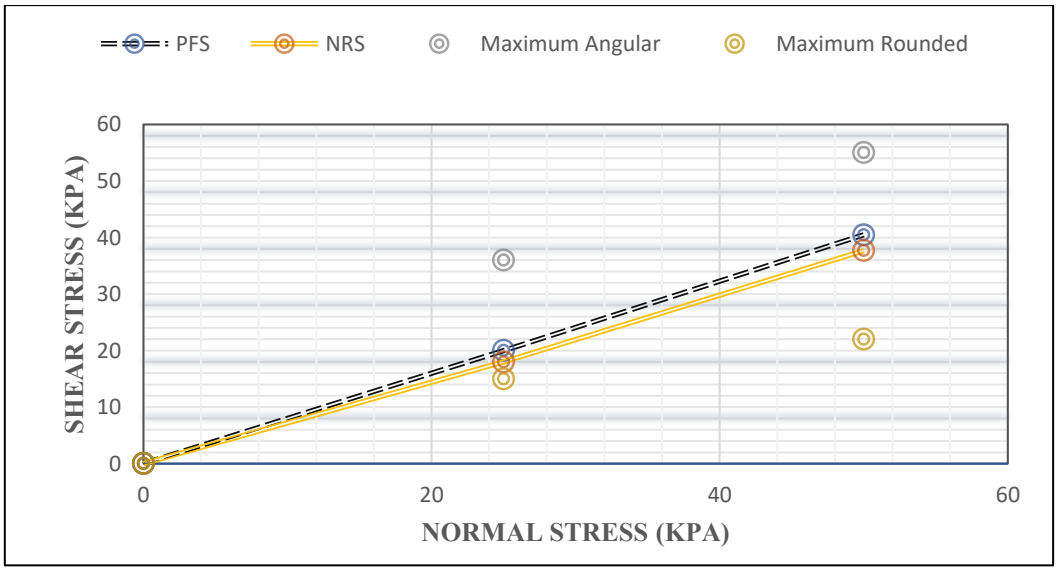


Fig. 5. Direct shear PFS and NRS

https://doi.org/10.5593/sgem2024/6.1/s26.33

3.4 Soundness Test

According to IS: 2386 (Part-V)- 1963 [21], evaluating the soundness test for PFS by immersing the sample in sodium sulphate (Na_2SO_4) for 16 hrs to 18 hrs and then drying the sample in the oven at 105ºC to 110ºC for 4 to 16 hrs. This cycle of immersing and drying was conducted for 14 days. The observed value of weight loss in the sample was 8%, which is within the permissible limit as per IS:383- 2016 (Not more than 10% after 5 cycles) [9]. The PFS may resist the change in volume when subjected to weathering action. As per the visual inspection, the shape and size of PFS particles had no change.

3.5 Alkali Silicate Reaction

The specimen size of 280mm x 25mm x 25mm mortar bars were cast by using PFS and cement as per ASTM C1260 [22]. This test was carried out as per ASTM C1260 [22] to evaluate the expansion of the specimen when they are open to exposure to an alkaline environment. The mortar bars immerse in 1M NaOH solution for 14 days at 80ºC. The observed average expansion of the three mortar bars was 0.07% after 16 days of the cycle (Table 5). The permissible limit as per IS: 383-2016 [9] is 0.1% after 16 days, the PFS expansion is within the permissible limit as per Indian Standard.



(a)



(b)

Fig. 6. PFS Mortar bars: (a) before ASR (b) after ASR

3.6 Scanning Electron Micrograph

This test was carried out on PFS using JSM 6380C available in the Materials Engineering Department of VNIT Nagpur. Scanning electron micrograph (SEM) was done on PFS to analyse the bonding of fly ash particles as shown in Fig 7.

From Fig 7 it was observed that there are some un-reacted fly ash particles due to the improper mixing process. Agarwal et.al also observed a similar result for GPS and they reported that the presence of unreacted fly ash particles behaves like filler to matrix, and also it helps to improve the strength of the concrete through the surface reaction of particles [8].

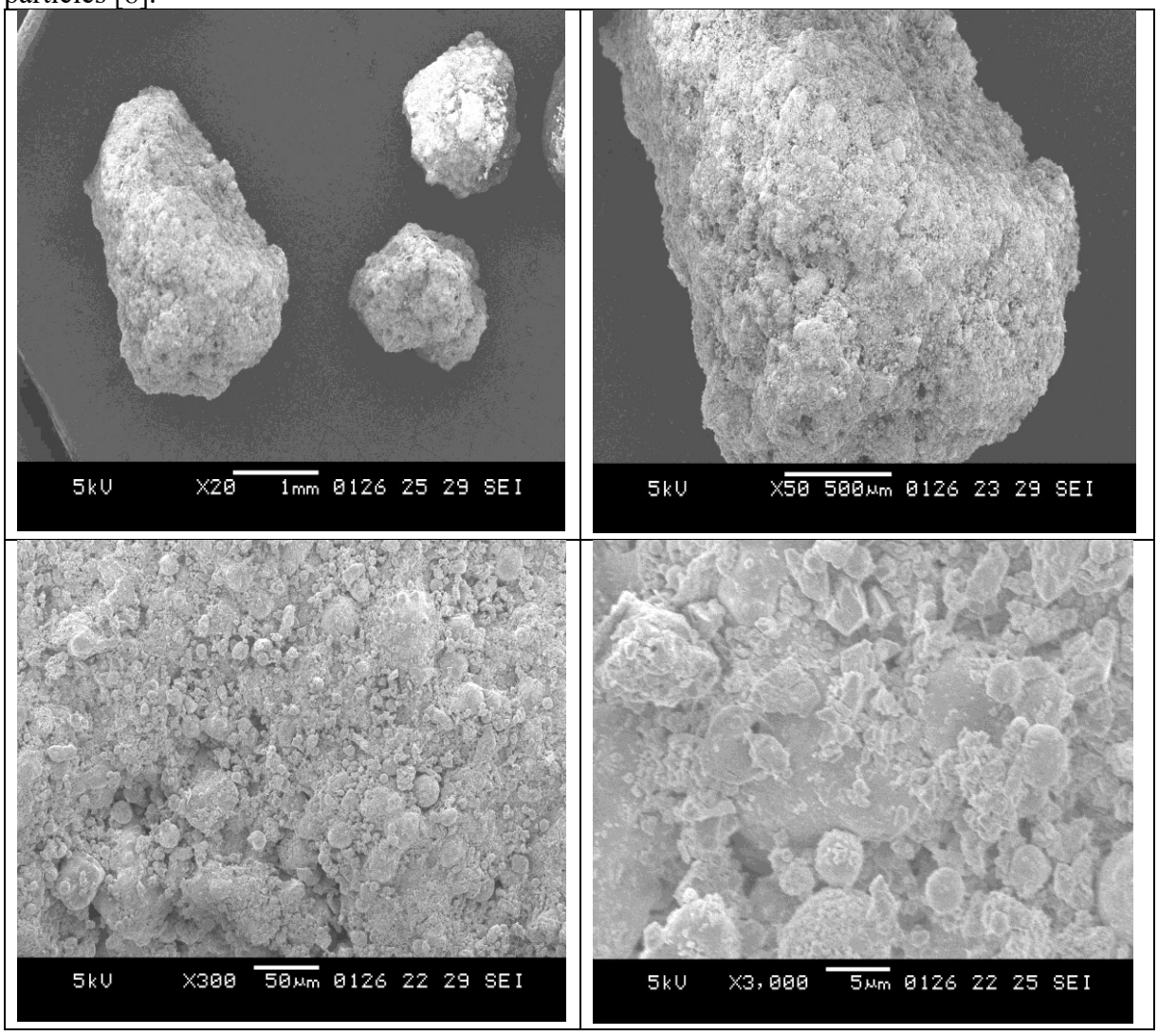


Fig. 7. SEM analysis PFS

3.7 X-ray Fluorescence (XRF)

The chemical analysis was done on PFS using XRF and is given in Table 6. The composition of PFS shows high silicon (SiO_2) and aluminium (Al_2O_3) with magnitudes of 57.56% and 29.78% respectively. The major component to develop PFS was fly ash, whereas fly ash contained SiO_3 and Al_2Sio_3 which is similar to cement. Hence, fly ash can be used in civil/mining engineering applications to reduce the environmental effect due to sand mining.

https://doi.org/10.5593/sgem2024/6.1/s26.33

Table 6 Chemical composition of PFS

Element	Composition
SiO_2	57.56
Al_2O_3	29.78
CaO	6.823
Fe_2O_3	3.485
TiO_2	1.365
K_2O	0.865
SO_3	0.426
V_2O_5	0.055
MnO	0.039

3.8 Compressive Strength

Cubes of grade M25 concrete were prepared with a W/C ratio of 0.5. Maintaining the cement content of 320 kg/m^3 in both the mix, the mix design adopted is shown in Table 7. Mix 1 contains NRS and in Mix 2, NRS was replaced with PFS. The mixes exhibited a flow of 95mm and 100mm for PFS and NRS respectively. The compressive strength was calculated as per IS 516: 1959 [23] and shown in Fig 9. Mix 2 containing PFS achieved compressive strengths of 18.14 MPa, 21.47 MPa, and 32.74 MPa at 3, 7, and 28 days respectively, whereas mix 1 containing NRS exhibited slightly higher compressive strengths of 19.57 MPa, 23.14 MPa, and 34.14 MPa at 3, 7, and 28 days respectively (Table 8). This indicates that there is a slight reduction of 4% in the 28 days compressive strength of the mix containing PFS. However, each mix satisfied the Indian codal limitation.

Table 7 Design Mix for M25 Grade of concrete

Mix	Cement (kg/m^3)	Water (kg/m^3)	NRS (kg/m^3)	PFS (kg/m^3)	Coarse aggregates (kg/m^3)		Average Slump (mm)
					20mm	10mm	
Mix 1 (or Control)	320	160	835	-	635	512	95
Mix 2	320	160	-	515	636	510	100

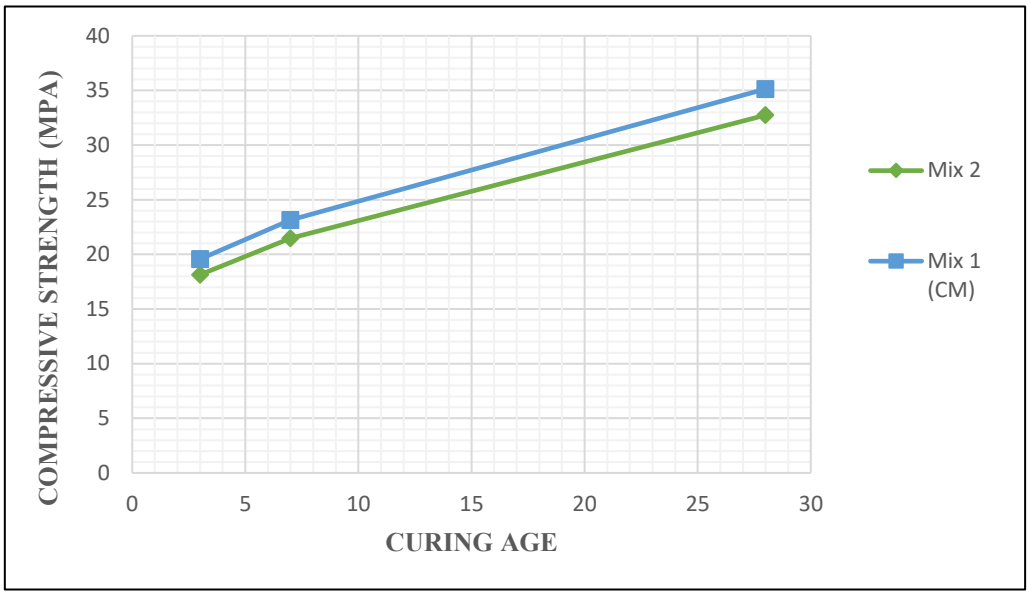


Fig 8. Compressive strengths of concrete with PFS and NRS

4. SUMMARY AND CONCLUSIONS

The aim of this study was to find the replacement of natural river sand (NRS) to reduce the environmental effect due to sand mining. An attempt was made to develop the artificial fly ash sand by mixing the fly ash, cement, and river sand at the proportion of 8:1:1 with the optimum dosage of polycarboxylate-based superplasticizer (PCE). The polycarboxylate-based fly ash sand (PFS) was compared with natural river sand in terms of physical and chemical properties. Various test has been performed on each sand as per the Indian Standard provision. Based on the properties of sand following conclusion has been made –

- The PFS achieved the specific gravity of 2.59 and NRS has 2.96. As per the IS: 383-2016 the value lies within the permissible limit. The particle size distribution curve indicates that PFS lies in Zone-I and coefficient of uniformity (Cu) = 4.35 and coefficient curvature of Cc = 1.8 classified as poorly graded sand (SP).
- The water absorption and pH value for PFS and NRS were observed as 3.58%, 11.6 and 2.1%, 8.38 respectively. However, these values satisfied the Indian codal provision. The PFS and NRS had friction angles of 41^0 and 37^0 respectively indicating that rounded and loosely packed.
- Soundness test was evaluated to resist the weathering action and observed 8% soundness and alkali-silica reaction was observed 0.07% respectively. Each value satisfied the Indian codal provision, indicating the durability of PFS.
- The chemical analysis of PFS using XRF was done and observed high silicon (SiO_2) and aluminium (Al_2O_3) with magnitudes of 57.56% and 29.78% respectively. Scanning electron micrograph (SEM) was done on PFS to analyse the bonding of fly ash particles. It was observed that there are some un-reacted fly ash particles due to the improper mixing process.
- The compressive strength of PFS and NRS was observed by casting the M25 grade concrete cubes. The observed values at 28 days for PFS and NRS are 32.74 MPa

https://doi.org/10.5593/sgem2024/6.1/s26.33

and 34.14 MPa, which indicate the PFS has achieved the 95.9% strength as that of NRS.

- With this study on the physical and chemical properties of sand as per Indian standards, conclude that PFS can be a good alternative to NRS to reduce the environmental effect due to sand mining.

REFERENCES

[1.] Express, B., & Service, N. (2018). Supreme Court stays order banning Tamil Nadu sand mining. *The New Indian Express*, *February 2018*.

[2.] Koehnken, L., & Rintoul, M. (2018). Impacts of Sand Mining on Ecosystem Structure, Process & Biodiversity in Rivers. In *Rivers, & Potential Geomorphic Transport Sediment Changes in Response to Sand Mining*.

[3.] Noufal E., R., & Manju, U. (2016). I-sand: An environment friendly alternative to river sand in Reinforced Cement Concrete constructions. *Construction and Building Materials*, *125*, 1152–1157. https://doi.org/10.1016/j.conbuildmat.2016.08.130

[4.] Rentier, E. S., & Cammeraat, L. H. (2022). The environmental impacts of river sand mining. In *Science of the Total Environment* (Vol. 838). Elsevier B.V. https://doi.org/10.1016/j.scitotenv.2022.155877

[5.] Nanthagopalan, P., & Santhanam, M. (2011). Fresh and hardened properties of self-compacting concrete produced with manufactured sand. *Cement and Concrete Composites*, *33*(3), 353–358. https://doi.org/10.1016/j.cemconcomp.2010.11.005

[6.] Kanthi, A. E. (2014). Studies on Partial Replacement of Sand with Flyash in Concrete. *European Journal of Advances in Engineering and Technology*, *1*(2), 89–92.

[7.] Siddique, R. (2003). Effect of fine aggregate replacement with Class F fly ash on the abrasion resistance of concrete. *Cement and Concrete Research*, *33*(11), 1877–1881. https://doi.org/10.1016/S0008-8846(03)00212-6

[8.] Agrawal, U. S., Wanjari, S. P., & Naresh, D. N. (2017). Characteristic study of geopolymer fly ash sand as a replacement to natural river sand. *Construction and Building Materials*, *150*, 681–688. https://doi.org/10.1016/j.conbuildmat.2017.06.029

[9.] Bureau of Indian Standards. *IS 383: 2016, Indian Standard Coarse and Fine Aggregate for Concrete-Specification*.

[10.] Titiksh, A., & Wanjari, S. P. (2021). Sustainable pavement quality concrete containing ultra-high volume fly ash in the presence of a novel superplasticizer. *Case Studies in Construction Materials*, *15*(June), e00603. https://doi.org/10.1016/j.cscm.2021.e00603

[11.] Bureau of Indian Standards. *IS 8112: 2013 Indian standard Ordinary Portland Cement, 43 Grade - Specification*.

[12.] Bureau of Indian Standards. *IS 1727-1967 Methods of test for pozzolanic materials*.

[13.] ASTM C618 - 03. (2010). Standard Specification for Coal Fly Ash and Raw or Calcined Natural Pozzolan for Use West Conshohocken, PA, 2001. *Annual Book of ASTM Standards*, *C*, 3–6.

[14.] Bureau of Indian Standards. *IS 2386-6 (1963): Methods of test for aggregates for concrete, Part 6: Measuring mortar making properties of fine aggregates*.

[15.] Bureau of Indian Standards. *IS 2386-3 (1963): Methods of test for aggregates for concrete, Part 3: Specific gravity, density, voids, absorption and bulking*.

[16.] Bureau of Indian Standards. *IS 2386-1 (1963): Methods of Test for Aggregates for Concrete, Part I: Particle Size and Shape*.

[17.] Bureau of Indian Standards. *IS 1498 (1970): Classification and identification of soils for general engineering purposes*.

[18.] Rao, S. M., & Acharya, I. P. (2014). Synthesis and Characterization of Fly Ash Geopolymer Sand. *Journal of Materials in Civil Engineering*, *26*(5), 912–917. https://doi.org/10.1061/(asce)mt.1943-5533.0000880

[19.] Bureau of Indian Standards. *IS 2720-13 (1986): Methods of test for soils, Part 13: Direct shear test*.

[20.] Bureau of Indian Standards. *IS 2720-26 (1987): Method of test for soils, Part 26: Determination of pH value*.

[21.] Bureau of Indian Standards. *IS 2386-5 (1963) Methods of Test for Aggregates for Concrete, Part 5: Soundness*.

[22.] *ASTM (2001b) Standard Test Method for Potential Alkali Reactivity of Aggregates (Mortar-Bar Method). C1260 West Conshohocken, PA, 2001*. (n.d.).

[23.] Bureau of Indian Standards *IS 516 (1959), Method of Tests for Strength of Concrete*.

https://doi.org/10.5593/sgem2024/6.1/s26.33

EVALUATION OF THE INITIAL VOLUME STABILITY OF CURRENT CEMENTS

Dr. Božena Dohnálková[1]

Dr. Jiří Grošek[1]

Tomáš Zavřel[1]

Dr. Theodor Staněk[2]

[1] Centrum dopravního výzkumu, v.v.i. (Transport Research Centre), **Czech Republic**
[2] Výzkumný ústav stavebních hmot, a.s. (Research Institute for Building Materials), **Czech Republic**

ABSTRACT

In the context of the pressure to reduce the production of CO_2 emissions in cement manufacturing, cement plants are significantly changing their product portfolios. Changes in the composition of cement products also lead to changes in their properties. This paper focuses on the monitoring and non-standard evaluation of initial volume stability. Several different types of currently used cements produced in various cement plants in the Czech Republic and Slovakia in 2022 and 2023 were tested using the "initial volume stability test". The test results included in this article describe defects forming in the test samples at the initial stage of the cement setting and hardening. The test can be used to observe the possible differences in the properties of the same cement types from different sources, as well as the variability in the properties of one cement type within a production batch.

Keywords: cement, volume stability, defects, concrete, mortar

INTRODUCTION

The basic ingredient for the production of Portland cement is Portland cement clinker, which is created by firing suitable raw materials (limestone, clay and other components) at a temperature of around 1450°C. Hydration is the chemical reaction between cement (binder) and water associated with the processes that create the solid structure of the concrete (mortar). It is a continuous and long-term process. The first stages of hydration are crucial for the integrity of the solid structure being formed.

Standards primarily describe the mechanical properties of cement. Cement strength is usually monitored at the basic testing age of 28 days. However, it is possible to measure the strength at other ages as well, for example at the age of 2 days, 7 days, 14 days, 56 days, 90 days, etc. Durability parameters of cement, such as the risk of cracks and other defects developing in the first hours or days of hydration in a solid structure that is still forming, are now either unsatisfactory (e.g. volume stability according to Le-Chatelier's method) or they are not monitored at all.

The cause of this criticism is the reduced durability of some exterior concrete pavement structures (or their components). The worst situation is probably in road construction, where we are sometimes seeing extremely reduced material durability of concrete. There is a difference between material durability and fatigue durability, as fatigue

https://doi.org/10.5593/sgem2024/6.1/s26.35

durability is specifically considered during the design and dimensioning of road structures, unlike material durability. Several cases have been even reported where sections of road concrete pavement had to be dismantled due to material degradation, even as early as three years after construction.

The properties and quality of the cement are also crucial for the achievable material durability of the concrete. Cement plants are currently under strong pressure caused by the necessity to reduce their CO_2 emissions and the production energy intensity. Consequently, the support of standards changes the cement production and the product portfolio of cement plants. New cements contain increased levels of slag, fly ash, ground limestone, pozzolans, calcined shale or silica fume.

The current trend in cement production focuses on reducing the content of Portland clinker while emphasizing the critical requirement of maintaining strength as the primary consideration. The simplest solution for this separated target is increasing grind fineness. However, this approach poses a risk with regard to the durability of future mortars and concretes, as volume changes tend to increase with higher grind fineness. The defects formed in the hydrating structure facilitate the penetration of external aggressive substances from the environment.

Many authors prefer using the dilatometry method to monitor volume stability such as shrinkage during hydration of cementitious materials [1-3]. However, some defects or failures are not measurable, especially during the initial hydration phase. One possible quick, new test, which is also suitable for construction site laboratories, is the evaluation of the volume stability of cements, including the initial hydration phase, using the initial volume stability test. This test is a non-standard test that offers a more accurate assessment of cement mortar behaviour and presents new opportunities for evaluating the risk associated with cement behaviour in relation to the material durability of concretes [4-6].

MATERIALS AND METHODS

The delivered cements were tested using a non-standard test focusing on initial volume stability. A detailed description of the procedure for conducting and evaluating the initial volume stability test is given in the “Methodology for testing the volume stability of hydraulic binders” [7].

The test was primarily developed and validated for all structural road pavement layers containing cement (both cover and base layers bonded with cement). The key to assessing the level of risk associate with specific cement or hydraulic binders is given in Table 1 of the document [7].

The initial volume stability test consists of manual mixing a recipe with a basic dose of binder (usually 240 g), an appropriate amount of water is added (water/cement ratios w/c = 0.42, w/c = 0.5, and w/c = 0.58). The use of any additives (e.g. aerating, plasticizing, etc.) is excluded. The prepared cement mortar is poured onto a non-absorbent pad and sensitivity of cements to mixing water and other defects (bleeding, failures, segregation etc.) are assessed at specified ages: first during the preparation of the samples, then 24 hours and 14 days after mixing.

RESULTS

Between 2022 and 2023, twenty-three cements were successively tested using the initial volume stability test method, of which sixteen were obtained directly from cement plants; the remaining ones were development cements, which are not further discussed in this paper. The aim was to improve the properties of those cements that did not demonstrate sufficient initial volume stability.
This paper deals in detail with the testing and comparison of the initial volume stability of the tested cements from cement plants divided into groups according to the harmonised standard EN 197-1, specifically:

- Portland cement CEM I (three specimens);
- CEM II/B-M cements (four specimens);
- composite Portland cements CEM II/B-S (four specimens);
- composite Portland cements CEM II/A-LL (three specimens);
- blast-furnace cement CEM III/B (two specimens).

The initial volume stability test was monitored for water/cement ratios of w = 0.42, w = 0.5, and w = 0.58, as shown in Figure 1 and minimum and maximum measured spreading for each cement class show Table 1. Sensitivity of cements to mixing water and defects and failures of current cements were observed.

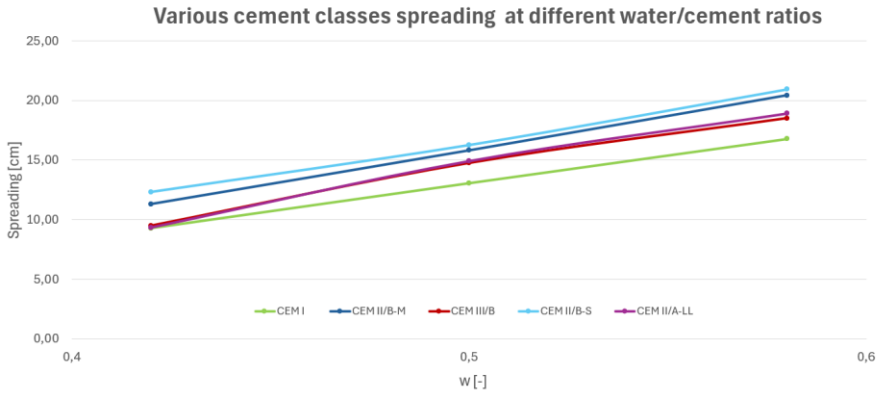


Figure 1: Spreading of testing samples for various cement classes at different water/cement ratios

Table 1: Minimum and maximum measured spreading for each cement class

Cement marking	w=0.42	w=0.5	w=0.58
CEM I	10,25 - 15,00	13,75 - 19,5	19,5 - 25,00
CEM II/B-M	9,75 - 13,00	13,25 - 18,00	18,25 - 22,00
CEM III/B	9,25 - 9,75	14,5 - 15,00	18,25 - 18,75
CEM II/B-S	9,50 - 15,00	12,50 - 19,75	18,00 - 24,00
CEM II/A-LL	9,00 - 10,00	14,75 - 15,00	18,75 - 19,00

https://doi.org/10.5593/sgem2024/6.1/s26.35

DISCUSSION

1. Sensitivity of cements to mixing water

In terms of measured spreading (water sensitivity), cements CEM II/B-S and CEM I 42.5 R show the most significant differences. The amount of water in concrete/cement mortar has a fundamental impact on the initial course of cement hydration and on the development of a solid structure. In particular, it affects the formation and development of cracks, mortar/concrete creep, and the pore structure of cement paste in general.
The initial volume stability test confirmed that admixtures mixed into cements exacerbate the effect of water dosage errors, increasing the fluidity of the cement mortar. If plasticisers were also used (they are not used in the initial volume stability test), the sensitivity to water dosage errors would be even greater. Table 1 shows the minimum and maximum measured values of spreading of the tested cements along with their corresponding specific water/cement ratios. The variability in the spreading among these groups highlights the unique properties of each cement.

2. Defects and failures of current cements

All cements exhibited the same defects. No dependence on either the strength class or the general marking of the type of admixture was confirmed for the admixed cements. Achieving a homogeneous consistency was easy for some cements, while other cements formed clumps that were very difficult to break up when mixed with water by hand.
After 24 hours, one frequently observed defect was the sporadic appearance of surface pits ranging from shallow to deep, with diameters up to 1 mm. This defect was often related to the cement's susceptibility to slight foaming (Figure 2).

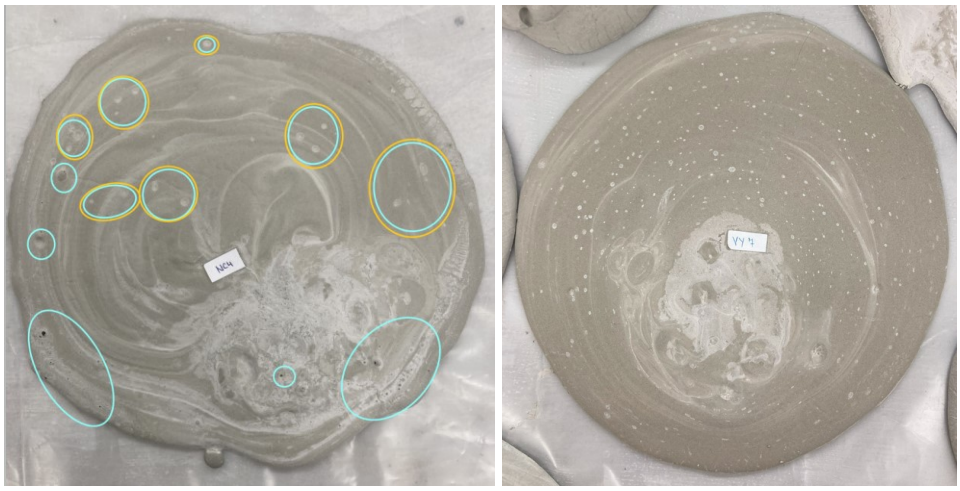


Figure 2: Defect manifested in forming of surface pits

Samples with higher water/cement ratio had markedly raised edges. According to the methodology [7], this places them in the group of “high-risk” cements. Furthermore, various microcracks were observed quite frequently. They were formed when the test specimens were about one to three days old and usually closed spontaneously by the age of eight days. However, they did not disappear completely, they reappeared when the surface of the test specimens were soaked with water after the test, see Figure 3.



Figure 3: Apparent closure of cracks w=0.5, sample age (a) 4 days, (b) 14 days, c) 14 days after soaking in water

In other test samples, the cracks were constant and remained pronounced until the end of testing. After peeling the samples and removing them from the pad, cracks were also found on the bottom side, but not all of them extended through the entire structure of the sample (Figure 4).

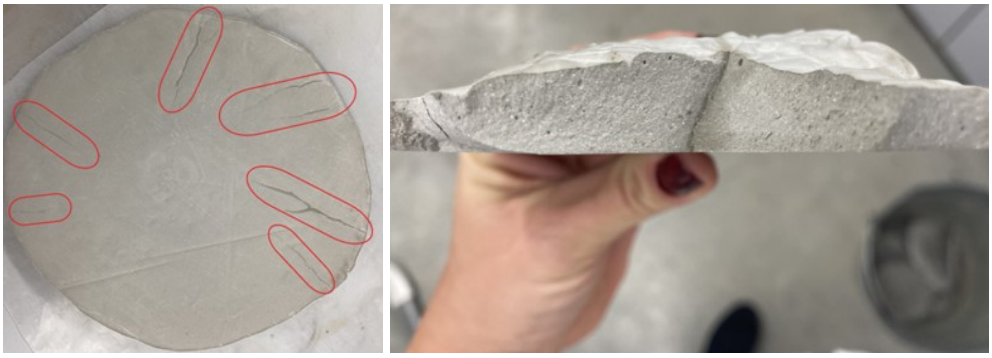


Figure 4: Cracks on the bottom side and extending through the entire sample structure

Probably the most frequent defect of the test specimens across the individual groups was the occurrence of wrinkles, predominantly radial. After the completion of testing and subsequent moistening with water for control, microcracks, cracks or a network of cracks were found on the samples, with some extending through the entire height of the cement test sample (Figure 5).

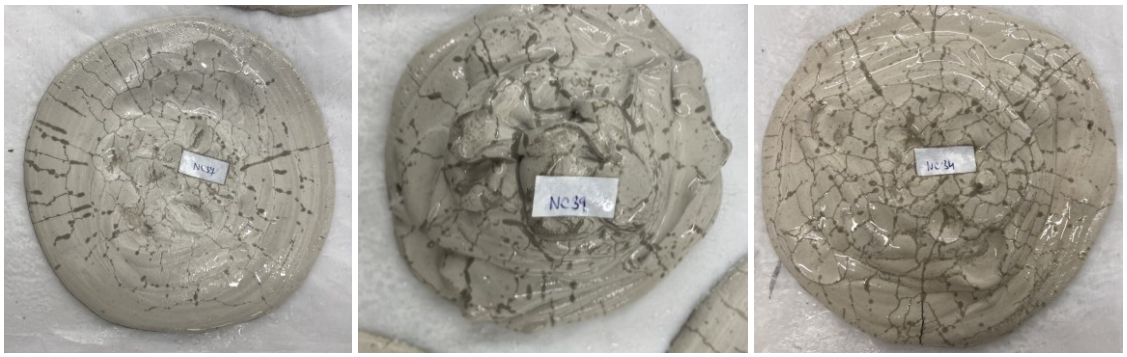


Figure 5: Network of wrinkles/cracks after moistening the samples with water

Another defect observed on the cement samples at 24 hours of age was the presence of surface crystals, which subsequently spontaneously disappeared after a few days, even under laboratory conditions (at 20°C and 50% relative humidity). There was a strong

https://doi.org/10.5593/sgem2024/6.1/s26.35

tendency for segregation of cement components in most samples (Figure 6). Segregation is more pronounced at higher water/cement ratios w=0.50 and above. In extreme cases, it was a full-body segregation of the test samples.



Figure 6: Surface crystals and segregation of cement components

CONCLUSION

Laboratory testing of current cements for initial volume stability found that the certain cement components exacerbate water sensitivity. Consequently, the test samples prepared from these cements exhibit higher values of spreading. This is likely to place higher demands on the accuracy of water dosing at the mixing units, the production, transport and compaction of the concrete mix. These prospects are not good for road construction.

In the course of long-term laboratory testing using the initial volume stability test method, new defects occurred in the new cements analysed. The new cements containing slag exhibited the smallest differences in volume stability compared to their previous behaviour, while the cements containing limestone showed the largest differences. An unexpected problem arose from the inhomogeneity observed in some of the new cements, even within the delivered sample, where the components partially segregated even in the bulk state during handling the packaging. For this reason, it will be necessary to check the quality of the delivered cement more rigorously and frequently in the future.

One of the new defects observed was the formation of temporary surface crystals. They are typically formed 24 to 48 hours after the samples are prepared. With a few exceptions, these crystals disappeared spontaneously even under dry laboratory conditions within 3 to 8 days. Further investigation into the potential complications caused by these crystals will require more detailed laboratory testing.

In new cements, two main processes related to volume instability occur in parallel between the mixing time and the cumulative age of 14 days. The first is the initial hydration of the clinker minerals, the second includes a range of physical reactions caused by the additives. These physical processes are most commonly visually manifested on the samples by the alternating formation and closing of thin hairline cracks. This behaviour has been observed in many cements and at different water/cement ratios. With a few exceptions, the cracks formed within 24 hours and gradually closed so that when the sample was 14 days old, they were only visible after the surface was wetted. The behaviour of these cracks in samples aged over 14 days has not been monitored. The occurrence and frequency of wide cracks (more than 0.2 mm)

are reduced at the expense of an increase in the frequency of thin and hairline cracks, or the surface netting.

The effect of utilising admixtures and additives to enhance volume stability varied, yielding success in some cases and not in others. In the search for additives and admixtures for cements, it became clear that each cement had to be treated individually. No general dependency was found either on the cement class or on the current standard marking of cements. Moreover, for certain cements, only a narrow dosing range of additives and admixtures proved effective, as both higher and lower doses reduced or even eliminated the enhancement achieved in volume stability of the samples. In general, the use of cement additives and admixtures tends to slightly reduce spreading of cement pastes.

The increased tendency for segregation of the cement components is another problem concerning the new cements. It is manifested on the surface by the contrasting colour distribution of dark and light areas. Segregation is most evident at higher water/cement ratios. In concrete, therefore, a tendency for the lighter components to leach out of the cements cannot be ruled out. It is essential to address this issue, and it is recommended to produce concrete in a manner that excludes (minimises) this phenomenon.

The most common defects observed on the surface of samples made of new cement include the appearance of wrinkles, mostly radial. These apparently closed wrinkles represent de facto future open cracks. Clear evidence of the possible existence of a crack is often only conclusive after slightly wetting the surface of the sample with water; according to [7], this can be done only after the initial volume stability test is completed. Wrinkles on the surface of cement samples pose a risk in terms of potential material disintegration.

In some cases, the quality of the cement was found to vary even within the same package. It has been found and verified that the properties of current cements with regard to initial volume stability can be optimised by suitable additives or admixtures. However, a certain consistency of individual cement production batches needs to be preserved and maintained. To verify the consistency of the production of individual cement batches, presented non-standard initial volume stability test can be used as a simple and technologically uncomplicated method of verifying the initial volume stability of cements.

In conclusion, laboratory testing of current cement types focusing on initial volume stability has revealed that the new cements behave differently in the non-standard initial volume stability test compared to the behaviour of the old (previously used) cements. Today, simply knowing a particular cement marking does not provide a universally valid indication of the defects and failures observed in this test. Laboratory testing of cements in terms of initial volume stability has shown that the real properties and behaviour of cement cannot be universally predicted solely from knowledge of the specific cement marking.

ACKNOWLEDGEMENTS

This article was produced with the financial support of the Ministry of Transport within the programme of long-term conceptual development of research institutions.

https://doi.org/10.5593/sgem2024/6.1/s26.35

REFERENCES

[1] Zhutovsky, S.; Kovler, S. Chemical shrinkage of high-strength/high-performance cementitious materials. Int. Rev. Civ. Eng. 2010, 1, 110–118.

[2] Charron, J.P.; Marchand, J.; Bissonnette, B. Early-age deformations of hydrating cement systems: Comparison of linear and volumetric shrinkage measurements. In Proceedings of the International Conference on Early Age Cracking in Cementitious Systems (EAC'01); Bentur, A., Ed.; RILEM Publications: Haifa, Israel, 12 March 2001

[3] Hammer, T.; Heese, C. Early age chemical shrinkage and autogenous deformation of cement pastes. In Proceedings of the 2nd International Research Seminar on Self-Desiccation and Its Importance in Concrete Technology; Persson, B., Fagerlund, G., Eds.; Lund University: Lund, Sweden, 1999; pp. 7–13.

[4] Nevosád, Z.: Aggresive external Conditions and Durability of Concrete, Failures of concrete structures, RILEM, Štrbské Pleso, 1993.

[5] Nevosád, Z., Chupík, V.: Cold recycling of pavement, X. seminár Ivana Poliačka, ISBN 80-969365-3-0, Slovenská cestná spoločnosť a Stavebná fakulta STU Bratislava, 2005, str. 121-127.

[6] Nevosád, Z.: Development of secondary admixed cements with increased volume stability, BETÓN 2019, ISBN 978-80-8076-138-7, str.81-87, JAGA GROUP, s.r.o. Bratislava, Vysoké Tatry – Štrbské Pleso, 2019.

[7] Grošek, J. Nevosád, Z., Dohnálková, B., Zavřel, T., Methodology for testing the volume stability of hydraulic binders. 2023. Certified methodology UDS_223, Transport Research Centre, v.v.i.

FLUOROGRAPHENE-DOPED MAGNESIUM OXYCHLORIDE CEMENT COMPOSITES FOR CONSTRUCTION

Ing. Martina Záleská, Ph.D.[1, 2]

prof. Ing. Milena Pavlíková, Ph.D.[1]

Ing. Adam Pivák, Ph.D.[1]

prof. Ing. Zbyšek Pavlík, Ph.D.[1]

prof. Ing. Ondřej Jankovský, Ph.D.[2]

[1]Department of Materials Engineering and Chemistry, Faculty of Civil Engineering, Czech Technical University in Prague, **Czech Republic**
[2]Department of Inorganic Chemistry, Faculty of Chemical Technology, University of Chemistry and Technology, **Czech Republic**

ABSTRACT

In addition to excellent mechanical, physical and chemical parameters, magnesium oxychloride cement (MOC) composites offer numerous environmental benefits, particularly with regard to the necessary reduction of carbon dioxide emissions associated with the production of Portland cement based building materials. However, the limitation to the wider use of MOC is its low water resistance. Therefore, the possibility of improving the water resistance of magnesium oxychloride cement (MOC) composites by nano-adjustment using fluorographene (FG) was the subject of the research presented. A tannic acid (TA)-based surfactant was used to uniformly disperse the FG particles. The effect of FG added at the dosage of 0.2% and 0.5% by weight of the MOC binder in the MOC mixture was investigated and characterized by the assessment of the mechanical, basic structural and microstructural properties of the hardened composites. Particular attention was paid to the analysis of water resistance, for which the hygric parameters and the softening coefficient were measured after immersing the samples in water for 24 hours.

The results obtained showed that FG in the amount of 0.2 wt% of the binder improved the water resistance, while 0.5 wt% of FG in the MOC binder gave results comparable to those of the reference sample. Since FG-doped MOC composites retained the excellent mechanical and structural parameters of MOC, the improvement in water resistance may enable them to more widely exploit their advanced properties and eco-efficiency in construction practice.

Keywords: magnesium oxychloride cement, fluorographene, construction industry, water resistance

INTRODUCTION

In order to achieve the climate-neutrality objective set out in the European Climate Law, the binding European Union 2030 climate target shall be a domestic reduction of net greenhouse gas emissions by at least 55 % by 2030 compared to 1990 levels [1]. The cement industry is one of the largest CO_2 emitting sectors of the economy, with the

https://doi.org/10.5593/sgem2024/6.1/s26.36

direct CO_2 emissions intensity of cement production remaining broadly stable over the last five years and estimated to increase slightly in a near future [2]. Therefore, the development of new low-carbon materials will be necessary in order to reduce CO_2 emissions. Magnesium oxychloride cement (MOC) is one of the most promising alternatives to Portland cement due to its low carbon footprint, ability to sequestrate CO_2 from the atmosphere over its service life, and excellent performance [3, 4].

MOC is an air setting binder consisting of magnesium oxide (MgO), magnesium chloride ($MgCl_2$) and water. The main hydration products, Phase 5 ($5Mg(OH)_2 \cdot MgCl_2 \cdot 8H_2O$) and Phase 3 ($3Mg(OH)_2 \cdot MgCl_2 \cdot 8H_2O$), determine the high strength of this material. MOC's outstanding properties include rapid setting, excellent bonding to a wide range of aggregates, fire, corrosion and abrasion resistance [5, 6]. Common MOC applications are industrial flooring, fire protection and lightweight panels. However, in contact with water, Phase 5 and Phase 3 decompose into $Mg(OH)_2$, which is linked to a reduction in mechanical properties. As a result, due to the poor water resistance of MOC, its general application is limited to the indoor environment [7, 8]. Various additives are currently being investigated to improve the water resistance of MOC, including fly ash, silica-fume, foamed glass, phosphate and carbon-based nanomaterials [5-9].

One of the carbon-based nanomaterials is fluorographene (FG), a two-dimensional (2D) stoichiometric graphene derivate with exceptional physical and chemical properties. FG is an inert material characterized by chemical stability in various solvents, high hydrophobicity and thermal stability (with beginning of decomposition between 300-400°C). Due to its hydrophobic surface properties, FG has been employed in anti-corrosion and self-cleaning coatings, as well as in analytical and environmental processes [10]. Hydrophobicity, a desired property to increase the water resistance of MOC, is nevertheless a limiting factor for the uniform dispersion of FG in the MOC binder. As a surfactant for the homogeneous dispersion of the applied carbon-based nanoadditives, tannic acid (TA) has been successfully used in previous studies [9, 11].

This study was carried out to evaluate the effect of fluorgraphene added at 0.2 and 0.5 wt% to the MOC binder, together with a tannic acid surfactant, on the properties of MOC-based composites. The series of tests included the determination of basic structural, microstructural and mechanical properties. The water resistance assessment consisted of measuring water absorption at atmospheric pressure and the examination of the softening coefficient after 24 hours of exposure to water.

EXPERIMENTAL

The MOC composites were produced using MgO (p.a. purity, Penta, Czech Republic) and $MgCl_2 \cdot 6H_2O$ (p.a. purity, Lachner, Czech Republic). Three fractions of silica sand (Filtrační písky, Ltd., Czech Republic) with grain sizes of 0-0.5 mm, 0.5-1.0 mm and 1.0-2.0 mm in a weight ratio of 1:1:1 were used as filler. Fluorographene (Industrial Fluorinated Graphene, ACS Material, LLC, USA) was applied at 0.2% and 0.5% by weight of the MOC binder. Tannic acid (TA) (Carl Roth GmbH+Co. KG, Germany) was added as a surfactant to ensure homogeneous dispersion of the FG particles in the MOC binder; the dosage was 0.2% by weight of MOC. The formulation of the MOC composites is shown in Table 1. The prepared materials were named MOC-REF (MOC binder with TA), MOC-FG-0.2 (MOC binder with TA and 0.2 wt% FG), and MOC-FG-0.5 (MOC binder with TA and 0.5 wt% FG).

Table 1: Formulation of studied composites

Material	m [g]					
	MgO	$MgCl_2 \cdot 6H_2O$	Sand	FG	TA	Water
MOC-REF	532.4	537.1	1597.2	0	2.8	333.2
MOC-FG-0.2	532.4	537.1	1597.2	2.8	2.8	333.2
MOC-FG-0.5	532.4	537.1	1597.2	7.0	2.8	333.2

In the preparation of MOC composites, the first step consisted of mixing the $MgCl_2$ solution with TA or TA+FG using a mechanical rotor-stator homogenizer Ultra-Turax T-18 (IKA, Germany) for 5 min at 20,000 rpm. This prepared solution was then mixed with the MgO powder and silica sand in a planetary-type mortar mixer. The fresh mixtures were poured into 40 × 40 × 160 mm prismatic moulds and air cured for 28 days under laboratory conditions. Manufactured composites are shown in Figure 1.



Figure 1: 28-day samples: MOC-REF, MOC-FG-0.2, MOC-FG-0.5 (from left)

Among the basic structural properties, bulk density ρ_b [kg/m^3], specific density ρ_s [kg/m^3] and total open porosity Ψ [%] were determined. Bulk density was measured on the gravimetric principle following EN 1015-10 [12]. Specific density was obtained using a Pycnomatic ATC helium pycnometer (Thermo Scientific). Prior to measurement, the MOC composite samples were first dried in a vacuum drier at 60 °C. Based on the knowledge of the bulk and specific density values, the total open porosity was obtained. The relative expanded uncertainty of porosity determination was 2 %, that of bulk density 1.4 %, and 1.2 % for the specific density.

Mercury intrusion porosimetry (MIP) was used to investigate the microstructural parameters of the prepared MOC composites using a set of Pascal series porosimeters (Pascal 140 and Pascal 440, Thermo Fisher Scientific).

https://doi.org/10.5593/sgem2024/6.1/s26.36

Compressive and flexural strength were tested according to EN 1015-11 [13]. The 40 × 40 × 160 mm prismatic samples were used to measure the flexural strength f_f [MPa]. For the evaluation of the compressive strength f_{c0} [MPa], the sample fragments from the flexural test were used. The loading area in the uniaxial compressive strength test was 40 mm × 40 mm. The Vikasonic apparatus (Schleinbinger Geräte, Germany) was used to determine the dynamic Young's modulus E_d [GPa] in the ultrasonic velocity test. The expanded combined uncertainty was 1.4% for both strength tests and 2.3% for the ultrasonic velocity test.

The influence of fluorographene on the water resistance of the modified MOC composites was evaluated in terms of the softening coefficient α_{24} [%] and the 24-h water absorption W_{a24} [%] measurement. W_{a24} was determined by immersing samples in water at atmospheric pressure in accordance with EN 13755 [14]. The expanded combined uncertainty of W_{a24} assessment was 1.2%, and 2.0% for α_{24}. The softening coefficient α_{24} was calculated using equation (1)

$$\alpha_{24} = \frac{f_{c24}}{f_{c0}} \cdot 100, \tag{1}$$

where f_{c24} is the compressive strength of 28 days air cured samples then immersed in water for 24 hours [MPa] and f_{c0} is the compressive strength of 28 days air cured samples [MPa].

RESULTS AND DISCUSSION

As shown in Table 2, FG at 0.2 wt% slightly increased both bulk and specific densities and decreased total open porosity compared to the reference sample, while FG at 0.5 wt% had the opposite effect. This can probably be attributed to the fact that the applied dosage of 0.5 wt% was already too high and that an uneven dispersion of this highly hydrophobic material could occur.

Table 2: Basic structural parameters of MOC composites

Material	Bulk density [kg/m^3]	Specific density [kg/m^3]	Total open porosity [%]
MOC-REF	2022.0 ± 28	2263.1 ± 27	10.7 ± 0.2
MOC-FG-0.2	2045.2 ± 29	2272.5 ± 27	10.0 ± 0.2
MOC-FG-0.5	1956.2 ± 27	2242.2 ± 27	12.8 ± 0.3

From the results presented in Table 3 and Figures 2, 3 it is clear that MOC-FG-0.2 exhibits enhanced microstructural parameters in comparison with the MOC-REF sample. The total pore volume and the average pore diameter were reduced by 12.9 % and 30.5 %, respectively. Conversely, in accordance with the basic structural characteristics, the microstructural parameters of the MOC-FG-0.5 were slightly worse than those of the MOC-REF.

Table 3: Microstructural parameters of MOC composites obtained by MIP

Material	Total pore volume [cm^3/g]	Average pore diameter [µm]
MOC-REF	0.0805	0.0246
MOC-FG-0.2	0.0701	0.0171
MOC-FG-0.5	0.1015	0.0255

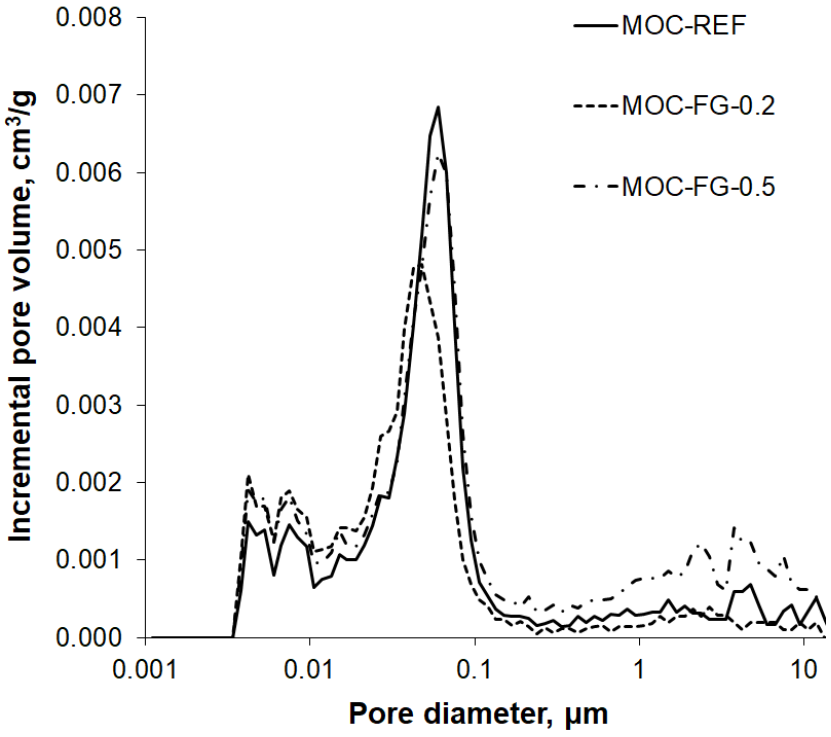


Figure 2: Incremental pore volume distribution of MOC composites

https://doi.org/10.5593/sgem2024/6.1/s26.36

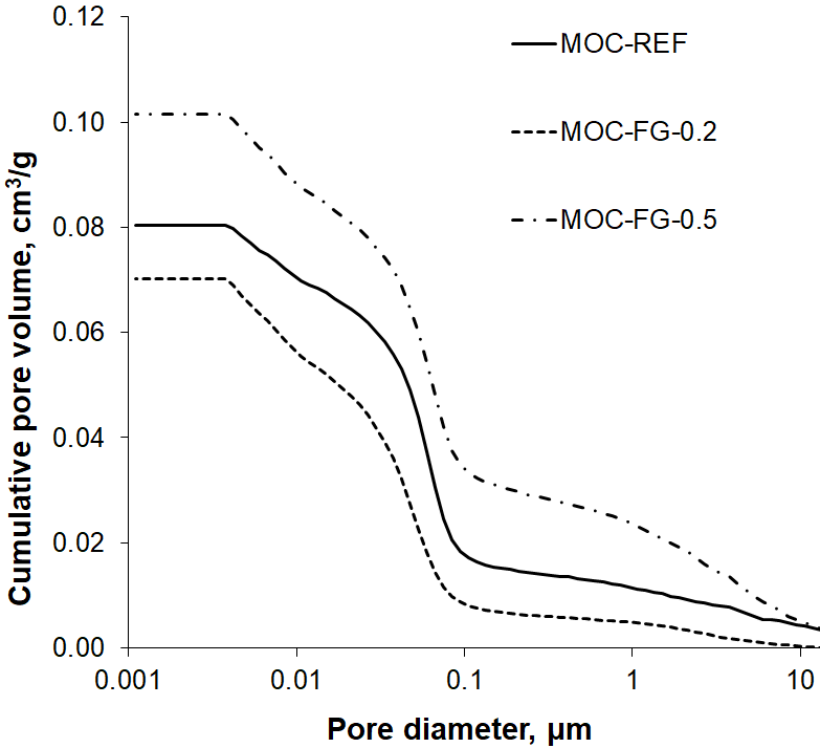


Figure 3: Cumulative pore volume of MOC composites

The compressive and flexural strength, together with the dynamic Young's modulus, are given in Table 4. Generally, it can be stated that all samples possess excellent mechanical parameters. The addition of FG had no effect on the flexural strength and resulted in a slight decrease in the compressive strength and Young's modulus. The compressive strength and the Young's modulus were reduced by 6.0 % and 5.3 % for MOC-FG-0.2 and by 9.6 % and 14.2 % for MOC-FG-0.5 as compared to the MOC-REF sample.

Table 4: Mechanical properties of MOC composites

Material	Compressive strength [MPa]	Flexural strength [MPa]	Young´s modulus [GPa]
MOC-REF	86.6 ± 1.2	23.4 ± 0.3	35.8 ± 0.8
MOC-FG-0.2	81.4 ± 1.1	23.7 ± 0.3	33.9 ± 0.8
MOC-FG-0.5	78.3 ± 1.0	23.4 ± 0.3	30.7 ± 0.7

Table 5 shows the compressive strength of the samples after 24 hours in water, the softening coefficient and the water absorption values. It can be seen that FG at 0.2 wt% had a beneficial effect on both the water absorption and softening coefficient. The enhancement in water resistance achieved can be associated with the improved microstructural parameters of MOC-FG-0.2 and hydrophobicity of FG. However, the higher amount of FG did not affect either the softening coefficient or the water absorption, as is apparent from the comparison of the data obtained for MOC-FG-0.5

and MOC-REF samples. This can mainly be attributed to the overall higher porosity of MOC-FG-0.5.

Table 5: Softening coefficient and water absorption of MOC composites

Material	Compressive strength	Softening coefficient	Water absorption
	f_{c24}	α_{24}	W_{a24}
	[MPa]	[%]	[%]
MOC-REF	53.8 ± 0.8	62.1 ± 1.2	3.42 ± 0.04
MOC-FG-0.2	53.8 ± 0.8	66.1 ± 1.3	3.26 ± 0.04
MOC-FG-0.5	49.1 ± 0.7	62.7 ± 1.3	3.46 ± 0.04

CONCLUSION

In this study, the influence of nano-adjustment using fluorographene together with the tannic acid as surfactant on the basic structural, microstructural, mechanical and water resistance parameters of MOC composites was investigated. The results showed that FG at 0.2 wt% of the MOC binder refined the microstructure in terms of reducing both the total pore volume and the average pore diameter. This, together with the hydrophobic nature of FG, led to an improvement in water resistance compared to the MOC-REF sample, i.e. an increase in the softening coefficient and a reduction in water absorption. The MOC-FG-0.2 composite also showed excellent mechanical and structural parameters. However, the higher FG content of 0.5 wt% resulted in a slight increase in total open porosity and decreased compressive strength, while water resistance was maintained at the same level as the reference. In conclusion, nano-adjustment of MOC with fluorographene is a promising approach to improve its water resistance, which may contribute to widening the range of applications of eco-friendly MOC composites in the building industry. Nevertheless, further studies aimed at the homogeneous distribution of nano-dopant are necessary together with the analysis of the optimal proportion of FG in composite mixture.

ACKNOWLEDGEMENTS

The research was supported by Czech Science Foundation Grant No. 23-05194M - High-strength and water-resistant MOC composites with secondary fillers: contribution of 2D carbon-based nanomaterials and their combinations. The research conducted at CTU Prague was financed by the Grant Agency of the Czech Technical University in Prague, under project No. SGS23/OHK1/3T-002/23 - Research and development of high performance building composites.

REFERENCES

[1] Regulation (EU) 2021/1119 of the European Parliament and of the Council of 30 June 2021 establishing the framework for achieving climate neutrality and amending Regulations (EC) No 401/2009 and (EU) 2018/1999 (‘European Climate Law’).

[2] International Energy Agency. Available online: https://www.iea.org/energy-system/industry/cement#tracking (accessed on 17 January 2024).

https://doi.org/10.5593/sgem2024/6.1/s26.36

[3] Chang Ch., An L., Dong J., Zheng W., Wen J., Yan F., Xiao X., Study on deterioration process of magnesium oxychloride cement under environment of dry-wet cycles, Materials, vol. 16, 1817, 2023.

[4] Aiken T., Russel M., McPolin D., Gavin B., Nugent L., Bagnall L., Effect of molar ratios and curing conditions on the moisture resistance of magnesium oxychloride cement, ASCE Journal of Materials in Civil Engineering, vol. 34, 04021426, 2022.

[5] Guan B., He Z., Wei F., Wang F., Yu J., Effects of fly ash and hexadecyltrimethoxysilane on the compressive properties and water resistance of magnesium oxychloride cement, Polymers, vol. 15, 172, 2023.

[6] Lauermannová A.-M., Jankovský O., Sedmidubský D., Lojka M., Pavlíková M., Pivák A., Záleská M., Pavlík Z., Case study on MOC composites enriched by foamed glass and ground glass waste: Experimental assessment of material properties and performance, Case Studies in Construction Materials, vol. 18, e01836, 2023.

[7] Zhu Y., Li W., Liu W., Yang L., Wang L., A new approach to improving the water resistance of MOC-solidified sludge using HCO_3^- ions, Construction and Building Materials, vol. 401, 132959, 2023.

[8] He P., Poon Ch. S., Tsang D. C. W., Effect of pulverized fuel ash and CO2 curing on the water resistance of magnesium oxychloride cement (MOC), Cement and Concrete Research, vol. 97, pp 115-122, 2017.

[9] Lauermannová A.-M., Jiříčková A., Sedmidubský D., Pavlíková M., Záleská M., Pivák A., Pavlík Z., Jankovský O., Graphene- and MWCNT-reinforced magnesium oxychloride composite modified by tannic acid, FlatChem, vol. 37, 100459, 2023.

[10] Chronopoulos D. D., Bakandritsos A., Pykal M., Zbořil R., Otyepka M., Chemistry, properties, and applications of fluorographene, Applied Materials Today, vol. 9, pp 60-70, 2017.

[11] Zhang X., Liu M., Zhang X., Deng F., Zhou C., Hui J., Liu W., Wei Y., Interaction of tannic acid with carbon nanotubes: enhancement of dispersibility and biocompatibility, Toxicology Research, vol. 4, pp 160-168, 2015.

[12] EN 1015-10 Methods of Test for Mortar for Masonry - Part 10: Determination of Dry Bulk Density of Hardened Mortar, CEN, 1999.

[13] EN 1015-11 Methods of Test for Mortar for Masonry - Part 11: Determination of Flexural and Compressive Strength of Hardened Mortar, CEN, 2019.

[14] EN 13755 Natural stone test methods - Determination of water absorption at atmospheric pressure, CEN, 2008.

FUNCTIONALITY OF TWO-COAT SYSTEM FOR CONCRETE PROTECTION AND REPAIR

Prof. Ing. Zbysek Pavlik, Ph.D.[1]

Ing. Adam Pivak[1]

Prof. Ing. Milena Pavlikova, Ph.D.[1]

[1] Faculty of Civil Engineering, Czech Technical University in Prague, **Czech Republic**

ABSTRACT

This paper presents the experimental evaluation of the effectiveness of a newly developed two-coat system (TCS) for the protection and repair of concrete. The optimized system consists of a penetrating layer of modified low-viscosity resin of BPA (bisphenol A) type and a top coat based on aliphatic polyisocyanate resin of HDI (hexametyl diisocyanate) type. TCS was applied to reference concrete specimens, which were subjected to various tests to evaluate their basic physical properties, mechanical strength, hygric properties, freeze-thaw resistance and resistance to de-icing salts. The application of TCS reduced the porosity, enhanced the freeze-thaw resistance, and greatly decreased the water absorption coefficient and 24-h water absorption. The treated specimens exhibited high resistance to de-icing salt even up to 125 testing cycles. Taking into consideration the fact that the control samples without any surface modification were completely cracked by coupled salt crystallization and freeze-thaw action, the improvement in the properties of treated concrete was quite substantial and promising for full-scale application on construction sites.

Keywords: concrete repair and protection, two-coat system, synthetic epoxy resin, mechanical strength, freeze-thaw resistance, water absorption, de-icing salts scaling

INTRODUCTION

The durability of concrete is one of the key aspects that affect the life and functionality of buildings and structures. Twice as much concrete is used in construction as all other buildings materials together [1]. Concrete properties and durability are influenced by a number of factors, among the most important being the quality of the virgin materials used, the correct ratio of concrete components, proper mixing and processing technology. Subsequent maintenance and protection against adverse environmental factors such as high humidity, excessive moisture, low [2] or elevated temperatures [3], mechanical stresses [4] and chemical influences [5] is also necessary. Good quality concrete should last for tens to hundreds of years, but its actual durability is always influenced by the specific conditions of use and care. It is therefore important to pay attention to all aspects of the production process and application of concrete to ensure that its durability is as high as possible. Problems associated with the durability of concrete structures commonly originate from degradation of the incorporated materials. While the initial deterioration of these materials does not represent an immediate safety risk, it cumulatively generates a potential threat to the integrity of the overall structure.

https://doi.org/10.5593/sgem2024/6.1/s26.37

Repair and rehabilitation of existing damaged concrete structures is one of the most important construction activities worldwide. The finance used to repair damaged structures often exceeds the funds used to build new ones [6]. Given the economic importance of the problem of concrete durability, a number of approaches have been developed to provide better and more durable concrete or reinforced concrete structures. Among them, the use of concrete surface modification as a convenient instrument to protect and improve concrete elements [7,8] has gained considerable popularity in recent years, particularly for its effectiveness in reducing infiltration of aggressive substances from the environment and their consequent harmful action. Several solutions have been developed to protect and repair concrete surface, all of which have their advantages and limitations. Therefore, novel multifunctional materials and their multilayer systems are being sought and investigated. In compliance with the current trend, a new type of two-coat polymer system designed for surface protection and repair of concrete is experimentally tested and its effectiveness evaluated.

MATERIALS & METHODS

The two-coat polymer-based system (TCS) for the protection and repair of concrete was applied to reference concrete specimens (C_{Ref}) made of C30/37 class structural concrete. The optimized system was manufactured by Coming Plus, Inc. (Zlatníky, Czech Republic) and consisted of a penetrating layer of modified low-viscosity resin of BPA (bisphenol A) type and a top coat based on aliphatic polyisocyanate resin of HDI (hexametyl diisocyanate) type. The cast specimens were 150 mm cubes, standard prisms (40/40/160 mm^3) and circular plate specimens 120 mm in diameter and 25 mm thick. Where necessary, samples were cut from the original shapes. The samples with TCS were labelled C_{TCS}. The application of TCS on the surface of concrete specimens is shown together with the cutting of the reference concrete specimen in Figure 1.

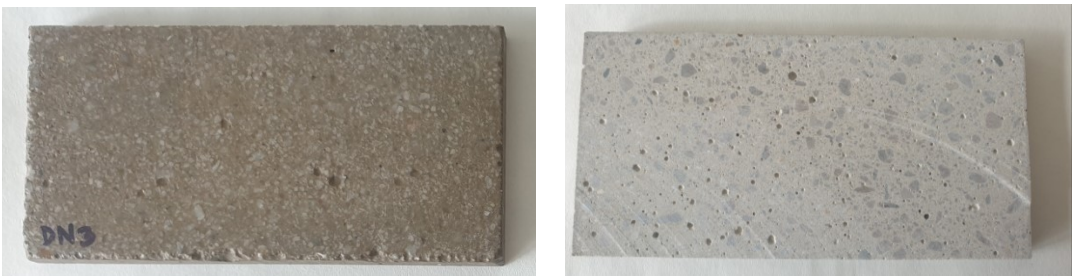


Figure 1: Treated concrete surface (left), reference concrete cut (right)

The experiments and tests performed included the evaluation of the effect of TCS-based surface treatment of concrete on its basic structural, mechanical, hygric and durability properties. The investigated material parameters and the methods and standard used are summarized in Table 1. A total of 100 freeze-thaw cycles were performed and the resulting frost resistance coefficient *k* [%] was calculated as the ratio of the compressive strength of the specimens subjected to freeze-thaw cycles and the control specimens stored freely in the laboratory. The durability assessment in regard to resistance to de-

icing salts was done in accordance with the ČSN 73 1326 [9]. As the de-icing salt, 3% solution of NaCl was used. The storage of samples (40 mm cubes) in an automatic freezing box is shown in Figure 2. The measured data were expressed as a cumulative mass loss per cross section area of a sample exposed to NaCl solution.

Table 1: Measured parameters and applied testing methods

Parameter, property	**Symbol, unit**	**Standard, method**
Specific density	ρ_s [kg·m^{-3}]	helium pycnometry
Dry bulk density	ρ_b [kg·m^{-3}]	EN 12390 -7 [10]
Total open porosity	φ [%]	calculated from ρ_s, ρ_b [11]
Compressive strength	f_c [MPa]	EN 12390-3 [12]
Flexural strength	f_f [MPa]	EN 1015-11 [13]
Dynamic elastic modulus	E_d [GPa]	ultrasonic pulse technique
Water vapor permeability	δ [s]	EN ISO 12572 [14]
water vapor resistance factor	μ [-]	EN ISO 12572 [14]
Water absorption coefficient	A_w [kg·m^{-2}·s$^{-1/2}$]	EN 1015-18 [15]
24-hour water absorption	W_{a24} [kg·m^{-2}]	EN 772-11 [16]
Frost resistance coefficient	k [%]	ČSN 73 1322 [17]
Mass loss	ρ_a [g·m^{-2}]	ČSN 73 1326 [9]



Figure 2: Testing of the resistance to de-icing salts – samples placed in an automatic freezing box

https://doi.org/10.5593/sgem2024/6.1/s26.37

RESULTS & DISCUSSION

The basic physical parameters of the reference concrete and the surface-treated concrete are shown in Table 2. Partial sealing of concrete surface and formation of surface impregnation film resulted in increase of dry bulk density, i.e. decrease of porosity. This is a very promising result in terms of reducing the penetration of moisture and dissolved pollutants into the internal structure of the concrete.

Table 2: Basic physical properties of concrete

Sample	ρ_b [kg·m^{-3}]	ρ_s [kg·m^{-3}]	φ [%]
C_{Ref}	2173 ± 30	2610 ± 31	16.7 ± 0.3
C_{TCS}	2227 ± 31	2575 ± 31	13.5 ± 0.3

The hygric properties of the tested samples are shown in Table 3. Both the values of water absorption coefficient A_w and 24-h water absorption W_{a24} were greatly reduced by the surface modification of concrete. The decrease of A_w was 95.2% and that of W_{a24} was 92.9%, respectively. Based on the changes in hygric performance of the treated concrete samples, the applied TCS can be classified as a waterproofing agent. The ability to transfer water vapor was partially reduced by the coating, but this characteristic is not as important for concrete performance as the liquid moisture parameters. In addition, the increase in water resistance factor was only 10.6%.

Table 3: Hygric properties of concrete

Sample	A_w [kg·m^{-2}·s$^{-1/2}$]	W_{a24} [kg·m^{-2}`]	δ [s]	μ [-]
C_{Ref}	0.021	3.64	2.0E-12	99.6
C_{TCS}	0.001	0.26	1.9E-12	104.9

The values of mechanical parameters and frost resistance coefficient are presented in Table 4. The surface modification improved all the measured mechanical parameters. Similarly, frost resistance was enhanced by TCS as compared to the reference concrete samples. The frost resistance coefficient k was for CTCS samples that underwent 75 and 100 freeze/thaw cycles even higher than 100%.

Table 4: Mechanical parameters and frost resistance coefficient

Sample	f_c [MPa]	f_f [MPa]	E_d [GPa]	Frost resistance coefficient k (%)			
				25 cycles	50 cycles	75 cycles	100 cycles
C_{Ref}	34.4	8.9	31.1	85.2	77.3	82,1	92.3
C_{TCS}	36.4	9.7	36.7	81.5	85.5	101.3	109.1

The resistance to de-icing salt, in our case 3% NaCl solution, is shown in Table 5. After 50 cycles, the reference concrete samples were completely decomposed, as shown in Figure 3. Sealing the concrete surface with TCS greatly improved its resistance to deicing salts. The CTCS samples withstood 125 freeze/thaw cycles while partially immersed in NaCl solution without significant damage and structural degradation. The enhanced resistance to de-icing salts can be used to repair or protect concrete in structures that will be exposed to solutions of de-icing salts used for winter maintenance of roads and pavements during their service life.

Table 5: Resistance to de-icing salts

Sample	**Mass loss ρ_a [g·m^{-2}]**	**Number of cycles**	**Classification of damage**
C_{REF}	-	50	Sample disintegration
C_{TCS}	14.2	125	No visible damage

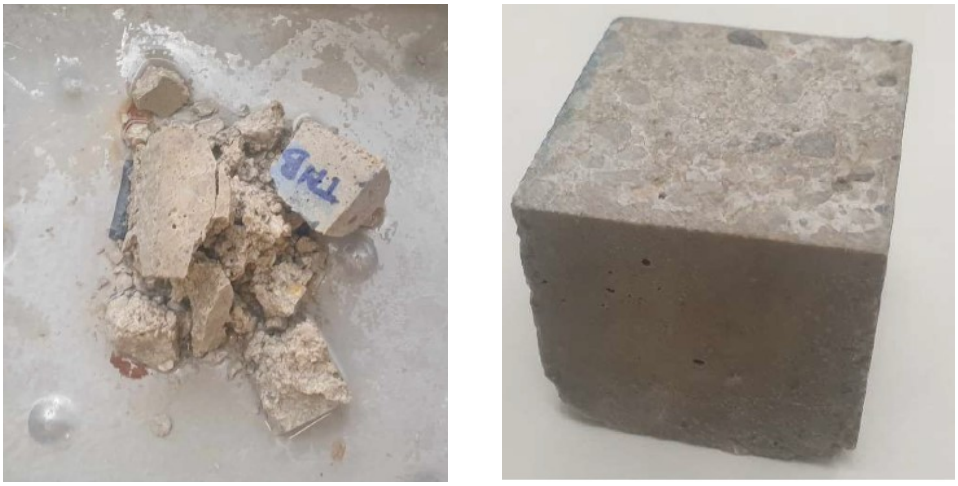


Figure 3: De-icing salt resistance test: Damage of sample C_{Ref} after 25 freeze-thaw cycles (left), sample C_{TCS} after 125 cycles (no apparent damage)

CONCLUSIONS

In this study, two-coat system based on a combination of low-viscosity resin of BPA type and aliphatic polyisocyanate resin of HDI type was tested as a prospective surface treatment of concrete for improving its durability and properties related to ability to withstand harsh conditions and chemically induced damage. The applied TCS formed a surface film on the concrete specimens, which resulted in their decreased porosity, significant reduction in moisture transport and improved resistance to frost and de-icing salts. Since the surface-treated specimens showed excellent durability, increased strength and reduced moisture absorption capacity, the tested TCS can be considered as

https://doi.org/10.5593/sgem2024/6.1/s26.37

an effective and functional modifier of concrete properties, enabling its protection and, if necessary, also the repair of partially cracked concrete.

ACKNOWLEDGEMENTS

Authors greatly acknowledge the financial support received from the Technology Agency of the Czech Republic under project No FW03010256 - Development and research of advanced materials for the protection and repair of concrete structures. The authors are grateful to F. Fára from company Coming Plus, Inc. for preparing and supplying the samples.

REFERENCES

[1] Gagg, C.R., Cement and concrete as an engineering material: An historic appraisal and case study analysis, Engineering Failure Analysis, vol. 40, pp. 114-140, 2014.

[2] Yang, W., Liu, L., Wu, W., Zhang, K., Xiong, X., Li, C., Huang, Y., Zhang, X., Zhou, H., A review of the mechanical properties and durability of basalt fiber recycled concrete, Construction and Building Materials, vol. 418, 134882, 2024.

[3] Li, Q., Li, H., Liang, T., Effect of non-intumescent fireproof coating on the durability of concrete exposed to elevated temperature, Construction and Building Materials, vol. 404, 133211, 2023.

[4] Ma, D., Zhang, M., Cui, J., A review on the deterioration of mechanical and durability performance of marine-concrete under the scouring action, Journal of Building Engineering, vol. 66, 105924, 2023.

[5] Zhao, G., Shi, M., Fan, H., Cui, J., Xie, F., The influence of multiple combined chemical attack on cast-in-situ concrete: Deformation, mechanical development and mechanisms, Construction and Building Materials, vol. 251, 118988, 2020.

[6] Ma, C.-K., Apandi, N.M., Sofrie, C.S.Y., Ng, J.H., Lo, W.H., Awang, A.Z., Omar, W., Repair and rehabilitation of concrete structures using confinement: A review, Construction and Building Materials, vol. 133, pp. 502-515, 2017.

[7] W. Yu, Z. Wenhua, W. Peipei, P. Yilin, Z. Yunsheng, Study on preparation and strengthening mechanism of new surface treatment agent of concrete at multi-scale, Construction and Building Materials, vol. 346, 128404, 2022.

[8] T. Kudo, K. Komatsu, A. Nakamura, O. Ito, A. Suzuki, M. Yamamura, T. Shimomura, H. Saitoh, Sealing of near-surface voids on cement concretes by combined application of metal-ethylenediaminetetraacetic acid complex solutions and high-heat treatment via hydrogen/oxygen coupled flame, Construction and Building Materials, vol. 301, 124029, 2021.

[9] ČSN 73 1326 – Determination of the resistance of the surface of cement concrete to the action of water and chemical de-icing agents, ÚNM, Prague, Czech Republic, 1984 (in Czech).

[10] EN 12390-7, Testing hardened concrete – Part 7: Density of hardened concrete, European Committee for Standardization (CEN), Brussels, Belgium, 2019.

[11] M. Záleská, M. Pavlíková, J. Pokorný, O. Jankovský, Z. Pavlík, R. Černý, Structural, mechanical and hygrothermal properties of lightweight concrete based on the application of waste plastics, Construction and Building Materials, vol. 180, pp. 1-11, 2018.

[12] EN 12390-3, Testing hardened concrete – Part 3: Compressive strength of test specimens, European Committee for Standardization (CEN), Brussels, Belgium, 2019.

[13] EN 1015-11, Methods of test for mortar for masonry – Part 11: Determination of flexural and compressive strength of hardened mortar, European Committee for Standardization (CEN), Brussels, Belgium, 2019.

[14] EN ISO 12572, Hygrothermal performance of building materials and products – Determination of water vapour transmission properties – Cup method, ISO, Geneva, 2016.

[15] EN 1015-18, Methods of Test for Mortar for Masonry – Part 18: Determination of Water Absorption Coefficient Due to Capillarity Action of Hardened Mortar, European Committee for Standardization (CEN), Brussels, Belgium, 2002.

[16] EN 772-11, Methods of test for masonry units – Part 11: Determination of water absorption of aggregate concrete, manufactured stone and natural stone masonry units due to capillary action and the initial rate of water absorption of clay masonry units, European Committee for Standardization (CEN), Brussels, Belgium, 2011.

[17] ČSN 73 1322, Determination of frost resistance of concrete, CNI, Prague, 1969 (in Czech).

https://doi.org/10.5593/sgem2024/6.1/s26.37

IMMOBILISATION OF HEAVY METALS IN FLY ASH-DIATOMITE MODIFIED MAGNESIA CEMENT COMPOSITE

Ing. Adam Pivak[1]

prof. Ing. Milena Pavlikova, Ph.D.[1]

Ing. Martina Zaleska, Ph.D. [1]

assoc. prof. Mgr. Jana Nabelkova, Ph.D.[1]

prof. Ing. Zbysek Pavlik, Ph.D.[1]

[1]Department of Materials Engineering and Chemistry, Faculty of Civil Engineering, Czech Technical University in Prague, **Czech Republic**

ABSTRACT

Every day, human activities generate large amounts of solid waste. To ensure the quality of the environment, waste must be further treated to prevent it from accumulation in landfills. In the case of materials that cannot be recycled or reused, such as municipal solid waste, burning in waste incineration plants to generate heat or electricity appears to be the appropriate solution of such waste disposal. However, combustion processes generate residues, such as bottom or fly ash, which must be stored. Fly ash generally contains heavy metals and other contaminants. If it is disposed in landfills, the contained substances may pollute the environment with dust, leach into the soil, and contaminate the groundwater. Therefore, it is important to find an alternative way to dispose fly ash, such as incorporation into building materials, which must provide sufficient and save immobilisation of heavy metals. The objective of the presented research was to utilize fly ash from waste incineration plant and diatomaceous earth in magnesia-based composites in the form of microfillers. The investigation focused on the determination of the material properties of the hardened composites with emphasis on the ability to immobilise heavy metals. Incorporation of fly ash and diatomaceous earth resulted in increased porosity and water absorption. The mechanical strength was also affected and reduced by the incorporation of both microfillers. On the other hand, the immobilisation test showed that the heavy metals contained in the fly ash were safely immobilised in the material and thus they are not able to be further released into the environment. In this way, hazardous waste can be safely treated and reused, and the amount of waste in landfills can be reduced.

Keywords: municipal waste disposal, fly ash, heavy metals, leaching, diatomite, magnesium composite

INTRODUCTION

Due to human activity, a large amount of municipal solid waste (MSW), i.e., household, institution, and industry waste, is produced [1]. According to UNEP [2], more than 2 kg of MSW is produced daily per person in North America. The development and improvement of living conditions and the predicted growth of population makes MSW management a difficult challenge due to increasing costs, complexity of waste materials and strict legislation on their disposal [1, 3]. An appropriate MSW disposal method, so

https://doi.org/10.5593/sgem2024/6.1/s26.38

that it is not deposited in a landfill, is burning in waste incineration plants to generate heat or electricity.

Although energy recovery is one of the optimal methods for MSW treatment, which significantly reduces the waste volume by up to 90 % [4], this method also has certain limitations. There is the incineration risk that the residues will contain environmentally toxic substances, such as heavy metals (HMs). When this waste is landfilled, heavy metals can be released into the soil, air, or groundwater, which can affect soil quality, flora and pose a potential health hazard to humans [5]. Therefore, it is essential to study alternative and sustainable strategies for the management of this type of waste. One of the ways to prevent the release of HMs is to immobilise them in the matrix of composite material, for example, cement-based [6, 7]. Such materials can be disposed of in landfill or further utilised, while heavy metals are chemically sealed within the material matrix, and their release is hindered.

Magnesium-potassium-phosphate cement (MKPC), a composite that is formed by the reaction of dead-burned magnesite (calcined at 1500-2000 °C) and potassium phosphate [8]. It is considered to have suitable properties to immobilise heavy metals. The advantages of MPC include rapid solidification and increased strength even at very low temperatures, fire resistance, low shrinkage, or the ability to stabilise toxic compounds and nuclear wastes. It also has the advantage of absorbing atmospheric CO_2, so it is considered an alternative to Portland cement composites with lover environmental impact [9].

This study investigates MKPC-based composite materials modified with fly ash, coming from incineration of MSW and containing heavy metals, and diatomite. The primary objective of this research is to evaluate the characteristics of the hardened composites, namely structural properties, and mechanical resistance. The combined use of MKPC, fly ash, and diatomite as a sorbent has the potential to create a novel composite material with valuable properties for the construction industry capable to solidify and immobilise HMs.

EXPERIMENTAL

Three type of composites were prepared and tested. Samples were composed of dead burned MgO (Slovenské magnezitové závody a.s., Jelšava, Slovak Republic) mixed with tap water, monopotassium phosphate, borax (LachNer, s.r.o., Czech Republic) which was used as retarding admixture, and silica sand (Filtrační písky s.r.o., Chlum u Doks, Czech Republic). Silica sand was combined from three size fractions (PG1, PG2 and PG3) in a weight ratio of 1:1:1 with a total fraction of 0/2 mm. The modifications were carried out by adding fly ash from the municipal waste incineration plant as a source of heavy metals and diatomite that served as a sorbent with high specific surface area (2095 $m^2 \cdot kg^{-1}$). The use diatomite was a product of LB Minerals, s.r.o., Czech Republic. The content of selected heavy metals (Cr, Cu, and Zn) in fly ash, determined by an atomic absorption spectroscopy (AAS), is shown in Table 1.

Table 1: AAS analysis of selected heavy metal contents in studied fly ash.

Substance	Cr	Cu	Zn
Content ($mg \cdot kg^{-1}_{solid}$)	92.7	538.7	6616.5

The chemical composition of MgO, fly ash, and diatomite obtained by X-ray fluorescence analysis (EDXRF spectrometer, ARL QUANT'X, Thermo Scientific) is listed in Table 2.

Table 2: The chemical composition of MgO, Fly ash and diatomite.

Material	SiO_2	CaO	Al_2O_3	Fe_2O_3	MgO	K_2O	SO_3	Na_2O	K_2O	Cl
					(mass %)					
MgO	0.8	2.5	4.9	8.2	82.6	0.1	0.2	0.3	0.1	-
Fly ash	2.7	48.8	3.2	1.6	0.9	3.5	12.9	5.1	3.5	18.3
Diatomite	81.7	0.2	13.8	1.6	0.9	1.0	0.1	-	0.6	-

The reference mixture (REF) was composed of MgO paste with silica sand only. Mixtures modified with the addition of 20 wt.% of fly ash (calculated as 20% weight ratio of MgO+KH_2PO_4) and combination of fly ash and diatomite (in total 20 wt.%) were labelled as FA and FA/D, respectively. The composition of all studied composites is listed in Table 3.

Table 3: Composition of studied mixtures.

Mixture	composition in ($kg \cdot m^{-3}$)						
	MgO	KH_2PO_4	Sand	H_2O	Borax	Fly ash	Diatomite
REF	762	265	895	269	45	-	-
FA	762	265	895	347	45	180	
FA/D	762	265	895	347	45	90	90

All samples were cast into plastic moulds (40 mm × 40 mm × 160 mm) and left to harden for 24 hours in a laboratory conditions (T = 21 ± 2 °C, RH = 35 ± 5 %). Then were the samples demoulded and cured for another 27 days under the same conditions. Given that the presence of HMs and their potential release into the environment makes the treatment of this waste a significant challenge, the structural characteristics, resistance to mechanical loading and concentration of the heavy metals leached from the hardened composites were investigated (Figure 1) in accordance to EN 1015-10 [10], EN 1015-11 [11] and EN 13657 [12], respectively. Summary of all performed tests including their expanded combined uncertainties (where available) is listed in Table 4.

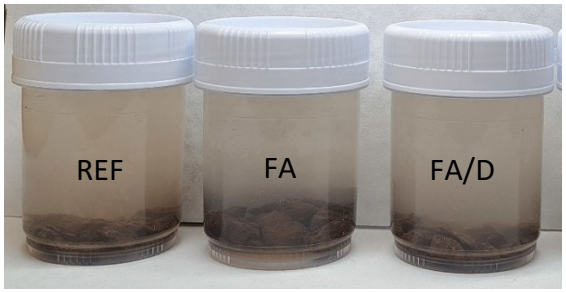


Figure 1: Leaching of HMs from the prepared composites: samples REF, FA, FA/D (from left).

https://doi.org/10.5593/sgem2024/6.1/s26.38

Table 4: List of tests performed for 28-days cured samples.

Measured characteristic	Method	Units	Instrument	Expanded combined uncertainty	Methodology according to standard
Bulk density	Gravimetry	$kg \cdot m^{-3}$	-	1.4 %	EN 1015-10 [10]
Specific density	Helium pycnometry	$kg \cdot m^{-3}$	Pycnomatic ATC	1.2 %	-
Porosity	Mercury intrusion porosimetry	%	Pascal 140+440	-	-
Pore diameter	Mercury intrusion porosimetry	µm	Pascal 140+440	-	-
Flexural strength	Three-point bending test	MPa	Heckert PF 100	1.4 %	EN 1015-11 [11]
Compressive strength	Uniaxial strength test	MPa	Heckert PF 100	1.4 %	EN 1015-11 [11]
Elasticity modulus	Ultrasonic pulse velocity	GPa	Vikasonic	2.3 %	-
Heavy metal content	Atomic absorption spectroscopy	mg/kg solid	Agilent 280FS AA		EN 13657 [12]

RESULTS AND DISCUSSION

The basic structural characteristics of the hardened composites are shown in Table 5. The addition of fly ash and the combination of fly ash and diatomite resulted in increased porosity, while the specific density remained basically intact. The highest increase in porosity (by 7 %) was recorded when mortar was modified with fly ash alone, while fly ash combined with diatomite increased porosity by nearly 6 %.

Table 5: Basic structural characteristics of studied composites.

Mixture	Bulk density ($kg \cdot m^{-3}$)	Specific density ($kg \cdot m^{-3}$)	Porosity (%)	Average pore diameter (µm)
REF	2102 ± 25	2776 ± 33	21.1 ± 0.40	0.025
FA	1926 ± 23	2792 ± 33	29.1 ± 0.06	0.048
FA/D	1830 ± 22	2776 ± 33	26.9 ± 0.05	0.043

Moreover, the addition of both fly ash and diatomite also affected the pore size distribution. As shown in Figure 2, the highest pore volume of REF sample was in the range from 0.005 µm to 0.01 µm. There is also a sign of pores with diameter around 4 µm. Both modifications affected the pore diameter at lower diameter range and resulted

in increase of the pores with diameter greater than 0.1 μm, which may influence the mechanical strength of the mixtures.

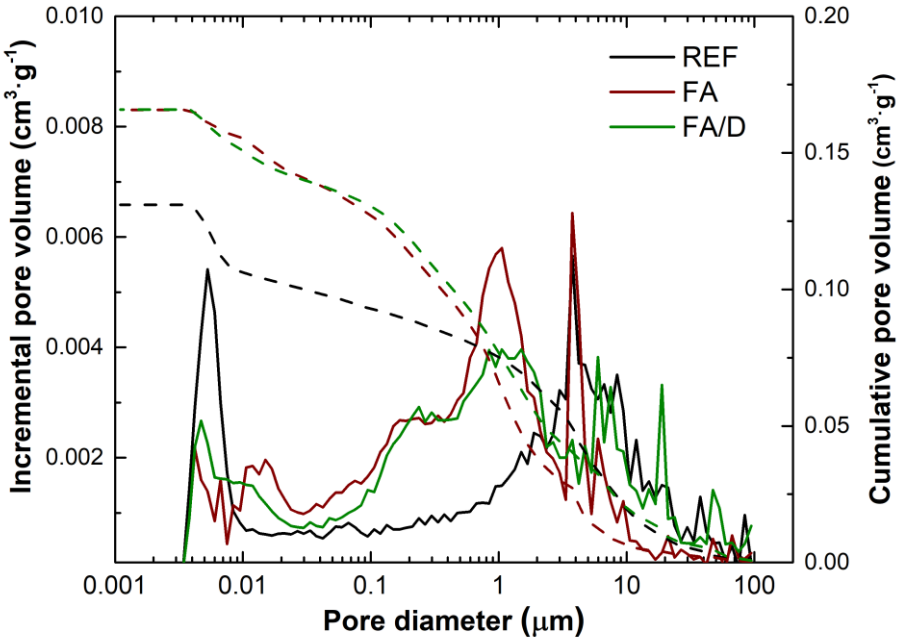


Figure 2: Pore volume of tested samples.

The results of mechanical parameters measurement (Table 6) show that the addition of fly ash or blend of fly ash and diatomite significantly dropped all mechanical parameters tested. Flexural strength was reduced by 40 % for FA composite. The composite with mixture of FA/D exhibited the flexural strength value of 3.99 MPa, less than half of the initial control value.

On the other hand, the lowest compressive strength was observed for the FA sample (by 72 %). The compressive strength of FA/D was lower by 59 %. It should be noted that the amount of the used admixtures was relatively high compared to the amount of MgO used. Studies investigating the possibilities of fly ash application in MKPC composites [13, 14] conclude that the reduction in strength is due to the lower amount of precipitated products, which are the main bearer of the composite strength.

Although the fly ash acts only as a microfiller, its admixing may have caused the absorption of part of the mixing water, affecting the hydration of MKPC. In combination with the increased porosity of the FA and FA/D composites, this also resulted in a reduction in their overall mechanical strength.

https://doi.org/10.5593/sgem2024/6.1/s26.38

Table 6: Mechanical characteristics of studied mortars.

Mixture	Flexural strength (MPa)	Compressive strength (MPa)	Young's modulus (GPa)
REF	7.95 ± 0.11	38.56 ± 0.54	12.82 ± 0.29
FA	4.79 ± 0.07	10.92 ± 0.15	6.82 ± 0.16
FA/D	3.99 ± 0.06	16.11 ± 0.23	6.29 ± 0.15

As can be seen in Figure 2, the maximum leachable concentrations of chromium, copper, and especially zinc reaches relatively high values. By applying the fly ash to the MKPC composite, the leaching of these specific heavy metals investigated was almost prevented. Comparing the resulting concentrations with, for example, the regulation on waste management of the Czech Republic, i.e., Regulation No. 273/2021 [15], fly ash studied is not suitable for engineering purposes such as landscaping, backfilling, or landfilling. On the other hand, the concentrations of HMs in the leachates from the hardened MKPC-based composites were safely bellow limit values. The obtained results thus clearly demonstrate the suitability of this type of composite material for immobilisation and stabilisation of HMs.

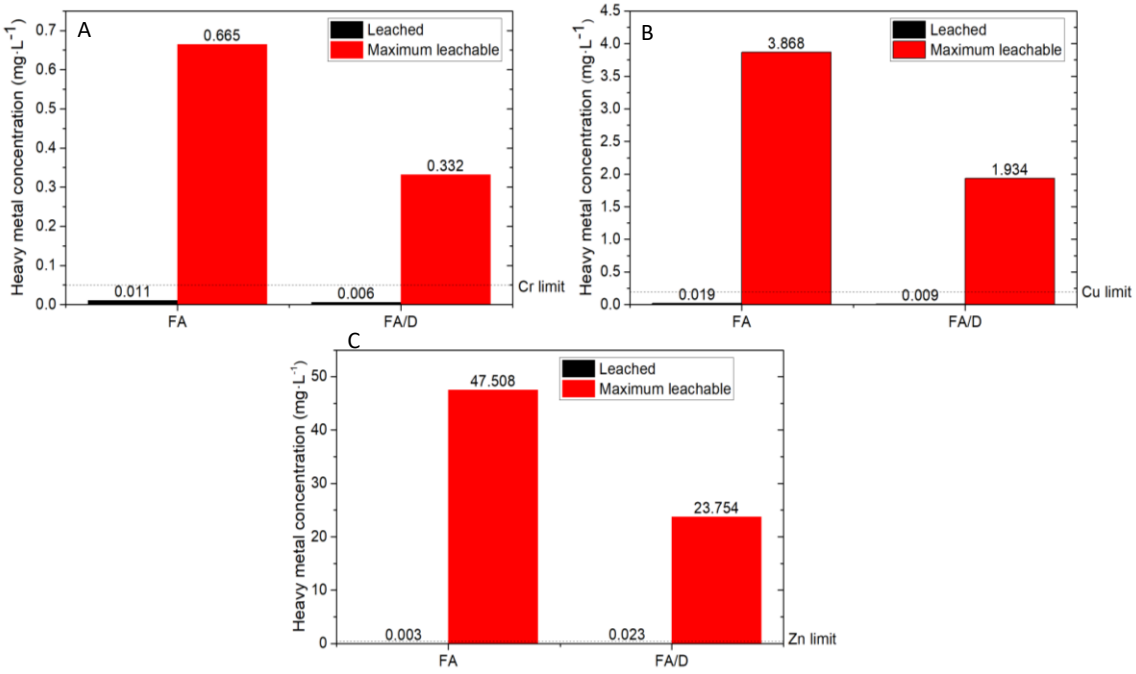


Figure 2: Concentration of Cr (A), Cu (B) and Zn (C) in the leaches and the maximum leachable.

The immobilisation rate, i.e. the ratio of the actual measured concentrations to the maximum that can be leached, listed in Table 7, shows the effectiveness of the modified MKPC composite in immobilising HMs. In the case of chromium, the immobilisation rate varied around 98%. For Cu and Zn, the immobilisation rate reached almost 100%.

Table 7: Immobilisation rate of the modified composites.

Mixture	Immobilisation rate (%)		
	Cr	Cu	Zn
FA	98.4	99.5	100.0
FA/D	98.1	99.5	99.9

CONCLUSIONS

The presented study demonstrates the effectiveness of MKPC-based composite in immobilising heavy metals contained in fly ash microfiller combined with diatomaceous earth, which served as sorbent with high specific surface area and complex morphology. The immobilisation rate of chromium, copper, and zinc by MKPC was approaching 100% in all cases. This means that the concentration of the leached heavy metals was safely below the limit values. However, changes in the microstructure, especially in the porosity of the composite, and consequently a large decrease in the mechanical resistance were observed for the composite with the fly ash and diatomaceous earth blend.

Despite the negative impact on the mechanical strength, when the heavy metal-containing fly ash was incorporated into the MKPC-based composite, these metals were effectively captured and did not leach into the surrounding environment. Thus, this method of using fly ash from a municipal waste incineration plant can be considered environmentally friendly and sustainable. Furthermore, there is a potential to improve the overall characteristics of the hardened composites by optimising their formulation to produce a high-performance material capable to immobilise high levels of toxic heavy metals.

ACKNOWLEDGEMENTS

Authors greatly acknowledge the financial support received from the Czech Science Foundation under project No. 23-04744S – Research of heavy metals immobilization in alternative low-carbon composites. The conference fees and travel expenses were covered from the project of the Grant Agency of the Czech Technical University in Prague No. SGS23/149/OHK1/3T/11, which is also greatly acknowledged.

REFERENCES

[1] Sondh S., Upadhyay D.S., Patel S., Patel R.N. A strategic review on Municipal Solid Waste (living solid waste) management system focusing on policies, selection criteria and techniques for waste-to-value, Journal of Cleaner Production, vol. 356, 131908, 2022.

[2] UNEP, Global Waste Management Outlook 2024: Beyond an age of waste – Turning rubbish into a resource, Nairobi, 2024.

[3] Czekała W., Janczak D., Pochwatka P., Nowak M., Dach J., Gases Emissions during Composting Process of Agri-Food Industry Waste, Applied Sciences, vol. 12, 9245, 2022.

[4] Arvanitoyannis I.S., 15 - Waste Management in Food Packaging Industries, Food Science and Technology, Waste Management for the Food Industries, pp 941-1045, 2008.

https://doi.org/10.5593/sgem2024/6.1/s26.38

[5] Ungureanu E.L., Mustatea G., Toxicity of Heavy Metals, Environmental Impact and Remediation of Heavy Metals. IntechOpen. 2022.

[6] Giergiczny Z., Król A., Immobilization of heavy metals (Pb, Cu, Cr, Zn, Cd, Mn) in the mineral additions containing concrete composites, Journal of Hazardous Materials, vol. 160, pp 247-255, 2008.

[7] Záleská M., Pavlíková M., Pivák A., Nábělková J., Pavlík Z., Heavy Metals Immobilization In Coal Combustion Fly Ash-Portland Cement Composites, 23rd SGEM International Multidisciplinary Scientific GeoConference, Bulgaria, pp 561-567, 2023.

[8] Waaling S.A., Provis J.L., Magnesia-Based Cements: A Journey of 150 Years, and Cements for the Future?, Chemical Reviews, vol. 7, pp 4170–4204, 2016.

[9] Haque M.A., Chen B., Research progresses on magnesium phosphate cement: A review, Construction and Building Materials, vol. 211, pp 885-898, 2019.

[10] EN 1015-10 Methods of test for mortar for masonry - Part 10: Determination of dry bulk density of hardened mortar, European Committee for Standardization (CEN), Brussels, 1999.

[11] EN 1015-11 Methods of test for mortar for masonry - Part 11: Determination of flexural and compressive strength of hardened mortar, European Committee for Standardization (CEN), Brussels, 2019.

[12] EN 13657, Characterization of waste - Digestion for subsequent determination of aqua regia soluble portion of elements, European Committee for Standardization (CEN), Brussels, 2002.

[13] Yang Y., Liu Y., Yan Z., Chen,Z., High-Temperature Resistance of Modified Potassium Magnesium Phosphate Cement, Materials, vol. 15, 8967, 2022.

[14] Zheng D., Ji T., Wang C., Sun C., Lin X., Hossain K.M.A., Effect of the combination of fly ash and silica fume on water resistance of Magnesium–Potassium Phosphate Cement, Construction and Building Materials, vol. 106, pp 415-421, 2016.

[15] Regulation No. 273/2021 Sb., Vyhláška o podrobnostech nakládání s odpady (in Czech), Annex 5, available online at: https://www.zakonyprolidi.cz/cs/2021-273 (accessed Appril 12, 2024).

IMPROVEMENT OF PHYSIOLOGICAL DATA COLLECTION BY IMPROVING SENSOR ACCURACY BASED ON THE SENSOR LOCATION

PhD Angel Dogeanu[1]

[1]Technical University of Civil Engineering of Bucharest, **Romania**

ABSTRACT

Heart rate (HR) is a fundamental physiological parameter that reflects cardiovascular health and fitness levels. Accurate HR monitoring is essential for diagnosing medical conditions, guiding physical training, and monitoring stress and recovery. With the increased development of wearable devices, the new direction of research appeared in the field of personalized comfort based on the physiological response and closing the HVAC control loop based on the occupant's involuntary reaction. This article reviews current HR monitoring technologies, evaluates their precision, and examines the effects of technology used, subject's skin tone and sensor position to obtained the most accurate HR measurement. Lower reading performance are observed with the increase of skin tone on vol Luscan scale for PPG sensor. Based on the results, ECG is the best sensor that can be used in the field compared with PPG sensor, but there are improvements that can increase the PPG sensor performance by using twisted wristband mode or by increasing the LED intensity with reduced battery life as a drawback.

Keywords: Physiological response, pulse, Heart Rate sensor, smart building, energy efficiency

INTRODUCTION

Buildings consume 40% of global final energy consumption [1] and more than 50% of this energy is used to ensure the occupants' thermal comfort through the HVAC (Heating, Ventilation, and Air Conditioning) systems [2] and several approaches aimed at energy reduction such as night ventilation [3] and shading design having an important influence on the indoor environment[4, 5] Thermal comfort is defined as "the condition of mind that expresses satisfaction with the thermal environment and is assessed by subjective evaluation" as defined by ASHRAE in the ASHRAE Standard 55 [6], indicating that thermal comfort is only determined by one's subjective judgment about the surrounding thermal environment. Accurate real-time thermal comfort assessment is essential and critical in thermal comfort satisfaction, intelligent HVAC system control, and energy conservation in the building sector. Is well known that the hypothalamus (a small region located at the base of the brain) plays a crucial role in numerous homeostatic processes, including temperature regulation, hunger, thirst, and circadian rhythms. The methods used by hypothalamus automatically, without user's interference, to achieves thermoregulation is using the following mechanisms: **Thermosensors**: The hypothalamus contains thermosensitive neurons that detect changes in blood temperature. Peripheral thermoreceptors in the skin also send temperature information to the hypothalamus via the spinal cord, **Autonomic Responses**: In response to temperature changes, the hypothalamus activates autonomic responses such as vasodilation or vasoconstriction, sweating, and shivering and **Behavioural Responses**:

https://doi.org/10.5593/sgem2024/6.1/s26.39

The hypothalamus influences behavioral responses to temperature changes, such as seeking a cooler or warmer environment, adjusting clothing, or altering physical activity levels. Many of the actions used by hypothalamus are taken way before the thermal discomfort is installed being a proactive approach. Several studies highlighted the variation of HR during different thermal perception of the body related to surrounding environment. Therefore, we consider HR measurement as a milestone in the implementation of personal thermal comfort control in sustainable green building.

METHODS AND MATERIALS

a. Devices:

The wearable sensors domain become very interesting for many companies in the field of wearable wristband and sport trackers. Several companies including Apple, Samsung, Huawei[7] and Fitbit[8] have applied and have been approved by different national and international associations to market these sensors as a form medical device to detect arrythmia[9]. These devices typically employ different types of sensors to measure heart rate, each with its own operating principles, advantages, and disadvantages. The most used heart rate sensors in wristbands are based on photoplethysmography (PPG) and, to a lesser extent, electrocardiography (ECG). Based on their technology there are several advantages and disadvantages. Therefore, **photoplethysmography** (PPG) [10] is an optical technique used to detect blood volume changes in the microvascular bed of tissue. PPG sensors in wristbands typically consist of a light-emitting diode that emits light (green, red, IR) and a photodetector (measure the amount of light either transmitted through or reflected by the skin). On contrast, **Electrocardiography** (ECG) measures the electrical activity of the heart. In wristbands, ECG sensors typically consist of conductive electrodes that detect the electrical signals produced by the heart with each beat with electrodes placed on the skin to detect electrical impulses generated by the heart and, usually, a proprietary signal processor that processes the electrical signals to determine the heart rate.



Figure 1: a)PPG (Apple watch 1); b)ECG (Huawei watch 3); c) PPG (PolarOH1)

Each solution has it's advantages and disadvantages starting from sensor size, energy consumption and impact of external factors such as ambient light, skin tone, motion artifacts and skin contact imperfection that influence the measurement performance.

Apple Watch 1 sensor is a clasic PPG sensor with good performance in ideal conditions (sensor tightly connected to the skin, no external light influence), Huawei ECG is more accurate in all condition but increase the energy consumption (is sensitive to skin eletrodes contact movement) and Polar OH1 is equipped with 6 leds that increase the illuminance level but diminish the battery life and measuring sampling (battery life is less than 5h).

b. Protocol

Sensor position static conditions

The measurement protocol imply to test the use of heart rate sensors implemented on the Apple Watch 1 (PPG sensor), Huawei Watch 3 Pro (ECG sensor), Polar OH1 (improved PPG sensor), as presented in Figure 1 and to validate measurements using a medical-grade fingertip SpO2 sensor. The study will assess the best position of the heart rate sensor based on the technology in controlled environment, in static conditions, without external disturbance.

Experiment parameters are presented in Figure 2

Nr	Parameter	Unit	Value
0	1	2	3
1	Indoor temperature	[C]	26
2	Outdoor temperature	[C]	33-35
3	Relative humidity	[%]	45%
4	Activity level	[-]	Seated office
5	Clothing level	[-]	Summer

Figure 2: Study parameters

The sensor positions monitor1ed during the study were as follows: **Wrist** (for Apple Watch 1 – [A] and Huawei Watch 3 Pro- [H])**; Upper Arm** (Polar OH1 – [P]); **Ankle (**for A/H/P**); Twisted wrist (A/H); Finger** (for the medical-grade SpO2 sensor).

We calculated the mean absolute error for each sensor calculated against the medical grade SpO2 sensor. The values obtained are presented in the table below for a measurement sample of subjects that comply with heart health interval (heart rate between 60-100 in passive seated activity) all other subjects with higher HR values (more than 100) were excluded from the statistical evaluation because there might be other causes that might impact the study and this factors influence cannot be, for now, interpreted. The data collected included age (rounded up or down), height, weight to be able to calculate BMI (Body Mass Index)**Error! Reference source not found.**, differentiation are made based on the scale presented in Figure 3, skin tone type 2:

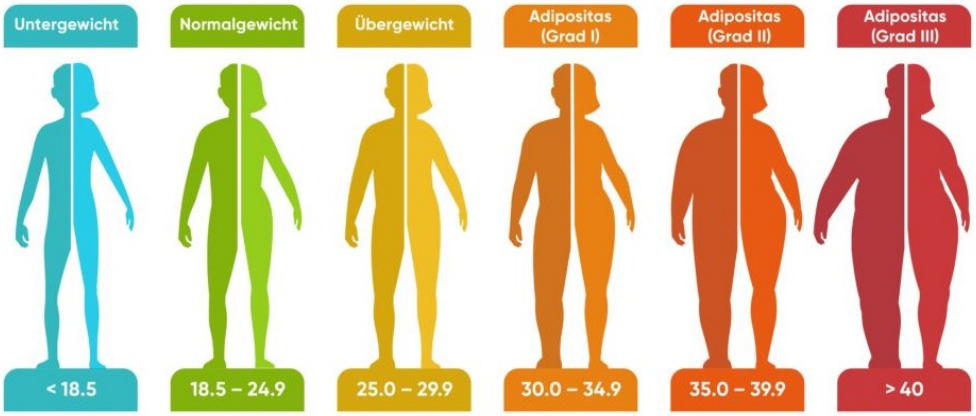


Figure 3: Body Mass Index scale

https://doi.org/10.5593/sgem2024/6.1/s26.39

Table 1: Subjects age gender and BMI

Subject	Gender	BMI	Age
1	2	3	4
S1	M	20,7	29
S2	M	23.2	32
S3	F	24.3	58
S4	F	25.1	42
S5	M	25.9	40
S6	M	27.6	46
S7	F	25.5	24
S8	F	19.9	28
S9	M	24.8	26
S10	M	34.7	29

Table 2: Measurements in static conditions

Subject	Wrist			Twisted wrist			Ankle			Upper arm	Finger	MAEv		
	A	H	P	A	H	P	A	H	P	P	SpO2	A	H	P
1	2	3	4	5	6	7	8	9	10	11	12	13	14	15
S1	70	68	68	69	68	67	69	68	68	67	68	1.33	0.00	0.5
S2	80	83	83	81	83	83	81	83	83	83	83	2.33	0.00	0
S3	82	86	86	85	86	85	82	86	85	85	86	3.00	0.00	0.75
S4	85	88	87	87	88	87	85	88	87	88	88	2.33	0.00	0.75
S5	89	92	92	91	92	92	90	92	92	92	92	2.00	0.00	0
S6	81	86	86	83	86	85	84	86	85	85	86	3.33	0.00	0.75
S7	75	78	77	77	78	77	75	78	77	78	78	2.33	0.00	0.75
S8	78	79	79	79	79	79	78	79	79	79	79	0.67	0.00	0
S9	82	85	86	85	85	85	83	85	86	84	85	1.67	0.00	0.75
S10	80	86	85	82	87	86	85	87	87	87	83	2.00	3.67	3.25

Mean average error was calculated for each sensor reading and the results were presented on the last tree columns in Table 2**Error! Reference source not found.**

Based on the final measurement for subject S10 and the conclusion of this session is that the ECG sensor is more accurate than even the medical grade SpO2 sensor. For subject S10 the increased BMI and body fat layer has an important influence on the PPG sensor reducing it's performance.

Sensor reading – dynamic scenario

This session was made to determine the accuracy of readings in dynamic situations (climb up the stairs). There were two subjects that voluntarily offered to participate in the study. There were mounded tree bracelets and a finger sensor (P on the upper arm, A to the right wrist, H on left wrist, SpO2 on the finger).

Before starting the climb the subjects rest on a chair for 5 minutes. The climb was at a fast rate with a speed of approximately 10 second / floor. At each floor the pulse was recorded, and the subject continued to the next floor.

Table 3: Dynamic pulse reading

Subject	Wrist		Upper arm	Finger	MAEv		
	A	H	P	SpO2	A	H	P
1	2	3	4	5	6	7	8
User 1							
Ground	72	74	74	75	4.00	1.33	1.33
Level 1	78	88	88	89	12.36	1.12	1.12
Level 2	94	115	115	116	18.97	0.86	0.86
Level 3	122	136	135	134	8.96	1.49	0.75
User 2							
Ground	80	82	82	82	2.44	0.00	0.00
Level 1	99	105	104	105	5.71	0.00	0.95
Level 2	108	126	126	125	13.60	0.80	0.80
Level 3	131	142	143	143	8.39	0.70	0.00

The data shows important differences between PPG [A] and ECG[H] and we can only conclude that the sensor is too slow and does not provide fast response in dynamic scenario, this conclusion is based on the fact that Apple does not disclose the reading frequency for Apple Watch 1 therefore, we can assume that the reading frequency is low. The results cannot be compared with P or H sensors readings that are able to provide reliable data in dynamic mode. However, for static studies A showed good results within 5% range. As a conclusion the dynamic scenario needs to be thoroughly conducted in the future with other sensors.

Influence of skin tone

During this session five subjects were invited to participate during the measurement session The subjects were invited to participate, were informed about the scope of the measurement session, duration, measurement protocol, expected outputs and how their personal data will be processed and anonymized. All of them were with BMI in normal range.



Figure 4: Samples from the skin tone measurements sessions

To evaluate the influence of skin tone, the von Luschan scale[11] was used and thereafter it was transposed to Fitzpatrick scale [12] details six different skin types as presented in Figure 5.

https://doi.org/10.5593/sgem2024/6.1/s26.39



Figure 5: Skin tone assessment scale

The five subjects were assessed only in relation of their pulse reading using two wearable sensors (A for twisted wristband /H standard wristband) and SpO2 (medical grade), regardless of their previous activity, level of comfort.

Table 4: Results of the skin tone measurements session

No	User	Gender	Skin tone		Pulse			Error	
[-]	[-]	[-]	Von Luscan	Fritz-patrick	Normal PPG	Twist PPG	ECG	N PPG	Tw PPG
0	1	2	3	4	6	7	8	9	10
1	Sst1	Male	27	6	88	92	101	12.87	8.91
2	Sst2	Male	25	6	102	107	114	10.53	6.14
3	Sst3	Male	29	6	95	102	110	13.64	7.27
4	Sst4	Male	34	6	80	86	94	14.89	8.51
5	Sst5	Male	21	4	70	72	76	7.89	5.26

The results are presented in table 4. It is highlighted that the reading error increases with the skin tone, see columns 9&10. The contact between the watch and skin was tight not to introduce any contact error. The measurements underlined the same pattern in terms of increased performance as in the static scenario. SpO2 has an internal verification mechanism that do not display any value until is considered correct.

DISCUSSION

There are several findings from the current study. One of the most important is that the sensor performance is highly important therefore, ECG will always be more accurate than PPG regardless of the location, position, BMI or skin tone. In the skin tone study ECG sensor was considered as baseline. The skin tone influence in PPG measurements showed a higher impact in wrist and ankle location due to higher skin pigmentation and lower influence in the twisted wrist mode due to lower skin thickness. Also, the higher skin pigmentation, the higher error was recorded.

To improve the PPG performance and diminish the skin tone influence we identify that the use of the wristband in a twisted mode reduces the reading errors. Therefore, it is recommended that manufacturers create a twisted wristband version to maintain the usage of PPG sensor within their devices due to cost, size and energy efficiency and/or include a software adjustment in the setup app to collect skin tone (by picture or user self-declaration) and/or increase the LED brightness if preliminary tests require it.

Even if, in the field of medical grade HR monitoring ECG sensors are used, it is highly recommended that the remaining equipment to be replaced with improved version (change from PPG to ECG to mitigate errors generated by skin tone) for example in SpO2 devices because skin tone could have an influence on the medical readings having a future impact on patient health assessment.

LIMITATIONS

Our study has limitations. During the measurement session we only used the devices available on the market, therefore there might be other manufacturers that might implement improved algorithms that could mitigate the skin tone influence.

The number of different skin tone persons available for the measuring period was limited but is still providing relevant information for the studied protocol.

It is acknowledged that measurements were made in controlled environment to ensure repeatability of the sessions, in real life scenario the influence of the errors generated by sensor precision will impact the collected data.

We are aiming to increase the number of subjects with increased skin tone and find an open-source PPG sensor that offers full control of the sensors parameters (brightness, sampling rate, alter the measurement algorithm, etc). This will be the focus of future research.

CONCLUSION

This paper presents the results obtained in a controlled environment, the reliability of 3 types of wristband devices in static conditions aiming to determine the best position in terms of pulse reading based on sensor type and skin tone. We found that ECG sensor is very precise, and it is not influenced by skin tone, body fat layer or other external influences. It can be used with outstanding results in all studied positions and moreover, it can be even more precise than SpO2 medical grade. PPG sensor is efficient at wrist and ankle but the precision decrease with skin tone increasing on Fitzpatrick scale, an improvement was identified by mounting in twisted wristband position. In terms of skin tone an improvement was highlighted by using Polar OH1 sensor due to increase illuminance of the sensor.

These preliminary conclusions highlight the necessity of taking into consideration the skin tone factor and the need to reevaluate the measuring protocol in application that need to read HR. Therefore, there are several directions that need to be studied by manufacturers or integrators:

1. PPG sensors need to be integrated in bracelets that are wrist twisted (inner wrist mounted) and/or correction factor need to be included in the reading algorithm to compensate the skin tone. For example, Polar OH1 increased LED intensity performed better in comparison to other PPG.

2. ECG sensor was not influenced by sensor location or skin tone being an reliable sensor. We consider that integrators and app developer to integrate skin tone as input parameter and alter the measurement protocol in line with sensor technology and sensor location.

3. Ankle pulse readings showed similar values like wrist measurements. This direction might be developed in the future by manufacturers.

https://doi.org/10.5593/sgem2024/6.1/s26.39

4. To be able to take into consideration the HR as parameter for thermal comfort and thermal sensation assessment, sensor improvement and easy access to read data need to be provided.

REFERENCES

This study was supported by research funding grant UTCB-GNAC-ARUT- 33.

[1] Perez-Lombard;, L., J. Ortiz;, and C. Pout;, *A review on buildings energy consumption information.* Energy and Buildings, 2008. **40**(4): p. 394.

[2] 2Vakiloroaya, V., et al., *A review of different strategies for HVAC energy saving.* Energy Conversion and Management, 2014. **77**: p. 738-754.

[3] Udrea, I., S. Cananau, and R.-T. Popa *On Energy Efficiency of Night Window Shutters for a Non-Residential Building in Three Major Romanian Cities*. Buildings, 2024. **14**, DOI: 10.3390/buildings14010187.

[4] Udrea, I. and V. Badescu, *Usage of solar shading devices to improve the thermal comfort in summer in a Romanian PassivHaus.* SIMULATION, 2019. **96**(5): p. 471-486.

[5] Udrea, I. and R.T. Popa. *Exterior shades energy efficiency for a mixt, office-residential building in Bucharest*. in *2017 International Conference on ENERGY and ENVIRONMENT (CIEM)*. 2017.

[6] ASHRAE, *''Thermal environmental conditions for human occupancy,'' ANSI/ASHRAE Standard 55-2004, American Society of Heating, Refrigerating and Air-Conditioning Engineers, Atlanta, GA*. 2004.

[7] Niu, Y., et al., *Diagnostic validation of smart wearable device embedded with single-lead electrocardiogram for arrhythmia detection.* DIGITAL HEALTH, 2023. **9**: p. 20552076231198682.

[8] Lubitz, S.A., et al., *Detection of Atrial Fibrillation in a Large Population Using Wearable Devices: The Fitbit Heart Study.* Circulation,2022. **146**(19):p. 1415-1424

[9] Cheung, C.C., A.D. Krahn, and J.G. Andrade, *The Emerging Role of Wearable Technologies in Detection of Arrhythmia.* Canadian Journal of Cardiology, 2018. **34**(8): p. 1083-1087.

[10] Banik, P.P., et al. *Development of a Wearable Reflection-Type Pulse Oximeter System to Acquire Clean PPG Signals and Measure Pulse Rate and SpO2 with and without Finger Motion*. Electronics, 2020. **9**, DOI: 10.3390/electronics9111905.

[11] Charoenngam, N. and S. Sriussadaporn, *Darker Skin Color Measured by Von Luschan Chromatic Scale and Increased Sunlight Exposure Time Are Independently Associated with Decreased Odds of Vitamin D Deficiency in Thai Ambulatory Patients.* Journal of Nutrition and Metabolism, 2021. **2021**(1): p. 889-993.

[12] Johnson, R.A. and T.B. Fitzpatrick, *The Horizons of Health19. The Skin*, H. Wechsler, J. Gurin, and G.F. Cahill, Editors. 1977, Harvard University Press. p. 278-286.

POLYMERIC COATING FOR THE INSULATION, PROTECTION AND SURFACES FINISHING OF THE REINFORCED BUILDINGS CONCRETE EXPOSED TO CORROSIVE ENVIRONMENTS

Prof. dr. ing. hab. Ion Rusu[1]

Senior Lecturer dr. chem. Loredana Judele[2]

Assoc. prof. dr. ing. hab. Daniel Lepadatu[1,2]

[1] Technical University of Moldova, **Republic of Moldova**
[2] Gheorghe Asachi Technical University from Iasi, **Romania**

ABSTRACT

In this paper, there are presented the characteristics of reinforced concrete structures that are subjected to a corrosive environment. These structures allow for the appearance and opening of short-term and long-term cracks within certain limits during operation, as well as the variation in the moisture of the concrete depending on the ambient humidity. The basic nature of the concrete allows it to react with acids, while its increased porosity enables the absorption of liquids and gases, including aggressive ones, increasing its permeability. The basic recipes for these special concretes are presented, along with the minimum requirements for the necessary and mandatory coatings for isolating and protecting structures exposed to such corrosive environments. It has been proven that only polymeric coatings can ensure their protection in highly aggressive environments, whether gaseous or liquid. The operating conditions of reinforced concrete structures such as bridges, underpasses, pumping and wastewater treatment stations, poles, and foundations of industrial buildings with aggressive production environments are described, including food industry containers and reservoirs for storing potable and technical water. The results of experimental research regarding the design and development of complex polymer coatings intended for protecting the concrete of these structures confirm the effective provision of isolation and anticorrosive protection, adhesion to concrete, and increased resistance to cracking, as well as enhanced chemical and biological resistance and low (reduced) permeability to water and aggressive liquids. We can also mention here that there are disadvantages to using polymer coatings, primarily those related to the harmfulness of their production, as well as issues concerning their resistance to high temperatures. The designed polymeric coating also possesses hygienic and sanitary properties that meet the requirements of health authorities and do not affect the quality of food products with which it may come into direct contact.

Keywords: polymeric coating, building concrete, corrosive environment

INTRODUCTION

A significant portion of the reinforced concrete elements of industrial enterprises, bridges, underpasses, dams and dikes, pumping and wastewater treatment stations, reservoirs for storing technical and potable water, food industry enterprises, technological installations, and other buildings are periodically or almost continuously subjected to the actions of

https://doi.org/10.5593/sgem2024/6.1/s26.42

aggressive environments, including liquids, temperature and humidity variations, deformations, static and dynamic load actions, and the actions of microorganisms, which cause the temporary degradation of concrete [1]. The destructive actions on reinforced concrete constructions are primarily caused by acids, which, in contact with $Ca(OH)_2$ in the concrete, form calcium salts. These salts, possessing a certain solubility in water, dissolve and are removed from the concrete, gradually increasing its porosity and reducing its mechanical strength [2].

The mechanical strengths of reinforced concrete constructions are reduced as a result of the action on the concrete of microorganisms, which are present in food products, wastewater, high-humidity and poorly ventilated rooms [3]. Practice has demonstrated that the tendency to increase the corrosion resistance of concrete, exploited in contact with aggressive environments (microorganisms and under conditions of water filtration through concrete), cannot be achieved solely by modifying its composition, if the viability of these constructions is not ensured [4]. The necessary viability of these constructions can only be ensured by finishing and isolating their surfaces with various coatings, including polymeric ones [5, 6]. The current tendency to ensure corrosion protection of concrete constructions solely by isolating their surfaces with materials more resistant than concrete is not sufficiently justified or correct and requires the development of new polymer coatings with properties corresponding to the operating conditions [7].

The use, for this purpose, of coatings with known lacquers and paints, which possess high adhesion, mechanical and chemical resistance, does not provide sufficient anticorrosive protection for concrete (used in constructions exploited under high aggressive conditions) [7]. During the exploitation of reinforced concrete constructions, there is a reduction in the quality of lacquer and paint coatings, with their subsequent degradation. The causes of this phenomenon are: reduction of adhesion of the coatings to the protected surface; appearance of water at the concrete-coating interface; partial degradation of concrete at the concrete-coating interface due to the permeability of coatings by acids; low crack resistance of polymeric coatings [8, 9]. A method of protection of reinforced concrete constructions, exploited in aggressive conditions, can be used for concrete insulation of polymer cement compositions. Additionally, a number of characteristics of concrete such as high basicity, a certain porosity and roughness of the surface, the tendency to appear and develop cracks as a result of the actions of dynamic and static forces, shrinkage and other factors, considerably complicate the possibility of developing efficient protective coatings for concrete.

RESULTS

Based on these considerations for the protection of construction concrete, operated in aggressive wet conditions, a complex polymer coating based on varnishes and paints has been developed, which possesses properties of insulation, finishing and increased anti-corrosion protection, due to increased adhesion and resistance to cracking, chemical and microbiological resistance.

The complex polymer coating consists of:
- primer PC 0241 based on chlorosulphide polyethylene varnish;
- elastic substrate PC 734 based on chlorosulphide polyethylene varnish;
- intermediate layer EE 737 based on epoxy resin type ED-20;
- enamel layer EE 7116 based on epoxy resin type ED-20.

The total thickness of the polymer coating is between the limits of 320...400 μm.
The primer PC 0241 ensures increased adhesion of the entire coating and figure 1 shows the dependence of its adhesion related to the addition content of expansive cement.

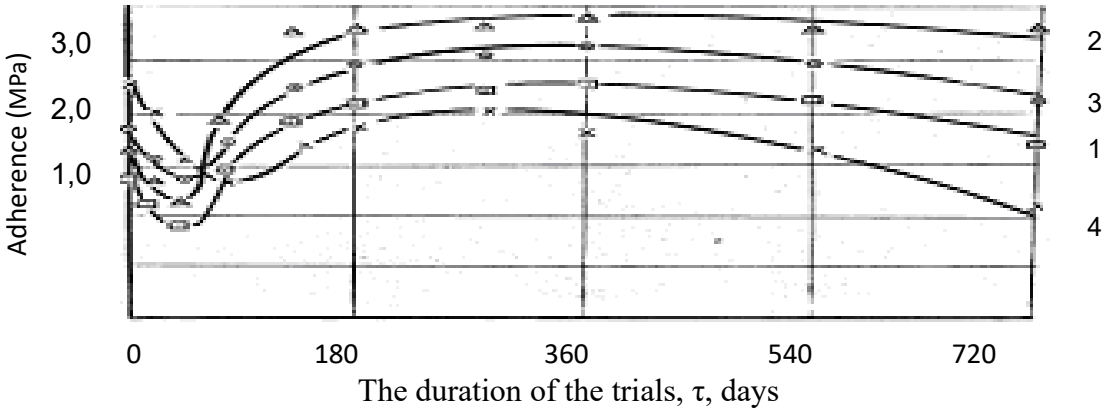


Fig. 1. Modification of adhesion (A) of polymer coatings depending on the content of expansive cement and the duration (τ, days) of the action of the liquid environment:
1- expansive cement 10 %; 2 - expansive cement 20 %; 3 - expansive cement 30 %;
4 – without the addition of expansive cement

The primer applied to the concrete surface, due to its porous structure, soaks into its superficial layer. In the case of water diffusion, having molecules smaller than the molecules of organic acids, they reach the surface of the primer, penetrate it and cause hydration of the expansive cement. By increasing in volume, the expansive cement contributes to the increase in volume of the primer, which in turn increases the frictional force between it and the concrete surface, thus increasing adhesion.

The elastic substrate PC 734 depending on its thickness increases the cracking resistance of the complex polymer coating (Figures 2 and 3).

https://doi.org/10.5593/sgem2024/6.1/s26.42

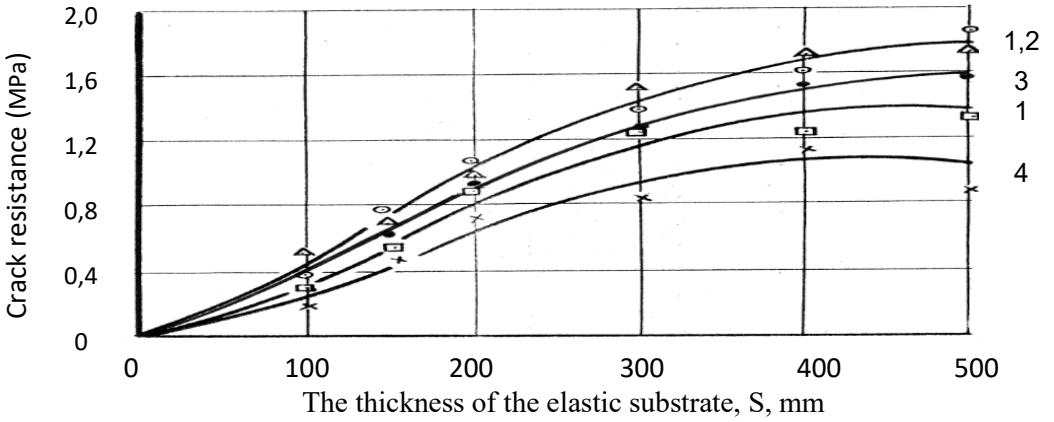


Fig. 2. Dependence of the cracking resistance of the coating on the thickness of the elastic varnish-based substrate PC-734

1 – elastic substrate based on PC-734 varnish without topcoats; 2 – with final coating layers based on LFE fluoroplastic epoxy varnish – 32 lhn; 3 – with final coating layers based on polyurethane UR-293; 4 – with final coating layers based on A-15-0 copolymer; 5 - with finished coating layers based on ED - 20 brand epoxy resin.

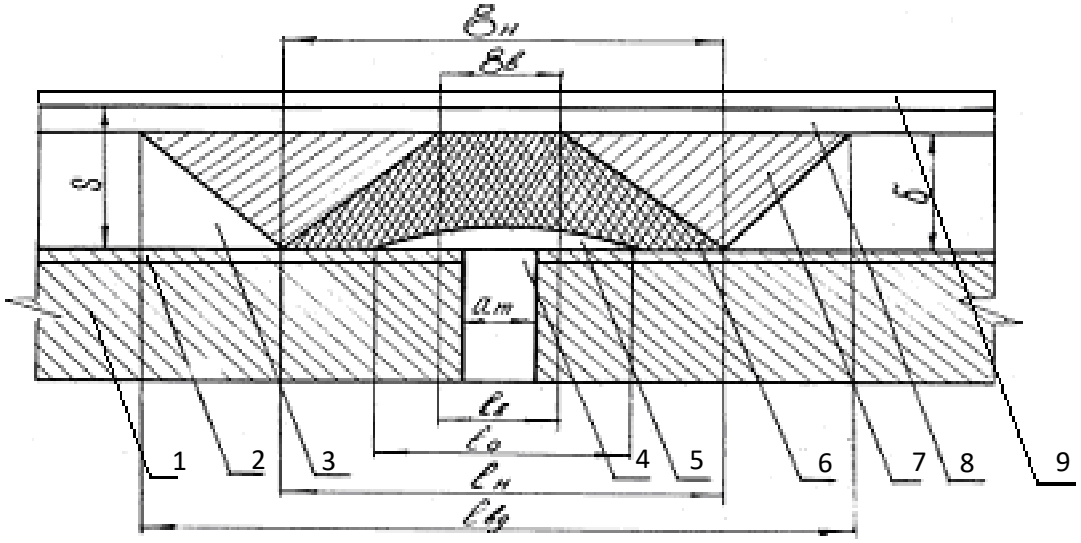


Fig. 3. Polymeric coating model for the appearance and development of cracks in concrete, the distribution of relative deformations (ε) and the stretching zones (l) in the elastic substrate. a_m – the width of the open crack; S – the total thickness of the coating; δ – the thickness of the elastic substrate; ε_H, l_H – in the adhesive layer; ε_B, l_B – in the upper layer, l_0 – the length of the sector from the detached elastic substrate; l_{Bg} – the upper length of the sector of the deformed elastic substrate.

1 – concrete layer; 2 – concrete layer impregnated with primer; 3 – the elastic substrate of the coating; 4 – the crack in the concrete; 5 – the detachment area of the coating; 6 – the stress distribution area in the deformed cover; 7 – the area of the deformed cover; 8 – the intermediate layer of the coating; 9 –the final layer of the coating.

The EE-737 interlayer reduces acid permeability through the polymer coating due to the addition of Cu 2-8 cS cationite in the form of Ca2+ (Figure 4).

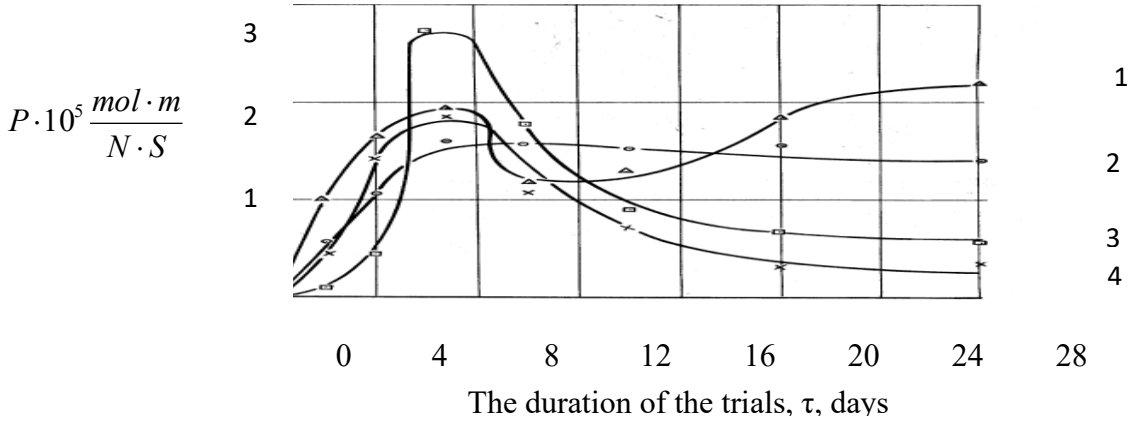


Fig. 4. Changing the permeability (P) of water and aggressive liquid media over time through the film based on the epoxy resin ED-20

1 – film based on ED-20 epoxy varnish; 2 – film based on epoxy enamel EE737; 3 – ED-20 epoxy varnish film with Cu 2-8 cS cation addition in the form of H^+; 4 – ED-20 epoxy lacquer film with addition of Cu cationite 2-8 cS in form Ca^{2+}. The developed complex polymer coating has the following characteristics: adhesion to concrete, MPa, minimum – 2.1 MPa; shock resistance, cm, minimum – 45; bending strength, cm, minimum – 16; water absorption, %, maximum – 4; water permeability, kg/(m•s•Pa), maximum – $0{,}5 \cdot 10^5$.

DISCUSSION

The health authority in the Republic of Moldova has approved the use of these developed polymeric coatings for direct contact with all liquid food products (wines, juices, sulfited products, beer, dairy products, potable water) and solid food products (flour, sugar, combined feed), as well as for isolating and finishing the plastered surfaces of rooms used for pharmaceutical production. The developed comprehensive coating has been implemented in finishing, isolating, and anticorrosive protection works for constructions (interior surfaces of reservoirs for storing various food products, bunkers for receiving raw materials (fruits and vegetables), floors, walls, ceilings). Additionally, it can be used to protect reservoirs for storing potable and technical water, and pharmaceutical production enterprises in the Republic of Moldova and Ukraine (with a service life of 10 to 15 years). With some minor modifications in composition, the developed comprehensive polymeric coating can also be used for anticorrosive protection of metal constructions (including reservoirs) in the food, light, chemical, construction materials, wood processing, and energy industries.

CONCLUSION

1. The maximum adhesion of primers after 300-320 days of contact with water is explained by the absorption of water and the swelling of the film-forming substance and concrete, caused by osmotic phenomena and increased frictional forces between them.

https://doi.org/10.5593/sgem2024/6.1/s26.42

2. The increased adhesion value of primers containing expansive cement is due to the volumetric increase during its hydration, which correspondingly causes the overall primer volume to increase, completely filling the pores, voids, cavities, and irregularities of the concrete. The frictional forces that arise between the concrete and the primer further contribute to the increased adhesion of the primer to the concrete.

3. The maximum adhesion value of the primer containing an expansive cement additive in the amount of 30 mass units is ensured by the maximum volumetric increase of the primer without destroying the integrity of the film-forming material.

4. The crack resistance of polymeric coatings depends on the thickness of the elastic substrate based on PC-734 lacquer and the elasticity of the coating layers. There is a directly proportional relationship between the crack resistance of the polymeric coatings and the elasticity of their layers.

5. The increase in crack resistance of polymeric coatings occurs due to the stretching of the elastic substrate over the cracks formed in the concrete, absorbing all the deformations, and consequently over the upper layers of the polymeric coatings.

6. For polymeric coatings with final covering layers based on ftoroplast-epoxy lacquer LFE-32 lnh, copolymer A-15-0, polyurethane lacquer UR-293, and epoxy resin ED-20, a crack resistance greater than 0.3 mm is ensured with the thickness of the elastic substrate based on PC-734 lacquer equal to 70, 80, 100, and 120 μm, respectively.

ACKNOWLEDGEMENTS

The researches of this paper were realized with the support of project: *Models, systems and technologies for energy efficiency, decarbonization and digitalization of processes in energy, industry, construction and transport*, Project financed by Technical University of Moldova – Institutional financing no. 4/FI from 22.02.2024, Republic of Moldova.

REFERENCES

[1] Shishkina A. A., Shishkin A. A. Ways to improve the durability of concrete. Collection of theses of the International Scientific and Technical Conference, Hydraulic Engineering and Transport Construction, Odessa May 28-29, 2020, p. 132-134.

[2] Kanaeva E. A., Khudyakov A. V. Impact of various types of acids on reinforced concrete structures. — Text : immediate // Young scientist. — 2023. — № 24 (471). — P. 94-97. URL: https://moluch.ru/archive/471/104256/ (accessed: 07.06.2024).

[3] Loginova S. A., I. N. Goglev. On the issue of increasing the biostability of concrete and reinforced concrete bridge supports. https://vestnik.cstroy.ru/jour/article/view/178?locale=ru_RU

[4] NCM E.04.04:2016. Environmental Protection/Corrosion Protection Design of Constructions. Chisinau 2016, 157 p. Approved by the order of the Ministry of Regional Development and Construction no. 153 of 16 Dec. 2016 with application of 01 July 2017.

[5] Ovchinnikov I. G., A. And. Likverman, O. N. Rasporov et al. Corrosion protection of metal and reinforced concrete bridge structures by the method of coloring/– Saratov: Kubik Publ., 2014. 504 p. (In Russian).

[6] Rusu I. V., Frunze A. N. Defects of paint coatings. Proceedings of the International Technical Seminar, Modeling and Optimization of Building Composites. Odessa, November 16-17, 2017, p. 78-81.

[7] Gara An. A., Gara A. A. Properties of Protective Epoxy Polymer Solutions in Contact with Water and Oil Products. Proceedings of the International Seminar, Modeling and Optimization of Building Composites, Odessa, November 21-22, 2019, p. 17-22.

[8] Pichugin A. P., Banul V. V., Batin M. O., Nikitenko K. A. Permina A. V. Study of the Process of Structural Formation and Forecasting of Operational Properties of Protective Polymer Coatings. Proceedings of the International Technical Seminar Modeling and Optimization of Building Composites. Odessa, Oct 27-28, 2016, p. 91-95.

[9] Kudryashov A. Yu., Batin M. O., Pichugin A. P., Nikitenko K. A. Optimization of impregnation of building materials with polymers in the control of diffusion parameters. Proceedings of the International Technical Seminar "Modeling and Optimization of Building Composites". Odessa, November 16-17, 2017, pp. 54-58.

https://doi.org/10.5593/sgem2024/6.1/s26.42

RETROREFLECTIVE GUARDRAIL BEAMS TO IMPROVE TRAFFIC SAFETY

Dr. Jiří Grošek[1]

Dr. Michal Janků[1]

Jakub Motl[1]

Leo Jeniš[2]

[1] CDV - Transport Research Centre, **Czech Republic**
[2] Likal, **Czech Republic**

ABSTRACT

One of the main monitored parameters related to road traffic safety is the visibility of road facilities and how they are perceived by drivers. Areas where visibility is suddenly limited, or where road sections become unclear due to inadequate design and technological arrangements, pose significant safety risks. Monitoring the optical properties of the applied coating surface, particularly its retroreflection and colour, is crucial for traffic safety. The paper describes research leading to the design of a system of measures to increase overall road safety and reduce the accident rates through the use of special retroreflective guardrail beams with retroreflective coating. As part of the research, experiments were also carried out to test the effect of the retroreflective guardrail beams on drivers' attention, as well as their potential improvement in visual perception using special eye-tracking system on site. Integrating new technologies into road facilities and investigating the human factor in various situations/driver conditions will significantly reduce risks in critical road sections. Additionally, an extended service life for road facilities should be achieved as a secondary outcome of this research.

Keywords: polymer coating, guardrail, crash barrier, retroreflection

INTRODUCTION

Application of coatings is particularly advantageous for steel elements exposed to corrosive or otherwise degrading environments. Plastic coatings can be applied using various methods and different types of polymers, depending on the intended use. Several common types of coating are used in various industrial sectors [1, 2]. The application of these coatings is often more suitable and cost-effective than replacing steel with stainless materials or performing galvanisation [3]. Furthermore, these methods are used also for aesthetic reasons. Coatings are also used to protect elements that are exposed to mechanical stresses which may lead to wear of some parts [4, 5].

There are some known coating applications for public spaces furniture or sections of roadways, which help enhance their service life. These applications include railings, public lighting poles or dowels in concrete pavements [6]. However, the use of polymer coatings on steel guardrail beams (in Britain known as crash barriers) remains uncommon. On the other hand, galvanised steel guardrails are commonly used.

https://doi.org/10.5593/sgem2024/6.1/s26.43

Reflective tapes or reflectors are commonly used on guardrails to increase visibility at night. Their service life and resistance to effect in critical areas degrade quickly, due to factors such as road cleaning and winter maintenance (de-icing salts, snow, mechanical damage, etc.). More extensive use of coating applications for road features significantly mitigates the above-mentioned drawbacks and addresses some of the related problems.

Optical parameters are one of the most important characteristics of road features and the minimum retroreflective class is monitored for the retroreflective materials according to standards and regulations. In addition, it is necessary to consider the effects on drivers and other road users. There are elements on roads that distract drivers' attention (e.g. billboards), while other elements may be difficult for drivers to perceive. To guarantee innovativeness, it is necessary to consider measurements to evaluate distraction and attention-grabbing effects. One potential approach includes evaluation and measurement with the use of an eye-tracking system, which was tested in the present research project. The system enables recording of a scene as perceived by the individual under investigation, tracking the movement or eye fixation in the videorecording, including subsequent evaluation. The post-analysis aims to identify differences between monitored objects (guardrails), time of perception of those objects, and the driver's reaction to them. In the analyses we focused on the visible course of the centre of view and all relevant physiological parameters of the eyes, including eye fixation, shifts and aims of sight, blinking and blinking rate, duration of closed eyelids, pupil size and movement, and others. On the basis of these parameters, we subsequently determined what the investigated individual saw, for how long and whether the individual was able to recognize the seen element, or whether they passed it without noticing.

As part of the research project, several samples of guardrail beams were created and tested under real conditions with the use of special devices detecting the effects of optical properties of coatings on drivers. The application technology was monitored and adjusted during the production to ensure the best quality surface preparation in terms of adhesion (jetting, degreasing). Furthermore, efforts were made to reach the required coating thickness and homogeneous retroreflective properties over the whole element surface.

MATERIALS AND METHODS

Throughout the research project, various mixture compositions were tested with different ratios of components, admixtures and technological application procedures. The most suitable for mixing of the development mixture was PHC-AH by Icosa, typically available in various colour shades, wherein colour pigments by Panax were added. Thermoplastic powder PHC-AH used for the surface treatment, supplied as a basic colourless powder specially developed for hard protective surfaces, provided perfect adhesion to the surface and allowed for addition of glass microspheres in order to achieve retroreflective properties. This special powder is based on a mixture of polyethylene and polyamide (partly from recycled components). This polymer coating showed high resistance to scratching and abrasion, good electric resistivity, i.e. low conductivity, surface water repellence, resistance to elevated temperatures (particularly in production), and chemical stability.

Other commercially available types of thermoplastics that were tested showed inferior resistance, i.e. they were too fragile. A big technological problem arose due to

granularity of coloured thermoplastic powder and glass microspheres, where it was impossible to perform homogenization of individual components. Additionally, the different melting temperatures of thermoplastics, glass microspheres and pigments posed another challenge. Consequently, achieving a sufficiently homogeneous coating layer with even thickness proved to be technologically impossible.

Continuous measurements of coefficient of retroreflection were conducted to develop a mixture using testing samples (Fig. 1) both in a laboratory of Transport Research Centre and in situ. Zehntner ZRS 6060 was used for measuring retroreflection (Tab. 1). The measurement was carried out in accordance with the EN 12899-3 standard [7]. Based on the measured values, average values and extended measurement uncertainties were determined for every test. The measurement results were used as a basis for adjusting the percentage amount of glass microspheres as the retroreflective component in the mixture.

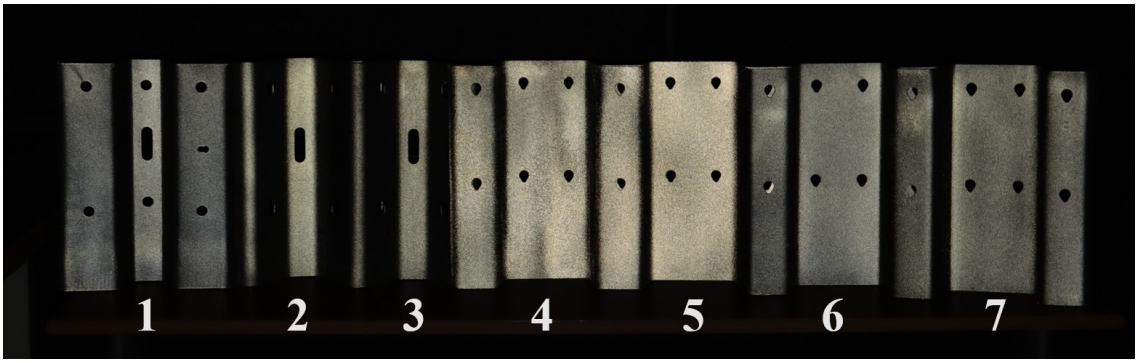


Figure 1: Set of coated guardrail samples

Table 1: Results of retroreflection measurements of guardrail samples

Sample	Coefficient of retroreflection R_A [cd·lx^{-1}·m^{-2}]		
	observation angle α = 0.2°	observation angle α = 0.33°	observation angle α = 2°
1	5.0	4.5	0.5
2	11.5	9.2	0.7
3	8.5	7.0	0.6
4	16.0	11.4	0.8
5	20.0	14.0	0.9
6	8.0	6.7	0.6
7	7.8	6.5	0.7

In order to prove in situ properties and evaluate the driver's perception, the research team designed two measurements that monitored retroreflective properties of grey coating on guardrail beams. The first measurement performed in situ involved monitoring of the properties of a guardrail with a traditional galvanised surface alongside the newly developed retroreflective coating (Fig. 2).

https://doi.org/10.5593/sgem2024/6.1/s26.43

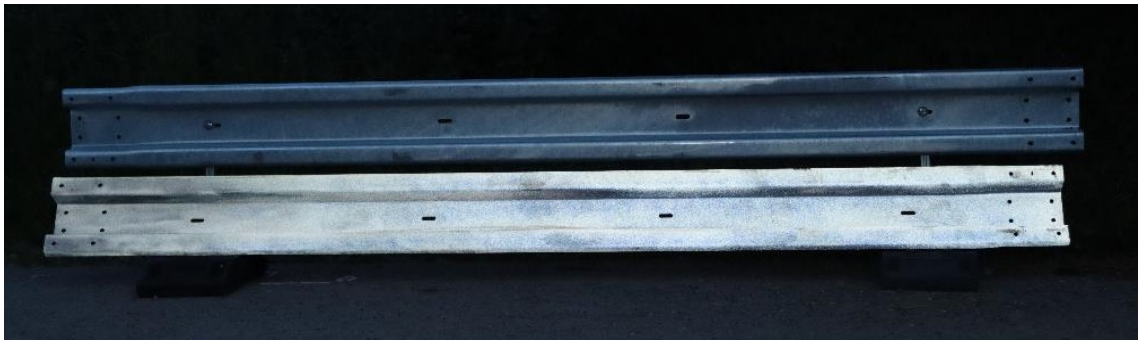


Figure 2: Difference in reflectance of guardrails without/with retroreflective coating

The aim was to measure the luminance distribution of the guardrail, which is used for luminance (reflectance) comparison of guardrails. In order to determine the luminance distribution, which is defined as a measure of luminosity, a luminance analyser PDA LumiDisp was used. This device is a specially calibrated camera equipped with a filter and evaluation software. The range of measurement is 0.001 – 10 000 000 cd/m^2. In order to determine the luminance distribution of the guardrail (both in its commonly used state and with polymer retroreflective surface treatment) the measurement was performed during nighttime hours. First, a guardrail without retroreflective surface treatment was installed. Subsequently, the measurements were taken at several distances from the guardrail increasing in 10-metre intervals (10, 20, 30, 40, 50, 60, 70, 80, 90, 100 m). A vehicle illuminating the guardrail with its passing beam was position at each of the specified distances. The measuring device was mounted in the vehicle in such way that the sensor was at the eye level (Fig. 3). The measurements were subsequently repeated with the retroreflecting guardrail beam.

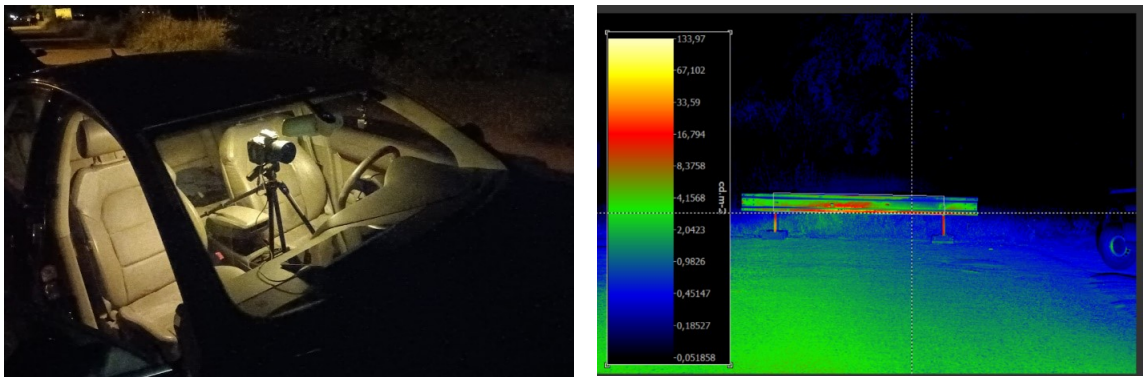


Figure 3: Location of luminance analyser in the vehicle (left), example of evaluation of luminance maps in software Lumidisp (right)

The second measurement in situ involved monitoring of properties of a guardrail with the newly developed retroreflective coating on the section of road I/47 between Ivanovice na Hané and Vyškov. The section for the night measurement trip was approx. 6.7 km long. At the end of the section, the vehicle turned back and drove along the same route. The evaluated section of the road segment was located approx. 5.2 km from the start, it was an intersection of the roadway I/47 and a private road. In this place the modified guardrail beams were installed onto the existing steel guardrails. The guardrail beams were curved, designed to be used on inner curves (Fig. 4).



Figure 4: Installation of guardrail beams with retroreflective coating (left) and view of the illuminated element during a night trip (right) on road section

The aim was to monitor and subsequently analyse several trips undertaken by a group of selected volunteers using the eye-tracking system under different defined conditions (with/without installed retroreflective guardrails) and analyse data from these measurements. The volunteers were informed about the general course of the testing trip, they were only given such instructions to be able to drive through the predefined route using their own driving style and preferred speed. The use of passing beam and high beam was left to the volunteers' preferences. Before their trip every volunteer was equipped with the eye-tracking device and briefly instructed on its specific features, particularly focusing on the appropriate use and proper fitting of the glasses on the face. Calibration was performed according to the manufacturer's manual and the measurement started. The volunteers were not disturbed during their ride and only questions concerning their route were answered. Each volunteer completed a short questionnaire about themselves before the ride and provided feedback about the course of the ride as well.

The eye-tracking device allowed to monitor and analyse distractions and/or points attracting attention of the test subjects, i.e. indicating where the sight of the subject focuses. Other functions used included recording of a scene as perceived by the subject, marking of movement and fixation of the eyes to the videorecording, including the following evaluation. The eye-tracking system records pupil movements using an accurately positioned camera mounted on the special glasses. The system consists of glasses which include a mounted camera monitoring the test subject's field of vision and a camera monitoring the test subject's right eye. These system components are controlled by a measuring and recording laptop with special software where all video recordings are stored (Fig. 5). The measurement result is an image (Fig. 6) which can be complemented with fixation data (focused eye position in a medium) and the route between individual focus positions. The system is designed to monitor the test subject's (driver's) line of sight and effectively evaluate their vision and eye reactions. The result includes the evaluation of the driver's reaction time, a degree of effects on the driving style, and overall assessment of improvement from the viewpoint of the tested volunteers (through a questionnaire survey). Regarding safety, we focus on the duration of eye fixation on the guardrail as well as on the number of eye fixations during the testing. These two aspects are directly related to the driver's need to get orientated

https://doi.org/10.5593/sgem2024/6.1/s26.43

under reduced visibility using these infrastructure elements (i.e. guardrail beams). The hypothesis underlying this measurement is that the duration of eye fixation on a clearly visible element would be shorter than on a less visible element in the close vicinity of the road. An element that is clearly visible even under reduced visibility conditions will help drivers stay oriented during their ride. Drivers thus get information on the curve earlier (or rather from a greater distance) if a given element is better visible.



Figure 5: Eye-tracking system for monitoring of eye movements and determination of areas of interest from driver's viewpoint



Figure 6: Processing of recording and eye-tracking measurement evaluation

RESULTS

The measured luminance distribution values are shown in the following Figure 7 for individual types of guardrails. The results indicate that light reflectance is significantly higher for the guardrail with retroreflective coating. Specifically, the guardrail equipped with polymer coating reaches on average approx. a four times higher value in comparison with the traditional guardrail. The deviation at the point 30 m from the guardrail is caused by unevenness on the test section.

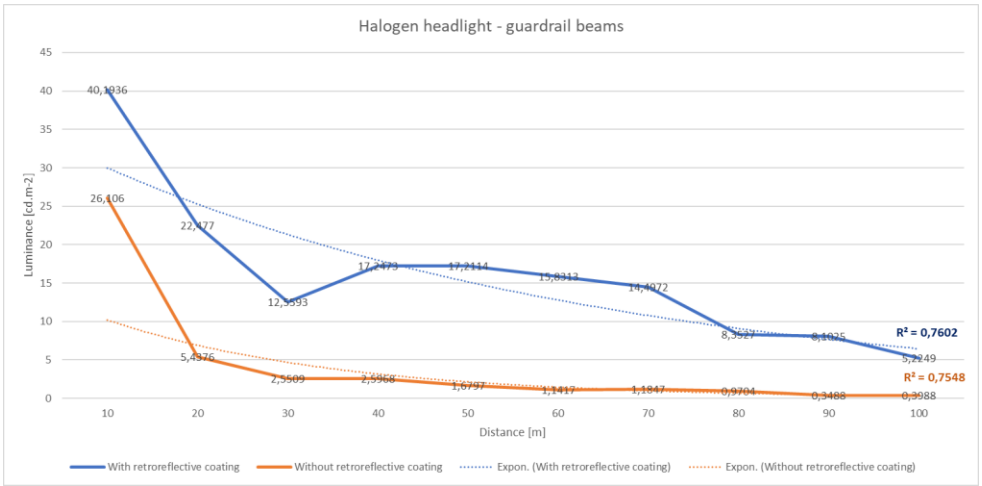


Figure 7: Distribution of headlight luminance on guardrail beams

The results of the second in situ measurement show different average durations of eye fixation on the infrastructure element based on its surface treatment – without / with polymer coating. Regarding the variant without polymer coating, the average eye fixation duration reached 0.992 s, while in the case of the variant with polymer coating the average duration of eye fixation on the infrastructure element was 0.750 s. In addition, there are significant differences between the minimum and maximum duration of eye fixation among individual test subjects depending on the guardrail surface treatment.

DISCUSSION

The measured retroreflection coefficient values of the test samples of guardrails with a polymer coating reach up to 20 $cd \cdot lx^{-1} \cdot m^{-2}$, which is up to 50 times lower compared to the reflectors of delineator posts. Although these measured values appear to be relatively low, thanks to the larger reflective surface, guardrails are more visible compared to delineator posts. On the basis of testing, it was verified that these values are sufficient and that higher values could lead to a negative perception (driver distraction) when passing through the given section.

In terms of road traffic safety, the concept of reaction time is crucial. It consists of three parts (sensory impulse registration, situation evaluation, and reaction to the situation). This process takes approx. 1.5 second under the assumption the driver is fully concentrated on driving. In a situation when the driver is distracted by various distractors (use of a mobile phone, impact of advertisements or billboards, etc.), their reaction time is significantly longer. These distractors very frequently include a visual fixation which is not directly focused on the traffic situation. Additional infrastructure, such as guardrails, apart from safety functions (e.g. protection of vehicles from leaving the road, protection from hitting a solid obstacle outside the road, e.g.), also have a self-explanatory purpose to guide drivers on their way and improve orientation at reduced visibility conditions. This function is greatly enhanced when the guardrail does not excessively attract the driver's attention, but instead provides the driver with information in shortest possible time.

The results show that a guardrail with polymer retroreflective coating can convey information to the driver in shorter time. Therefore, the driver has more time to pay attention to driving and focus their sight on the given traffic situation. Thus, the guardrail with polymer coating does not function as a distractor, but rather as a clearly visible element which guides the driver in shorter time than a standard guardrail without polymer retroreflective coating.

CONCLUSION

The paper describes several procedures, methods, and partial result evaluations. The authors focused in detail on the research activities not only for the evaluation and interpretation of laboratory test results, but also on monitoring of drivers' behaviour. The complex and often overlapping research activities were focused on developing and testing of new types of polymer coatings intended to improve road traffic safety and road service life.

https://doi.org/10.5593/sgem2024/6.1/s26.43

Several elements of guardrail beams with grey coating an admixture of glass microspheres were prepared within the project. The coating technology was adjusted during the development to ensure the coating application yielded the highest possible effectiveness and quality (thickness, colour, retroreflection, etc.). At the testing sections, the driver's reaction time, degree of influence during driving, and retroreflection under illuminated guardrail were measured. The measurement results from the testing sections also proved that this solution is suitable in terms of drivers' perception during driving. Drivers' reaction time was carefully evaluated and showed the viability of the solution. In addition, the drivers provided positive feedback to the installation of the guardrail with retroreflective coating via a questionnaire survey, further advocating for the implementation of the new solution.

Now, preparations are underway to verify the operational properties on another testing section with a higher accident rate, and it is expected that the solution will contribute to reducing the accident rate. Furthermore, the material properties also inherently position polymer coatings as an effective protection of steel against corrosion. The next planned phase of the research will focus on comparing the LCA of the polymer coating versus the conventional surface treatment by galvanisation. The aim will be to develop polymer coatings with a low carbon footprint and long service life for road facilities.

ACKNOWLEDGEMENTS

This article was produced with the financial support of the Ministry of Transport within the programme of long-term conceptual development of research institutions.

REFERENCES

[1] Xu H., Zhang, Y., A Review on Conducting Polymers and Nanopolymer Composite Coatings for Steel Corrosion Protection, Coatings, vol. 9/issue 6, 2019, DOI: 10.3390/coatings9120807.

[2] Ates M., A review on conducting polymer coatings for corrosion protection, Journal of Adhesion Science and Technology, vol. 30/issue 14, pp 1510–1536, 2016, DOI: 10.1080/01694243.2016.1150662.

[3] Motlatle A.M., Ray S.S., Ojijo V., Scriba M.R., Polyester-Based Coatings for Corrosion Protection, Polymers, vol. 14/issue 16, 2022, DOI: 10.3390/polym14163413.

[4] Krupička A., Johansson M., Hult A., Use and interpretation of scratch tests on ductile polymer coatings, Progress in Organic Coatings., vol. 46/issue 11, pp 32-48, 2003, DOI: 10.1016/S0300-9440(02)00184-4.

[5] Briscoe B.J., Sinha S.K., Scratch Resistance and Localised Damage Characteristics of Polymer Surfaces – a Review, Materialwissenschaft und Werkstofftechnik, vol. 34/issue 10-11, pp 989-1002, 2003, DOI: 10.1002/mawe.200300687.

[6] Zuzulova A., Grosek J., Janku M., Experimental Laboratory Testing on Behavior of Dowels in Concrete Pavements, Materials, vol. 13/issue 10, 2020, DOI: 10.3390/ma13102343.

[7] EN 12899-3 Fixed vertical road traffic signs - Part 3: Delineator posts and retroreflectors, 2008.

SOLID RESIDUES FROM THE COBUSTION OF BIOMASS – HEAVY METALS CONTAMINATION AND POSSIBLE REUSE

Prof. Ing. Milena Pavlíková, Ph.D.[1]

Ing. Martina Záleská, Ph.D.[1]

Assoc. Prof. Mgr. Jana Nábělková, Ph.D.[1]

Ing. Adam Pivák[1]

Prof. Ing. Zbyšek Pavlík, Ph.D.[1]

[1] Faculty of Civil Engineering, Czech Technical University in Prague, **Czech Republic**

ABSTRACT

This manuscript presents the comprehensive chemical and physical analysis of two types of biomass ashes derived from power and heat generation in order to highlight their positive parameters and properties and to propose the way for their safe reuse in the production of building materials. The analysis of biomass ashes included the assessment of chemical composition, dry matter content, loss on ignition, particle size distribution, Blaine fineness, dry powder density, specific density, pozzolanic activity, SEM morphology and microstructure. Emphasis was placed on the analysis of heavy metals content. The results of comprehensive physical and chemical tests proved the potential use of the investigated biomass ashes in the production of construction materials in the form of active component of blended binders or mineral fillers, while ensuring safe disposal of environmentally hazardous waste from energy production. Thus, it will be possible design and develop new eco-efficient materials with low carbon footprint enabling heavy metals stabilization and immobilization.

Keywords: biomass ash, safe disposal, health and environmental risks, leachability of heavy metals, pozzolanic activity, ash classification

INTRODUCTION

Problems related to the climate crisis, such as global warming or the melting of the glaciers in the Arctic and the South Pole, are currently being discussed by scientists and the general public [1]. These issues are associated with the burning of fossil fuels such as coal or oil and the depletion of natural resources for use in industry, transportation, construction, etc. Combustion of fossil fuels is the greatest contribution to the total CO_2 emissions which are widely believed to play a key role in global warming [2]. In this regard, any alternative in energy production can reduce greenhouse gas emissions. Currently, biomass combustion is considered as a promising alternative for energy generation, reducing the cost of energy and the negative environmental impact of its production. The number of biomass power plants is expected to increase dramatically in the near future due to the higher energy potential of biomass, its availability, eco-efficiency and sustainability. According to Carrasco et al. [3], the number of biomass power plants will increase by 210% by 2030. However, the safe disposal and reuse of

https://doi.org/10.5593/sgem2024/6.1/s26.44

biomass ash, an unavoidable by-product of biomass combustion, poses new challenges. Currently, biomass ash is often landfilled or discarded, which can pose serious environmental risks to groundwater resources and soil. If contaminated with heavy metals, it can cause environmental pollution due to heavy metal leaching [4,5]. Therefore, to prevent human health problems and pollution of the living environment, it is necessary to minimize the negative environmental and economic impacts of biomass ash landfilling and to safely reuse it in accordance with the circular economy principles [6]. Although intensive research on biomass ash treatment is currently underway [7-9], the problems associated with heavy metal contamination and potential leaching have not been fully understood and solved [10]. Therefore, the manuscript reports the analysis of two types of biomass ashes to evaluate their ability to be used in the composition of low-carbon building materials.

MATERIALS & METHODS

Two biomass ashes from the Lublin region, Poland, were analyzed. For comparison, CEM I 42.5 R produced in Radotín, Czech Republic by Českomoravský beton, a.s. (Heidelberg Materials CZ) was used. The first ash comes from a large-scale fluidized bed combustion of biomass for heat and power generation. The original biomass consisted of 80% wood chips and 20% biomass from fruit orchards. The second ash was produced during the incineration of old wooden roof structures made of pine wood. The incineration was carried out in a boiler with a fixed grate and a water jacket.

Physical and chemical analyses of biomass ashes were performed. The chemical composition was measured by ARL QUANT'X, Energy Dispersive X-ray Fluoroscence (EDXRF) spectrometer (Thermo Scientific). Among the physical parameters of BAs, dry matter content, loss on ignition, bulk density, specific density and Blaine fineness were tested. To measure the dry matter content (dry matter mass) m_{dm} [%], the samples were dried at 105 °C and the moisture content by mass m_w [%] present in each ash was determined. The loss on ignition LOI [%] was measured according to EN 15169 [11]. The loose bulk density ρ_p [g·cm^{-3}] was measured as a function of compaction time, i.e. for samples compacted up to their full compaction. The specific density ρ_s [g·cm^{-3}] was determined by helium pycnometry principle using a Pycnomatic ATC [Thermo Scientific] pycnometer. The specific surface area (Blaine fineness) was measured by an automatic Blaine air peremability tester UTCM 0280 (UTCM) in compliance with EN 196-6 [12]. The particle size distribution was analyzed by a laser diffraction technique working apparatus Analysette 22 Micro Tec plus (Fritsch). Surface morphology and microstructure were observed with the desktop SEM apparatus Phenom XL G2 (Thermo Fisher Scientific) with a CeB6 electron source, equipped with an SDD detector. The images were obtained at a secondary electron detection (SED) and backscattered electron detection (BSD) setups with a primary electron acceleration voltage of 5 kV. Pozzolanic activity of ashes was analyzed in the modified Chapelle test [13] which was carried out using the procedure described by the French norm NF P 18-513 [14]. The results were expressed in mg $Ca(OH)_2$ fixed by 1g of BA. Concentration of heavy metals in BAs was determined by atomic absorption spectroscopy (AAS) on a SOLAAR S iCE 3000 instrument (Thermo Scientific). The samples were digested in aqua regia.

RESULTS & DISCUSSION

Table 1 shows the chemical composition of the investigated BAs in oxide form as measured by EDXRF spectrometer. Both ashes contained high levels of CaO, indicating their self-cementing properties. On the other hand, the sum of the content of potentially hydraulic oxides (CHO), i.e. $SiO_2 + Al_2O_3 + Fe_2O_3$, was 17.61% for BA1 and 29.78% by weight for BA2. Therefore, the investigated BAs cannot be classified as pozzolanic admixtures, since the limit value for CHO is set by ČSN EN 450-1 [15] at > 70% by weight. Similarly, prior to 2019, ASTM C618 used the sum of $SiO_2 + Al_2O_3 + Fe_2O_3$ to classify fly ash - Class F had CHO > 70 wt% and Class C had CHO in the range of 50-70 wt%. In the current version of the specification (ASTM C618 [16]), both types of fly ash require CHO > 50 wt%. There are also some other fly ash requirements that apply to the production of cement-based materials, such as concrete. ASTM C618 [16] specifies a maximum limit for SO_3 content, which must be < 5 wt%. None of the biomass ashes tested meets this limit. EN 450-1 [15] defines limits for the content of MgO and P_2O_5, which must be < 4 wt% and 5 wt%, respectively. In the case of BA1, the concentration of MgO was higher than required.

Table 1: Chemical composition of biomass ashes

Biomass ash type	**BA1**	**BA2**
Compound	**Content [wt%]**	
CaO	46.11	43.74
K_2O	10.95	9.45
SiO_2	8.91	22.89
MgO	6.92	4.16
SO_3	6.54	6.91
MnO	4.95	0.86
Al_2O_3	4.73	5.07
P_2O_5	4.03	3.47
Fe_2O_3	4.01	1.82
ZnO	1.08	0.12
Cl	0.81	0.68
BaO	0.28	0.17
TiO_2	0.23	0.40
Ta_2O_5	0.15	-
SrO	0.14	0.15
ZrO2	0.04	0.05
Rb_2O	0.04	0.02
Co_3O_4	0.03	0.01
IrO_2	0.01	-
PbO	0.02	0.01
CuO	0.02	0.02

The physical parameters of BAs are presented in Table 2. The moisture content in both BAs was low, complying with the maximum limit for moisture in ashes to be used as a constituent of the blended binder. The LOI was also low and met the maximum prescribed by the EN 450-1 standard [15]. Blaine fineness of biomass ashes is even

https://doi.org/10.5593/sgem2024/6.1/s26.44

higher than that of Portland cement. This is the result of the complex structure of ash particles and their morphology (see Figures 2, 3).

Table 2: Physical properties of biomass ashes and Portland cement

Material	m_{dm} [%]	m_w [%]	LOI [%]	ρ_p [g·cm^{-3}]	ρ_s [g·cm^{-3}]	Blaine fineness [cm^2·g^{-1}]
BA1	99.71	0.29	1.5	0.894	2.443	5819.3
BA2	99.23	0.77	4.4	0.576	2.573	5544.4
CEM I 42.5 R	-	-	-	-	3.059	3982.9

Particle size distribution curves obtained by laser diffraction are shown in Figure 1. The particle size distribution parameters are summarized in Table 3. Although the BAs have not been mechanically processed by grinding, they are only slightly coarser than Portland cement.

Table 3: Particle size distribution parameters

Material	d_{10} [µm]	d_{50} [µm]	d_{90} [µm]
CEM I 42.5 R	8.8	25.0	38.3
BA1	21.9	38.2	59.3
BA2	22.5	33.1	45.2

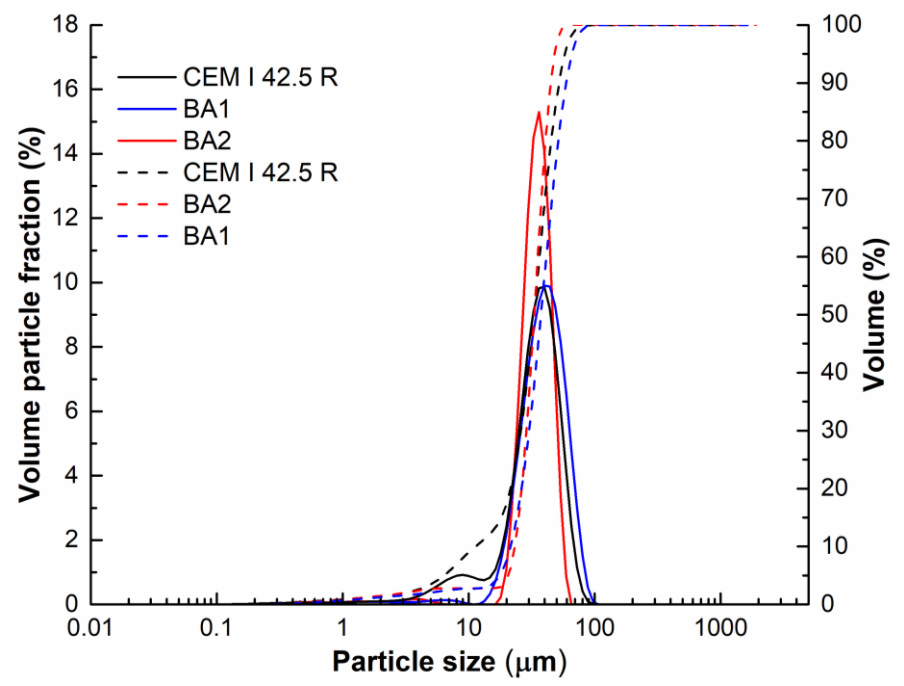


Figure 1: Particle size distribution of BAs and cement

SEM images of BAs are shown in Figures 2, 3. Secondary electron detection (Figure 2) enabled to observe particles of irregular angular shape, needle shape and ball-shapped. Back scattering (Figure 3) identified discrete and open pores of ash particles, which was the reason of their high specific surface. In BA2, the wood residues are visible.

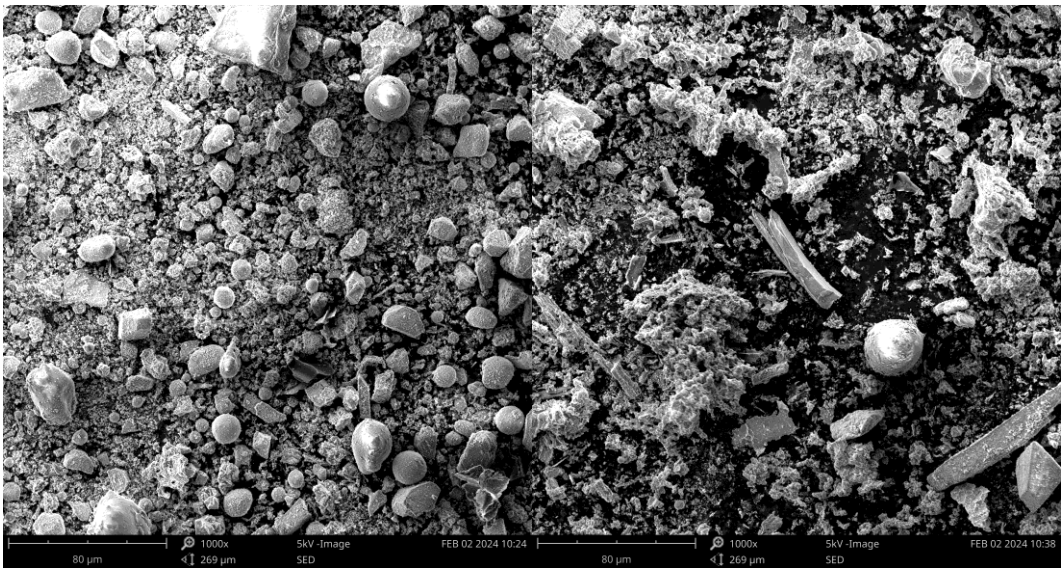


Figure 2: SEM images of BA1 (left) and BA2 (right) - SED

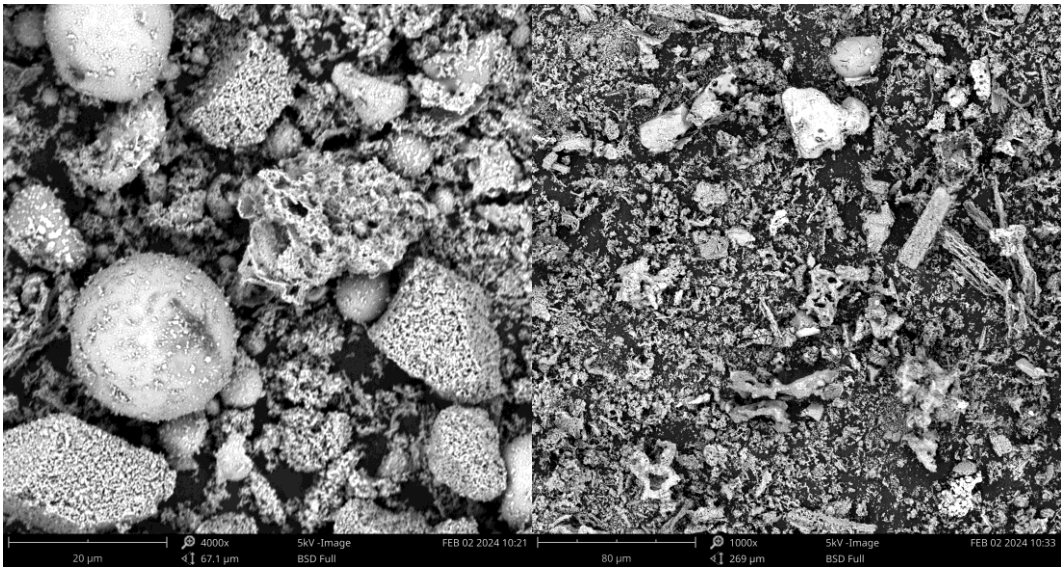


Figure 3: SEM images of BA1 (left) and BA2 (right) – BSD

The BAs studied fixed only 20 and 15 mg of $Ca(OH)_2$ by 1 g of BA1 and BA2, respectively. The ashes were therefore classified as not pozzolana active, which is in agreement with their chemical composition. On the other hand, a high CaO content will definitely allow their reaction with water and the formation of hardened substances.

The concentration of heavy metals (HMs) measured in dry matter of BAs is introduced in Table 4. The content of HMs was classified according to the Czech Regulation No. 273/2021 – Regulation on waste management, Annex 5 [17]. The exceeded limits are marked in red. Concentrations of As and Zn were higher than those prescribed for safe management of the waste in the form of backfilling. Therefore, safe disposal of the investigated BAs is necessary and must always be considered before their reuse.

https://doi.org/10.5593/sgem2024/6.1/s26.44

Table 4: Concentration of HMs in dry matter [mg/kg]

Ash /HM type	Pb	As	Ni	Cu	Ba	Hg	Zn	Cr	Cd
BA1	16.99	42.36	9.87	22.41	264.58	0.14	239.05	17.38	0.72
BA2	43.69	54.91	15.1	95.67	91.2	-	3483.9	16.4	0.36

CONCLUSIONS

Two types of biomass ashes were extensively analyzed and tested. Based on the acquired data, chemical composition and physical parameters of BAs, they can be used as fillers in construction composites or as part of blended binders. In a future research, their safe disposal as filler of PC-based composites and MKPC-based composites will be investigated, including the leachability tests of the contained heavy metals.

ACKNOWLEDGEMENTS

Authors greatly acknowledge the financial support received from the Czech Science Foundation under project No. 23-04744S - Research of heavy metals immobilization in alternative low-carbon composites. The scholarship of A. Pivák has been partially supported by the Grant Agency of the Czech Technical University in Prague, grant No. SGS23/OHK1/3T-002/23 - Research and development of high performance building composites.

REFERENCES

[1] Wang, L., Gi, T., Feng, G., Wang, Z., Wang, H., Han, Y., He, J., Du, S., Li, K., He, J., Green utilization of biomass by-product poplar leaf ash: A novel eco-friendly cementitious material for cement mortar replacement, Construction and Building Materials, vol. 393, 132025, 2023.

[2] Zhao, X., Zhu, H., Sikerwar, V.S., Zhao, M., Partk, A.-H.A., Fenell, P.S., Shen, L., Fan, L.-S., Biomass-based chemical looping technologies: the good, the bad and the future, Energy and Environmental Science, vol. 10, 1885, 2017.

[3] Carrasco, B., Cruz, N., Terrados, J., Corpas, F.A., P´erez, L., An evaluation of bottom ash from plant biomass as a replacement for cement in building blocks, Fuel, vol. 118, pp. 272–280, 2014.

[4] Katare, V.D., Madurwar, M.V., Experimental characterization of sugarcane biomass ash – a review, Construction and Building Materials, vol. 152, pp. 1-15, 2017.

[5] Tekin, İ., Dirikolu, İ., Gökçe, H.S., A regional supplementary cementitious material for the cement industry: Pistachio shell ash, Journal of Cleaner Production, vol. 285, 124810, 2021.

[6] Martinez-Lage, I., Velay-Lizancos, M., Vazquez-Burgo, P., Rivas-Fernandez, M., Vazquez-Herrero, C., Ramirez-Rodriguez, A., Martin-Cano, M., Concretes and mortars with waste paper industry: Biomass ash and dregs, Journal of Environmental Management, vol. 181, pp. 863–873, 2016.

[7] Tosti, L., van Zomeren, A., Pels, J.R., Dijkstra, J.J., Comans, R.N.J., Assessment of biomass ash applications in soil and cement mortars, Chemosphere, vol. 223, pp. 425–437, 2019.

[8] Athira, G., Bahurudeen, A., Rheological properties of cement paste blended with sugarcane bagasse ash and rice straw ash, Construction and Building Materials, vol. 332, 127377, 2022.

[9] Castillo, D., Cruz, J.C., Trejo-Arroyo, D.L., Muzquiz, E.M., Zarhri, Z. Gurrola, M.P., Vega-Azamar, R.E., Characterization of poultry litter ashes as a supplementary cementitious material, Case Studies in Construction Materials, vol. 17, e01278, 2022.

[10] Pavlík, Z., Záleská, M., Pavlíková, M., Pivák, A., Nábělková, J., Jankovský, O., Jiříčková, A., Chmel, O., Průša, F., Simultaneous immobilization of heavy metals in MKPC-based mortar—Experimental assessment, Materials, vol. 16, 7525, 2023.

[11] EN 15169, Soil, waste, treated biowaste and sludge – Determination of loss on ignition, European Committee for Standardization (CEN), Brussels, Belgium, 2021.

[12] EN 196-6, Methods of testing cement –

Part 6: Determination of fineness, European Committee for Standardization (CEN), Brussels, Belgium, 2018.

[13] Záleská, M., Pavlíková, M., Pavlík, Z., Classification of a-SiO_2 rich materials, Materials Science Forum, vol. 824, pp. 33-38, 2015.

[14] NF P 18-513, Pozzolanic Addition for Concrete – Metakaolin. Definitions, Specifications and Conformity Criteria. Annex A., AFNOR, La Plaine Saint-Denis, France, 2009.

[15] EN 450-1, Fly ash for concrete - Part 1: Definition, specifications and conformity criteria, European Committee for Standardization (CEN), Brussels, Belgium, 2012.

[16] ASTM C618 – 19, Standard Specification for Coal Fly Ash and Raw Calcined Natural Pozzolan for Use in Concrete, ASTM International, West Conshohocken, PA, United States, 2019.

[17] 273/2021 Sb., Vyhláška o podrobnostech nakládání s odpady (in Czech), Annex 5, available online at: https://www.zakonyprolidi.cz/cs/2021-273 (accessed February 5, 2024).

https://doi.org/10.5593/sgem2024/6.1/s26.44

STUDY OF REACTION TO FIRE IN HYBRID_BASED CORE INSULATORS INTENDED FOR THE OF VACUUM INSULATION PANELS

Prof. Ing. Jiří Zach, Ph.D.[1]

Ing. Petra Zachová[1]

Ing. Jitka Peterková, Ph.D.[1]

Ing. Vítězslav Novák, Ph.D.[1]

Bc. Jindřich Havelka[1]

[1] Brno University of Technology/Faculty of Civil Engineering, **Czech Republic**

ABSTRACT

The core insulators of vacuum insulation panels are mostly made from inorganic raw materials with a high SiO_2 content, either in the form of nanoparticles or microfibers, while the proportion of organics is usually up to 3 %. The contribution is devoted to the study of reaction to fire in hybrid insulation materials made from a combination of nano SiO_2-based particulate raw materials and organic-based fibrous raw materials, where the total proportion of organics is significantly greater than 3 %. Considering that it is a mixture of inorganic nanoparticles and organic microfibers with a total higher bulk density, the resulting behavior of these insulators in the field of reaction to fire is different from classic insulators (both fibrous and particulate). In the case of hybrid core insulators, which are the subject of the published study, the organic fibers are obtained by recycling old paper (municipal waste) and substitute part of the nano SiO_2 in the core insulator. In this way, it is possible to significantly improve the environmental parameters of vacuum insulation panels with minimal deterioration of functional properties and durability. The paper describes how the substitution of SiO_2 with organic microfibers will affect the key fire properties, especially the reaction to fire.

Keywords: vacuum insulation panels, core materials, reaction to fire, cellulose fibers, nano SiO_2

INTRODUCTION

The reaction to fire of building materials is one of the most important properties of building materials incorporated in building structures. Within the EU, the CPR (Regulation (EU) No 305/2011 of the European Parliament and of the Council) [1] prescribes the obligation to determine the reaction to fire performance of most construction products placed on the market. The actual requirements in terms of the required fire safety performance of buildings and individual structures are then determined in each country by national legislation and standards. In the case of insulation materials, the minimum reaction to fire class "E" according to EN 13501-1 is usually required [2]. This year, among other things, the Energy Performance of Buildings Directive EU/2024/1275 [3] has been amended and it will now be necessary to declare the amount of CO_2 per 1 m^2 in kg CO_2 eq/m^2 for building structures over a reference period of 50 years. Calculations shall be made according to EN 15978 [4]. In

https://doi.org/10.5593/sgem2024/6.1/s26.45

addition, there is a further tightening of requirements in the field of energy performance of new and existing constructions, which means that it is necessary to look for other ways to improve the thermal performance of (mainly) existing buildings even in cases where it is not possible to use conventional ETICS type insulation systems [5]. In areas where high thermal resistance must be achieved within the small thickness of the insulation material, it is possible to successfully use superinsulating materials, where among the most effective (in terms of thermal insulation properties) are vacuum insulation panels (VIP) [6, 7]. These materials were mainly used in refrigeration and white goods, but gradually they started to be used in the construction industry and in the last 5 years they have also started to be used in the automotive and logistics industries [8, 9]. In the construction sector, there is already a harmonised European standard for these materials [10], so they are gradually becoming a common part of building structures. In the construction sector, most of these products are based on core insulators made of nano SiO_2 (precipitated and fumed nano silica). In order to reduce the cost and environmental burden, many scientific teams are trying to use alternative raw materials based on secondary and easily renewable raw materials for the production of VIPs [11].

The reaction to fire of building materials is classified according to EN 13501-1 [2] and is one of the most important properties of building materials. Building materials are classified according to their reaction to fire into the following classes: A1 (non-combustible materials), A2, B, C, D, E, F (combustible materials):

- Class F - Class F classifies organic materials that are considered flammable. This class is the lowest and is therefore completely free of requirements.

- Class E - material classified in Class E must be tested in accordance with EN ISO 11925-2 [12],

- Class D, C, B - material classified in Class D, C or B must be tested according to EN ISO 11925-2 and EN 13823 [12, 13],

- Classes A1 and A2 - these classes are mostly non-flammable inorganic materials with very small amounts of organic fillers. Tests are carried out (depending on the specific class) according to EN ISO 1182 [14], EN 13823 [13] and EN ISO 1716 [15].

In the case of vacuum insulation panels, the main concern is the barrier foil, which is made up of a combination of polymer foils and aluminium foil, so VIPs are usually classified as reaction to fire class E. The core insulators themselves are most often of reaction to fire class A1 or A2, as they are made up of mainly inorganic fibres or nanoparticles [8]. In the framework of research work at Brno University of Technology, in cooperation with the University of Ljublana and TURVAC, a study of the behaviour of hybrid VIP matrices made of SiO_2 nanoparticles and microfibres obtained from paper recycling in terms of reaction to fire was carried out.

MATERIALS AND METHODS

The test samples were made of pyrogenic nanosilica from Wacker Chemie Aerosil 200 and microfibres obtained by recycling paper from CIUR Czech Republic with a length of up to 300 microns. In addition, viscose fibres with a thickness of 1.2 dTex were used for production. The test samples were made with a blend of silica and cellulose fibres from paper in the following proportions: 100:0; 90:10; 80:20; 70:30; 60:40 and 50:50.

Viscose fibers were used at 3 % of the raw material weight to achieve mechanical properties. The test specimens were produced in the size of 200x200x40 mm by pressing with a pressure of 300 kPa. These samples were then used to produce cut samples for small flame source ignitability testing according to EN ISO 11925-2 [12] in the size of 200 x 90 mm. The residues were sampled for determination of combustion heat according to EN ISO 1716 [15]. Testing was always carried out on the edge and on the surface separately (always on a separate group of test specimens). In addition, cylindrical samples were made by pressing into a mould with a diameter of 45 mm and a height of 50 mm for the determination of fire resistance according to EN ISO 1182 [14].

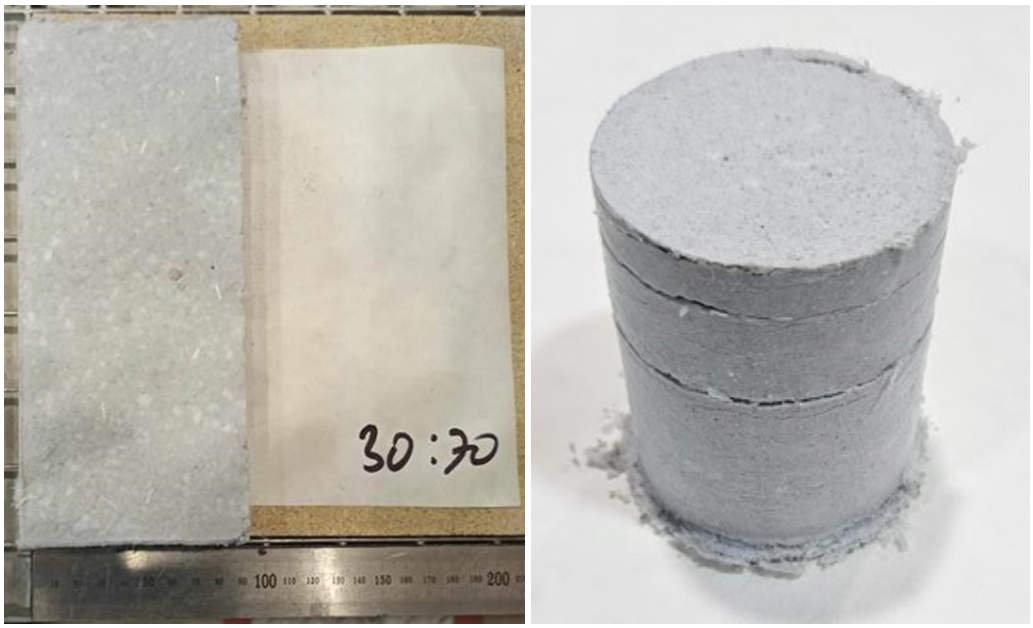


Figure 1. Photographs of the test specimen with composition 30:70 for the small flame test according to EN ISO 11925-2 (left) and for the fire test according to EN ISO 1182 (right)

MEASUREMENT RESULTS

Test samples of hybrid core insulations with varying ratios of nanofibres and cellulose microfibres were tested for small flame ignitability according to EN ISO 11925-2 [12]. The measurements were carried out on two sets of samples per surface and per edge. The exposure time was chosen for class "D" and better flame exposure for 30 s. During the test, neither ignition nor flammability was observed in any of the samples and in no case did the flame height exceed 150 mm. Therefore, the flame height was measured for comparison of the samples. The results are shown in the following table 1.

The determination of the heat of combustion according to EN ISO 1716 [15] was also carried out. The measurements were carried out by combustion in an IKA calorimeter. The results are given in the following table 2.

https://doi.org/10.5593/sgem2024/6.1/s26.45

Table 1. Evaluation of small flame ignitability

Ratio (Cellulose:Nanosilica)	Bulk density [kg/m^3]	Surface test - incandescence height [mm]	Edge test- incandescence height [mm]
0:100	181	41.0	39.0
10:90	182	48.0	45.0
20:80	190	47.5	43.0
30:70	175	43.0	48.5
40:60	172	59.5	43.5
50:50	172	62.0	52.0

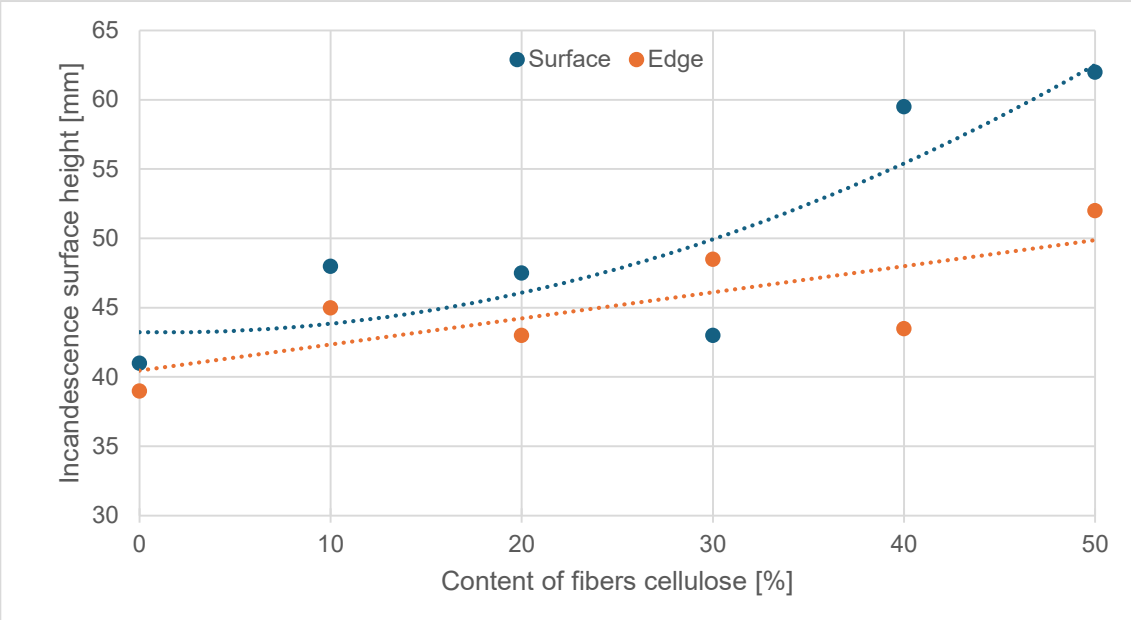


Figure 2. Surface ignition height in the small flame source ignition test as a function of cellulose fibre content

Table 2. Results of the determination of the heat of combustion on test samples of hybrid core insulators

Ratio (cellulose:nanosilica)	Combustion heat [MJ/kg]			
	1	2	3	Average
0:100	0.000	0.000	0.000	**0.000**
10:90	3.294	2.664	3.025	**2.994**
20:80	3.773	3.740	3.805	**3.773**
30:70	5.685	5.519	5.472	**5.559**
40:60	6.949	6.482	6.663	**6.698**
50:50	8.827	8.700	8.337	**8.621**

As can be seen from the results, the values correspond to the composition of the samples and the assumed combustion temperatures, where nanosilica is unburnable and therefore

has a combustion heat of 0 MJ/kg, while for cellulose fibres the combustion heat ranges from 15 to 18 MJ/kg depending on the specific fibre composition and cellulose content [16].
Furthermore, the determination of non-combustibility according to EN ISO 1182 [14] was carried out when the test samples were exposed to a temperature of +750°C. This test appeared to be crucial in terms of classification and behaviour of the samples when exposed to fire.

Table 3. Evaluation of fire resistance according to EN ISO 1182

Ratio (Cellulose:Nanosilica)	Temperature increase ΔT [°C]	Loss of weight Δm [%]	Sustained flamming t_f [s]
0:100	3.6	7.5	0
10:90	22.3	23.0	19
20:80	57.8	23.0	44
30:70	83.5	40.8	71
40:60	89.9	29.5	106
50:50	86.7	46.3	144

As can be seen from the test results in Table 3, the amount of cellulose fibres has a significant effect on all the properties observed during the test. As far as temperature rise is concerned, only a sample with 10% cellulose fibres would pass Class A2(A1). Similarly, in terms of flame burn time, only a sample with 10% cellulose fibres would pass. In terms of loss of weight, all samples would pass both A2 and A1.

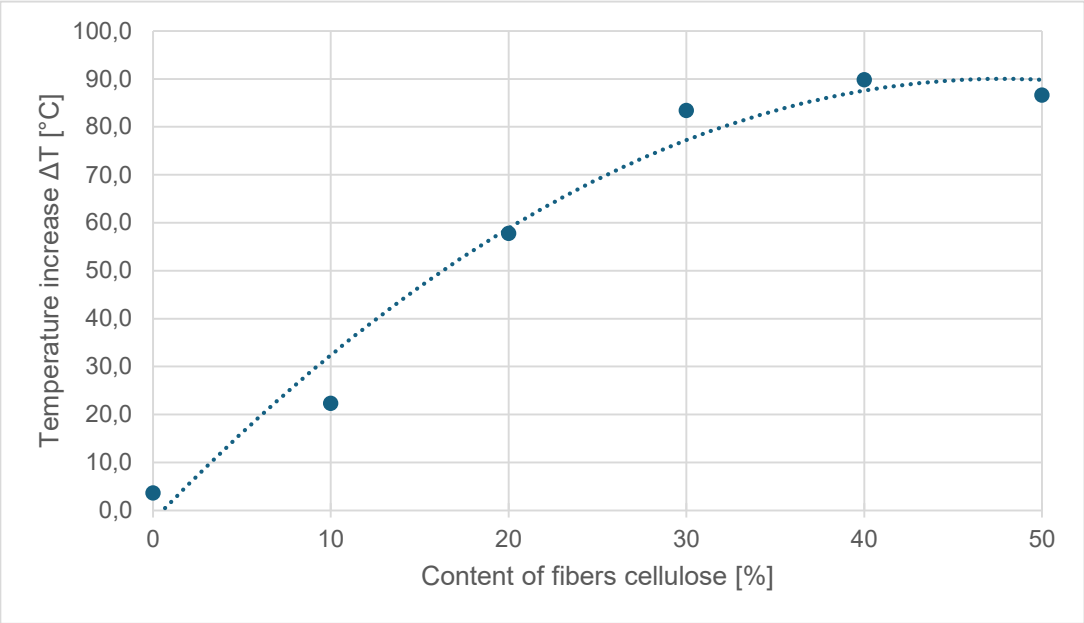


Figure 3. Temperature rises in non-combustibility test as a function of cellulose fibre content

https://doi.org/10.5593/sgem2024/6.1/s26.45

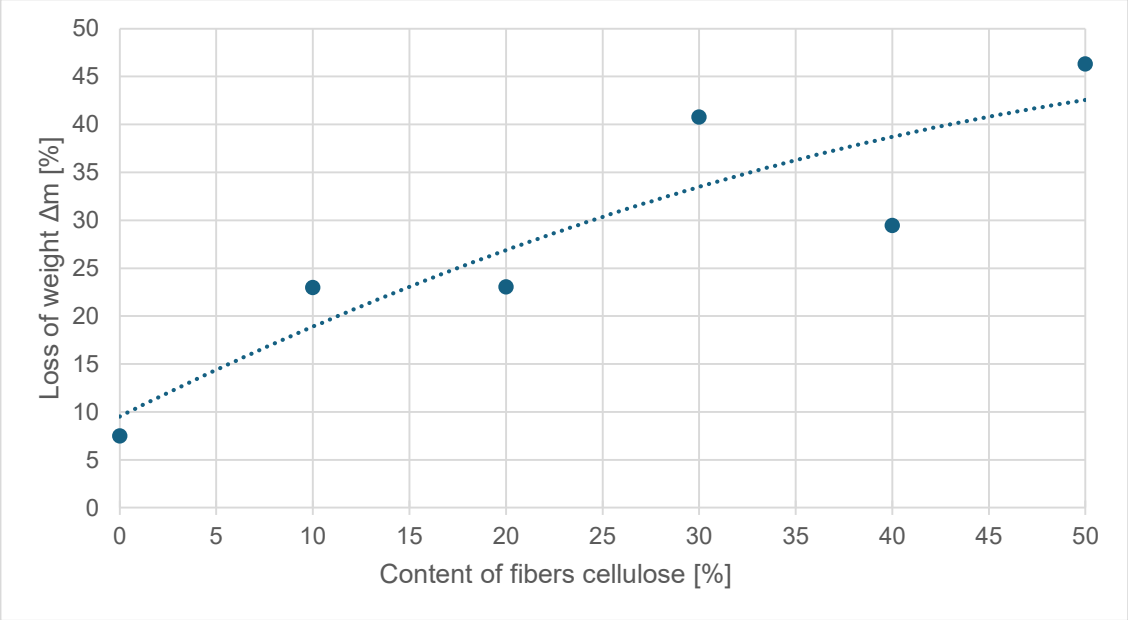


Figure 4. Loss in mass in the non-combustibility test as a function of cellulose fibre content

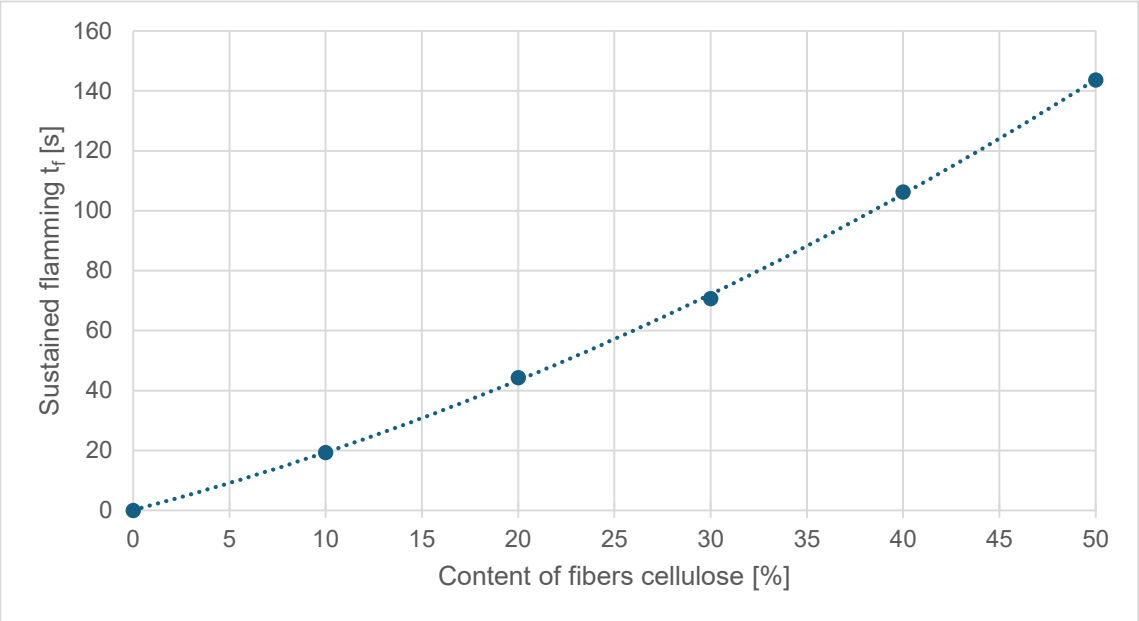


Figure 5. Flame burning time in the non-combustibility test as a function of cellulose fibre content

DISCUSSION

The measurement results confirmed the initial assumptions that the addition of organic cellulose fibers will have an effect on all measured parameters. However, the behavior was different within individual trials. In the case of small flame source ignition test, the

negative effect of whole vine fibers on the test result was proven, however, all the samples passed the test and none of the samples ignited during the test.

In the case of combustion heat, the test result corresponded to the assumption based on the composition of the samples and the combustion heat of individual components. What was interesting here was that the heat of combustion was not measured for the sample with 100% of nanosilica, the test result was equal to 0, even though the sample contained a small proportion of viscose fibers. However, this small amount was so insignificant from the point of view of the test result that it was equal to the accuracy of the given measurement, therefore the overall test result was 0 MJ/kg.

In the case of the test of non-combustibility, the results were, according to initial assumptions, connected to the content of the organic component, which burned at a temperature of 750°C. However, the result of the test was slightly different from the results of tests for other building materials of a similar composition [17], because non-flammable nanosilica provides thermal protection during the test and prevents rapid combustion of the organic component.

CONCLUSION

The results of the experiments conducted show that the hybrid core insulators for the production of VIP exhibit relatively good properties in terms of reaction to fire. From the point of view of the current classification of VIP with class 'E', the use of organic cellulose fibres as a substitute for nanosilica is not a problem. It can be expected that a hybrid insulator with a fibre content of up to 50% can be classified in much higher reaction to fire classes. However, a larger scale test according to EN 13823 would be required for classification. However, based on the results of the flammability test, it is believed that achieving class "D" should be realistic. Overall, the results were very interesting and it can be concluded that the use of hybrid core insulators made up of a combination of nanosilica and secondary cellulose fibres is realistic and the hybrid panel composition does not pose any major problems in terms of the fire performance of the resulting VIP.

For stand-alone applications and in terms of the overall contribution to fire performance of the hybrid core insulator, it is believed that a 10% replacement of nanosilica with cellulose fibres will still allow the resulting insulator (without barrier film) to be classified as Class A2 [2].

ACKNOWLEDGEMENTS

This paper was elaborated within the bilateral research project between the Czech Republic (GAČR 22-09616K) and the Republic of Slovenia (project No. N2–0258) “Study of thermal properties and reduced life cycle impact of alternative hybrid eco-nanomaterials under low pressure”.

REFERENCES

[1] Regulation (EU) No 305/2011 of the European Parliament and of the Council, 2011.

[2] EN 13501-1. Fire classification of construction products and building elements - Part 1: Classification using test data from reaction to fire tests, 2019.

https://doi.org/10.5593/sgem2024/6.1/s26.45

[3] Energy Performance of Buildings Directive EU/2024/1275

[4] EN 15978. Sustainability of construction works – Assessment of environmental performance of buildings – Calculation method, 2012.

[5] EAD 040083-00-0404, January 2019.

[6] Vajó, B., Lakatos, A., Super Insulation Materials-An Application to Historical Buildings, Buildings, vol. 11/issue 11, pp 525, 2021.

[7] Yuk, H., Choi, J., Kim, Y., Chang, S. J., Kim, S., Historic building energy conservation with wooden attic using vacuum insulation panel retrofit technology, Building and Environment, vol. 230, 2023.

[8] Brunner, S., Ghazi Wakili K., Stahl T., Binder B., Vacuum insulation panels for building applications—Continuous challenges and developments, Energy and Buildings, vol. 85, pp. 592-596, 2014.

[9] Zach, J.; Novák, V.; Peterková, J.; Bubeník, J.; Košir, M.; Božiček, D.; Krejza, Z., The Use of Advanced Environmentally-friendly Systems in the Insulation and Reconstruction of Buildings, Buildings, vol. 13/issue 2, pp2 1-15, 2023.

[10] EN 17140. Thermal insulation products for buildings - Factory-made vacuum insulation panels (VIP) – Specification, 2021.

[11] Almeida, F.A., Corker, J., Ferreira, N., Neto, M.A., Fan, M.Z., Beyrichen, H., Caps, R. Alternative low cost based core systems for vacuum insulation panels, Ciencia & Tecnologia dos Materiais, vol. 29/issue 1, pp. E151-E156, 2017.

[12] EN ISO 11925-2. Reaction to fire tests - Ignitability of building products subjected to direct impingement of flame - Part 2: Single-flame source test, 2023.

[13] EN 13823. Reaction to fire tests for building products - Building products excluding floorings exposed to the thermal attack by a single burning item, 2022.

[14] EN ISO 1182. Reaction to fire tests for building products - Non-combustibility test, 2023.

[15] EN ISO 1716. Reaction to fire tests for products – Determination of the cross heat of combustion (calorific value), 2018.

[16] Dorez, G., Ferry, L., Sonnier, R., Taguet, A., Lopez-Cuesta, J.M., Effect of cellulose, hemicellulose and lignin contents on pyrolysis and combustion of natural fibers, Journal of Analytical and Applied Pyrolysis, vol. 107, pp. 323-331, 2014.

[17] Fangrat, J, On non-combustibility of commercial building materials, FIRE AND MATERIALS, Volume41, Issue2, ISSN: 0308-0501

SUSTAINABILITY ANALYSIS OF COPPER SLAG AND REPLACEMENT FOR CONCRETE

María José Pérez Verbal[1]

Marcos Diaz González[2]

Andrés Gabriel César Torres[3]

Dr. Mauricio Pradena-Miquel[4]

[1]Departamento de Ingeniería Civil, Universidad de Concepción, **Concepción, Chile**
[2]Department of Construction Sciences, Metropolitan Technological University, Dieciocho, **Santiago de Chile 161, Chile**
[3]Universidade de São Paulo, Escola Politécnica, Departamento de Engenharia de Transportes, **São Paulo, SP, Brazil**
[4]Facultad de Ingeniería, Arquitectura y Diseño, Universidad San Sebastián, Lientur 1457, **Concepción 4080871, Chile**

ABSTRACT

Chile is one of the largest copper producers in the world, which implies a significant generation of waste, particularly copper slag (CS). On the other hand, the high demand for concrete mixes generates a high consumption of natural aggregates as sand. However, specialized literature indicates that the fine aggregate can be partially replaced by CS keeping (or improving) the concrete properties. Then, this paper presents a sustainability analysis of the partial replacement of fine aggregate of concrete by CS. The magnitude of the benefits that would be obtained from recycling at an environmental, economic, and social level will be directly associated with the legislation and will condition the responsibility of the producer regarding their waste. In addition, aggregate extraction is reduced having an extra positive effect in the natural capital. Finally, there are social benefits associated mainly to the improved quality of life of the population surrounding the landfills of CS.

Keywords: copper slag, sustainability analysis, concrete, legislation

INTRODUCTION

It is estimated that approximately 24.6 million tons of slag are generated in the global copper industry according to Gorai [1]. The Comisión Chilena del Cobre, also report that Chile is the largest copper producer worldwide and the third in terms of smelter copper production according to the Chilean Mining data, generating 2.2 tons of copper slag (CS) for one ton of copper produced, being also a large producer of these. This generates extensive areas of accumulation of this waste, negatively impacting the environment. To avoid continuing with this accumulation, recycling alternatives are being sought for CS.

On the other hand, Petek and Ostertag [2] estimated that each year more than 11 billion tons of concrete are manufactured worldwide and, according to the concrete dispatch index provided by the web of the Cámara Chilena de la Construcción, it is estimated that in Chile there is a total of 20 million annually for the data of the year 2021.High

https://doi.org/10.5593/sgem2024/6.1/s26.46

demand generates a large consumption of aggregates, estimated at approximately 10 million m3 per year [3]. These activities generate environmental impacts due to the energy and emissions associated with the extraction and crushing of aggregates, as well as other negative environmental and hydrological effects. In this context, the use of waste as a replacement for natural aggregates in concrete is very attractive.

The study by Al-Jabri [4] asserts that CS have mechanical and chemical characteristics that allow them to be used in concrete mixes as a partial replacement of aggregates. According to Cendoya [5], Al-Jabri [4], Thomas [6], Wu [7] and other studies, replaced CS as fine aggregates in concrete mixtures, obtaining optimum results of up to 40% replacement in terms of strength and Thomas [6] in terms of durability. The same values were found for mortar mixtures by Borkowsky [8] and Al-Jabri [4].

In addition to the purely technical aspects related to materials, it is important to perform a more comprehensive analysis that allows visualizing the potential and limitations of the joint from environmental, social, manufacturing, and legislative perspectives. In this sense, Ashby [9] proposes a comprehensive method for the analysis of material joints for sustainable development, where in this case it would be associated with the use of CS as a sustainable alternative for the partial replacement of fine aggregate in concretes.

METODOLOGY

According to the above, the optimum percentage of use of CS in mortars and concretes is defined, being this the basis for the sustainability evaluation. The sequence of the working method is shown in Figure 1, be an evaluation performed using the five-step method delivered by Materials and Sustainable Development by Ashby [9]. This method consists of defining the problem and objectives of the project, identifying the stakeholders, researching concrete facts, analyzing the facts through a judgment on the impact on the three capitals (social, environmental, and manufactured) and finally a reflection on implementing the project and its benefits.

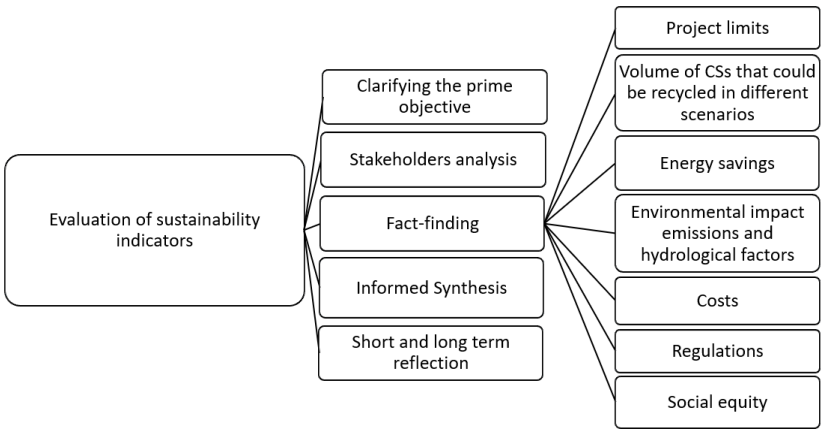


Figure 1. Method delivered by Materials and Sustainable Development (Adapted from Ashby [9]).

In the investigation of facts, the project limits associated with the life cycle according to ISO 14040 (2006) are established. To know these limits, a review is made of the international and national legislation on the responsibility of the waste generated by the producing companies and, in addition, of the uses that this waste currently has as a

replacement for natural fine aggregate. This seeks to analyze what will be the life cycle evaluated in the following stages.

Then, different cases are generated to know the volume of CS that could be recycled in different scenarios. Recycling volumes are estimated considering the amount of CS generated annually by each of the copper smelters in Chile, producing approximately 2.2 tons of CS per ton of copper produced. In addition, it is assumed that the transport distances for CS are comparable to the transport distances for natural fine aggregates (NFA), so that areas close to existing smelters are considered.

Subsequently, an estimate is made of the savings that this project generates in terms of energy and environmental impact emissions. The impacts associated with hydrological factors generated by excessive aggregate extraction are also identified, as well as the social benefits of the project if implemented. In addition, the regulatory requirements that this waste must meet in order to be used as fine aggregate in concrete mixes were identified.

RESULTS

Problem definition and objectives

The large volume of accumulated CS in landfills has the potential to contaminate soils and water in the sector, which prompts the generation of a use for this waste and avoid these environmental impacts. The objective of the articulation is to reduce the accumulation of CS by using it as a partial replacement material for NFA in concrete mixes, recycling at least half of the CS generated annually in Chile. The time scale would be mainly associated with the change in legislation, where the REP Law (Ley N°20920, 2016) is considered as a criterion, specifically the decree associated with the priority product, considerate a time scale of 10 years.

Stakeholders

It is necessary to identify the project stakeholders in order to be respected and involved. At the same time, it seeks to avoid obstructions or frustrations of the purpose of the project itself according to Ashby [9]. Figure 2 shows the individuals and the dependence of one on the other by arrows.

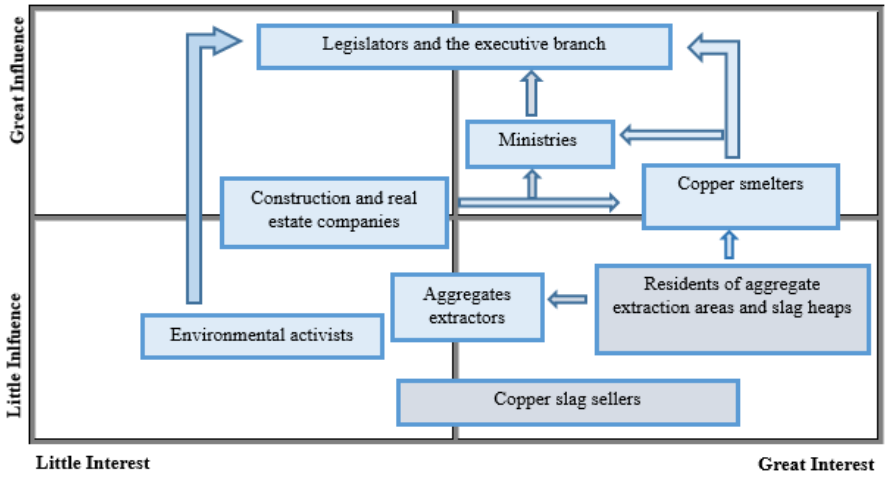


Figure 2. Influence vs interest of stakeholders.

https://doi.org/10.5593/sgem2024/6.1/s26.46

Investigations of the facts

According to data provided by the University of Concepción (Codelco CS) and Borkowsky [8], it is considered that the physical properties between CS from different mining companies in Chile are similar. On the other hand, the volume of CS generated annually by the seven smelters that currently exist in Chile is estimated, according to their respective productions in the years 2018-2019, gives us a total of 1.107.965 m3 per year.

Project boundaries

In different parts of the world, the existing approach is basically to seek economic growth at the expense of environmental degradation. The transition from this traditional approach to a more sustainable one is based on finding a better eco-efficiency of production and consumption systems [10]. To achieve this, the principle of generating worldwide standards that create prevention measures and/or internal costs for the industry returns to the foregoing. This de-linking is achieved in the European Union, where the creation of environmental awareness and legislation have been fundamental.
For other hands, we have the legislations. In Australia, a National Waste Policy was published, which represents a new commitment to sustainable development, including the internalization of environmental costs by companies and the polluter pays principles [11]. In the European Union through Directive 2006/21 (2006) expresses the waste management of industries having as objective that: "they must ensure adequate waste management plans for the prevention or minimization, treatment...and encourage the recovery of extractive waste by recycling". The Indian regulation restricts the use of soils for construction works within a radius of 100 kilometers around a thermoelectric plant, in addition the cost of transporting Coal must be borne by the producing company (Government of India, 2018). And OECD countries published Extended Producer Responsibility (EPR) Manual Guide (ENV/EPOC/WPRPW, 2015-16), which states that: "a producer's responsibility for a product extends to...assuming responsibility for collecting products at the end of their useful life and sorting them before their final treatment, ideally, recycling...can enable producers to exercise their responsibility either by providing the necessary financial resources or by assuming the operational and organizational aspects of the municipalities' process". Chile being part of the OECD countries, assumed the REP law N°20920 (2016).

Regarding the life cycle, it is assumed that the costs associated with the de-linking of environmental degradation and production should be assumed by the producing companies, supported by legislation. ISO14040 (2006) defines the life cycle assessment (LCA) as a technique for determining the environmental aspects and potential impacts associated with a material. Figure 3 shows the stages of the LCA of a material, in this case, concrete mixes.

To perform the LCA it is necessary to define its limits and assignments. A simplification of this is generated called Streamlined LCA, limiting it only to the differences of the two-alternative. The bounded cycle is based on the similarities that are supported by the following assumptions: (1) It is assumed that the material transport distance in both cases will be comparable. (2) It is assumed, according to the legislation previously exposed, that the recycling process of the CS is the responsibility of the

producing company (economically and environmentally). (3) The replacement of sand by CS as fine aggregate generates equivalent concrete mixes.

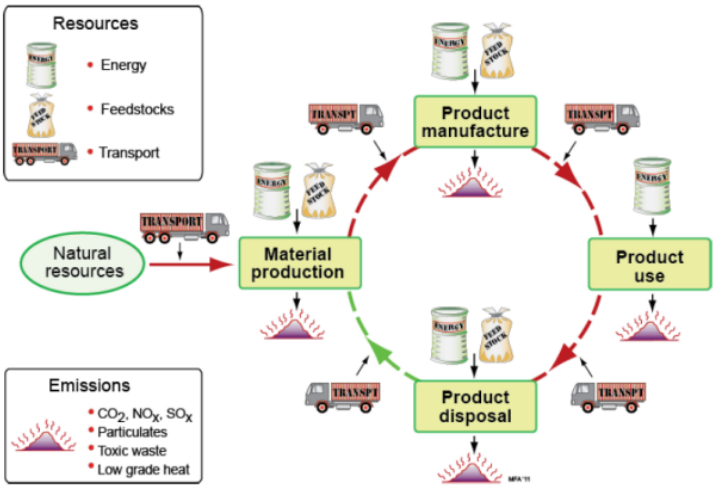


Figure 3. Product life cycle, Ashby [9].

Therefore, the analysis focuses on the differences generated in the production stage of the material. These differences are basically due to the energy and emissions required for the extraction of the NFA and its processing.

Materials and manufacture

The volume of CS that could be recycled is expressed according to masonry, stucco mortars and concrete walls and, in remaining concrete applications, according to the Concrete Dispatch Index provided on the website of the Cámara Chilena de la Construcción the volume of national concrete dispatch for 2019 is 8718534 m3. The value per region is generated urban settlement in hectares per region.

The values of possible recycling were calculated for two different cases, firstly, how much a macrozone (from Arica y Parinacota to Bernardo O'Higgins) could recycle considered the area with mining in operation. In the second case, was evaluated how much each mining region could recycle according to its own CS production.

The results obtained in both cases are given in table 1. Where we can observe that there is a great difference between both cases, since the "macrozone" considers the Metropolitan Region (MR) which has the highest urban demand in all the regions of Chile. Therefore, it is important to consider the MR, since according to the results it is obtained that it can recycle more than 100% of the leftover CS from both surrounding regions (Valparaíso and Bernardo O'Higgins).

Energy

The energy required to produce river fine aggregate corresponds to 69 MJ/t (in diesel), which would be equal to 184 MJ/m3 of sand, assimilated to that given by Venkatarama and Jagadish [12] corresponding to 175 MJ/m3. Table 2 presents as an example the energy savings that would be obtained in case of "Macrozone". The value of 184 MJ/m3 was used for the calculation.

https://doi.org/10.5593/sgem2024/6.1/s26.46

Table 1. Cases results.

	Macrozone	Per region
Mortars app	4%	0,9 - 4 %
Concrete walls	10%	2,4 – 11,1 %
Remaining concrete	50%	6,7 - 46 %
Total	64%	10 - 61,1 %

Table 2. Energy savings for Macrozone' case.

Application	**Energy savings [GJ]**
Mortar application	7.208
Concrete walls	20.079
Remaining concrete applications	97.358
Total	124.645

Emissions

Aggregate extraction and production generate emissions, where Pradhan [14] exhibits the environmental impacts associated with 1 m3 of river sand. As an example, the impacts that could be saved in "Macrozone" case, are set out in Table 3 where the following are considered: Abiotic depletion (ADP), Abiotic depletion due to fossil fuels (ADP), global warming potential (GWP), Depletion of ozone layer (ODP), Formation of tropospheric ozone photochemical oxidants (POCP), Acidification potential (AP) and Eutrophication potential (EP).

Table 3. Associated environmental impacts.

Impact category	Unit	Impacts per m3 of sand	Macrozone Case
ADP	kg Sb eq	1,84 E-05	13,11
ADP (fossil fuels)	MJ	3,65 E+01	25.964.664
GWP	kg CO2 eq	2,69 E+00	1.916.152
ODP	kg CDC-11 eq	1,23 E-07	0,09
POCP	kg C2H4 eq	1,09 E-03	776,36
AP	kg SO2 eq	1,86 E-02	13.248
EP	kg PO4-3 eq	2,42 E-03	1.724

Hydrological Factors

The intervention of natural watercourses for aggregate extraction generates changes in their slope, deformations and disturbances in their geometry, flow structure and flow velocities. Aggregate extraction generates a sediment deficit, where the downstream erosion process begins according to Gatica [13]. Alterations range from geometric changes of the section to destabilization of slopes due to changes in flow patterns and sediment balance, channel deepening and bed armoring according to Kondolf [15]. This is why there are cases where aggregate extraction has endangered bridges, roads and slopes.

Costs

As explained above, the difference between the process associated with the new alternative and the traditional process is specifically the extraction of the NFA. The rest

of the process is considered the same, assuming that the cost of producing the CS would be associated with the producing company.

Synthesis

After gathering the necessary information to generate an evaluation of the articulation, it is necessary to know the final impacts of the events on the three associated capitals presented in Table 4.

Table 4. Project impact in three capitals.

	Human capital	**Environmental capital**	**Manufacturing capital**
Materials	(+) Added value in sustainable construction.	(+) Large volume of waste recycling and reduction of extractions.	(+) Less dependence on finite resources.
Energy	-	(+) Lower associated energy.	-
Environmental	(+) Better quality of life for neighbors.	(+) Reduction of environmental impact emissions and improvements by reducing NFA extraction.	-
Legislation	-	-	(-) Modification of the regulations and legislations.
Economic	-	-	(+) There is no associated cost or need for new technology.
Social	(+) Satisfaction with waste recycling.	(+) Reduction of contamination in the areas surrounding the extraction of aggregates.	(-) Acceptance of the material by construction companies is unknown.

Table 4 shows that more positive than negative factors are identified in the implementation of the project. The great challenge lies in modifying the current legislation and regulations.

CONCLUSION

The sustainability analysis revealed that in the best scenario, between 58% and 64% of the CS generated annually could be recycled, resulting in significant environmental benefits. These benefits include reduced impacts on river hydrology and quarries due to decreased aggregate extraction, and the utilization of slag waste. Additionally, there are social benefits, such as improved quality of life for residents near extraction areas and increased awareness of recycling and environmental issues. These benefits are linked to entrusting CS grinding to producers, which would require changes in Chilean legislation to include clear and specific producer responsibility for waste management.

The project could further improve by increasing recycling volumes through subsidies for transporting waste to distant regions. Given the expected population growth and rising demand for construction materials, CS recycling presents a viable alternative. Recycling rates could also be enhanced by expanding the applications for CS use.

https://doi.org/10.5593/sgem2024/6.1/s26.46

REFERENCES

[1] Gorai B., Jana R. K., Characteristics and utilization of copper slag – a review, Conservation and Recycling (39), pp 299-313, 2003.

[2] Petek A. and Ostertag C., Life-Cycle Assessment of High-Strength Concrete Mixtures with Copper Slag as Sand Replacement, Hindawi, Advances in Civil Engineering, 2009.

[3] Uribe P., Explotación y venta de áridos en la comuna de Puerto Montt. Universidad Austral de Chile, 2011.

[4] Al-Jabri K.S., Al-Saidy H., Ramzi T., Effect of copper salg as a fine aggregate on the properties of cement mortars and concrete, *Construction Building Materials,* 25, 933-938, 2011.

[5] Cendoya P. Efecto en la Resistencia de las escorias de fundición de cobre como agregado fino en el comportamiento resistente del hormigón. *Revista chilena de ingeniería,* 17(1), 85-94, 2009.

[6] Thomas J., Thaickavil N., Abraham M.P., Copper or ferrous slag as substitutes for fine aggregates in concrete. *Advances in Concrete Construction,* 6, 545-560, 2018.

[7] Wu W., Zhang W., Ma G., Optimum content of copper slag as a fine aggregate in high strength concrete. *Materials and Design* 31, 2878-2883, 2010.

[8] Borkowsky A. Estudio de la falla de corte de morteros de pega con escorias de fundición de cobre. *Universidad de Concepción, Chile*, 2018.

[9] Ashby M., Materials and Sustainable Development. Un enfoque dinámico y multidimensional. *Ed. Mundiprensa,* 2016.

[10] Hendriks C.F., Vogtlander J.G., Janssen G.M.T., The eco-cost/value ratio, a tool to determine the long-term strategy of de-linking economy and environmental ecology. *International Journal of Ecodynamics,* 109, 67-77, 2006.

[11] Gumbley W., An analysis of regulatory Strategies for Recycling and Re-Use of Metlas in Australia. *Resources,* 3(2), 395-415, 2014.

[12] Venkatarama and Jagadish. Embodied energy of common and alternative building materials and technologies. *Energy and Buildings,* 35, 129-137, 2003.

[13] Gatica C., Formulación de un modelo de optimización para la gestion de sedimentos en la zona alta del río Maipo. *Universidad de Chile, Chile,* 2010.

[14] Pradhan S., Tiwari B.R., Kumar S., Barai S., Comparative LCA of recycled and natural aggregate concrete using Particle Packing Method and conventional method of design mix, *Journar of Cleaner Production, 228, 679-691,* 2019.

[15] Kondolf G.M., Geomorphic and environmental effects of instream gravel mining. *Landscape and Urban Planning, 28, 225-243*, 1994.

THE ASSESSMENT OF STRENGTH PROPERTIES OF HISTORICAL MORTARS FOR SUSTAINABLE RENOVATIONS

Eng. Jaroslav Pokorný, Ph.D.[1]

Doc. Eng. Jan Fořt, Ph.D.[1]

Eng. Lenka Scheinherrová, Ph.D.[2]

Eng. Tomáš Navara[1]

Eng. David Javorský[3]

[1] Department of Civil Engineering, Faculty of Technology, Institute of Technology and Business, **Czech Republic**
[2] Department of Material Engineering and Chemistry, Faculty of Civil Engineering, Czech Technical University in Prague, **Czech Republic**
[3] National Heritage Institute of the Czech Republic, Regional Office in České Budějovice, **Czech Republic**

ABSTRACT

Old buildings, in particular, those coming from the first half of 20th century often suffer with increased dampness in masonry coming from different sources. Some of them, however, have aesthetically rendered valued facades which are worth saving. For the design of new alternative mortars for renovation interventions, it is essential to obtain properties of original renders. Mechanical properties of mortars are in general assessed on standardized test samples; however, this approach cannot be always well applicable for in situ taken mortars or rendering materials. This paper is devoted to the specification of complex experimental procedure allowing to effectively obtain strength parameters of in situ collected renders which will be comparable with laboratory produced alternative mortars. Throughout this paper the detailed description of in situ collected renders sampling procedure is provided. Further, the adjusted approach of flexural strength testing in three-point arrangement and compressive strength tests for both cut renders samples and laboratory prepared alternative mortars is outlined. The suitable set up of testing procedures of materials coming from old or historical buildings introduces a key area for obtaining experimental relevant data being the bases for their sustainable renovations.

Keywords: renders, old buildings, strength properties, testing procedure, sustainable renovation

INTRODUCTION

In our history mortars intended for bonding, plastering and rendering applications were common part of masonry structures in the construction industry. For their production many different locally available raw materials were used [1]. Accordingly, each mortar type contained, in particular, different filling material – sand. In general, sands were

https://doi.org/10.5593/sgem2024/6.1/s26.47

mined in rich deposits, and with regard to the particular location contained a different amount of clay particles giving the final product various plasticity. Considering mortars composition thought the history, the binding materials also changed considerably. At the beginning of 20th century, a lime hydrate or hydraulic lime were a common input material for rendering mixes. With advancing time and with the development of industrial processes of Portland clinker production, Portland cement became more widespread binding component. Used binders have a significant effect on strength properties of applied renders, and also on their overall durability [2]. Except of a binder type, mortars also often contained mineral admixtures with pozzolanic properties [3]. Buildings coming from the first half of 20th century are not often categorized among historical buildings or buildings with the label of cultural heritage, however, some of them have aesthetically interesting valued facades. In general, old buildings suffer with increased dampness in masonry coming from different sources [4]. The dampness occurrence is in many cases connected with non-functional, damaged or missing horizontal water-proved insulation [5]. High moisture rate in masonry structures may cause a serious irreversible deterioration of rendering mortars caused by freeze-thaw cycles, high concentrated salts etc. High valuable facades are worth saving, and thus new mortars types for sustainable renovation and retrofitting innervations must be formulated. Accordingly, it is necessary to specify the composition and, in particular, physical and mechanical properties of original renders, in order to provide compatible alternative materials [6]. With respect to the EN 1015-11 [7] strength related properties of mortars on standardized specimens for laboratory testing are assessed. However, collecting mortars, renders or plasters samples on a site (in situ) often is not possible to obtain, on the one hand, in a large extent and, on the other hand, in layers thicker than 20 mm.

This work describes modified approach to effectively obtain strength parameters of in situ collected renders and to be comparable with laboratory produced alternative mortars. The paper provides a comprehensive description of samples preparation and applied adjusted method of strength properties testing. Data gained in this way can be considered as the suitable base for sustainable renovations.

EXPERIMENTAL

Several potential buildings which were built in the first half of the 20th century and having hard mortars-based facades located in the Czech Republic were subjected the local inspection and also the performance of a basic construction-technical survey by experts from the National Heritage Institute of the Czech Republic together with cooperating institutions. After aforementioned analysis, own physical collections of renders on selected buildings were taken. The places of physical innervations in facades were chosen in dependence on their orientation to the cardinal points, their current state of surface and also the occurrence of a locally appearing deteriorations. The main aim of the collections was to obtain the complex and intact samples of renders which become a suitable material base for the comprehensive experimental investigation including the assessment of physical properties, mechanical resistance and others. Accordingly, the optimal approach turned out to be a combination of cutting tools and manual methods using flat cut chisels. Firstly, the place of a collection was bordered with an angle grinder equipped with a diamond blade intended for concrete and masonry cutting. In the next step, flat cut chisels having different sizes were applied in

order to separate the plaster from the substrate. The challenge was, on the one hand, to obtain the intact sample and, on the other hand, to minimize a damage of the substrate. Example of a render sample collected directly from the facade of a building is shown in **Figure** 1. For one collecting point two samples were taken, if possible. The average size of a sample was approx. (250 x 150) mm^2.



Figure 1: Example of a render sample directly cut from the facade of a building.

With the focus on strength properties of mortars, flexural and compressive strengths, these material features according to the EN 1015-11[7] are assessed. In this standard, typical experimental samples with the shape of prism and the size of (40 x 40 x 160) mm^3 for strength tests are considered. The usual way how to obtain a mortar sample from masonry provides core drills or local sampling performed with a destructive approach. Considering historical buildings or buildings with valuable façades the extent and size of sampling is very limited. The question is how to approach to in-situ taken collections from historical and other buildings and to prepare test samples for strength properties determination which can provide good comparable base with laboratory prepared mortar samples.
In this case when plate collections of renders with usual area of (250 x 150) mm^2 and thickness around 20 mm, test specimens for strength properties testing with a diamond circular saw were cut (see in **Figure 2**). The size of specimens with regard to the prevailing thickness of renders of (20 x 20 x 100) mm^3 was chosen. Material observation of collected renders samples showed that these contained in all cases a fine aggregate with the maximum size up to 4 mm only. Thus, it was possible to approach to lower cross-section area of (20 x 20) mm^2.



Figure 2: Cutting of renders (left) and cut prismatic sample (20 x 20 x 100) mm^3(right).

https://doi.org/10.5593/sgem2024/6.1/s26.47

For the comparison purpose, an expediently prepared mortar in laboratory was made. The binding blend was consisted of lime hydrate CL 90 Čertovy schody (Lhoist, Ltd., Czech Republic) and CEM II/A-LL 32,5 R (Heidelberg Materials CZ, Corp., Czech Republic) in the weight ratio corresponding 2:1. The mined sand of the fraction 0/4 mm, provided by Mane Holding, Plc., Czech Republic, served as a filler material and was mixed with the binder blend in 3:1 by weight. The water to binder ratio (w/b) ensuring suitable consistency of fresh mortar of 160 x 160 ± 5 mm (EN 1015-3 [8]) was established 0.72. Fresh mortar mix were blended in the laboratory mixer E095 (Matest, S.p.A., Italy), whereas subsequently was placed into iron molds allowing to prepare six prisms with dimensions (20 x 20 x 100) mm^3 at particular step. Test samples were stored in laboratory conditions, with the temperature of 20 ± 1 °C and relative humidity 45 ± 5 %, covered by plastic foil and wet once per day by water spraying for overall curing period of 28 days. Comparison of a cut specimen from collected render and casted laboratory prepared specimen is depicted in **Figure 3**.
Mechanical tenting of modified samples was caried out with the usage of the hydraulic press Matest – Servo Plus Evolution (Matest, S.p.A., Italy), and the detailed description of flexural and compressive strength determination via following text parts is provided. The combined expanded uncertainty, considering in minimum 10 test specimens, for both procedures does not exceed 8 %. Bulk density values were assessed according to the methodology described in the EN 1015-10 [9].



Figure 3: Comparison of a cut sample from a render (left) and a casted sample from a laboratory produced mortar (right).

RESULTS AND DISCUSSION

Both, cut and casted samples, after curing period were subjected to the strength properties testing. The fundamental principle of strength tests from the EN 1015-11 [7] was adopted. However, in the case of flexural strength testing in three-point arrangement the procedure and equipment were modified. There was designed the supplementary equipment which can be easily installed to the regular set intended for tenting of standardised (40 x 40 x 160) mm^3 specimens. The main change consists in the shortening the distance between supports to 60 mm, whereas the length of modified render specimens as well as mortar samples was limited with the size of 100 mm. Given equipment further decrease the distance between the loading element and bearing supports, in order to be suitable for placement and loading of adjusted samples with the cross-sectional area of (20 x 20) mm^2. With regard to the different types of collected renders, the loading rate for flexural tests of 20 $N \cdot s^{-1}$ as the optimal value was set. After flexural tests the broken parts of prims with uneven ends were cut with the diamond

circular saw, and thus a pair of samples with clearly definable dimensions for compressive strength tests were obtained. The press loading process of regular halves of prisms was cried out in hydraulic press equipped with massive load plates, whereas each sample was centrally placed between plates and tests with the loading rate of 0.1 $kN \cdot s^{-1}$. The choice of loading rates in both flexural and compressive strength tests was made with consideration of prevailing test duration between 30 and 90 s.



Figure 4: Flexural strength test (left) and the supplementary equipment for three-point flexural test on modified samples (right).

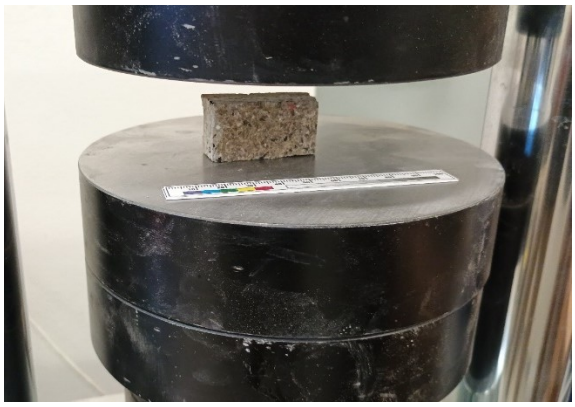


Figure 5: Compressive strength test on cut half of prism.

First set of strength-related data obtained on cut and laboratory prepared specimens are given in **Table 1**. In both cases the compressive strength exceeds average value of 2.5 MPa. The average flexural strength reached values under 1.0 MPa, when higher values for cut samples, and compared with laboratory prepared mortars, were observed. The modified procedure of flexural and compressive strength testing on (20 x 20 x 100) mm^3 turned out to be a promising approach with regard to the measuring uncertainty moving about 8 %, with an assumption of high number of test samples.

Table 1: Strength properties of cut and prepared mortars.

Sample	Bulk density [$kg \cdot m^{-3}$]	Compressive strength [MPa]	Flexural strength [MPa]
Cut	1 762	3.4 ± 0.2	0.9 ± 0.1
Prepared	1 740	3.1 ± 0.3	0.8 ± 0.1

https://doi.org/10.5593/sgem2024/6.1/s26.47

CONCLUSION

The paper comprehensively described and discussed the possibility of sampling and strength properties testing of in situ taken renders and comparative mortars made in laboratory condition. Unlike the recommendation of EN 1015-11 [7], strength tests were performed on prisms with dimensions of (20 x 20 x 100) mm^3 and with the use of the supplementary equipment for the thee-point flexural test arrangement on modified samples. Practical tests and obtained data showed the suitability of applied approach for in situ collected render samples, and compared with laboratory produced alternative mortars. Relevant strength properties of old/historical renders constitute an important input parameter curtail for sustainable renovations of valued facades made from hard renders.

ACKNOWLEDGEMENTS

The authors gratefully acknowledge the financial support received from the Ministry of Culture of the Czech Republic, under project DH23P03OVV012.

REFERENCES

[1] Vejmelková E., Keppert M., Keršner Z., Rovnaníková P., Černý R., Mechanical, fracture-mechanical, hygric, thermal, and durability properties of lime-methakalolin plasters for renovation of historical buildings, Construction and Buildings Materials, vol. 31, pp 22-28, 2012.

[2] Almeida L., Silva A.S., Veiga R., Mirão J., 20th Century Mortars: Physical and Mechanical Properties from Awarded Buildings in Lisbon (Portugal)—Studies towards

Their Conservation and Repair, Buildings, vol. 13, 2468, 2023.

[3] Maravelaki-Kalaitzaki L., Bakolas A., Karatasios I., Kilikoglou V., Hydraulic lime mortars for the restoration of historic masonry in Crete, Cement and Concrete Research, vol. 35, 1577-1586, 2005.

[4] Jerman M., Scheinherrová L., Medveď I., Krejsová J., Doleželová M., Bezdička P., Černý R., Effect of cyclic wetting and drying on microstructure, composition and length changes of lime-based plasters, Cement and Concrete Composites, vol. 104, 103411, 2019.

[5] Pokorný J., Ševčík R., Šál J., Zárybnická L., Žák J., Lightweigth concretes with improved water and water vapor transport for remediation of damp induced buildings, Materials, vol. 14, pp 1115-1126, 2007.

[6] Veiga M.R., Velosa A.L., Magalhães A.C., Evaluation of mechanical compatibility of renders to apply on old walls based on a restrained shrinkage test, Materials and Structures, vol. 40, 5902, 2021.

[7] EN 1015-11, Methods of test for mortar for masonry – Part 11: Determination of flexural and compressive strength of hardened mortar, CEN, Brussels, 1999.

[8] EN 1015-3, Methods of test for mortar for masonry – Part 3: Determination of consistence of fresh mortar, CEN, Brussels, 2000.

[9] EN 1015-10, Methods of test for mortar for masonry - Part 10: Determination of dry bulk density of hardened mortar, CEN, Brussels, 1999.

THE EFFECT OF DIFFERENT DEGRADATION ENVIRONMENTS ON CHLORIDE CONTENT AND CARBONATION IN CONCRETE

Dipl. Eng. et Dipl. Eng. Kristýna Hrabová, Ph.D. [1]
Dipl. Eng. Dita Vořechovská, Ph.D. [2]
Dipl. Eng. Tomáš Mazán[1]
Dipl. Eng. Dominik Lisztwan[1]
Dipl. Eng. Dalibor Kocáb, Ph.D. [1]
Prof., RNDr. Pavla Rovnaníková, CSc.[3]
Assoc. Prof., Dipl. Eng. Petr Konečný, Ph.D. [4]

[1]Brno University of Technology, Faculty of Civil Engineering, Institute of Building Testing, **Czech Republic**
[2]Brno University of Technology, Faculty of Civil Engineering, Institute of Structural Mechanics, **Czech Republic**
[3]Brno University of Technology, Faculty of Civil Engineering, Institute of Chemistry, **Czech Republic**
[4]VŠB – Technical University of Ostrava, Faculty of Civil Engineering, Institute of Structural Mechanics, **Czech Republic**

ABSTRACT

Different forms and combinations of degradation attacks cause the damage of concrete and reinforced concrete structures. Among the most usual belong ingress of chlorides and carbonation that influence the quality of the concrete and also affect its ability to protect reinforcement. The resistance of concrete against the mentioned attacks is given also by other surrounding conditions, like temperature, mechanical load, etc. In this paper, experimental findings are presented focused on the investigation of the effect of three different degradation environments, namely freeze-thaw cycles, immersion in salt solution and placing in carbonation chamber, on concentration of chlorides and degree of carbonation in concrete profile. The degradation environments were varied in order to compare the effect of each environment separately and also the effect of combined environmental action.

Keywords: concrete, service life, durability, chlorides, carbonation

INTRODUCTION

Concrete is a construction material that is widely used in the construction industry for its positive properties. The material has been used for centuries and currently faces high demands for its quality and environmental friendliness [1,2]. Building structures are constantly influenced by mechanical, dynamic, climatic, and degradation factors. The exposure of concrete to external environments can lead to its degradation over time, which can result in its deterioration. When concrete fails or deteriorates prematurely, it requires the removal of the concrete, the disposal of the concrete in landfills, the need

https://doi.org/10.5593/sgem2024/6.1/s26.48

for new raw materials and energy, as well as human and financial resources to repair and/or replace the existing concrete structure [3].

Different environments exhibit various mechanisms that lead to damage. The extent of damage varies depending on the exposure time in the environment and the degree of aggressiveness. In the case of embedded concrete in structures and in contact with the surroundings, exposure to weather conditions is closely related to temperature changes. Changes in temperature cause negative effects on concrete, especially in conjunction with water and moisture. The influence of low temperatures causes the generation of hydraulic pressure in pores, leading to the displacement of unfrozen water into the system of unfilled gel pores and the disruption of the cement matrix. The formation of ice is relatively slow, but the displaced water has nowhere to escape in the dense microstructure, and if it reaches a pressure level that exceeds the tensile strength, concrete failure occurs [4,5].

One major cause of durability problems of reinforced concrete is the ingress of external chloride ions into the cover zone, which can attack the steel reinforcement [6]. The diffusion coefficient for chloride ingress into concrete is a crucial parameter describing the resistance against chloride penetration and is important for the durability of reinforced concrete structures vulnerable to chloride-induced corrosion. Predicting the aging of concrete structures affected by reinforcement corrosion is complex due to the intricate mechanical and chemical phenomena involved, as well as their random nature [7,8]. Among other degrading influences, carbonation of concrete can occur due to the ingress of atmospheric CO_2, leading to a lowering of the pH of concrete which can result in corrosion of the steel reinforcement. Additionally, the reaction of calcium hydroxide and calcium silicate hydrate with CO_2 forms calcite, which precipitates within the pores, altering concrete properties [9]. Aggressive environments act on the concrete embedded in structures through various mechanisms, and in the case of exposure to multiple unfavourable environments simultaneously, synergy may occur, leading to a greater overall impact of the aggressive environment. In this paper, experimental findings are presented focused on the investigation of the effect of three different degradation environments, namely freeze-thaw cycles, immersion in salt solution and placing in carbonation chamber, on concentration of chlorides and degree of carbonation in concrete profile. The degradation environments were varied in order to compare the effect of each environment separately and also the effect of combined environmental action.

MATERIALS AND METHODS

A large experimental program is presently in process including the exposure of samples in harsh environments causing degradation of concrete and testing of concrete specimens on various parameters to quantify the effect of degradation on concrete quality. Concrete specimens were prepared from concrete C 30/37, XF4, S4, Cl 0.2, D_{max}=16 mm according to ČSN EN 206+A2 [10]. Composition of concrete mixture is given in Table 1.

Table 1 The composition of concrete mixture

	[kg/m^3]
CEM II/A-S 42,5R	400
Aggregate 0/4 Bratčice	752
Aggregate 4/8 Olbramovice	204
Aggregate 8/16 Olbramovice	755
Water – total/effective	165/152
Superplasticising admixture	2.8
Air-entraining admixture	0.5

Small cylinders of 100 mm diameter and 200 mm length were prepared for durability-related tests. After 3 months of maturing in the water, cylinders were cut into concrete discs of approximately 65 mm in height. These specimens were coated on the sides with epoxy so that the attacked area could only be the cut surface. The special treatment was provided for part of the samples subjected to carbonation. After 1 month of maturing in water, the samples were dried for 2 months under the temperature of 45°C. Generally, all the specimens were coated and subjected to degradation effect in the age of 3 months.



Figure 1 Concrete samples (discs)

Chloride concentration assessment

The samples had been soaked in a salt solution for 3 months before being combined and homogenized for analysis. The ratio between the wetted area of the test concrete discs and the volume of the solution should be between 20-80 [11]. In our case, we chose a ratio of 72.3. Technical salt and demineralized water were used to prepare the solution. The container was covered during the test to prevent evaporation.

https://doi.org/10.5593/sgem2024/6.1/s26.48

Carbonation

The concrete discs were placed in carbonation chamber for 3 months. An important factor is the concentration of carbon dioxide in the test chamber environment, which may decrease due to consumption in the degradation process, therefore the concentration needs to be monitored and maintained at a set value. The exposure environment used in our case was 80% concentration of oxide carbon dioxide, 85 ± 5 % relative humidity and 20 ± 2 °C. Two types of samples - saturated and dried - were placed in the carbonation chamber.



Figure 2 Carbonation chamber

Freeze-Thaw Testing

In this test, the specimens are subjected to alternate freezing and thawing for the required number of cycles. Before the test itself, it is important that the test specimens are stored in a water bath to saturate the specimens. The number of freezing cycles is a multiple of 25, in total, 100 cycles were performed. The measurement is based on the standard ČSN 73 1322 [12]. The test is carried out in time intervals, during which there are specified isothermal holds for 4 hours in case of a temperature of -18°C and 2 hours in case of a temperature of 20°C.

Synergistic effect

Some concrete samples were exposed to a combination of environmental action. One of them is a combination of freeze-thaw cycles (100 cycles) and immersion in salt solution (for 3 months) and the second is a combination of freeze-thaw cycles (100 cycles), immersion in salt solution (for 3 months), drying of discs (for 2 months, at a temperature of 45°C) and placing in carbonation chamber (for 3 months).

After exposure to degradation, the samples were cut into individual layers at the depths of 1.5, 3.5, 5.5, 7.5, 9.5 and 11.5 mm. These layers were ground and tested in the laboratory for the concentration of chlorides and pH in water leaches.

RESULTS AND DISCUSSION

The experiment presents findings focused on the investigation of the effect of three different degradation environments, namely freeze-thaw cycles, immersion in salt solution and placing in carbonation chamber, on concentration of chlorides and degree of carbonation in concrete profile.

In this study, we present the experimental measurements after three months of exposure in chloride environment (three samples – A, B and C) and two samples after three months of exposure in carbonation chamber (one saturated and one dried). Other concrete samples were exposed to a combination of environmental action. One of them is a combination of freeze-thaw cycles and immersion in salt solution and the second is a combination of freeze-thaw cycles, immersion in salt solution and carbonation. Experimental results are given in Tables 2 and 3, separately for each environmental action. Figures 3 and 4 show the same results graphically.

Table 2 Degree of carbonation quantified via pH [-] after exposure to different degradation environments

Average depth [mm]	Reference	Chlorides 91 days (A)	Chlorides 91 days (B)	Chlorides 91 days (C)	Carbonation (saturated)	Carbonation (dried)	Synergy (Freeze+Cl)	Synergy (Freeze+Cl+CO_2)
0.750	12.503	11.910	11.710	12.030	12.480	9.200	12.450	11.200
2.500	12.503	12.230	12.170	12.320	12.560	9.150	12.560	11.610
4.500	12.503	12.270	12.330	12.360	12.580	9.630	12.510	11.690
6.500	12.503	12.280	12.380	12.390	12.660	10.470	12.550	11.550
8.500	12.503	12.310	12.350	12.360	12.640	10.840	12.560	11.360
10.500	12.503	12.320	12.360	12.360	12.650	11.320	12.580	11.480

https://doi.org/10.5593/sgem2024/6.1/s26.48

Table 3 Concentration of chlorides [%] after exposure to different degradation environments

Average depth [mm]	Reference	Chlorides 91 days (A)	Chlorides 91 days (B)	Chlorides 91 days (C)	Carbonation (saturated)	Carbonation (dried)	Synergy (Freeze+Cl)	Synergy (Freeze+Cl+CO_2)
0.750	0.006	0.472	0.421	0.536	0.020	0.022	0.520	0.381
2.500	0.006	0.421	0.461	0.375	0.020	0.009	0.460	0.388
4.500	0.006	0.335	0.389	0.289	0.020	0.014	0.270	0.345
6.500	0.006	0.281	0.322	0.159	0.010	0.021	0.230	0.274
8.500	0.006	0.207	0.265	0.163	0.020	0.014	0.140	0.212
10.500	0.006	0.165	0.188	0.142	0.010	0.015	0.100	0.159

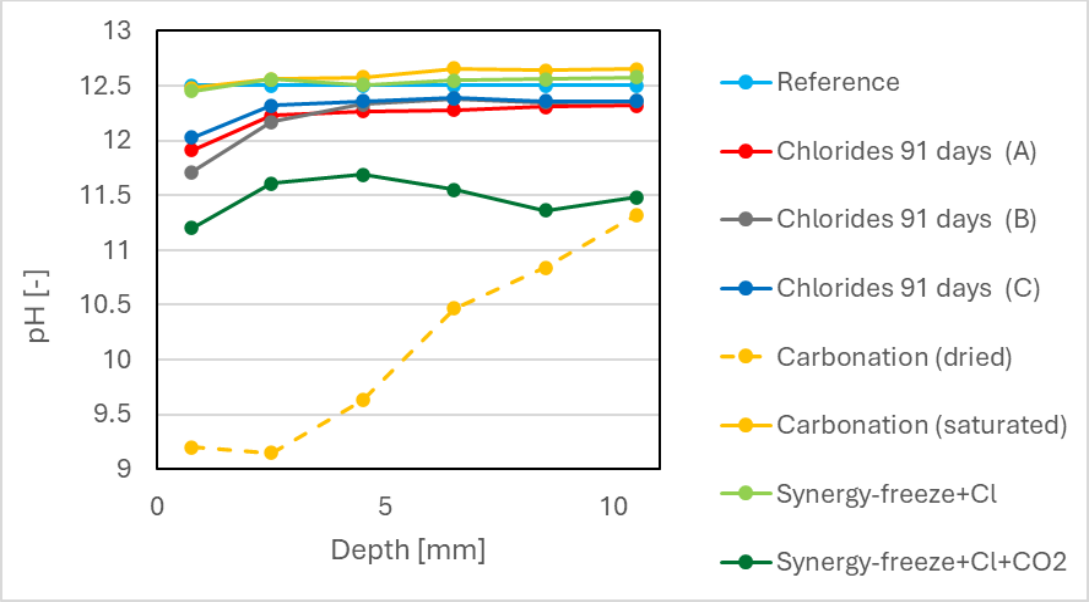


Figure 3 The pH values in concrete profile after exposure to various degradation environments

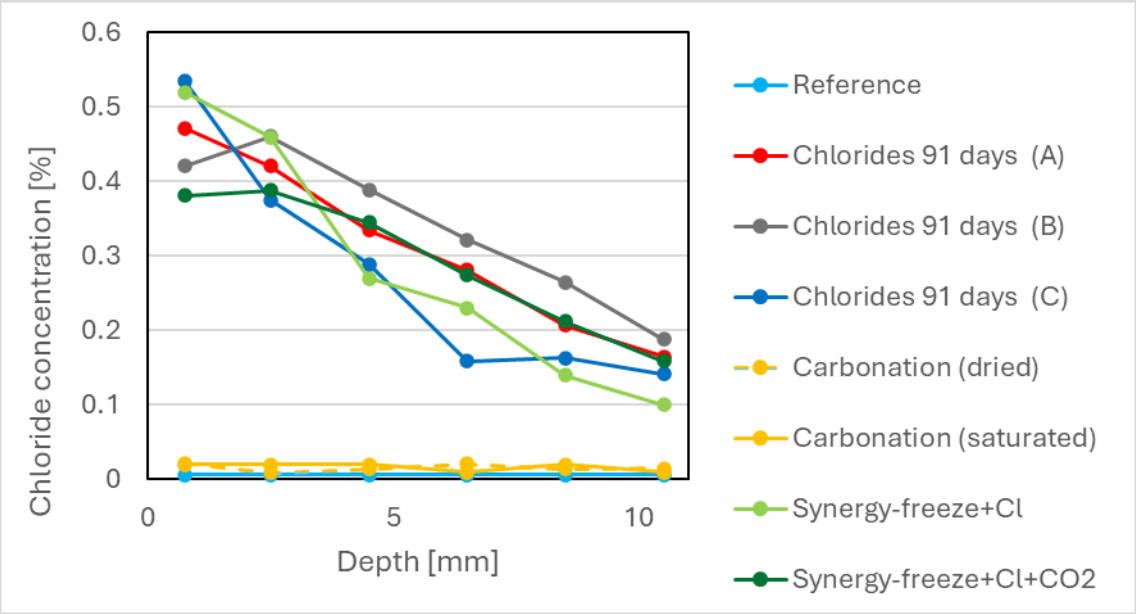


Figure 4 The chloride concentrations in concrete profile after exposure to various degradation environments

Figure 3 shows that the effect of degradation environments on degree of carbonation affects the sample exposed to carbonation, specifically the sample that was dried before being placed in the carbonation chamber. No effect was found for saturated carbonation. In case of synergy, pH was influenced for synergistic effect of all three environments – freeze, Cl and CO_2. Figure 4 shows that the effect of degradation environments on concentration of chlorides appears for samples that were exposed to chloride solution and for synergy. As expected, level of chlorides is almost zero for samples placed in the carbonation chamber.

CONCLUSIONS

Various types of deterioration attacks lead to the deterioration of concrete and reinforced concrete structures. Common factors include the penetration of chlorides and carbonation, which impact the concrete's quality and its ability to protect the reinforcement. This study examines the impact of three different degradation environments - freeze-thaw cycles, exposure to salt solution, and exposure to a carbonation - on the level of chlorides and extent of carbonation within the concrete profile. The results show that the effect of degradation environments on degree of carbonation affects the samples exposed to carbonation, specifically the sample that was dried before being placed in the carbonation chamber and sample exposed to combined effect of freeze + Cl + CO_2. The effect of degradation environments on concentration of chlorides appears for samples that were exposed to chloride solution and for combined effect of freeze + Cl and freeze + Cl + CO_2.

https://doi.org/10.5593/sgem2024/6.1/s26.48

ACKNOWLEDGEMENTS
This outcome was achieved with the financial support of the Czech Science Foundation, project No. 22-19812S and specific research project No. FAST-S-23-8279 at Brno University of Technology.

REFERENCES

[1] Favier, A., Wolf, C., Scrivener, K., Habert, G. A *sustainable future for the European Cement and Concrete Industry.* ETH Zurich. 1(1), pp. 1-97, 2018.

[2] Hrabová, K., Lehner, P., Ghosh, P., Konečný, P., Teplý, B. *Sustainability Levels in Comparison with Mechanical Properties and Durability of Pumice HighPerformance Concrete.* Applied Sciences. vol. 11(11), pp. 1-13, 2011.

[3] Konečný, P., Horňáková, M., Lehner, P., Rovnaníková, P., Sýkora, M. *Model uncertainty in diffusion coefficient for chloride ingress into concrete*, Elsevier, Procedia Structural Integrity. vol. 31, issue 1, pp. 147-153, 2021.

[4] Gong, F., Jacobsen, S. *Modeling of water transport in highly saturated concrete with wet surface during freeze/thaw*, Cement and Concrete Research. Vol. 115, pp. 294-307, 2019.

[5] Bonnet, S., Balyssac, J.P. *Combination of the Wenner resistivimeter and Torrent permeameter methods for assessing carbonation depth and saturation level of concrete*, Construction and Building Materials, Vol.188, pp. 1149-1165, 2018.

[6] Ueli, M. *Angstm Challenges and opportunities in corrosion of steel in concrete*, Materials and Structures, vol. 51:4, 2018.

[7] Zhang, D., Shao, Y. *Effect of early carbonation curing on chloride penetration and weathering carbonation in concrete*, Construction and Building Materials, vol. 123, pp. 516-526, 2016.

[8] Bao, J., Wei, J., Zhang, P., Zhuang, Z., Zhao, T. *Experimental and theoretical investigation of chloride ingress into concrete exposed to real marine environmen*t, Cement and Concrete Composites, vol. 130, 2022.

[9] Ekolu, S.O. *A review on effects of curing, sheltering, and CO_2 concentration upon natural carbonation of concrete*, Construction and Building Materials, vol. 127, pp. 306-320, 2016.

[10] EN 206:2013+A2:2021 Concrete – Specification, performance, production and conformity.

[11] Nordtest NTBuild 443, Nordtest Method: Accelerated Chloride Penetration into Hardened Concrete, Nordtest, Esbo, Finland, 1995.

[12] EN 73 1322 Determination of Frost Resistance of Concrete (in Czech); ÚNMZ: Prague, Czech Republic, 1968.

UNSTEADY STATE THERMAL ANALYSIS OF GLULAMINATED TIMBER ELEMENTS SUBJECTED TO FIRE

Lecturer Dr. Ing. Ruxandra Erbașu [1]

Assist. Dr. Ing. Ioana Teodorescu [1]

PhD Ress. Andrei Sabău [1]

Lecturer Dr. Ing. Daniela Țăpuși [1]

[1] Technical University of Civil Engineering Bucharest, **Romania**

ABSTRACT

The paper presents the procedures of introducing the unsteady state numerical analysis domain for simulating the mechanical behavior of glue laminated timber (glulam) elements when subjected to high temperatures. For any analysis applied to characterize the fire resistance of wood, glue laminated timber implicitly, the unsteady state numerical analysis domain must be applied, considering the heat propagation, humidity percentage loss and the overall change of the mechanical characteristics of the components through a phenomenon that can be simulated as phase transformation. Behavior of glued laminated timber when subjected to fire is equally influenced by the behavior of adhesives in the cross section composition together with the wood lamellas. Even the focus of fire resistance analysis was on the characteristics and properties of wood, the type of adhesive is of great importance also. The current adhesives used, like phenolic or aminoplastic offer good mechanical properties and satisfactory results in terms of strength, durability or fire resistance, for which provisions and details are already included in standards. The paper studies the delamination when structural element is subjected to high temperatures with discussion if localized effects relate to sectional behavior.

This paper is based on the background offered by a research project aiming to develop a testing system for the mechanical behavior of some new configurations of glulam composite materials (comprising different wood essences and adhesives) when subjected to high temperatures.

The need for this type of analysis is becoming more topical due to the trend of replacing with bio-renewable materials (wood) structural elements from materials whose production is energy-intensive (especially steel and cement) within the framework of the European policy "Green New Deal" to reduce greenhouse gas emissions, of which the construction industry is responsible for approximately 40-50%.

Keywords: glulam, adhesive, fire resistance, flash-over, delamination

INTRODUCTION

Recent climate targets and concerns point the construction industry towards a broader use of natural materials such as wood, and engineered wood products. Because fire safety is one of the main public concerns when it comes to the structural use of wood and wood composites, material science developments need to focus on all the materials forming composite products, and their environmental impact when subjected to high temperatures

https://doi.org/10.5593/sgem2024/6.1/s26.49

(fire load cases). In order to ensure a good global mechanical behavior under fire loads for composite members it is important to have good information regarding the thermal behavior and thermo-mechanical behavior of each component as well as the thermo-mechanical behavior of the whole structural element.

As such, obtaining real scale test data for this kind of fire behavior involves expensive and sophisticated testing procedures. Prototypes for new adhesives may be modeled numerically by using data obtained from simple procedures, in order to conclude whether or not building the real scale prototype is a worthwhile endeavor.

The present paper presents a coupled temperature-displacement transient finite element analysis that uses a cohesive, temperature dependent contact behavior in order to model the adhesive of an engineered wood product, loaded by a time dependent temperature boundary condition. Such a model may be used to evaluate the global behavior of adhesives in the previously mentioned conditions.

MATERIALS AND METHODS

The paper refers to the development of a model used for checking the feasibility of numerical simulation of glued spruce wood stack in terms of fire exposure. A simplification of the model to allow convergence control in this research stage was to ignore the mass loss of wood during pyrolysis as well as the influence of high temperatures upon the resistance model of wood. The decay of the glue properties used in glulam elements during a short-term exposure (1 hour) to the standard fire temperature curve (Fig. 1) outpaces the decay of the element cross-section as well as the mechanical properties of the wood, so that the focus was cast on the de-lamination effect of a two-board beam subjected to shearing during a standard fire (Fig. 2).

The wood is modeled as an orthotropic material having the properties defined according to [1]. The material orientations are described in Fig. 3. The thermal damage model for the adhesive was considered as a 3-domain piecewise linear behavior (Fig. 4) derived from the contribution [2].

The analysis consists of a transient coupled temperature-displacement step lasting 3600 seconds, with a maximum allowed temperature change per increment of 5°C and the temperature load was defined according to Fig. 1, applied on the bottom face of the beam, where the fire exposure is expected.

The mechanical load was applied instantaneously at the beginning of the step as a combination of own weight and a uniformly distributed pressure of 25kPa acting as a shearing action on the lateral faces of the beam components.

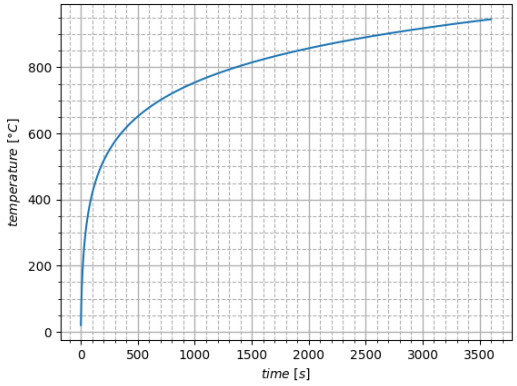


Fig. 1 Standard fire curve defined by SREN 1991-1-2 [4].

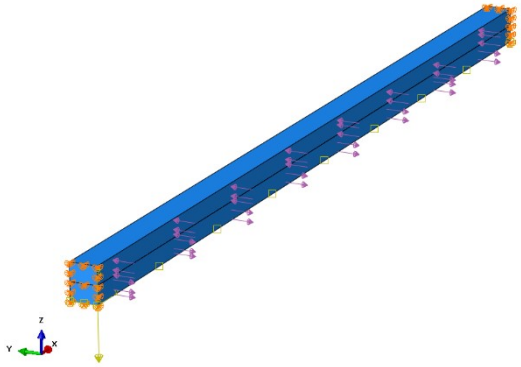


Fig. 2 Model and loads

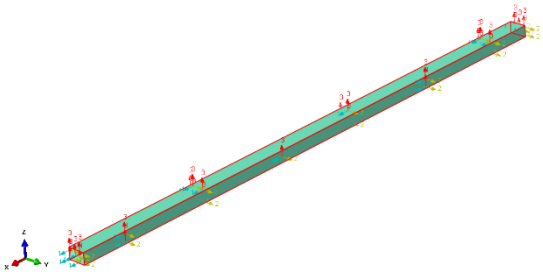


Fig. 3 Material orientations for orthotropic definition of the wood (spruce)

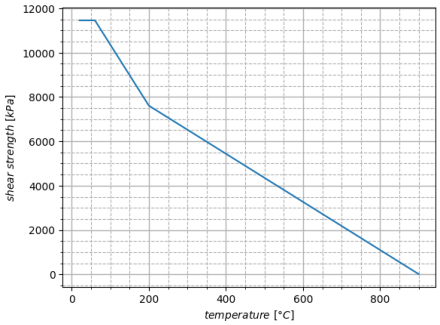


Fig. 4 Adhesive thermal damage model [2]

RESULTS

The validation of the appropriate lapse of time was checked comparing the first and the last computation frames where it was noticed that the complete dissipation of heat occurred.

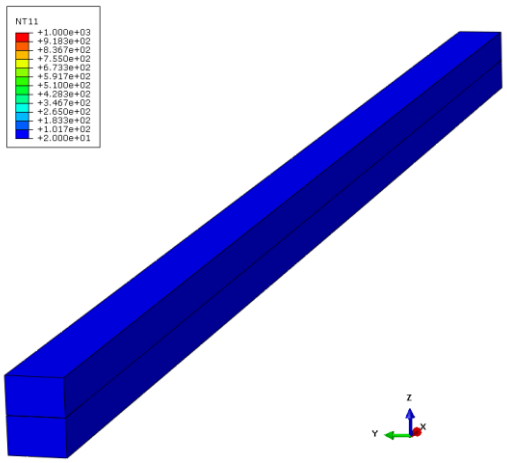


Fig. 5 Nodal temperatures at t=0.5s

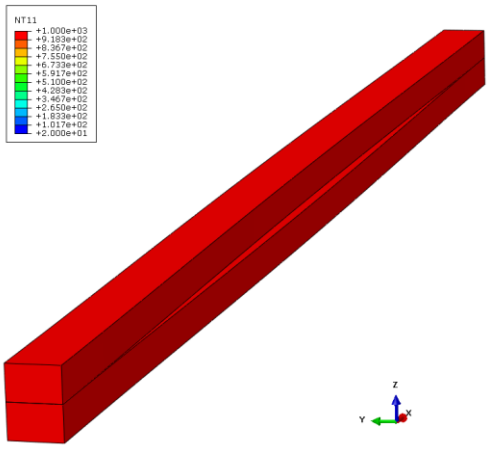


Fig. 6 Nodal temperature at t=3600s

https://doi.org/10.5593/sgem2024/6.1/s26.49

The previous choice was made despite the actual heatsink effect of the elements supported by the beam that would otherwise lead to a temperature distribution such as the one in Fig. 7. This phenomenon is important in a flash-over event, however, it induces temperature and heat distribution complexity interfering with the aimed purpose of the analysis, namely the behaviour of the interface.

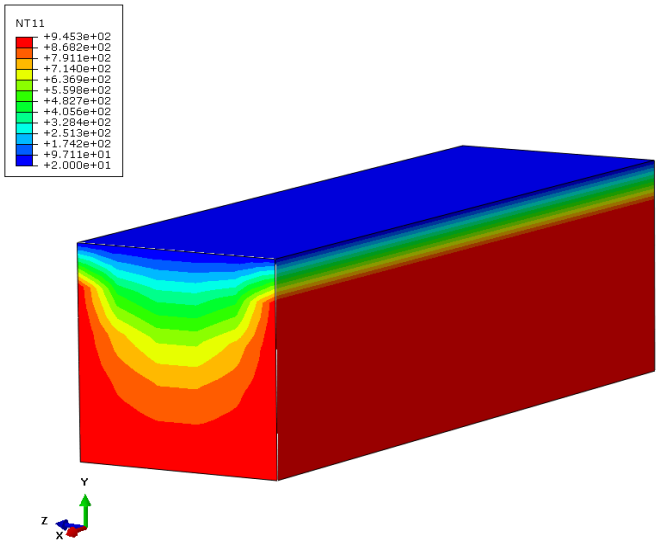


Fig. 7 Heat sink effect of elements above (illustrative model, not included in the paper herein)

In order to study the effect of the fire upon the contact interface, it was created a synthetic field containing the difference between the parameters of interest at the initial and final time increments.

The shear slip along the global y axis is highlighted in Fig. 8, while the contact shear stresses in the last step, when the effect of the fire curve is fully developed (Fig. 1) are shown in Fig. 9 along axis y.

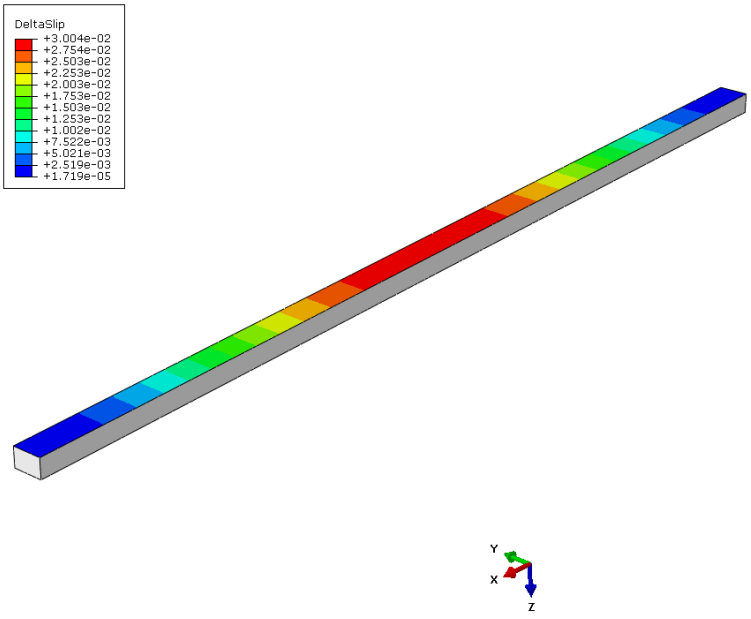


Fig. 8 Difference between Slip strain of contact surface at t=3600s and t=0.5s

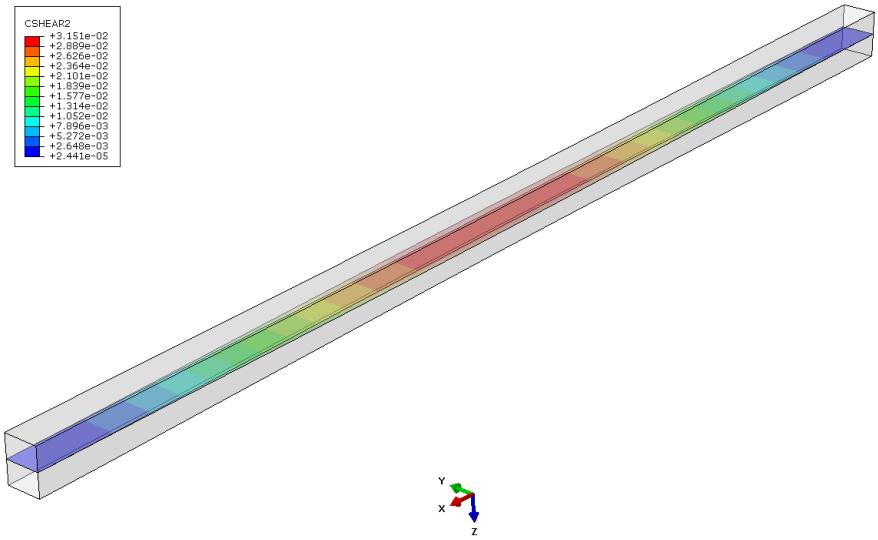


Fig. 9 Contact shear distribution along y axis at t=3600s

The overall displacement effect of the fire curve was captured using another synthetic field containing the difference between the displacement at the end of the analysis and at the first time increment as shown in Fig. 10. The distribution of stresses at the mid-section of the beam, was captured as-is for the von-Mises stresses at the beginning of the analysis (t=0.5s - Fig. 11) and at the final time increment (t=3600s - Fig. 12). These figures show the shift in the stress state of the wooden components due to the decay of the adhesive during the thermal loading.

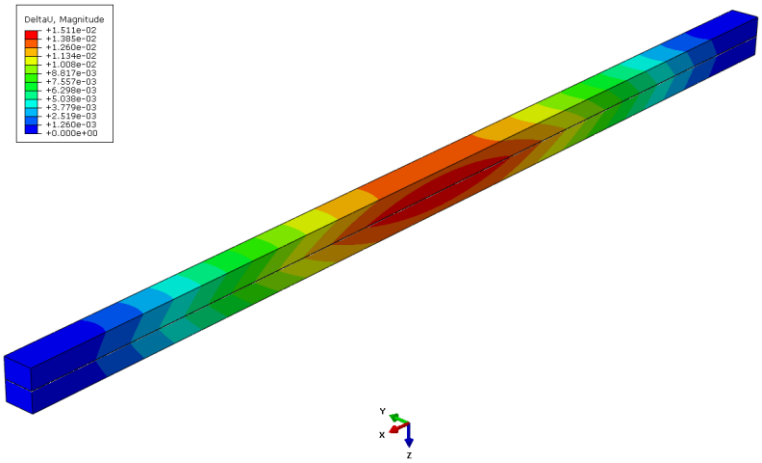


Fig. 10 Displacement difference at the end of the transient analysis

The delamination effect is shown in Fig. 13 and Fig. 14 as the cross-section of the components get loaded by a regular bending and shear stress-effect which shifts into two independent beams when the interface is unable to bear any more loads.

In order to showcase the fire effect at the glued interface, the nodes presented in Fig. 15 are monitored over the analysis time period, together with the parameter of interest and nodal temperature at said node over the analysis time.

The results are displayed in figures Fig. 16; Fig. 17 and Fig. 18. The selected nodes in Fig. 15, are located at the glued interface in the mid-section of the beam, and were

https://doi.org/10.5593/sgem2024/6.1/s26.49

denoted in the figures according to their coordinate along the global y-axis (as 0,25,50,75,100,125,150mm).

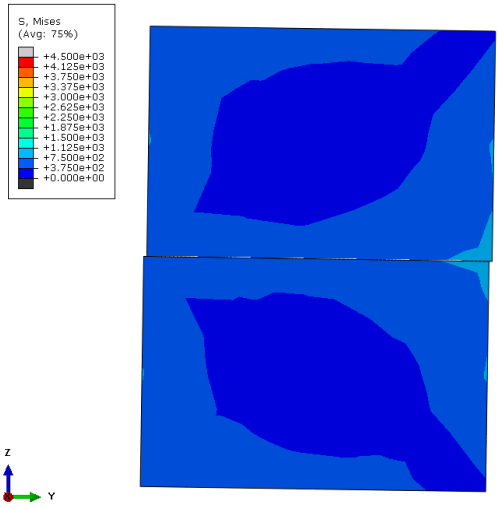


Fig. 11 Von-Mises Stress at mid-section at t=0.5s

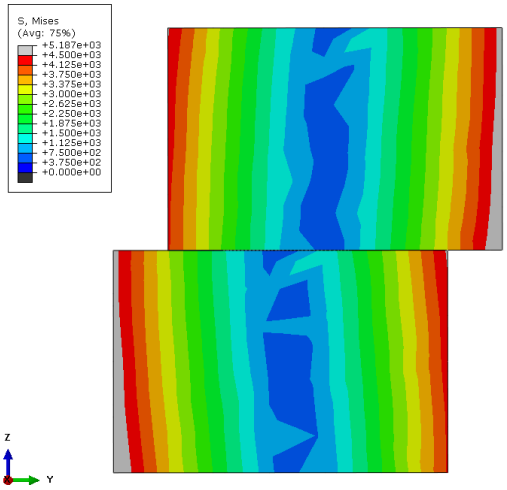


Fig. 12 Von-Mises Stress at mid-section at t=3600

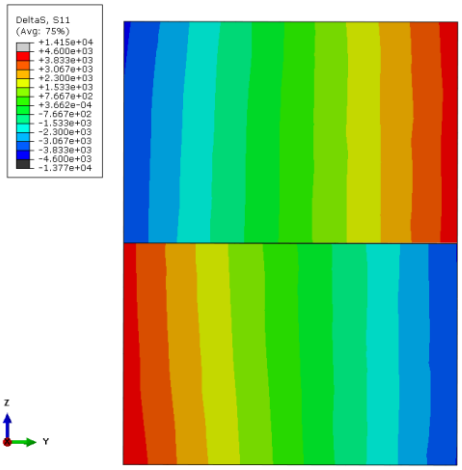


Fig. 13 Supplementary cross-sectional stress at the end of the fire

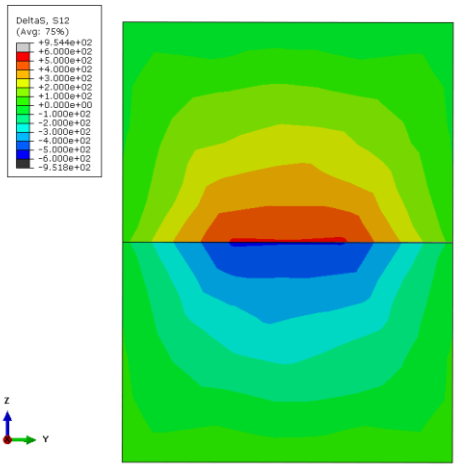


Fig. 14 Supplementary shear stress at the end of the fire.

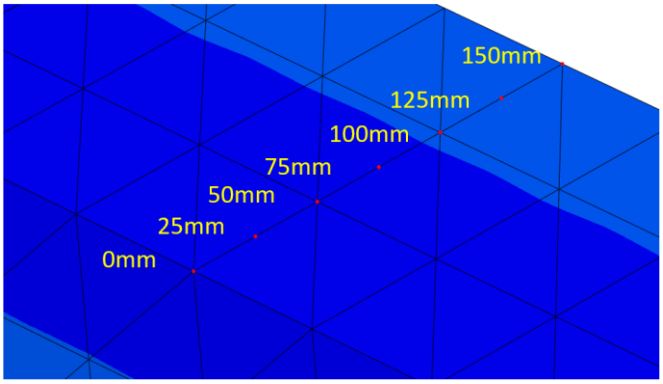


Fig. 15 Node positions to be monitored at the mid-section of the beam

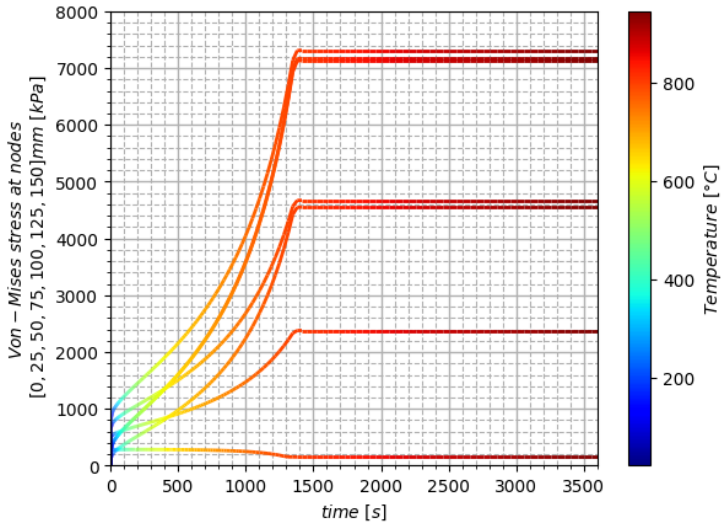


Fig. 16 Von-Mises stresses at the nodal positions in the mid-section of the beam

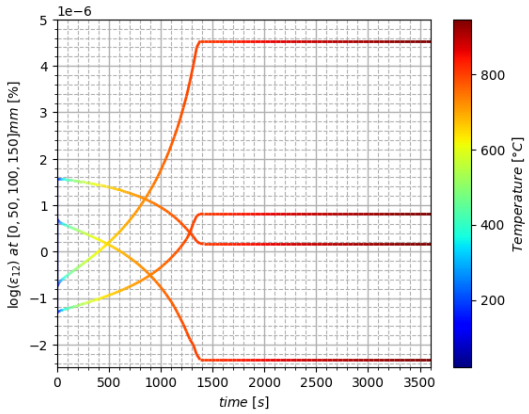


Fig. 17 Logarithmic shear strain at the element nodes in the mid-section of the beam

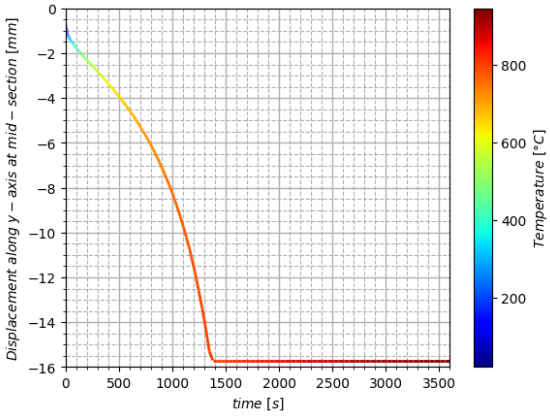


Fig. 18 Displacements over time-temperature at the middle node of the mid-section

DISCUSSION

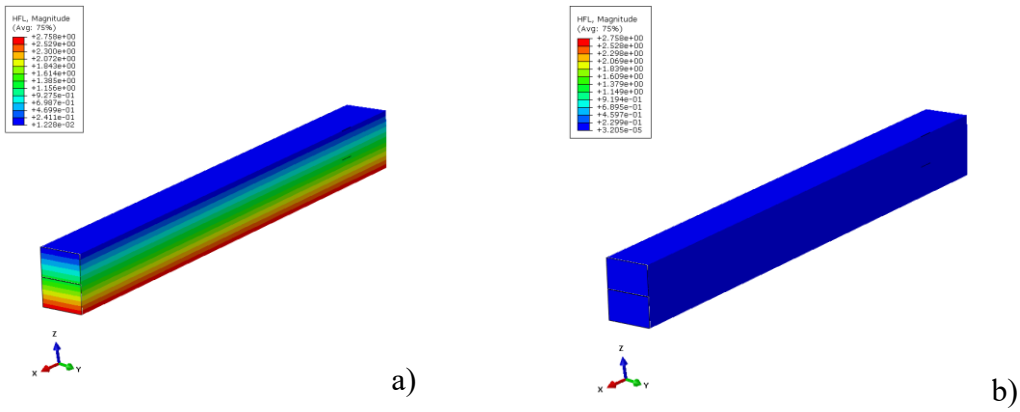


Fig. 19 Heat-flux magnitude at the initial (a) and final (b) time increments

https://doi.org/10.5593/sgem2024/6.1/s26.49

The transient analysis data presented in Fig. 16; Fig. 17 and Fig. 18, show that the properties of the modelled glued contact follow the design fire curve Fig. 1 closely, up to the point where the degradation advances far enough so that the change in mechanical properties leads to delamination.

The transient analysis also showed that for the standard fire curve, the high-temperature domain corresponds to a minimal heat-flux, and does not capture the post-flashover domain that experimental data showcases [3]. This is a limitation of employing the standard fire curve Fig. 1.

CONCLUSION

The paper showcases the effect of delamination of glulam elements subjected to the standard fire curve, stressing the importance of a proper model for the adhesive used in the construction of composite glulam elements. The proper capture of the delamination phenomena presented in this paper is very useful in determining potential evacuation times, as shown in Fig. 16, Fig. 17 and Fig. 18. This type of transient analysis may be used as an instrument for evaluating laminated timber elements, subjected to different fire load cases, without resorting to complex and expensive prototypes. Monitoring values of interest at set nodes, is a useful tool also in adjusting the numerical model to include experimental data.

Another point of interest is represented by the possibility of developing such models that incorporate also pyrolysis damage models, and more complex fire curve. Further developments in regards to these elements should be compared with the load-case presented in the paper, in order to enable designers to use the standard fire curve as a benchmark. For certain load cases, it is clear that the behavior of the adhesive is a determining factor in the global mechanical behavior of the composite element. It is clear that this kind of modelling can provide great insights into the usefulness of new adhesive models, developed by simple tests, in order to define their constitutive law.

ACKNOWLEDGEMENTS

This paper was published within the frame of the research grant $\boldsymbol{GNaC_{2023}^{ARUT}}$ “Evaluarea Comportării Materialelor Compozite pe Bază de Lemn la Temperaturi Înalte - PYROSTOP” funded by the Technical University of Civil Engineering Bucharest.

REFERENCES

[1] D. E. Kretschmann, "Mechanical Properties of Wood," in Wood Handbook Wood as an Engineering Material, U.S. Department of Agriculture, Forest Service, Forest Products Laboratory, 2010, pp. 100-145.

[2] A. Bernaczyk, A. Wagenführ, C. Terfloth, T. Krystofiak, J. Lincke and P. Niemz, "Investigations into the Influence of Temperature on the Tensile Shear Strength of Various Adhesives," Materials, vol. 16, no. 18, 2023.

[3] M. a. P. D. Blagojevic, "A new curve for temperature-time relationship in compartment fire," Thermal Science, vol. 15, pp. 339-352, 2011.

[4] ASRO, "SR EN 1991-1-2," Monitorul Oficial, 2004.

SECTION GREEN DESIGN

AND SUSTAINABLE ARCHITECTURE

BIM APLICATIONS IN THE DESIGN OF DEEP FOUNDATIONS FOR WIND TURBINES

Bogdan Chelaru[1] ,
Cătălin Onuțu[1] **,**
Adrian Alexandru Șerbănoiu[1]
[1] Gheorghe Asachi Technical University of Iaşi, Faculty of Civil Engineering and Building Services, **Romania**

ABSTRACT

This paper outlines three key processes: 3D modeling based on the technical records, data mapping to objects in the Building Information Modelling (BIM) model, and data extraction from the model.

Access to energy is a critical concern on the modern society, but equally important of how the energy is obtained. The methods used should be efficient enough to minimize adverse environmental impact, which holds significant importance in today's energy production landscape.

In the case of non-load-bearing subsoil, high structural loads or special requirements of the building, a deep foundation with drilled piles is required for a planned structure. The structure described in this paper is a deep foundation, utilized for onshore wind turbine design. This type of foundations can support largest wind turbine generators in operation. As the turbines are increasing in size, gravity are approaching to the limits of both their capacity and economical limit.

The focus of this research is to provide an accessible and easy-to-use BIM methodology for capturing and managing information derived from the technical documentation, and evidence gathered during the construction phase. The integrated meta data covers information across written parts, drawings, in-situ, and laboratory test results, planning registers, cost registers, sustainability criteria's identification and application and predicted performance in time of the described elements. Future endeavors will be directed towards automating the process of Building Information Modeling (BIM), by developing custom scripts designed to automatically generate elements for similar structures.

The findings contribute to the advancement of BIM methodology as a key tool for guiding informed decision making for green wind farms projects.

Keywords: Drilled Piles, Deep Foundation, Wind Turbine, Building Information Modeling (BIM), Laboratory Concrete Testing

1. INTRODUCTION

A wind turbine foundation serves as the critical anchor for the entire structure, must support the weight and dynamic loads of the turbine, provide stability and support against the forces generated by the rotating blades and external environmental factors. Several sustainable foundation types and approaches are available for onshore wind

https://doi.org/10.5593/sgem2024/6.1/s27.50

turbines. The onshore wind turbine foundations can be separated into two types: (i) spread foundations and (ii) piled foundations.

Piled foundations include a varied selection of technical methodologies designed to augment the load-bearing capacity of soil under circumstances where conventional shallow foundation designs fail to satisfy criteria such as load-bearing capacity, restricted differential settlement, or requisite rotational rigidity. Classified within the category of "deep foundations," in contrast to the conventional "shallow foundation" paradigm, piled foundations represent one facet of deep foundation solutions, alongside alternatives such as soil replacement and soil injection methods.

State-of-the-art

Building Information Modelling (BIM) it is a digital representation of physical and functional characteristics of places, typically buildings, structures, that enables the design, construction, and operation of a facility.

The integration of Building Information Modeling (BIM) enables a holistic and methodical strategy for construction project management, promising effectiveness, and accuracy across the entire spectrum of the Architectural, Engineering, and Construction (AEC) Industry [1]

Building Information Modeling (BIM) is a process supported by various tools, technologies, which involves the generation and management of digital representations of physical and functional characteristics of a construction. These representations or digital models are shared among stakeholders to support decision-making about an assets throughout its lifecycle, which includes all the project phases: initiation, planning, execution, operation, and eventual demolition.

One crucial aspect of Building Information Modeling (BIM) involves combining a three-dimensional digital graphic representation with comprehensive quantitative and qualitative data applied to its essential elements. This integration is defined through different BIM dimensions, like 4D, 5D, 6D, and 7D. A 4D model is employed for planning or simulation purposes, a 5D model emphasizes cost analysis, a 6D model prioritizes sustainability factors, and a 7D model encompasses operation and facility management tasks [2, 3]

The complexity of Building Information Modeling (BIM) is associated to the Level of Development (LOD), which defines the level and precision of geometry required for 3D BIM models. This specification outlines BIM elements within different building systems at various stages of their development and use during the design and construction phases. The LOD specification entails six distinct levels of development: LOD 100 (Conceptual), LOD 200 (Approximate Geometry), LOD 300 (Precise Geometry), LOD 350 (Precise Geometry with Connections), LOD 400 (Fabrication-ready Geometry), and LOD 500 (Operational, As-built Models) [4-7]

An essential consideration revolves around the identification of the suitable Levels of Development (LOD) and Levels of Information (LOI). In the framework of this study, the preferred approach entails adopting a low LOD and an elevated LOI. More precisely, for structural components, an LOD 200 for the drilled piles and foundation was adopted, and an LOD 350 for the anchor cage components. Simultaneously, an LOI 350 was employed, for all the elements, to establish an understand the properties associated with the objects.

Objectives

This paper outlines three consecutive stages: i) gathering data from technical documentation, ii) generating the BIM model using Revit software; iii) producing the deliverables of the BIM model. These three stages were applied following a series of activities:

a) Analysis of Information - Examining data gathered from technical archives,

b) Setup of Revit Template File - Configuring the Revit template file to align with the project's specifications,

c) Data mapping into the BIM model - Linking data through instance and type parameters within the BIM Revit model.

d) Extraction of Output - Extracting the finalized output from the BIM model for subsequent analysis and reporting purposes.



Fig. 1. Proposed methodology to generate the BIM model

2. CASE OF STUDY: DEEP FOUNDATIONS FOR WIND TURBINES

Piled deep foundations serve as crucial structural elements in the construction of wind turbines, facilitating stability and load-bearing capacity in various soil conditions.

Piled deep foundations represent a common solution to the unique structural requirements posed by wind turbine installations, especially in regions with challenging soil conditions or variable terrain. This introduction outlines the importance of deep foundations in wind energy projects and sets the stage for a detailed examination of piled foundation technologies. The design of piled deep foundations for wind turbines involves a meticulous consideration of factors such as soil properties, turbine specifications, environmental loads, and regulatory requirements.

Piled deep foundation construction system

The solution chosen for this paper is indirect foundation on drilled piles embedded into the base ground. The piles are distributed radially, 1.00m from the perimeter of the raft foundation, at a radius of 9,00m from its center, and at equal intervals. The length of the

https://doi.org/10.5593/sgem2024/6.1/s27.50

piles can vary, in reality, from one location to another, based on the recommendations of the geotechnical study.

The general foundation slab is circular in shape with a diameter of 20.00m. The minimum height of the slab (external) is 1.00m, while the maximum height is 3.05m.

3. METHODOLOGY

The methodology applied in this case study aims to provide a comprehensive BIM methodology outlining the BIM requirements. It is structured into three distinct phases: i) Data Acquisition, ii) Generation of the BIM model, and iii) BIM model deliverables.

i) Data acquisition

The initial stage of the process requires examining the gathered data, which explains the methodology employed in this paper. Therefore, the BIM model was developed to capture and interpret data from various sources and formats, such as: technical project documentation, in-situ, and laboratory test results, planning and cost registers, sustainability criteria's identification and application, estimated performance in time and warranty and other web databases,

ii) Generate de BIM model

The goal of this stage was to set up a semi-automated methodology that would bring together all data that covers information across written parts, drawings, in-situ and laboratory test results, planning registers, cost registers, sustainability criteria's identification and application and predicted performance in time of the described elements. The modeling process commences with setting up the building levels. Subsequently, the process involves creating the bored piles, foundation slab and the anchor cage. Within Revit, personalized data can be formatted as project parameters, which can then be associated with objects to facilitate the insertion of information, such as: geometrical data; data from technical projects; data from the construction phase.

iii) BIM model deliverables

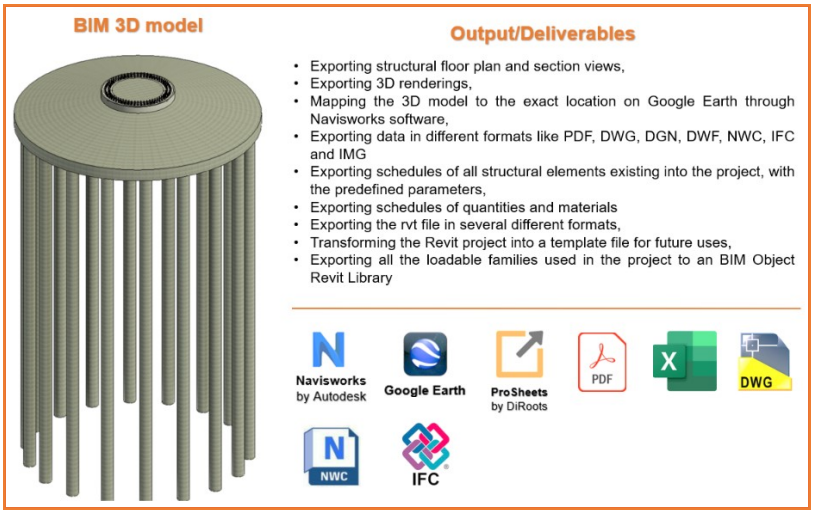


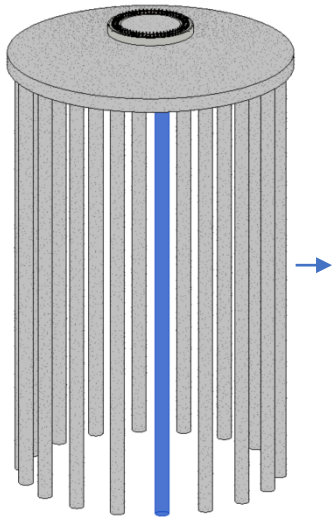
Fig. 2. BIM model deliverables

This phase essentially involves the identification of achievable or deliverable output, such as structural plan views, section views, elevation views, detail views, 3D views, 3D renderings, results from in-situ and laboratory tests, planning records, cost registers, sustainability criteria's records, records of test defects, as well as any other pertinent Asset Information Model (AIM). This data can be integrated into the Revit BIM model through project parameters associated with each type of structural element [1].

Mapping data to Revit project parameters

Revit project parameters include attributes that can be incorporated into a project file. To rationalize the organization of data resulting from project and construction phase, instance project parameters were formulated and applied to building elements that meet specific criteria.

a)



b)

TUI_Concrete bored piles
TUI_Drilled pile_Ø1000 mm

Structural Columns (1) | Edit Typ

Data	
TUI_Drilling company	Company name
TUI_Pile type description	Bored piles
TUI_Pile number	P1
TUI_Pile length (m)	0.0000 m
TUI_Pile diameter (m)	0.0000 m
TUI_Minimum Cement Content (kg/m3)	300
TUI_Water cement ratio	0.55
TUI_Pile Concrete class	C30/37
TUI_Exposure class	XA1
TUI_Pile reinforcement weigth (kg)	2039.200000
TUI_Steel class	BSt500S
TUI_Steel Ra (Mpa)	500
TUI_Pile coordinate in X	Value
TUI_Pile coordinate in Y	Value
TUI_Platform number	Platform XY
TUI_Planning_Dilled shaft date	yyyy-mm-dd
TUI_Planning_Drilled shaft planned date	yyyy-mm-dd
TUI_Planning_Drilled shaft delay (in days)	Value
TUI_Planning_Pouring pile date	yyyy-mm-dd
TUI_Planning_Pouring pile planned date	yyyy-mm-dd
TUI_Planning_Pouring pile delay (in days)	Value
TUI_Pile head demolition date	yyyy-mm-dd
TUI_Concrete in-situ test_Description	Pile Integrity Test (PIT)
TUI_Pile Integrity In-situ Test (PIT) with ultrasound_Date	yyyy-mm-dd
TUI_Pile Integrity In-situ Test (PIT) with ultrasound_Result	Aproved / Aproved with comments / Rejected
TUI_Pile Integrity In-situ Test (PIT) with ultrasound_Defect	Discontinuity/Segregation/Soil inclusion
TUI_Concrete compressive strength test (7 days)_Date	yyyy-mm-dd
TUI_Concrete compressive strength test (7 days)_Results (%)	Value
TUI_Concrete compressive strength test (28 days)_Date	yyyy-mm-dd
TUI_Concrete compressive strength test (28 days)_Results (%)	Value
TUI_Cost_Drilling equipment mobilization to site in € (per unit)	0.00
TUI_Cost_Drilling equipment in € (per unit)	0.00
TUI_Cost_Drill crew labor in € (per unit)	0.00
TUI_Cost_Reiforcement cage in € (per unit)	0.00
TUI_Cost_Reiforcement cage transport in € (per unit)	0.00
TUI_Cost_Reiforcement cage installation in € (per unit)	0.00
TUI_Cost_Concrete in € (per unit)	0.00
TUI_Cost_Pooring concrete crew labor in € (per unit)	0.00
TUI_Cost_Drilling fluid / slurry in € (per unit)	0.00
TUI_Cost_Drilling fluid / slurry crew labor in € (per unit)	0.00
TUI_Sustainability_Concrete batch plant distance from site (in KM)	Value
TUI_Sustainability_Concrete travel time (in min)	Value
TUI_Sustainability_Reinforcment cage transport travel time (in hours)	Value

Fig. 3. Drilled pile, a) BIM model element b) BIM dimensions characterization through the instance parameters mapped to the element

https://doi.org/10.5593/sgem2024/6.1/s27.50

The Revit families considered for the BIM model were native families like walls, floors, columns, and framing. In accordance with BIM principles, seven distinct "dimensions" are acknowledged: 3D modeling, 4D time-related information, 5D cost analysis, 6D sustainability, 7D life cycle and maintenance. The instance and type parameters generated and associated with each structural element encompass data across all five dimensions previously mentioned (refer to Fig. 3).

FUTURE APLICATIONS

BIM solutions represent significant progress in integrating data processes, enhancing the flow and ongoing updates. The current BIM model can also incorporate data referring to the physical and chemical attributes of utilized materials.

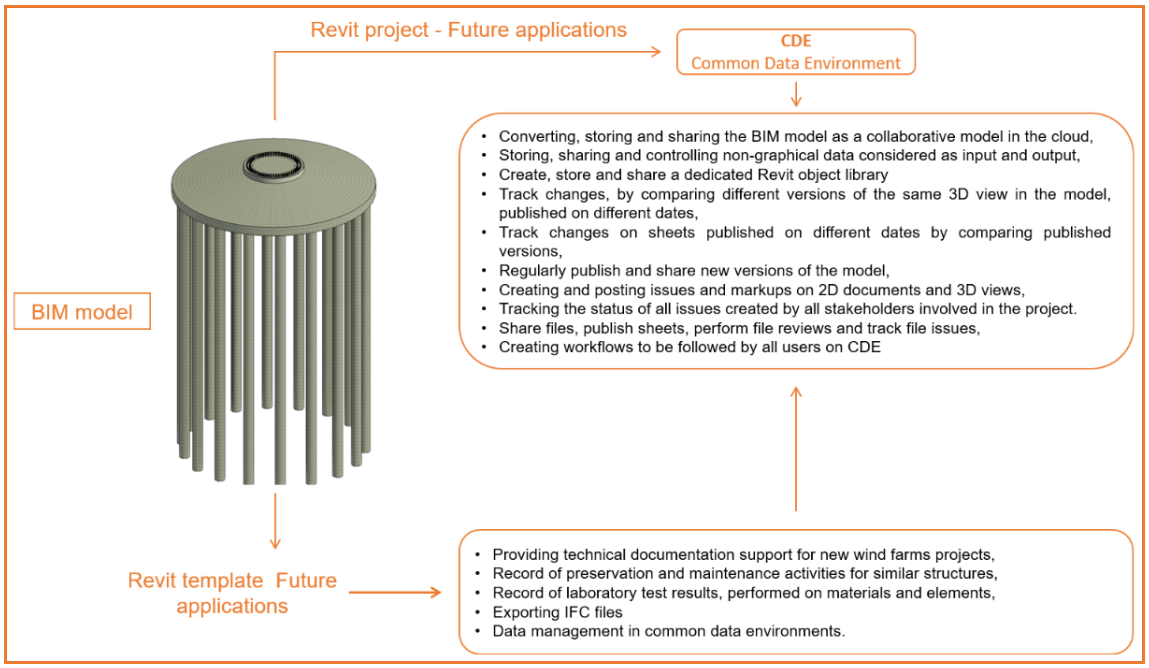


Fig. 4. Future applications

Benefits of BIM process for wind farms projects

The potential applications of BIM in the energy sector are diverse, contingent upon the scope and purpose of the project, and offer the following advantages:

- Providing accurate documentation,
- Providing efficient collaboration among stakeholders involved in similar projects,
- Parametric smart object libraries produce objects that can precisely describe individual features covering virtual representations of existing constructive elements, necessitating modeling only once.

Limitations of BIM process for wind farm projects

Several constraints of Building Information Modeling (BIM) and the research challenges associated with the wind farms projects could be highlighted:

- Parametric smart object libraries, since if a specific style is not present in the parametric libraries, they need to be manually modified.
- Visualization between 3D model and metadata: The metadata listed on previous chapters as well as the ways to embed them into the 3D models revealed that this connection was made semi-automatically through tables/spreadsheets and database.
- BIM implementation requires managing and interpreting fragmented data from different sources, to create accurate models.

Challenges of BIM for wind farms projects

In addressing the challenges posed by Building Information Modeling (BIM) for wind farms projects, future research towards the following key areas are imperative:

i) Automated Generation of Metadata in BIM Models - Explore approaches to integrate metadata into BIM models.

ii) Automatic Generation of Structural elements in BIM Models - Investigate techniques for the automatic generation of structural and architectural components within (BIM). This process could leverage Dynamo Scripts, Revit add-ins, or other modeling software to enhance efficiency and accuracy.

iii) Automation of Engineering Workflows - Develop and implement automated engineering workflows tailored to the unique characteristics of wind farms assets.

iv) Integration of Game Technology Applications - Assess the viability of incorporating game technology applications as a solution to optimize the modeling process for wind farms models.

4. CONCLUSION

The innovative approach presented in this study introduces a methodology applicable not only to deep foundations for wind turbines but also adaptable for other type of structures and constructions. This automation enhances productivity, eliminates errors in task outcomes, repetitive tasks, and provide a valuable benefit-cost. This study presents a systematic methodology where data collected from the project technical documentation, as well as results from the construction phase, are qualitatively described and seamlessly integrated into the Building Information Modeling (BIM) model. The BIM methodology applied accurately facilitates exploration and complex analysis of proposed interventions in various scenarios. The methodology serves as a robust foundation for collaborative approaches, making it well-suited for wind farms projects. Implemented with the goal of establishing a consistent knowledge base for the specific structures, the methodology acts as a valuable decision-making and management tool throughout the asset's life cycle. Therefore, the suggested approach provides new perspectives within the field of creating and managing such projects in a unique and innovative way.

https://doi.org/10.5593/sgem2024/6.1/s27.50

ACKNOWLEDGEMENTS

This research received funding from Gheorghe Asachi Technical University Doctoral School in the framework of Bogdan Chelaru Ph.D. Study Programme.

REFERENCES

[1] Chelaru, B., Onuțu, C., Ungureanu, G. and Șerbănoiu, A. A., Integration of point cloud, historical records, and condition assessment data in HBIM, Automation in Construction. 161 (2024) pp.105347. https://doi.org/10.1016/j.autcon.2024.105347.

[2] Baik, A., From point cloud to Jeddah Heritage BIM Nasif Historical House – case study, Digital Applications in Archaeology and Cultural Heritage. 4 (2017) pp.1-18. https://doi.org/10.1016/j.daach.2017.02.001.

[3] López, F. J., Lerones, P. M., Llamas, J., Gómez-García-Bermejo, J. and Zalama, E., A Framework for Using Point Cloud Data of Heritage Buildings Toward Geometry Modeling in a BIM Context: A Case Study on Santa Maria La Real De Mave Church, International Journal of Architectural Heritage. 11 (7) (2017) pp.1-22. https://doi.org/10.1080/15583058.2017.1325541.

[4] Chen, S.-H. and Xue, F., Automatic BIM detailing using deep features of 3D views, Automation in Construction. 148 (2023) pp.104780. https://doi.org/10.1016/j.autcon.2023.104780.

[5] Monchetti, S., Bartoli, G., Betti, M., Facchini, L., Rougier, E. and Zini, G., The research project "CHARMING PISTOIA": an integrated HBIM project for preservation and maintenance of heritage structures, Procedia Structural Integrity. 44 (2023) pp.1988-1995. https://doi.org/10.1016/j.prostr.2023.01.254.

[6] Pocobelli, D. P., Boehm, J., Bryan, P., Still, J. and Grau-Bové, J., BIM for heritage science: a review, Heritage Science. 6 (1) (2018) pp.30. https://doi.org/10.1186/s40494-018-0191-4.

[7] Volk, R., Stengel, J. and Schultmann, F., Building Information Modeling (BIM) for existing buildings — Literature review and future needs, Automation in Construction. 38 (2014) pp.109-127. https://doi.org/10.1016/j.autcon.2013.10.023.

BIM STRATEGY, IMPLEMENTATION AND EXPECTATIONS IN EDUCATIONAL PROGRAM

Lect. Dr. Marina Lute[1]

Lect.Dr. Luminita Fekete-Nagy[1]

[1] Politehnica University Timisoara, **Romania**

ABSTRACT

We are living in an information dense world, where the sustainability is key. Even though civil engineering projects are highly technical, they require precise planning and clear communication channels to be successful and achieve this purpose. For this, in recent years, all around the world, various entities and decision boards worked to put together a set of rules to define and standardize the interaction between all the involved stakeholders (e.g. investors, designers, builders, and operators). Using the BIM (Building Information Modelling) concept the project can be modelled with all its connections and all the disciplines can interact in real time with very little friction, and optimize the green space requirements. The educator role into this field is to accommodate the future professionals with the concept and use of it, taking into account the present regulations and create the correct inter-professional connection in order to obtain a comprehensive design and execution object that can work all specialties involved and obtain a clean design together with a clean construction execution. The present work shows the path that we use in our department to include the BIM design into our present program and the results obtained with the first graduates that used this concept into their activity.

Keywords: BIM education, building information modeling, construction industry productivity, BIM guidelines

INTRODUCTION

With the world around us becoming more technologically advanced every day, many countries shown great interest in BIM implementation. According to [1], BIM is defined as a collaborative way of working, underpinned by digital technologies that unlock more efficient methods of designing, creating and maintaining our assets. Messner et al. [2] defines BIM as a process focused on the development, use, and transfer of a digital information model of a building project to improve the design, construction, and operations of a project. Published in 2019, the ISO 19650 – Part 1 [3] and BS EN ISO 19650-2 supersede BS 1192 (principles) and PAS 1192-2 (capital delivery phrase). The document outlines the concepts and principles for information management at a stage of maturity described as “building information modelling (BIM)”. It defines BIM as “use of a shared digital representation of a built asset to facilitate design, construction and operation processes to form a reliable basis for decisions”. The document also provides recommendations for a framework to manage information including exchanging, recording, versioning and organizing for all actors.

https://doi.org/10.5593/sgem2024/6.1/s27.51

GLOBAL SITUATION

Building digitalization – which is in fact a short definition for BIM started with software developers during seventies (Fig. 1), and continued on this line with the Autodesk acquire of the software and inclusion into its own platform. The line of development was implemented by cooperation between UK and USA companies during 70-80 decades, and creation of an incipient platform that connected multiple versions of dedicated architectural, structure, HVAC, urbanism software that could be connected into one general software that could integrate all of the above.

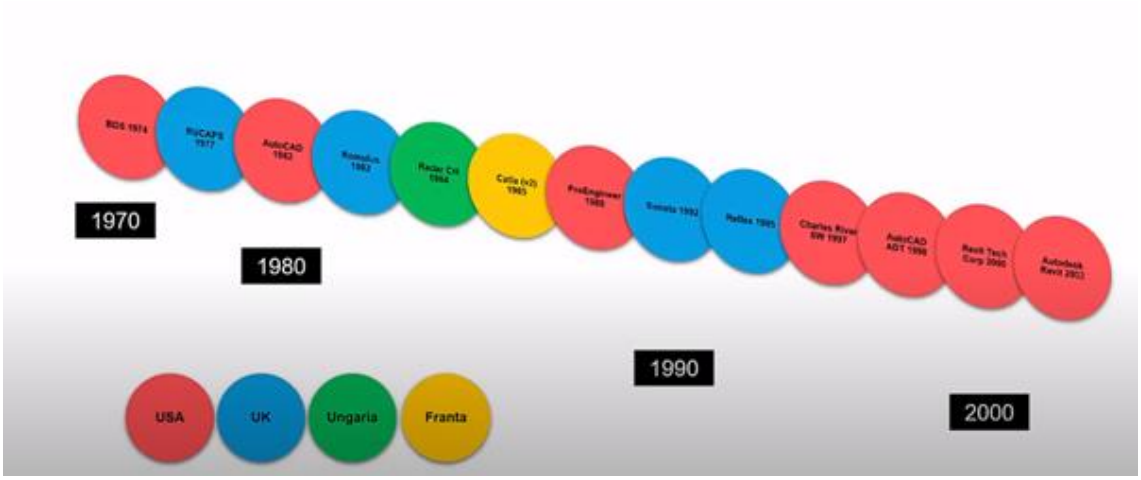


Fig. 1. BIM History

Next step was the involvement of governments into standardisation of the movement and implementation of general requirements regarding agreed general file format, efficient management of information, minimum workout template. Thereby, in Europe was agreed over publication of 17 ISO standards regarding the information management over the whole life span of the construction object, a free format called “ifc” to “carry” information between all existing software platforms, and the levels of information for each step in the way, starting with design – authorization, construction and building maintenance. Moreover, the gain of the process is that the ISO standards development involved 31 participant members and developed around 20 standards on the subject.

As a conclusion, the private sector was the initiator of the movement, the public sector took lead to develop BIM guidelines to instruct and standardize BIM implementation in construction projects, private sector took charge in education of industry, but less enthusiasm was found in educational public system for this subject.

NATIONAL SITUATION

Even if BIM is not mandatory, Romania is increasingly focusing on implementing BIM. Professional associations and companies are promoting the use of BIM in private projects. Up to this point, in Romania, the use of BIM was promoted by privately owned companies (usually international corporations) and few large and well-established design companies. The fast pace re-development of industrial parks led to

projects of increasing complexity and more demanding clients that requires changes in the concept, design and even construction phase. In order to be able to provide high quality work in such conditions, a more effective and efficient interdisciplinary coordination of architecture-structure-installations is required.

Building on past success stories regarding BIM projects (e.g. better cash flow planning, more precise execution schedule, improved facility management, planning of building extensions, including MEP) investors started demanding BIM compliant projects. For design companies, the use of BIM is not a simple choice. Due to the lack of a comprehensive central database for specific components and to lack of trained engineers, at this point the implementation effort is sustained by each individual company.

		Concept & Design Planning			
		Scope of works	Detailed scope of works after the kick of meeting and additional input	Concept Design development	Concept design delivery
Client	Project director	creates and deliver to the team leader the scope of works together with the financial and legal	creates and deliver the detailed version of the scope of works upon the harmonization of all the	participate to the regular meetings and gives his input and feedback with regards and	receives the concept design and verify the compliance with the
	Project manager				
	Cost control				
	Legal			kept informed	kept informed
Engineer	Team leader	analyze and distribute to the design team	brings their professional input and helps the Client to obtain the necessary additional information	verify the compliance of the design works with the Client expectations; evaluate the risks	receives the concept design and verify the compliance with the Client request
	Project managers (by specialties)	Receive			
	Cost control	Receive			
	Health & Safety	Receive		kept informed	kept informed
	Legal	Receive		kept informed	kept informed
Contractor	Coordinator	Receive, analyze, distribute to his team together with his professional input		coordinates the activity of the design team and the information exchange	deliver to the Client the concept design
	Architecture team	Receive and analyze in coordination with the entire team		develop the architectural part in coordination with all the other specialties	
	Structure design team	Receive and analyze in coordination with the entire team		develop the building structure in coordination with all the other specialties	
	MEP team	Receive and analyze in coordination with the entire team		develop the MEP in coordination with all the other specialties	
	Geotechnical engineer	Receive		prepare and deliver the geotechnical study	provides additional information on request
	Cadastral engineer	Receive		prepare the related works necessary to obtain the building permit	provides additional information on request
	Fire fighting consultant	Receive and analyze in coordination with the entire team		gives the related input for all the specialties involved, in order to obtain in the end an compliant design	provides additional information on request
	Environment consultant	Receive and analyze in coordination with the entire team		gives the related input for all the specialties involved, in order to obtain in the end an compliant design	provides additional information on request

Fig. 2. BIM History

Figure 2 presents an example for the responsibility's matrix used for complex projects in Romania. In a first phase, the activities described by the sub-matrix C1-F13 have been assimilated and integrated in BIM flows by various platforms. In a subsequent development, the activities depicted in line 15 have been integrated in the construction – design collaboration. As before stated, BIM is not a 'one-size fits all' approach and it cannot be used instead communication, but it can enhance the communication flow. To support further development, local design and engineering companies created professional alliances to cover all disciplines i.e. lines 5-9 from Figure 3 for Engineering, respectively 10-17 lines for the Design Contractor.

https://doi.org/10.5593/sgem2024/6.1/s27.51

Another natural step of development was for engineering and contractor companies to adopt the client requested platforms and attend trainings provided by local representatives of these platforms.

The tendency of inclusion for BIM requirements in the bidding stage appeared in 2020, after the translation of first 2 standards in Romanian i.e. SR EN ISO 19650-1:2019 and SR EN ISO 19650-2:2019. The standards translation was supported by national professional associations, as national e.g. AICPS [4] or private platforms e.g. http://bimtech.ro/ , which were also involved in creating discussion platforms related to the development directions of the national norms in the field. The standards and the related national annexes are currently under debate in order to create of the national BIM framework.

In the execution phase, the interdisciplinary cooperation is currently present only between the designers. In most cases (about 90%), the deliverables are related to transport of raw material, inventory, reporting, execution tracking, and heavy equipment shipment and the communication is limited to Excel files created outside BIM platforms and sent via e-mail.

The professional community is waiting for the involvement of the authorities for the creation of the legal framework to implement this system for government investments in all phases: design, execution and time tracking of construction behaviour. On this line, in December 2020, the construction industry was identified to have an increased competitive potential, consequently MDLPA– the Romanian Ministry for Development, Public Works and Administration) has started the development of a technical regulations for management and monitoring of BIM generated information.

The AICPS review magazine [5] presented a successful story of BIM implementation in its 2019 issue for the Constanța port extension. Since project inception, the client demanded real time information management to control and optimize the investment cash flow and execution. The designer decision was to use an exclusive 3D model in a CDE (Common Data Environment) to correlate all involved disciplines. The article concludes that the decision to use of BIM in accordance to SR EN ISO 19650-1 led to a reduction of design time, effective correlation between the numerical design model and detailing software, collision avoidance and more.

EDUCATIONAL DEVELOPMENT

As previously shown, BIM development was entirely a private effort, both in development, implement and educational process. First discussion for BIM implementation took place just at the beginning of 2020, and a proposal for an optional course was accepted for 2021. The need for action was highlighted during a process with two sides: on one side, the first normative on BIM management was raised in public debate and pointed out the fact that the future building authorizations will be based only on BIM documents, and on the other side a national survey among the professionals gave the results in December 2020 - https://bimtech.ro/2020/11/18/sondaj-gradul-de-maturitate-bim-in-romania/ with very poor results. Some significant answers has shown that from a pool of 32% architects, 35% structural engineer and the rest of

33% HVAC + roads + topographical engineers the following degree of knowledge are present:

- 34.6% found the subject for the first time in the last 5 years
- 67.7% did not know about international standards institutes regarding the subject
- 40% did not know about the ISO 19650 standard

But a strong percent of 69.2% considered that BIM concept is a revolutionary one for the industry.

Due to this lack of knowledge, the course was split into 2 parts: a theoretical one and a practical one.

The theoretical part covered the following issues:

- General notions: what is BIM, why we need BIM, BIM uses, current and future trends, implementation levels and requirements, situation in the world and why is not everybody using BIM
- Frames: dimensions of BIM, the tri-axial BIM framework, BIM levels of maturity, BIM levels of development

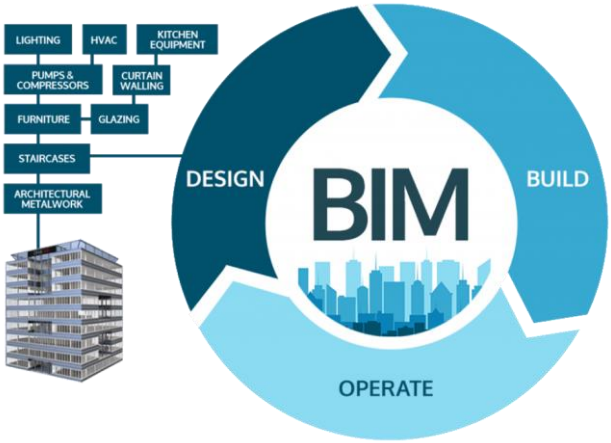


Fig. 3. BIM Management

- Management (fig 3): BIM guidelines, BIM definitions and abbreviations, specific roles and responsibilities, information management cycle, project execution planning procedure

The practical part involved a design of a building made by students on a certain design platform that cover the following subjects:

- Creation of architectural construction object into a collaborative software
- Import the architectural model into the structural software, automatic choice of structural elements, connection between architecture and structure files
- Turn to computational structure software, make structural calculus, export it to structural design

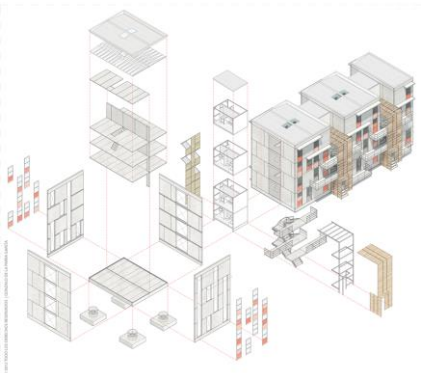


Fig. 4. BIM structure

- Make reinforcement plans for certain elements, make structural changes and collaborate to architectural file for collisions

https://doi.org/10.5593/sgem2024/6.1/s27.51

CONCLUSION

The BIM concept was introduced by industry in order to cut the losses on financial part of building construction, and was imposed in some way to state authorities, education being the last one to be involved in the process. The first steps in introducing the courses was rejected both by educators and students, who reluctantly accepted to look into the subject only after the implementation of first norms in 2022.

The optional course has shown that the implementation must be started earlier, with the bases of design that must be changed to 3D and use of collaboration software, and each technical design studied should show its part as a BIM component. A general project as the one presented above must follow all this effort in order to be well understand and ready to be used in professional life by students.

In this current situation it is expected that the new professionals that finish studies to be reluctant to use BIM strategy due to their lack of knowledge and complexity of subject, and it is expected that the subject to grow suddenly when the authorization process will be made only on the basis of digital models, as shown in the present BIM norms that are in the public debate.

REFERENCES

[1] Blackwell B., Industrial strategy: government and industry in partnership Building Information, HM Government, 2012;

[2] Messner, J., Anumba, C., Dubler, C., Goodman, S., Kasprzak, C., Kreider, R., Leicht, R., Saluja, C., Zikic, N., BIM Project Execution Planning Guide, Version 3.0. Computer Integrated Construction Research Program, The Pennsylvania State University, BIM Project Execution Planning Guide – Version 2.2 – Simple Book Publishing (unizin.org), 2019

[3] ISO 19650-1:2018 Organization and digitization of information about buildings and civil engineering works, including building information modelling (BIM) - Information management using building information modelling - Part 1: Concepts and principles, 2018

[4] Onofrei C., Avem standardele de BIM SR EN ISO 19650-1:2019 si SR EN ISO 19650-2:2019 in limba română. Ce găsim in ele și ce ne mai este necesar să le folosim eficient, AICPS Review 3-4/2019, pp 69-84

[5] Dogaru P., Krkljus D., Ghencea A., Tudose C.C., Dida L., Terminalul nou de cereale de la Dana 80, Port Constanța Sud – Provocările și perspectivele unui proiect grandios, AICPS Review 3- 4/2019, pp 58-68

DIGITAL TWIN OF BRATISLAVA CITY FOR ESTIMATION OF SUSTAINABLE ENERGY PRODUCTION AND UTILIZATION

Ing. arch. March. Roman Hajtmanek, PhD. Univ. Assoc. Prof.[1]

Mgr. art. Martin Uhrík, PhD. Assoc. Prof.[1]

Ing. arch. Vladimír Hain, PhD. Univ. Assoc. Prof.[1]

Ing. arch. Alexander Kupko[1]

[1]Slovak University of Technology, **Slovakia**

ABSTRACT

The paper outlines the process of data collection and processing undertaken to develop a digital twin of the central region of Bratislava city, focused on evaluating its capacity for generating solar and wind energy on an urban scale. Data sources included airborne laser scanning, provided as 3D point clouds, older existing polygonal 3D models, and other available map documents, which were processed to generate a comprehensive polygonal model with semantic information across different layers as buildings, vegetation, water bodies, paved and unpaved terrain. The outcoming digital twin was then used to calculate solar energy potential of the city using Ladybug tools (incident radiation) and weather data from a reference year. The results were compared to the calculations using the model r.sun (total irradiation) with satellite weather data within the GrassGIS software. The newly created digital twin of the city was published as physical model with digitally projected information layers at an exhibition and it will be also published online to be used as inputs to discussions on sustainable energy strategies for smart city development. The model will be further utilized in analysis of wind energy potential using OpenFoam and in statistical models predicting urban heat island formation and popularity of public spaces evaluated by their inhabitants.

Keywords: smart city, digital twin, solar energy, wind energy, sustainability

INTRODUCTION

Efforts to mitigate the climate crisis focus on transitioning from fossil fuels to renewable energy. This transition involves responsible energy production and consumption, as emphasized in global strategic documents like the UN 2030 Agenda's 17 Sustainable Development Goals [1]. Achieving these goals requires data-driven, energy-oriented design strategies to optimize efficiency and sustainability, including minimizing heat losses, increasing renewable energy use, and optimizing energy flows in urban environments.

Through the recording of big data, it is now possible to determine the state of our cities with unprecedented fidelity. Managing this data, however, poses a significant challenge, necessitating the use of computational models for the visualization and optimization of data from various sources. These virtual representations, known as digital twins, enable the testing of potential scenarios, thus aiding in the planning of a more sustainable future.

https://doi.org/10.5593/sgem2024/6.1/s27.52

One major challenge with sustainable energy sources like solar and wind is their variability; excess energy is generated during optimal conditions, but insufficient energy is produced during calm or cloudy conditions. A digital twin of a city visualizes potential energy gains throughout the year, supporting sustainable energy use and addressing local energy fluctuations.

This approach ensures energy-deficient areas, such as historic city centers, are supplied by energy-surplus districts using clean-energy appliances. Integrating these systems helps minimize infrastructure adjustments and reduce overall city energy demand.

The article describes a case study of sustainable energy assessment in Bratislava's digital twin. Besides energy data, this digital twin will integrate layers such as traffic patterns, historic buildings, planned developments, green spaces, noise and shadow maps, key viewpoints, and flood control measures. This method supports strategic planning and sustainable energy solutions, enhancing urban sustainability.

DIGITAL TWIN OF THE CITY

Digital twin is a virtual representation of a physical object, system, or process in high fidelity. It acts as a digital equivalent to its real-world counterpart, enabling real-time monitoring, simulation, and analysis. Digital twin bridges the gap between the physical and digital by using continuous feedback from the physical world to accurately predict the behavior of its real-world counterpart, aiming to enhance its design and manufacturing processes. [2]

The digital twin of the city is a digital model that utilizes continuously collected spatial and temporal data from infrastructure and organizational systems to analyze city functioning. Its applications include managing energy consumption [3] or monitoring air quality [4].

A distinctive feature of city’s digital twin is its emphasis on integrating ongoing data streams from both infrastructure and human activities. For instance, emotion mapping in the city collected citizen feedback to visualize spatial data on public sentiment. This qualitative analysis informs urban planning by highlighting areas needing improvement and enhancing the design of public spaces to foster positive interactions. [5]

Moreover, integrating predictive capabilities into digital twins using accumulated data streams facilitates proactive decision-making processes [6]. The aggregation of this data within a single digital twin of the city leads to a more comprehensive processing of this information and the exploration of statistical correlations between them through machine learning [7]. As a result, the machine learning models can supplement missing data, such as detecting various features [8] and subsequently predict the emergence of urban heat islands. [9]

SUSTAINABLE ENERGY ASSESSMENT

To assess the potential for sustainable energy production in the city, a comprehensive 3D digital model is essential. The 3D model covering the central part of Bratislava city was created with Bratislava Castle in the west, and Ružinov to the east. It extends from main train station in the north to Einsteinova street in the south.

The model was created using several data sources: Level of Detail 2 (LoD2) building models provided by Eurosense company [10], scanned point clouds of buildings, terrain,

and vegetation obtained from airborne laser scanning conducted by the Geodesy, Cartography and Cadastre Authority of the Slovak Republic [11]. The resolution of the scanned data is approximately 20 x 20 cm, with Slovakia being scanned annually, allowing for yearly updates of the model.

The initial LoD2 building models of Bratislava's central area contained numerous incorrectly oriented faces and degenerated geometries. The first step involved exporting data from the GIS to repair the geometry in segments using MS 3DBuilder. This software, designed for 3D printing, has robust capabilities for automatically repairing degenerated mesh geometries and filling holes. Subsequently, the models were manually refined.

The remaining 6866 buildings were modeled by students using airborne laser scanning point clouds as part of the Digital Instruments of Architecture II course. The modeling tasks were evenly distributed among the 154 students using a script in Grasshopper software, with each student modeling approximately 45 buildings in LoD2.

Terrain and vegetation models were also derived from airborne laser scanning data, classified into buildings, vegetation, and terrain categories. These data were imported into CloudCompare software, and the Delaunay 2.5D algorithm was applied to create a 3D mesh.

The final models, including buildings in LoD2, vegetation, and terrain relief, were collected and optimized in Rhinoceros 3D (Figure 1) to simulate solar radiation with Ladybug Tools and wind patterns using Butterfly and OpenFoam [12]. Additionally, a 1 x 1 raster height map was generated in QGIS from the scanned data, allowing for solar radiation calculations using the r.sun algorithm in GrassGIS. The results from these simulations were then compared for accuracy and consistency. Both methods were executed on the same computer, equipped with an Intel Core i7-9700F CPU and 16 GB of RAM.



Figure 1: The 3D model of central part of Bratislava city divided to layers of buildings in LoD2, terrain and vegetation. Source: Authors

Solar energy assessment with Ladybug

The Ladybug plugin utilizes defined time intervals and location data to create a discretized sky dome model consisting of 145 patches, based on the Tregenza subdivision method. Each patch is assigned specific solar radiation values. The sky luminance distribution is calculated using Perez expressions. The irradiance of each sky patch is derived from direct normal and diffuse horizontal irradiance values, recorded in the EnergyPlus Weather file, which contains reference year climate data. The sky model serves as a pre-processor for calculating the radiation on specific mesh faces. [13]

https://doi.org/10.5593/sgem2024/6.1/s27.52

For the digital twin of Bratislava, annual solar irradiation was calculated using the inputs: a 3D digital model, reference year data from the EnergyPlus weather file for the Bratislava area, a sky dome with 145 patches, and a ground reflectance of 0.2.

Solar energy assessment with r.sun in GrassGIS

The r.sun module calculates beam irradiance from the solar constant and Linke's turbidity factor, refined by Kasten. Diffuse radiation is computed using Linke's turbidity factor, and the algorithm includes ground-reflected radiation dependent on albedo values. For overcast conditions, the clear-sky index obtained from satellite data is used [14]. Explicit formulas are detailed in publications by Hofierka and Šúri [15]. The outcome is solar irradiation in $Wh.m^{-2}$ per day.

To calculate annual solar irradiation for the Bratislava digital twin, inputs included a height map with a 1x1 m resolution, a solar constant of 1367 $W.m^{-2}$, an albedo value of 0.2 for terrain reflectance, monthly Linke's turbidity factors for the city area, and monthly clear-sky indices from the Helio-Clim-1 satellite-derived database. The annual solar irradiation was calculated by scripting the irradiation of a sample day for each month with related coefficients, multiplying the sample day irradiations by the number of days in the respective month, and then summing them.

Wind energy assessment

The environment for assessing wind energy was established using Butterfly and OpenFOAM [12] to calculate outdoor airflow dynamics. The analysis produces calculated wind velocity and pressure, which are visualized in 3D at predefined time steps (Figure 2). Given the substantial computational time required, the detailed analysis of the entire city model will be conducted in future research.

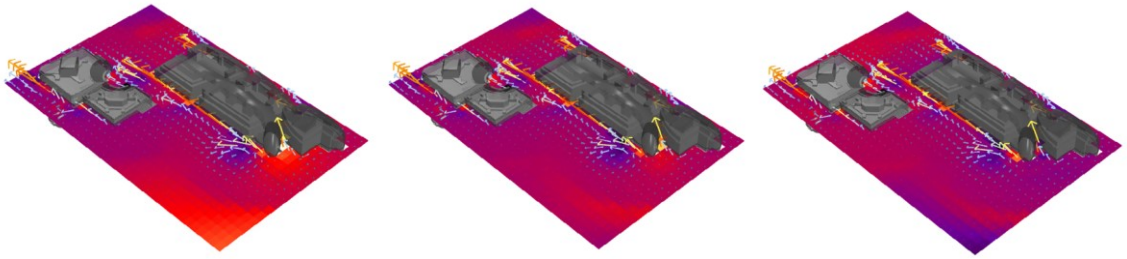


Figure 2: Analysis of outdoor airflow dynamics in specified time steps on models of Slovak National Theater and Eurovea buildings. Source: Authors

RESULTS

Annual solar radiation analysis on the digital model of Bratislava was conducted using both GrassGIS and Ladybug. GrassGIS demonstrated significantly faster performance, generating the output raster map in 12 hours. Notably, GrassGIS is efficient in memory usage and provides a responsive progress bar throughout the computation. However, it only generates a raster map, leaving façade evaluations unaddressed. The map resolution depends on the height map resolution, which was 1 x 1 meter in this case. GrassGIS calculates solar irradiation for a sample day of each month, allowing the results to be used for tracking solar radiation fluctuations throughout the year. (Figure 3)

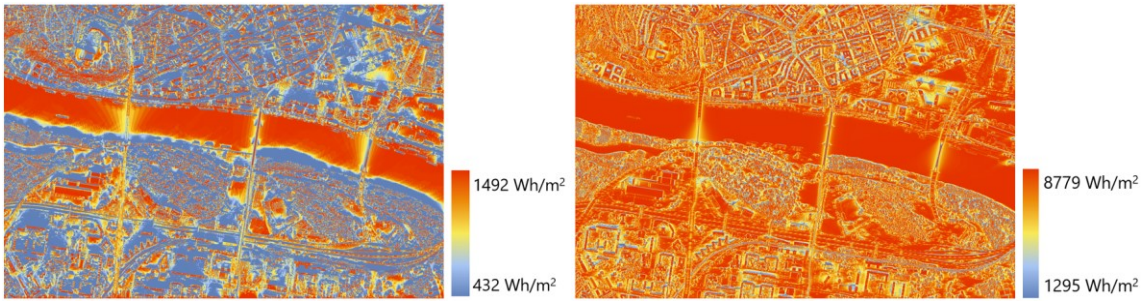


Figure 3: Solar radiation analysis on laser scanned data. Left: irradiation in winter day. Right: irradiation in summer day. Source: Authors

In contrast to GrassGIS, Ladybug took significantly longer to complete the solar radiation analysis, with the process finishing in 7 days. One drawback of Ladybug is the absence of a progress bar and responsiveness during calculations, leaving the user uncertain if the process is still running or has crashed. Due to the requirement for a single continuous run and high memory consumption, the city model had to be divided into two parts: one for the northern bank of the Danube and one for the southern bank.

Despite these challenges, Ladybug provides a detailed 3D mesh outcome, including façade analysis, offering a higher level of detail. The analysis resolution is determined by the number of mesh triangles, with higher resolutions requiring more time. The results are calculated using a cumulative sky component, producing an irradiated mesh for a predefined time interval over the cumulative period. To track solar irradiation fluctuations throughout the year, the entire process must be repeated for each month.

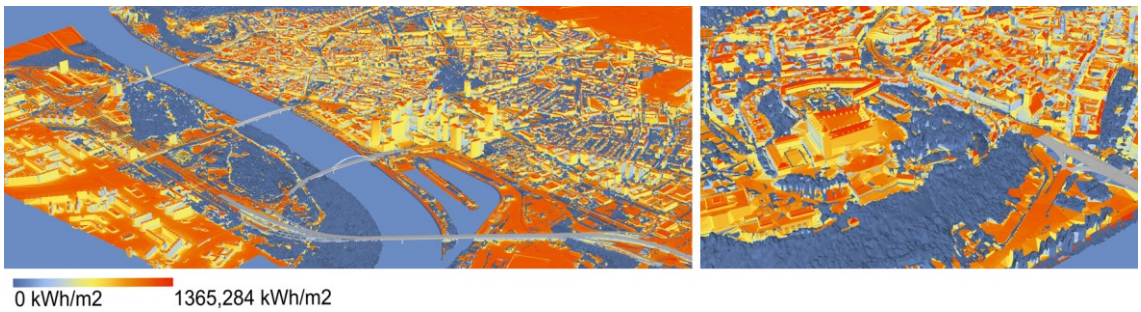


Figure 4: Solar radiation analysis of Bratislava 3D model. Solar incident radiation per one year. Source: Authors

The calculated analytical layers were visualized using Rhinoceros 3D modeling software. The values were encoded via RGB colors assigned to the vertices in the mesh geometry, accompanied by a legend. This colored mesh could then be exported to Three.js for online visualization. [16] Another visualization technique involved displaying the data on a physical model of the city, illuminated from beneath with an LCD screen, making it suitable for public exhibitions. This approach enhances communication with city inhabitants and facilitates decision-making among city institutions and authorities. (Figure 5)

https://doi.org/10.5593/sgem2024/6.1/s27.52

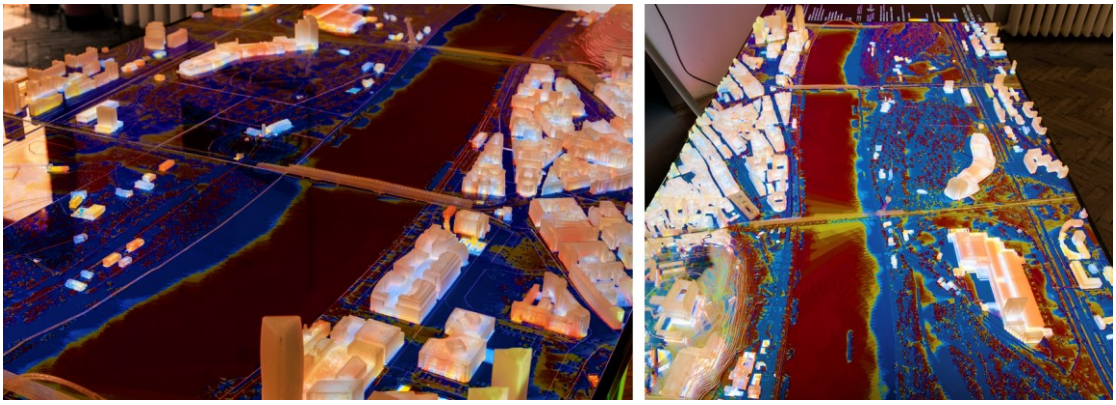


Figure 5: Physical model with visualization of solar irradiation. Source: Authors

The outcomes of the calculation were subject to further analysis. According to local regulations, photovoltaic (PV) appliances cannot be installed on historical buildings, rendering the historical center inefficient for solar energy production. Similarly, rivers and public spaces are also inefficient for this purpose. Consequently, the historical part of the city must be supported by other, more efficient areas. By excluding non-efficient parts of the city, buildings with higher potential for solar energy production are highlighted. These areas become even more visible after applying a blurring effect to the image, further emphasizing the zones with the highest potential. (Figure 6)

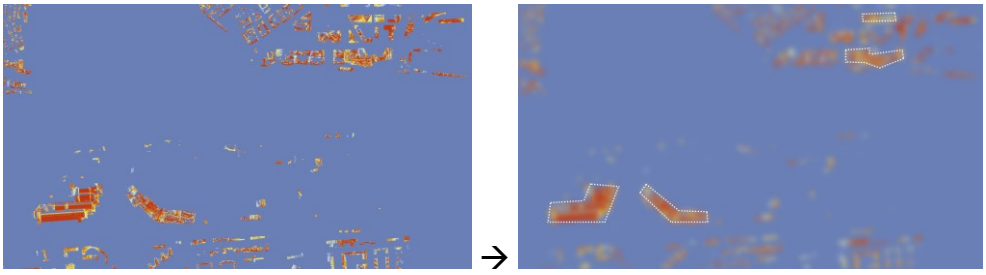


Figure 6: Solar radiation analysis with excluded public spaces, rivers and historical center (blue color). Right: blurred image with highlighted zones with highest potential.

DISCUSSION

The described analysis with the blurred image is qualitative and depends on image readability. However, a more quantitative approach could incorporate distances to less efficient city parts, allowing energy-deficient buildings to be complemented by nearby efficient ones. Optimizing connections between buildings would form efficient clusters and save resources for infrastructure construction.

However, these analyses are limited as they only display solar irradiation. The actual energy obtained will be lower due to PV panel efficiency (15-20%) and distribution. Seasonal fluctuations also impact energy needs: heating in winter with less sunlight, potentially supplemented by wind power and cooling in summer. Conditions vary in spring and autumn, necessitating monthly analyses to align solar and wind data for addressing energy fluctuations.

CONCLUSION

Upon reviewing analytical tools, Ladybug and Butterfly emerge as effective instruments for assessing solar impact and wind flow, particularly due to their 3D capabilities. With improved techniques and sufficient time, the resolution of analyses can be increased. On the other hand, when assessing hourly radiation patterns, GrassGIS proves more efficient as its computation is faster, allowing for better monitoring of radiation patterns, albeit in a 2D raster map format.

Determining the possible amount of energy gained can motivate the installation of renewable energy appliances in both the private and public sectors. In the public sector, this strategy could support the improvement of sustainable infrastructure managed by local municipal authorities, funded through taxes from commercial developments. By installing renewable energy appliances on buildings and parcels owned by the municipality, authorities retain full control over these infrastructure improvements and their future management.

After consolidating data in the digital twin of the city, further correlations can be explored. For example, relationships between vegetation density, wind patterns, solar irradiation, and satellite-measured temperatures could help predict urban heat islands. Similarly, correlations between physical parameters and space popularity could inform predictions of the popularity of new spaces during design phases.

ACKNOWLEDGEMENT

This article was developed with thanks for the support by the subsidy projects 23-05-02-B UrbanGraphica, 031STU-4/2022 Multidimensional model. The model was developed with help of FAD students on the courses Architecture and Mixed reality, Instruments of Digital Design II and within Data[LAB] studio.

REFERENCES

[1] United Nations General Assembly, Transforming our World: The 2030 Agenda for Sustainable Development. Resolution Adopted by the General Assembly on 25 September 2015. Online: sdgs.un.org/2030agenda (accessed 5th of June 2024).

[2] Abbas S., Ali Tarlani B., Amir S. J., Mohammadsadegh N., Ahmad G. L., Mohsen A., Application of artificial intelligence in digital twin models for stormwater infrastructure systems in smart cities. Advanced Engineering Informatics, Vol. 61/Issue 102485, 2024. ISSN 1474-0346, doi.org/10.1016/j.aei.2024.102485

[3] Francisco, A., Mohammadi, N. & Taylor, J. E. Smart city digital twin-enabled energy management: toward real-time urban building energy benchmarking. J. Manag. Eng., Vol. 36/ Issue 2, 2019. doi.org/10.1061/(ASCE)ME.1943-5479.0000741

[4] Lin, Y. & Cheung, W. Developing WSN/BIM-based environmental monitoring management system for parking garages in smart cities. J. Manag. Eng., Vol. 36/Issue 3, 2020. doi.org/10.1061/(ASCE)ME.1943-5479.0000760

[5] Nováček, O., Open planning: Qualification of urban space parameters from end user's perspective. ALFA , Vol. 11/Issue 3, 2020. Online: alfa.stuba.sk/wp-content/uploads/2020/11/03_2020_Novacek-1.pdf ISSN 2729-7640

https://doi.org/10.5593/sgem2024/6.1/s27.52

[6] Lu, Q., Parlikad, A. K., Woodall, P., Ranasinghe, G. D., Heaton, J. Developing a Dynamic Digital Twin at a Building Level: using Cambridge Campus as Case Study. International Conference on Smart Infrastructure and Construction 2019 (ICSIC) Vol. 36, pp 67–75, 2019. doi.org/10.17863/CAM.38523

[7] Petrova-Antonova, D., Ilieva, S., Digital Twin Modeling of Smart Cities. Human Interaction, Emerging Technologies and Future Applications III, Springer Link. pp 384–390,2020. doi.org/10.1007/978-3-030-55307-4_58

[8] ArcGIS. Use deep learning for feature extraction and classification. Online: doc.arcgis.com/en/imagery/workflows/resources/using-deep-learning-for-feature-extraction.htm (accessed 5th of June 2024).

[9] Pan, X., Mavrokapnidis, D., Ly, H.T. et al. Assessing and forecasting collective urban heat exposure with smart city digital twins. Sci Rep Vol. 14/Issue 9653, 2024. doi.org/10.1038/s41598-024-59228-8

[10] Eurosense, LiDAR measurements. Online: www.eurosense.com/products#Aerial-imagery (accessed on 5th of June 2024).

[11] Geodesy, Cartography and Cadastre Authority of the Slovak Republic, Airborne Laser Scanning. Online: www.geoportal.sk/en/zbgis/als/ (accessed on 5th of June 2024).

[12] Mackey, Ch., Galanos, T., Norford, L., Roudsari, M. S., Wind, Sun, Surface Temperature, and Heat Island: Critical Variables for High-Resolution Outdoor Thermal Comfort. Proceedings of Building Simulation 2017: 15th Conference of IBPSA, 2017. doi.org/10.26868/25222708.2017.260

[13] Robinson, D., Stone, A. Irradiation Modelling Made Simple: The Cumulative Sky Approach and Its Applications. Proceedings of the PLEA 2004, Eindhoven, Volume 2, pp. 1255–1259, 2004. Online: alexandria.tue.nl/openaccess/635611/p1153final.pdf (accessed 5th of June 2024).

[14] Solar Radiation Data. Satellite-derived database HELIOCLIM-1. Online: www.soda-pro.com/help/helioclim/helioclim-1-overview (accessed 5th of June 2024).

[15] Hofierka, J., Šúri, M., The solar radiation model for Open source GIS. Proceedings of the Open Source GIS-GRASS Users Conference. 2002.

[16] Hajtmanek, R. UrbanGraphica. Online: urbangraphica.mixedrealityarchitecture.eu (accessed 5th of June 2024).

THE EFFECTIVENESS OF THE RECONSTRUCTION OF HISTORIC COUNTRY HOUSES

Ing. Arch. Jaroslava Rolínková

Faculty of Architecture, Czech Technical University in Prague, **Czech Republic**

ABSTRACT

In the Czech Republic, despite the high demand for housing, a large number of houses remain unoccupied. Many of them are falling into disrepair, especially in the countryside. And at the same time, new houses, without architectural and urban planning qualities, are growing right next to them on agricultural land.

In my work, I deal with how to adapt these old houses to the current requirements for family housing. This includes requirements for energy savings for the indoor environment, especially thermal comfort. Therefore, during renovations, the house's outer shell is insulated and heating changes are made. Walls, ceilings, floors and roofs are insulated with thermal insulation, windows are replaced with new, thermally insulating ones, and air-conditioning units with recuperation are installed in the houses. These are very expensive measures. That's why I ask myself whether they are all necessary in terms of return on investment.

In addition, these interventions significantly change the appearance of the building and the entire environment. These modifications are not always carried out correctly and may damage the building and worsen living conditions.

Based on partial calculations of energy efficiency, I am dealing with how individual building modifications are beneficial for reducing energy efficiency and whether their contribution pays off financially, taking into account the costs.

I have narrowed my interest to buildings of historical, rural character, which are built from locally available, natural and recycled materials, perfectly adapted to their environment.

Keywords: historic country houses, renovation, energy efficiency, sustainability, return on investment

INTRODUCTION

Historic houses require regular maintenance in order to be habitable, and housing requirements also change. Therefore, it is necessary to carry out construction modifications.

A typical Czech historical country house had one heated living room, a black kitchen with a fireplace, pantries (spaces for storing food) and stables for animal husbandry.

https://doi.org/10.5593/sgem2024/6.1/s27.53

With a change in lifestyle, economic spaces lose their function, and on the contrary, more living space is required. The current housing standard is a private living room for each resident, a bathroom, a kitchen, a user-friendly and adjustable heating system and a good thermal standard and the associated low operating costs. Building modifications are also necessary due to the natural degradation of materials and the lack of technical infrastructure.

Construction work

A common problem with historic country houses is the lack of living space and lack of sanitary facilities, so it is necessary to adjust the layout. That is if we want to live comfortably as we want the inevitable today.

New heating system

Historical buildings had one heated room. The heat source was a furnace, a tiled stove or a tiled stove. Solid wood was almost always used as fuel. The disadvantage of this system is precisely the one heated room and the need to regularly add wood to the fire. This system is disadvantageous if all residents leave the house in the morning and return to a cold house only in the evening. A new heating solution is therefore associated with the change in layout. This is usually solved according to the way the object is used. Central heating with a biomass boiler (pellets, solid wood), gas or electricity or a heat pump is common. As with new houses. These systems allow the regulation of the interior temperature, and the possibility of tempering to a lower temperature to avoid damage to the object due to large temperature fluctuations during the heating break. If an old heater is preserved in the house during the reconstruction, it remains preserved or is replaced with a suitable replica.

Historic buildings in the countryside, which were not modernized during the second half of the 20th century, are often not connected to utility networks - water, sewerage, gas, except for electricity. Or they are not connected enough.

These mentioned modifications are almost always necessary, and therefore they will not be mentioned in the next part of the text.

Other construction modifications carried out in historic rural buildings are related to the reduction of energy requirements and the reduction of the influence of soil moisture. In the case study, I show what construction modifications can be made to the house and what their contribution is to reducing energy consumption.

I therefore ask myself the following questions: Is it worth investing in reducing the energy intensity of historic rural buildings?

What is the return on these investments?

MATERIALS AND METHODS

This text evaluates the return on the costs incurred to reduce the energy demand of the building.

The energy efficiency of the building was evaluated step by step, for each structural modification separately and then for all modifications at once. In this way, the contribution of individual building modifications and the overall reduction in energy consumption was evaluated. Energie 2021 calculation tool was used.

Based on the obtained data on energy needs and current energy prices (for the 1st quarter of 2024), the building's operating costs and their reduction in individual steps were calculated.

The reduction in operating costs was compared with the cost of building modifications.

The quoted prices are analogously based on budgets for the reconstruction of buildings with the same or similar types of structures and building elements. The budgets used were professionally processed by Radek Sláma during the last two years in the BUILDpower S program. The prices in the Budgets were given in Czech crowns. For this text, they were converted to euros at the rate of €1 per CZK 25. Prices include material and work.

Simple payback is given as the payback period - how long it will take for the savings to cover the construction costs.

CASE STUDY

The evaluated object is a miner's house in Láz u Příbrami. It is a single-storey residential house of a rural character with an unheated attic and small associated outbuildings with an L-shaped floor plan, with a north-south orientation of the residential part.

The house was built in the 1860s and was gradually expanded and rebuilt. First, it was extended by adding a stable, followed by other additions to farm premises in the northern part of the property. A wooden glazed porch was added to the original house, which was later extended, so that today it lines almost the entire eastern side of the house and connects all parts of the house. Most recently, a carriage house was added, perpendicular to the residential building. The current form of the house dates from the first half of the 20th century [1].

The first floor consists of an entrance network with a completed bathroom, a hall oriented to the south, a second living room, originally probably a chamber and other spaces, formerly of an economic nature. The ground in the attic of the building occupies the entire area above residential and non-residential rooms. It was used to store hay.

The house was uninhabited for several years and began to deteriorate without regular maintenance. Reconstruction work is currently underway, and the living area has been expanded to include former farm premises.

https://doi.org/10.5593/sgem2024/6.1/s27.53



Figure 1 - Evaluated object (origin: Ing. arch. Michal Profant)



Figure 2 - floor plan of the object being solved - original condition (origin: Ing. arch. Michal Profant)

Modifications considered:

- Replacement of windows
- Insulation of floors in the field and their ventilation
- Ceiling insulation
- Partial wall insulation
- Repair of the existing glazed veranda - an element of passive solar architecture
- Installation of new shutters

RESULTS

When all planned modifications are included in the calculation of the building's energy efficiency, it will be significantly reduced.

The original total required energy for heating, lighting and hot water heating would be 378 kWh/m²·year. With an energy reference area of 146.3 m², the total energy requirement per year would be 55.3 MWh.

The average energy price in the EU was €0.0763 per 1 kWh in the 1st quarter of 2024 [2]. This would mean that the total cost of running the facility was €4,320.

Returnability of individual steps of construction modifications

New windows

If replacing the windows reduces the energy demand by 4 Kwh/m²· year, the operating costs will be €4175. This means an annual saving of €145. The price of one new casement window of the same type as the original windows is around 1700 euros. In the house there are these 4 windows and 2 new doors (approx. €1400 each) and 4 (€270) small windows and one new door. The replacement of all the hole fillings would thus amount to approximately €10,680. The return on such an investment would be greater than 73 years. Given that manufacturers declare a service life of 50 years on average (30-80 years, depending on the specific material and surface treatment) and maintenance costs are not included, investing in new windows is not worth it from the point of view of saving operating costs. It is therefore advisable to replace windows only at the moment when their service life ends. Heat leaks can be reduced by adding seals or refurbishing with replacement of heat-insulating glass in the original frames.

New insulated floors

New insulating ventilated floors with quality brick paving throughout the house would save 53 Kwh/m²· This would reduce running costs by €693 every year. The price of 1 m2 of ventilated floor can be up to €320/m2 of clean floor area in a building of 98 m2. The total price of floor reconstruction can thus rise to €31,360. The total payback of this reconstruction will be 45 years.

Taking into account the technical condition of the building and the materials and structures used, investing in new floors is a must in any case. If quality materials are

https://doi.org/10.5593/sgem2024/6.1/s27.53

used, brick pavers have a service life of decades. Ventilation from the terrain and soil moisture will bring additional savings in the need for plaster repairs. From this point of view, the payback period seems acceptable.

Ceiling insulation

Insulation of the ceiling structure from the ground is a fairly simple and non-invasive intervention that can save up to €566 per year. Total heating costs could reach €26,280. In this case, the return on investment would be 46 years.

Porch repair

Another possible way to reduce the energy demand of the building is to repair the existing veranda to serve as an element of passive solar architecture. An element used to preheat the outside air for ventilation and insulation of the eastern facade of the building. The wooden veranda is partially glazed. The restoration, including the repair of the wooden and glass parts, should be around €4,000. With annual energy cost savings of €368, the return on investment will be 11 years.

Investing in the renovation of the veranda is not only about reducing the energy demand, but also about renovating a significant artistic element of the facade of the building.

Installation of new shutters

Shutters are a completely new element. But we can find similar houses from the same period that have shutters. It is possible to install them from the inside and outside. In the summer they can protect against overheating, in the winter they can increase the insulating capabilities of the windows. They also ensure privacy and increase security. New wooden shutters with adjustable slats for all the windows in the house would cost €4,600. Their contribution would bring a saving of €176 every year. The return on the investment will thus be 26 years.

For clarity, all data were entered in one table:

	total required energy [Kw/m²year]	total required energy [Mwh]	Cost [€]	Saving [€]	Investment [€]	Returnability [years]
Original state	378	55,3	4320	-	-	-
New windows	374	54,7	4175	145	10 680	73
Floor	325	47,6	3627	693	31 360	45
Ceiling	337	49,3	3762	566	26 280	46
Insulation	275	40,2	3069	1251	11 700	9,5
Veranda	354	51,8	3952	368	4 000	11
Shutter	371	51,2	4141	176	4 600	26
All building modifications	**149**	**21,8**	**1663**	**2657**	**88 620**	**33**

The total payback period for all these investments would be 33 years.

DISCUSSION

The answer to the question of whether it is worthwhile to invest in reducing the energy demand of historic rural buildings is equivocal. It is important to consider which building modifications are necessary. We have to start from the current technical condition of the building and also the mode in which we want to use the house.

If the building will only be used as a holiday home or will only be inhabited during the warmer part of the year, it is not worth investing too much in reducing energy consumption.

If we are going to live in the house permanently for the whole year, it is definitely desirable to reduce the energy consumption. We also have to take into account the durability of the materials used.

Specifically, in the case of replacing old windows, it is better to leave the existing windows (if they are functional) and only perform repairs or overhauls and, for example, replace the glazing or add seals.

The answer to the question of what "is the return on these investments" is quite accurate. These are decades. With a long return on investment, it pays to use long-lasting materials and structures, such as high-quality ceramic tiles, breathable plasters and high-quality wood. The price of the materials is often a smaller part of the construction costs, and the price for the work does not change.

CONCLUSION

Reconstruction of historical buildings is very expensive. Therefore, it is often necessary to consider what construction modifications are necessary and really beneficial for the building and its residents. A number of construction modifications that lead to a reduction in energy efficiency must be carried out due to the poor condition of the building. For example, new floors that, in addition to insulation against heat loss, protect structures from the effects of ground moisture. It will also make it possible to carry out new water and sewage installations or the installation of underfloor heating.

It is also suitable to insulate parts of constructions with low thermal insulation, where the return on investment is very short. In the case of replacing windows that are functional and only do not meet thermal technical standards, the investment may not bring the intended savings. Especially if the payback would be longer than the life of the windows.

Nevertheless, I believe that reconstructing historical objects makes sense. One of the reasons is that these houses meet the requirements for sustainable construction. Another reason is that it is not necessary to build additional green areas and agricultural land. The historical and socio-cultural significance of traditional architecture in the cultural Czech landscape is a matter of course.

ACKNOWLEDGEMENTS

I would like to thank Michal Profant for providing the basis for the calculations and his own drawing co-commentation for the reconstruction of his house.

https://doi.org/10.5593/sgem2024/6.1/s27.53

REFERENCES

[1] PROFANT, Michal. Stavebně historický průzkum: Dům v Lázu. 2019.

[2] KURZY.CZ. Elektřina únor 2024 v EUR. Online. Kurzy.cz. 2024. Dostupné z: https://www.kurzy.cz/komodity/cena-elektriny-graf-vyvoje-ceny/202402-eur-1kWh. [cit. 2024-03-30].

[3] Rolínková, J.; Vyoralová, Z. Možnosti snižování energetické náročnosti historických venkovských objektů In: 14th Architecture in Perspective 2022 / 14. Architektura v perspektivě 2022. Ostrava: Vysoká škola báňská - Technická univerzita Ostrava. Fakulta stavební, 2022. s. 209-215. ISBN 978-80-248-4646-0.

EVOLUTION AND DISTRIBUTION OF GREEN COVER AND ITS INFLUENCE ON URBAN PLANNING, THE CASE OF THE HISTORIC CENTRE OF LOJA, ECUADOR

Assoc. Prof. Valarezo-Jaramillo Sandra[1]

Assoc. Prof. Aguirre-Maldonado Eduardo[1]

Assoc. Prof. Dr. Balcázar-Arciniega Cristian[1]

Assoc. Prof. Alvarado-Rodríguez Lorena[1]

[1]Universidad Técnica Particular de Loja – Architecture and Urbanism Departament, **Ecuador**

ABSTRACT

Changes in land use and architectural renovation are a normal process in historic urban centres, and as a consequence there are changes in the occupation of properties, such as the loss of vegetation cover and filtering soils that could be integrated into the urban green system, which is now almost entirely concentrated in the public space. In this study, a series of orthophotographs of the historic centre of the city of Loja were analysed to determine the changes in vegetation cover and its distribution among squares, parks and private properties. The study puts into context the way in which the city has modified the extent of green cover throughout its modern history. An analysis of aerial imagery was carried out using a pixel classification technique to determine the proportion of area per pixel analysed, and maps were produced to study the distribution of urban greenery in the study area and compare its radius of influence in each period studied. The results show how the historic centre is becoming detached from the urban green system, reducing the presence of green cover on private properties and concentrating on the public space of squares and parks in the centre. This study also explores strategies to protect and increase the distribution of green areas, which can contribute to the reduction of environmental problems in the city.

Keywords: green coverage, urban green system, historical analysis, orthophotography, sustainable urban planning.

INTRODUCTION

The urbanization speed is one of the main concerns of the current century; the proposal of new sustainable areas for living must take into account aspects such as the water and carbon cycle, rainwater harvesting, mitigation of the heat island effect, preservation of biodiversity, recreational spaces and air quality that contribute to the physical and mental health of people [1]; all of these characteristics are related in one way or another to Urban Green Spaces (UGS). Densification and growth of urbanized areas is a recurrent phenomenon in the face of population growth; urban sprawl involves the shrinking of natural areas, while in consolidated urban centres, densification is a strategy to mitigate horizontal sprawl. However, the creation of urbanized land does not always imply a reduction in green space, especially in cases of low urbanization and in the outer rings of urban areas [2]; on the other hand, the degradation of vegetation is not

https://doi.org/10.5593/sgem2024/6.1/s27.54

inevitable in modern cities, and the presence of urban green space does not imply vegetation quality, although the reduction of green space deprives residents of its benefits [3]. The study of UGS distribution patterns complements green area per capita indicators, making it possible to analyze areas lacking green space in order to intervene with the limited resources of urban space [4]. The identification of green areas can be done through a grid-based survey on aerial photographs, taking into account the relationship between resolution and scale to define a polygon, while applying a grid-based survey processed with ArcGis [5][6].

Urban centres are shaped by development and reflect social dynamics, allowing us to understand the speed of urban change over time and to project its possible impact on the quality of urban space in order to design mitigation strategies. However, an understanding of the evolution of the distribution of UGS in these historic centres allows establish the degree of impact of the increase or decrease of green areas in terms of social and environmental sustainability, and to understand how the city is missing out on the opportunity to integrate the environmental benefits of distributed green space.

MATERIALS AND METHODS

Study area

Located in the southern region of Ecuador, the city of Loja (3°59'35.3" S, 79°12.253' W) covers an area of 192,800 hectares (Figure 1) and has a temperate humid Cfbi climate according to the Köppen classification. The case study is the historic centre with an area of about 100 ha, spread over 90 blocks. The old town, founded in 1548, preserves the outlines of the imperial Hispanic urban planning, including a checkerboard morphology characterized by narrow streets and regular blocks, places of worship and public squares.

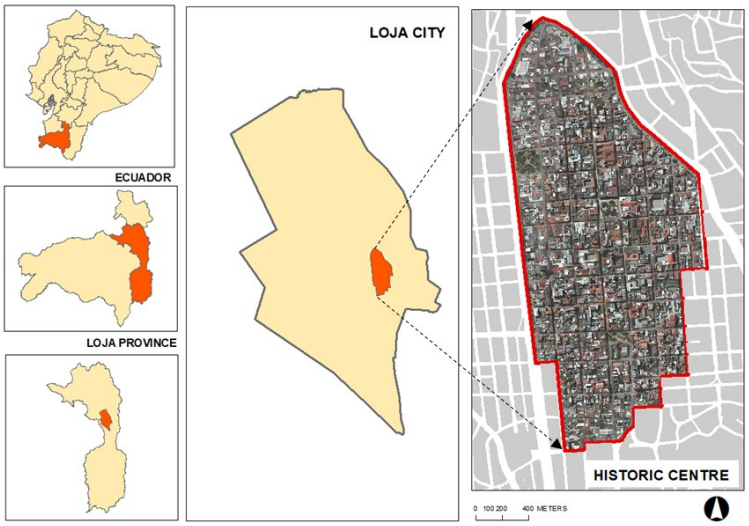


Figure 1: Historic centre of Loja city in 2023.

The first buildings also followed the archetypes of the Spanish villa of the time, spaces around a central area with vegetation, built with construction systems based on raw earth for the main structure, wood and terracotta materials for the roof, a construction system that would prevail in later centuries, with partial modifications based on the incorporation of new technologies. Between 19th and 20th centuries, the city

underwent a period of significant transformation, not only due to changes in infrastructure, but also to the division of land and the diversification of public and private land uses, driven by the city's population growth. In the last decades of the twentieth century, urban regeneration projects were carried out in an attempt to improve the conditions of the space through actions that intervened mainly in the restoration of buildings and urban infrastructure, while the intervention in green areas is still a pending issue to be integrated.

Study method

The study of the evolution of the distribution of UGS is based on the historical collection of orthophotographs of the study area (1767.79m NS, 779m EW), the existing collected files include the years 1960, 1984, 2003, 2010 taken by the Military Geographic Institute of Ecuador, while the orthophotography of the most recent year (2023) was developed based on a Metashape photogrammetric survey using a multirotor drone Enterprise Series. The scale for the older photographs is 1:10000 and for the most recent 1:1000. In order to interpret the presence and distribution of UGS, a recognition of green areas observed in grid-based (100mx100m), The green area is identified and delineated by pixels in each image examined using ArcGIS 10.4.1 software, the mapping unit for the identification of UGS is 0.3m/pixel. The pixels classified as urban vegetation were identified in private and public properties in the historic centre, the total values of urban vegetation were obtained for the five historic orthographies (Table 1). In addition to the identification of UGS, seven categories of areas that make up the historic centre and are related to urban vegetation are quantified. Finally, in order to determine the degree of concentration of UGS over time, three zones that make up the historic centre were classified: the founding nucleus, the expansion zone of this nucleus and the edges of the historic centre. The spatial analysis criteria based on the density of green areas and marked areas and their comparison from 1960 to 2023 are used to evaluate the changes in the areas of these zones, determining the degree of loss or expansion of the UGS presence based on their distribution.

Table 1: Occupancy of different uses within an urban area, measured in square meters (m^2), in different time periods.

Year	Buildings	Parking lot	Green Front Urban Retreats	Natural ground surface, unvegetated	Green on property (rear retreats)	Green in public spaces	Tracks
1960	446006.04	0.00	0.00	81160.29	274971.46	3429.89	195792.13
1984	584372.52	19894.18	4102.68	54318.49	106251.62	12066.07	225519.91
2003	666429.80	18098.13	2188.83	12500.63	74258.72	10921.93	226330.18
2010	683381.14	21282.82	2080.92	10916.52	56093.41	10569.03	226404.15
2023	693590.16	35933.75	1729.16	4012.87	38527.81	10530.11	226404.15

RESULTS

Figure 2 illustrates the evolution of land use in the historic centre of Loja, Ecuador, from 1960 to the present. The figure highlights the significant increase in the built-up area, mainly occupied by buildings, which represented 44% in 1960 and 70% today. The built-up area in the blocks has increased as a result of the densification that urban

https://doi.org/10.5593/sgem2024/6.1/s27.54

centres experience in their development, with the consequence that the area designated as green areas or areas without vegetation cover has significantly decreased, reducing the availability of green areas in the historic centre.



Figure 2: Evolution of land use in the historic centre of Loja city in different periods.

The main area occupied to increase the built-up area is the UGS, which decreases from 27% to 5% between 1960 and 2023. The increase in built-up area has also implied a demand for parking spaces, which both leads to the occupation of non-built-up areas, such as set-aside land, and reduces the likelihood of maintaining green cover in the historic centre. On the other hand, the distribution of UGS has been exponentially reduced at the edges and in several block cores, this phenomenon has accelerated in the first decades of the 21st century, the concentration of green areas in the most central areas has been maintained in squares and parks.

DISCUSSION

Figure 3 shows the evolution of the occupation of the different uses in the historic centre of the city of Loja. Based on the conservation of historic structures, urban centres limit their scope, while experiencing changes in relation to the most flexible space available to be modified, such as the unbuilt spaces where the UGS are present. In this line, the presence of green areas in the historic centre over the last 50 years indicates a progressive reduction, the decreases in the percentage of UGS area are mostly on the

edges (86% between 1960 and 2023), while in the most central area of the city the UGS tend to be preserved almost exclusively in public space, which can be explained by the dissociation of private properties from the urban green system, as they seek to make full use of the rentable area (Figure 4).

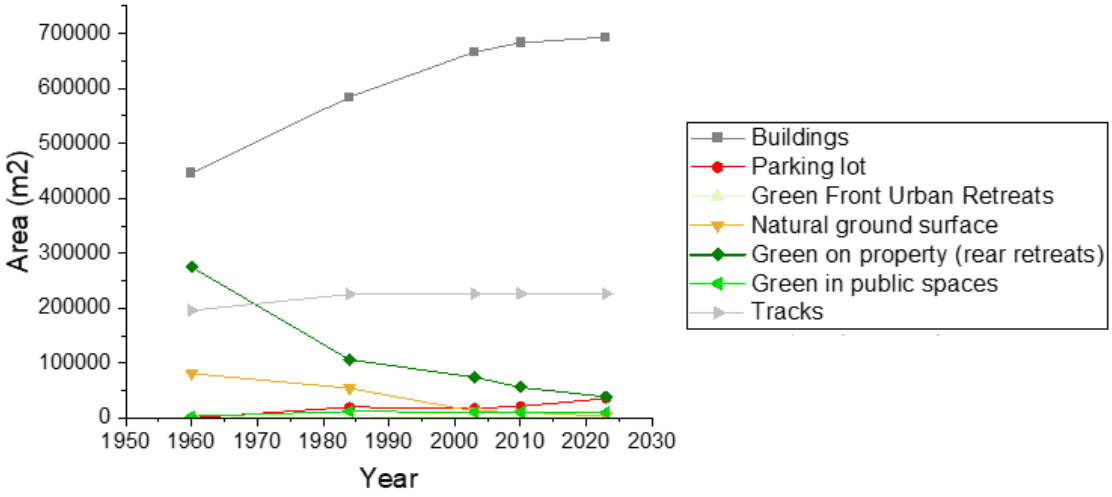


Figure 3: Evolution of the occupation of the different uses in the historic centre of the city of Loja, Ecuador

On the other hand, the spatial needs that force the occupation of the UGS may lead to other issues in other areas of urban sustainability. The observed changes in land use have potential implications for the environmental, social and economic aspects of the historic centre.

Environmental impacts: The reduction in green space could lead to an increase in the heat island effect, a reduction in air quality and a reduction in biodiversity. Social impacts: The loss of green space could reduce opportunities for recreation, relaxation and social interaction within the historic centre. Economic impacts: Increased demand for space could increase property values and potentially affect the affordability of housing in the historic centre. In addition to the loss of urban green space, Loja's reliance on small urban green public spaces (SPUGS) highlights the importance of incorporating sustainable urban development principles into urban planning and design. This includes:

First, to ensure their continued availability to the community, existing SPUGS AND UGS must be protected from development or encroachment [7].

Second, to implement optimization strategies to improve the accessibility of SPUGS and UGS [4]. This includes: (a) Identifying and revitalizing existing UGS. Revitalization can be achieved by providing amenities such as children's play areas, seating, or selecting materials that promote lower surface temperatures and higher humidity to create more thermally comfortable public spaces that encourage use and social interaction [8]. It is also important to ensure that UGS designs are inclusive and accessible to people of all abilities. (b) Locate and use spaces that are not being used for SPUGS and UGS development. This can be done on vacant or unused land, or by adding vegetation to roofs, balconies and vertical surfaces of existing buildings. (c)

https://doi.org/10.5593/sgem2024/6.1/s27.54

Facilitate access to SPUGS for non-motorized users by improving the overall connectivity and accessibility of the UGS network. It is therefore essential to connect existing SPUGS to public transport routes and stops, to encourage residents to use sustainable transport to access green spaces, and to establish a network of well-connected and accessible UGS that ensures equitable distribution.

Third, moving to a 15-minute city model would allow residents to access essential services within a 15-minute walk or bike ride of their homes, promoting sustainable and equitable urban development [9].

Fourth, reducing reliance on private cars can help improve air quality and create more space for pedestrian-friendly areas and SPUGS.

Finally, involving residents in the planning and implementation of improvement initiatives is essential to ensure that solutions meet their needs and aspirations. Implementing improvements in a phased manner, prioritizing the most critical interventions and addressing other aspects gradually, can ensure a manageable and sustainable approach.



Figure 4: Distribution of UGS on centre of Loja city in different periods.

CONCLUSIONS

Land use changes in the historic centre of Loja, Ecuador, pose environmental, social and economic challenges. The loss of green space can cause heat island effects, reduce air quality and affect biodiversity. Spaces for recreation and social interaction are also being lost. On the other hand, the increasing demand for space increases property values and could affect housing affordability.

To address these impacts and promote sustainable urban development, principles such as protecting existing green spaces, optimizing their accessibility, moving towards a 15-minute city model, reducing dependence on the private car and actively involving residents in planning need to be implemented. A phased implementation of these strategies, prioritizing the most critical interventions, will ensure a sustainable and manageable approach.

The need for built space in historic urban centres accelerates the reduction of green spaces, as a result of which the distribution reduces their presence and concentrates them mostly in the public space, thus reducing the capacity of the urban green system to integrate and provide environmental benefits in the urban space. For this reason, the conservation of the built heritage in historic centres must also consider its relationship with the original green space and propose alternatives to restore its presence and influence.

REFERENCES

[1] J. Maas, S. M. E. van Dillen, R. A. Verheij, and P. P. Groenewegen, “Social contacts as a possible mechanism behind the relation between green space and health,” Health Place, vol. 15, no. 2, pp. 586–595, Jun. 2009, doi: 10.1016/j.healthplace.2008.09.006.

[2] W. Fu, Y. Lü, P. Harris, A. Comber, and L. Wu, “Peri-urbanization may vary with vegetation restoration: A large-scale regional analysis,” Urban For Urban Green, vol. 29, pp. 77–87, Jan. 2018, doi: 10.1016/j.ufug.2017.11.006.

[3] S. Yu et al., “Does urban growth mean the loss of greenness? A multi-temporal analysis for Chinese cities,” Science of The Total Environment, vol. 898, p. 166373, Nov. 2023, doi: 10.1016/j.scitotenv.2023.166373.

[4] K. Xue, K. Yu, and H. Zhang, “Accessibility analysis and optimization strategy of urban green space in Qingdao City Center, China,” Ecol Indic, vol. 156, p. 111087, Dec. 2023, doi: 10.1016/j.ecolind.2023.111087.

[5] Y. Chen et al., “Inequalities of urban green space area and ecosystem services along urban center-edge gradients,” Landsc Urban Plan, vol. 217, p. 104266, Jan. 2022, doi: 10.1016/j.landurbplan.2021.104266.

[6] G. Yang et al., “Identifying the greenhouses by Google Earth Engine to promote the reuse of fragmented land in urban fringe,” Sustain Cities Soc, vol. 67, p. 102743, Apr. 2021, doi: 10.1016/j.scs.2021.102743.

[7] Gavrilidis, A. A., Popa, A.-M., Onose, D. A., & Gradinaru, S. R. Planning small for winning big: Small urban green space distribution patterns in an expanding city. *Urban Forestry & Urban Greening*, *78*, 127787. 2022

https://doi.org/10.5593/sgem2024/6.1/s27.54

[8] Maldonado, E. A., Jaramillo, S. V, Rodríguez, L. A., Arciniega, C. B., & Salazar, S. O. Impact of unsealed surface pavements on air temperature and humidity in public spaces. *Proceedings of International Structural Engineering and Construction*, *11*(1). 2024. https://doi.org/10.14455/ISEC.2024.11(1).SUS-06

[9] Wang, T., Li, Y., Chuang, I.-T., Qiao, W., Jiang, J., & Beattie, L. (2024). Evaluating the 15-minute city paradigm across urban districts: A mobility-based approach in Hamilton, New Zealand. *Cities*, *151*, 105147.

ILHA DE MOÇAMBIQUE AND ITS BUFFER ZONE – PROPOSAL FOR A LANDSCAPE STRUCTURE

Assist. Prof. Dr. Rute Sousa Matos[1]

Assist. Prof. Dr. Paula Simões[2]

Assist. Prof. Dr. Desidério Batista[3]

[1]University of Évora, Investigation Centre in Art and Artistic Research, **Portugal**
[2]University of Évora, Investigation Centre in Art and Artistic Research, **Portugal**
[3]University of Algarve, Centre of Studies on Archaeology, Arts and Heritage Sciences, **Portugal**

ABSTRACT

The high risk of natural disasters to which Ilha de Moçambique (IM) and its Buffer Zone (BZ) are naturally exposed and the demographic explosion it has suffered increased the loss of ecological wealth, biodiversity and the mischaracterization of the cultural identity it holds. Thus, there are required urgent measures for its values safeguard, preservation and valorization. The primary objective of this proposal is to improve the sustainability of IM and BZ enhancing its development trough landscape and urban planning. The proposal will target a multifunctional and sustainable landscape structure trough food production, protection of environment, resources, biodiversity and leisure promotion. This structure will articulate the IM open spaces with the ones of the BZ. Methodology will include: collecting information about the target area as a basis to all project decisions; work cartography production; a Productive Landscape Component Map; a Continuous Landscape Component Map; a Productive and Continuous Landscape Structure Plan. The expected results are: improvement of resources preservation, biodiversity and environmental quality; increasing of community gardens area; increasing of public open spaces; decreasing construction on ecological sensitive areas; recovering ecosystems and biodiversity; increasing awareness and cooperation of communities and regional authorities; increasing local Nature-Culture based tourism; increasing local economy.

Keywords: Ilha de Moçambique; Landscape structures; Multifunctionality; Sustainability

INTRODUCTION

According to [1], Mozambique has significant natural resources and a unique biodiversity, of which Ilha de Moçambique (IM) is an example.

Urbanisation will play an increasingly important role in the development of coastal Mozambique, namely IM, transforming its economy and supporting green economic growth. In this way, landscape-based urban planning responds to the challenges of rapid urbanisation by integrating urban development with environmental planning to improve liveability and resilience [2].

https://doi.org/10.5593/sgem2024/6.1/s27.55

As well as giving the country its name, IM has been on the Indian Ocean shipping routes since the 10th century. It was Mozambique's 1st capital and it was a strategic trading point where people from different parts of the world met [3]. Thus, it presents a rich architecture and is an exceptional example of an urban dichotomy resulting from cultural diversity between people of different backgrounds and cultures. IM's landscape, history, and culture give it two distinct but complementary urban systems: The city of Pedra e Cal (PC) and the city of Macuti [4].These cities are interdependent and reflect a mixture of popular knowledge as well as urban development within an urban and cultural *continuum.* It's cultural values, in terms of its urban setting and its intangible heritage as well as the social integrity embedded in the site's material heritage, were the reason why IM was declared a World Heritage Site by UNESCO in 1991.

At present, IM includes a buffer zone (BF), which incorporates a strip of continental territory, as well as several small islands in its vicinity: Cabaceira Pequena, Cabaceira Grande, Vila do Mossuril, Lumbo, Sanculo and Djembesse and all the islands – Sete Paus, Goa and Sena.

This area has a great diversity of marine habitats that are favorable to the development of plant and animal species. The continental strip includes mangroves, herb and seaweed beds and coral reefs. Within it is a mosaic of agricultural crops, uncultivated grasslands and secondary coastal grasslands. Inside this landscape, mangroves, dune vegetation, riparian forest, scrub and swamp vegetation can be found [5]. The beaches of the continental strip and the islands are also part of the natural heritage, as are the marine resources.

However, despite the recognition of the Outstanding Universal Value (OUV) of the Island's Cultural Heritage which includes its natural, ecological and biodiversity wealth, and the efforts to ensure its conservation, the Island suffers from several problems. These are due both to the high risk of natural disasters to which it is naturally exposed and to the demographic increase it has suffered. This has resulted in an increase in risks and a loss of ecological wealth and biodiversity, a misrepresentation of the cultural identity and a widening socio-economic gap between the inhabitants of Macuti and the City of PC, which contributes to the existing division between the residents.

There are several sources of pressure on the heritage that pose risks to the effective conservation and sustainable management of the IM and the BF. The main factors include coastal erosion, cyclones and types of use of natural resources, demographic pressure and sanitation, levels of poverty and social vulnerability, accelerated degradation of the heritage, and the conflict of interest [6].

The value and authenticity of the Island is therefore in danger of being compromised unless concrete measures are taken to improve living conditions through the effective implementation and monitoring of territorial management plans and instruments. A reversal of the degradation situation may occur, which is the challenge to which this plan proposal, perfectly framed in the contemporary Green Cities Strategy and in [7] and [8], intends to contribute.

The main objective of this plan is to significantly improve the sustainability of IM and its BZ promoting its development through landscape and urban planning. In particular, the project will aim to create a multifunctional and sustainable landscape structure through the presence of food production, protection of the environment, resources and biodiversity and leisure [9]. This structure will link and articulate the IM open spaces and these with those of the BZ.

The methodology will include: collection of information about the target area as a basis for all plan decisions; production of working cartography, namely a Productive Landscape Component Map; a Continuous Landscape Component Map and a Productive and Continuous Landscape Structure Plan. The expected results are: improvement of resource preservation, biodiversity and environmental quality; increase in the area of community gardens; increase in public open spaces; decrease in building on ecologically sensitive areas; recovery of ecosystems and biodiversity; increase in awareness and cooperation of local communities and regional authorities; increase in nature-culture based solutions and community-based tourism; increase in local economy.

MATERIALS AND METHODS

This is a transdisciplinary proposal. It must bring together a team with complementary skills, combining scientific knowledge and experience in the implementation of sustainable urban and landscape planning measures, local institutions, stakeholders, managers and international organizations. In addition, the implementation of strategies and measures with local communities, which will provide the proper functioning of the plan, is fundamental [10].

It will include tasks designed and planned to achieve the objectives, namely the collection of essential information about the target area; an operational plan to guide all the process; the production of cartography; the production of a productive landscape component map; the production of a continuous landscape component map; the production of a productive and continuous landscape structure plan; the implementation of the plan; monitoring the impact of the plan, i.e. socio-economic impact, environmental function, cost-effectiveness; communication and dissemination to the general public and to the nature-culture tourism public; promotion of environmental education and technical and scientific dissemination activities; promotion of networking with other plans; and finally, plan management activities.

For the Productive Landscape Component map we will use the collected information related to the agricultural potential of the soils. Agricultural areas from planning models as well as those identified in land use maps will be selected. Then the areas of soils classified as low alluvial and colluvial and their subsequent association in a single area are selected. The areas dedicated to the agricultural use of the soil, together with the areas that are not occupied in the urban soil, conjugated with the patches of soils with agricultural potential, constitute the "productive component of the landscape" [11,12].

The delineation of the map of the continuous landscape component - ecological structure - is based on the information collected and associated with ecologically sensitive areas. These are the protection of mangroves and special habitats, the protection of coastal corridors and the protection of coral reefs and seagrass in coastal resorts, beaches of the continental area, small islands and marine resources. In terms of cartography, the land use map, the topographic map, the hydrological map and the vegetation map will be used. The continuity of the landscape is still valued for the integration of all open spaces and cultural sites in the IM and BZ. It forms a network of pedestrian and recreational spaces that crosses the entire island and the BZ, allowing the connection between the urban areas and the natural and cultural values of the surrounding rural areas. The existence of this structure will be decisive for the creation of a future network of paths and places that will connect ecological and productive

https://doi.org/10.5593/sgem2024/6.1/s27.55

landscapes, intensifying their level of use and creating an articulation between rural and urban spaces. The existing heritage values should act as reference elements in the landscape [12]. This information is provided by the data collected in heritage maps, cultural site maps and open spaces maps.

After determining the areas added to the productive and continuous components of the landscape, the conjugation of the two determines the areas to be added for the construction of a multifunctional landscape structure [11, 12].

According to this structure, it is expected to implement an area of community allotment gardens, to identify the ecological areas to be protected and to improve and create open spaces. In this sequence, there will be four interpretive routes: Ilha de Moçambique (1000m); Cabaceira Grande (1500m); Vila do Mossuril (900m) and Lumbo (800m), linking open spaces, ecological areas and allotment gardens. Along these routes, it will promote outdoor leisure activities such as sports, theatre, dance or reading.

The awareness of the population about the importance of sustainability, natural values, heritage, community allotment gardens, open spaces and conservation of the heritage is fundamental. But also its future preservation, communication and dissemination tasks as well as monitoring will be decisive for the success of the implementation plan. These actions will be carried out through the creation of websites, information panels, information leaflets, surveys, questionnaires, exhibitions, TV reports, briefings, visits, educational activities for schools and local population, development of educational projects for primary and secondary schools, field trips, school competitions, seminars, field workshops for communities and stakeholders, scientific events and publication of a field guide on natural and cultural values.

RESULTS

This proposal is designed to achieve the following results:

- Improve resource conservation, biodiversity and environmental quality in accordance with our objective, including the protection of ecologically sensitive areas and systems. The quality should be reflected in the diversity of species and in a well-framed and consistent ecological structure. This means the effective improvement of the current state. This is a very important result, as it means reversing the current process of degradation and moving from a "vulnerable state" to a "good state" in the medium term;

- Increasing the area of community allotment gardens in accordance with our goal, including horticulture, cereals and orchards.

- Increasing the number of public open spaces, improving existing ones and promoting outdoor activities, well-being and human health .

- Reducing construction and edification on ecologically sensitive areas, namely primary dunes, mangrove cutting, waterproofing of private and public open spaces through their identification, delimitation and legal protection by including them in a fundamental ecological structure. This will also contribute to the recovery of ecosystems and biodiversity, the reduction of flooding, erosion and other natural disasters.

- Test the effectiveness of all the management techniques and methods used, ensuring their transfer and replication in at least 2 other territories. To reach at least 50,000 people (through direct contacts, visits to the website, social networks and online

platforms, downloads of the handbook and videos/visualizations. Increasing the awareness, motivation, skills and cooperation of communities and regional authorities.

- Increasing local tourism based on nature and culture with the introduction of traditional and popular building techniques and materials, footpaths, cultural routes, nature observation and interpretation.

- Improvement of the local economy through financial imports and job creation.

As climate change is a major threat to Mozambique, this proposal will help to reduce its impact and thus improve its future viability. The main actions of the plan will also contribute to reducing vulnerability to climate change. This will be done by increasing resilience: by protecting the ecologically sensitive areas, creating an ecological structure and reducing the impact of two of the main drivers of ecological problems - floods and cyclones [16]. Therefore, communication and dissemination tasks will be fundamental to transfer knowledge to other areas. This will be crucial and a tool to address the impacts of climate change in the communities involved.

The proposal addresses the following project possibilities: i) projects to improve sustainability; ii) projects to improve urban and landscape planning; iii) projects to improve the conservation status of habitat types or species of community interest, unless their status is ‘favorable/secure’ and not ‘declining’ or ‘unknown’ according to the most recent overall assessments; iv) projects to improve biodiversity; v) projects to improve urban agriculture; vi) projects to improve urban open spaces; vii) projects to improve green corridors and green infrastructures.

The main objective of this proposal is to improve the sustainability of IM and BZ by enhancing their development through landscape and urban planning. To achieve this, we propose several management practices to improve the quality of environmental protection, food production and recreational activities. The proposed planning tasks will achieve this, as well as improving the economy and sociability.

DISCUSSION

A number of authors [2, 9, 11-12], among others, at the national and international level, from different disciplinary fields, have called for a new model of urban planning that guides action on the city in its landscape and heritage dimension. This is achieved through the formulation of a new urban planning and design, to establish a positive dialectic between cities, the peripheries and between these and the surrounding rural space; between built and open spaces; and between these and the behaviors and needs of the population; thus contributing to the environmental sustainability and social equity of the urban region.

This socioecological-based urbanism, required by the social, economic and territorial evolution of the last decades, is based on principles and urban design and planning on a landscape scale, considering the effects and requirements of sustainable development.

In urban planning, the presence of nature, characterized by the diversity and continuity of systems, requires a concept that brings together urban design and open space design, as well as a relationship with the landscape, where its multifunctionality and sustainability as a productive, cultural and recreational space should be guaranteed. [13] proposed this relationship in his Green Plan for Lisbon, [2] addressed it in his Landscape Urbanism, on a fundamentally ecological basis, [14] comes up with an

https://doi.org/10.5593/sgem2024/6.1/s27.55

essentially productive landscape structure. [9] advances a return to the multifunctionality of the landscape in urban space, combining in landscape structures the functions of protection, recreation and production, which are fundamental to the energy and food crisis we are experiencing. In these landscape structures, urban agriculture and natural habitats are considered not only as a factor of production and protection, but also as having a great potential for social, economic, ecological, cultural and aesthetic recreation [9, 11]. As such, we consider them as fundamental structures in the reconceptualization of urban spatial planning, in this case of IM. According to [15], the planning proposal that tends to maintain or introduce agriculture as a green urban infrastructure is positively received by the local population and local administrators, as they consider it fundamental for the aeration and animation of the city, acting as an interstitial agriculture as if it were the fingers of a hand.

This approach to urban design and planning for the IM and its BF is fully in line with current international and national guidelines.

To ensure the success of this process, the various actors should be closely involved, including local communities and stakeholders, politicians, professionals, public authorities, scientists, institutions, non-governmental organizations and others.

The communication and dissemination of this plan model is extremely important, as it will make possible to raise the awareness of the local population, visitors and all those concerned with environmental and cultural issues and the need to preserve them [16].

The relevance of this proposal is clear, given the current economic, environmental and social context, as well as the expected results: Activation and use of underused or abandoned spaces in a socially and environmentally productive way; simultaneous appearance of a wide variety of articulated activities; increase in biodiversity; increase in sustainability; adaptation to ever-changing urban conditions; reduction of health risks and related environmental risks, improvement of living conditions for residents and increase in integrated and identity tourism [17], among others. It is essential that the quantification and qualification of these results be demonstrated and evaluated through a cost-benefit analysis and added value in relation to the reference situation, as this will lead to greater political and social acceptance and enable the development of a sustainable city - inclusive, food secure, productive and environmentally healthy (Fig.1).

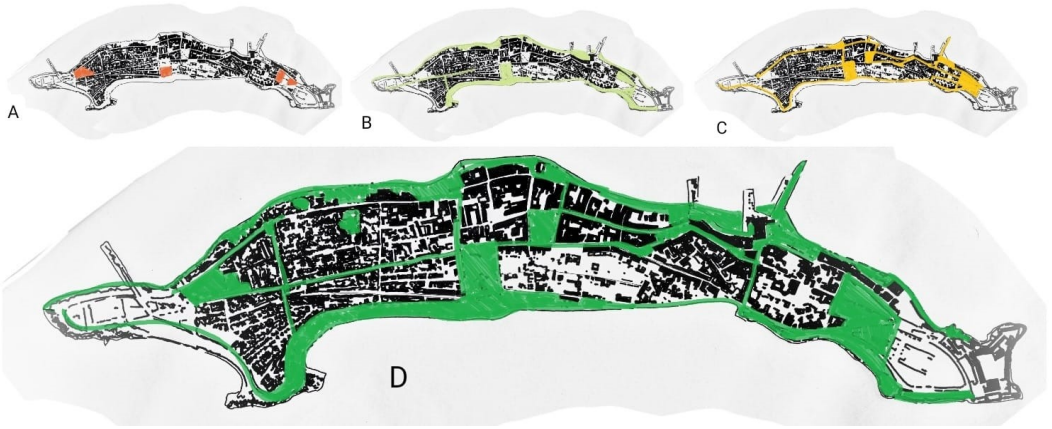


Fig. 1 - A. Productive spaces; B. Ecologic spaces; C. Public spaces; D. Landscape Structure; Source: Author's sketches.

CONCLUSION

As an added value, this plan proposal will contribute to the development of Africa in terms of sustainability, as defined by: i) the World Heritage Committee, ii) the Recommendations on Urban Historic Landscapes approved by UNESCO, iii) the Agenda 2063 entitled "The Africa We Want", iv) the United Nations (UN) 2030 Agenda for Sustainable Development, v) the New Urban Agenda UN-Habitat. At the national level, by the Government's Five-Year Program 2015-2019. At the level of Nampula Province by: i) the Nampula 2020 Strategic Development Plan, ii) the Master Plan for Disaster Risk Reduction (PDRRD) 2017-2030, which is guided by the priorities established in the Sendai Framework for Disaster Risk Reduction. Specifically for the IM, by the Law no. 10/88 of 22 December, which provides for the legal protection of the material and immaterial goods of the Mozambican cultural heritage.

Overall, this planning approach will bring the following benefits:

- Environment, food production, outdoor activities, socialization, improved knowledge and professional skills.
- Improving the quality of the urban and rural environment and landscape not only in the IM and BZs but also in the surrounding communities through transfer and replication efforts.
- Increasing the sustainability of IM and BZs by reducing overuse and inappropriate use of land, resources and natural and cultural values.
- Improving the ecosystem services provided by the landscape structure by increasing biodiversity, protecting resources and promoting the practice of urban agriculture.
- Improving the quality of life through the practice of sports and outdoor activities.
- Incorporating best practice measures into regional and local policies.
- Reducing the carbon footprint associated with inappropriate practices.
- Local economic growth, both by promoting new income opportunities related to food production and by promoting specialized market niches.

Some of these benefits include the creation of synergies between international and national environmental policies and the integration of results from previous international projects, namely the Sendai Disaster Risk Reduction (SDRR) project mentioned above.

The sustainability of this proposal is enhanced by the partnerships established between institutions, communities, private companies and public authorities. In the medium and long term, as the sustainable landscape structure is expected to continue, environmental and economic benefits are expected to continue beyond the project.

ACKNOWLEDGEMENTS

Funding: This research was funded by FCT Fundação para a Ciência e Tecnologia, Ministério da Ciência, Tecnologia e Ensino Superior, SFRH/BSAB/143118/2018, for a period of 4 months. The paper was financed with Nacional Funds through FCT – Portuguese Foundation for Science and Technology, within the scope of the project: CHAIA/UÉ (UI&D112)/2020 – [Ref.ª UIDB/00112/2020].

https://doi.org/10.5593/sgem2024/6.1/s27.55

REFERENCES

[1] World Bank, 'Data – Mozambique'. Available online: http://data.worldbank.org/country/mozambique (assessed on 19 set 2019)

[2] Waldheim, C., The landscape urbanism reader*;* Princeton Architectural Press: New York, USA, 2006.

[3] Barradas, R., Ilha de Moçambique, estórias da sua história; GAPI-Sociedade de Investimento: Maputo, Moçambique, 2018.

[4] Eroy, S., Proposta preliminar/recomendação: Valores arquitectónicos e urbanísticos para o processo de selecção das casas, Community tourism Project, Fundação da Ilha de Moçambique, Slums, museums or rethinking site-specific architectural practice? Traditional building techniques world heritage and sustainable development in Ilha de Moçambique, 2013.

[5] Rasoolimanesh, S., M.; Badarulzaman, N.; Jaafar, M. City Development Strategies (CDS) and Sustainable Urbanization in Developing World, Procedia - Social and Behavioral Sciences, vol. *36,* pp 623-631, 2012.

[6] Silva, N.B.F., Relatório de trabalho de campo sobre património natural, Universidade Eduardo Mondlane: Maputo, Moçambique, 2017.

[7] UN-Habitat Country Programme Mozambique 2018-2021, Available online, https://unesdoc.unesco.org/ark:/48223/pf0000246143, (assessed on 13 Out 2019).

[8] The New Urban Agenda, Available online, https://habitat3.org/the-new-urban-agenda/ , (accessed on 15 Mai 2020).

[9] Matos, R., A Reinvenção da Multifuncionalidade da Paisagem em Espaço Urbano – Reflexões, PhD, Universidade de Évora, Évora, 2011.

[10] Katz, P., The New Urbanism: Toward an architecture of community, McGraw-Hill, New York, USA, 1994.

[11] Valente, D., Matos, R., Batista, D., Simões P., Urban Agriculture: a way to a sustainable complementary between the City and the Countryside, 14th International Multidisciplinary Scientific GeoConference & Expo SGEM 2014, Section 27, Green Design and Sustainable Architecture, Albena, Bulgaria, 19-25 June, 2014.

[12] Matos, R. S., Nguyen, H., Phan., P., Phan, T., A Landscape Structure Proposal for a Sustainable Development – Quy Nhon City, Springer: Singapore, 2020,10, 915-920.

[13] Ribeiro Telles, G., Plano verde de Lisboa, Edições Colibri, Lisboa, Portugal, 1997.

[14] Viljoen, A., CPULs, continuous productive urban landscapes – designing urban agriculture for sustainable cities, Architectural Press, Elsevier, Oxford, England, 2005.

[15] Donadieu, P., Campagne urbane, una nuova proposta di paesaggio della città, Donzelli Editore, Roma, Itália, 2006.

[16] Asse, A., Relatório de trabalho de campo do processo de revisão do plano de gestão e conservação da Ilha de Moçambique 2018-2022, Kaleidoscópio, pesquisa em políticas públicas e urbanas, Maputo, Moçambique, 2018.

[17] Chiluvane, A., Ilha de Moçambique como destino turístico: desafios e oportunidades, Universidade Eduardo Mondlane, Maputo, Moçambique, 2018.

INFLUENCE OF A FACADE BASED ON GABIONS AND PLANTS ON THE INDOOR AIR TEMPERATURE IN A TROPICAL CLIMATE OF THE AMAZON REGION

PhD. Balcázar- Arciniega, Cristian[1]

Arq. Román- Vargas, Patricio[2]

Assoc. Prof. Aguirre- Maldonado, Eduardo[3]

Assoc. Prof. Valarezo- Jaramillo, Sandra[4]

Assoc. Prof. Alvarado- Rodríguez, Lorena[5]

[1] Departamento de Arquitectura y Urbanismo/ Universidad Técnica Particular de Loja, **Ecuador**
[2] Departamento de Arquitectura y Urbanismo/ Universidad Técnica Particular de Loja, **Ecuador**
[3] Departamento de Arquitectura y Urbanismo/ Universidad Técnica Particular de Loja, **Ecuador**
[4] Departamento de Arquitectura y Urbanismo/ Universidad Técnica Particular de Loja, **Ecuador**
[5] Departamento de Arquitectura y Urbanismo/ Universidad Técnica Particular de Loja, **Ecuador**

ABSTRACT

The present research evaluated a façade alternative to reduce the indoor temperature of buildings in the Ecuadorian Amazon (Yantzaza, Ecuador). Three scale models were compared: one with a gabion facade and leafy vegetables (onion, lettuce, basil, chamomile, and cabbage), one with a gabion facade only, and one with a clay brick (traditional) facade. Thermal data from inside the models were analyzed in March (warmest month) and January (coldest month). The results showed that between 13:00 and 15:00 in January and March 2021, the facade with plants reduced the indoor temperature up to 2°C more than the traditional facade. Cultivated facades increase thermal inertia without the need for additional materials or insulation, making it an environmentally beneficial solution. This research could be useful for designing cooler and more sustainable homes and buildings in hot climates.

Keywords: Green facades, bioclimatic architecture, Amazon, indoor temperature, sustainability

INTRODUCTION

Building facades play a fundamental role in the functionality, aesthetics and sustainability of structures. One of their main functions is environmental control, regulating the transfer of heat between the interior and exterior, which is crucial for maintaining a comfortable temperature inside the building [1]. In a context of growing concern for urban sustainability, green facades are presented as a promising alternative to integrate nature into cities without taking up land. Vegetation systems on the exterior walls of buildings are being used to address the challenges of food security and carbon footprint in urban areas [2].

https://doi.org/10.5593/sgem2024/6.1/s27.56

Recent research has focused on the concept of green facades with the following approaches: (a) Life Cycle Assessment (LCA), which compares green facades with conventional building solutions to assess their environmental impact [3]; (b) Cool and shade, the relative contribution of evapotranspiration and shade to the cooling provided by green facades was studied [4]; (c) Thermal performance, firstly, the thermal performance of green facades was evaluated for one year in a Mediterranean climate [5], on the other hand, experimental measurements and numerical simulations have been used to study the thermal effect of green facades [6].

In addition, other research has focused on the concept of Productive Facades (PF), which combine photovoltaic (PV) panels with vertical cultivation (VF) planters, focusing on aspects such as (a) Acceptance, through surveys of building occupants in Singapore, their acceptance of the concept of productive facades has been evaluated [7]; (b) Architectural quality, the architectural characteristics of the productive facades have been analyzed and design recommendations have been made [8]; (c) Comparative study, three productive facade alternatives were compared: a building without photovoltaic energy and vertical cultivation, a building with vertical cultivation and trellised photovoltaic panels, and a building with double skin facade, internal cultivation and photovoltaic energy [9].

Overall, research shows that green facades can reduce energy consumption, mitigate urban heat, and improve air quality, while productive facades can generate renewable energy, produce food, and improve building aesthetics. In addition, research on green and productive facades should focus on optimizing their design, improving their efficiency, extending their benefits, and ensuring their long-term viability.

This study has an innovative approach relevant to the context of the Ecuadorian Amazon. It focuses on the development of a green façade system using locally available building materials and recycled elements, such as plastic bottles, to grow leafy vegetables and reduce the indoor air temperature of buildings.

MATERIALS AND METHODS

Table 1. Descriptive statistics of outdoor air temperature measurements (°C)

Month	N	Mean	Standard error of mean	Statistical deviation	Minimum	Q1	Median	Q3	Maximum
January	5.00	28.88	0.57	1.27	27.40	27.87	27.40	30.09	30.78
March	5.00	30.61	0.19	0.42	30.03	30.23	30.57	31.02	31.08

Table 2. Descriptive statistics of outdoor relative humidity measurements (%)

Month	N	Mean	Standard error of mean	Statistical deviation	Minimum	Q1	Median	Q3	Maximum
January	5.00	66.28	2.02	4.52	59.31	62.27	67.46	69.69	71.62
March	5.00	73.98	1.68	3.76	70.23	71.04	72.15	77.84	79.38

The experiment was conducted in the canton of Yantzaza, located in southern Ecuador and northeast of the province of Zamora Chinchipe (latitude -3.84, longitude -78.77, at an altitude of 1008 meters above sea level). The climate of the canton is classified by the Köppen system as Cfb, a tropical oceanic climate with short summers.

Climatological data from 2007 to 2020, recorded by the National Institute of Meteorology and Hydrology (INAMHI), were collected to define the warmest month (March) and one of the coldest months (January). The experimental test was carried out over a period of 10 days, 5 of them in the month with the highest environmental thermal values (March 2021) and the other 5 days in one of the months with the lowest temperature values (January 2021), with a daily exposure of 12 hours. The data were obtained using a digital thermohygrometer model "WSTK-103 Digital Weather Station RCC DCF" with three available sensors and an accuracy of ±1°C (less than -0 ~ 50°C) ± 5% (less than 25°C, 30~80%rH). The descriptive statistics of the outdoor air temperature and relative humidity measurements for the months of January and March of 2021 are shown in Tables 1 and 2.

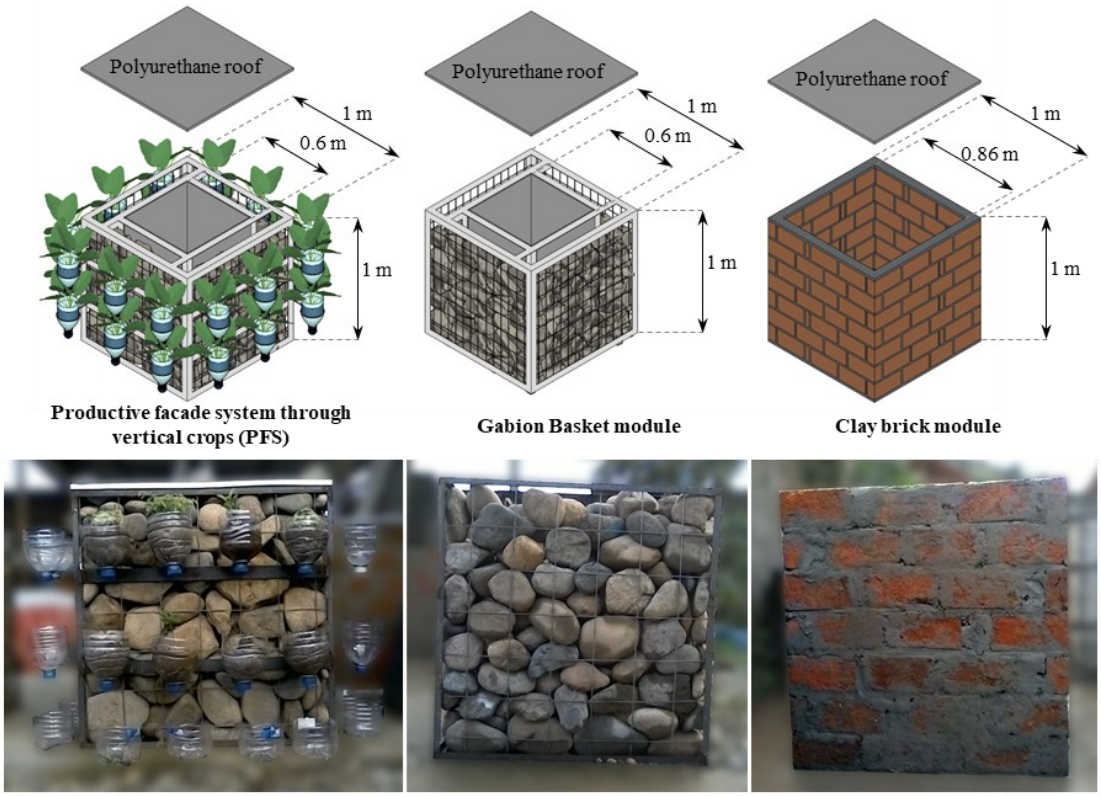


Figure 1: Features of the experimental modules

Figure 1 schematizes the configuration of the experimental modules designed to simulate building envelopes and provide heat transfer data, information used to evaluate the thermal performance of the different materials and construction systems proposed. The three experimental modules were exposed to the same climatic, orientation and ventilation conditions and had similar characteristics: volume of 1 m^3, placed on a reinforced concrete floor and covered with 2 cm thick polystyrene sheets.

The distinctive aspects of the scale models are described as follows: (1) Productive Facade System through vertical crops (PFS) module consisted of a gabion basket or wire mesh structure filled with local stones and supporting 5-liter PET plastic bottles with vertical crops of leafy vegetables (onion, lettuce, basil, chamomile, and kale). (2) The gabion basket module, which consists only of a gabion basket or wire mesh structure filled with stones. In the first two modules, the gabions were lined internally with 0.8 cm thick fiber cement panels. Finally, (3) The clay brick module was

https://doi.org/10.5593/sgem2024/6.1/s27.56

constructed with 25 cm x 12.5 cm x 7 cm clay bricks (length, width and thickness) and cement mortar.

Regarding the location of the thermohygrometer: the base monitor was placed on one of the experimental modules to measure the outside air temperature, while the sensors were placed inside the experimental modules, in the middle of the face opposite to the surface exposed to solar radiation.

RESULTS

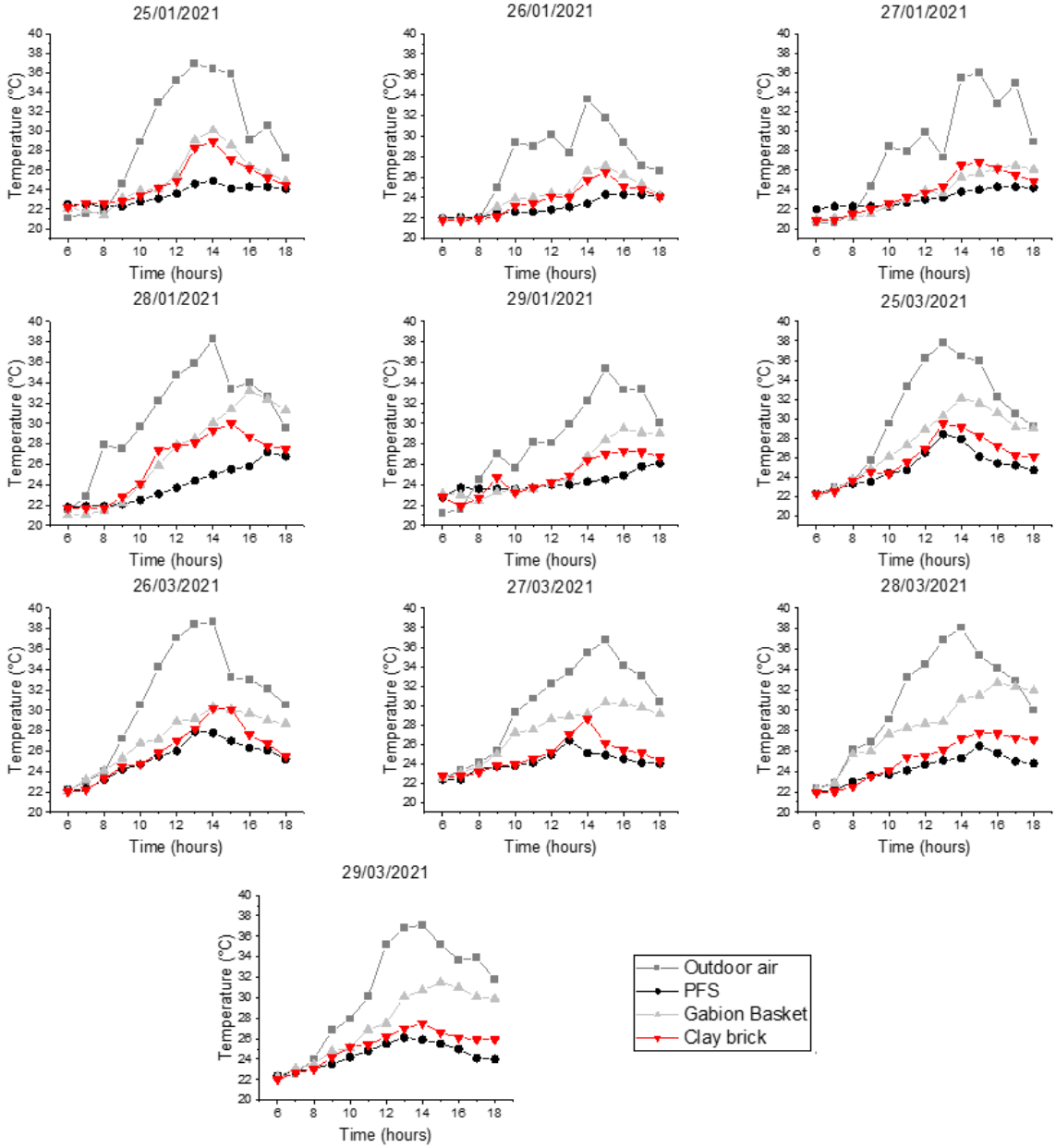


Figure 2: Temperature measurements for the months of January and March 2021

To ensure the accuracy and reliability of the measurements, it was ensured that they were made under similar environmental conditions: the measurements of the air outside and inside the experimental modules were made at the same time during several days in two different months, with little or no exposure to wind. The influence of wind shadows

(aerodynamic shading) was also avoided: the modules were placed at a distance of 2 meters from each other. In addition, the areas of the surfaces exposed to radiation were the same.

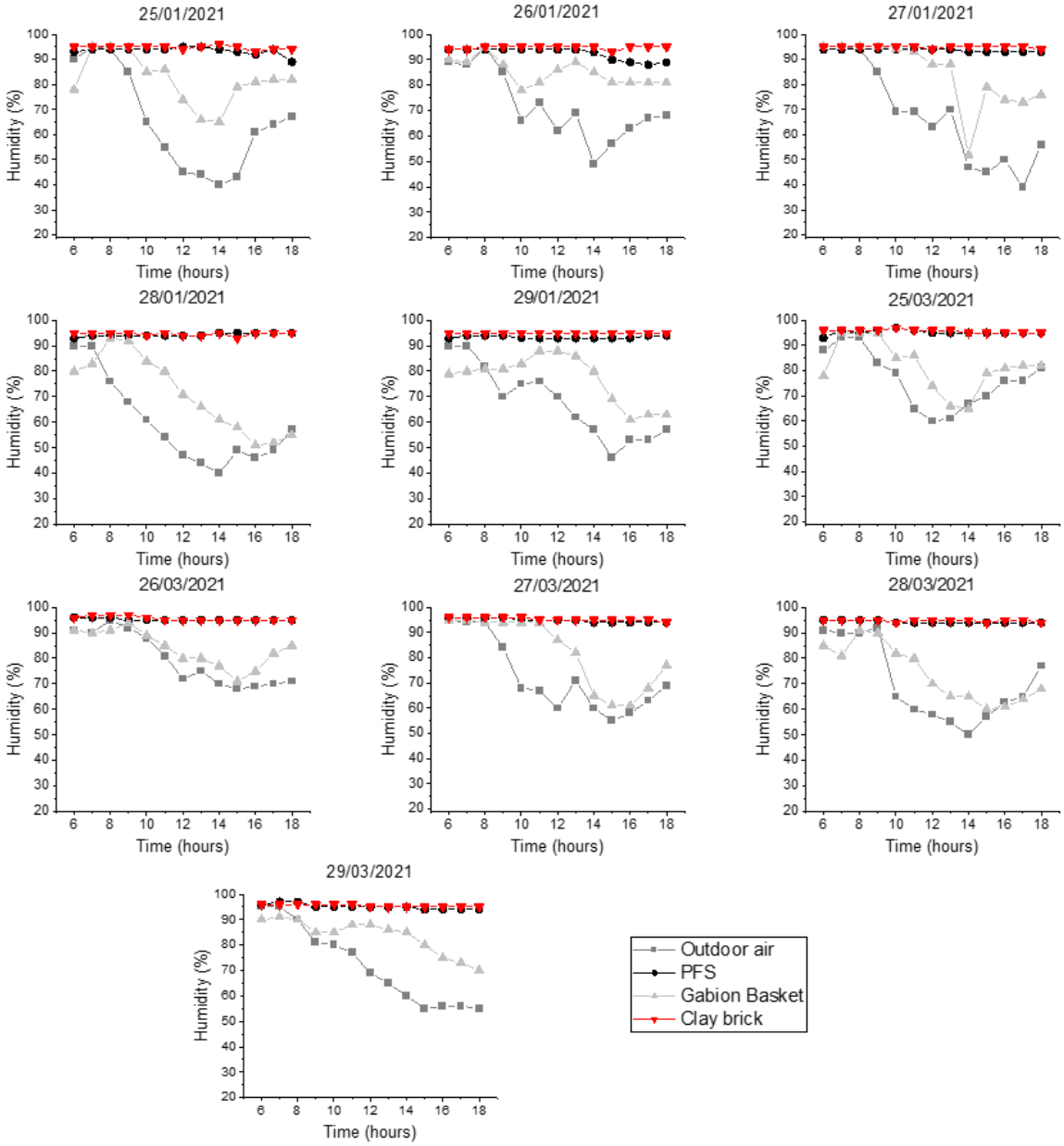


Figure 3: Humidity Measurements for the Months of January and March 2021

Figure 2 shows the results of the outdoor air temperature and humidity measurements and the indoor air temperature and humidity measurements of the experimental modules in the months of January and March 2021. The highest indoor and outdoor temperature peaks were recorded between 13:00 and 15:00. During all the measurements, the temperature evolution graph of the PFS module, formed by the line connecting the data points, showed a lower slope than that of the other two modules. This means that the surfaces of the PFS module store and release heat more slowly than the surfaces of the other two modules. In other words, PFS has a higher thermal inertia. If we compare PFS with the "gabion basket", the incorporation of the productive green facades allowed to

https://doi.org/10.5593/sgem2024/6.1/s27.56

increase the thermal inertia without the need of more material (higher volume or density) or the incorporation of insulation, which is beneficial for the environment. In addition, in buildings they can provide benefits such as (1) Reduced temperature fluctuations: The higher thermal inertia dampens temperature fluctuations, resulting in a stable indoor temperature and less need for air conditioning. (2) Thermal comfort: A more stable indoor temperature improves the thermal comfort of the occupants, especially in hot climates. Finally, (3) Energy efficiency: The reduced need for air conditioning reduces the building's energy consumption.

Figure 3 shows the results of the outdoor humidity and indoor humidity measurements of the experimental modules in January and March 2021. On the one hand, the facades of the "Gabion Basket" module significantly reduced the relative humidity of the indoor air compared to the facades of the "Clay brik" experimental module. This could be explained as a function of the temperature increase, which reduces the humidity of the air. In the absence of renovation, the humidity is not eliminated, but localized on the porous surfaces of the internal coating. On the other hand, the facades of the PFS module can very slightly reduce the evolution of the indoor humidity in relation to the facades of the experimental "Clay brik" module. This can be attributed to the shading and evapotranspiration effects of the plants that cool the facades, reducing the radiant temperature contributions and therefore the operating temperature inside the box. Permeable facades, as proposed for the experimental module "Gabion Basket" and PFS, improve the natural air circulation, essential architectural aspects to be considered in the Amazonian climate.

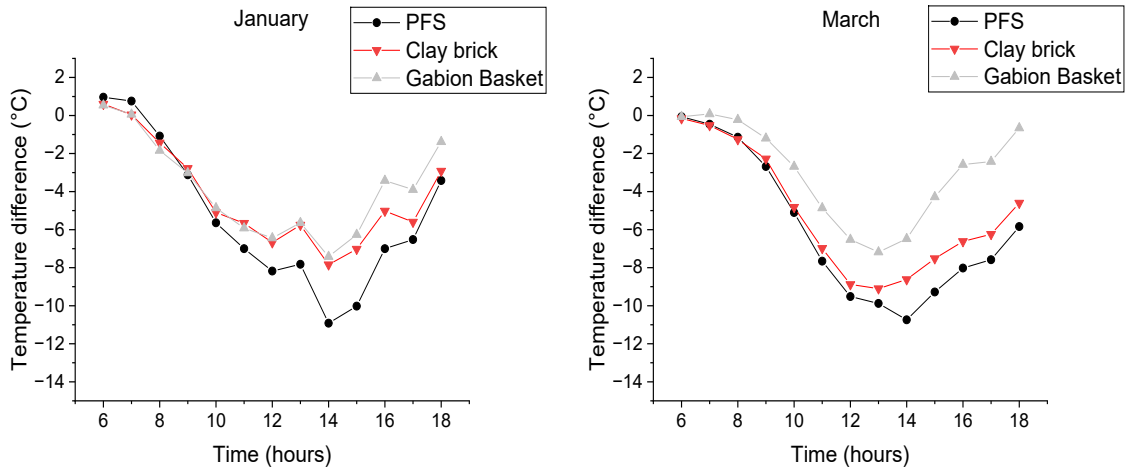


Figure 4: Arithmetic mean of the difference between the indoor and outdoor temperatures of the scaled modules, averaged over 5 days in January and 5 days in March

DISCUSSION

Finally, Figure 4 shows the arithmetic mean of the difference between the indoor and outdoor temperatures of the experimental modules. The temperature difference tells us how much the temperature has changed in a given time interval. In this investigation, measurements were taken every hour. A positive value indicates that the temperature has increased, while a negative value indicates the opposite. In addition, the greater the temperature difference, the greater the rate of heat transfer. In other words, the facades of the PFS module transfer less heat than the other two modules. This can be explained

by three phenomena: (1) Shadows cast by the vegetation: The vegetation of the PFS module creates shadows that protect the stone facades from direct solar radiation, thus reducing heat gain, (2) Evapotranspiration: The process of evapotranspiration, in which plants release water vapor, absorbs energy in the form of latent heat, cooling the surrounding air and facades, and (3) Low thermal diffusivity: The PFS module's low thermal conductivity façade system slows heat transfer into the module, dampening temperature fluctuations. The lower heat transfer in the facades of the PFS module results in an internal temperature difference between this module and the others, especially during the critical hours of higher solar radiation (between 13:00 and 15:00). In January, this difference is 2°C to 3°C, while in March it is reduced to 0.5°C to 2°C.

CONCLUSION

The research presented highlights the potential of PFS module facades to improve the thermal performance of indoor spaces. At the same time, the "Gabion Basket" module facades can regulate indoor humidity.

The combination of shading, evapotranspiration, and low thermal diffusivity in the PFS module facades reduced heat transfer. In a building, this can be defined as an increase in thermal inertia, a reduction in energy consumption for air conditioning, and a greater sense of comfort for the occupants, especially during the hottest hours.

Combining PFS facades with bioclimatic design could improve air performance and increase the benefits in terms of temperature and humidity regulation. It is recommended that research be extended to different climates to better understand the performance of PFS and gabion basket facades in a variety of climatic conditions.

REFERENCES

[1] S. Bianchi, C. Andriotis, T. Klein, and M. Overend, “Multi-criteria design methods in façade engineering: State-of-the-art and future trends,” Build Environ, p. 111184, 2024.

[2] A. Tablada and V. Kosorić, “Vertical farming on facades: transforming building skins for urban food security,” in Rethinking Building Skins, Elsevier, 2022, pp. 285–311.

[3] I. Blanco, G. Vox, E. Schettini, and G. Russo, “Assessment of the environmental loads of green façades in buildings: a comparison with un-vegetated exterior walls,” J Environ Manage, vol. 294, p. 112927, 2021.

[4] R. Bakhshoodeh, C. Ocampo, and C. Oldham, “Exploring the evapotranspirative cooling effect of a green façade,” Sustain Cities Soc, vol. 81, p. 103822, 2022.

[5] R. Bakhshoodeh, C. Ocampo, and C. Oldham, “Impact of ambient air temperature, orientation, and plant status on the thermal performance of green façades,” Energy Build, vol. 296, p. 113389, 2023.

[6] W. G. Báez-García, E. Simá, M. A. Chagolla-Aranda, L. C. S. Herazo, and L. G. Carreto-Hernandez, “Numerical-experimental study of the thermal behavior of a green facade in a warm climate in Mexico,” Energy Build, vol. 311, p. 114156, 2024.

[7] V. Kosorić, H. Huang, A. Tablada, S.-K. Lau, and H. T. W. Tan, “Survey on the social acceptance of the productive façade concept integrating photovoltaic and farming

https://doi.org/10.5593/sgem2024/6.1/s27.56

systems in high-rise public housing blocks in Singapore," Renewable and Sustainable Energy Reviews, vol. 111, pp. 197–214, 2019.

[8] A. Tablada, V. Kosorić, H. Huang, S. S. Y. Lau, and V. Shabunko, "Architectural quality of the productive façades integrating photovoltaic and vertical farming systems: Survey among experts in Singapore," Frontiers of Architectural Research, vol. 9, no. 2, pp. 301–318, 2020.

[9] B. Nashaat, "Investigating the Performance of Indoor daylighting, and Thermal Performance in Residential Buildings Using Productive Façades," Port-Said Engineering Research Journal, vol. 27, no. 1, pp. 15–23, 2023.

MARGINAL CONDITIONS FOR MEASURING THE LIGHT TRANSMISSION OF WINDOWS

Ing. Dagmar Richtrová
Doc. Ing. Lenka Prokopová, Ph.D
Doc. Ing. Daniela Bošová, Ph.D.

Czech Technical University in Prague, Faculty of Architecture, Institute of Civil Engineering II, **Czech Republic**

ABSTRACT

Construction using 3D printer technology seems to be not just a passing trend and a growing number construction companies are approaching this new construction methodology. Although construction processes with printers are becoming standardized, it is also true that many other aspects must be considered in the design phase. Better this construction methodology becomes known, more architects and engineers will have to learn how to design these constructions, in the methods of statics, systems, etc. A very important point is the issue of thermal insulation. The designer must be able to ensure that these houses are correctly insulated, respecting all the canons required by the local laws because, like all constructions, this technology is also subject to obtaining the appropriate permits to be built. The research aims to provide an understanding of the correct thermal insulation methods so that the right standards can be ensured that are necessary and already in place for other types of construction.

Keywords: factor daylight, indoor environment of buildings, light transmission.

1. INTRODUCTION

Daylight transmittance of glazing can be measured on double-sided cleaned glazing in two ways. Either the diffused light transmittance coefficient is measured using a luxmeter, or the normal light transmittance coefficient is measured using a luminometer. In the laboratory, both methods of measurement are feasible. However, field conditions for already built-in windows favor a luminometer measurement. In this experimental measurement, therefore, a method that can be performed in the laboratory and on-site, a luminometer measurement, was used.

In determining the normal light transmittance coefficient, the luminance of the sky or other background is measured perpendicular to the surface of the material to be measured, and immediately afterwards the luminance of the same background is measured through an open aperture without the material to be measured. The normal light transmittance coefficient is equal to the ratio of the two luminances measured. The time interval between the two measurements must be very short to exclude the

https://doi.org/10.5593/sgem2024/6.1/s27.57

variability of daylight. This methodology is described in the technical standard [1]. The methodology is described very briefly and there is no substantial description of the boundary conditions to be taken into account. And it is the definition of the boundary conditions of light transmittance measurement that is of benefit to this research.

2. Description of experiment

The experimental measurement of the normal light transmittance factor of clear glass consisted in determining the influence of background colours and shades on the resulting values. The experiment involved six coloured matt homogeneous papers in a range of colours - white, bright yellow, light green, pale blue, red, black and the last background was a white diffuse substance. Measurements for these different backgrounds were carried out according to the standard methodology [1] using the Konica Minolta LS 110 luminometer – see Fig. 1, on which immediately consecutive values of brightness in cd/m^2 in two states were read in a short sequence, always with and without a glass sample. Each background was measured in a succession of ten repetitions. The resulting light transmittance factor was then calculated as the average of the luminance ratios of each repetition.

All measurements of the normal light transmittance factor were carried out on a sample sheet of clear glass with dimensions of 800 x 500 mm and a thickness of 3 mm. Sample of clear glass in tl. 3 mm was chosen because of the known normal value of daylight transmittance, which is 0,92 (-) [2].

In the same way, the normal light transmittance factor of the built-in glazing of hole fillings in existing construction structures and in laboratory can be determined.



Fig. 1: Luminometer Konica Minolta LS 110, source: photo archive doc. Ing. Daniela Bošová, Ph.D.

For the measurement itself, the perpendicular assembly of the measuring instrument - the luminometer, the measured material on bench No. 1 and the evaluated background on bench No. 2 was important, and the exact distance between the parts does not matter, as long as their position is not changed during the individual measurements. The measurement should take place in an evenly cloudy sky, thus eliminating direct solar

radiation, or its reflections, and the readings of the luminosity are relevant and stable at the same time.

For our experiment, the luminometer on a tripod was placed and rectified to a height of 0.9 – 1.0 m. Within 2 m of the luminometer, bench No. 1 was placed with a sample of clear glass. The glass was installed perpendicular to the luminometer. The location of the bench was precisely marked on the floor of the room and the outdoor terrain, so that the perpendicular position of the sample relative to the luminometer was preserved in both measuring states. At a further distance of 2 m from the measuring bench No. 1 with a sample of clear glass, another measuring bench No. 2 was installed for the location of the measured background. Both benches were installed horizontally and at the same time perpendicular to the direction of the luminometer placed on the tripod see Figure 2.

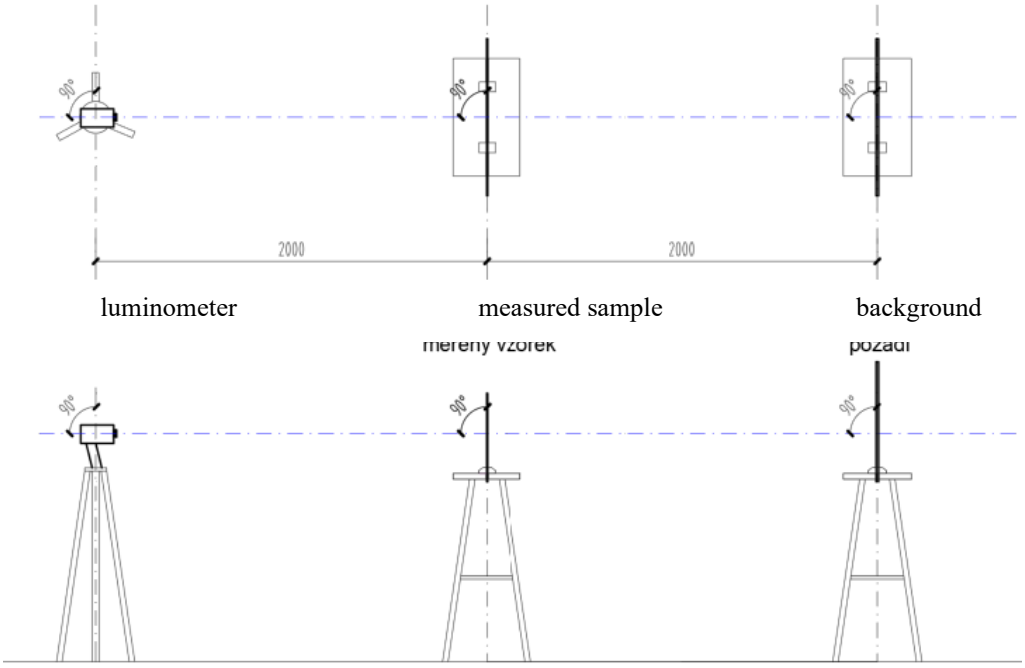


Fig. 2: Distribution scheme of the measuring assembly, (source: author's archive)

3. Background variants

It is easy to ensure a homogeneous background of ideal parameters in the laboratory, but it is very difficult to ensure these conditions on the building site for already built-in windows. The ideal background is a uniformly cloudy sky with constant brightness. However, this is not achievable for windows on lower floors and with high surrounding areas or greenery, while maintaining the verticity of the measurement. The experiment was thus aimed at creating the most favorable background that would bring minimal errors to the measurement.

The measurement of the normal light transmittance factor of clear glass was carried out on a homogeneous background in six different shades. The colours chosen corresponded to the basic colour range (white, yellow, green, blue, red and black) see

https://doi.org/10.5593/sgem2024/6.1/s27.57

Figure 3 and were intended to simulate e.g. the background of the facade of surrounding objects when measured in the field.

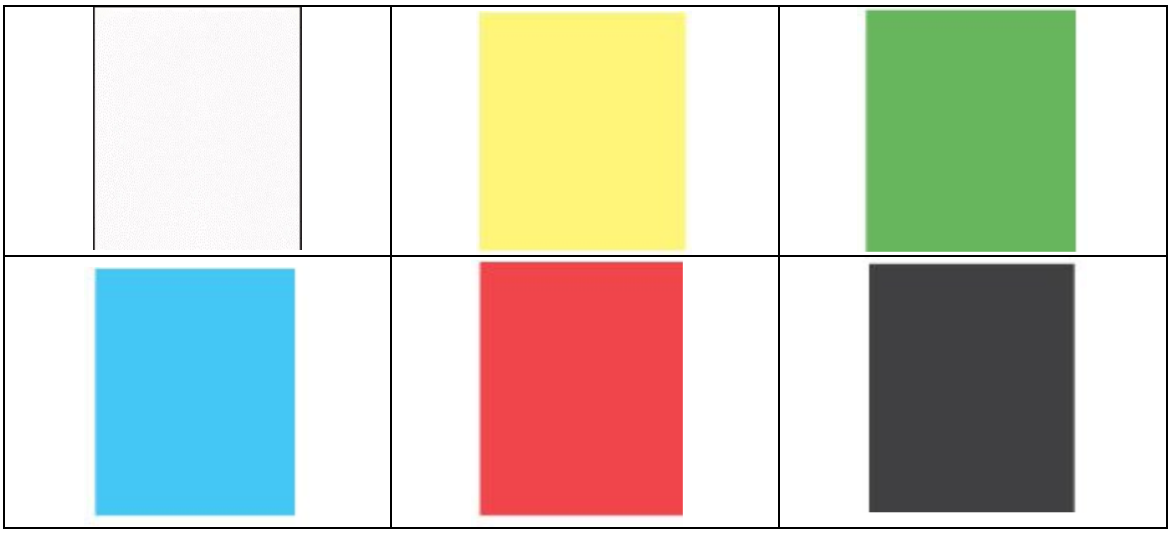


Fig. 3: Homogeneous background of used colours, (source: author's archive)

Another background was a switched-off diffusion substance in white, which evenly diffuses the passing light to ensure a constant brightness. This substance is used by the photographic and film professions. This substance can be installed in the laboratory and on the construction site in front of the measured material.

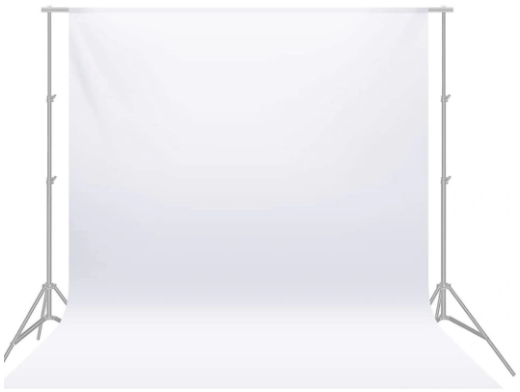


Fig. 4: Diffuse substance, (source: www.film-technika.com)



Fig. 5: Diffuse substance, (source: www.phototools.cz)

4. Comparison of results

Table below – Tab. 1 gives the resulting values of the measurement of the normal light transmittance factor $\tau_{s,nor}$ (-) of clear glass with different background variations. Measurements were made for ten repetitions each time.

Tab. 1: Measurement results $\tau_{s,nor}$ (-) for different backgrounds.

Number	white	yellow	green	red	blue	black	diffuse substance
1	0,940	0,940	0,948	0,956	0,963	0,991	0,905
2	0,935	0,935	0,938	0,972	0,967	0,997	0,912
3	0,918	0,918	0,950	0,953	0,933	1,008	0,923
4	0,913	0,930	0,969	0,981	0,963	0,995	0,916
5	0,930	0,926	0,951	0,953	0,925	0,999	0,902
6	0,926	0,931	0,917	0,955	0,954	1,003	0,909
7	0,931	0,954	0,955	0,961	0,968	1,022	0,901
8	0,954	0,922	0,923	0,971	0,964	1,031	0,927
9	0,922	0,923	0,950	0,960	0,960	1,058	0,958
10	0,923	0,936	0,947	0,956	0,953	1,055	0,955
$\tau_{s,nor}$ (-)	**0,929**	**0,932**	**0,945**	**0,962**	**0,955**	**1,016**	**0,921**

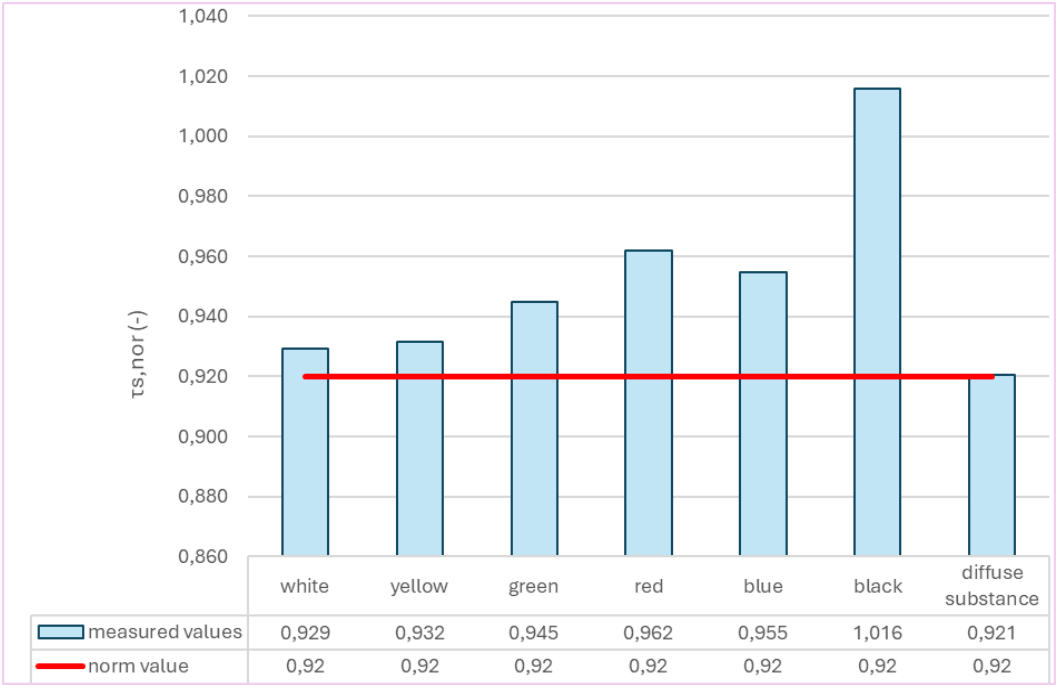


Fig. 6: Graphic representation of measurement results

https://doi.org/10.5593/sgem2024/6.1/s27.57

5. CONCLUSION

The experiment shows that the background plays a very important role in the measurement of the normal light transmittance factor of clear glass. According to the Czech standard ČSN 360011-2 [1], the background can be sky or other background, so it is not specified in any way in which colour the measured background should occur.

According to the measurements made, it is obvious that the darker the background behind the measured element, the higher the light transmission values in the normal direction of the measured element will come out. The results are significantly different and distorted. This effect is given by the ratio of the brightness of the cloudy sky from the horizon to the zenith. The standard conditions of the sky model should be in the ratio of brightness 1:3 from the horizon to the zenith. The daylight source thus does not have a constant luminous intensity and thus significantly affects the light transmission depending on the background during the measurement. The light diffuse substance behind the measured element simulates the standard conditions most accurately.

The best option seems to be the use of very bright to white background colours with constant brightness during the measurement.

ACKNOWLEDGEMENTS

This research was funded by Czech Technical University in Prague, Faculty of Archutecture reseaech project SGS22/195/OHK1/3T/15 and with financial support from the Faculty of Architecture of Czech Technical University in Prague.

REFERENCES

[1.] ČSN 36 0011-2 ZMĚNA Z1:2019 Měření osvětlení prostorů - Část 2: Měření denního osvětlení, 2019.

[2.] ČSN 73 0580-2 ZMĚNA Z1:2019 Denní osvětlení budov - Část 2: Denní osvětlení obytných budov, 2019.

NATURE A CONSTANT INSPIRATION FOR HUMAN BEINGS – AESTHETIC CHANGES IN ARCHITECTURE OVER THE CENTURIES

M. Eng. Arch. Ewa Kuhnert[1]

[1] Warsaw University of Technology, Faculty of Architecture, **Poland**

ABSTRACT

Since the prehistoric times, humans have been exploiting the immediate environment for various purposes, from the adaptation of caves for shelter to the subsequent transformation of the landscape for their own needs and this continues to the present day. The bio-inspiration movement in architecture, including bionic, biomorphic, and biomimetic architecture, is linked to the dynamic technological development initiated by the Industrial Revolution and later by the Digital Revolution. Each of these has influenced the epoch-specific representation and perception of architectural forms.
The aim of this paper is to provide a synthetic picture of the relationship between architecture and nature historically. This will provide a basis for further research in the field of biological architecture. **The hypothesis of the article is that we can identify two principal design approaches in contemporary architecture: a technological approach and an organic approach, which on occasion intertwine, particularly in terms of process and technical solutions.** The study uses an analysis of the literature on the history of architecture in the context of human-nature relations and contemporary architectural trends. The historical overview presented in the article will assist in conceptualising potential avenues of aesthetic evolution, while references to contemporary examples in the field of bio-inspiration will facilitate the characterisation of the trend in the shaping of architectural forms.

Keywords: nature, bioarchitecture, biology, innovation

INTRODUCTION

Architecture has historically been inextricably linked with the natural environment, with both raw materials and design inspiration drawn from the surrounding landscape. The evolution of human civilization has shaped human attitudes towards nature, which are reflected in the transformation of the landscape over the centuries. The industrial revolution and then the digital revolution catalysed new approaches to architectural form and function. The developments in technology and building materials have led to changes in design approaches, with an increasing emphasis on functionality and efficiency. This resulted in the emergence of new architectural styles, such as Modernism, Functionalism and Art Déco. These styles are characterised by elegance, functionality and the use of new materials, and they became emblematic symbols of the era [1]. In parallel with the emergence of modern artistic trends such as surrealism and abstractionism, biomorphic concepts evolved, encompassing the imitation of forms and structures found in nature. In the 21th century, the advent of digital technology is facilitating a reinterpretation of these concepts, influencing the direction of architectural design towards a biological approach.

https://doi.org/10.5593/sgem2024/6.1/s27.58

METHODS

Two research methods were used in this paper. The first is historical analysis, whose main research tools were historical data and documents, allowing us to delve into the contexts of architectural design from the past in order to gain insights relevant to the subject of the research. The second method used is a formal and processual analysis based on two selected contemporary examples. This interdisciplinary approach to design arts allows us to illustrate similarities and differences in approaches to shaping architectural forms.

MATERIALS

HISTORY CONTEXT OF NATURE INSPIRATION

It might be said that at the outset, humans used the environment in a minimally invasive way, adapting the nearest space for shelter. One might consider the ancient caves as an example. The rocks within these caves allowed for survival, and they also had a symbolic dimension for the peoples who inhabited them, as evidenced by the cave paintings (Ill.1.) [2]. Karst processes and the human activity involved in adapting the interior for their needs are expressions of early biomorphic architecture, where nature was the primary designer and man the secondary.



Ill.1. Interior of the *Lascaux Cave* in France. Left: Hall of Bulls, depicting bulls and deer animals; right: a narrow corridor decorated with paintings.

This primitive form of habitation evolved over time into more organised clusters of peoples, and their settlement was accompanied by the first buildings made of mammoth bones and skins [3]. At the time, architecture had a technical and logistical rather than philosophical significance, limited by the availability of materials and cognitive capacity. Over time, the construction of buildings improved, and the population no longer struggled just to survive, but dedicated their efforts to constructing buildings that met specific social needs. This resulted in the emergence of organised settlements that provided the means of livelihoods and enabled observation of the natural environment. This, in turn, facilitated an increased comprehension of the world and the development of a sense of purpose.

In ancient societies, people worshipped a multitude of deities, primarily associated with nature, atmospheric phenomena and supernatural beings. From antiquity, geometry facilitated the formation of objects in space and enabled the creation of a language with which to elucidate cosmological relationships [4]. With the development of craftsmanship, the technical possibilities offered the chance for greater freedom in

creation, and buildings began to rise higher above the horizon. The search for symmetry, rhythm and order in objects was an attempt to create beauty and perfection in the surrounding world. Nature was given symbolic meaning, often representing concepts of fertility, regeneration and cosmic order. Architectural structures were oriented towards celestial bodies or built in harmony with the natural landscape, reflecting respect for the natural world and its cyclical rhythms.

In the Middle Ages, Christian theology dominated artistic creation, with nature complementing its symbolic representation, such as illuminated manuscripts containing intricate depictions of flora and fauna. It was not until the Renaissance that artists were inspired anew by the natural world, this time in the context of scientific research. Artists such as Leonardo da Vinci and Albrecht Dürer looked closely at nature, conducting in-depth studies of the biological world (Ill.2). Their fascination with anatomy and botany, developed into a holistic study of nature based on observation of details, as well as attempts to understand wider relationships and regularities in nature [5]. This deeper insight into the natural world resulted several hundred years later in great discoveries that are still an important reference for the design context today.



Ill.2. A study of the nature of medieval artists. Left: Leonardo da Vinci, Botanical studies of irises, 1490; right: Albrecht Durer, *Hirschkäfer (Stag Beetle),* 1505.

INDUSTRIAL REVOLUTION

The Industrial Revolution has had a profound impact on numerous aspects of human life, fundamentally transforming the relationship between humans and nature. The advent of new technologies brought with it the development of novel materials and processes, and the prefabrication of building components became a common practice. Nevertheless, nature continued to serve as an inspiration for creative design, albeit in a somewhat altered form compared to previous eras. Technology enabled architects to integrate buildings more closely with their surroundings. This was exemplified by Frank Lloyd Wright's organic architecture, which experimented with different building

https://doi.org/10.5593/sgem2024/6.1/s27.58

techniques that combined innovative material solutions with the aesthetics and functionality of the building [1].

BIOMORPHISM AS A INTERDISCIPLINARY TERM

There can be no doubt that biomorphism has manifested itself in various human activities related to the shaping of space. The origin of the term is derived from the Greek words 'bios', meaning life, and 'morphe', meaning form, which literally means 'form of life' [6]. The biomorphism concept was first introduced in the late 19th century by zoologist and anthropologist Alfred Cort Haddon to describe patterns derived from animate sources [7]. However, the attempt to describe the phenomenon of what biomorphism is for a long time took place mainly in the field of art. This was when twentieth-century artists, fascinated by biological forms, used the term to describe difficult-to-define curved shapes inspired by nature [8]. The manifestations of biomorphism in art and architecture are diverse, reflecting the spirit of a particular era rather than a particular design style or direction. In the present era, biomorphism is defined as activities related to the development of solutions similar to those found in nature, which describe shapes based on curvilinear geometry, characterised by fluidity of forms and continuity of lines [6].

RESULTS

BIOARCHITECTURE NOW AND IN THE FUTURE

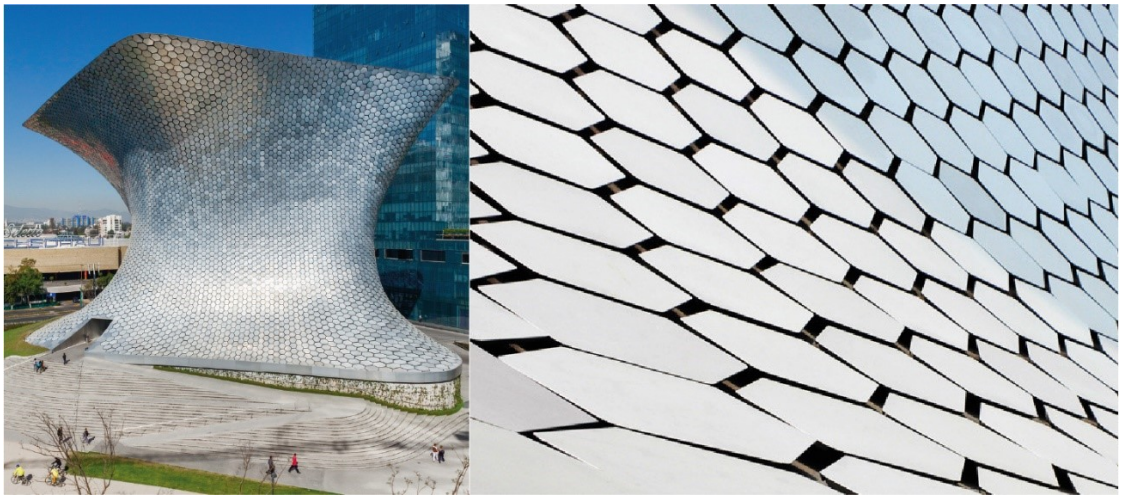
In contemporary architecture, biomorphic forms are manifested in various ways, including bioarchitecture, the expression of the creation of buildings that are in harmony with the natural environment. The fourth industrial revolution is once again transforming the relationship between humans and nature, and placing the designer in the role of an observer. The utilisation of patterns observed in nature is becoming increasingly prevalent in the context of design and technological solutions. One illustrative example is the study of micro- and nanostructures present in nature (insect wings, suction cups of marine animals) and their application in the creation of biomimetic materials with special properties. The convergence of diverse fields of study, evident in numerous research domains, facilitates the generation of innovative solutions that transcend conventional approaches, thereby facilitating the advancement of life sciences.

DISCUSSION

DEPENDENTS BETWEEN ARCHITECTURE, NATURE AND TECHNOLOGY

The relationship between nature and architecture and technology is multifaceted, and their interaction leads to improvements in form, function and design [9]. In contemporary architecture, two design trends can be observed in the work of engineers. The first is a technological approach, which involves the use of modern technologies in the design and construction of buildings. The second is an organic approach, which emphasises the integration of natural forms and materials into architectural designs. The first of these design trends refers to an approach in which modern technologies are used as an integral part of the design and construction process of buildings. Technological advances are used to create innovative, effective and functional architectural solutions. In this case, the form is an expression of experimentation with innovative structures and spatial arrangements that go beyond the traditional design framework. Furthermore, the

inspiration of nature is an additional component that is only relevant on a formal level. An illustrative example is the *Museo Somaya* in Mexico City (Ill. 3), where the organic shape and bespoke finish of the façade are the consequence of the utilisation of sophisticated technologies at both the design and construction levels.



Ill.3. *Museo Somaya*, Mexico City, 2011. Left: photo of realisation; right: building façade clad in hexagonal aluminium tiles resembling fish scales.

Conversely, there is design inspired by forms, patterns and processes found in nature, where technology is an enabling component, merely a tool to help reproduce natural patterns. An illustrative example is the *Research Pavillon* (2013-2014) (Ill.4) a collaborative project between the Institute for Computational Design (ICD) and the Institute of Building Structures and Structural Design (ITKE) of the University of Stuttgart. This project explored the application of biomimetics and advanced digital technologies in architecture. The primary source of inspiration for the pavilion was the structure of the beetle exoskeleton, which permitted the creation of a lightweight yet robust structure [10]. By analysing the structure of the insect's shell, the research team developed innovative design and manufacturing methods that allowed for the precise reproduction of natural structural patterns. In this instance, the process observed in nature provided both inspiration and specific design and manufacturing solutions that were subsequently implemented.



Ill.4. *Research Pavillon*, Stuttgart. 2013-2014. Left: view of a structure made up of dozens of modular panels; right: production of one panel consisted of machine winding fibers onto a frame.

https://doi.org/10.5593/sgem2024/6.1/s27.58

CONCLUSIONS

Since prehistoric times, the relationship between humanity and nature has been characterised by a dynamic and fluctuating interaction: from identification with the surrounding natural world, through fascination with biological structures, to the exploitation and use of raw materials for economic development. Currently, there is a gradual shift in the way we think about nature, which is inspiring creators and facilitating the development and integration of numerous fields of natural sciences into different research fields. The integration of numerous disciplines within natural sciences, coupled with the advancement of technology, is paving the way for an expanded design context. The advent of technology has accelerated the pace of change, with design trends observed over the past two decades, particularly those pertaining to technology and organic forms, directing architects to create buildings with distinct characters that embody the search for new ideas where nature plays a significant role. Designers are increasingly conceptualising the human as an equal to nature. This can be observed in the creation of organic architectural forms that emulate the natural world, both in terms of their formal characteristics and the processes involved in their construction. This approach equips designers with specific methods and techniques.

REFERENCES

[1] Curtis J., William R., *Modern Architecture Since 1900*, Phaidon Press, London 1996, pp. 53-131.

[2] Curtis G., *The Cave Painters: Probing the Mysteries of the World's First Artists*, Knopf, New York 2006.

[3] Bahn P.G. (ed.), 100 Great Archaeological Discoveries, Barnes and Noble, New York 1995.

[4] Randall E. L., Campbell F.E., *The Sacred Geometry of the Ancients: The Harmonious Design of the Universe*, Kessinger Publishing, 2003.

[5] Laurenza D., *Art and Anatomy in Renaissance Italy: Images from a Scientific Revolution*, Endeavour 30, no. 3, pp. 107-111, 2006. Doi:10.1016/j.endeavour.2006.08.003 (access: 10.05.2024).

[6] Agkathidis A., *Biomorphic Structures: Architecture Inspired by Nature. Biomorphic Structures: Architecture Inspired by Nature (Form + Technique)*, Laurence King Publishing, London 2017, p. 9.

[7] Botar O. I., *Biomorphism*, Routledge Encyclopedia of Modernism, Taylor and Francis, 2016. Doi:10.4324/9781135000356-REM770-1 (access 16.05.2024).

[8] Turowski A., *Biomorfizm w sztuce XX wieku. Między biomechaniką a bezformiem,* słowo/obraz terytoria, Gdańsk 2019, p. 19.

[9] Vitruvius, *On Architecture*, Granger F. (transl), Harvard University Press, Cambridge, London, 1914. https://www.chenarch.com/images/arch-texts/0000-Vitruvius-50BC-Ten-Books-of-Architecture.pdf (access: 29.05.2024).

[10] Sanalkumar S., *A collaborative computational approach towards the integrative design of Modular Architectural Fiber Composite Structure for ICD/ITKE Research Pavilion 2013-14*, 2019. https://www.researchgate.net/publication/335978527_A_collaborative_computational_approach_towards_the_integrative_design_of_Modular_Architectural_Fiber_Composite_Structure_for_ICDITKE_Research_Pavilion_2013-14 (access: 01.06.2024).

THE METHODOLOGY OF TECHNICAL DUE DILIGENCE FOR THE REHABILITATION OF AN ABANDONED BUILDING

Bogdan Chelaru[1]

Cătălin Onuțu[1]

Adrian Alexandru Șerbănoiu[1]

[1]Gheorghe Asachi Technical University of Iaşi, Faculty of Civil Engineering and Building Services, **Romania**

ABSTRACT

This paper outlines the methodology of a technical due diligence preparation for the reconsolidation process of an abandoned building. The structure highlighted in this paper is an existing but incomplete building that has been abandoned for more than over a decade. For this study a technical due diligence was performed to assess the current condition of the asset presented on the next chapters of this paper. A technical due diligence represent the research and analysis discovery process which helps to collect essential information about the physical and technical condition of one asset. Careful examination and analysis of technical documentation, along with on-site inspections, were crucial for providing a well-informed report. The results of the technical evaluation have required the presentation of essential intrusive tests. The final report provide a complete understanding of the current condition of the building, highlighting the risks associated with the completion of the construction. All of the findings can be interpreted and used as part of a project feasibility study. The new technical project, referring to reconsolidation and completion of the construction works, propose green solutions like integrating friendly practices and technologies to reduce carbon footprint, enhance energy efficiency, and promote sustainability.

The objective of this study is to identify the risks and outline the necessary work program to ensure the successful completion of the construction project.

Keywords: Technical Due Diligence (TDD), Technical Inspection, Condition Survey, Laboratory Concrete Testing

1. INTRODUCTION

The structure under consideration in this analysis, designed with a framed structural system, was part of a construction project initiated in 2008 but postponed in 2009. Currently, the construction is marked by partially implemented resistance elements. Primarily designated for office use, the building encompasses a substantial constructed area of approximately 94,000 m2, reaching a maximum height of 15 m. It includes a parking facility with approximately 1600 underground spaces, constituting around 70% of the Plot Occupancy Ratio (P.O.T.). After conducting an on-site technical inspection and analysing the relevant documentation, it has been concluded that the current physical condition of the construction is categorized as "Partially Executed Resistance Elements." The construction present the following identification features:

https://doi.org/10.5593/sgem2024/6.1/s27.60

- *Construction Height Regime*: The structure comprises three underground levels, one ground floor, and two levels above the ground floor,
- *Infrastructure Structural Solution*: The resistance structure is composed of reinforced concrete bearing walls (cast walls), drilled piles, and monolithic cast reinforced concrete slabs,
- *Superstructure Structural Solution*: The resistance structure includes reinforced concrete frames, monolithic reinforced concrete slabs without beams but with capitals, columns, and beams of monolithic reinforced concrete. The access stairs to the basement and floors are monolithic cast reinforced concrete. The roof is designed in both non-circulating and circulating terrace types.

The technical expertise, established through laboratory tests, follows to country legislation in conjunction with European standards in the field. Conclusive decisions are contingent upon a meticulous analysis of the technical documentation, encompassing information sourced from the local building administration, and findings derived from technical expertise conducted by independent laboratories specializing in comprehensive testing and analysis solutions for construction projects.

2. RESEARCH METHODOLOGY

The steps outlined in this chapter are summarized in Figure 1.

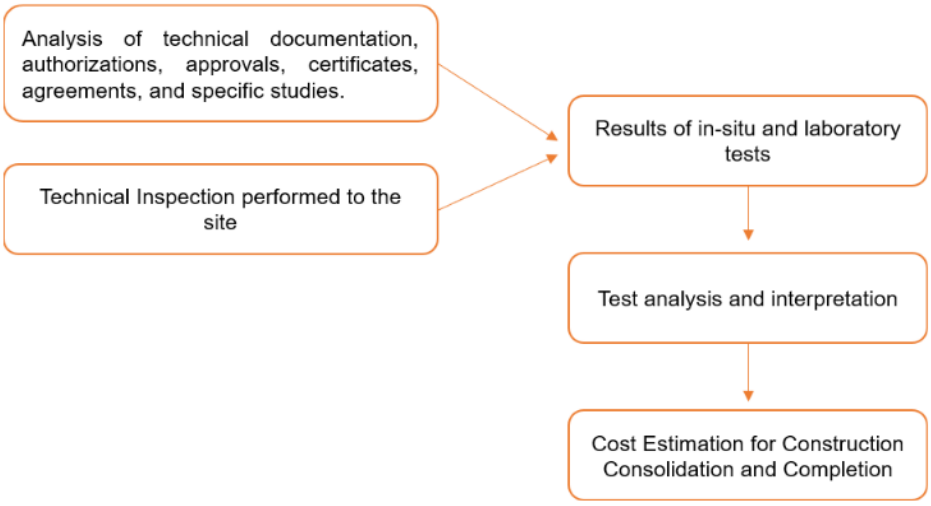


Fig. 1. Graphic Summary

Analysis and interpretation of existing technical documentation

The technical documentation provided for analysis and interpretation included the following: Project presentation in PowerPoint format; General architectural drawings in dwg and pdf formats (site location plans, plans for each underground and above-ground level, characteristic sections, and facades), Project layout details (Excel document); Partial information about the structural project obtained from the local municipality's physical archive (Structural Technical Project and Structural Execution Project, as well

as Drawings for Execution); Feasibility study; Energy Performance Certificates; Geotechnical Study.

Technical Visual Inspection (Condition Survey)

For a more accurate evaluation of the building's quality, the initial and crucial step include a visual inspection of the asset, followed by a detailed photographic report which identifies the degradation process of the structural elements, both surface and subsurface.

The superficial degradation elements under examination include space deterioration due to acts of vandalism, modification of concrete color, surface corrosion caused by exposure to climate conditions and environmental factors, as well as surface cracking.

In-depth degradation elements inspected include the deterioration of expansion joints, segregation of reinforced concrete elements, cracks in the concrete cover layer, infiltrations at expansion joint locations, identification of biological attack, carbonatation, and reinforcement corrosion, incomplete concrete finishing of structural elements, and the detection of waste in the concrete mix composition.

Laboratory Tests and Trials

The determination of whether to proceed with or end this project, was determined that specific laboratory tests will be realized. These include Core extraction and conducting compression tests on concrete samples; Measurement of carbonation in the extracted cores; Measurement of concrete cover; Measurement of chloride content in concrete. The methodology employed is based on the following European Standards and Regulations:

- [1] BS EN 206:2013 Concrete - specification, performance, production, and conformity (+A2:2021).
- [2] ISO 15686-1:2011 Buildings and constructed assets — Service life planning — Part 1: General principles and framework,
- [3] EN 1990:2002 Eurocode: Basis of structural design,
- [4] EN 1992-1-1:2004 - Eurocode 2: Design of concrete structures - Part 1-1: General rules and rules for buildings

The assessment of the compressive strength of concrete structures is an essential component in evaluating existing structures, providing data regarding the most important characteristic of concrete, its strength class. The choice of a specific testing method depends on factors such as the testing area, destructive effects produced, and the precision of the obtained results, more precisely, the margin of error obtained. The confidence level in assessing concrete strength will increase with the number of tests conducted. In this case, it has been determined, in collaboration with the technical expert that a high level of confidence can be achieved by extracting 40 cores distributed in 8 testing zones. The severity of the chemical attack phenomenon of concrete carbonation is linked to the quality of concrete, the thickness of the concrete cover over the reinforcement, and the degree of concrete compaction. Upon sampling the specimens, the measurement of concrete cover was also conducted (fig.10), using a PS 200 Ferroscan pacometer with electromagnetic waves. The objective of measuring the chloride content in concrete is to assess the environmental aggression caused by

https://doi.org/10.5593/sgem2024/6.1/s27.60

chloride attack on concrete and, consequently, the reinforcement, leading to its depassivation. A critical chloride content results in depassivation, affecting the concrete cover layer.

3. QUANTITATIVE, QUALITATIVE RESULTS, AND INTERPRETATIONS

Results of the Analysis of Existing Technical Documentation

The content of the virtual data room (VDR) and physical archive is deemed satisfactory. The accuracy and quality of the information described in the final report entirely reflect the content quality of both the virtual and physical archives. In general terms, the definition of the design theme, all analyzed technical documentation, can be considered up-to-date, and no adaptation or modification is required to comply with the current legal requirements. The seismic actions considered in the project align with the current regulations in force from the European updated standards. Information was requested regarding how the quality control system was ensured and implemented, with its objective being the definition and quantification of the compliance of delivered concrete to the construction site. It was noted that the quality control of the implemented concrete was not guaranteed, as there were no supporting documents, implemented procedures, norms, or entities involved in this process. Following the analysis of the technical documentation, it was concluded that the geotechnical report lacks sufficient information to justify the structural solution implemented by the designer, posing a high risk. This information has been communicated to the investor.

Conclusions of the Visual Technical Inspection

Following the visual technical inspection, no significant structural defects were observed that could have a significant impact on the structural behavior or integrity of the building. However, poor quality of some load-bearing elements such as beams, columns, and floor slabs was noted, along with signs of reinforcement bar corrosion due to the aggressive environment, inadequate concrete coverage, vertical and longitudinal cracks, and signs of segregation. Currently, the construction is not complete and cannot be categorized as in the "rough construction" stage, lacking masonry closures. The building is not connected to utilities such as water, sewage, or electricity. At the time of the visual technical inspection, the following findings were observed: Visible cracks in some reinforced concrete walls in the basement, Cracks in joint areas, Exposed and corroded reinforcement bars, Infiltrations, Concrete segregation, Concrete carbonation and reinforcement corrosion, Lack of concrete coverage and appearance of corrosion on reinforcement bars, Incomplete concreting of certain elements, Deterioration due to the lack of regular maintenance of structural elements exposed to aggressive agents, Signs of chemical aggression from chloride or sulfate salts, Signs of abrasion-induced aggression.



Fig. 2 - Concrete Segregation



Fig. 3 - Expansion Joint Degradation



Fig. 4 - Reinforced Concrete Column Sectioned



Fig. 5. Visible cracks on the waffle concrete slabs

The illustration (Fig.3) clearly highlights a significant concern: the insufficient coverage of concrete, resulting in potential infiltrations. This structural flaw poses a serious risk that demands immediate attention and remedial actions.

Given suspicions regarding the quality and conformity of the material used in the construction, in light of the deficiencies identified in the geotechnical report and supported by the conclusions of the visual technical inspection, it has become imperative to conduct a technical expertise.

Evaluation of in-situ concrete testing

Core extraction tests are inherently destructive due to their impact, and this method has been employed to ascertain compressive strength and compare it with a reference value. The tests were conducted on columns and slabs, distributed across various floors within the CC, CD, CE, CF, CG, CH, CI, CJ, CL zones (Fig. 6).

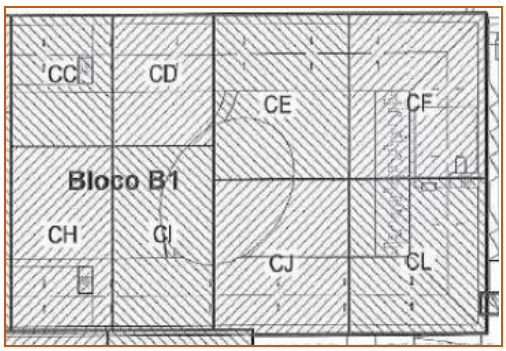


Fig. 6 – Core Extraction Zone



Fig. 7 – Test Samples – Slabs

https://doi.org/10.5593/sgem2024/6.1/s27.60



Fig. 8 – Test Samples - Columns

The results of concrete compression tests for the samples extracted from slabs (Fig. 7) and columns (Fig. 8) have indicated that the strength class corresponds to the one specified in the project, namely C30/37. Additionally, carbonation measurements were conducted on the core samples. The carbonation process indicate a decrease in the concrete pH from pH 13 to pH values of 8.5 – 9. These values fall below the necessary threshold that ensures passive conditions for reinforcement. The test results demonstrate a high probability, ranging from 17% to 47%, that the reinforcements may exceed the threshold for normal passive conditions, consequently leading to the oxidation of the iron in the reinforcement and the formation of rust, causing stresses beyond the concrete's tensile strength. As a result, the concrete layer protecting the reinforcement will detach, exposing it directly to corrosion through rusting.

The concrete cover thickness can be observed in the graphs below (Fig. 9 and 10). The concrete cover specified in the project is 35 mm, while the average obtained in the tests was 28 mm (if referring to individual values) and values ranging between 24 and 31 mm if referring to the values obtained in the sampling zones.

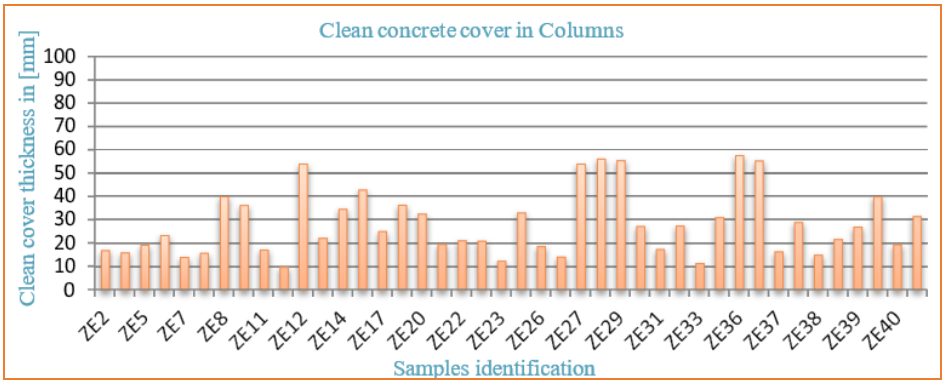


Fig. 9 – Values of clean concrete coverage in columns

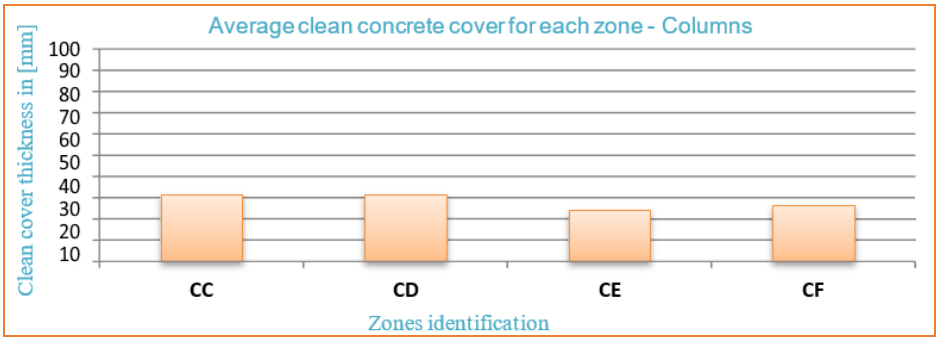


Fig.10 – Values of average clean concrete coverage for each zone in columns

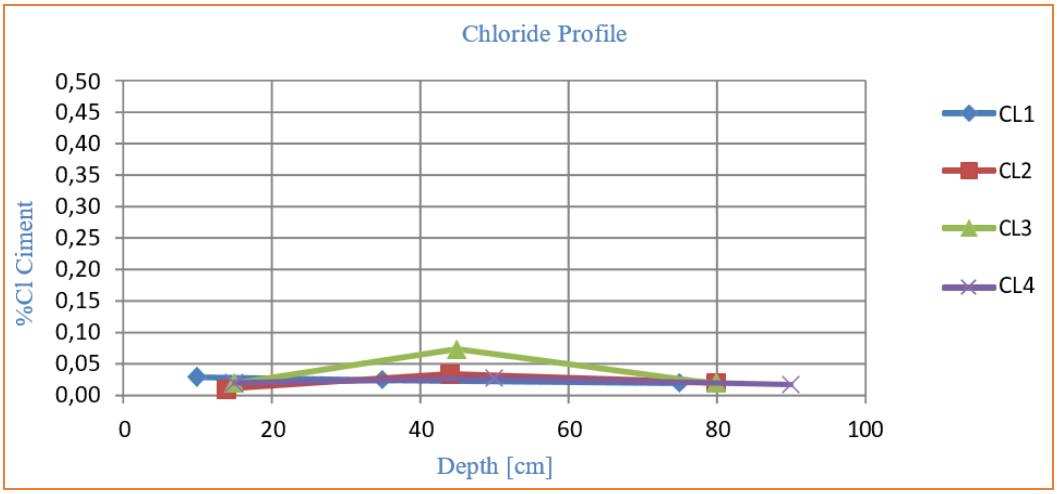


Fig. 11 – Average values of chloride content - per areas

The measurement of chloride content in concrete (Fig. 11) was conducted using the Rapid Chloride Test System (RCT). The maximum allowable chloride value according to the project specifications is 0.4%. The average measurements obtained from the conducted tests are well below the reference value.

As general recommendations for the future consolidation and completion of the construction, it is imperative to consider the necessary repairs and interventions related to the identified anomalies. All obtained results, laboratory test recommendations, as well as those from the experts, have been documented in a technical due diligence report. Following the analysis of the technical documentation, it was concluded that the geotechnical report lacks sufficient information to justify the chosen structural solution implemented by the designer.

4. CONCLUSIONS

In conclusion, the overall condition of the property was considered to be MEDIUM, having in consideration that has been abandoned for more than a decade. The construction quality was considered satisfactory with deviations in certain areas, where major interventions should be undertaken by the new owner to rectify the defects and errors committed by the initial contractor and designer. The identified risks are considered manageable, but repairs are required to improve the building condition.

The general construction risk profile of this property can be considered from LOW to MEDIUM, and regarding its impact on the surrounding environment, the risk is considered LOW. No signs of land contamination have been observed over the years, and current on-site activities do not pose a risk of soil or groundwater contamination. Structural consolidation of the construction have been identified and proposed.

https://doi.org/10.5593/sgem2024/6.1/s27.60

ACKNOWLEDGEMENTS

This research received funding from Gheorghe Asachi Technical University Doctoral School in the framework of Bogdan Chelaru Ph.D. Study Programme.

REFERENCES

[1] Institution, B. S., BS EN 206:2013 Concrete - specification, performance, production and conformity (+A2:2021), 2013. Website: pp. 21, Available from: https://www.thenbs.com/PublicationIndex/documents/details?Pub=BSI&DocId=332743

[2] (ISO), I. O. f. S., ISO 15686-1:2011 Buildings and constructed assets — Service life planning — Part 1: General principles and framework, 2011. Website: pp. 21, Available from: https://www.iso.org/standard/45798.html

[3] (CEN), E. C. f. S., EN 1990:2002 Eurocode: Basis of structural design, 1990. Available from: https://eurocodes.jrc.ec.europa.eu/EN-Eurocodes/eurocode-basis-structural-design.

[4] (CEN), E. C. f. S., EN 1992-1-1:2004 - Eurocode 2: Design of concrete structures - Part 1-1: General rules and rules for buildings, 1992. Website, Available from: https://eurocodes.jrc.ec.europa.eu/EN-Eurocodes/eurocode-2-design-concrete-structures.

VALORIZATION OF THE LANDSCAPE THROUGH THE APPLICATION OF MODERN ENERGY SOLUTIONS FOR THE CONSTRUCTION OF GREEN BUILDINGS AND THE DEVELOPMENT OF GREEN ARCHITECTURE

Assoc. Prof. Dr. Metodi Ivanov[1]

[1]Sofia University „St. Kliment Ohridski“, **Republic of Bulgaria**

ABSTRACT

The aim of this report is to assess the extent of valorization of the landscape in relation to the increase of energy efficiency and in the context of the construction of green buildings and the development of modern green architecture, which is responsible for the implementation of sustainable policies implemented in the field of environmental protection and the fight against climate change. This paper will review current trends in the development of green architectural design and the interrelationship with the application of modern energy solutions in the construction of green buildings in the construction of sustainable cities of the future. On the other hand, an explanation of the processes of increasing the value and potential of the landscape will be sought in order to highlight the influence of social cohesion and cultural continuity in the development of contemporary urban environments. This study will use administrative and institutional approaches in identifying current trends in the application of modern energy solutions applied in the territory of municipalities in the Republic of Bulgaria. Furthermore, it will seek answers to a number of questions related to the existence of a methodological framework in the identification of buildings to be upgraded through energy audits and retrofitting and the application of modern energy solutions. The experience of other EU Member States will also be examined to highlight good practices that can be applied in the country as well as other EU Member States with similar problems. On the other hand, an attempt will be made to develop a new methodological framework in the implementation of landscape resource assessment, through which to seek opportunities to improve existing strategies in the field of environmental protection and sustainable use of natural resources. Attention will also be paid to the development of ecotourism, sustainable agriculture and efforts to combat climate change.

Keywords: valorization of landscape, energy efficiency, climate change, environmental management and protection, green architecture.

INTRODUCTION

For the most part, European countries are attempting to preserve historic rural landscapes, which in turn represent and are part of Europe's cultural heritage. It can be noted that on the continent, traditional landscapes remained almost unchanged until the early twentieth century. It should also be noted that a significant proportion of cultural landscapes 'still possess high qualities in terms of the environmental services they provide, have the necessary tourist appeal, have maintained the production of high-quality food, have

https://doi.org/10.5593/sgem2024/6.1/s27.61

managed to preserve biodiversity, and have preserved the cultural and historical heritage they possess. The problems in recent years have been related to finding solutions to maintain them, both from a sustainable development and economic point of view [1]. A significant challenge related to the implementation of conservation and loan management policies individual countries, including Bulgaria, are facing is the preservation of terraced landscapes in terms of both historical and aesthetic importance and role as a resource in the field of agriculture and tourism, which is also confirmed by the research done by other researchers [2]. Mainly the changes associated with landscape changes are the result of:

- urban sprawl;

- the loss of many traditional farming systems;

- the intensification of agriculture in the most suitable areas for modern agricultural production;

- the abandonment of crops in mountainous or marginal areas[3].

The particularities are related to the degree of ongoing intensity in different regions and countries. The determination of landscape vulnerability is driven by the existence of different drivers, pressures, inherent characteristics and threats. Socio-economic, environmental, hydrogeological can be identified as the main ones for most regions. Climate change is increasingly leading to episodic local catastrophic events, such as the significant volume of heavy rainfall in some regions can lead to loss of life in addition to material damage. In addition, landslides are triggered and significant damage is caused not only to residential buildings but also to buildings intended for economic activity. For this reason, site management plans for potentially hazardous areas are now required in many places. The development of a management plan itself goes through the definition of strategies for the management of critical infrastructure in the threatened region. This is also where we need to point to the need for a wider understanding by local communities of the definition and perception of landscape by local people as an area of strategic importance for planning policies related to landscape conservation, management and planning. Therefore, local people should perceive the landscape as "an area perceived by people whose character is the result of the action and interaction of natural and/or human factors" [4]. Furthermore, the European Landscape Convention (ELC) defines the meaning of landscape policy as "means an expression by the competent public authorities of general principles, strategies and guidelines that permit the taking of specific measures aimed at the protection, management and planning of landscapes" . A "landscape management" as "means action, from a perspective of sustainable development, to ensure the regular upkeep of a landscape, so as to guide and harmonise changeswhich are brought about by social, economic and environmental processes; /. While the process of "landscape planning" "means decisive and forward-looking action to enhance, restore or create landscapes". The involvement and active participation of the public is crucial for the planning and implementation of landscape planning and management policies and should play a significant role in the decision-making process. As it is important to include and adopt ideas that are consistent with the values and interests of the public. On the other hand, the process of studying landscape transformations implies improving the link between the research conducted and the attitudes, views and needs of the population in the regions studied. However, it should be borne in mind that the populations that inhabit a given locality have critical perceptions and attitudes on issues of planning, integration and the impact of landscape change on people. Making an aesthetic assessment of a

landscape depends on many factors, some of the factors may be common to all regions studied and researched, while other factors are determined by the social context and changes occurring over time, both in the existing spatial system, the preserved and/or altered landscape, and by the society whose attitudes and trends are changing the environment. Evidence shows that not only rural but also urban landscapes have always been subject to drastic transformations as a result of the "dynamic interaction between natural and cultural forces in the environment"[5]. In carrying out the landscape planning process, the perception of the landscape and public participation in the preparation of a management plan for a specific area should be assessed by collecting the necessary data on the main existing problems and needs of the local population, and for this purpose, the opinion of the main social groups for whom landscape conservation is of interest in a given area can be studied. The planning and management of processes for the conservation of the uniqueness of a landscape implies the involvement and participation not only of farmers but also of all stakeholders, as well as the provision of the necessary institutional support for the implementation of a sustainable management model by the local community.

1. THE NEED TO IMPLEMENT LANDSCAPE PLANNING.

Priority in landscape planning decision-making should be given to the informed participation of the local public in carrying out the process of exploring co-management options, considering different adaptation alternatives, and integrating knowledge processes into the shaping of future landscape and nature management policies for a region. It should be noted that, in practice, the perceptions of residents and farmers often diverge, even though there may not be significant differences within the two groups, and even the particular socio-cultural characteristics may not statistically influence the opinions of the social group concerned. There is a tendency in surveys carried out in different rural areas for those actively involved in agricultural activities to have local ecological knowledge of the region compared to those not directly involved in agricultural activities, i.e. there is a different degree of sense of belonging to rural and agricultural culture by different sections/sections of the rural population, such as those working in the tourism industry. Furthermore, it should be noted that there is a high average age of farmers in rural areas, which is accompanied by the lower average level of education of farmers, but at the same time it is seen that there is a relatively low level of knowledge and awareness of the landscape by different social communities in different regions. On the other hand, there are different attitudes between farmers and inhabitants in terms of how they perceive the state of forests, which are perceived both as an important feature of the landscape and as a problem related to environmental protection and the fight against climate change. Often, local communities view and understand the local landscape as an environment that is surrounded by man-made surroundings through anthropogenic activities. On the other hand, the perception of tourism as a priority area of intervention in rural areas is a product of the existing long-standing conflict, which is both related to the creation of opportunities for heritage conservation and the creation of appropriate conditions for tourism development, which pass through the improvement of existing infrastructure and the construction of new infrastructure, which very often involves the implementation of landscape modifications. As a rule, World Heritage sites themselves attract large numbers of tourists, generating income and jobs as a result, but at the same time there are threats to the ecological and cultural integrity as a result of excessive numbers of tourists, which can also lead to a deterioration in the quality of life of the local

https://doi.org/10.5593/sgem2024/6.1/s27.61

population in the region. On the basis of the analysis carried out so far, one of the main problems can be identified in terms of creating the necessary conditions for rethinking the organisation of tourism services in a specific region and in a specific area where appropriate types of tourism need to be identified. In Bulgaria, tourism, which is concentrated in villages, is mainly one-day tourism and very little of the revenue actually goes to farmers, who, on the other hand, carry out the main activities of maintaining the territory and landscape of the settlement and the cultural and historical heritage sites. In other words, farmers in small settlements create the conditions for the preservation, maintenance and conservation of biodiversity and the territory, while at the same time maintaining their livelihoods through the transmission of knowledge and skills between generations.

2. WEAKNESSES OF THE AGRICULTURAL SECTOR AND THE IMPACT OF CLIMATE CHANGE ON ITS DEVELOPMENT.

In Bulgaria, the agricultural sector has significant weaknesses, on the one hand as a result of the fragmentation of ownership and on the other hand due to the lack of cooperation between farmers. In addition, there is a lack of interest of young people in agricultural activities, including a lack of initiative and association of local citizens in order to remove bushes from abandoned land and turn it back into arable land. Certainly local communities need to be fully aware of the vulnerability of their territory and the strong links between land abandonment, uncontrolled deforestation, which in turn can lead to an increase in hydrogeological risk in the region. In order to solve the above problems, on the one hand, it is necessary to increase the level of interest of the local population, which would put pressure on the organizations of public institutions to increase their support in the implementation of interventions related to the implementation of hydrogeological risk assessments, risks and safety of the built environment at different scales, planning, design and protection of residential, commercial and administrative buildings in the lands of settlements. The opportunities provided by the various rural development funds have a major role to play, as local communities should strive to increase efficiency in the use of funds related to environmental protection and biodiversity maintenance, as well as to preserve the condition of properties located above arable land in order to minimise possible hydrogeological problems. Priority should be given to the existence of opportunities to remove secondary vegetation in order to restore abandoned arable land and, on the other hand, given climate change and the increase in rainfall in many areas, which are increasingly leading to an increase in both river and rainfall flooding, attention must also be paid to the uncontrolled clearing of forest areas, which often not only leads to increased soil erosion but also to an increase in the risk of localised flooding. In this line of thought, the level of participation of the population should be significantly increased, not only by studying the perception of the landscape and the critical problems in the region, but in order to determine the needs and expectations for the implementation of various effective tools and activities related to the implementation of environmental protection measures.

3. ENERGY SECURITY AND EFFICIENCY IN THE CONTEXT OF CLIMATE CHANGE AND CLIMATE CHANGE RISKS AND THEIR IMPACT ON LANDSCAPE VALORISATION.

The need to improve energy efficiency in Bulgaria is imperative as it will contribute to limiting carbon dioxide emissions as well as help prevent climate change. By adopting

the Energy Efficiency Act, the country has implemented the requirements of Directive 2006/32/EC on the regulation of public policy relating to energy efficiency. In the Energy Efficiency Act, energy efficiency is introduced as a national priority with clearly defined commitments and support from the State for its development. The adopted law creates the necessary institutional, regulatory and financial conditions for the implementation of the national policy and its integration with the policies of the European Union. The Energy Efficiency Act established the Energy Efficiency Fund, and now the Energy Efficiency and Renewable Sources Fund, whose main objective is to manage the financial resources made available for investment projects for the development of energy efficiency, in accordance with the priorities set out in the annual energy efficiency programmes adopted by the Council of Ministers. In the adopted Integrated Energy and Climate Plan of Bulgaria for the period 2021-2030, which foresees a reduction of primary energy consumption by 27.89% and of final energy consumption by 31.67% [6], one of the measures is foreseen to be related to increasing the number of buildings with near-zero energy consumption, and it is also foreseen to improve the energy performance of buildings used by the public administration by at least 5% per year. In addition, measures related to increasing efficiency and reducing technological costs in electricity and natural gas distribution and heat transmission networks are foreseen. There are gaps at institutional level, which are related to the limited coordination between the institutions involved in energy renovation and the lack of coherence between the different energy efficiency programmes, so efforts should be directed towards improving coordination and communication. In addition, there is a lack of qualified energy auditors to carry out the projects with the necessary quality, a lack of training materials, of certification programmes for new auditors and for the companies that will implement the energy efficiency measures.

4. THE SPECIFIC CLIMATE CHANGE RISKS AND VULNERABILITIES IN THE COUNTRY'S AGRICULTURAL SECTOR THAT WILL AFFECT LANDSCAPE VALORISATION.

As a result of climate change, there is an increase in the frequency and magnitude of extreme weather events in Bulgaria with the most common hydrometeorological and natural disasters being :

- extreme precipitation and temperatures;
- storms;
- flooding;
- forest fires;
- landslides and drought.

In parallel, the number of deaths and casualties resulting from natural disasters is on the rise, indicating an increase in vulnerability to weather and climate. It is characteristic of the country that the vulnerability of the population and the economy to the impacts of climate change is increasing in regions characterised by relatively high levels of poverty, and on the other hand this is also the result of the increasing concentration of the country's population in several industrial and urban areas. The economic losses from weather and climate-related disasters are expected to increase as a result of the National Institute of Meteorology and Hydrology's projections of an increase in annual air temperature in

https://doi.org/10.5593/sgem2024/6.1/s27.61

Bulgaria by 2050, with projections ranging from 1.6°C to 3.1°C, and for 2080, with projected increases ranging from 2.9°C to 4.1°C. Naturally, these projected trends will affect biodiversity, terrestrial and aquatic ecosystems, as well as the water resources, agriculture and forestry sectors, and will affect society and the economy as a whole. Assessing the nature and extent of vulnerability to climate change is based on consideration of multiple factors, including such things as future environmental, economic and social changes. And, a major source of uncertainty is future greenhouse gas emissions, which in turn will alter radiative forcing. It is characteristic of Bulgaria that the vast majority of the country's regions belong to rural areas, where the population has lower incomes, there are no job opportunities, the proportion of the population of retirement and pre-retirement age is increasing, and also the majority of the rural population is at risk of poverty or social exclusion. The picture painted shows the continuing widening of the urban-rural divide, both in terms of social status and living standards in the country. The climate change scenarios developed for our country show an increased frequency of adverse weather events associated with an increase in the duration of droughts, an increase in heat waves, an increase in the proportion of intense rainfall events and possible potential flooding. The agricultural sector is highly vulnerable, but it should be noted that the risk of climate change impacts is unevenly distributed spatially, as different regions of the country differ in the likelihood of negative impacts from prolonged droughts and floods. The observed differences are also the result of the existence of dual farm structures, as well as the uneven distribution of land, which will result in differences in the degree of resilience and adaptive capacity between:

- large commercial farms, which are both economically more vulnerable to the impact of drought and flooding on crop yields but have significantly greater resources to invest in adaptation measures;

- while smallholder farms are socially and economically vulnerable to adverse weather events.

We will highlight the specific climate change risks and vulnerabilities in the country's agricultural sector, namely:

- changes in the length of the growing season;

- agrophenology, changes in the timing of the life cycle of agricultural crops in Bulgaria, which will affect the volume of yields.

- changes in yields of major crops as a result of projected temperature increases and reduced rainfall.

- the risk of pests and diseases spreading as a result of changes in temperature, humidity and atmospheric gas concentration.

- livestock production will be affected by the greater heat stress, which will affect reproduction, metabolism and health as a result of an increase in the rate of spread of pathogens.

- increasing the risk of drought, erosion, desertification and salinisation of soils, marginalisation and abandonment of farmland in areas where soils are lighter and vulnerable to erosion.

- Risk of water shortages as reduced rainfall levels will lead to reduced water storage and less water collected in irrigation reservoirs.

- Adverse impacts on fisheries and aquaculture as a result of declining water levels, which pose a serious threat to fish farming systems and may also lead to species loss[7].

These specific risks, or a combination of climate change risks and the vulnerability of the agricultural sector, will affect overall production and individual household production levels and living standards in the various affected regions of the country, and the ever-increasing vulnerability of agriculture to adverse climatic events will affect the well-being of the meat population and the livelihoods of many rural people will be threatened.

DISCUSSION

The valorization of the landscape implies to consider the mechanisms of landscape policy, as well as to analyze the process of landscape management, with significant attention to the possibilities of applying modern energy solutions in the construction of green buildings and the development of green architecture, since it should be borne in mind that the valorization of the landscape implies to apply sustainable policies, both in the field of environmental protection and the fight against climate change, and From a discussion point of view, when research is carried out in the field of valorisation of the landscape and the impact of climate change, a number of issues of an interdisciplinary nature are addressed, since topics related to the field of study of a number of different experts are addressed simultaneously, such as planners, architects, engineers, landscape architects, ecologists, economists, sociologists and financial management specialists, especially with regard to topics related to the planning and construction of protective architecture and landscape design Each of these experts could contribute to the identification of the elements, functions and services provided by the landscape in the context of the understanding of the landscape as a "key driver" for the development of the region, especially in terms of measures to be taken in "vulnerable regions". In addition, this study can be complemented and extended by presenting different specific risks or a combination of risks from climate change and vulnerability of economic sectors that will affect total production and individual household production levels and living standards in the different regions affected and studied. The ever increasing vulnerability especially in the agricultural sector to adverse climatic events will not only affect the well-being of the local population but will also affect the livelihood opportunities of many people living in vulnerable areas.

CONCLUSION

Ongoing climate change and predicted changes will increasingly lead to the occurrence of extreme weather events in different regions of the country and the world. Climate change is expected to lead to different impacts on different ecosystem types and biodiversity and ecosystem services will be affected to different degrees, but on the other hand, the annual increase in average temperatures could support the adaptation process by extending growing seasons or by increasing species migration in different natural ecosystems.

In conclusion, we can summarize the main vulnerabilities to climate change at different levels of biodiversity and ecosystems in Bulgaria:

- Loss of genetic diversity as climate change impacts on vulnerable/endangered species, some of which may be lost;

https://doi.org/10.5593/sgem2024/6.1/s27.61

- Disruption of species life cycles and phenological phases as climate change affects populations and ecosystem processes;

- Degradation of habitats, especially habitats at high altitude;

- Impacts on ecosystem service delivery through the implementation of regime shifts, which may have both positive effects in terms of increased growing season length, which may result in increased terrestrial ecosystem productivity. Or negative effects in terms of an increase in the number and duration of drought periods, which may in turn lead to a change in the composition of producers in terrestrial ecosystems, causing changes in their functioning and resulting in reduced provision of ecosystem services. The most vulnerable ecosystems in the country can definitely be identified as the forest areas along our southern border with the Republic of Turkey and the Hellenic Republic, as well as other lowland areas of the country. Inland wetland ecosystems are also vulnerable, as are shrubland and coastal ecosystems. In reality, the gradual climatic changes taking place and the onset of extreme weather events will affect all levels of biodiversity throughout the country, as well as influencing landscape change in different regions of the country. For this reason, the vulnerability and adaptive capacity to climate change of the biodiversity and ecosystem services of the threatened areas already mentioned should be assessed. This process requires the collection of data of appropriate quality over time, examining the impacts of climate change on ecosystem integrity characteristics.

Moreover, the energy sector will also be affected as a result of climate change, especially given that the country is already exposed to various natural hazards, including floods, droughts, forest fires, earthquakes and landslides. The increase in the number of extreme weather events is expected to cause damage and disruption to the energy sector, and we can expect energy infrastructure to be significantly affected, through frequent grid failures and/or temporary power outages, which in turn will lead to a number of challenges for the sector in the future related to planning strategies and taking measures corresponding to the emerging trends related to the expected climate change in the country. Particularly given that the energy infrastructure is vulnerable to a number of climatic stressors such as changes in temperature, rainfall, sea level rise and the occurrence of extreme events. Climate change will alter the intensity, frequency and distribution of extreme high temperatures, the amount of precipitation, and the number and frequency of storms will increase the vulnerability of all elements of the country's energy system. Climate change poses a significant challenge to the country's energy security, despite the energy sector being identified as resilient to the expected impacts in the period to 2035, as experts consider the energy infrastructure to be relatively well planned and maintained. Expected extreme weather events and gradual climate change will have an impact on forest landscapes, biodiversity and agriculture, as well as influencing demand for different types of tourism, possibly even reshaping the country's existing tourist destinations as a result of the increasing risk of damage to cultural sites, increased demand for transport, water and energy, and expected increased pressure on infrastructure. Climate change may lead to overexploitation of ecosystem services in specific regions, which are at risk from an increase in the number and frequency of expected extreme weather events. In this context, the protection and nurturing of landscapes and ecosystems in regions where an increase in the number and frequency of expected extreme weather events is expected should be planned. This protection planning process entails building and maintaining public places with protective architecture and landscape design against the occurrence of possible extreme weather events, and to this end our country can actively participate in the creation

of multidisciplinary courses for planners, architects, engineers, landscape architects, ecologists, economists, sociologists and financial management specialists to use their increased knowledge of climate change in the planning and construction of protective ar But in addition we should not forget that "the development of a city" or region is "more than just property management", because "due to the revolution of communications, a city is nowadays a space for relationships, very often virtual and urbanism is more than management paper and should seek an increase in the sense of belonging in citizens and their involvement in the development process of a city and the regions[8].

ACKNOWLEDGEMENTS

This text is the result of the implementation of the project "Landscape valorization models for regional development" with contract № KP-06-N65/11, funded by the Scientific Research Fund - MES.

REFERENCES

[1] Vos, W.; Meekes, H. Trends in European cultural landscape development: Perspectives for a sustainable future. Landsc. Urban Plan. 1999, 46, 3-14.

[2] Wei, W.; Chen, D.; Wang, L.; Daryanto, S.; Chen, L.; Yu, Y.; Lu, Y.; Sun, G.; Feng, T. Global synthesis of the classifications, distributions, benefits and issues of terracing. Earth-Sci. Rev. 2016, 159, 388-403.

[3] Santoro, A., Venturi, M., Agnaletti, M., Landscape Perception and Public Participation for the Conservation and Valorization of Cultural Landscapes: The Case of the Cinque Terre and Porto Venere UNESCO, available to https://www.mdpi.com/2073-445X/10/2/93 on 05.05.2024

[4] Council of Europe. The European Landscape Convention; Council of Europe: Strasbourg, France, 2000, available to https://rm.coe.int/16807b6bc7 on 03.05.2024

[5] Antrop, M. Why landscapes of the past are important for the future. Landsc. Urban Plan. 2005, 70, 21-34, available to https://www.sciencedirect.com/science/article/abs/pii/S016920460300207X on 03.05.2024

[6] Bulgaria's Integrated Energy and Climate Plan 2021-2030, available to https://www.me.government.bg/uploads/manager/source/VOP/obshtestveno%20obsajdane/INPEK/INPEK12.06.24.pdf on 05.05.2024

[7] National Climate Change Adaptation Strategy and Action Plan, available to https://faolex.fao.org/docs/pdf/bul222405.pdf on 05.05.2024.

[8] Todorov, L. Todorova, El., GIS-based location analysis for hospital site selection: A case study on National Children's Hospital in Sofia, Bulgaria, Journal of the Bulgarian Geographical Society, Volume 49 (2023), 3-15, DOI 10.3897/jbgs.e108502DOI 10.3897/jbgs.e108502, available to https://www.researchgate.net/publication/373159862_GIS-based_location_analysis_for_hospital_site_selection_A_case_study_on_National_Children's_Hospital_in_Sofia_Bulgaria on 05.05.2024

https://doi.org/10.5593/sgem2024/6.1/s27.61

SECTION SPACE TECHNOLOGIES

AND PLANETARY SCIENCES

A SCIENTIFIC AND ENGINEERING APPROACH FOR PLANETARY LAVA TUBES EXPLORATION

Homero Aguilar Diaz [1]

Gustavo Jamanca-Lino [1]

Yury Vasquez Charcape [2]

Daniel Suarez Zelada [1]

[1] Universidad Privada del Norte, **Peru**

[2] Universidad Nacional de Moquegua, **Peru**

ABSTRACT

Lava tubes are natural underground structures formed by volcanoes during magmatic eruption events. Their exploration has aroused undeniable interest in the scientific community because of their potential as future habitats capable of hosting human missions in the Solar System. Indeed, there are significant topographic features that indicate the existence of lava tubes on the Moon and Mars, offering natural shelter and environmental insulation for permanent planetary settlements. The article summarizes the geological process of lava tube formation based on an extensive review of the literature and introduces the relevance of geomechanical prospecting to interpret the surface stability for habitability, introducing the results obtained during the visit to The Hawaii Space Exploration Analog and Simulation (HI-SEAS) base and the region of the Mauna Loa volcano in Hawaii in 2021. The collected data would allow an estimate of the surface properties of these geological formations outside of Earth. In addition, different methodologies currently used in the mining and civil construction industries are discussed that can be transferred as spin-in technologies to complement the characterization of these formations on Earth. In fact, these underground structures are analog environments where it is possible to test different procedures and instruments and develop future space payloads to support the human exploration of the Moon and Mars, with potential terrestrial applications.

Keywords: lava tubes, Moon, Mars, human exploration

INTRODUCTION

Since the beginning of time, humanity's curiosity has always aspired to discover and unravel the great enigmas of the universe. The Moon and Mars represent possible destinations in this century for human exploration, providing essential data for its expansion along the solar system. This interest is based on relevant scientific objectives, the prospect of the long-term survival of mankind, and the potential exploitation of space resources. Future astronauts must survive space weather risks related to temperature variation, high radiation levels, and harsh surface conditions. The main risks are associated with temperature, radiation, micrometeorites, and regolith features [1].

https://doi.org/10.5593/sgem2024/6.1/s28.62

Temperature ranges from -249°C to 96°C (lunar poles), -153°C to 127°C (lunar equator) and -140°C to 20°C (martian equator) meaning a cruel environment for human adaptation and increasing the requirements of habitats and space suits to keep the body temperature at the appropriate values [2],[3]. The high doses of radiation in space represent another latent risk. For example, the value recorded on board the International Space Station (ISS) ranges between 0.4 and 1.1 microsieverts per day and 70-500 Sv per year [4]. In comparison, the maximum cumulative dose in ten years suggested by NASA for an astronaut is 2900 mSv[4], and the lethal dose for humans is about 10,000 mSv. Thus, missions on the lunar and martian surfaces need to be monitored for effective radiation countermeasures to be far below the risky limits. An additional hazard is associated with micrometeorites and regolith. Micrometeorites are micrometric-sized particles (5-100 microns) continuously hitting the lunar surface at a high speed (up to 70 km/s). Besides, the surface lunar regolith is abrasive, ultrafine (<1000 microns), and toxic, so this is one of the main challenges to mitigate [1]. On the other hand, although there are no micrometeorites on Mars, the presence of dust storms is an undesirable condition because of toxic regolith transportation contaminated by perchlorate salts [5].

Based on the challenges presented, it is suggested that astronauts settle in regions with natural protection to reduce the logistic requirements [6], applying the in-situ resource utilization (ISRU) philosophy. In this context, lava tubes offer natural underground channels that stand out as favorable geological locations for human expeditions, offering stable temperature environments, natural radiation bunkers, and protection against micrometeorites and dust. This paper discusses the formation process of lava tubes, their geomechanical surface values, and their importance as planetary refuges, in addition to proposing new methodologies for future scientific expeditions.

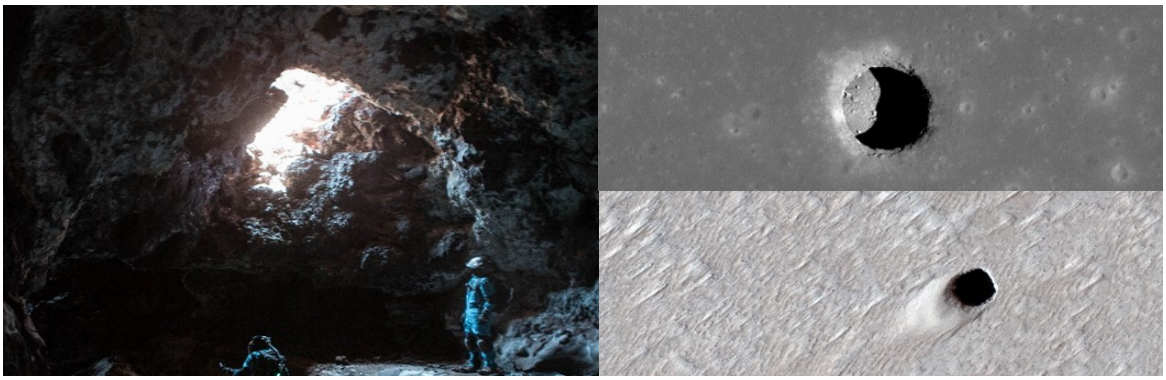


Figure 1. Planetary lava tubes: (Left) Pit and entrance to terrestrial lava tube in Hawaii. (Top right) Crater pit and possible entrance to lunar lava tube. (Bottom right) Crater pit and possible entrance to Martian lava tube. [7], [8].

MATERIALS AND METHODS

This article presents an overall study of planetary lava tubes on Earth, the Moon, and Mars. Indeed, lava tubes have gained a lot of importance in recent times, and this can be corroborated by the more than 34,000 studies related to this topic published in databases such as Scopus, Scielo, and Google Scholar. After a selection process, 28 documents were selected to develop the fundamental concepts presented as a summary.

In the first section of the results, the authors summarized the formation process of these underground locations using AutoCAD 2023. Secondly, the results section introduces the geomechanical data collected during May 2021 in the old lava flow and lava tube regions

near Mauna Loa volcano in the Big Island, Hawaii, during a scientific expedition to the base camp HI-SEAS. HI-SEAS is a scientific habitat located on the Big Island of Hawaii, at 2500 meters above sea level. The sampling and experiment locations were located using a GPS system and presented in this article using Google Earth. Sample collection and qualitative rock hardness evaluation were performed following the instructions of the rock scratch test and compared by visual inspection. The geomechanical data were gathered using a Schmidt Hammer brand DRC, serial number 20M0183N. This instrument was validated and certified by the Peruvian company Geoteknik. The experimental procedure follows the instructions of ASTM D5873. The rebound units obtained during the experiment were converted to Unconfined Compressive rock Strength (in MPa) using correlation curves with an R2 >0.91, from a preliminary calibration of rebound tests with compressional resistance experiments on concrete according to the standard UNI EN 12504 -2:2001. After interpreting the results, the authors identified 20 additional methods and procedures useful for lava tube prospection, specifying their current ASTM (American Society for Testing and Materials) code standard. These methods allow us to expand the data acquisition from lava tubes for future planetary missions.

RESULTS

Formation of lava tubes

On Earth, the formation of lava tubes (see Figure 2) starts when lava emerges from the volcano at a temperature of 1,100–1,200 C° [9] and a viscosity between 10^1 - 10^2 Pa*s [10] (in comparison, water viscosity is 10–3 Pa*s at 20°C [11]). During the event, regions in contact with air experiment with faster cooling compared to deeper layers, resulting in the formation of the hard "crust" as a thermal insulator layer. First, fragments of a solid crust dome grow over the lava flow (sequence in Figure 2 A). Second, there is a gradual accumulation of marginal portions of solidified lava, eventually forming a dome crust over the lava channel (Figure 2B). This layer could be formed by a continued accumulation of small solid fragments dragged by the mobile magma and deposited in the sinuosity of the lava flow, as illustrated in Figure 2C [10]. The lava tubes formed during this first stage begin with the addition of a thin layer of solidified lava that adheres to both sides of the channel (XA1). If the volume remains constant, the crust continues to grow towards the center of the channel until both sides, join the margins and achieve the conclusion of the dome (Figure 2 XA2). The crust continues to increase in thickness and length up to a critical level for collapse, where solidified fragments may break off when the lava flow level drops abruptly, forming pits along the formation (YA2) [10].

The second stage occurs during the fluctuations in the lava flow level circulating through the channel. It begins with small lava overflows on the external margins of the channel (Figure B2, B4); when these reach a significant magnitude, a thick layer of solidified lava is formed that might complete the domo and close the tube (Figure B5, B6, B7). If the volume of lava increases, it will cause the complete filling of the tube (Figure B8), resulting in a significant growth of the crust and resistance increasing (Figure B9); subsequently, the lava is evacuated, decreasing its volume and allowing the walls of the tube to cool and solidify along large extensions (Figure B10, B11, B12) [10]. While the shallow lava layer forms a crust, molten magma deeper continues flowing at a velocity of 10–30 km/h. Once all the lava is drained, it leaves an empty space like an underground

https://doi.org/10.5593/sgem2024/6.1/s28.62

cavern or mine labor of several meters and even kilometers in length, with a width and height ranging from 0.5 to 30 m [12], [13].

During the second stage, the intrusion of crust fragments floating over the lava and circulating the channel, reach narrow areas, so, they gradually accumulate and begin the dome formation process, finalizing the growth of upper and lower tube section (Figure 2 A3, B3) [10].Depending on terrain slope, and intensity of volcanic activity, lava tubes can be simple, sinuous, rectilinear, braided, or multi-level [12]. Mineralogically, lava tubes are formed by basaltic rocks with minerals such as olivine, plagioclase, and pyroxene, phenocrystals, and vesicular or porphyritic textures [14].

On Earth, main lavatubes are located in Hawaii (EU), Canarias (Spain), Iceland, Queensland (Australia), Sicily (Italy), Jeju Island (South Korea), and Galápagos (Ecuador) [12]. On the Moon, around Gruithuisen (34.618°−43.467°) and Marius Hills (13.603°−58.047°), possible underground cavities similar to collapse chains and pits have been identified [12]. While on Mars, several deep pits above ancient lava flows have been recognized as the entrance to these underground formations. Some examples are located in Arsia (−3.062°−123.930°) and Olympus Mons (19.456°−133.399°) [12]. Data from remote sensing has detected the existence of over 300 (Moon) and 1000 (Mars) geological features (see Figure 1) that suggest the presence of extra-terrestrial lava tubes [12] [15].

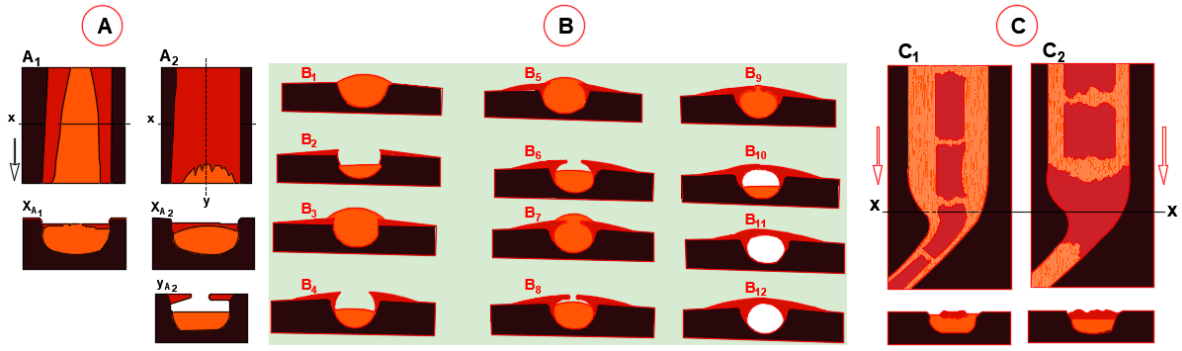


Figure 2. Lava tube formation process. Re-drawn by the authors using AutoCAD design based on the original graphics of J. López [10].

A Case study: geomechanics prospection in Hawaiian lava tubes

HI-SEAS, a scientific base operated by the International MoonBase Alliance is a highly valuable region because the habitat is located on ancient lava flows, with almost no presence of wildlife (neither animals nor plants), and because of the closeness to lava tubes [16]. The nearby area was used for scientific purposes by several space agencies, including NASA and research organizations, to simulate social interaction in isolation conditions for a future planetary human base [17] and to collect geologic samples. Indeed, Gustavo Jamanca-Lino, co-author of this article, visited this area in 2021 as a crewman of the analog team Selene IV. During the 14-day stay, the crew lived in complete isolation and performed a strict routine, including diet control, physical exercise, scientific experiments and exploration trips to lava tubes.

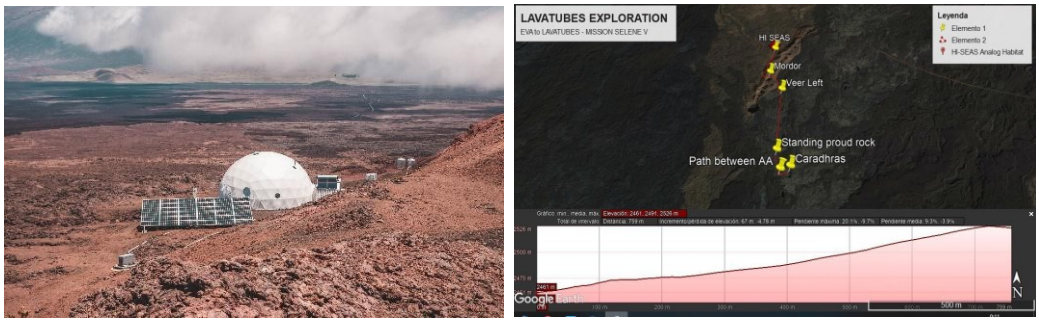


Figure 3. HI-SEAS base (left) and trekking distance to lava tubes (right) , including important reference regions of the old lava flow.

The role of Gustavo was as Space Resources Officer, and in addition to team activities, he performed a series of measurements of the geomechanics features of the floor and lava tubes walls, using the Schmidth Hammer test, to measure indirectly the Unconfined compressive rock strength (UCS) of the lava formations. The tests and sample collection were applied outside the base, first, on the basaltic floor formation denominated as "Mordor" and "Triple point", which are over 0.5 Km south of the HI-SEAS base (See Figure 3). The area denominated as triple point, presents three geological formations coexisting: Aa old lava flow (sample A), Smooth Pahoehoe old lava flow (sample B), and cinder material highly weathering (C). These regions are presented in Figure 4.

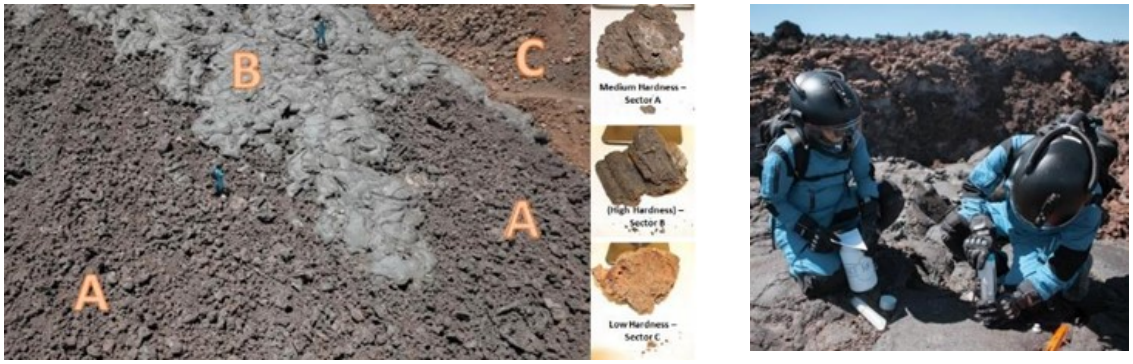


Figure 4. Activities into the old lava flow region, near HI-SEAS. (Left) Aerial view of triple point area. (Right) Geomechanics tests, in the photo Gustavo Jamanca-Lino and Michaela Musilova.

The first region corresponding to the Aa old lava flow (region A) contains angles and rock blocks because it is associated with a high velocity of magma deposition, expanding the molten material and preventing the formation of continuous layers; hence, it was impossible to get geomechanics data from this region due to the standard procedure suggesting a flat and uniform surface to reduce the experimental deviation and bias. The second location explored was the smooth Pahoehoe old lava flow (region B), which presents overlapping layers deposited on the surface with a smooth, continuous, and flat texture; in consequence, their origin and features are attributed to the low velocity of the magma during the formation. Thus, although the chemical and mineralogical composition is similar to Aa lava flow formation, the low velocity of deposition and magma displacing make the texture difference. Region C contains cinder and other materials very affected by erosion, with a low quantity of centimetric rocks. Because of the absence of a continuous solid layer, there was no testing there either. After the visual recognition of

https://doi.org/10.5593/sgem2024/6.1/s28.62

the area, a qualitative scratch test was applied over rock samples of 4–6 cm in diameter. Therefore, region B was identified as the highest hardness value.

The geomechanical data was measured at 20 different points in Region B. The rebound values were recorded in the range of N° rebound 16–23, which represents a UCS: 17–37 MPa. According to this, for future science campaigns, the surface presents enough resistance to allow the transit of small rovers and human crews without risk of trapping. However, the topography and blocks stability might restrict movement ability. Visually, it identifies some areas with weak layers that may break during continuous traffic. In comparison, most of these old lava flows have a resistance similar to that of common residential concrete surfaces (UCS: 17 MPa), while other areas are similar to high-hardness residential surfaces (UCS: 41 MPa). In contrast, the features of region A, which presents angular rocks, will make difficult the displacement of a robot system, and even sampling activities by humans pose falling risks. Region C, which is mostly formed by cinder and soil, would have enough resistance to support the movement of small rovers, but the fine granulometry is a potential risk for stucking.



Figure 5. Sampling and testing activities in lava tubes – Hawaii, U.S. In the photo Gustavo Jamanca-Lino

The second location visited was the lava tube region called Caradhras, 1 km from the base (see Figures 3 and 5). Several basaltic flows are revealed on the walls, probably from different and sequential volcanic events. Additionally, white spots appear on the roof and walls due to the interaction with microorganisms. The values of the basaltic floor range between N° rebound 20 - 29 (UCS: 42 - 67 MPa), and the walls range between N° rebound 32 - 38 (UCS: 58 - 78 MPa). These values are similar to those of underground mining tunnels, with a resistant classification of class R4 (uniaxial strength of 50 to 100 MPa). The rock formations are considered resistant and, for extreme security, might require additional support (e.g., wooden shoring for beams and pillars). The complete data obtained is described in figures 5 and 6.

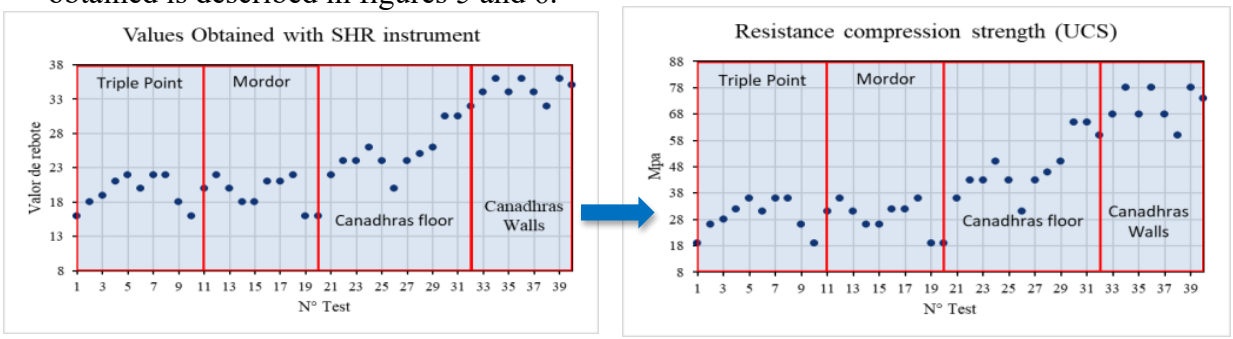


Figure 6. (Left) Compression resistance values obtained during the SELENE IV mission. (Right) Results converted to MPa.

DISCUSSION

The authors suggest the following activities for an extensive and complete characterization of a lavatube. The first set of procedures is related to the detection, shape, dip slope, and interconnection of these natural tunnels. Geophysical methods such as gravimetry, ground penetrating radar (GPR), seismic refraction, and electrical resistivity could be adapted for an aerial or ground survey of lava tubes and caverns close to the volcanic regions. Second, robotic systems (as rovers or drones teleoperated) could gather internal topographic data using LiDAR (Light Detection and Ranging or Laser Imaging Detection and Ranging) for a better description of the roughness and access.

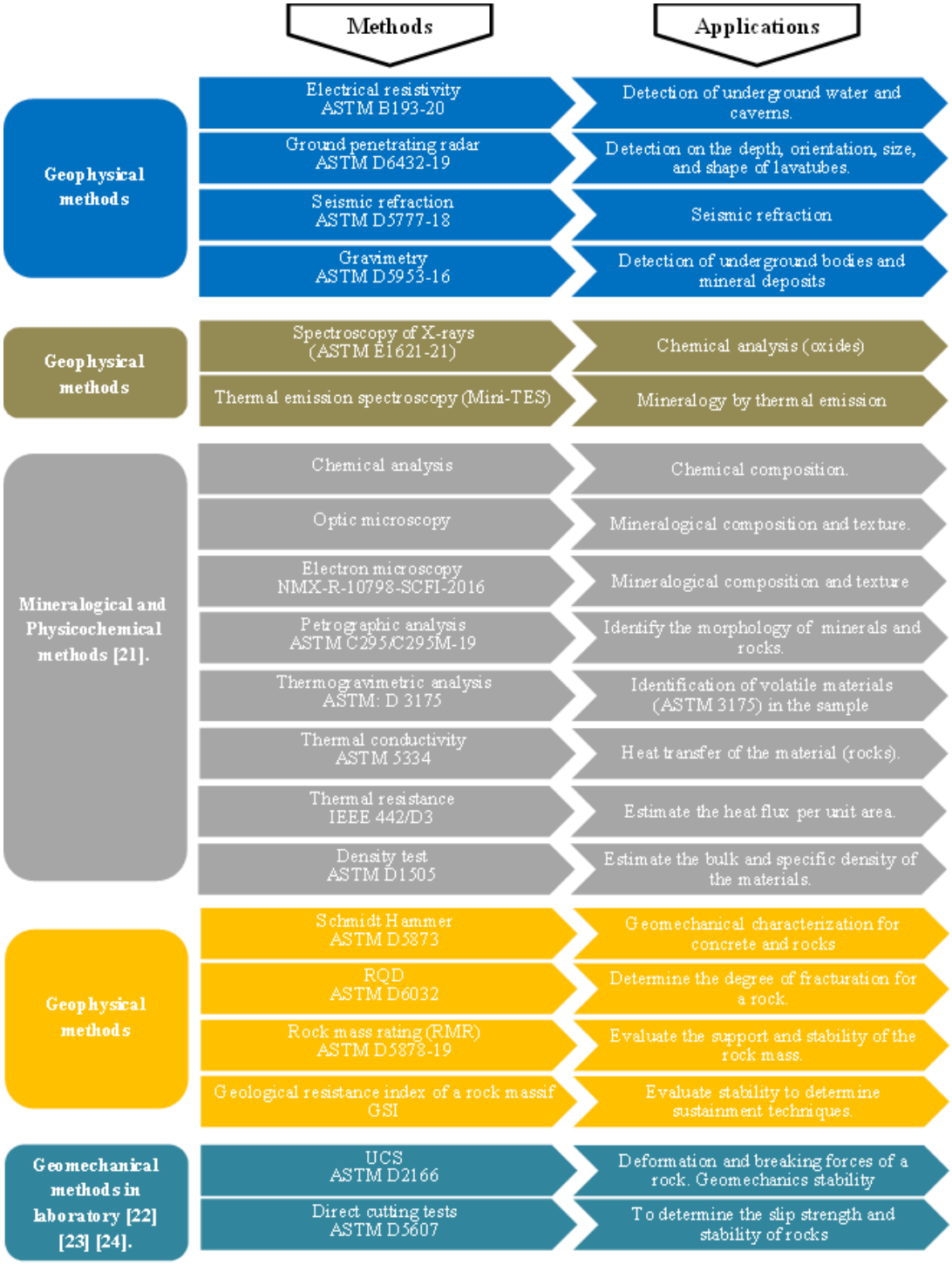


Figure 7. Geomechanics methods: In situ and in Laboratory, based on ASTM standards and [18-25].

https://doi.org/10.5593/sgem2024/6.1/s28.62

Finally, once the lava tube is detected and overall mapped, a crew or robotic system could explore geochemically in situ and geomechanic classify the formation. A good example of chemical and mineralogic in situ characterization is currently applied onboard the Perseverance and Opportunity by X-ray and thermal emission spectroscopy to explore Mars [18],[19].

According to the data collected on Hawaii, basaltic lava tubes would be qualified as "resistant" (R4), stable, and would not require additional support to withstand seismic events. These formations would be adequate for the construction of underground structures or facilities inside. With the purpose of guaranteeing the safety and continuity of operations [20], geomechanical tests used in underground mining to analyze tunnel quality, fracture resistance, and load capacity could be adapted for these environments. It includes the analysis of rock-quality designation (RQD), Cave Geomechanical Index (CGI), Barton's Q index and Rock Mass Rating (RMR) to determine the rocky massif stability. Data generated by these tests will be essential for the planning phase of geomechanical support, civil construction, and monitoring. Furthermore, the use of the Schmidt hammer could be adapted for an indirect measure of UCS, and visual systems (e.g., cameras and 3D mapping with LIDAR) could be used to detect the fractures in the walls and cavern roof for a quantitative evaluation. Based on the results obtained, it will decide the deployment of additional support (e.g., timber shoring for beams and pillars, reinforcing with shotcrete, or electrowelded wire meshes in local zones with a risk of collapse). By designing systems to evaluate the geomechanical properties and strength of these rock formations, engineers could conceive and refine appropriate civil construction designs for lava tubes on the Moon and Mars, such as habitats or research stations.

In addition. two important aspects to determine the genesis of the rock massif and their civil potential for human habitats are shallow hardness (ability to resist deformations or abrasions on its surface) and resistance (ability to withstand continuous forces or pressures). In lava tubes, both features vary according to the formation conditions, such as volcanic lava flows (basalts, trachytes, and phonolites) or volcanic pyroclast flows. While the first group is a uniform material with greater density and resistance, the second is made up of fragmented materials with high porosity and low density. In general, both groups appear very frequently alternately and intermixed, affecting the formation of the rock massif. Therefore, to meet the safety standards, it is necessary to conduct in situ and laboratory tests along different zones of the formation. This data allows us to model the geomechanic behavior of the underground formation and determine if it requires additional support systems to prevent collapses or sinking in the rocky structure. For the whole prospection activity, the authors suggest the list of methods described in Figure 7.

Lava tubes can be used as sources for planetary ore extraction and in-situ resource utilization activities. On Earth, basalt, rich in iron, is an essential resource for the construction of tools, machinery, and infrastructure. Similarly, on the Moon, basalt could meet the future demand for civil construction. Indeed, on the lunar surface, it is necessary to construct roads, habitats, and landing pads using in-situ materials. Techniques such as regolith sintering or casting have been proposed to fabricate bricks as support materials in planetary civil construction. Although these bricks would come as by-products of extraction activities, their formation involves intensive power consumption [26]. Conversely, lava tubes offer natural "bricks" that require only drilling and cutting operations, which are less power-intensive compared to the thermal operations mentioned

above. Therefore, the direct extraction of lunar basalts from lavatube formations is a competing technology for civil construction, and although it requires more evaluation, it should be considered along with other manufacturing technologies such as additive manufacturing, sintering, and casting. In fact, lunar basalts are a source of a homogeneous material with higher properties than lunar regolith, making them useful for additive manufacturing (3D printing) and unfolding a wide spectrum of possibilities in the manufacturing of structures and components. Thus, the lunar basalt would be a keystone in the development of civil construction settlements in space, increasing the economic potential value of lunar lava tubes.

In addition, lunar basalt is a rich source of oxygen, iron, and silicon, three of the main resources required for future lunar habitats. However, the utilization of lunar basalt for metallurgical activities requires the implementation of crushing and milling operations on the lunar surface. Although there is no yet an official study for comminution techniques on off-Earth surfaces and most researchers suggest processing directly the ultrafine regolith, the efficiency of a beneficiation stage using regolith is uncertain due to the degradation effect of lunar micrometeoroids, which have converted the original single-phase minerals into fractal mixed grains with two or three ore phases in the same grain, making the concentration techniques more challenging and reducing the chance to obtain high-pure concentrates[27].In contrast, the lava tube environment would preserve the original formation of minerals, making it more practical to concentrate basalt minerals directly than lunar regolith, to obtain high pure concentrates at high recovery levels. From an additional material sciences perspective, lunar basalt is a potential ore to produce wool fibers and glass sheets, benefiting various industries such as construction and solar energy by offering a local and sustainable source of these key materials. To close the suggestion of various technologies for a complete lava tube characterization, the authors present Figure 7, which is a list of official procedures used in the mining, civil and geotechnical industry in the characterization of underground formations.

Regarding astrobiological potential, on Earth, lava tubes are natural environments that host different microorganisms (Cyanobacteria, fungal mycelia, and diatoms) that can grow without sunlight conditions and absorb silica or iron as their microbial structure allows. Thus, it is possible that lava tubes could serve as potential refuges for ancient microbial life on Mars [11], and the acquisition of data must be addressed. Currently, NASA's Perseverance rover is using a variety of techniques to search indirectly for signs of life on the red planet, such as X-ray fluorescence (PIXL) [28], and the LIBS instrument (Laser-Induced Breakdown Spectroscopy) [29]. Similar strategies and methods for indirect and direct microorganisms' detection could be tested on lava tubes to find resistant chemotrophic organisms (microorganisms able to obtain nutrients from minerals) that could exist on the red planet.

Finally, the main interest of developing space technologies is their spin-off and dual use to solve current problems in our society. Mine collapses are one of the top causes of deceases in Peruvian and Latin American mining workers because the geomechanical characterization is not well completed or is based on manual biases methods. The authors suggest developing an explorer rover to prospect the geomechanical properties of an underground mining unit using a 3D imagen inspection system and penetrometers or mobiles Schmidt hammer to perform a complete RMR analysis, as well as geophysical devices to map the presence of geological faults. This information will be crucial to

https://doi.org/10.5593/sgem2024/6.1/s28.62

improving the accuracy of the detection and quantifying the collapse risk in situ, reducing human bias, automating the process, and saving important lives.

CONCLUSION

Lava tubes exploration can provide us with relevant information for the geological field and help us understand the history of surrounding volcanic eruptions and lava composition. Based on the collected data, we concluded that the geomechanical resistance along superficial lava flows is not constant and has a high standard deviation, affected by the proximity of transition zones, where the layers become brittle. Secondly, the rovers' and robots' trafficability is possible but lighter systems are preferable to prevent any damage in the brittle areas. In contrast, the floor inside lava tubes is stronger, the same as hard cement surfaces in industrial buildings, so it can support heavier rovers with more payload. In general, lava tube formations are stable and strong enough not to need geotechnical support, but additional considerations must be taken, such as the calculation of RMR, RQD, and GSI. Finally, safety strategies that include monitoring gasses are crucial to ensuring human expeditions. In addition to the scientific potential of terrestrial lava tubes, another interesting application could be related to the production of lightweight structural materials with high mechanical strength and thermal insulation capacity against ultraviolet and non-ionizing radiation. Beyond Earth, lava tubes are possible natural shelters for human settlements as protection on other planets. Finally, basalt resources into lava tubes along with shallow regolith are positioned as fundamental pillars in the expansion and development of humanity in space.

ACKNOWLEDGEMENTS

The authors express their gratitude to Dra. Gladys Ocharan for the support in the preliminary characterization of rocks. Also, to the crew Selene IV and the HI-SEAS scientific base operated by the International MoonBase Alliance, and Bader Al Moudah for the photographs. This paper was developed under the support of the ARIES Peruvian research group, a multidisciplinary team who are working on systems engineering for planetary exploration and environmental technologies. Finally, thanks to the Department of Research, Innovation, and Social Responsibility at the Universidad Privada del Norte, Peru; for the support received for the participation in SGEM 2024.

REFERENCES

[1]. C. Guerra, G. Jamanca Lino, S. Rincon Martinez, E. Rezich, I. Casasbuenas, “Geomechanics on the Moon. A prospecting mission architecture concept”, Proceedings of the International Astronautical Congress, IAC, 2022, 2022-September

[2]. Moon fact sheet. (2024, enero 11). Nasa.gov. https://nssdc.gsfc.nasa.gov/planetary/factsheet/moonfact.html

[3]. Mars fact sheet. (2024, enero 11). Nasa.gov. https://nssdc.gsfc.nasa.gov/planetary/factsheet/marsfact.html

[4]. D. Marín, “La radiación en el espacio”, mar. 2011.

[5]. G.Jamanca-Lino, W. Aoun, E. Roy, C. Carrière, A. Böttge, S. Grand, “REDMARS - Lowering the Perchlorate for agriculture on Mars and In-situ resource utilization”, Proceedings of the International Astronautical Congress, IAC, 2021, A5

[6]. D. Viúdez-Moreiras, “The ultraviolet radiation environment and shielding in pit craters and cave skylights on Mars”, Icarus, vol. 370, núm. 114658, p. 114658, 2021.

[7]. W. Steigerwald, “NASA’s LRO finds lunar pits harbor comfortable temperatures”, NASA, 26-jul-2022.

[8]. “HIRISE spots the mouth of a martian lava tube –”, NASA Mars Exploration. [Online]. Available: https://mars.nasa.gov/resources/26349/hirise-spots-the-mouth-of-a-martian-lava-tube/.

[9]. M. Detay y B. Hróarsson, “Túneles de lava. Investigación. Investigación y ciencia” (420), 62-67

[10]. J. López Ruiz y J. M. Cebriá, “Tipología de las Lavas generadas en Ambiente Subaéreo por las Erupciones Basálticas”, Revista de la sociedad española de mineralogía, p. 8, 2014.

[11]. R. B. Bird, W. E. Stewart, y E. N. Lightfoot. Viscosity of Liquids and Gases, 2ª edición, John Wiley & Sons, 2007, pag 10.

[12]. F. Sauro, R. Pozzobon, M. Massironi, P. De Berardinis, T. Santagata, y J. De Waele, “Lava tubes on Earth, Moon and Mars: A review on their size and morphology revealed by comparative planetology”, Earth Sci. Rev., vol. 209, núm. 103288, p. 103288, 2020.

[13]. R. J. Léveillé y S. Datta, “Lava tubes and basaltic caves as astrobiological targets on Earth and Mars: A review”, Planet. Space Sci., vol. 58, núm. 4, pp. 592–598, 2010.

[14]. Pedro Luis Ballarín. Biologia-Geologia.com, “Composición de los magmas”, Biologia-geologia.com.

[15]. G. E. Cushing, “Candidate Cave Entrances on Mars”, 2017.

[16]. M. Musilova, B. Foing, y H. Rogers, “Simulating lava tube exploration research during analog lunar and Martian missions at HI-SEAS in Hawaii”, EGUGA, pp. EGU21-14600, 2021.

[17]. A. Ganser y C. Lavery, Eds., Maritime Mobilities in Anglophone Literature and Culture. Cham: Springer International Publishing, 2023.

[18]. P. G. Node y Washington University, “Alpha particle X-ray spectrometer (APXS)”, Wustl.edu. [Online]. Available: https://an.rsl.wustl.edu/help/Content/About%20the%20mission/MER/Instruments/MER%20APXS.htm. [Consultado: 13-sep-2023].

[19]. “Mini-TES”, Nasa.gov. [Online]. Available : https://mars.nasa.gov/mer/mission/instruments/mini-tes/. [Consultado: 13-sep-2023].

[20]. L.E Hernández Gutiérrez & J.C Santamarta Cereza, Ingeniería geológica en terrenos volcánicos métodos, técnicas y experiencias en las Islas Canarias. Madrid: Ilustre Colegio Oficial de Geólogos, 2015.

[21]. J. C. Melgarejo, J. A. Proenza, y S. Gali y X. LL. Llovet, “Técnicas de caracterización mineral y su aplicación en exploración y explotación minera”, Scielo, 2010.

https://doi.org/10.5593/sgem2024/6.1/s28.62

[22]. A. Russo, I. Vela, E. Hormazabal, “Cuantificación del Índice de Resistencia Geológica Intacta para Macizos Rocosos en Ambientes Hipógenos”, MassMin, 2020.

[23]. S. Loaiza, G. Rodríguez, y M. Mulas, “Análisis de estabilidad de la cueva volcánica El Mirador de los 2 Túneles (Islas Galápagos, Ecuador) combinando métodos empíricos, numéricos, técnicas remotas y realidad virtual”, 2022.

[24]. G. Bastidas, O. Soria, M. Mulas, y L. Bordehore, “Análisis de Estabilidad y Riesgos Asociados a las Cuevas Vol- 2 cánicas de las Islas Galápagos: comparación de Métodos Empí- 3 ricos y Numéricos”, 2022.

[25]. L. Bermejo et al, “Técnicas de prospección geofísica aplicadas a yacimientos kársticos: Tomografía de Resistividad Eléctrica (ERT) en el Karst de Ojo Guareña”, 2014.

[26]. K. W. Farries, P. Visintin, S. T. Smith, and P. van Eyk, “Sintered or melted regolith for lunar construction: state-of-the-art review and future research directions,” Constr. Build. Mater., vol. 296, no. 123627, p. 123627, 2021.

[27]. G. Jamanca-Lino, “Concentration of lunar plagioclase for solar cells fabrication. An ISRU conceptual architecture,” in SGEM International Multidisciplinary Scientific GeoConference. EXPO Proceedings, 2023.

[28]. A. Aeroespacial, “El rover Perseverance de la Nasa empieza su búsqueda de signos de vida en Marte”, Actualidad Aeroespacial, 22-jul-2021.

[29]. Amazings & NCYT, Ed., Proponen un método de análisis rápido para encontrar huellas biológicas en Marte. 2021.

ANALYSIS OF GEOMAGNETIC DATABASES IMPACTING SPACE WEATHER

Dr. Laurentiu Asimopolos[1]
Dr. Natalia-Silvia Asimopolos[1]
Dr. Vijdea Anca-Marina[1]
Dinu Luminita[1]
Assist. Prof. Adrian-Aristide Asimopolos[2]
[1]Geological Institute of Romania, Bucharest, **Romania**
[2]National University for Science and Technology POLITEHNICA of Bucharest, Faculty of Transports, **Romania**

ABSTRACT

Through the complex analysis of the geomagnetic database of the Surlari Geomagnetic Observatory for over 80 years, corroborated with the data of other planetary observatories from the INTERMAGNET network, we have extracted the geomagnetic information that is correlated with the specific physical parameters of space weather domain.

Space weather refers to the conditions and phenomena occurring in outer space that can influence the near-Earth space environment. This concept includes a variety of events and conditions that occur outside the Earth's atmosphere and can affect various aspects of space activities and technology. At the same time, we used the Romanian geomagnetic database, regarding declination, inclination and the total geomagnetic field, made in ArcGIS based on measurements in Romanian airports. Correlating the historical geomagnetic data of the observatory with the Solar Cycles and variations of the solar emission, with the spatiotemporal evolution of the composition, density, speed of the solar wind and ionospheric effects, provides a tool for forecasting climate change, space weather and for rapidly quantifying the possible effects of extreme geomagnetic storms in mid-latitudes. The periodic update of absolute declination values from the Airport Secular Variation Network with the help of global models, national reference values determined from observatory records and in situ measurements highlights the dynamics of national declination anomalies in real time and represented a tool for risk assessment in a strategic field – National Air Traffic Security.

In this paper, we present the Fourier and wavelet analysis of geomagnetic data recorded at different planetary observatories, regarding geomagnetic storms. Fourier analysis highlights the predominant frequencies of the magnetic field components. Wavelet analysis provides information about the frequency ranges of magnetic fields, which contain long time intervals for average frequency information and short time intervals for highlight frequencies, details of the analyzed signals. Also, wavelet analysis allows us to decompose geomagnetic signals into different waves. The presented analyzes are significant for the study of the geomagnetic storm. Data for the following days after the storm showed a weakening of the disturbances and a transition to quiet days of the geomagnetic field. In both, the Fourier Transform and the Wavelet Transform, the evaluation of the transform involves the calculation of a scalar product between the

https://doi.org/10.5593/sgem2024/6.1/s28.63

analyzed signal and a set of signals that form a certain basis in the vector space of finite energy signals.

At the same time, we present in this paper the realization of the web-GIS application for the magnetic declination measurements carried out by the Surlari Geomagnetic Observatory in the period 2010-2023.

Keywords: Solar Cycle, geomagnetic storm, planetary geomagnetic indices, Wavelet analyses, Fourier analyses.

INTRODUCTION

The Sun has a greatest influence on the external magnetic field of the Earth and its space environment. Space weather is caused by many components such as: Solar flares (X-ray solar flashes), coronal mass ejections (CME), high speed solar wind and the solar energetic particles.

These and others refer to the effects that the Sun has on the solar system and Earth. When the solar activity is more intense, CMEs appear, and a mass is detached from the surface of the Sun, which can touch several terrestrial masses, and the solar wind is generated, which generates a series of effects, among which are geomagnetic storms (the sudden increase in the geomagnetic field of Earth).

The physical phenomena that appear, starting from Maxwell's equations, the classifications of geomagnetic storms and geomagnetic indices, are very well explained in the bibliography and specialized websites. The impact of geomagnetic storms on space weather and on critical infrastructures are of great interest to humanity.

There are geomagnetic databases on the servers of each observatory from the INTERMAGNET network, as well as global databases that take all the information from terrestrial observatories and satellite data, and through complex analysis and forecasting methods such as: Machine Learning, Deep Learning and Artificial Intelligence techniques, statistical-spectral methods and so on, can make forecasts two to three days before the occurrence of major geomagnetic disturbances.

For exemplification of geomagnetic studies, we used the magnetic data sampled at 1 minute from INTERMAGNET [9], for 24 planetary observatories and based on these data, we performed spectral analysis and wavelet analysis for the geomagnetic storms. We also performed wavelet coherence between these observatories.

CORRELATION OF GEOMAGNETIC DATA FROM THE SURLARI NATIONAL GEOMAGNETIC OBSERVATORY WITH SOLAR CYCLES AND VARIATIONS AND MEASUREMENTS FROM OTHER INTERMAGNET OBSERVATORIES

In this year, at maximum level of 25th Solar Cycle, the most important geomagnetic event was a storm dated March 24, 2024, whith *geomagnetic* three-hourly index Kp = 8,33 and Disturbance Storm-Time (Dst) = -222. The detailed mathematical methodology used in this paper is presented in [2], [4], [6], [7] and [8]. The part of applications in geomagnetism of this methodology is presented in [1], [3] and [5]. Data used are from [9] and software from [10]. Figure 1 shows the graphs as time series, made from the data

recorded at 24 INTERMAGNET observatories, for the period March 22 at 00:00 and March 26 at 00:00, with a sampling step of 1 minute, for the Surlari observatory (SUA), where the meaning of the colors is: - red represents the magnetic field in the North (X) direction; - the magnetic field in the East (Y) direction is represented in green; - the magnetic field in the vertical direction (Z) is represented in blue; - the Total magnetic field (F) is represented in black.

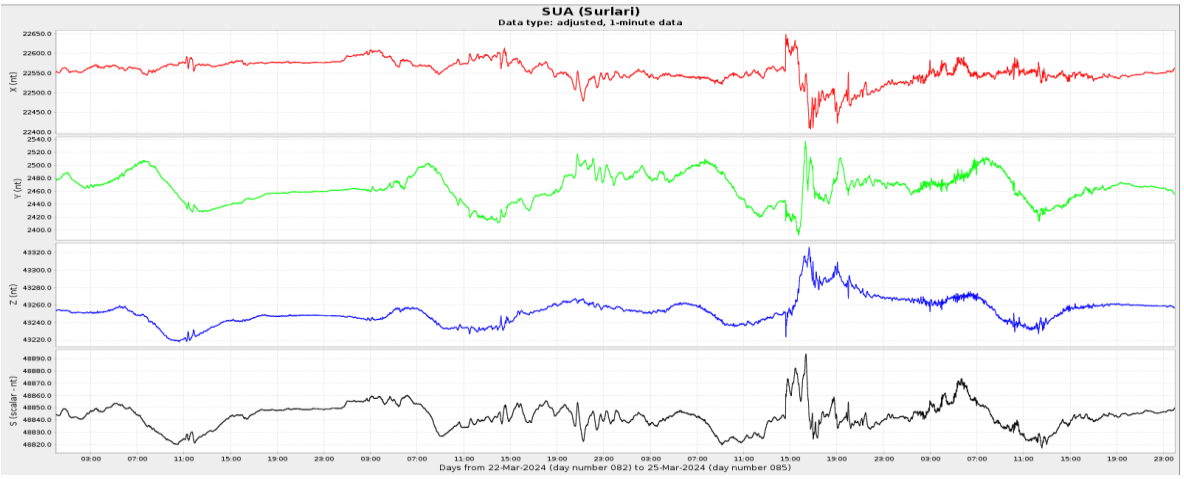


Fig. 1 – Magnetogram from Surlari Observatory (SUA), March 22-26, 2024

Wavelet methodology and other multiscale techniques can be used to analyze data at different time and frequency resolutions and to decompose signals and images into their various components. There are many techniques and wavelet functions to reduce dimensionality and extract discriminative features from signals and images to train ML and DL models. The Wavelet Toolbox in MATLAB allows us to interactively remove noise from the signals we are analyzing, being able to perform multi-resolution and wavelet analyses. To this end, the toolkit includes algorithms for continuous and discrete wavelet analysis, wavelet packet analysis, multiresolution analysis, wavelet scattering, and other multiscale analysis. We exemplify the wavelet analysis for two planetary observatories Surlari and Tatuoca in figures 2 and 3.

https://doi.org/10.5593/sgem2024/6.1/s28.63

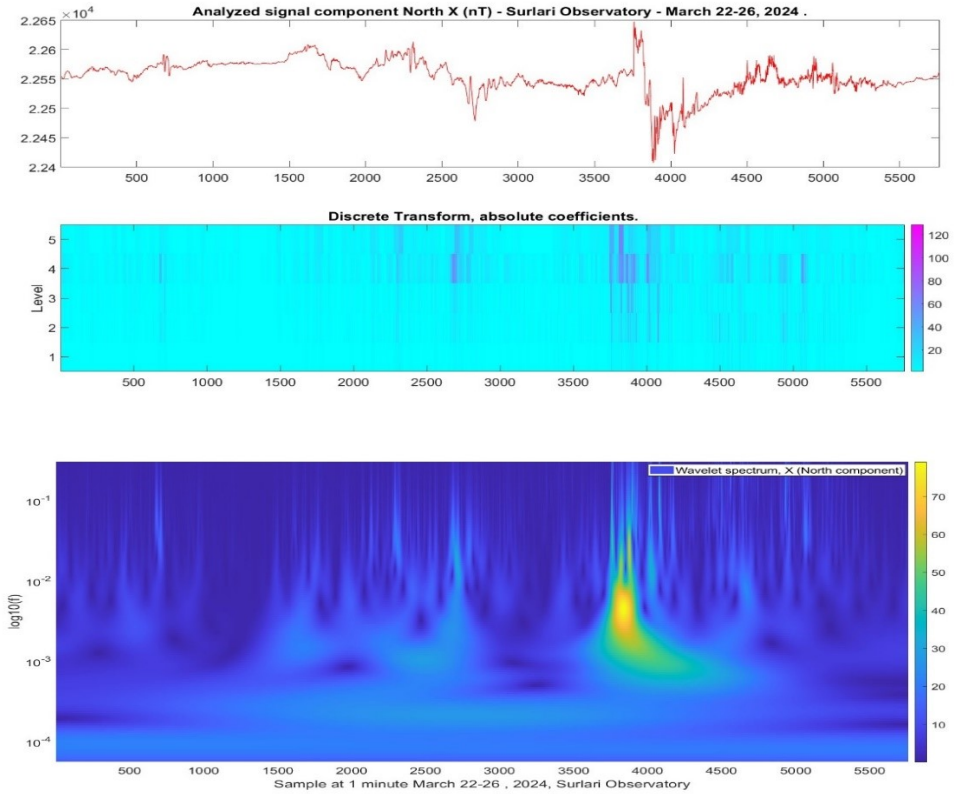


Fig. 2 – Wavelet analysis at Surlari Observatory, March 22-26, 2024, North (X)

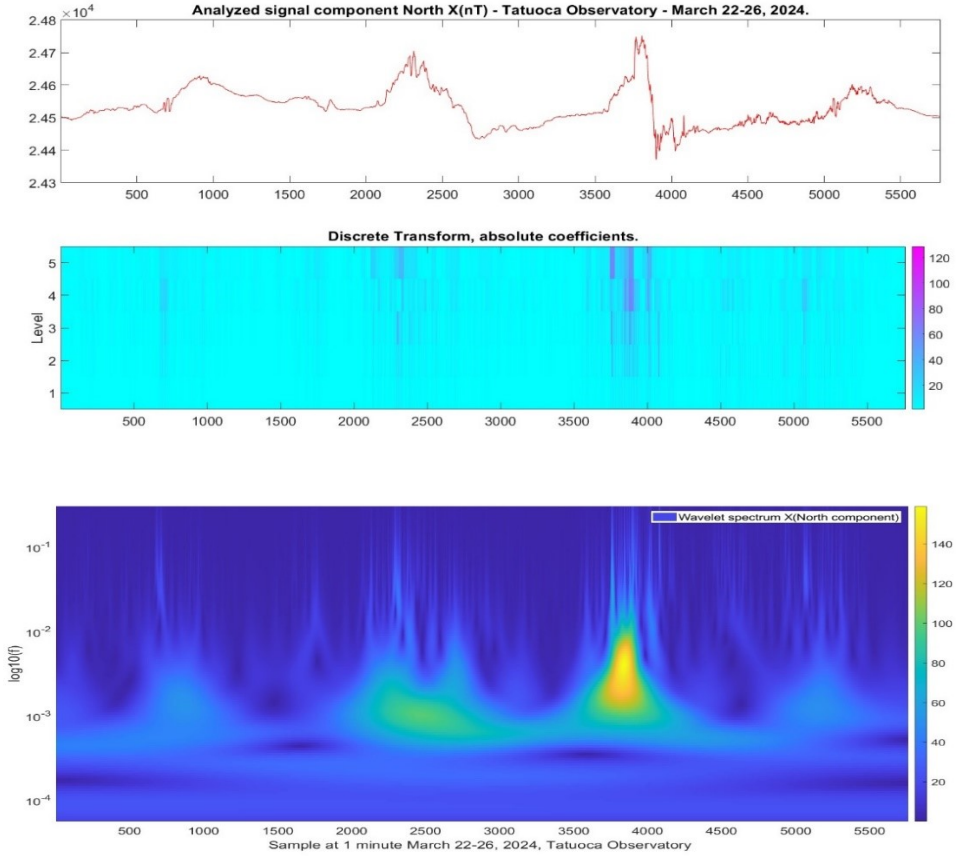


Fig. 3 – Wavelet analysis at Tatuoca Observatory, March 22-26, 2024, North (X)

The wavelet coherence defined by the function wcoherence(x,y) in Matlab, is a measure of the correlation between two real 1D vector signals of the same length x and y in the time-frequency plane.

Wavelet coherence is applicable to the analysis of non-stationary signals and uses the analytical Morlet wavelet, being able to detect events such as geomagnetic field anomalies, change points and transients. In figures 4, 5, 6 and 7 we can view the wavelet coherence for geomagnetic components (North, East, Vertical and Total) between Surlari and Tatuoca Observatories.

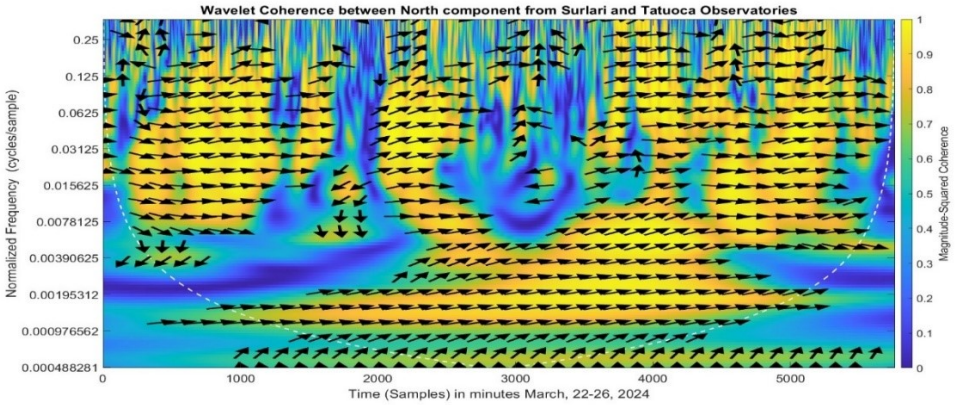


Fig. 4 – Wavelet coherence between Surlari și Tatuoca observatories, North (X)

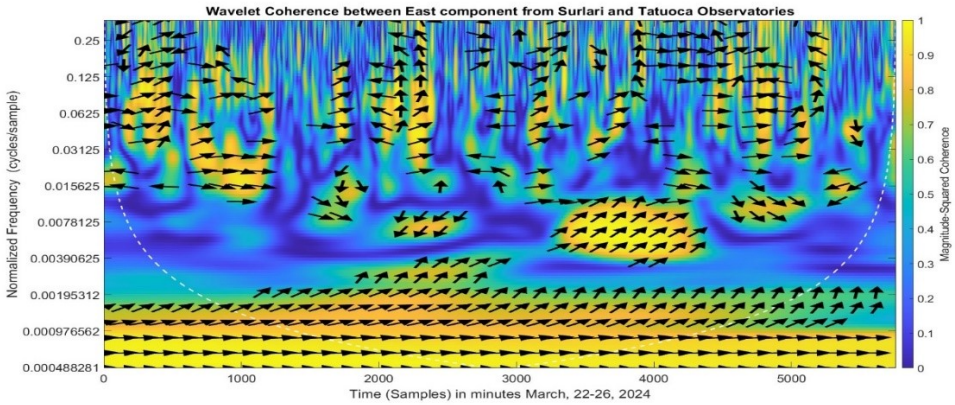


Fig. 5 – Wavelet coherence between Surlari și Tatuoca observatories, East (Y)

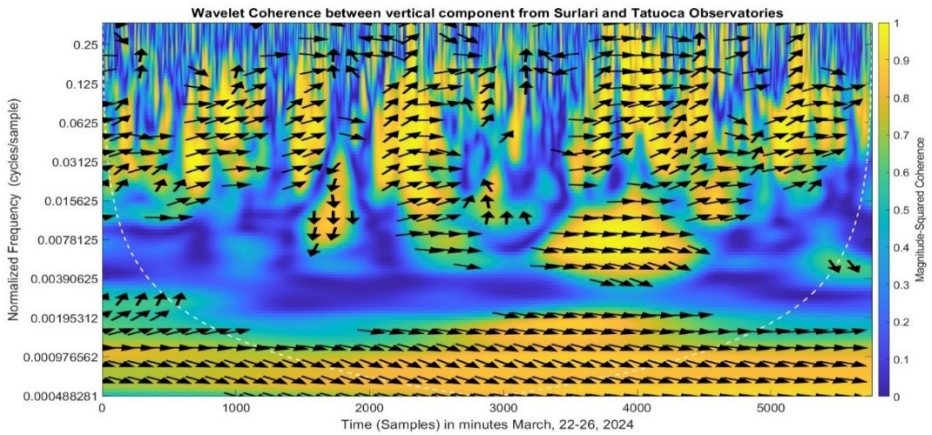


Fig. 6 – Wavelet coherence between Surlari și Tatuoca observatories, Vertical (Z)

https://doi.org/10.5593/sgem2024/6.1/s28.63

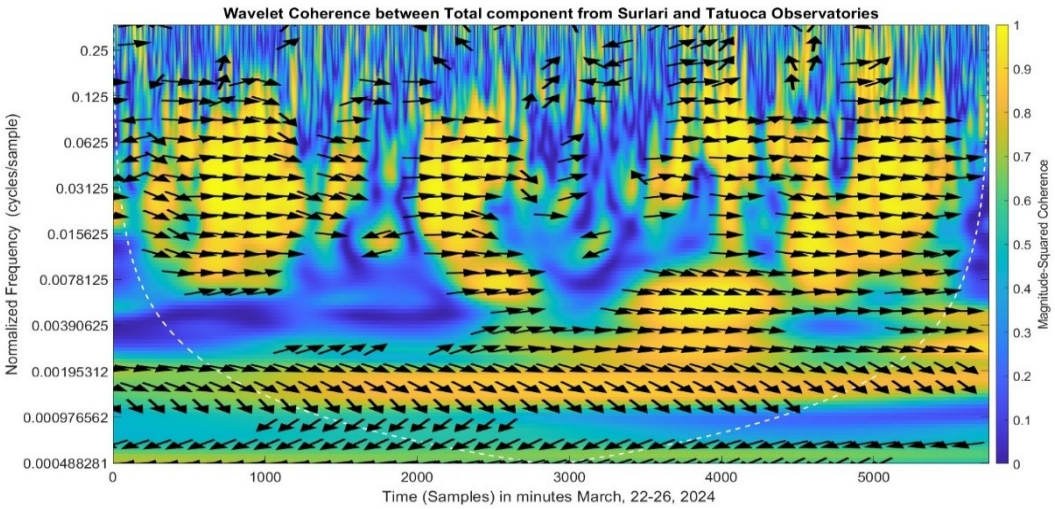


Fig. 7 – Wavelet coherence between Surlari și Tatuoca observatories, Total (F)

The arrows in the "wcoherence" plot indicate the phase relationship between the two signals at each time and frequency point (or period). The phase angle of the cross spectrum is the same as the phase difference between the signals.

The direction of the arrows in regions of high coherence can help to understand the phase relationship. For example, if the arrows point to the right, it indicates that the two signals are in phase (0 delay), and if they point to the left, it indicates an anti-phase relationship (1/2 cycle delay). A 1/4 cycle offset in a signal at a given frequency is indicated by a vertically pointing arrow.

Therefore, an arrow pointing in the northeast direction (between 0 and 1/4 cycle offset direction) corresponds to a delay of 1/8 cycle (half of 1/4) and similarly an arrow pointing in the northwest (between 1/4 and 1/2 cycle offset direction) corresponds to a 3/8 cycle delay (adding half of 1/4 to 1/4). Delays move counterclockwise.

REALIZATION OF THE WEB-GIS APPLICATION FOR MAGNETIC DECLINATION MEASUREMENTS FOR AIRPORTS IN ROMANIA

Was created, a web-GIS application on the site of Geological Institute of Romania, which can be viewed in an internet browser at the address: http://harti.igr.ro/masuratori_aeroporturi.

Figure 8 shows the thematic layers in the country-wide application.

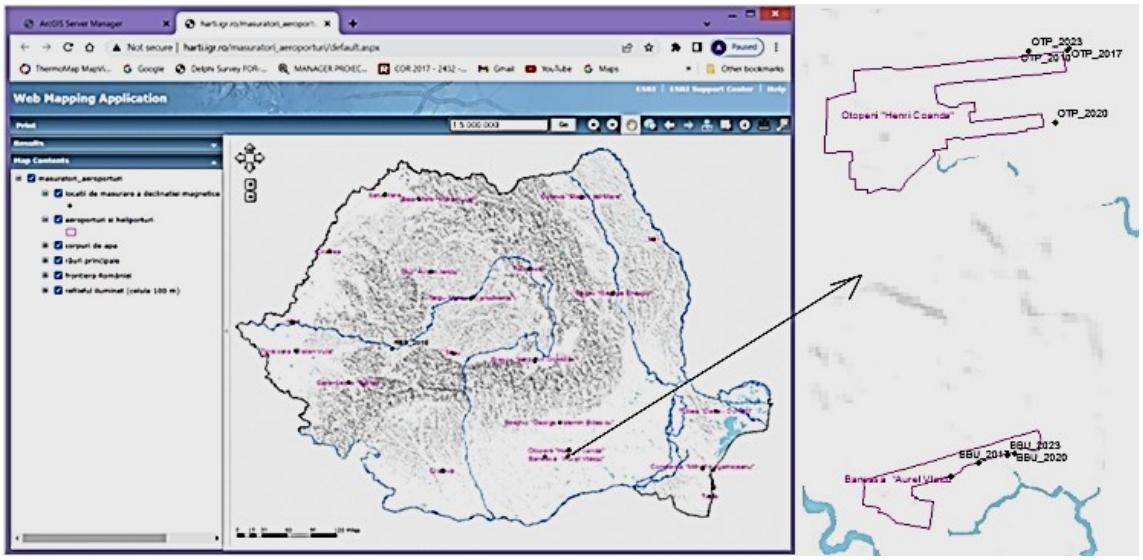


Fig. 8 - Web-GIS application regarding magnetic declination measurements in the period 2010-2023. On the right is a detail for the Otopeni and Baneasa airports that serve Bucharest; the years in which measurements were made and the values of the measured and calculated magnetic parameters are shown.

For this purpose, from the National Agency for Cadastre and Land Registration portal, the "Download TopRO50" section, the databases containing the polygons representing the airports, heliports and radio beacons for which the GIR performed geomagnetic measurements necessary for flight safety were downloaded, at the level of counties in Romania.

It was desired to use the standardized GIS databases for Romania according to the INSPIRE Directive in order to finally create a GIS application with correct data, approved at the national level. The address of Romania's download portal is http://geoportal.gov.ro/arcgis/apps/sites/#/inspire/.

All selected polygons were entered as "feature classes" in a "geodatabase file" - gdb extension. Where the databases did not contain newer airports (such as the one at Ghimbav, near Brasov, commissioned in 2022), the contour was drawn from Google Earth images.

CONCLUSION

From the analyzes performed, all the observatories in INTERMAGNET recorded simultaneous pulses during the geomagnetic storm, indicating a synchronous relationship between them. We used statistical, spectral and wavelet methods, which highlighted the strongest geomagnetic storm of the year 2024 (March 23-24), which had Kp=8.33 and Dst = - 220.

Fourier transform cannot show which of the harmonic components is present at a time in the geomagnetic data series. Wavelet analysis gives us three-dimensional information (time, frequency, amplitude) or a two-dimensional shape, when the amplitude is encoded by colour intensity levels. A first step in the wavelet analysis is Short Time Fourier Transform, applied successively with different narrow windows, for the best accuracy of

https://doi.org/10.5593/sgem2024/6.1/s28.63

time location. Increasing the window improves the resolution in frequency but decreases the resolution in time.

In wavelet analysis we can choose the many different mother functions and we can make the comparations between there.

The wavelet transform is one of the ways of representing the signals in the multi-resolution analysis where the analysed geomagnetic signal is described by a sequence of approximations that contain more and more information. Each level of approximation contains on the one hand all the information available at the previous level plus an additional detail component.

When geomagnetic data are processed by standard deconvolution algorithms, such as predictive deconvolutions, the data contain phase errors. These errors in wavelet phase arise because the time-series do not meet the strict requirements upon which deconvolution algorithms depend. Model based wavelet processing is a technique for correcting such phase errors.

To use specific Machine Learning, Deep Learning and Artificial Intelligence algorithms, as well as Auto-Regressive Integrated Moving Average, we need large databases, structured in training data for different parameters.

Based on forecast analysis we can get an estimate, but we get the maximum precision, only after the CME has occurred and we can visualize it through telescopes in the form of dark spots on the solar disk. From that moment, a geomagnetic storm is possible in an interval of two or three days.

The databases and the web-GIS application were created for the geomagnetic measurements made at the airports in Romania, being able to detail the location and the exact period when the measurements were made.

ACKNOWLEDGEMENTS

This paper was supported by Installation and Special Objective of National Interest (IOSIN) – Surlari National Geomagnetic Observatory, Core Program PN 23 39 04 01/2023 as well as by project AI-COSTSQO – Artificial Intelligence and Combined Survey Techniques for Stone Quarries Optimization, contract number: 305/2022 with UEFISCDI Romania. Also, we thank the national institutes that support them and INTERMAGNET for promoting high standards of magnetic observatory practice.

REFERENCES

[1] Asimopolos, N. S., Asimopolos, L.- 2018 - Study on the high-intensity geomagnetic storm from march 2015, based on terrestrial and satellite data, Micro and Nano Tehnologies & Space Tehnologies & Planetary Science, Issue 6.1, vol.18, pag. 593-600, ISBN 978-619-7408-50-8, ISSN 1314-2704, DOI: 10.5593/sgem2018/6.1

[2] Box,G.E.P. & Pierce, D.A. – 1970 - Distribution of the Autocorrelations in Auotoregressive moving Average Time Series Models. Journal of American Statistical Association 65. p. 1509-1526.

[3] Campbell W.H.- 1989 - Quiet daily geomagnetic fields - Reprint. - Basel; Boston; Berlin: Birkhiiuser, Aus: Pure and applied geophysics; Vol. 131, No.3

[4] Campbell W.H. – 2003 - Introduction to Geomagnetic Fields, Cambridge University Press, ISBN 978-0-521-52953-2, 1-350

[5] Clauer, C. R., McPherron, R. L. and Kivelson, M. G. – 1980 - Uncertainty in Ring Current Parameters due to the Quiet Magnetic Field Variability at Mid-Latitudes, J. Geophys. Res. 85, 633~3.

[6] Del Rosso M. P., Sebastianelli A. and Ullo S. L. – 2021 – Artificial Intelligence applied to Satellite- - based Remote Sensing data for Earth Observation, IET Telecommunications Series, 98, p. 1-221.

[7] El-Eraki M. A., Lethy A., Samy A., Deebes H.A. – 2018 - The disturbance storm time (Dst) index prediction using time delay neural network during some extreme geomagnetic storms, Academia Journal of Scientific Research 6(7): p. 295-302.

[8] Johansen, S. – 1991 - Estimation and Hypothesis Testing of Cointegration Vectors in Gaussian Vector Autoregressive Models. Econometrica 55, p. 1551-1580.

[9] https://www.intermagnet.org/

[10] https://www.mathwoks.com

https://doi.org/10.5593/sgem2024/6.1/s28.63

EXPENDITURE OPTIMAL CONTROL FOR A SATELLITE MOVING CLOSE TO THE LIBRATION POINT

Prof. DSc. L. K. Babadzanjanz[1]

Assoc. Prof. Dr. I. Yu. Pototskaya[1]

Assoc. Prof. Dr. Yu. Yu. Pupysheva[1]

Assoc. Prof. Dr. V. S. Korolev[1]

[1]St. Petersburg State University, **Russia**

ABSTRACT

Satellite motion control in the vicinity of the libration point with expenditure criteria is considered. Expenditure optimization is natural in the case, where it is necessary to keep mechanical system in the neighborhood of the equilibrium point for a long time. Disturbing factors from time to time distort this system unacceptably far from the equilibrium point, and we need to extinguish these deviations, using fuel or another resource, which reserves are limited.

Optimization of the satellite motion control according to this criterion is important not only from the economic and technical side, but also brings an environmental effect.

Features of the presented mathematical problem definition are following. While deviations from the equilibrium point are very small, its controlled motion can be by linear differential equations with constant coefficients. The admissible control is a piecewise polynomial function that blanks selected frequency components of the solution of linear equations at the terminated moment T. As the expenditure functional we use the integral of the sum of the control coordinates modules along the interval [0,T].

As the results of solving the problem, formulas and an algorithm for finding the control switching points satisfying the expenditure functional extremum necessary conditions are proposed.

Keywords: expenditure criteria, libration point, piecewise polynomial control.

INTRODUCTION

This article is a continuation of the research, which results were presented in previous works of the authors [1] – [4]. In this paper, the algorithm for finding the switching points of the satellite moving optimal control with the expenditure criteria close to the libration point is presented. Libration points are points where a small body (satellite or spacecraft) in a system of three bodies is in a state of relative equilibrium with respect to large bodies of this system (for example, Earth-Moon or Earth-Sun). Libration points have huge potential for space exploration [5] – [9]. Spacecraft located in their vicinity can remain relatively stable for a long time and perform their tasks longer. Nevertheless, disturbing factors from time to time distort the spacecraft unacceptably far from its equilibrium position, and we need to extinguish these deviations, using fuel, which

https://doi.org/10.5593/sgem2024/6.1/s28.64

reserves are limited. In order to maximize the useful stay of the spacecraft in space, fuel consumption must be saved. The engineering solution to this problem consists in sequentially switching thrusters that create multidirectional torques. To construct an optimal control mode for such thrusters it is necessary to find the time points of their switching.

Mathematical modeling of this problem has a number of features:

a) Linear ODE with constant coefficients are used to describe small deviations of the spacecraft from the equilibrium position;

b) Piecewise polynomial time functions are used to describe the control;

c) To describe the control purpose, that is, to minimize fuel consumption over time [0,T], the quality criterion in the form of the integral of the control coordinates modules sum along the interval [0,T] is used. In practice, this value is proportional to fuel consumption.

The solution to this mathematical formulation is the switching points for constructing optimal control. The mode of thrusters operation with this control will allow us to save fuel as much as possible.

THE PROBLEM DEFINITION OF CONTROL WITH EXPENDITURE CRITERIA IN LINEAR SYSTEMS

Let us consider a body of infinitesimal mass m_3, which at some time point is in the plane of motion of the attracting bodies m_1 and m_2 with zero speed relative to the rotating coordinate system. In order for the body m_3 to be in equilibrium position with respect to the other two attractive bodies, it is necessary to place it at a certain point, which is called the libration point. There are five such positions in total - two stable (triangular libration points) and three unstable (collinear libration points). Such points of the solar system bodies are of great interest for applied problems of space flight mechanics. They can be used to place communication satellites, to organize interplanetary communications, and many other problems [6].

The controlled satellite motion in the gravitational field of two attracting bodies in the vicinity of any of the five libration points is described by the Cauchy problem:

$$\frac{dx}{dt} = Ax + U(t),\ x(0) = x_0, \tag{1}$$

where $x(t) = (x_1, \dots, x_n) \in R^n$, $x_0(t) = (x_{1,0}, \dots, x_{n,0})$, $U(t) = (u_1, \dots, u_n) \in R^n$, A is a constant $(n \times n)$ matrix with real valued coefficients, and control $U(t)$ components u_k belong to the class of piecewise constant functions of time with a finite number of switching points:

$$u_k(t) = \sum_{i=1}^{r_k} \left[H\left(t - t_i^k\right) - H\left(t - \tau_i^k\right)\right]\alpha\left(t - t_i^k\right) +$$

$$+\sum_{i=1}^{q_k}\left[H\left(t-\widetilde{\tau_i^k}\right)-H\left(t-\widetilde{t_i^k}\right)\right]\beta\left(t-\widetilde{t_i^k}\right), \quad (2)$$

where

$$\alpha\left(t-t_i^k\right)=\left[a_k^0+a_k^1\left(t-t_i^k\right)+\cdots+a_k^m\left(t-t_i^k\right)^m\right]>0,$$

$$\beta\left(t-\widetilde{t_i^k}\right)=\left[b_k^0+b_k^1\left(t-\widetilde{t_i^k}\right)+\cdots+b_k^{\widetilde{m}}\left(t-\widetilde{t_i^k}\right)^{\widetilde{m}}\right]>0.$$

Two summands in (2) are positive and negative steps, where r_k is the number of positive steps and q_k is the number of negative steps; t_i^k, $\widetilde{t_i^k}$ are points of switching on control; τ_i^k, $\widetilde{\tau_i^k}$ - switching off control, and T is the last switching off point; H is the Heaviside function. Coefficients $a_k^0, a_k^1, \dots, a_k^m$ and $b_k^0, b_k^1, \dots, b_k^{\widetilde{m}}$ are given constants. The solution of Cauchy problem (1) with control (2) is a linear combination of the summands, corresponding to different eigenvalues of the matrix A. Such summands are called as frequency components of the solution. An admissible control is a kind of control as (2), such that it makes zero one selected frequency component of the solution at last moment T. If this selected component is symbolized by $\tilde{x}(T)$, this condition can be written as follows:

$$\tilde{x}(T)=0. \quad (3)$$

The functional which has to be minimized is as follows:

$$J=\sum_{k=1}^{n}\int_0^T|u_k(\theta)|d\theta. \quad (4)$$

It is called "the expenditure functional". The problem definition is the following: with fixed number of control steps r_k and q_k to find all switching points for an admissible control (including the last point T), that satisfy the necessary conditions of the expenditure functional extremum.

SATELLITE MOTION CONTROL IN THE VICINITY OF THE LIBRATION POINT

Let us consider two coordinate systems – inertial $BXYZ$ and rotating $Bxyz$ with the origin in the barycenter B of two attracting bodies (m_1, m_2). Motion plane is BXY. We write the motion equations of the point in the system $Bxyz$. The axis Bx is directed along the radius vector of the point m_1 all the time, the axis Bz coincides with the axis BZ of the inertial coordinate system. The angular rotation velocity of $Bxyz$ relative to $BXYZ$ is equal to the angular rotation velocity of the bodies relative to their barycenter.

The motion of the point in the circular restricted three-body problem is written (using canonical variables) [6]

$$\ddot{x}=\frac{(1-m)(x-x_1)}{\rho_{31}^3}-\frac{m(x-x_2)}{\rho_{32}^3}+x+2\dot{y}, \quad \ddot{y}=-\frac{(1-m)y}{\rho_{31}^3}-\frac{my}{\rho_{32}^3}+y-2\dot{x}.$$

https://doi.org/10.5593/sgem2024/6.1/s28.64

Here $\rho_{31} = \sqrt{(x-x_1)^2+y^2}$, $\rho_{32} = \sqrt{(x-x_2)^2+y^2}$, $m = m_2/(m_1+m_2)$, x_1, x_2 - centers of mass of attracting bodies. Coordinates of triangular libration points (L_4, L_5):

$$x^*_{4,5} = (1/2)(1-2m), y^*_4 = \left(\sqrt{3}/2\right), y^*_5 = \left(-\sqrt{3}/2\right).$$

The linearized equations of the satellite moving close to the triangular libration point with control $\dot{X} = AX + U$, where

$$A = \begin{pmatrix} 0 & 1 & 0 & 0 \\ 3/4 & 0 & a_k & 2 \\ 0 & 0 & 0 & 1 \\ a_r & -2 & 9/4 & 0 \end{pmatrix}, \quad X = \begin{pmatrix} \Delta x \\ \Delta \dot{x} \\ \Delta y \\ \Delta \dot{y} \end{pmatrix}, \quad U = \begin{pmatrix} 0 \\ u_1 \\ 0 \\ u_2 \end{pmatrix},$$

$a_k = (-1)^{\kappa}\left(2\sqrt{3}/4\right)(1-2m)$, k = 4,5; Δx, Δy, $\Delta \dot{x}$, $\Delta \dot{y}$ – small perturbations of normalized coordinates x, y and velocities $\dot{x}$, $\dot{y}$ in the vicinity of the libration point.

Thus, all values necessary for the application of the algorithm are presented. So, it is possible to use them to find the control switching points corresponding to the necessary conditions of the expenditure functional extremum in the problem of the satellite motion control in the vicinity of the triangular libration point. Similarly, the problem is solved in the neighborhood of collinear libration points.

THE ALGORITHM FOR FINDING THE SWITCHING POINTS

Let us make an assumption that among the eigenvalues of matrix A in system (1) there is a pair of pure imaginary eigenvalues $\pm i\,\mu$ with unit multiplicity. This pair describes an oscillation with frequency μ. There is an algorithm for finding the explicit formulas for switching points in our problem definition. As a first step of this algorithm let us split Cauchy problem (1) into two Cauchy problems. In order to do this, we make a linear substitution $x = B\xi$. Here $\xi = (y, z) = (y_1, y_2, z_1, \dots, z_{n-2}) = (\xi_1, \dots, \xi_n)$; B is nonsingular constant complex matrix, that can be chosen to satisfy the equality

$$B^{-1}AB = \begin{pmatrix} Y & 0 \\ 0 & Z \end{pmatrix}, \quad \text{where} \quad Y = \begin{pmatrix} i\mu & 0 \\ 0 & -i\mu \end{pmatrix};$$

and Z - some matrix which dimension is $(n-2)\times(n-2)$. Thus, from the Cauchy problem (1), we have derived two following Cauchy problems:

$$\dot{y} = Yy + V, \; y(0) = y_0, \tag{5}$$

$$\dot{z} = Zz + W, \; z(0) = z_0, \tag{6}$$

where

$$y_0 = Dx_0 = \left(y_{1_0}, y_{2_0}\right), \qquad z_0 = D_z x_0 = \left(z_{1_0}, \dots, z_{(n-2)_0}\right),$$

$$V = DU = (v_1, v_2), \quad W = D_z U = (w_1, \dots, w_{n-2}), \quad (V, W) = B^{-1}U,$$

$$B^{-1} = \begin{pmatrix} D \\ D_z \end{pmatrix}, \qquad D = \begin{pmatrix} d_{1,1} & \dots & d_{1,n} \\ d_{2,1} & \dots & d_{2,n} \end{pmatrix}, \quad D_z = \begin{pmatrix} d_{3,1} & \cdots & d_{3,n} \\ \vdots & \ddots & \vdots \\ d_{n,1} & \cdots & d_{n,n} \end{pmatrix}.$$

To solve the given problem, it's enough to consider only the problem (5).

The algorithm of this solution is presented in the form of the theorem [3].

The theorem. Let controlled motion of a mechanical system be determined by Cauchy problem (1) and $\lambda_{1,2} = \pm i\mu$ is a pair of pure imaginary nonmultiple eigenvalues of matrix A of this system (1). Then, if an admissible control (2) turns value $\tilde{x}(t) = \big(x(i\mu, T), x(-i\mu, T)\big)$ to zero, thus the switching points t_i^k, $\widetilde{t_i^k}$, τ_i^k, $\widetilde{\tau_i^k}$ corresponding to the necessary conditions of functional (4) extremum are determined by the following formulas:

$$\tau_i^k = \widetilde{\tau_i^k} \pm \mu^{-1}\pi \pm 2\mu^{-1}\pi l, \quad \tau_i^k = \tau_{i+1}^k \pm 2\mu^{-1}\pi \pm 2\mu^{-1}\pi l, \quad l \in Z, \tag{7}$$

$$t_1^k = t_k - \Delta_k, \quad \tau_1^k = t_k + \Delta_k, \quad \widetilde{t_1^k} = \widetilde{t_k} - \widetilde{\Delta_k}, \quad \widetilde{\tau_1^k} = \widetilde{t_k} + \widetilde{\Delta_k} \tag{8}$$

with using the results of unconstrained minimization on all variables of the functional

$$\Phi = L_1^2 + L_2^2 + \sum_{k=1}^{n} \left[\left(N_{1,m}^k\right)^2 + \left(N_{2,m}^k\right)^2 + \left(N_{1,\tilde{m}}^k\right)^2 + \left(N_{1,\tilde{m}}^k\right)^2 \right] \tag{9}$$

Here the values in the functional (9) are introduced by the following expressions:

$$N_{1,m}^k = \frac{\partial S}{\partial \Delta_k}, \quad N_{1,\tilde{m}}^k = \frac{\partial S}{\partial \widetilde{\Delta_k}}, \quad N_{2,m}^k = \frac{\partial S}{\partial t_k}, \quad N_{2,\tilde{m}}^k = \frac{\partial S}{\partial \widetilde{t_k}}, \tag{10}$$

$$S = M + \lambda_1 L_1 + \lambda_2 L_2,$$

$$M = \sum_{k=1}^{n} \left(r_k \sum_{l=0}^{m} a_k^l \frac{(2\Delta_k)^{l+1}}{l+1} + q_k \sum_{l=0}^{\tilde{m}} b_k^l \frac{\left(2\widetilde{\Delta_k}\right)^{l+1}}{l+1} \right), \tag{11}$$

$$L_1 = y'_{1_0} + \frac{1}{\mu} \sum_{k=1}^{n} \left(r_k \left[d'_{1k} C_{1,m}^k + d_{1k}^* C_{2,m}^k \right] - q_k \left[d'_{1k} C_{1,\tilde{m}}^k + d_{1k}^* C_{2,\tilde{m}}^k \right] \right) = 0,$$

$$L_2 = y_{1_0}^* + \frac{1}{\mu} \sum_{k=1}^{n} \left(r_k \left[d_{1k}^* C_{1,m}^k - d'_{1k} C_{2,m}^k \right] - q_k \left[d_{1k}^* C_{1,\tilde{m}}^k - d'_{1k} C_{2,\tilde{m}}^k \right] \right) = 0, \tag{12}$$

$$C_{1,\nu}^k = R_{1,\nu}^k(\gamma) \sin \mu (\varphi + \psi) + R_{2,\nu}^k(\gamma) \cos \mu (\varphi + \psi) -$$
$$- c_{1,\nu}^k \sin \mu (\varphi - \psi) - c_{2,\nu}^k \cos \mu (\varphi - \psi), \tag{13}$$
$$C_{2,\nu}^k = -R_{1,\nu}^k(\gamma) \cos \mu (\varphi + \psi) + R_{2,\nu}^k(\gamma) \sin \mu (\varphi + \psi) +$$
$$+ c_{1,\nu}^k \cos \mu (\varphi - \psi) - c_{2,\nu}^k \sin \mu (\varphi - \psi),$$

https://doi.org/10.5593/sgem2024/6.1/s28.64

$$R_{1,\nu}^{k}(\gamma)=\sum_{j=0}^{E\left(\frac{\nu}{2}\right)}\frac{(-1)^{j}}{\mu^{2j}}\left(\gamma_{k}^{2j}(2j)!+\sum_{l=2j+1}^{\nu}\gamma_{k}^{l}\frac{l!}{(l-2j)!}(2\psi)^{l-2j}\right),$$

$$R_{2,\nu}^{k}(\gamma)=\sum_{j=0}^{E\left(\frac{\nu+1}{2}\right)}\frac{(-1)^{j-1}}{\mu^{2j-1}}\left(\gamma_{k}^{2j-1}(2j-1)!+\sum_{l=2j}^{\nu}\gamma_{k}^{l}\frac{l!}{(l-2j+1)!}(2\psi)^{l-2j+1}\right), \quad (14)$$

$$c_{1,\nu}^{k}(\gamma)=\sum_{j=0}^{E\left(\frac{\nu}{2}\right)}\frac{(-1)^{j}}{\mu^{2j}}\gamma_{k}^{2j}(2j)!, \qquad c_{2,\nu}^{k}(\gamma)=\sum_{j=0}^{E\left(\frac{\nu+1}{2}\right)}\frac{(-1)^{j-1}}{\mu^{2j-1}}\gamma_{k}^{2j-1}(2j-1)!. \quad (15)$$

In formulas (13)-(15), if $\nu=m$, then $\varphi=t_k$, $\psi=\Delta_k$, $\gamma=a$. If $\nu=\widetilde{m}$, then $\varphi=\widetilde{t_k}$, $\psi=\widetilde{\Delta_k}$, $\gamma=b$. $E(s)$ means the quotient of real number s.

The value $2\Delta_k$ is the width of positive control step for u_k, t_k is the middle moment for this step. Correspondingly, $2\widetilde{\Delta_k}$ – the width of negative control step for u_k, $\widetilde{t_k}$ – the middle moment for this step. The values y'_{1_0} and $y^*_{1_0}$ are coefficients of the real and imaginary parts of y_{1_0} correspondingly. Coefficients λ_1, λ_2 are the Lagrange multipliers which allow to formulate the problem of unconstrained minimization of the functional (9). The values λ_1, λ_2, t_k, Δ_k, $\widetilde{t_k}$, $\widetilde{\Delta_k}$ are found numerically from solving this problem by LS method. After that, using (7), (8) formulas, it's possible to calculate all switching points for each index k.

Description of the algorithm of numerical solving was presented in previous works of the authors [2], [3].

CONCLUSION

Therefore, in the presented article, the problem of extending the spacecraft's working in outer space in the vicinity of the libration point is considered. This task is reduced to the problem of minimizing the fuel used by thrusters to stabilize spacecraft near its equilibrium position. The mathematical solution to this problem is to find the switching points of the optimal thrusters operation mode, which minimizes fuel consumption. Such minimization has not only an economic, but also an environmental effect, reducing the release of pollutants into space.

The use of only approximate numerical methods to solve a mathematical problem invariably leads to an accumulation of error, and, consequently, to inaccuracy of the solution. Only analytical methods and explicit formulas can provide accurate results. The greater their share in the algorithm used, the more accurate the solution.

This paper presents algorithm for constructing the expenditure optimal control of satellite motion in the vicinity of the triangular libration point. The algorithm for finding these switching points consists of analytical and numerical parts. The analytical part,

formulated in the form of the theorem, includes formulas (7)-(15) for further numerical implementation.

Description of the algorithm of numerical solving was presented in previous works of the authors [2], [4].

The results given in the theorem allow us to extinguish oscillations of the satellite moving close to the collinear libration point.

REFERENCES

[1] Babadzanjanz L.K., Pototskaya I.Yu., Pupysheva Yu.Yu., Control with Expenditure Criteria in Rotational Motion of the Satellite Moving along a Circular Orbit, Greece, AIP Conference Proceeding Vol.1648, American Institute of Physics, 2015, pp.1-4.

[2] Babadzanjanz L.K., Pototskaya I.Yu., Pupysheva Yu.Yu., Expenditure Optimization in a Problem of Controlled Motion of Mechanical Systems, Greece, AIP Conference Proceeding Vol.1738, American Institute of Physics, 2016, pp.1-4.

[3] Alesova I.M., Babadzanjanz L.K., Pototskaya I.Yu., Pupysheva Yu.Yu., Saakyan A.T., Piecewise polynomial control in mechanical systems, Greece, AIP Conference Proceeding Vol. 1863, American Institute of Physics, 2017, pp.1-4.

[4] Alesova I.M., Babadzanjanz L.K., Bregman A.M., Bregman K.M., Pototskaya I.Yu., Pupysheva Yu.Yu., Saakyan A.T., Piecewise constant control of linear mechanical systems in the general case, Greece, AIP Conference Proceeding Vol. 1978, American Institute of Physics, 2018, pp.1-4.

[5] Farquhar, R.W., Dunham, D.W. Use of Libration-Point Orbits for Space Observatories. In: Kondo, Y. (eds) Observatories in Earth Orbit and Beyond. Astrophysics and Space Science Library, vol 166. Springer, Dordrecht, 1990. https://doi.org/10.1007/978-94-011-3454-5_52

[6] Szebehely Victor, Theory of Orbits, Academic Press, New York, 1967.

[7] Ardaens J.S., D'Amico S. Control of formation flying spacecraft at a Lagrange point. DLR, 2008.

[8] Markeev A.P. Tochki libratsii v nebesnoy mekhanike i kosmodinamike [Vibration points in celestial mechanics and cosmodynamics]. Moscow, Nauka Publ., 1978 (in Russ.).

[9] Korolev V., Polyakhova E., Pototskaya I., Prospects Of Photogravitational Celestial Mechanics For Space Systems, Bulgaria, SGEM Conference Proceeding, 2023, 23 (6.1) pp. 439–446.

https://doi.org/10.5593/sgem2024/6.1/s28.64

LANDSLIDE SUSCEPTIBILITY MAPPING IN LUNAR SOUTH POLE REGION

Andrea Ermini[1,2]

Assoc. Prof. Riccardo Salvini[1]

Full Prof. Pier Simone Marrocchesi[3]

[1]Department of Physical Sciences, Earth and Environment and Centre of Geotechnologies, University of Siena, **Italy**

[2]National PhD Program in Space Science and Technology, University of Trento, **Italy**.
[3]Department of Physical Sciences, Earth and Environment, University of Siena, **Italy**

ABSTRACT

The study addresses a challenge in planetary exploration, focusing on landslide susceptibility on the Lunar South Pole Region (LSPR), fundamental for future lunar missions. Features like permanently shadowed regions and water ice deposits attract scientific attention but issues related to rugged terrain and dynamic geological processes must also to be considered. The photointerpretation of data from Lunar Reconnaissance Orbiter (LRO) mission, allowed to create a landslides inventory map. The Frequency Ratio (FR) model was applied to generate a landslide susceptibility map (LSM). Geological and morphological factors were derived from existing maps and LRO data. Peak Ground Acceleration (PGA) variation and epicentral distance were used to define seismic hazard zones. LSM accuracy was evaluated using the Area Under the Curve (AUC) method. The study allows to identify geological formations susceptible to seismic-induced landslides, aiding site selection for future lunar missions. This interdisciplinary approach integrates planetary geology, remote sensing, and GIS software and it contributes to lunar exploration and exploitation for scientific and resource purposes allowing to optimize the Moon involvement in solar system exploration.

Keywords: Moon, Lunar South Pole Region, Landslide Susceptibility Mapping

INTRODUCTION

Landslides are recognized as dominant geomorphic events of morphological evolution in most mountainous and hilly landscapes. These important geomorphological phenomena, which can often occur on steep slopes, have been widely studied on the Earth, both in subaerial [1] and submarine [2] environments. Similarly, different types of gravitational events have been observed on other planets and minor bodies such as the Moon [3]. This study aims to contribute to the understanding of landslide susceptibility on the lunar surface, focusing specifically on the Lunar South Pole Region (LSPR), which holds scientific and strategic importance for future lunar exploration endeavors. The LSPR has garnered increasing attention due to its geological features, including Permanently Shadowed Regions (PSRs) and volatile deposits such as water ice. Many space agencies are planning or actively working on lunar missions. For example, NASA's Artemis

https://doi.org/10.5593/sgem2024/6.1/s28.65

missions prepare to land the first woman and man near the south pole of Moon in 2024, followed by a series of advanced human and robotic missions, for which 13 candidate landing regions have been selected within 6° latitude from the South Pole. In this work, to evaluate the safety conditions, not only for the sites chosen for the Artemis lunar mission landing, but also for future missions, a Landslide Susceptibility Map (LSM) was created in LSPR. Starting from a landslide inventory map, created through the photointerpretation of data from the Lunar Reconnaissance Orbiter mission (LRO), the Frequency Ratio model (FR) was utilized to assess the probability of landslide occurrence in different zones. In this type of study, it is crucial to consider both causative factors, which influence the predisposition of an area to geomorphological phenomena over long periods, and triggering factors, which are short-term events that can originate landslides. Causative factors, represented by geological and morphological characteristics, derived from existing thematic maps and by the processing of Lunar Orbiter Laser Altimeter (LOLA) Digital Elevation Model (DEM). This activity has been carried within ESRI™ ArcGIS Pro software environment. Considering the studies already carried out on the Earth, many authors have analyzed the contribution of heavy rainfall [4] and earthquakes [5] as triggering factors of landslides. Similarly, on the Moon, in the absence of rainfall, recent scientific papers proposed by [6-7], assert that moonquakes, produced by lobate thrust fault scarps movement, have the greatest impact on regolith landslides that are triggered in the steepest slopes of impact craters. To include the contribution of moonquakes as a triggering factor into the FR model, it was decided to consider the PGA variation as function of epicentral distance, as suggested by previous studies [6-7]. Once the causative and triggering factors were implemented into the FR model and the LSM was produced, its accuracy was assessed by using the AUC method.

MATERIALS AND METHODS

Landslide inventory

Landslide inventory, in general, is produced by the systematic mapping of existing gravitational events using various techniques, including both fieldwork and the photointerpretation of aerial photographs or satellite image [8]. In this study, the identification and mapping of landslides on the lunar surface were obtained by the analysis of images from the Lunar Reconnaissance Orbiter Camera (LROC) Wide Angle Camera (WAC), at a spatial resolution of 100 meters, and hillshaded LOLA DEM (118 m/pixel resolution).

Based on work proposed by [9], to analyse the effect of gravity in slope failure mechanism, the landslides research was focused on probable post-impact gravitational event features, as opposed to terraces formed during the modification stage of impact cratering. The objective is to address mass movements propelled by the gravity, rather than those triggered by the energy released during the impact process itself. Figure 1a shows an example of post-impact crater landslide where dashed line and polygon indicate crown and the landslide body, respectively. The landslide inventory dataset, in the current version of the study, consists of forty-six landslides in total. For susceptibility mapping, landslide polygons were randomly divided into 70% for training and 30% for validation

datasets (Figura 1b). The training dataset was used for constructing the predictive model while the validation dataset was used for LSM validation.

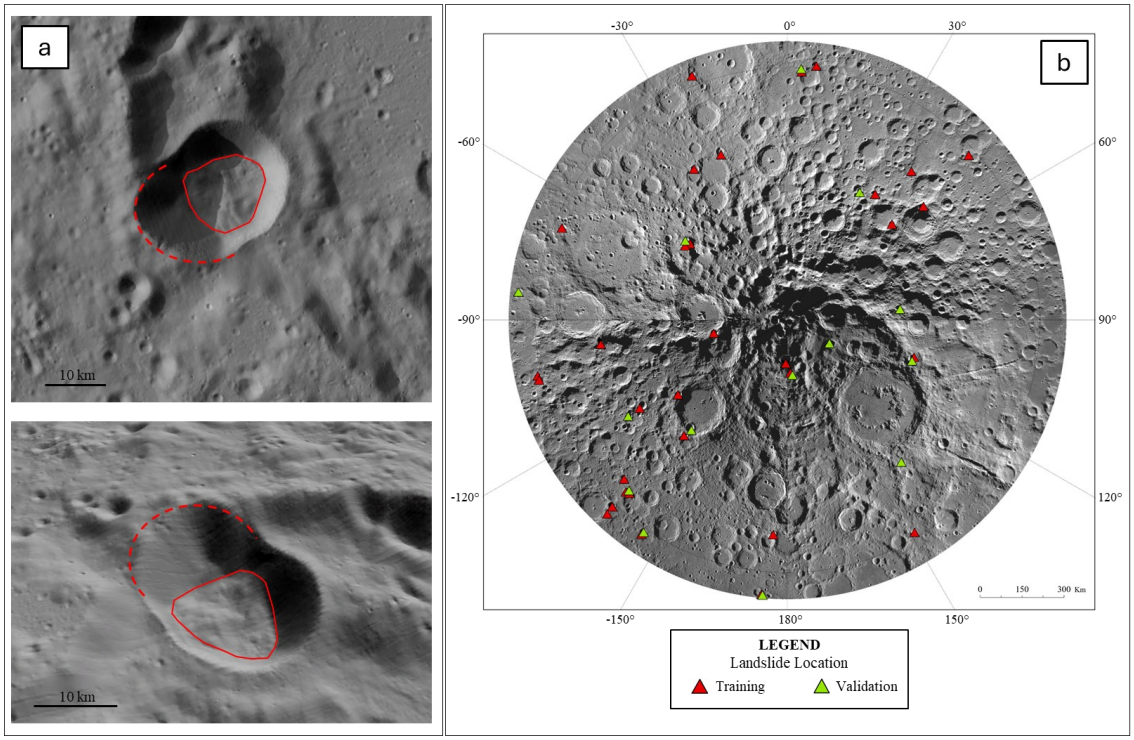


Figure 1: (a) Example of a landslide mapped through photointerpretation analysis: planimetric view with highlighted the crown and the landslide body (top); perspective view of the landslide (bottom). (b) Landslide locations subdivided in training and validation dataset in Lunar South Pole Region.

Causative and triggering factors

To conduct a landslide susceptibility analysis in the study area, a spatial database containing causative and triggering factors was created using the tools available within Esri™ ArcGIS Pro software. In this work, a total of four causative factors, including elevation, slope, aspect and geology (Figure 2) were used. The topographic parameters were derived from the elaboration of LOLA DEM, while the information regarding the outcropping lithologies was obtained by rasterizing the geological polygonal data provided by [10]. All these factors provide information about predisposition of the area to geomorphological phenomena over extended periods. Elevation is an important parameter to be considered for the analysis of landslide susceptibility in the LSPR. Firstly, it influences the distribution of local gravity which influences the slopes stability. Furthermore, it affects the thermal regime, with lower temperatures in higher regions. Aspect, instead, indicates the slopes dip direction and it determines variations in soil heating due to sun position. The consequent thermal differences can affect the physical-mechanical properties of the regolith and they can modify the slope stability conditions and the presence of materials on the lunar surface. The slope of the terrain in the LSPR is crucial for assessing landslide susceptibility. Steeper slopes increase the risk of collapses and terrain instability, directly influencing material distribution. The interaction of the slope with parameters like aspect and elevation provides further insights into lunar terrain dynamics. Finally, geology and soil composition play a fundamental role in slope stability analysis: terrains characterized by more cohesive rocks tend to be more stable.

https://doi.org/10.5593/sgem2024/6.1/s28.65

There are no strict rules that guide the selection and utilization of triggering factors in different statistical approaches for landslide susceptibility mapping: Basing on the data and information provided by [6-7], moonquakes generated by movements along lobate scarps faults are identified as possible triggering factors for post-impact crater landslides. Specifically, [6] states that considering the occurrence of moonquakes with Mw 1-4 along lobate scarps at focal depth of 1 km, the variation in PGA is a function of epicentral distance. This acceleration reaches a not-significant level (~ 0.03g) at father distances, which were estimated by [6] at 3, 12, 30 and 70 km, respectively, for M_w 1, 2, 3 and 4 moonquakes. Hence, four seismic hazard zones around each scarp were created (Figure 2e) and classified accordingly. Finally, all causative and triggering factor maps were converted into co-registered raster maps with the same coordinate system (Moon 2000 South Pole Stereographic) and the same pixel size (118 x 118 m). The weight of each causative and triggering factor was subsequently calculated by its relationship with the landslide locations.

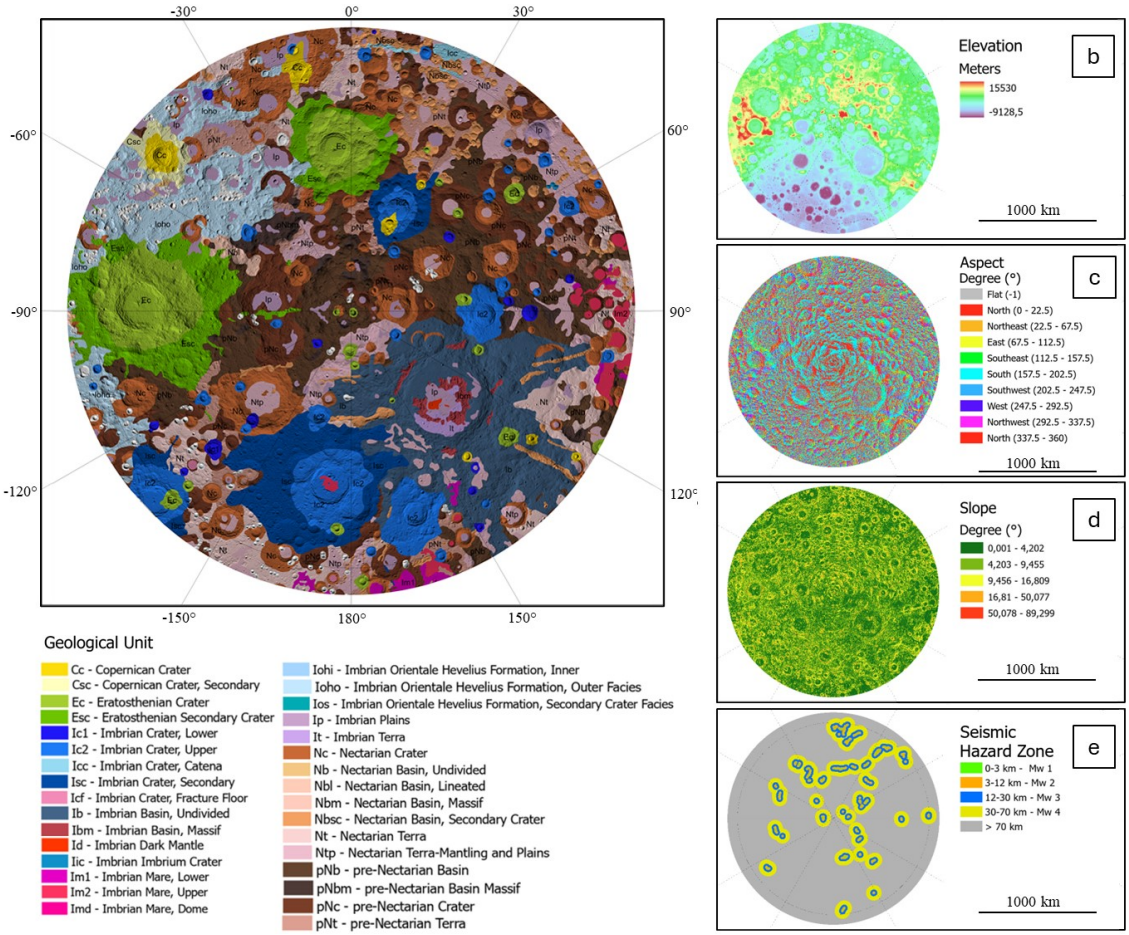


Figure 2: Landslide causative and triggering factors: Geology (a), modified by [10]; Elevation (b); Aspect (c); Slope (d); Seismic Hazard Zone (e).

Frequency Ratio (FR) model and validation

The Frequency Ratio (FR) is a bivariate statistical model widely used in landslide susceptibility mapping on Earth [11]. It calculates the ratio between the presence of landslides within each factor class compared to the total area of that class on the map. A FR of 1 indicates an average susceptibility, values greater than 1 suggest higher

susceptibility, while values below 1 indicate lower susceptibility. The FR was be obtained by the following Equation 1:

$$FR = \left[\frac{N_{pix}(SX_i)/\sum_{i=1}^{m} SX_i}{N_{pix}(X_j)/\sum_{j=1}^{n} N_{pix}(X_j)}\right] \quad (1)$$

where N_{pix} (SX_i) represents the number of landslide pixels in class i of the factor X; $N_{pix}(X_j)$ is the total number of pixels within factor X_j; m is the number of classes in factor X_i; and n is the total number of factors.
Consequently, LSM can be calculated by summing the FR of all of the factors according to the following Equation 2:

$$LSM = \sum_{j=1}^{n} FR_j \quad (2)$$

Once the landslide susceptibility map was produced, its validation is necessary in order to check its predictive accuracy. In the present study, the performance of the LSM produced by FR model, was evaluated using the AUC method that establishes the accuracy by creating success and prediction rate curves. The prediction rate curve indicates the model efficiency to predict future landslides and the comparison of the validation dataset with the landslide susceptibility map provides the prediction rate curve. The AUC values ranging from 0.5 to 1.0 are used to assess the model accuracy. The qualitative relationship between AUC and prediction accuracy can be classified as it follows; excellent (0.9-1.0); very good (0.8-0.9); good (0.7-0.8); average (0.6-0.7), and fair (0.5-0.6).

RESULTS

The FR model was used to find the correlation between the landslide locations and the classes of each causative and triggering factor (Figure 3a). The obtained landslide susceptibility map, shown in Figure 3b, allows the identification of zones with variable probability of landslides occurrence.
Moreover, the total surface of each susceptibility class was calculated, and it varies as it follows: Very low (229.31 km^2 – 29%); Low (226.54 km^2 – 29%); Moderate (227.77 km^2 – 29%); High (58.18 km^2 – 7%); Very High (42.31 km^2 – 5%).
Figure 4 shows the prediction rate accuracy of the LSM as computed by using the AUC method and the landslide validation dataset: the obtained AUC reaches a value of 61.85%.

DISCUSSION

This study represents a preliminary tentative approach to investigate the landslide susceptibility in the LSPR through a data-driven analysis of topographic and geological data. Aim of the work was to identify and to understand the factors that influence the potential regolith instability in LSPR. Using the FR model, it was possible to specifically identify the classes, within each causative and triggering factor, that could influence the landslide susceptibility (i.e., FR greater than 1). To what concerns the elevation parameter, which shows high FR values up to of 2.5 within the altitude range of - 3464 - 6388 m, some Authors [12] indicate a close direct correlation with the gravity which represent one of the most important causative factors for landslide events. To what concerns the aspect parameter, it must be said that FR values above 1 of N, NW and SW oriented slopes can be correlated with illumination conditions and, consequently, with temperature variations. In fact, the rate of diurnal temperature change is lower than 2 K/min on the Moon, but grain-scale stresses induced by diurnal temperature changes are

https://doi.org/10.5593/sgem2024/6.1/s28.65

about 100 MPa [13]. This magnitude of stress is comparable to the typical strength of lunar rocks [13]; temperature changes lead to the reorientation of grains, causing differential expansion of the material to the point of inducing movements.

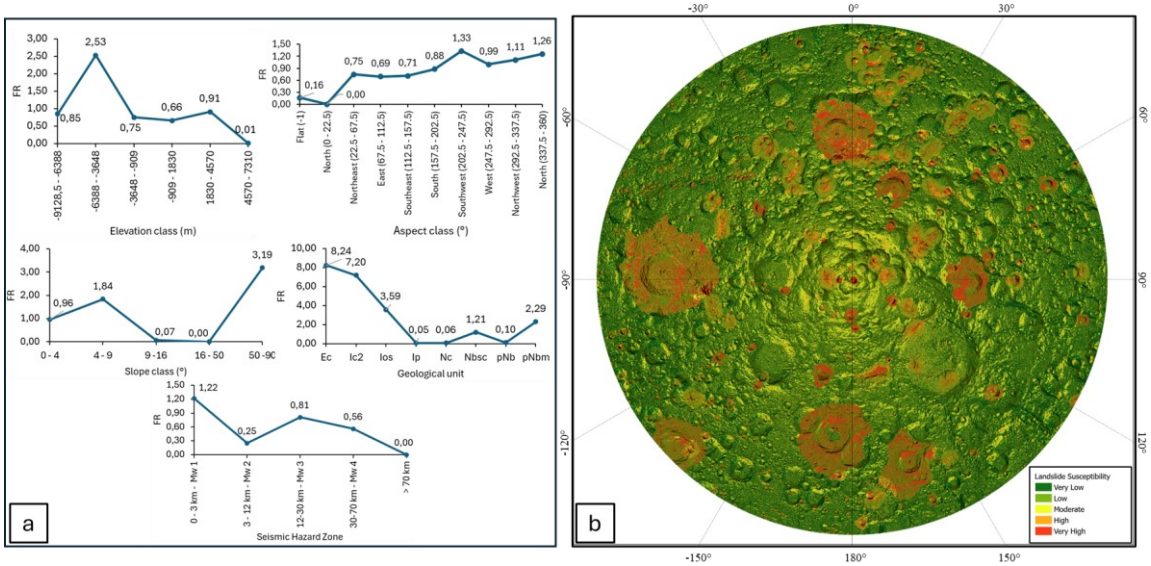


Figure 3: Results of the application of the FR model for each class of causative and triggering factors (a); Landslide susceptibility map of LSPR (b).

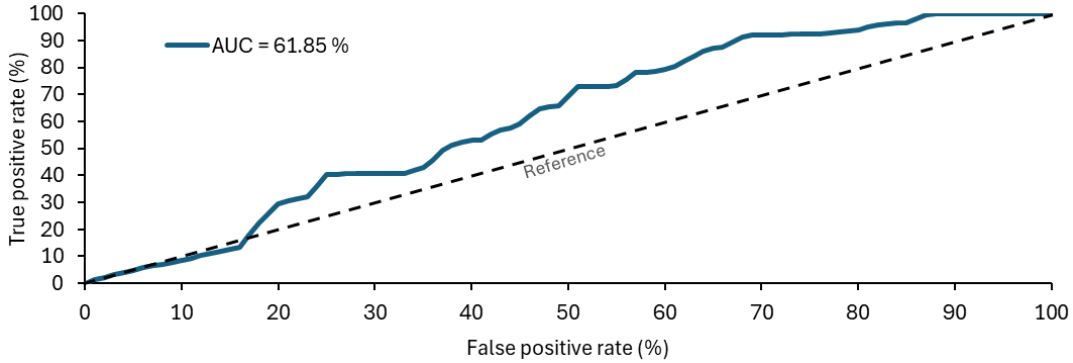


Figure 4: Result of the application of the Area Under the Curve (AUC) method.

Not only the stresses induced by temperature variations and gravity can be considered as guilty of failures: for example, analysing the FR of the slope parameter, it is possible to notice how it reaches values of 3.19, for the 50°-90° class, and again high values up to 1.84 for the 4°-9° class. The latter can be explained by considering that some of the mapped landslides have significant movements until their body settles on gentle slopes: their occurrence has anyhow an influence on the model results. However, of greater importance is the high FR value reached for the 50°-90° slope class. In fact, when the slope exceeds the internal friction angle of the lunar regolith, typically ranging between 25° and 50° [14], even a slight disturbance or change in environmental conditions can cause material displacement on the lunar surface. This can occur, for example, in presence of seismic activity, as highlighted by high value of FR reached for the seismic hazard zone 0-3 km – M_w 1 (i.e., FR = 1.22): the closer the lobate scarps are, the greater is the probability of landslides occurrence. Concerning the geology, high FR value was reached in geological unit in primary or secondary craters, where the rock material is weathered due to meteorite impacts that negatively affect the cohesion. The LSM, produced by the

application of FR bivariate model, indicates zones with high probability of landslide occurrence allowing for the identification of hazardous areas. Moreover, LSM highlights that 58% of LSPR surface has a low probability of landslide occurrence and this information can be useful for future landing planning and for feasibility analysis of equipment installation. The quality of the landslide susceptibility model is reflected in the AUC value, which stands at 61.85%, indicating a moderate predictive capability. This result can be explained by the use of a basic predictive model, like the FR one, and by the absence of causative factors such as temperature, both on the surface and in depth, and the water ice.

CONCLUSIONS

This study focuses on landslide susceptibility mapping in the Lunar South Pole Region which is a valuable information for future lunar missions. By utilizing Lunar Reconnaissance Orbiter data, a landslide event map was created and through the implementation of causative (elevation, slope, aspect and geology) and triggering factors (seismic hazard zone) in the Frequency Ratio model, the susceptibility map was created. This output allowed to differentiate zones according to their landslide occurrence probability and to analyse the contribution of each class of different causative and triggering factors. The landslide susceptibility map, that in the present version shows a moderate prediction capability, could be improved by using more advanced predictive models (ex. Weight of Evidence, Random Forest) and by implementing additional causative and triggering factors such as the surface temperature and the water ice distribution. In conclusion, the integration of planetary geology, remote sensing, and GIS facilitated comprehensive analysis of landslide susceptibility in LSPR that could be utilized in site selection for future lunar missions and to advance our understanding of the Moon in solar system exploration.

ACKNOWLEDGEMENTS

This paper was produced while attending the PhD program in Space Science and Technology at the University of Trento, Cycle XXXIX, with the support of a scholarship financed by the Ministerial Decree no. 118 of 2nd march 2023, based on the NRRP - funded by the European Union - NextGenerationEU - Mission 4 "Education and Research", Component 1 "Enhancement of the offer of educational services: from nurseries to universities" - Investment 4.1 "Extension of the number of research doctorates and innovative doctorates for public administration and cultural heritage"

REFERENCES

[1] Osawa H., Matsushi Y., Matsuura S., Okamoto, Semiempirical modeling of the transient response of pore pressure to rainfall and snowmelt in a dormant landslide. Landslides, 21, pp. 245–256, 2024;

[2] Nouri M., Rashidi, A., Montazeri Namin, M., Shugar D.H., Submarine landslide tsunami hazard assessment for the western Makran based on a deterministic approach, Natural Hazards,118, pp.1117-1136, 2023;

[3] Huang Y., Zhang J. Li B., Chen S., Slope Stability Analysis and Soil Mechanical Properties of Impact Craters around the Lunar South Pole, Remote Sensing, 16, pp 371, 2024;

https://doi.org/10.5593/sgem2024/6.1/s28.65

[4] Kincey M.E., Rosser N.J., Swirad Z.M., Robinson T.R., Shrestha R., Pujara D.S., Basyal G.K., Densmore A.L., Arrell K.J., Oven A., Dunant A., National-scale rainfall-triggered landslide susceptibility and exposure in Nepal, Earth's Future, 12(2), 2024;

[5] Micu M., Micu D., Havenith H.B., Earthquake-induced landslide hazard assessment in the Vrancea Seismic Region (Eastern Carpathians, Romania): Constraints and perspectives, Geomorphology, 427, 108635, 2023;

[6] Mishra A., Senthil Kumar P., Spatial and temporal distribution of lobate scarps in the lunar south polar region: Evidence for latitudinal variation of scarp geometry, kinematics and formation ages, neo-tectonic activity and sources of potential seismic risks at the Artemis candidate landing regions, Geophysical Research Letters, 49, 2022;

[7] Watters T.R., Schmerr N.C., Weber R.C., Johnson C.L., Speyerer E.J., Robinson M.S., Banks M.E., Tectonics and Seismicity of the Lunar South Polar Region, The Planetary Science Journal, 5(1), 22, 2024;

[8] Ardizzone F., Bucci F., Cardinali M., Fiorucci F., Pisano L., Santangelo M., Zumpano, V., Geomorphological landslide inventory map of the Daunia Apennines, southern Italy, Earth System Science Data, 15(2), pp. 753-767, 2023;

[9] Brunetti M.T., Xiao, Z., Komatsu G., Peruccacci S., Guzzetti F., Large Landslides in Lunar and Mercurian Impact Craters, 46th Lunar and Planetary Science Conference, The Woodlands, Texas, pp.1-2, 2015;

[10] Fortezzo C.M., Spudis P.D., Harrel S.L., Release of the Digital Unified Global Geologic Map of the Moon At 1:5,000,000 Scale, 51st Lunar and Planetary Science Conference, Lunar and Planetary Institute, Houston, TX, 2020;

[11] Xu K., Zhao Z., Chen W., Ma J., Liu F., Zhang Y., Ren Z., Comparative study on landslide susceptibility mapping based on different ratios of training samples and testing samples by using RF and FR-RF models, Natural Hazards Research, 4(1), pp. 62-74, 2024;

[12] Goossens S., Sabaka T.J., Nicholas J.B., Lemoine F.G., Rowlands D.D., Mazarico E., Neumann G.A., Smith D.E., Zuber M.T., High-resolution local gravity model of the south pole of the Moon from GRAIL extended mission data, Geophysical Research Letter, 41, pp. 3367–3374, 2014;

[13] Li K., Wang J., Shi Y., A review of studies on mass-movements on the Moon, Frontiers in Astronomy and Space Sciences, 10, 2023;

[14] Heiken G.H.V., David T., French B.M., Lunar Sourcebook, a User’s Guide to the Moon, Cambridge University Press, Cambridge, UK, 1991.

PROSPECT AND PROVOCATION OF SUSTAINABLE LUNAR ACTIVITIES

Dr. eng. cosm. Dumitru-Dorin Prunariu[1,2]

Prof. dr. eng. habil. Ildiko Tulbure[3,4,5]

[1]Romanian Space Agency, Bucuresti, **Romania**
[2]Association of Space Explorers, ASE - Europe, Illkirch – Graffenstaden, **France**
[3]University "1 Decembrie 1918", Alba Iulia, **Romania**
[4]Technical University of Cluj-Napoca, **Romania**
[5]Clausthal University of Technology, **Germany**

ABSTRACT

Technological advance has assured humanity's desire to increase its quality of life, anyway humanity is currently confronted with several global challenges, their complexity bases on their interconnectedness, and on fast changes in technological field. Present space activities are directed to explore the potential of diverse celestial bodies to have hosted life. In this context the Moon Village Association, MVA has as its main objective creating a global informal forum for governments, industry, academia for debating the Moon Village concept. MVA fosters cooperation for existing or planned global moon exploration programs by establishing the Global Expert Group on Sustainable Lunar Activities, GEGSLA. On a global level the United Nations Office for Outer Space Activities, UNOOSA, through its Committee, Policy, and Legal Affairs Section, CPLA provides main support to the United Nations Committee on the Peaceful Uses of Outer Space, UN-COPUOS. By the delegation of Romania, COPUOS has recently prepared a Proposal on a Consultative Mechanism on Lunar Activities, stating that lunar missions will for sure be carried out soon through efforts of space agencies and commercial stakeholders. In this context COPUOS is emphasizing the need to preserve the peaceful use of outer space by starting a new era of sustainable space exploration. This vision is urging global cooperation for shaping sustainable lunar activities, an Action Team on Lunar Activities Consultation, ATLAC, being proposed by the first author of this contribution. Therefore, some technical and operational issues are debated, which could be faced by lunar operators, being brought into debates by ATLAC with the goal of ensuring sustainable lunar activities.

Keywords: Space activities, Moon Village Association, UN-COPUOS, Sustainable Lunar Activities, ATLAC

INTRODUCTION

Currently humanity is confronted with several global challenges, as to be observed in Figure 1, as resource and energy consumption, environmental pollution and increase of world population being interconnected to each other making all this issue a complex one [12]. After defining 1987 the concept of sustainable development in the Brundtland-Report [5] and after accepting it as being the potential answer to overcome recognized challenges, other new debates started regarding its concrete applying manner.

https://doi.org/10.5593/sgem2024/6.1/s28.66

Nowadays the vision of human sustainability is debated from different points of view especially in scientific literature on a global level also referring to different issues regarding space flights and activities having the goal of moving to space [1, 9, 14].

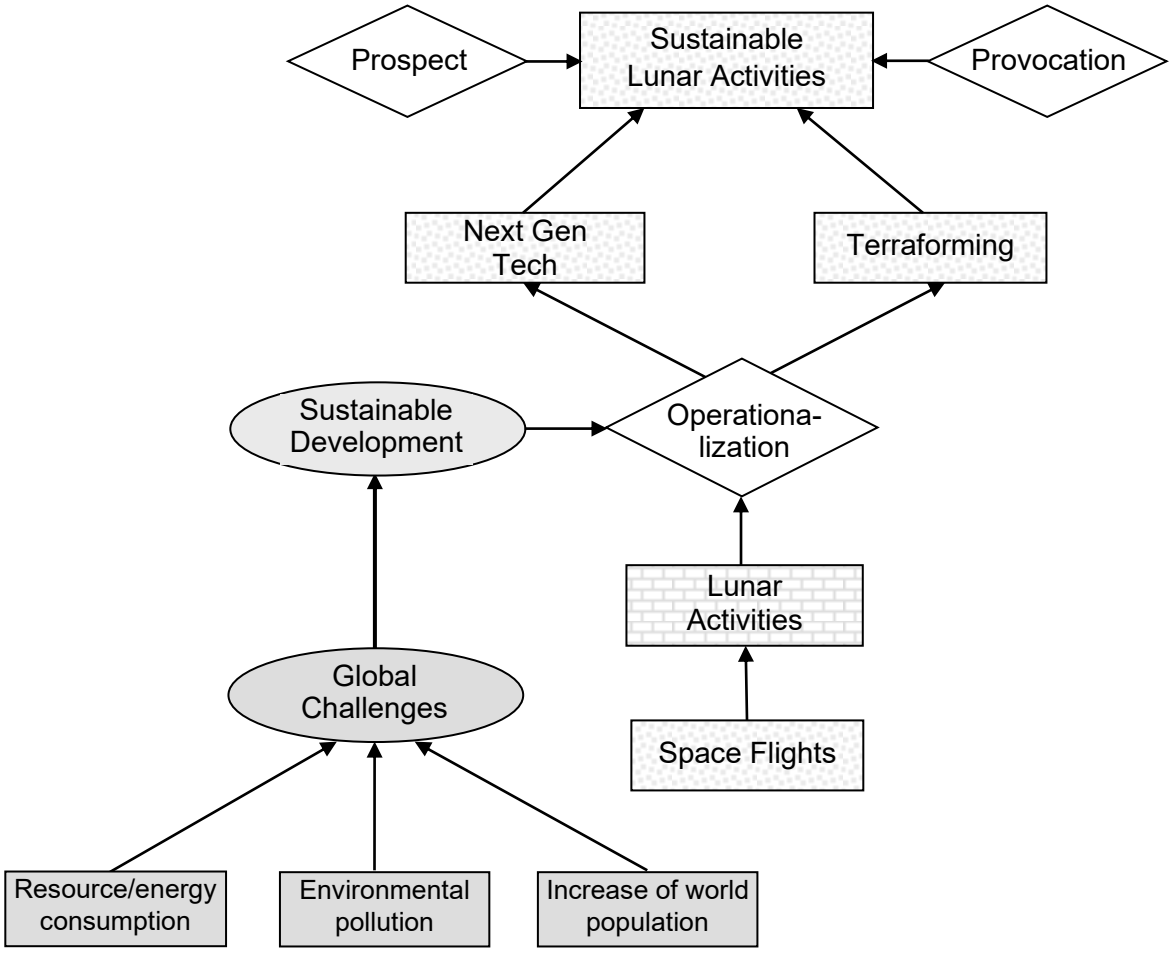


Figure 1: Global Challenges and Sustainable Development Operationalization by Sustainable Lunar Activities

It should be considered the fact that real concrete situations can be very different to each other in different regions and countries in the world [12]. Recently engaged debates to try finding best solution for sustainability operationalization highlighted the possibility of moving to space by intensifying space activities and encouraging ambitious initiatives and programs connected to terraforming other planets by shaping needed technological applications known as "Next Gen Tech" [1, 8, 9]. The future of space exploration is encouraged by registered technological innovation as well as by new policies and initiatives providing public and private sector the possibility to orient available know-how and future investments toward space exploration undertakings. It has been recognized on a global level the opportunity to adapt space exploration context for designing specific lunar activities as future space ventures in this innovative field of potential moving human beings to the Moon [1, 2, 4, 14].

MATERIALS AND METHODS

ACTIVITIES OF UN-COPOUS

Several debates have started by the Moon Village Association, MVA about potential lunar activities as well as about the Moon Village Concept, as to be noticed in Figure 2, and in this regard the Global Expert Group on Sustainable Lunar Activities, GEGSLA was established, whose expert member is the first author of this contribution [4, 7, 9]. The final goal of such activities is represented by the desire to grow the coordination of diverse space related activities to be started in this regard. The expert forum has as a goal to identify potential present and future prospect and provocation of lunar missions, as well as to try mitigating connected risks for assuring human sustainability in Space [4, 14]. Managing mentioned risks is a very provoking topic, and has a high relevance connected to existing and intended space activities in the idea to mitigate them in the future in other words to try de-risking future space operations [4, 12].



Figure 2: Moon Village Concept [10].

The generally accepted vision is allowing globally inclusive participation in future developments of space activities by human undertaking in space. GEGSLA has been pretty involved on a global level for succeeding in bringing space activities closer to interested scientists and public by different lunar stakeholders from industry, government, and academia [1, 3, 4]. On a global level UNOOSA, especially through its Committee, Policy, and Legal Affairs Section, CPLA offers important assistance to the UN-COPUOS, https://www.unoosa.org/. By the delegation of Romania, COPUOS has recently prepared a Proposal on a Consultative Mechanism on Lunar Activities, stating that lunar missions will be carried out soon through efforts of space agencies and commercial stakeholders. In this context COPUOS is emphasizing a need to preserve the peaceful use of outer space by starting a new era of sustainable space exploration [2, 4, 14].

It is to be mentioned in this context that a huge step forward connected to space activities especially connected to lunar activities has been made once humanity succeeded 1969 the first moon landing [6]. At that time this successful action represented a unique event, which encouraged human society to continue space activities especially connected to Moon prospecting. As a result, nowadays it can be stated that Moon Missions do not represent a rare event anymore, as since the start of the space age in the 1950s, more than 77 successful lunar missions have been registered.

https://doi.org/10.5593/sgem2024/6.1/s28.66

This number is expected to increase over the next decades as such flights will be more crewed space flights with soft landings, succeeding in the not far future to prove return missions, amongst others. Such kinds of flights will surely be planned in the future for single individuals and private entities. This courageous vision is nevertheless confronted with the main question of how to assure that such space flight activities are carried out in a sustainable manner being safe for human beings nevertheless assuring engaged continuously Moon exploration by sustainable lunar activities [4, 14].

Since its start, the intergovernmental Committee on the Peaceful Uses of Outer Space, COPUOS, whose leader has been for several years the first author of this paper, has continuously proceeded in trying to devise global governance of outer space affairs. In the meantime, COPUOS has succeeded in building international consensus for peaceful usage of outer space. In this way it shall be warrantied that Lunar activities are carried out on the base of fundamental principles of the *Outer Space Treaty*, which states that "the exploration and use of outer space, including the Moon and other celestial bodies, shall be carried out for the benefits and in interests of all countries" [13].

ABOUT MOON'S ENVIRONMENT

The Moon, presented in Figure 3, is a celestial body being the natural satellite of the Earth and having a radius of about 1,740 km. In its dimension the Moon is less than a third of the width of Earth. The distance between the Earth and the Moon is about 384400 km. On an astronomic scale the position of planets and celestial bodies remains not the same, all the system is a dynamic one meaning that movements are constantly registered. Following this idea it has been observed that the Moon is slowly moving away from the Earth, each year getting farther away by about an inch [6].

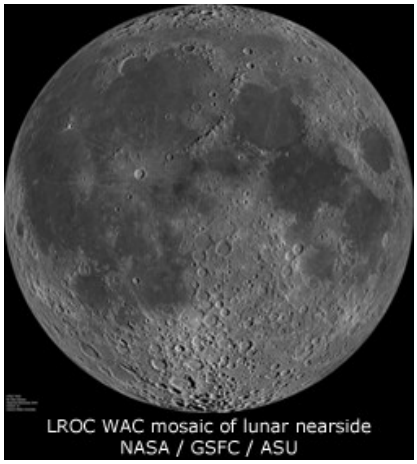


Figure 3: Lunar environment and surface

Anyway, several experiments performed recently by astronauts have confirmed that the Moon has a very thin atmosphere [11]. Lunar atmosphere is represented by a very sparse layer of gases surrounding the Moon. The atmosphere of the Moon, having a density of 100 molecules/cm^3, consists of He, Ne, Ar, and H_2. Other elements of the Moon's atmosphere, as for instance NH_3, CH_4, K, Na, and CO_2 are to be found in very small concentrations [11]. Most important elements of Moon's environment are represented by neutral gases, plasma, and some dust particles. These particles are generated especially by the interaction of lunar surface with space environment. The Moon's environment is characterized by various so-called "energetic particles",

particles associated with solar wind and solar flares, as well as galactic cosmic rays mostly consisting of protons, and electrons. The absence of a real atmosphere and of a magnetic field of the Moon has as a result that mentioned radiation directly interacts with its surface causing significant alteration of the uppermost material [6, 11].

ACTION TEAM ON LUNAR ACTIVITIES CONSULTATION, ATLAC

After having agreed on the Outer Space Treaty followed several initiatives and activities, foremostly addressing various aspects of lunar operations all of these being understood as an attempt to keep the main fundamental disposition of the Treaty regarding Outer Space activities having the goal to support humanity ambition to Terraforming other planets by relocating human beings in the Space [9, 13]. As a direct consequence it must be mentioned that COPUOS has supported in the last years diverse initiatives and activities addressing aspects of lunar operations by launching for instance the Working Group on the Legal Aspects of Space Resources. On the other side in the context of diverse activities carried out by COPUOS the delegation of Romania has recently prepared a proposal on launching a Consultative Mechanism on Lunar Activities, pointing out that the expectance is that lunar missions will be carried out soon through engaged efforts of space agencies and commercial stakeholders. In this context COPUOS is emphasizing the need to preserve the peaceful use of outer space, this being the main argument of its existence, by trying to support the beginning of a new era of sustainable space exploration. Having this understanding it means that there is an urgent need for global cooperation for shaping sustainable lunar activities, and in this regard an *Action Team on Lunar Activities Consultation, ATLA*C has been proposed by the first author of this contribution [2]. Therefore, several technical and operational aspects must be touched in different occasions just to prepare lunar operators on challenges which could be faced and being raised for debates by ATLAC for ensuring sustainable lunar activities. This Action Team has as a goal to start debates about potential lunar cooperation activities in view of common ambitious vision of bringing the benefits offered by space to all human beings [2, 14].

Connected to engaged initiatives and activities to succeed in carrying out sustainable lunar activities the organization of the United Nations Conference on Sustainable Lunar Activities on June 17 had as a main goal to strengthen existing dialogue about lunar activities and about international lunar collaboration and governance. It is a courageous initiative and for this there is a need to support cooperation among space agencies, scientific and legal experts, and relevant stakeholders from the public and private sector. A better understanding of various approaches of key actors trying to handle challenges will for sure enable identifying potential global coordination odds as a basis for future sustainable lunar activities. It is important to understand prospects and provocations to timely recognize ways of global coordination for getting sustainable lunar activities[14].

CONCLUSION

From made presentations have become clear that technological advance has also assured carrying out diverse space activities being directed to explore potentials of diverse celestial bodies to have hosted life. In this context established Global Expert Group on Sustainable Lunar Activities, GEGSLA is involved on a global level for bringing space activities closer to interested scientists and public by different lunar stakeholders from industry, government, and academia. In this context UN COPUOS is emphasizing the

https://doi.org/10.5593/sgem2024/6.1/s28.66

need to assure a peaceful use of outer space by starting a new era of sustainable space exploration. On the other side the Action Team on Lunar Activities Consultation, ATLAC, being proposed by the first author of this contribution has the vision of global cooperation for shaping *sustainable lunar activities*, considering specific technical and operational aspects, that could be faced by lunar operators. Intended humanity vision in moving to space has to be debated by following some actual recognized trends of NEXT GEN TECH for emphasizing prospect and provocation of *sustainable lunar activities*.

REFERENCES

[1] ASGARDIA - The Space Nation: Build the future through democracy and innovations. https://asgardia.space/en

[2] COPUOS, Proposal on a Consultative Mechanism on Lunar Activities – Non-Paper submitted by the Delegation of Romania, 2024, https://www.unoosa.org/documents/pdf/copuos/stsc/2024/np/STSC-2024-Non-Paper-Romania_Action-Team-on-Lunar-ConsultationsE.pdf

[3] Davis, M., Top 4 candidates in our solar system for terraforming, 2019, https://bigthink.com/surprising-science/terraforming-solar-system?rebelltitem=1#rebell titem1

[4] Global Expert Group on Sustainable Lunar Activities, GEGSLA, Recommended Framework and Key Elements for Peaceful and Sustainable Lunar Activities, 2023, https://swfound.org/news/all-news/2023/03/global-expert-group-on-sustainable-lunar-activities-releases-the-recommended-framework-and-key-elements-for-peaceful-and-sustainable-lunar-activities

[5] Hauff, V., (Ed), Our Common Future. The Brundtland Report of the World Commission on Environment and Development, Oxford Univ. Press, Oxford, 1987.

[6] Moon facts, https://science.nasa.gov/moon/facts/

[7] Moon Village Association, 2024. https://moonvillageassociation.org

[8] Next Gen Tech trends you should know about. https://www.techradar.com/news/10-next-gen-tech-trends-you-should-know-about

[9] Prunariu, D., D., Tulbure, I., Chances, and Challenges of Terraforming other Planets. In: O. Trofymchuk, B. Rivza (Ed.), Proceedings of 21st International Multidisciplinary Scientific GeoConference SGEM 2021, Albena, Vol. 21, "Space Technologies and Planetary Science", 2021. https://epslibrary.at/sgem_jresearch_publication_view.php?page=view&editid1=8241

[10] Guardian] The Guadian, Moon Village Concept attracts worldwide support, 2016, https://www.theguardian.com/science/2016/dec/02/moon-village-concept-attracting-worldwide-support-european-space-agency-lunar-outpost

[11] The Moon's Atmosphere! https://spacemath.gsfc.nasa.gov/Geometry/4Page26.pdf

[12] Tulbure, I., Technikbewertung – Vorlesungsskript (Technology Assessment). Institute for Applied Mechanics, Clausthal University of Technology, Germany, 2013.

[13] UNOOSA, Treaty on Principles governing the Activities of States in the Exploration and Use of Outer Space, including the Moon and other Celestial Bodies, 2022, https://www.unoosa.org/oosa/en/ourwork/spacelaw/treaties/introouterspacetreaty.html

[14] UNOOSA, Sustainable Lunar Activities, 2024, https://www.unoosa.org/oosa/en/ourwork/moon-mars-and-beyond/sustainable-lunar-activities-conference-2024.html

SUSTAINABLE AEROSPACE PROPULSION: THE SPINLOOP ROTARY ACCELERATOR WITH MAGNETIC LEVITATION FOR LOW EARTH ORBIT VEHICLE DEPLOYMENT

Piotr Mamczura[1]

Dawid Pękała[1]

[1] AGH University of Krakow, **Poland**

ABSTRACT

The main goal of this work is to present the SpinLoop Rotational Accelerator project as a preliminary module for accelerating space rockets destined for low Earth orbit. By utilizing magnetic levitation technology, which is also used in modern high-speed rail systems (including the thriving Hyperloop technology), it will be possible to design a device that imparts high velocity to the rocket immediately upon launch. This would reduce the amount of fuel the spacecraft would need, thereby decreasing its dimensions and construction costs. During the acceleration phase, the rocket would be positioned on a special platform that moves along a magnetic track. This platform would be responsible for bearing the load resulting from the rocket's mass and the centrifugal forces generated during acceleration. The platform itself would be attached to an arm mounted on a shaft, which would receive torque from the propulsion system equipped with an appropriately selected gearbox and an electric motor. The entire setup would be placed within a vacuum chamber tilted relative to the horizontal plane, minimizing air resistance and significantly reducing power requirements. Once the desired rotational speed is achieved (and the resulting linear velocity), the platform would detach from the arm and transition from the circular track to a straight track. After stabilizing the trajectory, the rocket would separate from the platform upon exiting the tube, utilizing the imparted velocity to pass through the thickest atmospheric layers. Finally, in the later stages of the flight, rocket engines would be activated to place the vehicle into the desired orbit. This project holds great promise for reducing the costs of launching payloads into near-space and could revolutionize space transportation.

Keywords: Rotary Accelerator, magnetic levitation, aerospace, LEO, sustainability

INTRODUCTION

In an era of progressive climate change, Mankind is looking for newer and newer ways to slow it down in such a way as not to stop the development of technology and to constantly improve the standard of living in every corner of the globe. This also applies to space transportation, which is already an indispensable part of our civilization. There are special hopes for the use of magnetic levitation (Maglev) in accelerating space vehicles in the initial phase of flight [1]. This technology would find its application in particular in placing payloads such as satellites in Low Earth Orbit (LEO). Building on this premise, the research aims to determine how a system employing magnetic levitation and rotary acceleration technologies can minimize fuel requirements and costs for spacecraft launches into LEO, while enhancing sustainability and reducing environmental impacts.

https://doi.org/10.5593/sgem2024/6.1/s28.67

One of the first attempts to use Maglev systems for spaceflight was the StarTram project (Figure 1) [2]. Its idea was to use a long linear magnetic track, ascending upwards, to accelerate space vehicles. The main disadvantage of this solution is the need to build an extensive infrastructure, directly affecting the cost of the project.

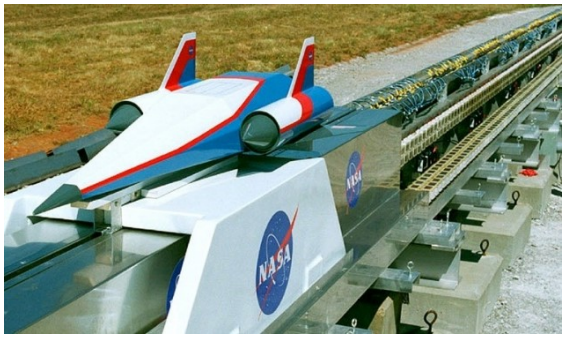


Figure 1. NASA StarTram, a track on test model scale for lower velocity magnetic launch assist. Source: NASA. (1999). Test model scale of StarTram [Photograph]. Public Domain. Source: https://commons.wikimedia.org/w/index.php?curid=15050169

Another interesting idea, which, however, does not use Maglev technology, is the SpinLaunch project (Figure 2). It assumes giving the rocket the necessary speed by accelerating it in rotation. The rocket would be placed in a special holder that is part of a rotating arm capable of carrying heavy loads. The arm would be rotated by a complex propulsion system consisting of shafts of considerable diameter, gears and electric motors, all of which could be powered by renewable energy sources. The whole would be housed in a vertically positioned chamber in which a near-vacuum pressure would prevail, to minimize the effect of air resistance on the power the engine would have to provide in order to accelerate the space vehicle to the appropriate speed. It would then be launched in the appropriate direction, into a tunnel isolated from its surroundings by means of appropriate membranes that the rocket would pierce during flight or through a system of pyrotechnically opened hatches. In this way, it would be possible to significantly reduce the impact that spaceflight has on the environment, especially during the initial phase of launch, when drag is greatest, and thus fuel consumption most significant.



Figure 2. SpinLaunch construction during launch test. Source: SpinLaunch. (2022). Source: https://www.spinlaunch.com/

However, this system carries certain limitations, the most noteworthy of which are the very high overloads acting on the rocket with its payload, of the order of up to 10,000 G [3]. The solution to this problem could be to increase the radius of rotation, however, in

order for the overload values to reach orders of magnitude acceptable to the human body, the radius would have to reach significant values, which directly affects the cost of manufacturing the system. For this reason, the concept focuses on transporting overload-resistant cargo, which could include selected satellites due to the high resistance of the electronics to overloads of up to 25,000 G [4]. Another potential drawback of the solution proposed by SpinLaunch is the design of the arm, which will be subjected to significant loads of various types, such as stretching and bending in two axes, resulting from centrifugal drag forces [5]. At the same time, these loads will be transferred to the shaft, causing it to twist and bend. All this, combined with the need to ensure an adequate level of safety and reliability of the entire system, makes it necessary to use a system consisting of components of considerable dimensions to accelerate a relatively small mass, after taking into account material allowances [6].



Figure 3. Delft Hyperloop. (2024). Delft Hyperloop capsule with visible LIM and levitation systems on the top [Digital Graphic]. Source: https://www.delfthyperloop.nl/our-pods/helios-iii-2024

To fully understand what the SpinLoop Rotary Accelerator is, it is also necessary to introduce the concept of the Hyperloop high-speed vacuum train initiated by Elon Musk [7]. Currently, many teams from around the world are researching and applying linear motors (LIM) and Maglev systems to propel and apply levitation to the pods [8]. With the development of these technologies (Figure 3), there is a great opportunity to develop them further, thereby improving their performance and lowering the costs associated with their manufacturing. SpinLoop was originally intended to be a system for accelerating Hyperloop cargo pods. Its general design involved moving the vacuum chamber to the horizontal plane and placing a track inside it to enable levitation. An arm was retained as the capsule's propulsion element [9], but this would be significantly relieved due to the transfer of the action of the dominant centrifugal force to the track.

MATERIALS AND METHODS

The development of the SpinLoop Rotational Accelerator integrated a multi-disciplinary approach using Computer-Aided Design (CAD) tools, particularly SolidWorks, to simulate and optimize the mechanical engineering aspects, ensuring robustness under real-world conditions. Advanced finite element analysis (FEA) [10] was essential for examining structural durability and assessing loads on individual components, identifying potential weak points, and optimizing mass while maintaining strength. Fluid dynamics tests and thermal simulations further helped with this analysis, providing a comprehensive understanding of the system’s response to various operational and environmental stresses [11]. These integrated simulations were critical for evaluating the aerodynamic properties

https://doi.org/10.5593/sgem2024/6.1/s28.67

of the design, significantly enhancing its efficiency and performance. This approach not only improved the accuracy of the design but also streamlined the development process by enabling virtual testing and modifications prior to the construction of physical prototypes, ensuring a well-optimized system ready for real-world application.

RESULTS

A project was proposed using the given methodology. Inspired by previously mentioned projects, a method has been developed to implement the SpinLoop Rotary Accelerator as a module for imparting the initial velocity to rockets. The rocket's mounting in a special holder at the end of the arm, as in the SpinLaunch project, has been replaced with mounting the rocket on a special platform connected to the arm, moving along a magnetic track inspired by the Hyperloop technology, enabling its levitation.

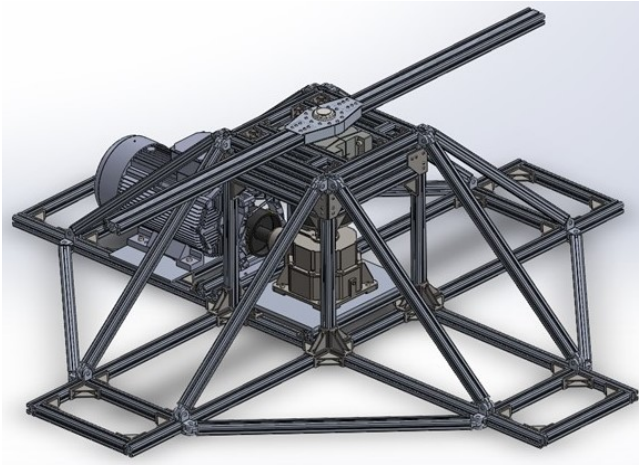


Figure 1. CAD Model of a prototype of the Rotary Accelerator in a scale. Source: own elaboration.

The structure (Figure 4) features a simple construction that minimizes complexity and reduces the risk of critical failures. This design includes a load-bearing frame that transfers loads and ensures stability, essential characteristics given the structural demands of the system.

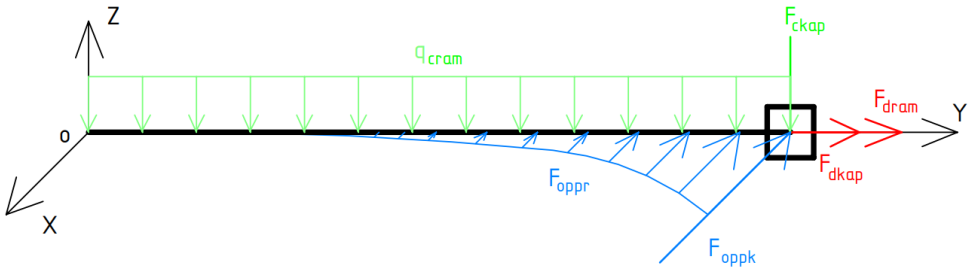


Figure 2. Diagram of forces acting on a moving arm: F_{oppr} – air resistance force on the arm, F_{oppk} – air resistance force on the platform, F_{dram} – centrifugal force on the arm, F_{dkap} – centrifugal force on the platform, q_{cram} – gravitational load on the arm, F_{ckap} – gravitational force on the platform. Source: own elaboration.

Understanding the forces acting on the system (Figure 5) was crucial for assessing structural integrity and ensuring the durability and stability of the system under operational conditions.

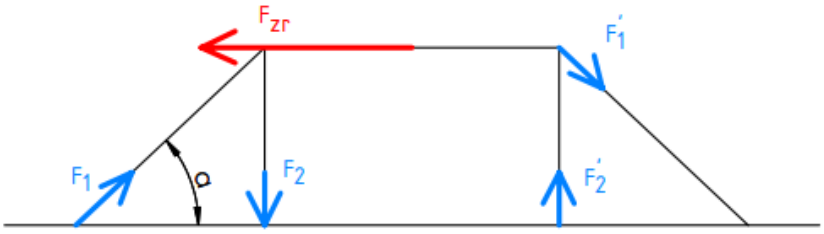


Figure 6. Diagram of forces acting on the frame in a side view: F_{zr} – force causing the breakage of the arm, forces marked in blue – reaction forces in the frame profiles.
Source: own elaboration.

Comprehensive force mapping (Figure 6) (Figure 7), was instrumental in ensuring that the frame could withstand both localized stresses and overall structural demands. The propulsion system of the Accelerator rotates a rotor, which includes an arm where the platform, using static magnetic levitation, attaches to the spacecraft. This configuration eliminates the need for a traditional wheeled chassis and incorporates active vibration damping, which is critical for maintaining rotor stability.

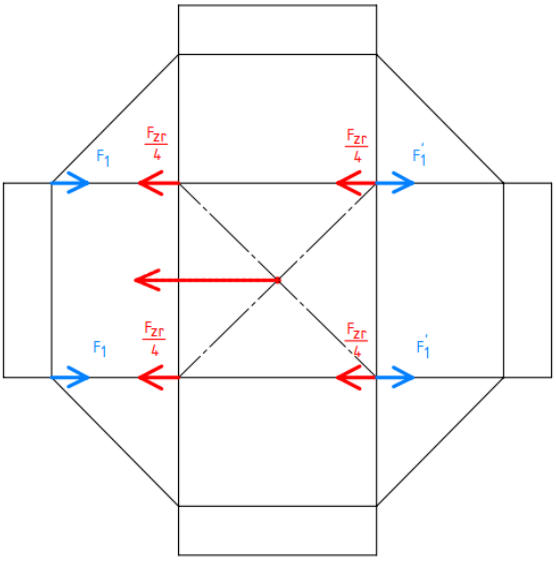


Figure 7. Diagram of forces acting on the frame in a top view: large red vector – force causing the breakage of the arm, small red vectors – forces breaking the arm distributed across key structural nodes, forces marked in blue – reaction forces in the frame profiles.
Source: own elaboration.

Additionally, calculating the forces acting on the shaft and identifying potential failure points (Figure 8) were crucial for reinforcing the structure to meet physical demands.

https://doi.org/10.5593/sgem2024/6.1/s28.67

Once the rocket reaches the target speed, it is detached in the specified direction and launched.

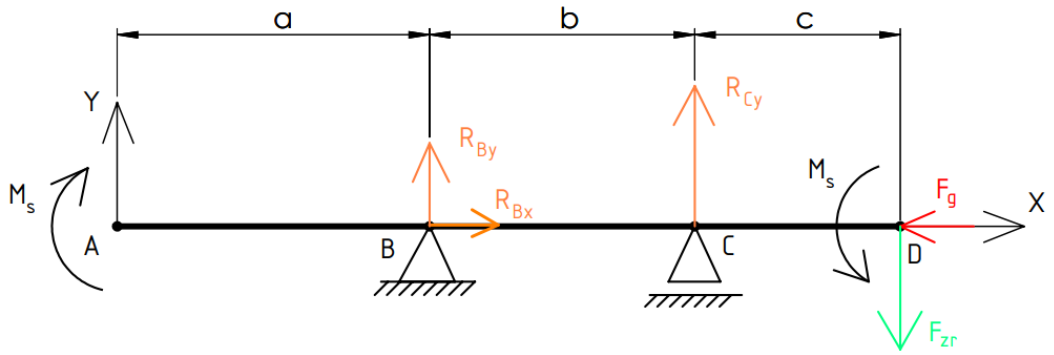


Figure 8. Diagram of forces acting on the shaft for the least favorable critical state: M_s – torque transmitted from the engine to the arm, R_{Bx} – reaction force in the x-axis at bearing point B, R_{By} – reaction force in the y-axis at bearing point B, R_{Cy} – reaction force in the y-axis at bearing point C, F_g – weight of the rotor, F_{zr} – force causing the breakage of the arm.
Source: own elaboration.

To enhance operational efficiency, the entire system is installed on a special foundation within a chamber maintaining 1% atmospheric pressure, significantly reducing air resistance and energy losses during acceleration. This fully electric system supports the use of green energy from renewable sources or nuclear reactions. Placing the structure in high-altitude areas takes advantage of lower atmospheric pressure and air resistance, and the natural slope of the terrain aids in positioning the structure at the optimal angle for the proper flight path of the rocket.

DISCUSSION

The SpinLoop Rotational Accelerator, an advancement over technologies like StarTram, integrates a rotary mechanism that minimizes infrastructure and mechanical wear, thus enhancing durability and optimizing rocket launch velocities while conserving fuel. This innovative system promises cost-effective transportation to LEO by providing high initial velocities through magnetic levitation and rotary acceleration, enabling the production of smaller, lighter, and more economical spacecraft. Its scalable design allows adaptation to diverse payload requirements, improving safety and reducing stress on structural components. The integration of a vacuum chamber enhances energy efficiency by lowering air resistance, and the placement of the launch system on a mountainside leverages lower air density at higher altitudes to decrease onboard fuel needs further. The system's compatibility with renewable energy sources aligns with sustainability goals, presenting an initial propulsion mechanism that allows rockets to traverse the densest layers of Earth's atmosphere with significantly reduced fuel requirements.

Despite these advancements, the technology confronts challenges. Especially the high centrifugal forces exerted on payloads, demand research into materials capable of withstanding such stresses without necessitating larger system sizes. Future research should focus on optimizing magnetic levitation and rotary systems to reduce energy consumption and enhance payload safety, with innovations in cooling superconductors poised to improve system efficiency and scalability. Addressing compatibility issues with existing launch platforms is crucial for seamless integration with conventional rocket propulsion

systems. Additionally, assessing the readiness of high-stress components like superconductors and evaluating the feasibility of initial investments are vital. A comprehensive lifecycle environmental impact assessment is essential to confirm the system's minimized environmental footprint, concentrating on component reuse and recycling. Moreover, a detailed cost-benefit analysis comparing SpinLoop with traditional and emerging launch technologies will elucidate capital and operational expenses and potential lifecycle savings, ensuring safety and reliability for both manned missions and high-value payloads.

CONCLUSION

The research on the SpinLoop Rotational Accelerator introduces an innovative approach to reduce the cost and environmental impact of launching rockets into LEO. Utilizing magnetic levitation, similar to high-speed rail systems, the SpinLoop system accelerates rockets during the initial launch phase, significantly decreasing fuel requirements and thus reducing the size and cost of spacecraft. The system's design is simple and scalable, minimizing failure risks and allowing for easy adaptation to various payload needs. Energy efficiency is enhanced by a vacuum chamber that reduces air resistance, and the use of green energy sources underscores its sustainability. Magnetic levitation minimizes mechanical wear, ensuring smoother acceleration crucial for sensitive rocket electronics. Additionally, the reduced fuel consumption directly lowers greenhouse gas emissions, aligning with global sustainability goals.

While the system offers substantial benefits, the high centrifugal forces involved may pose challenges to payload integrity, necessitating further research into materials and structural enhancements. Additional investigations are required to optimize magnetic levitation systems, develop cost-effective cooling solutions for superconductors, and explore the feasibility of scaling the technology for various payloads. Integrating SpinLoop with existing propulsion systems is also crucial for seamless transitions and mission success. Overall, the SpinLoop Rotational Accelerator promises a significant advancement in sustainable aerospace propulsion, offering cost-effective and environmentally friendly LEO vehicle deployment.

ACKNOWLEDGEMENTS

We extend our sincere gratitude to the entire Transpeed AGH team for their dedicated work on the SpinLoop Rotary Accelerator prototype and its applications in various fields. We offer special thanks to Mateusz Milczanowski for initiating and leading the initial efforts on this concept.

REFERENCES

[1] Yang W., Qiu M., Liu Y., Wen Z., Duan Y., Chen X., Levitation characteristics in an HTS maglev launch assist test vehicle, Superconductor Science and Technology, China, vol. 20, pp. 281-286, 2007.

[2] Powell J., Maise G., Paniagua J., Rather J., StarTram: A New Approach for Low-Cost Earth-to-Orbit Transport, IEEE Aerospace Conference Proceedings, USA, vol. 5, pp. 2569-2590, 2001.

[3] Li, J., Li, J., Qin, L., Liu, W., Wei, X., Gao, N., & Liu, Y., Optimal Design and Analysis on High Overload Buffer Structure of Passive Semi-Strapdown Inertial Navigation System, Sensors (Basel, Switzerland), Switzerland, vol. 20, 2020.

https://doi.org/10.5593/sgem2024/6.1/s28.67

[4] Lall, P., Pandurangan, A. R. R., Dornala, K., Suhling, J., Deep, J., & Lowe, R. (2019). Effect of Shock Pulse Variation on Surface Mount Electronics under High-G Shock. IEEE Intersociety Conference on Thermal and Thermomechanical Phenomena in Electronic Systems (ITherm), USA, vol. 18, issue 1, pp. 586-594.

[5] Razban, M., & Movahhedy, M., A speed-dependent variable preload system for high speed spindles, Precision Engineering-journal of The International Societies for Precision Engineering and Nanotechnology, United States, vol. 40, pp. 182-188, 2015.

[6] Aslanov, V., & Ledkov, A., Swing principle in tether-assisted return mission from an elliptical orbit, Aerospace Science and Technology, France, vol. 71, pp. 156-162, 2017.

[7] Prymon-Ryś E., Pękała D., Bieniek K., Gątkiewicz W., Survey of young adults' preferences and attitudes towards technology Hyperloop, Czasopismo Techniczne KTT: Kwartalnik Krakowskiego Towarzystwa Technicznego, Poland, vol. 143/issue 193, pp. 2–9, 2023.

[8] Musk, E., Hyperloop Alpha, SpaceX, USA, 2013

[9] Kuptsov V., Fajri P., Rasheduzzaman M., Magdaleno-Adame S., Hadziristic K., Combined Propulsion and Levitation Control for Maglev/Hyperloop Systems Utilizing Asymmetric Double-Sided Linear Induction Motors, Machines, Switzerland, vol. 10/issue 2, pp. 1-31, 2022.

[10] Choi, J., Development of an Automation Tool for the Three-Dimensional Finite Element Analysis of Machine Tool Spindles, vol. 24, pp. 166-171, 2015. https://doi.org/10.7735/KSMTE.2015.24.2.166.

[11] Bell, S., Blair, A., Wagner, L., Zou, V., Buendia, A., & Ashrafzadeh, F., Survey of Computational Fluid Dynamics Software for Rotational Purposes, Volume 5: Engineering Education, 2019. https://doi.org/10.1115/imece2019-11447.